INTERNATIONAL ATOMIC ENERGY AGENCY

INDC(BLR)-016
Distr. J+TU/EL

I N D C INTERNATIONAL NUCLEAR DATA COMMITTEE

Neutron Data Evaluation of ^{232}Th

V.M. Maslov[1], Yu.V. Porodzinskij[1], N.A. Tetereva[1]
A.B. Kagalenko[1*], N.V. Kornilov[1*]
M. Baba[2], A. Hasegawa[3]

[1]) Joint Institute of Nuclear and Energy Research – SOSNY
220109, Minsk-Sosny, Belarus
[2]) Cyclotron and Radioisotope Center, Tohoku University,
Sendai, Japan
[3]) Department of Nuclear Energy System, Tokai Research
Establishment, Japan Atomic Energy Research Institute,
Tokai-mura, Naka-gun, Ibaraki-ken

*) Permanent address: Institute of Physics and Power Engineering,
249020, Obninsk, Russia

March 2003

IAEA NUCLEAR DATA SECTION, WAGRAMER STRASSE 5, A-1400 VIENNA

Documents in the EL series are available in only limited quantities in hardcopy form. They may be downloaded in electronic form from http://www-nds.iaea.or.at/indc_sel.html or sent as an e-mail attachment. Requests for hardcopy or e-mail transmittal should be directed to services@iaeand.iaea.org or to:

Nuclear Data Section
International Atomic Energy Agency
PO Box 100
Wagramer Strasse 5
A-1400 Vienna
Austria

Produced by the IAEA in Austria
March 2003

INDC(BLR)-016
Distr. J+TU/EL

Neutron Data Evaluation of ^{232}Th

V.M. Maslov[1], Yu.V. Porodzinskij[1], N.A. Tetereva[1]
A.B. Kagalenko[1*], N.V. Kornilov[1*]
M. Baba[2], A. Hasegawa[3]

[1]) Joint Institute of Nuclear and Energy Research – SOSNY
220109, Minsk-Sosny, Belarus
[2]) Cyclotron and Radioisotope Center, Tohoku University,
Sendai, Japan
[3]) Department of Nuclear Energy System, Tokai Research
Establishment, Japan Atomic Energy Research Institute,
Tokai-mura, Naka-gun, Ibaraki-ken

*) Permanent address: Institute of Physics and Power Engineering,
249020, Obninsk, Russia

Abstract

Consistent evaluation of ^{232}Th measured data base is performed. Hauser-Feshbach-Moldauer theory, coupled channel model and double-humped fission barrier model are employed. Total, differential scattering, fission, capture and (n,*x*n) data are consistently reproduced as a major constraint for inelastic scattering cross section estimate. The direct excitation of ground state and higher band levels is calculated within rigid rotator and soft (deformable) rotator model, respectively. Structures evident in measured neutron emission spectra are correlated with excitation of levels of $K^{\pi} = 0^-$ and $K^{\pi} = 0^+$, 2^+ banbs. Prompt fission neutron spectra data are described. Average resonance parameters are provided, which reproduce evaluated cross sections in the range of 10-150 kev.

This work is performed under the Project Agreement B-404 with the International Science and Technology Center (Moscow). The Financing Party for the Project is Japan.

March 2003

Contents

1 Introduction

Nuclear data of ^{232}Th are very important for the novel fission, fusion and accelerator-driven system calculations. Optimization of these nuclear energy systems much depends on ^{232}Th neutron cross sections in unresolved resonance and fast neutron energy ranges. Capture as well as inelastic scattering data for ^{232}Th are rather discrepant. We will investigate the possibility of consistent reproducing cross section data in a statistical model of compound nucleus reactions and coupled channel optical model.

The total inelastic scattering cross section measured data below ∼1.5 MeV incident neutron energy [1, 2] predict different cross section trends for higher energies. There is also a systematic discrepancy of excitation functions of discrete levels data obtained by time-of-flight method [3] and by (n,n'γ) measurements [4]. The neutron inelastic scattering cross sections of available evaluated data files JENDL-3.2 [5], ENDF/B-VI [6], BROND-2 [7], JEF-2.2 [8] are discrepant up to ∼15% above ∼1 MeV. In ENDF/B-VI [6] and JEF-2.2 [8] evaluations excitation cross sections are provided only for the clusters of discrete levels above ∼700 keV, this might influence on the secondary neutron spectra. As distinct from the previous evaluations we proceed within full-scale Hauser-Feshbach theory and coupled channel optical model. Consistent description of total, elastic, fission and capture cross section data would provide an independent estimate of inelastic scattering cross section from threshold up to 20 MeV incident neutron energy. The important item for the total inelastic scattering cross section in a few MeV incident neutron energy range is the compound scattering to the ^{232}Th continuum levels and direct excitation of rotational and vibrational bands levels. For the former component the level density modelling above the pairing gap of even-even nuclide ^{232}Th is important. The competition of ^{232}Th(n,γn$'$) reaction to the "true" capture reaction (n,$\gamma\gamma$) also turns out to be dependent on the target nucleus ^{232}Th level density at excitations just above the pairing gap. Collective bands structure of ^{232}Th is similar to that of ^{238}U, while the actual positions of vibrational octupole $K^\pi = 0^-$, $\beta-$vibrational $K^\pi = 0^+$, $\gamma-$vibrational $K^\pi = 0^+$and anomalous rotational $K^\pi = 2^+$ band-heads are much different, i.e. β-band $K^\pi = 0^+$and $K^\pi = 2^+$ bands are ∼200-300 keV lower, while γ-band $K^\pi = 0^+$ is ∼150 keV higher. The consistent analysis of collective levels structure along with differential cross sections helps to assign the nature of $K^\pi = 0^+$ vibrational bands. The incoherent sum of compound and direct excitation for ground state $K^\pi = 0^+$, vibrational octupole $K^\pi = 0^-$, $\beta-$vibrational $K^\pi = 0^+$, $\gamma-$vibrational $K^\pi = 0^+$and anomalous rotational $K^\pi = 2^+$ band levels helps to derive coupling parameters fitting angular distributions of inelastic neutrons [3, 4, 9].

Measured neutron emission spectra are inclusive both of elastic, inelastic and

prompt fission neutron spectra (PFNS), detailed description of PFNS data for first- and multiple-chance fission is investigated. We will demonstrate that present description of inelastic scattering data reproduces neutron emission spectra [10, 12]. We demonstrate here that one needs the sophistication of direct scattering, level density modelling and PFNS representation to describe consistently the available measured data base for ^{232}Th.

2 Resolved resonance energy range

Region of resolved resonances in JENDL-3.2 [5], ENDF/B-VI [6], BROND-2 [7], JEF-2.2 [8] extends up to ∼4 keV. Here we will briefly review the status of resolved resonance parameters and provide average resonance parameters for cross section parameterization of total, capture, elastic and inelastic scattering cross sections in unresolved resonance energy range.

In ENDF/B-VI data file ^{232}Th resonance parameters were evaluated by Olsen [13] as weighted average of available data. Two bound resonances of Newman et al. [14] were adopted. Capture resonance integral for infinite dilution from 5 to 4000 eV $I\gamma = 85.544$ barn. Average capture width of 24.4 meV was assumed. Resonance parameters were tuned to achieve smooth connection to the thermal region at 5 meV, missed $p-$resonances and $1/v$ trend of capture cross section were taken into account.

We performed an extensive resonance parameter [13] analysis based on maximum likelihood estimate both of mean level spacing $\langle D_{l=0}\rangle$ and neutron strength function S_o [15]. Cumulative sum of $s-$resonances up to 4 keV is shown on Fig. 1. The solid line histogram corresponds to $s-$resonances set obtained by Olsen [13]. The dotted line histogram corresponds to BNL-325 [16] set of resonances. Stair-case plots almost coincide below ∼800 eV, at higher energies they are rather different, the former being much steeper. Proper account of missing of levels based on analysis of level spacing distribution and neutron width distribution gives estimate of average $s-$wave neutron resonance spacing as 17.380±0.600 eV. It would predict no missing of $s-$resonances up to ∼2.5 keV. Maximum likelihood estimate for BNL-325 [16] set of resonances predicts $\langle D_{l=0}\rangle = 16.566$ eV and missing of ∼10 $s-$wave neutron resonances up to 4 keV.

Cumulative sum of reduced neutron widths of $s-$resonances Γ_n^o is described with strength function estimate of $S_o = 0.94\times10^{-4}$ (see Fig. 2). The resolution function parameters as well as $\langle\Gamma_n^o\rangle$ and $\langle D_{l=0}\rangle$ are obtained by maximum likelihood method when comparing experimental distributions of reduced neutron width and resonance spacing with Porter-Thomas and Wigner distributions, modified for the resonance missing. The latter distributions will be called expected distributions. Figures 3 and 4 demonstrate comparison of predicted level spacing $D_{l=0}$ and reduced neutron width Γ_n^o distributions with resonance parameter set. Deciles on Fig. 3 show ten equal probability intervals

($P(x \leq x_{0.1}) = \int p(x)dx$ =0.1) for level spacing distribution $D_{l=0}$. Expected distribution which takes into account missing of weak resonances and unresolved doublets is not much different from Wigner distribution, that means that up to 4 keV we have rather pure $s-$resonance sample. This conclusion is supported by reduced neutron width distribution. Octiles on Fig. 4 show ten equal probability ($P(x \leq x_{0.1} = \int p(x)dx$ =0.1) intervals for Γ_n^o distribution. Figure 5 shows a comparison of cumulative Porter-Thomas distribution of reduced neutron widths. It seems that $s-$resonance parameters up to 4 keV are compatible with Wigner and Porter-Thomas distributions and there is almost no missing of levels.

3 Unresolved resonance region

In the unresolved resonance energy region of JENDL-3.2 [5], ENDF/B-VI [6], BROND-2 [7] and JEF-2.2 [8] provided average resonance parameters for $s-$, $p-$ and $d-$waves reproduce average cross section data rather differently.

In ENDF/B-VI data file average capture width is assumed to be $\langle\Gamma_\gamma\rangle = 21.3$ meV for $s-$and $d-$waves and 25.2 meV for $p-$waves, neutron $s-$wave strength function $S_o = 0.826\times10^{-4}$, while for $p-$wave $S_1 = 1.6\times10^{-4}$. Capture cross section in the energy range of 4 keV - 25 keV was evaluated by de Saussure and Macklin [17], at higher energies it was joined smoothly with the evaluation by Poenitz [18]. Capture width for $p-$wave $\langle\Gamma_{\gamma l=1}\rangle$ was increased up to 25.2 meV, while $\langle\Gamma_{\gamma l=0}\rangle$ and $\langle\Gamma_{\gamma l=2}\rangle$ were kept constant. Reduced $p-$wave neutron width $\langle\Gamma_n^1\rangle$ was varied to fit capture cross section, it has rather sophisticated shape: it decreases up to E_n ~30 keV and then sharply increases, while S_0, S_2, D_0, $D_1$and D_2 were kept constant. Potential scattering radius was assumed to be 9.72 Fm.

In JENDL-3.2 [5] unresolved resonance region of ^{232}Th is supposed to be from 3.5 keV up to 50 keV. In that case average resonance parameters $\langle\Gamma_\gamma\rangle = 21.2$ meV and $\langle D_{l=0}\rangle$=18.64 eV were adopted. At 10 keV neutron strength functions $S_0 = 0.93\times10^{-4}$, $S_1 = 1.96\times10^{-4}$ were obtained. Total cross section was normalized to the total cross section at E_n ~24 keV measured by Kobayashi et al.[19] by increase of potential scattering radius which was assumed to be R =10.01 Fm. Evaluated total cross section follows the trend predicted by recent measurements by Grigoriev et al. [20]. Reduced $s-$ and $p-$wave neutron widths $\langle\Gamma_n^0\rangle$ and $\langle\Gamma_n^1\rangle$ were varied to fit capture and total cross sections, they follow generally decreasing trend up to ~20 keV, then increase and abruptly decrease above 40 keV, while $d-$wave strength function S_2 was kept constant.

In BROND [7] ^{232}Th data file resonance parameters (both resolved and unresolved) are represented as a mixture of two isotopes with identical masses and concentrations. The first one resembles data for $s-$ and $d-$ waves, while the second one for $p-$wave, for energy ranges 4.65 - 200 keV and 2.25-200 keV respectively. Another peculiarity is large difference of potential scattering radii for $s-$ and $p-$ waves: $R_{l=0}$=9.65 Fm, $R_{l=1}$= 7.0 Fm, respectively.

Average resonance parameters of previous evaluations produce capture cross sections which are not much different, but total cross section seems to be rather different, especially that of JEF-2.2 [8] (by ∼3 b). The latter peculiarity is due to low scattering radius value R= 8.9874 Fm.

3.1 Average resonance parameters

The assumed lower energy of present unresolved resonance energy region is 4 keV, the end-point of resolved resonance region, the upper energy is 150 keV. We suppose $s-$, $p-$ and $d-$wave neutron-nucleus interactions to be effective. Average resonance parameters $S_o = (.94 \pm 0.7) \times 10^{-4}$, $\langle D_{l=0} \rangle$= 17.38 eV, Γ_γ =21.3 meV would be applied for cross section calculation from 4 keV up to 150 keV.

3.1.1 Neutron resonance spacing

Neutron resonance spacing $\langle D_J \rangle$ was calculated with the phenomenological model, which takes into account the shell, pairing and collective effects. The main parameter of the model $\widetilde{a}$ was normalized to the observed neutron resonance spacing $\langle D_{l=0} \rangle$ = 17.38 eV.

3.1.2 Neutron width

Average neutron width is calculated as follows

$$\langle \Gamma_n^{lJ} \rangle = S_l \langle D_J \rangle E_n^{1/2} P_l \nu_n^{lJ}, \tag{1}$$

where P_l is the transmission factor for the $l-$th partial wave, which was calculated within black nucleus model, ν_n^{lJ} is the number of degrees of freedom of Porter-Thomas distribution (see Table 1). The p-wave neutron strength function S_1 = 2.15×10^{-4} $(\mathrm{eV})^{-1/2}$ at 10 keV was calculated with the optical model, using the deformed optical potential, described below. This value was obtained fitting total and capture cross sections.

3.1.3 Radiative capture width

Energy and angular momentum dependence of radiative capture width are calculated within a two-cascade γ-emission model with allowance for the (n,γn') reaction competition to the (n,$\gamma\gamma$) reaction. The (n,$\gamma\gamma$) reaction is supposed to be a radiative capture reaction. The radiative capture width was normalized to the value of $\langle \Gamma_\gamma \rangle$.

3.1.4 Neutron inelastic width

Average neutron inelastic width is calculated as follows

$$\langle \Gamma_{n'}^{lJ} \rangle = S_l \langle D_J \rangle (E_n - E_1)^{1/2} P_l (E_n - E') \nu_{n'}^{lJ}, \tag{2}$$

where $\nu_{n'}^{lJ}$ is number of degrees of freedom of Porter-Thomas distribution (see Table 1). For actual compound nucleus states, formed by $s-$, $p-$ and $d-$wave neutrons one obtains

$$\begin{aligned}
\langle \Gamma_{n'}^{0,1/2} \rangle &= S_2 \langle D_{1/2} \rangle (E_n - E_1)^{1/2} P_2 (E - E_1) \cdot 2, \qquad (3)\\
\langle \Gamma_{n'}^{1,1/2} \rangle &= S_1 \langle D_{1/2} \rangle (E_n - E_1)^{1/2} P_1 (E_n - E_1),\\
\langle \Gamma_{n'}^{1,3/2} \rangle &= S_1 \langle D_{3/2} \rangle (E_n - E_1)^{1/2} P_1 (E_n - E_1) \cdot 2\\
\langle \Gamma_{n'}^{2,3/2} \rangle &= S_0 \langle D_{3/2} \rangle (E_n - E_1)^{1/2} + S_2 \langle D_{3/2} \rangle (E_n - E_1)^{1/2} P_2 (E_n - E_1) \cdot 2\\
\langle \Gamma_{n'}^{2,5/2} \rangle &= S_0 \langle D_{5/2} \rangle (E_n - E_1)^{1/2} + S_2 \langle D_{5/2} \rangle (E_n - E_1)^{1/2} P_2 (E_n - E_1) \cdot 2
\end{aligned}$$

3.1.5 Fission width

Fission widths are calculated within a double-humped fission barrier model. Energy and angular momentum dependence of fission width is defined by the transition state spectra at inner and outer barrier humps. We constructed transition spectra by supposing the axiality and mass symmetry at inner saddle and mass asymmetry at outer saddle. Number of degrees of freedom ν_f^{lJ} of Porter-Thomas distribution is defined in Table 1.

Table 1
Number of degrees of freedom

l, J	ν_n^{lJ}	$\nu_{n'}^{lJ}$	ν_f^{lJ}
0,1/2	1	2	3
1,1/2	1	1	3
1,3/2	1	2	4
2,3/2	1	1	4
2,5/2	1	1	4

3.2 Average cross sections in the region 10-150 keV

3.2.1 Total cross section

Total cross section data base is rather controversial below $E_n \sim 40$ keV. Measurements of transmissions were made by Grigoriev et. al. [21] from 2 eV up

to 100 keV, they argue that resonance structure is important for total cross section estimate up to $E_n \sim 100$ keV. This data are claimed to take into account a self-shielding correctly and appear to be systematically higher than previous measurements by Grigoriev et. al. [20]. Both these measurements are compatible nevertheless with total cross section data by Poenitz et. al. [22] above $E_n \sim$ 40 keV and Vertebnij et. al. [23, 24]. Data by Hibdon et. al.[25] appear to be systematically lower than data by Grigoriev et. al. [20, 21]. Optical model calculations could reproduce the data trend predicted by data by Vertebnij et. al. [23, 24], Poenitz et. al. [22] as well as cross section values by Grigoriev et. al. [21] below $E_n \sim 4$ keV. Fitting the data by Grigoriev et. al. [21]. in the 4-40 keV energy range would correspond to rather high value of $s-$wave neutron strength S_0. Present estimate of total cross section is compatible with $S_0 = 0.94 \times 10^{-4}$ and $S_1 = 2.15 \times 10^{-4}$, predicted by optical model. Total cross section, calculated with optical model up to 150 keV, could be reproduced assuming a decreasing trend of S_o strength function values above ~50 keV and S_1 and S_2 strength function values linear decrease above ~100 keV (see Fig. 6), adopting potential radii from optical model calculations. In JENDL-3.2 potential scattering radius is $R =$ 10.01 Fm, while we assume $R = 9.429$ fm, that is why our estimate of total cross section is discrepant with that of JENDL-3.2.

3.2.2 Capture cross section

There are a number of measurement of ^{232}Th neutron capture cross section covering unresolved resonance energy range. All available differential data sets are shown in Fig. 7. Most of them are discrepant well outside claimed statistical errors. Below is given brief description of neutron capture measurements.

Forman et. al. [26] have measured capture cross section at $E_n =$ 2-30 keV. ^{232}Th sample was placed at a flight path of 250 m from neutron source (underground nuclear explosion). The capture gamma rays have been measured by Moxon-Rae detector. The incident neutron flux was measured using ^{6}Li(n,t) monitor reaction. No information is given about experimental errors, that decreases weight of these data, which predict rather flat cross section shape above ~10 keV.

Macklin et. al. [27] have measured capture cross section at $E_n =$ 3-700 keV. The investigated sample was placed at 40.123 meter flight path from neutron source. The liquid scintillation detector with pulse-height discrimination was applied for prompt gamma-ray detection. The incident neutron flux was measured using ^{6}Li(n,t) monitor reaction (no information is given about ^{6}Li(n,t) reaction cross section). These data were renormalised by Macklin and Winters [28] to remove an error in transforming measured neutron capture yields to neutron capture cross sections.

Poenitz and Smith [29] have measured capture cross section at $E_n =$ 58.4-850 keV. They have used large liquid scintillator tank as a prompt gamma-ray

detector. The ^{197}Au(n,γ) monitor reaction cross section of ENDF/B-IV was used for incident neutron flux determination. We renormalized these data to^{197}Au(n,γ) cross section of ENDF/B-VI [6].

Moxon [30] have measured capture cross section at E_n = 5.5-148 keV. Time-of-flight method, path length of 32.5 meters, was applied. Capture gamma rays have been registered by Moxon-Rae detector. The (^{10}B(n,α)) monitor reaction was used for incident neutron flux determination (cross section values are not given). No uncertainties are given with original data, however contributions from statistical effects, self-shielding, multiple scattering and normalization lead to the error of at least 14%, i.e. 10% statistical and 10% systematic contributions. The ^{232}Th(n,γ) cross section values are discrepant with most experimental data, predicting systematically lower cross for E_n = 5.5- 70 keV.

Kobayashi et. al. [31] have measured capture cross section at E_n = 1-408 keV. ^{232}Th(n,γ) cross section was measured relative to the ^{10}B(n,$\gamma\alpha$) cross section. They have used a pair of C_6D_6 liquid scintilators as capture gamma-ray detector. The investigated sample was located at 12 m flight path. Authors have used monitor reaction ^{10}B(n,α) cross section values of ENDF/B-V, we renormalized these data to ENDF/B-VI values [6]. (Kobayashi et. al. [31] also have measured capture cross section at 3 energy points using filtered neutron beams, we will dicuss this point below).

Grigoriev et. al. [32] have measured capture cross section at 0.0215-21.5 keV. The experiment was carried out with the γ-ray multisection liquid detector and battery of boron counters as neutron detector on the 120 m flight path of the pulsed reactor IBR-30. The group neutron cross sections are obtained with accuracy of 2-7%.

Most of the following measurements have been performed using Van de Graaf accelerators and T(p,n) and ^{7}Li(p,n) reactions as a neutron source. All these measurements suffer of one and the same disadvantage, i.e. low-energy background due to multiple neutron scattering on target sample, sample environment, air and experimental room. The quality of reported results strongly depends on the accuracy of the determination of relevant corrections.

Lindner et. al. [33] have measured capture cross section at the energy range E_n = 121- 2730 keV. The authors have used NaI gamma-ray detector and $\beta-$proportional counter to measure ^{232}Th sample activity, fission detector assembly included a gold coated silicon surface-barrier detector (^{235}U(n,f) monitor reaction) to determine incident neutron flux. We renormalized these data to ENDF/B-VI [6] data for ^{235}U(n,f) reaction cross section.

Linenberger et. al. [34] have measured capture cross section at the energy range of E_n = 3 - 390 keV. The authors have used ^{235}U(n,f) reaction for incident neutron flux determination. We renormalized these data according ENDF/B-VI [6] evaluated values. Cross section values are discrepant with most experimental data.

Miskel et. al. [35] have measured capture cross section at the energy range

E_n = 32 -990 keV. They have used ^{235}U(n,f) reaction for incident neutron flux determination, but cross section values are not available. Cross section values are discrepant with most experimental data.

Stupegia et. al. [36] have measured capture cross section at the energy range E_n = 191 - 1170 keV. Usual experimental technique was used, i.e. ^{7}Li(p,n) neutron source, ^{235}U(n,f) for neutron flux determination and β-counter to detect ^{233}Th $\gamma-$decay events. No information about experimental uncertainties and ^{235}U(n,f) cross section is provided, but ^{232}Th(n,γ) cross section values are discrepant with most experimental data.

Poenitz and Smith [29] have measured capture cross section at the energy range E_n = 244 - 2480 keV. The authors have used Ge(Li) coaxial gamma-ray detector to measure ^{232}Th sample activity and ^{235}U(n,f) for neutron flux determination. We renormalized these data to ENDF/B-VI evaluation [6] of ^{235}U(n,f) reaction cross section.

Hanna et. al.[37] have measured capture cross section at the energy range E_n = 16.5 -1230 keV. The authors have used photo-neutron source and NaI gamma-ray detector. No error analysis is provided, only statistical errors are given. Cross section values are discrepant with most experimental data.

Perkin et. al. [38] have measured capture cross section at E_n = 14.5 MeV. The authors have used T(d,n) reaction as a neutron source (440-keV deuterons bombarding tritium "layer" on Zr target) and end-window Geiger counter, calibrated with a 4π-β counter, to measure ^{232}Th sample activity and ^{27}Al(n,α) for neutron flux determination.

Jain et. al. [39] and Anand et. al. [40] have measured capture cross section at the energy ranges E_n = 350 - 680 keV and E_n = 425 and 950 keV, respectively. These experiments were performed using similar technique: lithium metal target as a neutron source, Ge(Li) high resolution γ-detector, ^{197}Au sample for incident neutron flux determination. We renormalized these data to ^{197}Au(n,γ) cross section of ENDF/B-VI [6].

Stavisskij and Tolstikov [41] have measured capture cross section at the energy range E_n = 313 - 964 keV. The authors have used T(p,n) reaction as a neutron source and ^{127}I(n,γ) reaction cross section for neutron flux determination. Data have been updated recently [42].

Tolstikov et. al. [43] have measured capture cross section at the energy range E_n = 11.5 - 102 keV. The authors have used ^{7}Li(p,n) reaction as a neutron source and ^{10}B(n,α) for neutron flux determination, the activity of irradiated sample has been measured by β-counter. Data have been updated recently [42].

Davletshin et. al. [44] have measured capture cross section at the energy range E_n = 370 - 2435 keV. This measurement was performed using convenient technique: low-weight solid tritium target as a neutron source, Ge(Li) high resolution γ-detector, ^{197}Au(n,γ) and ^{235}U(n,f) reactions for incident neutron flux determination. Corrections were made for neutrons scattered on material surrounding target. The authors give cross section values for ^{197}Au(n,γ) and ^{235}U(n,f) monitor

reactions, we used averaged values.

Wisshak et. al. [45] have measured capture cross section at E_n = 5 - 225 keV. ^{232}Th(n,γ) cross section was measured relative to the ^{197}Au(n,γ) cross section. Neutron energy was determined by time of flight method. Capture events were registered with 4π barium fluoride detector. High efficiency of capture events registration maintains an overall accuracy of $\prec$2 % for the energy range between 50 and 200 keV.

Capture cross section was measured by Karamanis et. al. [46] in the energy region E_n = 60 - 2000 keV. The characteristic $\gamma-$lines of the product nuclei ^{233}Pa were measured with a Ge detector. Cross section was measured relative to ^{197}Au(n,γ) cross section up to 1 MeV and to ^{235}U(n,f) cross section at higher energies. The authors have used ^{7}Li(p,n) and T(p,n) reactions as a neutron source. Cross section is close to JENDL-3.2 evaluation below 800 keV and above 1.4 MeV. Low cross section values are predicted from 800 keV up to 1.4 MeV. Numerical data are inaccessible.

There are some measurements of this ^{232}Th capture cross section near E_n =24 keV (Sb-Be source and filtered beams are used) and integral measurements. Capture cross section near E_n =24 keV has resonance structure, and "measured" values strongly depend on incident neutron spectrum [47, 48, 49, 51]. Filtered beams from reactor ([50]) give large spread of results without any possibility to renormalize these values. The situation with integral (reactor spectra ([52, 53, 54]) and 14 MeV assemblies [55]) experiments is absolutely the same: available information about neutron spectra for different measurements is incomplete.

Data by Miskel et. al. [35] and Hanna et. al. [37] predict rather high cross section level in the energy range between 30 and 600 keV. Data by Stupegia et. al. [36] also predict high capture cross section in the energy range between 200 and 1200 keV. Other capture data predict much lower cross section, though a number of discrepancies is observed.

Though measured data are discrepant well beyond claimed errors, a consistent data set could be selected and fitted within statistical model. Below $\sim$15 keV measured data by Wisshak et. al. [45] predict an upward trend, while data by Kobayashi et. al.[31] predict a downward trend. Renormalized by [28] data by Macklin [27] are compatible with data by Kobayashi et. al.[31] and Wisshak et. al. [45] in $\sim$10-150 keV energy range. Above $\sim$50 keV data by Poenitz and Smith [29] are compatible with data by Wisshak et. al. [45], Macklin [27] and Kobayashi et. al.[31].

The comparison of statistical theory calculation with measured data is shown on Fig. 7. The important peculiarities of the calculated capture cross section is the Wigner cusp above first excited level threshold of $\sim$49.369 keV. The contributions of $s-, p-, d-$wave neutrons to capture cross section are shown, the main contribution above $E_n \geq$ 10 keV comes from $p-$wave neutrons, while that of $d-$wave neutrons is only $\sim$30% lower than that of $s-$wave neutrons at $\sim$150 keV. The decrease of S_1strength function above 100 keV, from 2.15×10^{-4} to 1.9×10^{-4}

is essential for capture cross section description. Fit to average capture cross section data resulted in $s-$wave radiative strength function $S_{\gamma 0}$ =12.255×10^{-4} (Γ_γ = 21.3 meV and $\langle D_{l=0} \rangle$ = 17.38 eV). Detailed analysis of capture cross section description up to $E_n \sim 5$ MeV will be given below.

3.2.3 Inelastic scattering cross section

Inelastic scattering cross section sharply increases above 49.369-keV level excitation threshold and reaches ∼0.75 b at 150 keV. Direct scattering contribution to the 49.369-keV level excitation seems to be important above ∼100 keV, it amounts to ∼15% at 150 keV. Conventional ENDF/B processing codes (i.e. RECENT [56], NJOY [57]) exemplify Hauser-Feshach-Moldauer formalism and do not take into account direct scattering component of inelastic scattering. Total and capture data could be described within conventional Hauser-Feshach-Moldauer formalism, while it fails in case of inelastic scattering cross section above E_n ∼100 keV. The deficiency of Hauser-Feshbach-Moldauer formalism for inelastic scattering cross section calculation could be diminished by increasing inelastic neutron widths $\langle \Gamma_{n'}^{lJ} \rangle$ for the channels, giving major contributions to inelastic scattering. Figure 8 shows partial contributions to the inelastic scattering coming from (l, J)-channels. Major contribution comes from $p-$wave channels $(l = 1, J = 1/2)$ and $(l = 1, J = 3/2)$,the lowest comes from $s-$wave channel $(l = 0, J = 1/2)$, since only $d-$wave neutrons contribute to $\langle \Gamma_{n'}^{0,1/2} \rangle$ inelastic neutron width in exit channel. The intermediate level contribution comes from $(l = 2, J = 3/2)$ and $(l = 2, J = 5/2)$ entrance channels, when both $s-$wave and $d-$wave neutrons contribute to exit channel. That is correlated with partial contributions to capture cross section, when these $(l = 2, J = 3/2)$ and $(l = 2, J = 5/2)$ channels make the lowest contribution to the capture cross section. The direct contribution missing could be compensated by linear increase of S_1strength function in the exit inelastic channels to 3.0×10^{-4} $(\mathrm{eV})^{-1/2}$ at 150 keV. To keep capture cross section unaffected we should increase relevant capture widths in the same linear manner up to ∼15% at 150 keV.

3.2.4 Comparison of present and previous evaluated data

Figures 6, 7, 8 and 9 demonstrate $\sigma_{nt}, \sigma_{n\gamma}, \sigma_{nn'}$ and σ_{nn} for present and previous evaluations, while Figs. 10-14 compare reduced neutron widths $\langle \Gamma_n^{0lJ} \rangle$. A number of discrepancies are noticed in case of total (see Fig. 6) and elastic scattering (see Fig. 9) cross sections. JEF-2.2 [8] evaluated total and elastic scattering cross sections are ∼2 b lower than present and others estimates in unresolved resonance region. That is due to low value of potential scattering radius adopted in JEF-2.2 [8]. Capture cross sections in JENDL-3.2 [5], ENDF/B-VI [6] are JEF-2.2 [8] are represented with rather different radiation and neutron strength functions (see Table 2). The discrepancies in $S_{\gamma l}$ are compensated by different neutron strength

functions S_l. Differences are pronounced either in $s-$wave, $p-$wave and $d-$wave reduced neutron widths (see Figs. 10-14). Inelastic scattering cross section of ENDF/B-VI [6] is rather low up to 200 keV, while previous as well as present evaluations are compatible with measured data by Fujita et. al. [108] (see Fig. 8).

The advantage of present evaluation is that it provides average energy dependent parameters which reproduce evaluated cross sections, using conventional ENDF/B processing codes [56, 57] up to 150 keV. The price paid for that is slight increase of inelastic and capture widths for $p-$wave channels. Without that increase competitive inelastic width would correspond to inelastic scattering cross section, which is lower than inelastic cross section of smooth cross section file above 150 keV. That would be pronounced as a step in total cross section at 150 keV, since according to ENDF/B conventions, total cross section is calculated as a sum of elastic, capture, fission and inelastic scattering cross section, the latter is taken from tabulated cross section data file. The other cross sections are calculated using average energy dependent parameters. Present estimate of $D_{l=0}$ is consistent with adopted set of $s-$wave resonances, while estimates of S_l and $S_{\gamma 0}$ values are consistent with total and capture data trends. Non-smooth energy dependence of ENDF/B-VI [6] $p-$wave average resonance parameters and JENDL-3.2 [5] $s-$ and $p-$wave average resonance parameters seems to be unnecessary to reproduce total and capture cross sections up to E_n =150 keV.

Table 2
Average resonance parameters for ^{232}Th

	$D_{l=0}$,eV	Γ_γ,meV	$S_0 \times 10^{-4}$
JENDL-3.2	18.64	21.2	.93
ENDF/B-VI	17.35	25.5	.86
Present	17.385	21.3	.94

4 Optical Potential

A coupled channel model is employed for analysis of differential scattering and total cross section data. Another important application of coupled channel model is calculation of direct inelastic scattering contribution of discrete levels, five levels were assumed coupled. The direct excitation of ground state rotational band levels 0^+-2^+-4^+-6^+-8^+ is estimated within rigid rotator model. To calculate the direct excitation cross sections for β-vibration K^π= 0^+, γ-vibration K^π= 0^+, anomalous rotational $\gamma-$band K^π=2^+, as well as octupole $K^\pi = 0^-$ band levels a soft rotator model [58] was used.

Optical potential parameters by Haouat et. al. [59] are frequently used for n+^{232}Th interaction data analysis, coupling scheme being 0^+-2^+-4^+. We tried optical potential parameter search with 0^+-2^+-4^+-6^+-8^+ coupling scheme, using potential parameter values obtained for ^{238}U as starting ones. Optical potential parameters were defined by fitting total cross section data, angular distributions and $s-$wave strength function $S_o = 0.94\times10^{-4}$. The following potential parameters were obtained:

$$V_R = 45.722 - 0.334E_n, MeV, r_R = 1.2668\ fm, a_R = 0.6468\ fm$$
$$W_D = \begin{cases} 3.145 + 0.455E_n, MeV, & E_n \leq 8MeV, r_D = 1.25\ fm, a_D = 0.5246\ fm \\ 7.695\ MeV, & 10 < E_n < 20\ MeV \end{cases}$$
$$V_{SO} = 6.2\ MeV, r_{SO} = 1.120\ fm, a_{SO} = 0.47\ fm,$$
$$\beta_2 = 0.188, \beta_4 = 0.071$$

4.1 Total cross section

Total cross section data [22, 60, 61, 62, 63, 64, 65, 66, 67, 68, 69, 70, 71, 73, 74, 75, 76, 77] fit with present optical potential is shown on Figs. 15, 16, 17. Present total cross section is not much different from JENDL-3.2 [5] evaluation, which basically accepted optical potential parameters by Haouat et. al. [59], except the energy range of E_n= 1 - 4 MeV. Though the discrepancies are within the scatter of the measured data points, our estimate of total cross section closely follows in that energy range data trend by Poenitz et. al.[22, 65]. At incident neutron energies $E_n \lesssim 4$ MeV JEF-2.2 [8] evaluation predicts rather low total cross section, which is incompatible with total data base (see Fig. 16). This energy region is very important for the consistent estimation of first 2^+ level excitation cross section. At incident neutron energies above 10 MeV both ENDF/B-VI [6] and JEF-2.2 [8] evaluations predict low total cross section values (see Fig. 17).

Figure 18 shows the comparison of reaction cross sections, calculated with different coupled channels optical potentials. It will be shown below that the decreasing trend of the reaction cross section above ~10 MeV is very important for consistent measured data description. Elastic cross section data [74, 78, 79, 80, 81, 82, 83, 84, 85] shape is fairly reproduced (see Figs. 19,20). Present and JENDL-3.2 [5] calculated elastic scattering cross sections are compatible up to E_n=20 MeV with measured data by Haouat et. al. [59], Cox et. al. [78] and Iwasaki et. al. [74], while those of ENDF/B-VI [6] and JEF-2.2 [8] predict rather different trend.

4.2 Angular distributions

Elastic scattering angular distribution fit at 1.5 MeV is shown on Fig. 21. Figs. 22 and 23 demonstrate the angular distribution of inelastic scattered neutrons which excite 2^+ and 4^+ levels of ground state band. Overall data trends are reproduced

quite well, though the fit is much better in case of 4^+ level. At incident neutron energy of 2.4 MeV summed cross sections of elastic and inelastic scattering to 2^+ and 4^+ levels by Iwasaki et. al. [74] are shown on Fig. 24. Figures 25, 26, 27 show the same as figures 21, 22, 23 for the incident neutron energy of 2.5 MeV. At E_n =2.6 MeV summed cross sections of elastic and inelastic scattering to 2^+, $4^+$and 6^+ levels by Miura et. al. [12] also are reproduced (see Fig. 28). At E_n =3.4 MeV summed cross sections of elastic and inelastic scattering to 2^+ and 4^+ levels by Haouat et. al. [59] are reproduced (see Fig. 29). Partial contributions to the latter cross section are shown on Figs. 30, 31, 32, here the fit is poorer in case of 4^+ level. At E_n =3.6 MeV summed cross sections of elastic and inelastic scattering to 2^+, $4^+$and 6^+ levels by Miura et. al. [12] are reproduced (see Fig. 33) much better than in case of both JENDL-3.2 [5] and ENDF/B-VI [6].

Elastic scattering angular distributions at 4.5, 5.0, 5.5, 5.9, 6.5, 7.14, 7.5, 7.75, 8.03, 8.4, 9.06, 9.5, 10 and 14.1 MeV are compared with measured data [86, 87, 88, 89, 90, 91] on Figs. 34 - 47. Fits with our potential appear to be somewhat better at 4.5, 5.0, 5.5, 5.9, 6.5, 7.14 MeV incident neutron energy and equally good at 8.03, 8.4, 8.56 MeV. At higher energies of 9.06, 9.5, 10, 14.1 MeV scattering data to large angles (above $\sim 90^o$) are described rather poorly with any optical potential.

5 Statistical Model

Hauser-Feshbach-Moldauer statistical theory is employed for partial cross section calculations below emissive fission threshold. Fissioning and residual nuclei level densities as well as fission barrier parameters are key ingredients, involved in neutron-induced actinide cross section calculations. First, level density parameters are defined, using neutron resonance spacing $\langle D_{obs} \rangle$ estimates for ^{232}Th, ^{231}Th, ^{230}Th, ^{229}Th and ^{228}Th target nuclides, which are formed in neutron emission cascade reactions. Constant temperature level density parameters T_o, E_o, U_c are defined by fitting cumulative number of low-lying levels of ^{233}Th, ^{232}Th, ^{231}Th, ^{230}Th, ^{229}Th and ^{228}Th [15]. At incident neutron energies, when continuum levels are excited, width fluctuation correction is treated within Tepel et. al. [92] approach. Cross sections, calculated with statistical theory by Tepel et. al. [92] are matched to those calculated with Hauser-Feshbach-Moldauer statistical theory at the incident neutron energy equal to the energy of last discrete level. Then fission cross section of ^{232}Th target nuclide is calculated up to emissive fission threshold to extract fission barrier parameters, at higher incident neutron energies Hauser-Feshbach code STAPRE [93] is employed. Fission barrier parameters of ^{232}Th, ^{231}Th and ^{230}Th are defined by fitting observed fission cross section of ^{232}Th(n,f) above emissive fission threshold

In case of fast neutron ($E_n \leq 6$ MeV) interaction with ^{232}Th target nucleus, the main competing channels against neutron inelastic scattering are fission and

radiative neutron capture. Below there is an outline of the statistical model [94, 95] employed.

5.1 Cross Section Formula

Neutron-induced reaction cross section is defined as

$$\sigma_{nx}(E_n) = \frac{\pi \acute{\lambda}^2}{2(2I+1)} \sum_{ljJ\pi} (2J+1) T_{lj}^{J\pi}(E_n) P_x^{J\pi}(E_n) S_{nx}^{ljJ\pi}, \tag{4}$$

the compound nucleus decay probability $P_x^{J\pi}$ $(x = n, f, \gamma)$ is

$$P_x^{J\pi}(E_n) = \frac{T_x^{J\pi}(U)}{T_f^{J\pi}(U) + T_n^{J\pi}(U) + T_\gamma^{J\pi}(U)}, \tag{5}$$

where $U = B_n + E_n$ is the excitation energy of the compound nucleus, B_n is the neutron binding energy, E_n is the incident neutron energy, $T_{lj}^{J\pi}$ are the entrance neutron transmission coefficients for the channel $(ljJ\pi)$, I is the target nucleus spin. Decay probability $P_x^{J\pi}(E)$ of the compound nucleus with excitation energy U for given spin J and parity π, depends on $T_f^{J\pi}$, $T_n^{J\pi}(U)$ and $T_\gamma^{J\pi}(U)$, transmission coefficients of the fission, neutron scattering and radiative decay channels, $S_{nx}^{ljJ\pi}$ denotes partial widths Porter-Thomas fluctuation factor. Below incident neutron energy equal to cut-off energy of discrete level spectra the neutron cross sections are calculated within Hauser-Feshbach approach with correction for width fluctuation by Moldauer [96]. For width fluctuation correction calculation only Porter-Thomas fluctuations are taken into account. Effective number of degrees of freedom for fission channel is defined at the higher fission barrier saddle as $\nu_f^{J\pi} = T_f^{J\pi}/T_{f\,\max}^{J\pi}$, where $T_{f\,\max}^{J\pi}$ is the maximum value of the fission transmission coefficient $T_f^{J\pi}$. At higher incident neutron energies the Tepel et. al. [92] approach is employed, it describes cross section behavior in case of large number of open channels correctly.

5.2 Level Density

Level density is the main ingredient of statistical model calculations. Level density of fissioning, residual and compound nuclei define transmission coefficients of fission, neutron scattering and radiative decay channels. We will briefly discuss here level densities of even-even nuclide ^{232}Th and even-odd nuclide ^{233}Th.

The level densities were calculated with a phenomenological model by Ignatyuk et. al. [97], which takes into account the shell, pairing and collective effects in a consistent way

$$\rho(U, J, \pi) = K_{rot}(U, J) K_{vib}(U) \rho_{qp}(U, J, \pi), \tag{6}$$

where quasiparticle level density

$$\rho_{qp}(U,J,\pi) = \frac{(2J+1)\omega_{qp}(U)}{4\sqrt{2\pi}\sigma_{\perp}^{2}\sigma_{\parallel}} \exp\left(-\frac{J(J+1)}{2\sigma_{\perp}^{2}}\right), \tag{7}$$

$\omega_{qp}(U,J,\pi)$ is state density, $K_{rot}(U,J)$ and $K_{vib}(U)$ are factors of rotational and vibrational enhancement of the level density. The collective contribution of the level density of deformed nuclei is defined by the nuclear deformation order of symmetry. The actinide nuclei at equilibrium deformation are axially symmetric. The order of symmetry of nuclear shape at inner and outer saddles were adopted from calculations within shell correction method (SCM) by Howard & Möller [98]. For deformed axially symmetric nucleus

$$K_{rot}(U) = \sigma_{\perp}^{2} = F_{\perp}t, \tag{8}$$

where $\sigma_{\perp}^{2}$ is the spin cutoff parameter, $F_{\perp}$ is the nuclear momentum of inertia (perpendicular to the symmetry axis), which equals the rigid-body value at high excitation energies, where the pairing correlations are destroyed, experimental value at zero temperature and is interpolated in between, using the pairing model.

For triaxially asymmetric nuclides the rotational enhancement factor is

$$K_{rot}(U) = 2\sqrt{2\pi}\sigma_{\perp}^{2}\sigma\ . \tag{9}$$

Here, $\sigma^2 = F_{\parallel}\ t$ is the spin distribution parameter, t is thermodynamic temperature, $F_{\parallel} = 6/\pi^2 < m^2 > (1 - 2/3\varepsilon)$, where $< m^2 >$ is the average value of the squared projection of the angular momentum of the single-particle states, and ε is quadrupole deformation parameter. The closed-form expressions for thermodynamic temperature and other relevant equations which one needs to calculate $\rho(U,J,\pi)$ are provided by Ignatyuk et. al. model [97].

To calculate the residual nucleus level density at the low excitation energy, i.e. just above the last discrete level excitation energy where $N^{exp}(U) \sim N^{theor}(U)$, we employ a Gilbert-Cameron-type approach. The constant temperature approximation of

$$\rho(U) = dN(U)/dU = T^{-1}\exp((U-U_o)/T) \tag{10}$$

is extrapolated up to the matching point U_c to a phenomenological model by Ignatyuk et. al.[97] with the condition

$$U_c = U_o - Tln(T\rho(U_c)). \tag{11}$$

In this approach $U_o \simeq -n\triangle_o$, where $\triangle_o$ is the pairing correlation function, $\triangle_o = 12/\sqrt{A}$, A is the mass number, $n = 0$ for even-even, 1 for odd and 2 for odd-odd nuclei, i.e., U_o has the meaning of the odd-even energy shift. The value of nuclear temperature parameter T is obtained by the matching conditions at the excitation energy U_c.

In present approach the modelling of total level density

$$\rho(U) = K_{rot}(U)K_{vib}(U)\frac{\omega_{qp}(U)}{\sqrt{2\pi}\sigma} = T^{-1}\exp((U-U_o)/T) \tag{12}$$

in Gilbert-Cameron-type approach looks like a simple renormalization of quasiparticle state density $\omega_{qp}(U)$ at excitation energies $U < U_c$.We will illustrate cumulative number of levels description with constant temperature approximation for ^{233}Th and ^{232}Th nuclides. The cumulative number of observed levels for even-even ^{232}Th and even-odd ^{239}Th are compared with constant temperature approximation on Figs. 48 and 49. In case of ^{232}Th missing of levels above pairing gap ($\sim$1.2 MeV) is markedly pronounced. In case of ^{233}Th nuclide missing seems to be pronounced above excitations of 0.5 MeV.

Few-quasiparticle effects which are due to pairing correlations are essential for state density calculation at low intrinsic excitation energies either for equilibrium or saddle deformations. The step-like structure in ^{239}Pu(n,2n) reaction cross section was shown to be a consequence of threshold excitation of two-quasiparticle configurations in residual even-even nuclide ^{238}Pu [99]. The same effect is pronounced in ^{232}Th(n,γ) data description through (n,γn$'$) reaction competition. We argue that they are important also for reasonable fitting of inelastic scattering cross section data for even-even target nuclide ^{232}Th at low energies, typically below $\sim$2 MeV incident neutron energy. In case of even-odd fissioning nuclide ^{233}Th few-quasiparticle effects are also important for description of irregularities above fission threshold.

The partial $n-$quasiparticle state densities, which sum-up to intrinsic state density of quasiparticle excitations could be modelled using the Bose-gas model prescriptions [99, 100]. The intrinsic state density of quasiparticle excitations $\omega_{qp}(U)$ could be represented as a sum of $n-$quasiparticle state densities $\omega_{nqp}(U)$:

$$\omega_{qp}(U) = \sum_n \omega_{nqp}(U) = \sum_n \frac{g^n(U-U_n)^{n-1}}{((n/2)!)^2(n-1)!}, \tag{13}$$

where $g = 6a_{cr}/\pi^2$ is a single-particle state density at the Fermi surface, n is the number of quasiparticles. The important model parameters are threshold values U_n for excitation of $n-$quasiparticle configurations $n = 2, 4...$ for even-even nuclei and $n = 1, 3...$ for odd-A nuclei. [100].

Nuclear level density $\rho(U)$ of even-even nuclei above the pairing gap up to the four-quasiparticle excitation threshold was extracted by fitting total inelastic, capture and fission cross section data of ^{232}Th. The total level density for even nuclide ^{232}Th at equilibrium deformation, as compared with the Gilbert-Cameron-type approximation of $\rho(U)$ is shown on Fig. 50. The arrows on the horizontal axis of Fig. 50 indicate the excitation thresholds of even $n-$quasiparticle configurations. Below the excitation threshold U_2, i.e. within pairing gap the constant temperature model fits cumulative number of ^{232}Th levels [102].

In case of odd-even and even-odd nuclei the partial contributions of $n-$quasiparticle states $\omega_{nqp}(U)$ to the total intrinsic state density $\omega_{qp}(U)$ produces distinct "jump" only below three-quasiparticle excitation threshold U_3 (see Fig. 51). The arrows on the horizontal axis of Fig. 51 indicate the excitation thresholds of odd $n-$quasiparticle configurations. Nuclear level density $\rho(U)$ up to the three-quasiparticle excitation threshold U_3 is virtually independent on the excitation energy, since the intrinsic state density ($\omega_1 \sim g$) is constant. The numerical values of nuclear level density $\rho(U)$ parameters are defined by fitting ^{232}Th fission cross section data.

Main parameters of the level density model for equilibrium, inner and outer saddle deformations are as follows: shell correction δW, pairing correlation functions Δ and Δ_f, at equilibrium deformations $\Delta = 12/\sqrt{A}$, quadrupole deformation ε and momentum of inertia at zero temperature $F_o/\hbar^2$ are given in Table 3. For ground state deformations the shell corrections were calculated as $\delta W = M^{exp} - M^{MS}$, where M^{MS} denotes liquid drop mass (LDM), calculated with Myers-Swiatecki parameters [103], and M^{exp} is the experimental nuclear mass. Shell correction values at inner and outer saddle deformations $\delta W_f^{A(B)}$ are adopted following the comprehensive review by Bjornholm and Lynn [104].

Table 3

Level density parameters of fissioning nucleus and residual nucleus

Parameter	inner saddle	outer saddle	neutron channel
δW, MeV	1.5	0.6	LDM
$\triangle$, MeV	$\triangle_o + \delta^*$	$\triangle_o + \delta^*$	$\triangle_o$
ε	0.6	0.8	0.24
$F_0/\hbar^2$, MeV^{-1}	100	200	73

*)$\delta = \Delta_f - \Delta$ value is defined by fitting fission cross section in the plateau region.

6 Inelastic Scattering

Main competing channels against inelastic scattering are elastic scattering, capture and fission. The former is of overwhelming importance below ~2 MeV incident neutron energy. At higher energies fission channel competition is decisive.

6.1 Neutron Channel

The lumped transmission coefficient of the neutron scattering channel is given by

$$T_n^{J\pi}(U) = \sum_{l'j'q} T_{l'j'}^{J\pi}(E_n - E_{q'}) + \sum_{l'j'I'} \int_0^{U-U_c} T_{l'j'}^{J\pi}(E'_n)\rho(U - E'_n, I', \pi)dE'_n, \quad (14)$$

where $\rho(U-E'_n, I', \pi)$ is the level density of the residual nucleus. Levels of residual nuclide ^{232}Th are provided in Table 4. The entrance channel neutron transmission coefficients $T_{lj}^{J\pi}$ are calculated within a rigid rotator coupled channel approach. For the compound nucleus formation cross section calculation the cross sections of the direct excitation of ground state band levels were subtracted from the reaction cross section. The compound and direct inelastic scattering components are added incoherently.

The exit neutron transmission coefficients $T_{l'j'}^{J\pi}(E'_n)$ were calculated using the re-normalized deformed optical potential of entrance channel without coupling, which roughly describes a neutron absorption cross section. Below E_n ~5 MeV due to high fission threshold the main contribution to inelastic scattering on ^{232}Th comes from the compound processes. For ground state band levels the direct and compound components become comparable above ~2 MeV.

6.2 Ground State Rotational Band

The first excited level cross section is the most extensively studied, nonetheless the data points scatter a lot [2, 59, 24, 74, 105, 82] (see Fig. 52). Calculated inelastic cross section shape is controlled by competition with elastic neutron scattering. The compound component tends to be zero above E_n ~2.5 MeV. Using optical potential, which describes total cross section data, we could describe measured data base within Hauser-Feshbach-Moldauer [96] approach somewhat better than it was done in JENDL-3.2 [5] evaluation above ~2 MeV, while ENDF/B-VI [6] evaluation in the vicinity of the threshold seems to be too low, the same is true in case of JEF-2.2 [8] evaluation above ~1 MeV. The latter peculiarity is due to direct contribution missing.

The calculated cross section of 4^+-level excitation is different from the previous evaluations ENDF/B-VI [6] and JEF-2.2 [8] below ~2 MeV incident neutron energy (see Fig. 53). The difference of present and JENDL-3.2 [5] evaluations seems to be due to systematically lower direct contribution in present calculation, which is supported by measured data by Goswani et. al.[105].

On figures 54 and 55 angular distribution of inelastic scattered neutrons which excite 6^+ level of ground state band are compared with data by Kegel et. al. [9] at 2.4 and 2.8 MeV, respectively. Overall data trends are reproduced quite well, but it seems that angular -integrated cross sections were obtained based on inelastic cross section at 125° angle. This may explain why present 6^+- level

excitation cross section is about twice higher than data by Kegel et. al. [9] (see Fig. 56). We employ coupling schema of 0^+-2^+-4^+-6^+-8^+, direct contribution of 6^+-level excitation is predominant above ~3 MeV. Direct contribution should be virtually zero, when using coupling basis of 0^+-2^+-4^+. We may conclude, that 6^+- level excitation cross section evaluations of JENDL-3.2 and ENDF/B-VI are not pure calculations, they were just normalized to reproduce the trend predicted by measured data by Kegel et. al. [9].

Table 4
Levels of ^{232}Th

E, MeV	J^π	K^π	E, MeV	J^π	K^π
0.0000;	0^+	0^+	1.0231	6^+	2^+
0.049369;	2^+	0^+	1.0429	7^-	0^-
0.16212;	4^+	0^+	1.0499	6^+	0^+
0.3332;	6^+	0^+	1.0536	2^+	
0.5569	10^+	0^+	1.0729	2^+	
0.71425;	1^-	0^-	1.0775	1^-	
0.7303;	0^+	0^+	1.0787	0^+	0^+
0.7741;	2^+	0^+	1.0944	3^+	
0.7744;	3^-	0^-	1.1057	3^-	
0.7853;	2^+	2^+	1.1218;	2^+	0^+
0.827	10^+		1.1371	12^+	
0.8296	3^+	2^+	1.1433	4^-	
0.8730	4^+	2^+	1.1460;	7^+	0^+
0.8836	5^-	0^-	1.1483	4^+	0^+
0.8901	4^+	0^+	1.1825	3^-	
0.9604	5^+	2^+	1.2089	5^-	

6.3 Soft rotator model

There are two major experiments which explore inelastic scattering for levels between 0.7 MeV and 1.4 MeV up to E_n ~2 MeV. Time-of-flight technique was used to measure angular distributions of inelastic scattered neutrons by Ciarcia et. al. [3], these (n,n') data are complemented with (n,n'γ) measurements by Dave et. al. [4]. However, in a number of cases TOF- measurements are discrepant with cross sections inferred from (n,n'γ) measurements. At incident neutron energies above ~1.5 MeV cross sections obtained from (n,n'γ) in a ~70% of investigated cases are larger than (n,n') data. That might be due to possible feeding of the level of interest from higher lying levels. Gamma-ray spectroscopy is especially useful near level excitation threshold, where TOF technique has lower resolution. However, for these lower incident neutron energies the reliability of (n,n'γ) data depends on detailed knowledge of E0-transition contribution and internal

conversion coefficients, frequently that is not the case and then (n,n'γ)-data are systematically lower than TOF-data. Angle-integrated inelastic scattering cross sections were obtained measuring differential neutron scattering at 125° angle. For a number of incident neutron energies we could compare angular distributions of inelastic scattered neutron by Ciarcia et. al. [3] with calculated values.

Direct excitation of vibrational levels could be described within a soft rotator model [58]. Here the direct inelastic scattering component is due to excitation of octupole and quadrupole band levels. Direct excitation cross sections for γ-vibration $K^\pi = 0^+$, β-vibration $K^\pi = 0^+$, anomalous rotational $K^\pi = 2^+$ bands as well as first octupole $K^\pi = 0^-$ band levels are calculated for deformed non-axial, soft to quadrupole $\beta-$ and $\gamma-$vibrations rotator. Excitation energies of members of even-parity collective bands $K^\pi = 0^+$, 0^+, 2^+ and first octupole band $K^\pi = 0^-$,are reproduced up to $\sim$2 MeV [58].

Levels of $K^\pi = 0^-$ band (0.71425 MeV) are most sensitive to the octupole deformation parameter β_3,which slightly influence also the positions of other band levels. Another parameter which defines positions of levels of $K^\pi = 0^-$ band is the softness parameter to the octupole vibrations μ_ξ, this peculiarity prohibits unanimous definition of β_3-parameter by fitting $K^\pi = 0^-$ band levels' positions. When this coupling strength parameter β_3 is changed to fit angular distribution data, levels could be kept unaffected with this softness parameter μ_ξ. This procedure was followed in case of ^{238}U inelastic scattering data analysis [106]. Data for a group of octupole band levels by Plompen et. al. [107] up to $\sim$3 MeV helped to define uniquely β_3-parameter and softness parameter to the octupole vibrations μ_ξ. We adopted these parameter values for ^{232}Th, they allowed to reproduce the octupole band levels of ^{232}Th as well.

Levels of second $K^\pi = 0^+$ band (0.73035 MeV) are classified as quadrupole longitudinal $\beta-$vibrations, while levels of third $K^\pi = 0^+$ band (1.0787 MeV) - as quadrupole transversal $\gamma-$vibrations. Both are defined by softness parameters to respective vibrations μ_β and μ_γ. Anomalous rotational $\gamma-$band $K^\pi = 2^+$ levels are defined by non-axiality parameter γ_o.This band lies much lower ($\sim$300 keV) than respective band in case of ^{238}U, at the other hand this band lowering is accompanied by moving $K^\pi = 0^+$ band (1.0787 MeV) - that of quadrupole transversal $\gamma-$vibrations, to higher excitations (by $\sim$250 keV), than in case of ^{238}U nuclide. Moreover, quadrupole longitudinal $\beta-$vibration band also is lowered as compared with relevant band of ^{238}U nuclide by $\sim$250 keV. That means that within soft rotator model ^{232}Th nuclide is much softer with respect to quadrupole longitudinal $\beta-$vibrations, which is pronounced in higher μ_β parameter values. As regards quadrupole transversal $\gamma-$vibrations, static non-axiality parameter γ_o for ^{232}Th is higher than in case of ^{238}U. It was fitted to the position of anomalous $\gamma-$band $K^\pi = 2^+$, which is appreciably lower than in case of ^{238}U. This masks possible difference of softness to transversal $\gamma-$vibrations of ^{232}Th and ^{238}U, i.e. μ_γ parameter values differ only slightly (see Table 5).

Actually the calculations of direct inelastic scattering cross sections were made

adding each of 17 levels of K^π= 0^+, 2^+, 0^- band levels (see Table 6), one by one, to the 0^+-2^+-4^+-6^+-8^+ coupling basis, instead of the last 8^+-member of ground state rotational band, since the coupling with ground state band levels is the strongest for any band level. This procedure only slightly changes total and reaction cross sections, the same response is to the increase of coupling basis, i.e. from 3 to 5 levels within a rigid rotator model.

Table 5
Deformation parameter values for soft rotator model

Nuclide	β_2	β_4	$\hbar\omega_o$,MeV	μ_β	μ_γ	γ_o	β_3	μ_ξ
^{232}Th	0.188	0.071	0.725	0.279	0.279	0.187	0.052	0.626
^{238}U	0.195	0.078	0.989	0.216	0.29	0.146	0.052	0.626

Differential scattering data for negative and positive parity level excitations were employed to fix reliable values of equilibrium deformation parameters.

6.3.1 Octupole, $\beta-, \gamma-$vibration and $\gamma-$ bands

Differential scattering data for incident neutron energies 1.2 and 1.5 MeV by Ciarcia et. al.[3] predict slight forward/backward peaking of inelastic scattered neutrons, which excite band-head level of K^π= 0^- band (see Figs. 57, 58). Calculated curve almost reproduces the angular distribution at 1.5 MeV. It seems that assumption of angular isotropy in obtaining angle-integrated inelastic scattering cross section might lead to rather small error. Evaluated curves of ENDF/B-VI [6], JEF-2 [8] and JENDL-3.2 [5] are rather discrepant with measured data on 0.71425 MeV (J^π=1^-) of K^π=0^- band level (see Fig.59). Calculated curve is compatible with data by Ciarcia et. al.[3] up to E_n $\sim$1.6 MeV, however our predicted direct scattering contribution is much lower than in case of previous evaluations.

Differential scattering data for incident neutron energies 1.2 and 1.5 MeV by Ciarcia et. al.[3] again predict forward/backward peaking of inelastic scattered neutrons, exciting band-head level of K^π= 0^+ band (see Figs. 60, 61), it is also pronounced in calculated curves, which reproduce data shape, except forward angles. Angle-integrated data by Ciarcia et. al.[3] and by Dave et. al. [4] are severely discrepant, however our calculated curve is compatible with (n,n') data by Ciarcia et. al.[3] and once again supports assumption made by Ciarcia et. al.[3] that (n,n'γ) data might be lowered due to undetected E0($0^+ \rightarrow 0^+$) transition.

Differential scattering data forE_n = 2 MeV by Ciarcia et. al.[3] for neutrons, exciting band-head levels of octupole K^π= 0^- and β-vibration K^π= 0^+ bands are shown on Fig. 63. At higher incident neutron energies of 2.4 and 2.8 MeV these calculated differential cross section shows strong back-ward peaking (see Figs. 64, 65). For the angles in the range of 30°-150° calculated curve resembles measured data by Kegel et. al. [9] structure rather closely, though it seems to be

systematically higher. Summed inelastic scattering cross section, shown on Fig. 66, follows the trend predicted by data by Ciarcia et. al.[3] up to E_n ~2 MeV and by Kegel et. al. [9] at higher energies. It seems that the direct contribution component for the 0.71425 MeV (J^π=1$^-$) of K^π=0$^-$ band level should be ~2 times lower than that predicted in JENDL-3.2 [5] evaluation.

Inelastic scattering cross section for the level second levels of β-vibration band 0.7741 MeV (J^π=2$^+$) and octupole band 0.71425 MeV (J^π=3$^-$) are compared with JENDL-3.2 evaluation on Figs. 67 and 68. Differential scattering data by Ciarcia et. al.[3] for this unresolved doublet for incident neutron energies 1.2 and 1.5 MeV predict rather smooth distribution of inelastic scattered neutrons (see Figs. 69, 70). Summed cross section for these levels is compared with measured data on Fig. 71. Though (n,n') and (n,n'γ) cross sections are compatible for the incident neutron energies around ~1.5 MeV, above ~1.5 MeV calculated cross section is much lower than (n,n γ) data predict. This closely resembles the situation shown on Fig. 66 for the band-heads of octupole K^π= 0$^-$ and β-vibration K^π= 0$^+$ bands.

The next level is the band-head of anomalous rotational band K^π= 2$^+$ lying at 0.7853 MeV. Differential scattering data for incident neutron energy of 1.2 MeV by Ciarcia et. al.[3] predict rather smooth distribution of inelastic scattered neutrons, for higher energy of 1.5 MeV peaking at 90° is reproduced only qualitatively (see Figs. 72, 73). Direct scattering contribution predicted for 0.7853 MeV (J^π= 2$^+$) is compatible with (n,n') data trend, (n,n'γ) data by Dave et. al. [4] predict much higher cross section. JENDL-3.2 [5] evaluation largely overestimates the direct contribution and follows the trend predicted by (n,n'γ) data by Dave et. al. [4] (see Fig. 74).

For the next member of this K^π= 2$^+$ band, lying at 0.8296 MeV (J^π= 3$^+$), differential scattering data for incident neutron energy of 1.2 and 1.5 MeV by Ciarcia et. al.[3] predict rather smooth distribution of inelastic scattered neutrons (see Figs. 75, 76), for still higher energy of 2 MeV measured data seem to be too high, strong forward peaking also could not be reproduced (see Fig. 77). This may explain the discrepancy of calculated and (n,n') measured cross section data above ~1.5 MeV (see Fig. 78).

Differential scattering cross section for the composite levels of octupole, $\beta-$vibration and γ-bands and J^π= 10$^+$ level of ground state rotational band in the 0.774-0.830 MeV excitation energy range have been measured by Kegel et. al. [9] for E_n =2.4 and 2.8 MeV (see Figs. 79, 80). Calculated differential scattering cross section is compatible with measured data for E_n =2.4 MeV and overestimates the data at E_n =2.8 MeV. Inelastic cross section is shown on Fig. 81, present calculation is compatible with measured data by Ciarcia et. al.[3] and Kegel et. al. [9] up to E_n ~2.7 MeV, at higher energies the latter data predict too steep decrease of the cross section. It seems that direct contribution in JENDL-3.2 evaluation is again largely overestimated. The same is true for the third member of anomalous rotational band K^π= 2$^+$ lying at 0.873 MeV (J^π=

4^+) (see Fig. 82).

Figure 83 shows the description of data for unresolved doublet of two levels, 0.8836 (J^π= 5^-), third member of octupole K^π= 0^- band, and 0.8901 (J^π= 4^+) - third member of $\beta-$vibration K^π= 0^+ band. For incident neutron energies below 1.5 MeV calculated curve somewhat underestimates (n,n') data, but is still higher than (n,n'γ) data. At higher incident neutron energies (n,n'γ) data are higher than calculated cross section, this favors the assumption that there some unobserved gamma-ray transitions in (n,n'γ) experiment by Dave et. al. [4].

Differential scattering cross section for the composite of three levels in the 0.883$\sim$0.890 MeV excitation energy range have been measured by Kegel et. al. [9] for 2.4 and 2.8 MeV (see Figs. 84, 85). Data scatter a lot, so we could reconcile calculated curve with measured data only for E_n =2.4 MeV. Inelastic cross section for this group of levels is shown on Fig. 86. It seem that direct contribution in JENDL-3.2 evaluation is again largely overestimated. Our calculated curve follows (n,n') data by Ciarcia et. al.[3] below $\sim$1.5 MeV and tendency, predicted by Kegel et. al. [9] data above E_n $\sim$2 MeV, though the latter data seem to be too low because of misinterpreted angular distribution for E_n $\gtrsim$2.4 MeV. The same kind of calculated curve discrepancy with measured (n,n'γ) data above $\sim$1.7 MeV is evident.

Differential scattering data for fourth member of anomalous rotational band K^π= 2^+ lying at 0.9604 MeV (J^π= 5^+) at incident neutron energies of 2.0, 2.4 and 2.8 MeV by Ciarcia et. al.[3] predict rather high cross section with forward peaking, which could not be reproduced with present version of soft rotator model (see Figs. 87, 88, 89). Cross section data scatter a lot, direct contribution in this case is rather low and calculated curve is discrepant with (n,n'γ) data above $\sim$1.7 MeV in the same way as before (see Fig. 90). It is compatible with measured data by Kegel et. al. [9] only above $\sim$2.6 MeV.

Cross section for the 1.0536 MeV level was measured both by Ciarcia et. al.[3] and Dave et. al. [4], they are drastically different, the former data being much higher. Spin-parity assignment for this level is rather controversial: Chan et. al. [101] assume this level being the band-head of K^π= 2^- octupole state, ENSDF [102] assigns only spin value J= 2. Calculated cross section is not much sensitive to the parity of this level (see Fig. 91) and remains compatible with (n,n') data. We adopted J^π= 2^+ here, since there are a number of inconsistencies in assigning spin-parity to this level in [101].

Differential scattering data for the levels lying at excitations between 0.7 and 1.05 MeV, i.e. β-vibration K^π= 0^+, anomalous rotational K^π= 2^+ bands as well as first octupole K^π = 0^- band levels, were measured by Baba et. al. [12] (see Fig. 92), our calculation is rather compatible with these data, as distinct of previous measurements [11] for the levels lying at excitations between 0.7 and 0.9 MeV (see Fig. 93).

Level lying at 1.0729 MeV (J^π= 2^+) is not attributed to any band within the present model. Calculated cross section is discrepant with the data by Dave et.

al. [4] in the same way as for most other levels. Direct contribution in JENDL-3.2 evaluation is rather high, while it is missing in present approach (see Fig. 94).

Cross section for the excitation of the band-head of γ-vibration band $K^\pi = 0^+$ was measured only with (n,n'γ) method. Calculated curve is discrepant with the data above $\sim$1.5 MeV being systematically lower. Calculated direct contribution is almost three times lower than that of JENDL-3.2 [5] evaluation (see Fig. 95). Data for the triplet 1.0729 MeV ($J^\pi = 2^+$), 1.0775 MeV ($J^\pi = 1^-$) and 1.0787 MeV ($J^\pi = 0^+$) obtained by (n,n') and (n,n'γ) methods are compared on Fig. 96. Calculated curve is compatible with (n,n') data above $\sim$1.8 MeV. Direct scattering is included only for 1.0787 MeV ($J^\pi = 0^+$) level, band-head of γ-vibration band $K^\pi = 0^+$, that of JENDL-3.2 [5] is much higher.

The next pair of levels 1.0944 MeV ($J^\pi = 3^+$) and 1.1057 MeV ($J^\pi = 3^-$) was resolved in measurement by Dave et. al. [4], the former level cross section is much discrepant with calculated cross section as if there are unobserved decay branches in the (n,n'γ) measurements. The spin-parity assignment for this level is controversial, Chan et. al. [101] assume that this is $J^\pi = 2^-$ level of octupole $K^\pi = 1^-$ band. For this spin-parity values calculated cross section changes shape only a bit (see Fig. 97). Cross section data for the excitation of 1.1057 MeV ($J^\pi = 3^-$) level are discrepant with a calculated cross section being higher up to E_n $\sim$1.5 MeV and lower at higher energy . This doublet was unresolved in (n,n') measurement , comparison of measured (n,n'), (n,n'γ) and calculated cross sections is presented on Fig. 99. Measured data are rather discrepant below E_n $\sim$1.5 MeV, being consistent in the energy range 1.5 $\sim$ 2 MeV. Calculate curve nicely describes (n,n') measurement data [3], while JENDL-3.2 evaluation follows (n,n'γ) measurements.

The second member of γ-vibration band $K^\pi = 0^+$ lies at 1.1218 MeV ($J^\pi = 2^+$). Calculated excitation cross section is compatible with measured (n,n') and (n,n'γ) data, which are almost consistent (see Fig. 100). The cross section for the excitation of the third member of γ-vibration band $K^\pi = 0^+$,1.1483 MeV ($J^\pi = 4^+$), is measured combined with excitation cross section of 1.1433 MeV ($J^\pi = 4^-$) level. Calculated curve nicely follows the (n,n') data trend up to E_n $\sim$2 MeV, which are markedly higher than (n,n'γ) data below $\sim$1.5 MeV (see Fig. 101). The discrepancy between (n,n') and (n,n'γ) data might be attributed to E0 transition from 1.1483 MeV ($J^\pi = 4^+$) level to the $J^\pi = 4^+$ level of ground state band.

Calculated cross section of 1.1825 MeV ($J^\pi = 3^-$) level is compatible both with (n,n') and (n,n'γ) data, except to anomalous data points around E_n $\sim$1.4 MeV. Evaluation of ENDF/B-VI follows the strange shape, predicted by these two data points (see Fig. 102).

In most cases calculated cross sections for excitation of discrete levels and group of levels of γ-vibration $K^\pi = 0^+$, β-vibration $K^\pi = 0^+$, anomalous rotational $K^\pi = 2^+$ bands as well as first octupole $K^\pi = 0^-$ band levels are in nice agreement with (n,n') method measured data up to $\sim$3 MeV. Measured data derived by (n,n'γ) method were supposed in most cases overestimate inelastic scattering

cross section above E_n ~1.5 MeV and underestimate it at lower energies, or in the whole energy range, in a number of cases. This conclusion, made by Ciarcia et. al.[3], was never supported by the detailed statistical nuclear reaction model calculations. Present investigation, taking into account direct excitation of γ-vibration $K^\pi = 0^+$, β-vibration $K^\pi = 0^+$ and anomalous rotational $K^\pi = 2^+$ bands levels, seems to be the first trial.

Table 6
Coupling scheme for ^{232}Th

			1.1483; 4^+	
		1.1460; 7^+		
			1.1218; 2^+	
			1.0787; 0^+	
		1.0499; 6^+		
	1.0429; 7^-			
				1.0231; 6^+
				0.9604; 5^+
		0.8901; 4^+		
	0.8836; 5^-			
				0.8730; 4^+
				0.8296; 3^+
				0.7853; 2^+
	0.7744; 3^-			
		0.7741; 2^+		
		0.7303; 0^+		
	0.71425; 1^-			
0.3332; 6^+				
0.16212; 4^+				
0.049369; 2^+				
0.0000; 0^+		n_β=1	n_γ=1	
$K^\pi = 0^+$	$K^\pi = 1^-$	$K^\pi = 0^+$	$K^\pi = 0^+$	$K^\pi = 2^+$

6.4 Total inelastic cross section

Calculated total inelastic cross section is compared with measured data [82, 2, 108, 1] on Fig. 103. The data measured by Glazkov et. al. [2] and Smith et. al. [82] are inconsistent above E_n ~1 MeV. Data measured by Smith et. al. [1] should be complemented with the inelastic scattering cross sections for ground state band levels, since they were subtracted from measured scattered neutron spectra along with elastic scattering component. The calculated curve describes the measured

data [1, 2, 108] within errors. The contribution of direct excitation of ground state band levels, γ-vibration $K^{\pi}= 0^{+}$, β-vibration $K^{\pi}= 0^{+}$, anomalous rotational $K^{\pi}= 2^{+}$ bands as well as first octupole $K^{\pi} = 0^{-}$ band levels is shown to be ~15% of total inelastic cross section below ~6 MeV. The step-like dependence of total inelastic scattering cross section above ~1 MeV incident neutron energy seems to be compatible with measured data base. The calculated curve is consistent with JENDL-3.2 [5] evaluation up to ~2 MeV incident neutron energy. Figure 104 shows the comparison of continuum scattering contribution to total inelastic cross section of JENDL-3.2, ENDF/B-VI [6] and present evaluation, the curves are rather different in energy dependence, especially up to E_n ~6 MeV.

Above emissive fission threshold evaluations of inelastic scattering cross section differ by ~30%, present estimate being intermediate. The discrepancy with JENDL-3.2 evaluation might be attributed to overestimated contribution of pre-equilibrium neutron emission, the opposite is true with respect to ENDF/B-VI [6] and JEF-2 [8] evaluation.(see Fig. 105). In our calculations pre-equilibrium neutron emission contribution is defined by description of secondary neutron spectra and consistent description of ^{232}Th(n,f) and ^{232}Th(n,2n)reaction cross sections.

7 Capture cross section

Calculated ^{232}Th capture cross section is dependent on radiative strength function value, i. e. on level densities of ^{233}Th and ^{232}Th nuclides as well as inelastic neutron scattering competition. We will check the consistency of measured data base with calculated capture cross section up to E_n ~5 MeV.

Measured data are discrepant well beyond claimed errors, a consistent data set could be selected and fitted within statistical model. Below ~15 keV measured data by Wisshak et. al. [45] predict an upward trend, while data by Kobayashi et. al.[31] predict a downward trend. Renormalized by [28] data by Macklin [27] are compatible with data by Kobayashi et. al.[31] and Wisshak et. al. [45] in ~10-150 keV energy range. Above ~50 keV data by Poenitz and Smith [29] are compatible with data by Wisshak et. al. [45], Macklin [27] and Kobayashi et. al. Above E_n ~ 150 keV data by Kobayashi et. al.[31] demonstrate an upward trend, which is at variance with data trend by Lindner et. al. [33]. It was concluded that renormalized by [28] data by Macklin [27] for E_n ~ 3-700 keV are compatible with data by Kobayashi et. al.[31] in ~3-400 keV energy range. Data by Wisshak et. al. [45] in ~5 - 225 keV energy range are compatible with both data sets, except for incident neutron energies below ~15 keV, where the latter data predict sharply increasing trend of capture cross section. Above ~50 keV data by Poenitz and Smith [29] are compatible with data by Wisshak et. al. [45], Macklin [27] and Kobayashi et. al.[31]. Data by Davletshin et. al. [44] predict rather low capture cross section above E_n ~400 keV.

7.1 Radiative capture channel

The dipole radiative strength function for ^{233}Th $\gamma-$decay was calculated using Lorenz' parameterization of actinide absorption cross section data at low energies (<7 MeV). The higher multipolarity transitions are neglected. The radiative transmission coefficient

$$T_{\gamma}^{J\pi}(U) = \frac{2\pi C_{\gamma}}{3(\pi hc)^2} \int \varepsilon_{\gamma}^2 \sigma_{\gamma}(\varepsilon_{\gamma}) \sum_{I=|J-1|}^{I=J+1} \rho(U-\varepsilon_{\gamma}, I, \pi) d\varepsilon_{\gamma}, \tag{15}$$

was calculated using Lorenz' parameterization of photoabsorption cross section $\sigma_{\gamma}(\varepsilon_{\gamma})$

$$\sigma_{\gamma}(\varepsilon_{\gamma}) = \sum_{i=1}^{2} \sigma_{\gamma i} \frac{\varepsilon_{\gamma}^2 \Gamma_{Gi}^2}{(\varepsilon_{\gamma}^2 - E_{Gi}^2)^2 + \varepsilon_{\gamma}^2 \Gamma_{Gi}^2}. \tag{16}$$

The respective parameters being fitted to actinide photoabsorption data at low energies [109]: $\sigma_{\gamma 1} = 250\ mb$, $\sigma_{\gamma 2} = 300\ mb$, $E_{G1} = 10.5\ MeV$, $E_{G2} = 14\ MeV$, $\Gamma_{G1} = 2.5\ MeV$, $\Gamma_{G2} = 4.5\ MeV$, C_{γ} is the normalizing coefficient.

At incident neutron energies higher than ∼1 MeV, the competition of neutron emission at the second cascade, i.e. after first γ-quanta emission should be included. Then "true" capture reaction cross section (n,$\gamma\gamma$) is defined using transmission coefficient $T_{\gamma\gamma}^{J\pi}(U)$ defined in a two-cascade approximation as

$$T_{\gamma\gamma}^{J\pi} = \frac{2\pi C_{\gamma 1}}{3(\pi hc)^2} \int \varepsilon_{\gamma}^2 \sigma_{\gamma}(\varepsilon_{\gamma}) \sum_{I=|J-1|}^{I=J+1} \rho(U-\varepsilon_{\gamma}, I, \pi) \frac{T_{\gamma}^{I\pi}}{T_f^{I\pi} + T_{n'}^{I\pi} + T_{\gamma}^{I\pi}} d\varepsilon_{\gamma}\ , \tag{17}$$

The last term of the integrand describes the competition of fission, neutron emission and γ-emission at excitation energy $(U-\varepsilon_{\gamma})$ after emission of first γ-quanta, $C_{\gamma 1}$ is the normalizing coefficient. That means transmission coefficients $T_{\gamma}^{I\pi}$, $T_{n'}^{I\pi}$ and $T_f^{I\pi}$ are defined at excitation energy $(U-\varepsilon_{\gamma})$. The neutron emission after emission of first $\gamma-$quanta strongly depends on the ^{232}Th residual nuclide level density at excitations just above paring gap [110].

The contribution of (n,γn$'$)$-$reaction to inelastic scattering cross section is defined by $T_{\gamma n'}^{J\pi}$ value. The energy dependence of (n,γn$'$) reaction transmission coefficient $T_{\gamma n'}^{J\pi}$ was calculated with the expression

$$T_{\gamma n'}^{J\pi} = \frac{2\pi C_{\gamma 1}}{3(\pi hc)^2} \int \varepsilon_{\gamma}^2 \sigma_{\gamma}(\varepsilon_{\gamma}) \sum_{I=|J-1|}^{I=J+1} \rho(U-\varepsilon_{\gamma}, I, \pi) \frac{T_{n'}^{I\pi}}{T_f^{I\pi} + T_{n'}^{I\pi} + T_{\gamma}^{I\pi}} d\varepsilon_{\gamma}\ , \tag{18}$$

At incident neutron energies above fission threshold competition of fission is important [111]. The contribution of (n,γf)-reaction to fission cross section is

defined by $T_{\gamma f}^{J\pi}$ value. The energy dependence of (n,γf) reaction transmission coefficient $T_{\gamma f}^{J\pi}$ was calculated with the expression

$$T_{\gamma f}^{J\pi} = \frac{2\pi C_{\gamma 1}}{3(\pi hc)^2} \int \varepsilon_\gamma^2 \sigma_\gamma(\varepsilon_\gamma) \sum_{I=|J-1|}^{I=J+1} \rho(U-\varepsilon_\gamma, I, \pi) \frac{T_f^{I\pi}}{T_f^{I\pi} + T_{n'}^{I\pi} + T_\gamma^{I\pi}} d\varepsilon_\gamma \ , \quad (19)$$

7.2 Data analysis

Measured data are discrepant well beyond claimed errors, a consistent data set could be selected and fitted within statistical model. Below ~15 keV measured data by Wisshak et. al. [45] predict an upward trend, while data by Kobayashi et. al.[31] predict a downward trend. Renormalized by [28] data by Macklin [27] are compatible with data by Kobayashi et. al.[31] and Wisshak et. al. [45] in ~10-150 keV energy range. Above ~50 keV data by Poenitz and Smith [29] are compatible with data by Wisshak et. al. [45], Macklin [27] and Kobayashi et. al. Above $E_n \sim 150$ keV data by Kobayashi et. al.[31] as well as renormalized data Macklin [27] demonstrate an upward trend, which is at variance with data trend by Lindner et. al. [33]. Above ~50 keV data by Poenitz and Smith [29] are compatible with data by Wisshak et. al. [45], Macklin [27] and Kobayashi et. al.[31]. Data by Davletshin et. al. [44] predict rather low capture cross section in the energy range of E_n ~400 - 1400 keV, which is systematically discrepant with data by Lindner et. al. [33] and Poenitz and Smith [29].

Data by Anand et. al. [40] are compatible with data by Pönitz and Smith [29] and data by Lindner et. al. [33] in the energy range of 400-900 keV, while data by Jane et. al. [39] predict rather low capture cross section above 350 keV. Data by Hanna et. al. [37] predict the lowest cross section above ~1 MeV.

For incident neutron energy up to E_n ~150 keV capture cross section is defined solely by radiation strength function value adopted from resonance energy region. For higher incident neutron energies calculated cross section is rather sensitive to the level density of ^{233}Th at low excitation energies. Figure 106 demonstrates the sensitivity of calculated cross section to the level density of ^{233}Th below three-quasiparticle excitation threshold. The lowest estimate of ^{233}Th level density produces the highest level cross section due to normalization of calculated radiative strength function to the observed value $S_{\gamma 0}$ =12.255×10^{-4}. Adopted capture data description is shown on Fig. 107. The important peculiarities of the calculated capture cross section is the cusp above first excited level threshold of ~49 keV up to ~800 keV, another one is the cross section drop from ~800 keV up to ~1.2 MeV (see Fig. 106). The latter drop is evident in data by Lindner et. al. [33], it might be correlated with strong increase of inelastic scattering competition due to increase of residual nuclide ^{232}Th number of levels (see Fig. 48). Present calculation is compatible with evaluation of JENDL-3.2 up to E_n ~250 keV. At higher energies evaluation of JENDL-3.2 follows the data trend by Davletshin et.

al. [44]. Evaluation of ENDF/B-VI is systematically higher than present evaluation in the energy range of 100 - 1000 keV. The $(n, \gamma n')$ reaction competition to the "true" capture $(n, \gamma\gamma)$ reaction competition is rather strong above ~1 MeV incident neutron energy. Figure 108 shows the cross section of $(n, \gamma n')$ reaction and the cross section of $(n, \gamma x)$ reaction, which is the sum of $\sigma_{(n,\gamma\gamma)}$ and $\sigma_{(n,\gamma n')}$ cross sections. The competition of $(n, \gamma f)$ reaction to the "true" capture (n,$\gamma\gamma$) reaction is inessential for ^{232}Th$(n, \gamma\gamma)$ reaction due to low fission probability of ^{233}Th nuclide.

8 Fission Cross Section

Fission data fit is used as a major constraint for inelastic scattering, capture, (n,2n) and (n,3n) cross sections estimation. Consistent description of measured data might justify a validity of level density description and fission barrier parameterization. There are a number of vibrational resonances in neutron-induced fission cross section of ^{232}Th target nuclide below E_n ~2.5 MeV. These resonances are interpreted as transmission resonances for the splitted outer fission barrier hump, then the fission barrier is triple humped. We will describe fission cross section for incident neutron energies $E_n \gtrsim 2.5$ MeV in a double humped fission barrier model, treating intermediate and outer fission barriers as a single barrier. For lower incident neutron energies we will describe the overall trend of measured data and the normalize calculated cross section to the measured data.

8.1 Fission Channel

Neutron-induced fission of ^{232}Th could be treated in a double humped fission barrier model as a two-step process, i.e. a successive crossing over the inner hump A and over the outer hump B. Hence, the transmission coefficient of the fission channel $T_f^{J\pi}$ (U) can be represented as

$$T_f^{J\pi}(U) = \frac{T_{fA}^{J\pi}(U) T_{fB}^{J\pi}(U)}{(T_{fA}^{J\pi}(U) + T_{fB}^{J\pi}(U))}. \tag{20}$$

The transmission coefficient $T_{fi}^{J\pi}(U)$ is defined by the level density $\rho_{fi}(\varepsilon, J, \pi)$ of the fissioning nucleus at the inner and outer humps (i = A,B, respectively):

$$T_{fi}^{J\pi}(U) = \sum_{K=-J}^{J} T_{fi}^{JK\pi}(U) + \int_0^U \frac{\rho_{fi}(\epsilon, J, \pi) d\epsilon}{(1 + \exp(2\pi(E_{fi} + \epsilon - U)/h\omega_i))}, \tag{21}$$

where the first term denotes the contribution of low-lying collective states and the second term that from the continuum levels at the saddle deformations, ϵ is the intrinsic excitation energy of fissioning nucleus. The first term contribution due to

discrete transition states depends upon saddle symmetry. The total level density $\rho_{fi}(\epsilon, J, \pi)$ of the fissioning nucleus is determined by the order of symmetry of nuclear saddle deformation.

Inner and outer fission barrier heights and curvatures as well as level densities at both saddles are the model parameters. Fission barrier height values and saddle order of symmetry are strongly interdependent. The order of symmetry of nuclear shape at saddles were adopted from shell correction method (SCM) calculation by Howard and Möller [98]. According to shell correction method (SCM) calculations by Howard and Möller [98] the inner barrier was assumed mass and axially symmetric, outer barrier is assumed axially symmetric and mass-asymmetric.

8.1.1 Fission transmission coefficient, level density and transition state spectrum

Fission cross section data of ^{232}Th exhibits threshold shape, modulated by vibrational resonance. To fit the data shape above E_n ~3 MeV the different behavior of level densities of even-odd and even-even nuclei at low excitation energies should be taken into account. Adopted level density description allows to describe qualitatively subthreshold cross section shape (see Fig. 109). Incident neutron energy $E_3 = U_3 + E_{fA(B)} - B$ correspondent to excitation of three-quasiparticle states is $\sim$ 3.4 MeV. The one-quasiparticle neutron states of even-odd fissioning nuclide, lying below the three-quasiparticle states excitation threshold define the shape of fission cross section below incident neutron energy of $E_n \leq E_{fA(B)} + U_3 - B_n$. At higher excitation energies three-quasiparticle states are excited. Two-quasiparticle states in even residual nuclide ^{232}Th could be excited at incident neutron energies $E_n > U_2$. At lower energies fission cross section shape is controlled by one-quasiparticle state density. The transition state spectra were constructed using values of $F_0/\hbar^2$ at the inner and outer saddles shown in Table 7.

Table 7
Transition spectra band-heads Z-even, N-odd nuclei

inner saddle		outer saddle	
K^π	E_{K^π}, MeV	K^π	E_{K^π}, MeV
$1/2^+$	0.0	$1/2^+$	0.0
$5/2^+$	0.08	$1/2^-$	0.0
$1/2^-$	0.05	$3/2^+$	0.08
$3/2^-$	0.0	$3/2^-$	0.08
		$5/2^+$	0.0
		$5/2^-$	0.0

Each one-quasiparticle state in odd fissioning nucleus is assumed to have a rotational band built on it with a rotational constant, dependent upon the respective saddle deformation. We construct the discrete transition spectra up to ~100 keV, using one-quasiparticle states by Bolsterli et. al. [113, 114]. The discrete transition spectra, as well as continuous level contribution to the fission transmission coefficient are dependent upon the order of symmetry for fissioning nucleus at inner and outer saddles. The negative parity bands $K^{\pi} = 1/2^-$,$3/2^-$, $5/2^-$ ... at outer saddle are assumed to be doubly degenerate due to mass asymmetry. With transition state spectra thus defined the fission barrier parameters are obtained.

8.2 Fission Data Analysis

Measured data for ^{232}Th fission cross section [115, 116, 117, 118, 119, 120, 121, 122, 123, 124, 125, 126] below 3 MeV are rather consistent. At higher incident neutron energies there are some systematic differences in first plateau region. We will reproduce the date trend by Fursov et. al. [125] (see Fig. 110). One-quasiparticle neutron states of even-odd ^{233}Th fissioning nuclide, lying below three-quasiparticle states excitation threshold define the shape of ^{232}Th fission cross section below incident neutron energy of ~3.4 MeV. At higher energies three-quasiparticle states are excited.

9 Cross sections above emissive fission threshold

At higher incident neutron energies when fission reaction of ^{232}Th, ^{231}Th, ^{230}Th or ^{229}Th compound nuclides is possible after emission of 1, 2, 3 or 4 neutrons, the observed fission cross section is a superposition of non-emissive or first chance fission of ^{233}Th and xth-chance fission contributions. These contributions are weighted with a probability of x neutrons emission before fission. For fixed statistical model parameters of residual nuclei ^{232}Th, ^{231}Th, ^{230}Th or ^{229}Th, fissioning in (n,nf), (n,2nf), (n,3nf)or (n,4nf) reactions, the behavior of the first-chance fission cross section σ_{f1} should make it possible to reproduce the measured fission cross section σ_f of ^{232}Th. A consistent description of measured data on the (n,f) and (n,2n) reaction cross sections for the ^{232}Th target nuclide up to 20 MeV enables one to consider the estimates of σ_{f1} and fission probability $P_{f1}$of the initial compound nuclei ^{233}Th as fairly realistic.

9.1 Fission cross section

Fission cross section of ^{232}Th, shown on the Fig. 111 demonstrates a step-like structure, relevant to contribution of (n,$x$nf) reactions to total fission cross sec-

tions for $x = 1, 2, 3$. First-chance fission cross section slowly increases with energy. Contribution of first-chance fission appears to be sensitive to level density of residual nuclide ^{232}Th. The behavior of the first-chance fission cross section σ_{f1} is obviously related to the energy dependence of the first-chance fission probability of the $A+1$ nucleus P_{f1}:

$$\sigma_{f1} = \sigma_r(1 - q(E_n))P_{f1}. \tag{22}$$

Once the contribution of first neutron pre-equilibrium emission $q(E_n)$ is fixed, the first-chance fission probability P_{f1} of the ^{233}Th compound nuclide depends only on the level density parameters of fissioning and residual nuclei. Actually, it depends on the ratio of shell correction values δW_{fB} and δW_n. We shall consider the adopted $\delta W_{fA(B)}$ estimates (see Table 3) to be effective, provided that δW_n are obtained with the liquid drop model. The trend of the first-chance fission cross section σ_{f1} shown in Fig. 111 could be treated as a manifestation of the shell effects in first-chance fission probability. Sharp increase of observed fission cross section above (n,nf) fission reaction threshold and rather steep decrease up to (n,2nf) fission threshold is due to fission probability of ^{232}Th. Contributions of partial $x-$chance fission reactions to the observed fission cross sections is shown on Fig. 112. Up to (n,2nf) fission reaction threshold contribution of ^{232}Th(n,nf) reaction is higher than in case of ^{238}U(n,f) reaction. It would be directly pronounced in (n,nf) pre-fission spectra contribution to the prompt fission neutron spectra (see below). Contribution of second-chance fission of ^{232}Th compound nuclide is sensitive to the level density of fissioning nuclide ^{232}Th. Estimate of ^{232}Th $\langle D_{obs} \rangle = 0.45$ eV, obtained by systematics of average resonance parameters [15] is consistent with pre-equilibrium contribution into first neutron spectrum and subsequent sharing of $\sigma_r = \sigma_{n,f1} + \sigma_{n,nx}$ reaction cross section into first-chance fission and neutron emission cross sections. Cross section of ^{231}Th(n,f) reaction is shown on Fig. 113, it corresponds to (n,nf) fission contribution to observed fission cross section ^{232}Th(n,f) (see Fig. 111). Contributions of (n,2nf) and (n,3nf) reactions correspond to consistent description of ^{232}Th(n,2n) cross sections. So it can be stated that we have got effective estimate of σ_{f1} which corresponds to consistent fit of ^{232}Th(n,f) and ^{232}Th(n,2n) reaction cross section data.

9.2 ^{232}Th(n,2n) cross section

There are a number of measurements of ^{232}Th(n,2n) reaction cross section. We carried out an exhaustive examination of measured data, including error analysis and data renormalization, using updated values of appropriate standard and reference data. In most of them the authors used activation technique to measure ^{231}Th activity. In most cases the activity of the irradiated thorium sample was determined by the weighted average of the values calculated from the intensity

of the same gamma peaks using Ge(Li) detector.

9.2.1 Measured data

The energy dependence of ^{232}Th(n,2n) reaction cross section in a wide energy range has been measured in 3 experiments (in all of them D-d reaction has been used as a neutron source).

Tewes et. al. [127] (8.4 - 15.1 MeV, 13 points), they used recoil proton counter telescope to measure incident neutron flux (the monitor reaction was H(n,n), no information given about cross section values used).

Butler and Santry [128] (6.51 - 20.4 MeV, 18 points), they used ^{32}S(n,p) reaction for incident neutron flux determination. We renormalized original ^{232}Th(n,2n) cross section values using up-to-date evaluation of monitor reaction ^{32}S(n,p) cross section [6].

Raics et. al. [130] (6.745 - 14.84 MeV, 16 points), authors used ^{56}Fe(n,p), ^{27}Al(n,α) and ^{238}U(n,f) monitor reactions for incident neutron flux determination. The neutron flux has been determined as weighted average value from these reactions, updated cross section values were used, no additional renormalization is required.

The energy dependence of ^{232}Th(n,2n) reaction cross section near 14 MeV has been measured in the next 3 experiments (in all of them the T-d reaction has been used as a neutron source):

Prestwood and Bayhurst [131] (12.13 - 14.93 MeV, 12 points), ^{238}U(n,f) reaction has been used for incident neutron flux determination. We can not renormalize these data because reference on monitor cross section is incorrect.

Karius [133] (12.99 - 18.13 MeV, 9 points), neutron flux was measured with a proton recoil stilbene detector (the monitor reaction was ^{1}H(n,n)).

Filatenkov et. al. [138] (13.48 - 14.83 MeV, 9 points). Most recent experiment, very thin sample - metallic thorium was used, weight 13 mg, purity 100%. The monitor reactions ^{27}Al(n,α) and ^{93}Nb(n,2n) were used for neutron flux determination.

The cross section near 14 MeV point has been measured in the next 4 experiments (in all works T-d reaction has been used as a neutron source).

Perkin and Coleman [134] (14.1 MeV), 2.25×2.25 inch sodium iodide crystal has been used as a γ-detector, so the prescribed uncertainty in detector efficiency ($\sim$3%) seems too optimistic. The authors used ^{27}Al(n,α) monitor reaction for neutron flux determination. No information about monitor reaction cross section values is available.

Phillips [135] (15.0 MeV), associated α-particle counting technique was applied for neutron flux determination. Massive sample - two grams of thorium dioxide and krypton filled proportional counter for γ-detection were used.

Chatani and Kimura [136] (14.5 MeV), average neutron energy was determined by the cross section ratio of ^{90}Zr(n,2n) and ^{93}Nb(n,2n), using two Zr and

two Nb foils, placed at a distance of 1.5 cm from Ti-T target. The reaction cross section ratio for this position was 1.57, then corresponding average neutron energy of 14.5±0.2 MeV was obtained. The time dependence of the neutron flux was monitored using a moderator type neutron dose rate meter located at a distance of ∼2 m from Ti-T target. For neutron flux determination ^{27}Al(n,α) monitor reaction was used (reaction cross section values taken from [6]).

Zysin et. al. [137] (14.7 MeV), low-voltage linear accelerator and (T-d) reaction as a neutron source and mixture of the thorium oxide-dioxide (0.2 g) as a sample, were used. They used 3 monitors - ^{238}U(n,f) cross section and cumulative yields of ^{99}Mo and ^{140}Ba fragments in ^{238}U(n,f) reaction for neutron flux determination and 4-π β-detector for sample activity measurement. We renormalized original ^{232}Th(n,2n) cross section value using up-to-date evaluation [6] of ^{238}U(n,f) cross section.

Cochran and Henkel [129] (7.03 and 15.97 MeV), only cross section values are given, no other information about this work is available.

Batchelor et. al. [139] (7 MeV). Time-of-flight technique was used for secondary neutron spectrometry. They used massive thorium sample (cylinder 5 cm long, 2.50 cm diameter with a 1.0 cm diameter axial hole). Neutron flux has been determined against ^{1}H(n,p) elastic scattering. The ^{232}Th(n,2n) cross section value was extracted from model calculations (they varied optical potential parameters to describe the observed neutron spectra). There was a number of corrections (multiple scattering, angular integration, detector threshold etc.), therefore the estimated accuracy (270±13 mb) looks too optimistic.

9.2.2 ^{232}Th(n,2n) data analysis

All existing experimental data are shown on Figs.114, 115. Several older data [127, 128, 137, 134, 131] disagree with more recent measurements.

In JENDL-3.2 (n,2n) reaction cross section was calculated using evaporation model by Segev [141], it follows the trend predicted by Tewes et. al. [**?**] data and predicts rather low cross section above ∼13 MeV. The reason is missing of pre-equilibrium contribution in first neutron spectra. ENDF/B-VI and JEF-2.2 evaluations follow data trend by Butler et. al. [128] and are consistent with other renormalized data around 14 MeV. Evaluated cross section of JEF-2.2 predicts too high level of hard energy tail of ^{232}Th(n,2n) cross section. Below ∼13 MeV previous evaluations are much lower than recent data by Raics et. al. [130], which might be considered consistent with data by Butler et. al. [128], since there is much scatter in the latter data set.

Estimates (n,3n) reaction cross sections for ^{232}Th are presented on Fig. 116. Cross section of (n,3n) reaction is less sensitive to pre-equilibrium neutron emission contribution. Calculated curve, shown on the Fig. 116 is just the result of fitting fission reaction cross sections. Evaluated (n,3n) reaction cross section of JENDL-3.2 is ∼20% higher than present calculation. It seems that reflects the

differences of (n,2n) reaction cross sections, the same is true in case of (n,3n) reaction cross section of JEF-2.2, which is much lower.

10 Neutron emission spectra

Measured neutron emission spectra provide a complementary information on inelastic scattering cross section for discrete and continuum levels of target nucleus. Emission spectra inclusive of both fission and scattered neutrons were measured by Baba et. al. [10] at 1.2, 2.03, 4.25 and 14.05 MeV, Miura et. al.[12] at 2.6, 3.55 and 11.8 MeV, at a number of angles: 30°, 45°, 60°, 120°. To compare the calculated emission spectra, prompt fission neutron spectrum should be added to that of inelastic scattered neutrons. First we will describe the approach used for prompt fission spectrum calculation and then return to the discussion on neutron emission spectra.

10.1 Prompt fission neutron spectra

Prompt Fission Neutron Spectra (PFNS) for ^{232}Th have been calculated with the model that was previously applied for ^{238}U PFNS data analysis. Here is enclosed a brief survey of measured PFNS data.

10.1.1 Experimental data

For the first chance fission incident neutron energy range the available PFNS were measured at E_n =1.49 MeV [142] (Fig.117), E_n =2 MeV [10](Fig. 118), E_n =2.9 MeV [143] (Fig.119) and E_n =4.1 MeV [144], at higher incident energy the PFNS were measured at E_n =7 MeV [145] (Fig.120), E_n =14.6 MeV [143, 146] (Fig.121) and E_n =17.7 MeV [146] (Fig.122). Time-of-flight method with monoenergy neutron source was used. The neutron detector efficiency was measured relative to standard neutron source (^{252}Cf(sf)) [142, 10, 145, 146] or was calculated with Monte Carlo method [10], [144].

In [142, 10, 144] metal ^{232}Th sample has been used. Energy range of fission neutrons $E \gtrsim E_n$ was investigated in these experiments. In [143, 145, 146] fast ionization chambers loaded with ^{232}Th layers were applied for selection of fission events and for timing of neutron spectrometer. In [143, 146] the some amount of ^{252}Cf was incorporated into one of the fissile layers. This latter data would be susceptible only to small systematic error due to loss of fragments in the fission chamber.

10.1.2 Model for PFNS evaluation

In the energy range of first chance fission the PFNS are calculated as sum of two Watt distributions [147]:

$$S_i(E, E_n) = 0.5 \cdot \sum_{j=1,2} W_i(E_n, E_n, T_{ij}(E_n), \alpha) \tag{23}$$

where

$$T_{ij} = k_{ij} \cdot \sqrt{E^*} = k_{ij} \cdot \sqrt{E_r - TKE + B_n + E_n} \tag{24}$$

is the temperature parameters for nucleus "i" and light and heavy fragments (j=1,2) for nucleus "i", E_n is the incident neutron energy, α is the ratio of the total kinetic energy (TKE) at the moment of the neutron emission to the TKE value at full acceleration. Free parameter α was fitted to the PFNS experimental data. The ratio of "temperatures" for light and heavy fragment r=1.248 is the second semi-empirical fitting parameter, it slightly varies from one target nucleus to another.

Above emissive fission threshold the PFNS are described by the equation:

$$\begin{aligned} S(E, E_n) &= \nu^{-1}(E_n)(\nu_o(E_n) \cdot \beta_o(E_n) \cdot S_o(E, E_n) + \\ &\quad \nu_1(E_n) \cdot \beta_1(E_n) \cdot S_1(E, E_n) + \beta_1(E_n) \cdot P_{11}(E, E_n) + \\ &\quad \nu_2(E_n) \cdot \beta_2(E_n) \cdot S_2(E, E_n) + \\ &\quad \beta_2(E_n) \cdot [P_{21}(E, E_n) + P_{22}(E, E_n)] + ..., \end{aligned} \tag{25}$$

$$\int P_{ij}(E, E_n) dE = 1,$$

$$\nu(E_n) = \sum_{i=0} [\nu_i(E_n) + i) \cdot \beta_i(E_n)], \tag{26}$$

where subscript i =0, 1, 2... denotes i-th chance fission reaction of the $A+1$, A, $A-1$... nucleus after emission of i pre-fission neutrons, $\beta_i(E_n)$ is the i-th chance fission contribution to the observed fission cross section, $\nu_i(E_n)$ is the number of the prompt fission neutron for these nuclei, $S_i(E, E_n)$ is PFNS spectrum without pre-fission neutrons, $P_{ik}(E, E_n)$ is the spectrum of k-th pre-fission neutron for $i-$th chance fission. To calculate total PFNS, $\nu_i(E_n)$, $\beta_i(E_n)$ and T_{ij} values should be known.

The contributions of i-th chance fission reactions $\beta_i(E_n)$ to the observed fission cross sections, pre-fission neutron spectra $P_{ik}(E, E_n)$ and average neutron energy $<E_{ik}>$ were calculated as described in [148]. The pre-equilibrium pre-fission neutron emission was also taken into account.

The excitation energy U_i of the nucleus $A_i = A + 1 - i$ after emission of i-neutrons was calculated as:

$$U_i = E_{ri} + B_n + E_n - \sum_j (B_j + \langle E_{ij} \rangle), \tag{27}$$

where B_j is the neutron binding energy. This allows to estimate the excitation energy of fission fragments as $E^* = E_r + U - TKE$ and calculate the $T_{ij}(E_n)$ energy for each nucleus in the chain.

The systematic [149] for first chance fission reactions was used to estimate $\nu_i(E_n)$. In [149] the $\nu_i(E_n)$ values were evaluated for spontaneous and neutron-induced fission for a number of actinide nuclei within the experimental errors. We assumed that excitation energy U_i is brought into A_i nucleus with the reaction: $n + A_i - 1 \rightarrow fission$. Incident neutron energy in this hypothetical reaction equals to $U_i - B_{i-1}$. In this way the $\nu_i(E_n)$ functions for all isotopes in the chain $A+1, A, A-1$ were evaluated. In case of the ^{232}Th compound nucleus $\nu_i(E_n)$ was fitted to experimental data on ^{232}Th(n,f) reaction.

At the incident neutron energies $E_n \gtrsim$10 MeV there is a discrepancy between new experimental data [143, 146] and present model calculation. To reconcile calculated and measured PFNS data we assume [106] that CMS energy per one nucleon E_{v0} should be reduced according to the equation:

$$E_v = \alpha \cdot \alpha_1 \cdot E_{v0}, \tag{28}$$

α_1=1 for E_n<10 MeV and α_1=0.7 for E_n>12 MeV and linearly interpolated for 10<E_n<12 MeV. This correction was made either for non-emissive and emissive fission reactions.

10.1.3 Spectrum of pre-fission neutrons

To calculate neutron energy distributions of (n,$x$nf) and (n,xnγ), x = 1, 2, 3 reactions we use a simple Weisscopf-Ewing evaporation model taking into account fission and gamma-emission competition to neutron emission. The pre-equilibrium emission of first neutron is fixed by the description of high energy tail of ^{232}Th(n,2n) reaction cross section (see Fig. 114) and ^{232}Th(n,f) reaction cross section (Fig.111). This feature is parameterized within a conventional exciton model similar to that used in STAPRE [93] code, we get the main parameter of the exciton model, that is the matrix element $M^2 = 10/A^3$. Partial contributions of emissive and non-emissive fission reactions, shown on Fig. 113, were fitted. First neutron spectra for the ^{232}Th(n,nf) reaction is the sum of evaporated and pre-equilibrium emitted neutron contributions. Second and third neutron spectra for ^{232}Th(n,$x$nf) fission reactions are assumed to be evaporative. Pre-fission neutron spectrum, especially hard energy tail of ^{232}Th(n,nf) reaction, is sensitive to the description of fission probability of ^{232}Th compound nuclide near fission threshold (see below).

10.1.4 Comparison with experimental PFNS data

Calculated spectrum reproduce the experimental data by Boykov et. al. [143] for E_n =2.9 MeV incident neutron energy in the energy range of the secondary

neutrons from 0.2 MeV up to 10 MeV. Measured data [142] show strong increase at low energy that can not be reproduced with present model. At PFNS energy range higher than ∼3 MeV measured data contradict to present and previous evaluations of JENDL 3.2 [5] and ENDFB/-VI [6]. It seems that this results is overloaded by systematic errors. The data by Baba et. al.[10, 144] on PFNS were investigated in the limited energy range $E>E_n$. However, one may conclude that present model is compatible with these data also.

In the domain of emissive fission one can see the same tendency as in ^{238}U(n,f) reaction [106]. The low energy component due to pre-fission neutrons strongly influences on the PFNS shape. The calculated spectra are compatible with measured data [143, 145, 146] (Figs. 120, 121, 122). For ^{232}Th neutron-induced fission the contribution of pre-fission neutrons from (n,nf) reaction to the observed PFNS in fission neutron energy range $E_{th} \sim E_n - B_f$ is much more pronounced than in case of ^{238}U(n,f) reaction (see Figs.123, 124, 125), where PFNS for ^{232}Th(n,f) and ^{238}U(n,f) reactions are compared). Actually the energy dependence of PFNS for fission neutron energies $E_n \lesssim E_{th}$ resembles the shape of fission probability of ^{232}Th or ^{238}U nuclide, respectively. Figure 126 shows the comparison of data on fission probability of ^{232}Th, measured in ^{230}Th(t,pf) reaction [150] with calculated fission probability of ^{232}Th for the reaction ^{231}Th(n,f). The latter fission probability fits measured fission cross section of ^{232}Th(n,f) above emissive fission (n,nf) reaction threshold (see Fig. 111). The decreasing trend of ^{232}Th(n,f) above $E_n \gtrsim$7.5 MeV (see Fig. 111) is correlated with rapid increase of ^{232}Th(n,2n) reaction cross section. The contribution of ^{232}Th(n,nf) reaction cross section to the observed fission cross section ^{232}Th(n,f) is shown on Fig. 112. For $E_n \lesssim 10$ MeV contribution of (n,nf) reaction to the observed fission cross section in case of ^{232}Th target is higher than in case of ^{238}U target. The difference of fission probability measured in transfer (t,pf) reactions from that inferred from neutron-induced reactions for incident neutron energies $E_n \lesssim$1 MeV is well-known [151]. The straightforward comparison of fission probabilities on Fig. 126 ignores that difference. It is due to different compound spin populations in transfer and neutron-induced reactions. However in both cases sharp decrease of ^{232}Th nuclide fission probability above fission threshold up to ∼10 MeV excitations is observed. For incident neutron energy of 14.6 MeV it produces much stronger pick around ∼8 MeV energy of the secondary neutrons than in case of ^{238}U(n,f) reaction. One do not needs such strong energy dependence of ^{238}U fission probability to fit observed ^{238}U(n,f) reaction cross section. Consequently, fission probability for ^{238}U is of more flat shape above fission threshold (see Fig. 127).

10.2 Prompt fission neutron number ν

Prompt fission neutron number ν was calculated with the same model as PFNS, taking into account pre–fission neutron emission. A brief survey of measured data on ν is provided below.

10.2.1 ν measured data

Glendenin et. al. [152] have measured ν-values for E_n=2 - 14.7 MeV. They used ^{7}Li(p,n) and D(d,n) reactions for neutron generation below E_n =5 MeV and above E_n =5 MeV, respectively. The ν-values were calculated from fission fragments yields using conservation of mass rule. The ^{238}U(n,f) monitor reaction has been used to provide approximate fission rate. The fission yields were transformed to the absolute scale by normalization of measured mass distribution to 200-percent total yield. The thermal induced neutron fission of ^{235}U was used to check $\gamma-$ intensities of decay data. No data about fission cross sections and fission fragment yields are available.

Howe [153] has measured ν-values for E_n=1.084 - 48.9 MeV. Linac was used for neutron production, time-of-flight technique was applied to determine the incident neutron energy. Prompt fission neutrons were detected by a liquid scintillator located near the fission chambers with layers of ^{232}Th and ^{235}U, which was used as a standard. We renomalized the results of this work using modern values of ν for ^{235}U [6].

Conde and Holmberg [154] have measured ν-values for E_n=1.42 - 14.9 MeV. They used Van de Graaff neutron source and large liquid scintillator for detection of fission neutrons. The ^{232}Th ν-values were measured against to ^{252}Cf(sf) one (ν=3.775). We renomalized their data using modern value of ν=3.7661 [6]. The error given is statistical only.

Batchelor et. al. [155] have measured ν-values for E_n=3 - 7 MeV. The tritium and deuterium gas targets and pulsed proton accelerator were used as a neutron source. The prompt fission neutrons were detected by the well-shielded organic scintillator with pulse shape discrimination, the TOF technique was applied to reduce neutron background. The (n,p) elastic scattering cross section was used for incident neutron flux determination.

Mather et. al. [156] have measured ν-values for E_n=1.39 - 4.02 MeV. The authors used Van de Graaff neutron source and a large liquid scintillation counter loaded with gadolinium to detect fission neutrons. The ^{232}Th ν-values were measured relative to ^{252}Cf(sf) (ν=3.782$\pm$0.024).

Frehaut et. al. [157] have measured ν-values for E_n=2.37 - 14.74 MeV. The authors used the T(p,n) and D(d,n) reactions in gas target and tandem Van-de-Graaff accelerator as a neutron source. The time of flight techniques has been used in order to discriminate against fissions induced by secondary neutrons. The ^{232}Th ν-values were measured against to ^{252}Cf(sf) one (ν=3.732), a deposit of ^{252}Cf was present in the fission chamber.

Caruana et. al. [158] have measured ν-values for E_n=1.35 - 16.0 MeV. They used Van de Graaff accelerator neutron source (T(p,n) and T(d,n) reactions) and a large liquid scintillator tank for detection of fission neutrons. The ^{232}Th ν-values were measured against to ^{252}Cf(sf) one (ν=3.745).

Prokhorova and Smirenkin [159] have measured ν-values for E_n=1.48 - 3.27

MeV. The authors used a Van de Graaff accelerator neutron source (T(p,n) reaction) and assembly of 36 $^{10}BF_3$ counters for prompt fission neutrons detection. They measured the ratio $\nu(^{232}Th)/\nu(^{235}U)$.

Malinovskij et. al. [160] have measured ν-values for E_n=1.35 - 6.35 MeV. The authors used the T(p,n) and D(d,n) reactions on solid targets and Van de Graaff accelerator as a neutron source, the ionization chamber was used as a fission events detector. The energy uncertainty was ~30-40 keV for E_n ≤3.7 MeV and ~80 keV for E_n=5-6 MeV. The ^{232}Th ν-values were measured against ^{252}Cf(sf) (ν=3.733).

Kuzminov [161] has measured ν-values for E_n=2.3, 3.75 and 15.7 MeV. The author used the T(p,n) and T(d,n) reactions on solid targets and Van de Graaff accelerator as a neutron source and the assembly placed in paraffin moderator BF_3 filled proportional counters as a fission neutrons detector. He measured the ratio $\nu(^{232}Th)/\nu(^{235}U)$. We renomalized this data using modern values of $\nu(^{235}U)$ ([6]).

Smith [162] has measured ν-values for E_n=1.4 MeV. The ^{7}Li(p,n) reaction was used as a neutron source. They measured ^{232}Th ν-value relative to ^{238}U (ν=2.63).

Bondarenko et. al. [163] has measured ν-values for E_n=4 MeV. The authors used D(d,n) reaction in solid target mounted on Van de Graaff accelerator as a neutron source and the assembly placed in paraffin moderator BF_3 filled proportional counters as a fission neutrons detector. They measured the ratio $\nu(^{232}Th)/\nu(^{235}U)$.

In the following measurements the deuteron-tritium reaction in tritium-titanium target was used for the production of ~14 MeV neutrons.

Leroy [164] has measured ν-values for E_n=14.2 MeV. BF_3 counters surrounding the fission chamber were used to detect prompt fission neutrons in coincidence with fission fragments. ^{232}Th ν-value was measured relative to ^{238}U (ν=4.55±0.15 at 1.42 MeV). Feu [165] has measured ν-values for E_n=14.7 MeV. The information given is not enough for result renormalization. Johnstone [166]has measured ν-values for E_n=14.1 MeV. Coincidences between fission events in parallel plate fission chamber and neutron detected by BF_3 proportional counter were registered. The ^{235}U(n,f) reaction was used to calibrate detector. No information is given about monitor reaction cross section values.

All measured data are shown in Fig.128. We renomalized when necessary original data using modern ν values for ^{235}U and ^{238}U [6]. One can see that several old data sets [152, 159, 161] and all "one energy point" measurements [162], [163], [164], [165] and [166] are discrepant with other measurements. Other data are consistent with of recent measurements by Howe[153], Frehaut et. al.[157] and Malinovskij [160].

10.2.2 $\nu-$value analysis

To calculate the ν-value energy dependence for ^{232}Th up to 20 MeV we should know ν-values for ^{231}Th, ^{230}Th and ^{229}Th target nuclides, which contribute to the observed ν-value via emissive fission processes. We describe the energy dependence of ν-value for the first-chance fission of ^{232}Th(n,f) reaction [153] using two energy intervals - from thermal energy point to E_n =3.8 MeV and from E_n =3.8 to E_n =6 MeV. The slope of linear curve in first energy interval was chosen to describe experimental data in MeV-energy region together with thermal point ν-value (2.175) for ^{232}Th(n,f). Then we fixed ν-value (2.327) at 3.8 MeV and define the slope for second energy interval (E_n =3.8-6 MeV). This is shown as a solid line in Fig. 128. We applied the same approach in case of ^{229,230,231}Th isotopes also, but dependencies were shifted according to thermal values ν_{th}. Thermal point ν-values were taken from evaluation [149]. The complete set of first-chance ν-values for ^{229,230,231,232}Th target nuclides is shown in Table 8.

At incident neutron energies number of prompt fission neutron $\nu(E_n)$ was calculated as

$$\begin{aligned}\nu(E_n) &= \beta_o\nu_o(E_n) + \beta_1(1 + \nu_1(E_n - B_{nA} - \overline{E}_1)) + \\ &\quad \beta_2(2 + \nu_2(E_n - B_{nA} - B_{nA-1} - \overline{E}_1 - \overline{E}_2)).\end{aligned}$$

Here, $\nu_i(E_n)$ is a prompt fission neutron number for ith fissioning nucleus, B_{nA} - neutron binding energy for the A nucleus, $\overline{E}_i$- average energy of ith neutron. Fig. 129 shows the partial contributions to the observed prompt fission number up to E_n =20 MeV. Bump in $\nu-$value above (n,nf) reaction threshold is once again due to pre-fission neutrons emitted in ^{232}Th(n,nf) reaction.

Table 8
The evaluated first chance ν-values for ^{229,230,231,232}Th isotopes.

Target	ν(th)	ν(3.8 MeV)	ν(6 MeV)
^{229}Th	1.919	2.071	2.447
^{230}Th	2.080	2.232	2.608
^{231}Th	1.981	2.133	2.509
^{232}Th	2.175	2.327	2.703

10.3 Neutron emission spectra analysis

There are a number of discrepancies in neutron emission spectra of evaluated data files JENDL-3.2 and ENDF/B-VI with measured data, which might be attributed to the inconsistencies of partial inelastic cross sections for observed discrete levels [12]. Model calculations were performed to interpret neutron emission spectra from ^{232}Th, measured by Baba et. al. [10] for incident neutron energies E_n = 1.2, 2.03, 4.25, 6.1 and 14.05 MeV, by Baba et. al.[168] for E_n = 18 MeV

and by Miura et. al. [12] for E_n =2.6, 3.55 and 11.8 MeV. For incident neutron energies below emissive fission threshold we attribute these inconsistencies mainly to estimates of inelastic cross sections of first octupole band ($K^\pi = 0^-$) levels and levels of $\beta-$ and $\gamma-$vibration and anomalous rotational γ-bands ($K^\pi = 0^+, 2^+$).

The direct excitation of ground state rotational band levels 0^+, 2^+, 4^+ and 6^+ was estimated within rigid rotator model. To calculate the direct excitation cross sections for $\beta-$, $\gamma-$ vibration and anomalous rotational $\gamma-$band ($K^\pi = 0^+$, 2^+) as well as octupole (K^π=0^-) band levels a soft rotator model was employed. Due to high fission threshold in case of ^{232}Th+n interaction the main contribution to inelastic scattering at low incident neutron energies comes from the compound processes. With increase of incident energy the influence of discrete level excitation diminishes, while the role of continuum level excitation grows.

Figures 130-145 show the description of measured emission spectra for incident neutron energies below or slightly higher than emissive fission threshold and the comparison of present calculations with JENDL-3.2 evaluation [5]. Structures evident in measured emission spectra for incident neutron energies of ∼1.2 - 6.1 MeV could be correlated with excitation of discrete levels of various collective bands. The elastic and inelastic scattering to 2^+, $4^+$and 6^+ levels of ground state rotational band contribution were added to the inelastic scattered and prompt fission neutrons. They were broadened using model resolution function of Gaussian type with a constant resolution width. PNFS labels prompt neutron fission spectra. For the lowest incident neutron energy $E_n = 1.2$ MeV measured by Baba et. al. [10] emission spectra for the angles 60° and 120° are described almost equally good (see Figs. 130, 131). Arrows on figures show emitted neutron energy, corresponding to excitation of $\beta-$, $\gamma-$ vibration and anomalous rotational $\gamma-$bands as well as octupole band levels. One more bump due to excitation of levels of $\gamma-$ vibration band was predicted. For incident neutron energy $E_n = 2.03$ MeV present calculation reproduces angle-integrated data by Baba et. al. [10] (see Fig. 132). It is evident that excitation cross sections for $\beta-$, anomalous rotational γ- and octupole bands in JENDL-3.2 evaluation [5] is too high, while for the cross sections $\gamma-$ vibration band levels - too low. For higher incident neutron energy $E_n = 2.6$ MeV neutron emission spectra by Miura et. al. [12] for 120° are reproduced better than for 60° (see Figs. 133, 134, 135). Overestimation of discrete level excitation cross sections in JENDL-3.2 evaluation [5] is again evident (see Fig. 133). For incident neutron energy $E_n = 3.55$ MeV structures evident at lower energies disappeared, however present calculation reproduces bump in angle-integrated data Miura et. al. [12] (see Fig. 136) in the vicinity of broad elastic peak, while estimate of JENDL-3.2 seems to be distorted by overestimated excitation cross sections for $\beta-$, $\gamma-$ vibration and anomalous rotational $\gamma-$bands as well as octupole band levels. Emission spectra by Miura et. al. [12] for 60° and 120° are reproduced better than for 30° (see Figs. 137, 138, 139). This might be due to lowering contribution of elastic scattering at higher angles. For incident neutron energy $E_n = 4.25$ MeV present calculation reproduces angle-integrated

data by Baba et. al. [10] (see Figs. 140) better than JENDL-3.2 evaluation for secondary neutron energies corresponding to excitation on levels above 0.7 MeV. Emission spectra by Baba et. al. [10] for 120° are reproduced somewhat better than for 45° (see Figs. 141, 142), bump in the vicinity of elastic peak is still present. For incident neutron energy $E_n = 6.1$ MeV present calculation and JENDL-3.2 evaluation fail to reproduce angle-integrated data by Baba et. al. [10] (see Figs. 143). However, for forward scattering (θ =45°) emission spectra data are underestimated in the energy range of 2.5 - 5 MeV(see Figs. 144), while back-ward scattering (θ =120°) emission spectra data [10] are reproduced quite well (see Fig. 145). Summarizing, it is evident that neutron emission spectra data by Baba et. al. [10] and Miura et. al. [12] for backward angles are fitted. With increase of incident energy the influence of discrete level excitation diminishes, while the role of continuum level excitation grows.

To calculate neutron energy distributions of (n,xnγ) and (n,$x$nf), x = 1, 2, 3 reactions we use a simple Weisscopf-Ewing evaporation model taking into account fission and gamma-emission competition to neutron emission. The pre-equilibrium emission of first neutron is included. The hard component of neutron scattering spectra and high energy tail of ^{232}Th(n,2n) reaction cross section are interpreted as being due to the pre-equilibrium evaporation of neutrons. This feature is parameterized within a conventional exciton model, used in STAPRE [93] code. Pre-equilibrium contribution of first neutron spectrum was fixed by consistent description of (n,f) and (n,2n) reaction cross sections up to 20 MeV, we get the main parameter of the exciton model, that is the matrix element $M^2 = 10/A^3$. The charge conservation and transition rates renormalization were also employed. With all that in mind and in the STAPRE code [93] a pre-equilibrium emission fraction $q(E)$ leading to depletion of compound nucleus states population is obtained. It equals $\sim$0.035 at $E_n \sim 4$ MeV and increases up to $\sim$0.46 at $E_n \sim 20$ MeV. First neutron spectra for the (n,nx) reaction is the sum of evaporation and pre-equilibrium neutron contributions. Second and third neutron spectra are assumed to be evaporative.

On Figs. 146-154 data on neutron emission spectra at still higher incident neutron energies E_n =11.8 by Miura et. al. [12], E_n =14.05 by Baba et. al. [10] and E_n =18 MeV by Baba et. al. [168] are compared with present evaluation. "Bump" in case of 6.1-MeV spectra and flattening of secondary neutron spectrum of 11.8-, 14.05- and 18-MeV in the vicinity of elastic peak are supposed to be due to direct scattering on collective band levels. Figures 146 and 147 compare neutron emission spectra E_n =11.8 MeV for θ =60° and θ =120°, unfortunately the data description for backward emission is even worse, than for forward emission. Figures 148, 149 and 150 compare angle-integrated and measured for θ =45° and θ =120° neutron emission spectra for E_n =14.05 MeV, in this case the data description for backward emission is somewhat better, than for forward emission. The same conclusion could be made for neutron emission spectra for E_n = 18 MeV measured at θ =30°, θ =60° and θ =120° (see Figs.

151 - 154), though angle-integrated data also are reproduced quite well, while in JENDL-3.2 [5] neutron emission spectrum is overestimated in the energy range 5 - 10 MeV (see Fig. 151).

We have calculated 1st, 2nd and 3d neutron spectra for the (n,n'γ), (n,2n) and (n,3n) reactions. To compare with JENDL-3.2 [5] and ENDF/B-VI [6] evaluations, calculated spectra were summed up and tabular spectra for the (n,n'γ), (n,2n) and (n,3n) reactions were obtained. Figures 155-161 compare neutron spectra of (n,n'γ) reaction of JENDL-3.2 [5] and ENDF/B-VI [6] with present calculation. Average energies of first neutron spectra for JENDL-3.2 [5] and ENDF/B-VI [6] are compatible (see Table 9). Figures 162-167 show spectra of (n,2n) reaction for 8 - 20 MeV incident neutron energy, average energies of (n,2n) reaction neutron spectra of present and JENDL-3.2 [5] evaluation are compatible, while those of ENDF/B-VI [6] seem to be too low, especially at higher energies. Average energies of (n,3n) reaction neutron spectra of present and JENDL-3.2 [5] evaluation again are compatible, while those of ENDF/B-VI [6] are shifted to higher energies.

Table 9
Average energies of secondary neutron spectra

E_n,MeV	1st neutron average energy, MeV								
	(n,n')					(n,2n)	(n,n'f)	(n,3n)	(n,2n'f)
	Pres.	B-VI	J-3.2	BROND	JEF-2	Pres.	Pres.	Pres.	Present
3.0	0.65	0.68	0.73	0.76	0.80				
8.0	2.67	1.99	2.12	1.07	1.07	0.77	1.18		
14.0	9.26	9.24	8.52	1.08	1.08	3.01	2.61	0.92	0.49
20.0	15.3	15.2	14.5	1.08	1.08	9.78	2.88	2.58	2.18

	average neutron energy of (n,2n), MeV			average neutron energy of (n,3n), MeV		
E_n,MeV	Present	J-3.2	B-VI	Present	J-3.2	B-VI
8.0	0.56	0.54	0.51			
14.0	2.03	2.1	1.71	0.68	0.69	0.85
20.0	5.36	4.76	2.35	1.57	1.57	2.81

For incident neutron energy higher than emissive fission threshold, emissive neutron spectrum is deconvoluted, components of 1st, 2nd and 3d neutron spectra are provided, where applicable. Figures 172 and 173 show spectra of 1st neutron of the reaction (n,nx) and its partial contributions for (n,n'γ), (n,2n), (n,nf) (n,2nf), (n,3n) etc. reactions at incident neutron energy of 20 and 14 MeV. Partial neutron spectra are normalized to the contributions of appropriate cross sections to the (n,nx) reaction cross sections. Above $\sim$5.5 MeV energy of first emitted neutron, neutron spectrum is of pre-equilibrium nature only. Spectrum of

(n,n'γ) reaction actually is just hard energy tail of 'pre-equilibrium' component of first neutron spectrum. Spectrum of the first neutron of (n,2n) reaction is much softer, although 'pre-equilibrium' component still comprise major part of it. First neutron spectrum of (n,3n) reaction is actually of evaporative nature. First neutron spectrum of (n,nf) reaction has rather long pre-equilibrium high-energy tail. First neutron spectrum of (n,2nf) reaction, as those of (n,3n) and (n,4n) reactions, is of evaporative nature. Figures 174 and 175 show components of second neutron spectrum, they are evaporative, as those of third neutron spectra (see Fig. 176).

11 Conclusions

The statistical Hauser-Feshbach-Moldauer model calculation of neutron-induced reaction cross sections for ^{232}Th target nucleus shows the fair description of available data base on ^{232}Th+n total, elastic, fission, capture, inelastic scattering, (n,2n), prompt fission neutron spectra and neutron emission spectra. The same methods were applied previously for ^{238}U data analysis. Average resonance parameters were obtained which reproduce total, capture and inelastic cross sections from 4 keV up to 150 keV. Rigid rotator coupled channel model with present potential parameters gives fair description of differential inelastic scattering data for the ground state band levels. Collective bands structure of ^{232}Th is reproduced within soft deformable rotator model, which fairly describes differential inelastic scattering data for the $\beta-, \gamma-$vibration and anomalous rotation $\gamma-$band levels. It is shown that (n,n') inelastic data are compatible with statistical theory and soft rotator estimates of direct inelastic excitation of discrete levels. Double-differential neutron emission cross sections are shown to be consistent with present estimate of inelastic neutron scattering to the discrete and continuum levels. Radiative strength function alllows to describe capture cross section data in 4 keV - 5 MeV energy region. Consistent estimates of fission cross section data and prompt fission neutron spectra above emissive fission threshold give direct evidence of pre-fission (n,nf) reaction neutron influence on observed PFNS.

We assume that for incident neutron energy range of 4 keV - 20 MeV the reliability of present evaluated data file might be comparable with that of ^{238}U data file [106].

12 Acknowledgments

This work was supported by the International Science and Technology Center under the Project B-404 "Actinide Nuclear Data Evaluation", Funding Party Japan.

References

[1] Smith A.B., Guenter P.T., McKnight R.D., Proc. Int. Conf. Nuclear Data for Science and Technology, Antwerpen, Belgium, September 6-10, 1982, p. 39, K.H. Böckhoff, Ed., Holland (1982).

[2] Glazkov N.P., Atomnaya Energiya, 14, (4), 400, (1963).

[3] Ciarcia C.A., Couchell G.P., Egan J.J. et. al., Nucl. Sci. Eng., 91, 428 (1985).

[4] Dave J.H., Egan J.J., Couchell G.P. et. al., Nucl. Sci. Eng., 91, 187 (1985).

[5] JAERI-Data/Code, 98-006 (Part II), (Eds.) K. Shibata and T. Narita, (1998).

[6] Roussin R.W., Young P.G., McKnight R., Proc. Int. Conf. Nuclear Data for Science and Technology, Gatlinburg, USA, May 9-13, 1994, p. 692, J.K. Dickens (Ed.), ANS (1994).

[7] Blokhin A.V., Fursov B.I., Ignatyuk A.V. et. al., Proc. Int. Conf. Nuclear Data for Science and Technology, Gatlinburg, USA, May 9-13, 1994, p. 680, J.K. Dickens (Ed.), ANS (1994).

[8] Nordborg C., Salvatores M., Proc. Int. Conf. Nuclear Data for Science and Technology, Gatlinburg, USA, May 9-13, 1994, p. 680, J.K. Dickens (Ed.), ANS (1994).

[9] Kegel G.H.R., Aliyar A., Egan J.J. et. al., Bull. Am. Phys. Soc., Ser. II, 33(8), 1568, Paper AF 13 (1988).

[10] M.Baba, H.Wakabayashi, N.Ito, M.Ishikawa, K.Maeda, N.Hirakawa Report of INDC(NDS)-220, 1989, Report of INDC(Jap)-129/L (1989).

[11] Iwasaki T., Baba M., Hattori K. et al., Prog. NEANDC(J)-75, 1981.

[12] Miura T., Baba M., Ibaraki M. et. al. Proc. of the 1998 Symp. on Nuclear Data, November 19-20, 1999, JAERI, Tokai, Japan, JAERI-Conf., 99-002, p. 101 (1999).

[13] Olsen K.D. ORNL/TM-8056 , ENDF-319 (1982).

[14] Newman D.F., Leonard B.R., Jr. et. al., EPRINP-222, (1977).

[15] Maslov V.M.,Porodzinskij Yu.V. JAERI-Research 98-038, Japan (1998).

[16] Mughabghab S.F. Neutron Cross Section, vol.1, part B. z = 61-100. Academic Press, New York and London (1985).

[17] De Saussure G. and Macklin R.L., ORNL/TM-6161 (ENDF-255) (1977).

[18] Meadows J.W., Poenitz W.P., Smith A.B., et. al., ANL/NDM-35 (Feb., 1978).

[19] Kobayashi K., Fujita Y., Oosaki T. et. al., Nucl. Sci. Eng., 65, (2), 347 (1978).

[20] Grigor'ev Yu.V., Manturov G.N., Sinitsa V.V. et. al., FEI-2120 (1990).

[21] Grigor'ev Yu.V., Sinitsa V.V., Gundorin N.A., et. al., , VI International Seminar on Interaction of Neutrons with Nuclei, Dubna, Russia, May 13-16, 1998, p. 194 (1998).

[22] Poenitz W.P., Whalen J.F., Smith A.B., Nucl. Sci. Eng., 78, 333 (1981).

[23] Vertebnyj V.P., Kirilyuk A.L.,Gnidak N.L. et. al., 3rd All Union Conf. on Neutron Physics, 9-13 Jun, Kiev, 3, 151 (1975).

[24] Vertebnyj V.P., Murzin A.V.,. Pshenichnyj V.A. et. al., IAEA-410, 257 (1987).

[25] Hibdon C.T., Langsdorf A. Jr., ANL-5175, 7 (1954).

[26] Forman L., Schelberg A.D., Warren J.H. et. al. Phys. Rev. Lett., 27, 117 (1971).

[27] Macklin R.L.,Halperin J., Nucl. Sci. Eng., 64, 849, (1977).

[28] Macklin R.L., R.R. Winters Nucl. Sci. Eng., 78, 110 (1981).

[29] Poenitz W.P., Smith D.L., Report ANL-NDM-42 (1978).

[30] Moxon M.C., Report NP-17644, 1968 Moxon Thesis.

[31] Kobayashi K., Fujita Y., Yamamuro N., Nucl. Sci. Techn., 18, 823 (1981).

[32] Grigor'ev Yu.V., Kitaev V.Ya. et. al., ISINN-8, pp.68-74, Dubna (2000).

[33] Lindner M., Nagle R.J., Landrum J.H., Nucl. Sci. Eng., 59, 381 (1976).

[34] Linenberger G.A., Miskel J.A., Report LA-467 (1946).

[35] Miskel J.A., Marsh K.V., Lindner M., Nagle R.J., Phys. Rev., 128, 2717 (1962).

[36] Stupegia D.C., Smith A.B., Hamm K., Journ Inorg. Chem, 25, 627 (1963).

[37] Hanna R.C., Rose B., J. Nucl. Energy, 8, 197 (1959).

[38] Perkin J.L., O'Connor L.P., Coleman R.F., Proc. Phys. Society, 72, 505 (1958).

[39] Jain H.M., Anand R.P., Jhingan M.L., et. al., Int. Conf. on Neutron Physics and Nuclear Data for Reactors and Other Applied Purposes, AERE Harwell (1978).

[40] Anand R.P., Jain H.M., Kailas S., et. al., Annals of Nucl. Energy, 16(2), 87 (1989).

[41] Stavisskij Ju.Ja., Tolstikov V.A., Atomnaya Energiya, 10,(5), 508 (1961).

[42] Tolstikov V.A., IPPE Report No. 9913 (1998).

[43] Tolstikov V.A., Sherman L.E., Stavisskii Ju.Ja., Atomnaya Energiya, 15, (5), 414 (1963).

[44] Davletshin A.N., Teplov E.V., Tipunkov A.O. et. al.,Vopr. At. Nauki I Tekhn., ser.Jadernye Konstanty, 1, 41 (1992).

[45] Wisshak K., Voss F., Kaeppeler F., Nucl. Sci. Eng., 137, 183 (2001).

[46] Karamanis D., Petit M., et al., Nucl. Sci. Eng., 139, 282 (2001).

[47] Macklin R.L., Lazar N.H., Lyon W.S., Phys. Rev., 107, 504 (1957).

[48] Baldwin G.T., Knoll G.F., Nucl. Sci. Eng., 88, 123 (1984).

[49] Chaubey A.K., Sehgal M.L., Nucl. Phys., 66, 267 (1965).

[50] Chrien R.E.,Liou H.I.,Kenny M.J.et. al., Nucl. Sci. Eng., 72, 202 (1979).

[51] Belanova T.S., Atomnaya Energiya, 8, 549 (1960).

[52] Ivanov V.I., Markelov I.P., Tolstikov V.A., In: Proc. Int. Conf. Nuclear Data for Science and Technology, Kiev, 1, p.325 (1971).

[53] Belanova T.S.,Van'kov A.A.,Mikhaylus F.F. et. al., Atomnaya Energiya, 19, (1), 3 (1965).

[54] Zvonarev A.V., Kolyzhenkov V.A., Liforov V.G. et. al., VANT, ser. Yadernye Konstanty, 3, 67 (1990).

[55] Zagryadskiy V.A., Kraynev M.I., Markovskiy D.V. et. al., Report IAE-4480/8 (1987).

[56] Cullen D. PREPRO2000: 2000 ENDF/B Pre-Processing Codes.

[57] NJOY 94.10 Code System for Producing Pointwise and Multigroup Neutron and Photon Cross Sections from ENDF/B Data, RSIC Peripheral Shielding Routine Collection, ORNL, PSR-355, LANL, Los Alamos, New Mexico (1995).

[58] Porodzinskij Yu.V., Sukhovitskij E.Sh, Yadernaya Fizika, 59, 247 (1996).

[59] Haouat, Lachkar J., Lagrange Ch., et. al., Nucl. Sci. Eng. 81, 491 (1982).

[60] Foster D.G. jr, Glasgow D.W., Phys. Rev. C3, 576 (1971).

[61] Green L., Mitchell J.A., 71Knoxvill, 1, 325 (1971).

[62] Whalen J., Meadows J., ANL-7710, 12 (1971).

[63] Divadeenam M., Bilpuch E.G., Newson H.W., NCSAC-31, 218 (1970).

[64] Whalen J.F., Smith A.B., Nucl. Sci. Eng., 67, 129 (1978).

[65] Poenitz W.P., Whalen J.F., ANL-NDM-80 (1983).

[66] Coon J.H., Graves E.R., Barscall H.H., Phys. Rev., 88, 562 (1952).

[67] Walt M., Becker R.L., Okazaki A. et. al., Phys. Rev., 89, 1271 (1953).

[68] Manero F., Nuclear Physics, 65, 419 (1965).

[69] Deconninck G., Gonze A., Macq P. et. al., Journal de Physique, 22, 652 (1961).

[70] Tsukada K., Fuse T., Journal of the Physical Society of Japan, 15, 1994 (1960).

[71] Fasoli U., Toniolo D., Zago G. et. al., Nuclear Physics, Sect. A, 151, 369 (1970).

[72] Batchelor R., Gilboy W.B., Towle J.H., Nuclear Physics, 65, 236 (1965).

[73] Uttley C.A., Newstead C.M., Diment K.M., 66PARIS, 1, 165 (1966).

[74] Iwasaki T., Baba M., Hattori K. et. al., NEANDC(J)-75 (1981).

[75] Fillippov V.V., Nikolaev M.N., Atomnaya Energya, 15, (7), 493 (1963).

[76] Averchenkov V.Y., Veritennikov A.I., Soviet Physics Neutron, 191 (1961).

[77] Leroy J.L., Berthelot F.C., Pomelas E., Journal de Physique, 24, 826 (1963).

[78] Cox S.A. and Dowling E.E., ANL-7935 (1972).

[79] Walt M. and Barshall H.H., Phys. Rev. 93,1062 (1954).

[80] Hudson C.I. JR, Walker W.S., Berko S., Phys. Rev., 128, 1271 (1962).

[81] Batchelor R., Gilboy W.B., Towle J.H., Nuclear Physics, 65, 236 (1965).

[82] Smith W., Phys. Rev.,126, 718 (1962).

[83] Koester L., Knopf K., Waschkowski W., NEANDC(E)-252U,(5), 46 (1984).

[84] Kazakova L.Ya., Kolesov V.E., Popov V.I. et. al., EANDC-50 (1965).

[85] Popov V.I., Atomnaya Energya, 3, 498 (1957).

[86] Haouat G. et. al., NEANDC(E)-196 (1978).

[87] Smith A.B., Chiba S., Annals of Nuclear Energy, 23, 459 (1996).

[88] Buccino S.C. , Hollandsworth C.E., Bevington P.R., Zeitschrift für Physik, Section A,196,103 (1966).

[89] Schreder G., Hammer J.W., Grum W. et. al.,Int. Conf. on Nuclear Data for Science and Technol., Mito, Japan, 30 May - 3 Jun 1988 (1988).

[90] Hansen L.F., Pohl B.A., Wong C. et. al.,Phys. Rev., Part C, 34, 6, 2075 (1986).

[91] Dukarevich Ju.V., Djumin A.N.,Zhurnal Eksperimental'noi i Teoret. Fiziki 44,(1),130 (1961).

[92] Tepel J.W., Hoffman H.M., Weidenmuller H.A. Phys. Lett. 49, 1 (1974).

[93] Uhl M., Strohmaier B., IRK-76/01, IRK, Vienna (1976).

[94] Ignatjuk A.V., Maslov V.M., Proc. Int. Symp. Nuclear Data Evaluation Methodology, Brookhaven,USA, October 12-16, 1992, p.440, World Scientific (1993).

[95] Maslov V.M., Kikuchi Y., JAERI-Research 96-030 (1996).

[96] Moldauer P.A., Phys. Rev., C11, 426 (1975).

[97] Ignatjuk A.V., Istekov K.K., Smirenkin G.N. Sov. J. Nucl. Phys. 29, 450 (1979).

[98] Howard W.M., Möller P. Atomic Data and Nuclear Data Tables, 25, 219 (1980).

[99] Maslov V.M., Zeit. Phys. A, Hadrons & Nuclei, 347, 211 (1994).

[100] Fu C. Nucl. Sci. Eng. 86, 344 (1984).

[101] Chan D.W., Sheldon E. Phys. Rev. 26C, 861 (1982).

[102] Shmorak M., Nucl. Data Sheets, 36, 367 (1982).

[103] Myers W.O., Swiatecky W.J., Ark. Fyzik, 36, 243 (1967).

[104] Bjornholm S., Lynn J.E. Rev. Mod. Phys., 52, 725 (1980).

[105] Goswani G.C., Egan J.J., Kegel G.H.R. et. al., Nucl. Sci. Eng., 100, 48 (1988).

[106] Maslov V.M., Porodzinskij Yu.V., Baba M., Hasegawa A., Kornilov N.V., Kagalenko A.B., submitted for publication.

[107] Plompen A.J.M., Goddio C., Maslov V.M., Porodzinskij Yu.V. Proc. VIII International Seminar on Interaction of Neutrons with Nuclei, Dubna, Russia, May 17-20, 2000, p. 153, 2000.

[108] Fujita Y., Ohsawa T., Bugger R.M. et. al.,J. of Nucl. Sci. and Tech., 20, 983 (1983).

[109] Zhuchko V.E., Ostapenko Yu.B., Smirenkin G.N., Yadernaya Fizika, 28, 1978 (1170).

[110] Maslov V.M., Proc. Ninth Int. Symp. Capture Gamma-Ray Spectroscopy and Related Topics, Budapest, Hungary, October 8-12, 1996.

[111] Stavinskij V.S., Shaker M.O., Nucl. Phys., 62, 667 (1965).

[112] Maslov V.M. and Kikuchi Y., Nucl. Sci. Eng., 124, 492 (1996).

[113] Bolsterli M., Fiset E.O., Nucl. Sci. Eng., 63, 250 (1977)..,

[114] Nix J.R., Norton J.L. Phys.Rev., C 5, 1050 (1972).

[115] Behrens J.W., Browne J.C., Ables E., Nucl. Sci. Eng., 81, 512 (1982).

[116] Auchampaugh G.F., Plattard S., Hill N.W. et. al. Phys. Rev., Part C, 24, 505 (1981).

[117] Williams J.H., LA-520 (1946).

[118] Fabry Y A., Garlea I., IAEA-208, 2, 291 (1978).

[119] Kanda K.,Sato O.,Yoshida K. et. al. JAERI-M-85-035, 220 (1985).

[120] Kanda K., Imaruoka H.,Yoshida K. et. al. Radiation Effects, 93, 233 (1986).

[121] Meadows J.W., Int.Conf. on Nuclear Cross Sections for Technology, Knoxville, Tennessee, 22-26 Oct 1979, 479 (1979).

[122] Goverdovskij A.A., Gordjushin A.K., Kuzminov B.D.et. al., Atomnaya Energiya 60, (6), 416 (1986).

[123] Goverdovskij A.A., Gordjushin A.K., Kuzminov B.D.et. al., Atomnaya Energya 61, 380 (1986).

[124] Nordborg C., Conde H., Stroemberg L-G., 78HARWELL, 910 (1978).

[125] Fursov B.I., Baranov E.YU., Klemyshev M.P. et.al., Atomnaya Energya 71,(4),320 (1991).

[126] Zvonarev A.V., Kolyzhenkov V.A., Liforov V.G.et. al., Yadernye Konstanty 3, 67 (1990).

[127] Tewes H.A., Caretto A.A., Miller A.E. et. al., Report UCRL-6028-T (1960).

[128] Butler J.P., Santry D.C., Canadian Journal of Chemistry, 39, 89 (1961).

[129] Cochran D.R.F., Henkel R.L., Preprint WASH-1013, p.34 (1958).

[130] Raics P., Daroczy S., Csikai J. et. al., Phys. Rev/C, 32, 1, p.87, 1985; Report INDC(HUN)-029/L, IAEA (1990).

[131] Prestwood R.J., Bayhurst B.P., Phys. Rev., 121, 1438, 1961

[132] Smith, B. Am. Phys. Soc. 2, 196, (1957)

[133] Karius H., Ackermann A., Scobel W., J. of Physics part G (Nuclear Physics), 5, (5), 715 (1979).

[134] Perkin J.L., Coleman R.F., Nuclear Energy, 14, 69 (1961).

[135] Phillips J.A., Report of AERE-NP/R-2033 (1956).

[136] Chatani H., Kimura I., Annals of Nuclear Energy, 19, (8), 477 (1992).

[137] Zysin Yu.A., Kovrizhnykh A.A., Lbov A.A. et. al., Journal of Atomic Energy, 8, 360 (1960).

[138] Filatenkov A.A., Chuvaev S.V., Aksenov V.N. et. al., Report of INDC(CCP)-402 (1997).

[139] Batchelor R.,Gilboy W.B.,Towle J.H., Nuclear Physics, 65, 236 (1965).

[140] Raics P. Th(n,2n) cross-section investigation near 14 MeV neutron energy. Debrecen (1978).

[141] Segev M., Ann. Nucl. Energy, 5, 239 (1978).

[142] Sukhikh S.E., Lovchikova G.N., Vinogradov V.A., Zhuravlev B.V., Poljakov A.V., Sal'nikov O.A. Yadernye Konstanty, 3, 34 (1986).

[143] Boykov G.S., Dmitriev V.D., Kudyaev G.A., Ostapenko Yu.B., Svirin M.I., Smirenkin G.N. Yadernaya Fizika, 53, 628 (1993).

[144] Miura T., Win T., Baba M. et. al.l, Proc. of the 1999 Symp. on Nuclear Data, November 18-19, 1999, JAERI, Tokai, Japan, JAERI-Conf., 2000-005, p. 137.

[145] Lovchikova G.N. et. al.l, ^{232}Th PFNS at neutron energy 7 MeV, Meeting on PFNS properties. Mito (1988).

[146] Lovchikova G.N. et. al.l, XIV International Workshop on Nuclear Fission Physics, October 1998, Obninsk, p.72 (2000).

[147] Kornilov N.V., Kagalenko A.B., Hambsch F.-J. Physics of Atomic Nuclei 62, 173 (1999).

[148] Kornilov N.V., Kagalenko A.B., Maslov V.M. et. al. In: Proceedings of Trieste Conference on Nuclear Data for Science and Techology, Trieste, v. 1, p.940 (1997).

[149] Malinovskij V.V., VANT, Nuclear Data, 2, 25 (1987).

[150] Back B.B., Hansen O., Britt et al. Phys. Rev. 9, 1924 (1974).

[151] Arthur E.D., Trans. Am. Nucl. Soc., 1984 Annual Meeting, New Orleans, June 3-7, 1984, Vol. 46, TNSAO, p.759.

[152] Glendenin L.E., Gindler J.E., Ahmad I.,Henderson D.J., Meadows J.W. Phys. Rev. C, 22, 52 (1980).

[153] Howe R.E. Nucl. Sci. Eng., 86, 157 (1984).

[154] Conde H., Holmberg M. J. AF, 29, 33 (1965).

[155] Batchelor R., Gilboy W.B., Towle J.H. Nucl. Phys., 65, 236 (1965).

[156] Mather D.S., Fieldhouse P., Moat A. Nucl. Phys., 66, 149 (1965).

[157] Frehaut J., Bois R., Bertin A. Report of CEA-N-2196, 1981.

[158] Caruana J., Boldeman J.W., Walsh R.L. Nucl. Phys. A, 285, 217 (1977).

[159] Prokhorova L.I., Smirenkin G.N. Sov. Nucl. Phys, 7, 579 (1968).

[160] Malinovskyj V.V., Vorobjova V.G., Kuzminov B.D., Piksajkin V.M., Semjonova N.N., Valjavkin V.S., Solovjov S.M. Atomnaya Energiya, 54, 209 (1983).

[161] Kuzminov B.D. Sov. Nucl. Phys, 4, 241 (1961).

[162] Smith A.B., Nobles R.G., Cox S.A. Phys. Rev., 115, 1242 (1959).

[163] Bondarenko I.I., Kuzminov B.D., Kutsayeva L.S., Prokhorova L.I., Smirenkin G.N. Second UN Conf. on the Peaceful Uses of Atomic Energy, Geneva, 15, 353, 1958, Report 2187.

[164] Leroy J. Journ. de Physique (J. Phys. Radium), 21, 617 (1960.).

[165] Feu C. Journ. de Physique, 38, 273 (1977).

[166] Johnstone I. Report of AERE-NP/R-1912 (1956).

[167] Malinovskyj V.V. VANT, Nuclear Data, 1, 35 (1991).

[168] Baba M., Matsuyama S., Ito T., et. al. Proc. Int. Conf. Nucl. Data for Sci. and Technology, Julich, Germany, May 13-19, 1991, 349 (1991).

13 Figure captions

Fig. 1 Cumulative sum of levels of ^{232}Th.
Fig. 2 Cumulative sum of reduced neutron width of ^{232}Th.
Fig. 3 Level spacing distribution of ^{232}Th.
Fig. 4 Reduced neutron width distribution of ^{232}Th.
Fig. 5 Cumulative distribution of reduced neutron widths of ^{232}Th.
Fig. 6 Total cross section of ^{232}Th.
Fig. 7 Capture cross section of ^{232}Th.
Fig. 8 Inelastic scattering cross section of ^{232}Th.
Fig. 9 Elastic scattering cross section of ^{232}Th.
Fig. 10 Average reduced neutron width of ^{232}Th, l =0, J =1/2.
Fig. 11 Average reduced neutron width of ^{232}Th, l =1, J =1/2.
Fig. 12 Average reduced neutron width of ^{232}Th, l =1, J =3/2.
Fig. 13 Average reduced neutron width of ^{232}Th, l =2, J =3/2.
Fig. 14 Average reduced neutron width of ^{232}Th, l =2, J =5/2.
Fig. 15 Total cross section of ^{232}Th.
Fig. 16 Total cross section of ^{232}Th.
Fig. 17 Total cross section of ^{232}Th.
Fig. 18 Reaction cross section of ^{232}Th.
Fig. 19 Elastic scattering cross section of ^{232}Th.
Fig. 20 Elastic scattering cross section of ^{232}Th
Fig. 21 Differential elastic scattering cross section at 1.5 MeV.
Fig. 22 Differential scattering cross section to 2^+ level at 1.5 MeV.
Fig. 23 Differential scattering cross section to 4^+ level at 1.5 MeV.
Fig. 24 Differential scattering cross section at 2.4 MeV.
Fig. 25 Differential elastic scattering cross section at 2.5 MeV.
Fig. 26 Differential scattering cross section to 2^+ level at 2.5 MeV.
Fig. 27 Differential scattering cross section to 4^+ level at 2.5 MeV.
Fig. 28 Differential scattering cross section at 2.6 MeV.
Fig. 29 Differential scattering cross section at 3.4 MeV.
Fig. 30 Differential elastic scattering cross section at 3.4 MeV.
Fig. 31 Differential scattering cross section to 2^+ level at 3.4 MeV.
Fig. 32 Differential scattering cross section to 4^+ level at 3.4 MeV.
Fig. 33 Differential scattering cross section at 3.6 MeV.
Fig. 34 Differential scattering cross section at 4.5 MeV.
Fig. 35 Differential scattering cross section at 5.0 MeV.
Fig. 36 Differential scattering cross section at 5.5 MeV.
Fig. 37 Differential scattering cross section at 5.9 MeV.
Fig. 38 Differential scattering cross section at 6.5 MeV.

Fig. 71 Cross section of ^{232}Th: 0.741 MeV, 2^+ and 0.7744 MeV, 3^- levels excitation.
Fig. 72 Inelastic differential scattering cross section to 0.7853 MeV, 2^+ level at 1.2 MeV.
Fig. 73 Inelastic differential scattering cross section to 0.7853 MeV, 2^+ level at 1.5 MeV.
Fig. 74 Cross section of ^{232}Th: 0.7853 MeV, 2^+ level excitation.
Fig. 75 Inelastic differential scattering cross section to 0.8296 MeV, 3^+ level at 1.2 MeV.
Fig. 76 Inelastic differential scattering cross section to 0.8296 MeV, 3^+ level at 1.5 MeV.
Fig. 77 Inelastic differential scattering cross section to 0.8296 MeV, 3^+ level at 2.0 MeV.
Fig. 78 Cross section of ^{232}Th: 0.8296 MeV, 3^+ level excitation.
Fig. 79 Inelastic differential scattering cross section to 0.774 -0.830 MeV levels at 2.4 MeV.
Fig. 80 Inelastic differential scattering cross section to 0.774 -0.830 MeV levels at 2.8 MeV.
Fig. 81 Cross section of 0.774 -0.830 MeV levels excitation.
Fig. 82 Cross section of ^{232}Th: 0.873 MeV, 4^+.
Fig. 83 Cross section of ^{232}Th: 0.8836 MeV, $5^-$and 0.8901 MeV, 4^+ levels excitation.
Fig. 84 Inelastic differential scattering cross section to 0.873 -0.890 MeV levels at 2.4 MeV.
Fig. 85 Inelastic differential scattering cross section to 0.873 -0.890 MeV levels at 2.8 MeV.
Fig. 86 Cross section of 0.873 -0.890 MeV levels excitation.
Fig. 87 Inelastic differential scattering cross section to 0.9604 MeV, 5^+ level at 2.0 MeV.
Fig. 88 Inelastic differential scattering cross section to 0.9604 MeV, 5^+ level at 2.4 MeV.
Fig. 89 Inelastic differential scattering cross section to 0.9604 MeV, 5^+ level at 2.8 MeV.
Fig. 90 Cross section of ^{232}Th: 0.9604 MeV, 5^+ level excitation.
Fig. 91 Cross section of ^{232}Th: 1.0536 MeV, 2^+ level excitation.
Fig. 92 Inelastic differential scattering cross section to 0.7 - 1.05 MeV levels at 3.55 MeV.
Fig. 93 Inelastic differential scattering cross section to 0.7 - 0.9 MeV levels at 2.4 MeV.
Fig. 94 Cross section of ^{232}Th: 1.0729 MeV, 2^+ level excitation.
Fig. 95 Cross section of ^{232}Th: 1.0787 MeV 0^+ level excitation.
Fig. 96 Cross section of ^{232}Th: 1.0729 MeV, 2^+ + 1.0775 MeV, 1^- and 1.0787 MeV 0^+ levels excitation.

Fig. 133 Neutron emission spectrum of ^{232}Th for incident neutron energy 2.6 MeV.
Fig. 134 Neutron emission spectrum of ^{232}Th for incident neutron energy 2.6 MeV.
Fig. 135 Neutron emission spectrum of ^{232}Th for incident neutron energy 2.6 MeV.
Fig. 136 Neutron emission spectrum of ^{232}Th for incident neutron energy 3.55 MeV.
Fig. 137 Neutron emission spectrum of ^{232}Th for incident neutron energy 3.55 MeV.
Fig. 138 Neutron emission spectrum of ^{232}Th for incident neutron energy 3.55 MeV.
Fig. 139 Neutron emission spectrum of ^{232}Th for incident neutron energy 3.55 MeV.
Fig. 140 Neutron emission spectrum of ^{232}Th for incident neutron energy 4.25 MeV.
Fig. 141 Neutron emission spectrum of ^{232}Th for incident neutron energy 4.25 MeV.
Fig. 142 Neutron emission spectrum of ^{232}Th for incident neutron energy 4.25 MeV.
Fig. 143 Neutron emission spectrum of ^{232}Th for incident neutron energy 6.1 MeV.
Fig. 144 Neutron emission spectrum of ^{232}Th for incident neutron energy 6.1 MeV.
Fig. 145 Neutron emission spectrum of ^{232}Th for incident neutron energy 6.1 MeV.
Fig. 146 Neutron emission spectrum of ^{232}Th for incident neutron energy 11.8 MeV.
Fig. 147 Neutron emission spectrum of ^{232}Th for incident neutron energy 11.8 MeV.
Fig. 148 Neutron emission spectrum of ^{232}Th for incident neutron energy 14.05 MeV.
Fig. 149 Neutron emission spectrum of ^{232}Th for incident neutron energy 14.05 MeV.
Fig. 150 Neutron emission spectrum of ^{232}Th for incident neutron energy 14.05 MeV.
Fig. 151 Neutron emission spectrum of ^{232}Th for incident neutron energy 18 MeV.
Fig. 152 Neutron emission spectrum of ^{232}Th for incident neutron energy 18 MeV.
Fig. 153 Neutron emission spectrum of ^{232}Th for incident neutron energy 18 MeV.
Fig. 154 Neutron emission spectrum of ^{232}Th for incident neutron energy 18

MeV.
Fig. 155 Comparison of (n,n'γ) reaction neutron spectra of ^{232}Th for incident neutron energy 2MeV.
Fig. 156 Comparison of (n,n'γ) reaction neutron spectra of ^{232}Th for incident neutron energy 4 MeV.
Fig. 157 Comparison of (n,n'γ) reaction neutron spectra of ^{232}Th for incident neutron energy 6 MeV.
Fig. 158 Comparison of (n,n'γ) reaction neutron spectra of ^{232}Th for incident neutron energy 8 MeV.
Fig. 159 Comparison of (n,n'γ) reaction neutron spectra of ^{232}Th for incident neutron energy 12 MeV.
Fig. 160 Comparison of (n,n'γ) reaction neutron spectra of ^{232}Th for incident neutron energy 14 MeV.
Fig. 161 Comparison of (n,n'γ) reaction neutron spectra of ^{232}Th for incident neutron energy 20 MeV.
Fig. 162 Comparison of (n,2n) reaction neutron spectra of ^{232}Th for incident neutron energy 8 MeV.
Fig. 163 Comparison of (n,2n) reaction neutron spectra of ^{232}Th for incident neutron energy 10 MeV.
Fig. 164 Comparison of (n,2n) reaction neutron spectra of ^{232}Th for incident neutron energy 12 MeV.
Fig. 165 Comparison of (n,2n) reaction neutron spectra of ^{232}Th for incident neutron energy 14 MeV.
Fig. 166 Comparison of (n,2n) reaction neutron spectra of ^{232}Th for incident neutron energy 16 MeV.
Fig. 167 Comparison of (n,2n) reaction neutron spectra of ^{232}Th for incident neutron energy 20 MeV.
Fig. 168 Comparison of (n,3n) reaction neutron spectra of ^{232}Th for incident neutron energy 12 MeV.
Fig. 169 Comparison of (n,3n) reaction neutron spectra of ^{232}Th for incident neutron energy 14 MeV.
Fig. 170 Comparison of (n,3n) reaction neutron spectra of ^{232}Th for incident neutron energy 16 MeV.
Fig. 171 Comparison of (n,3n) reaction neutron spectra of ^{232}Th for incident neutron energy 20 MeV.
Fig. 172 Components of first neutron spectrum of ^{232}Th for incident neutron energy 20 MeV.
Fig. 173 Components of first neutron spectrum of ^{232}Th for incident neutron energy 14 MeV.
Fig. 174 Components of second neutron spectrum of ^{232}Th for incident neutron energy 20 MeV.
Fig. 175 Components of second neutron spectrum of ^{232}Th for incident neutron energy 14 MeV.

Fig. 176 Components of third neutron spectrum of ^{232}Th for incident neutron energy 20 MeV.

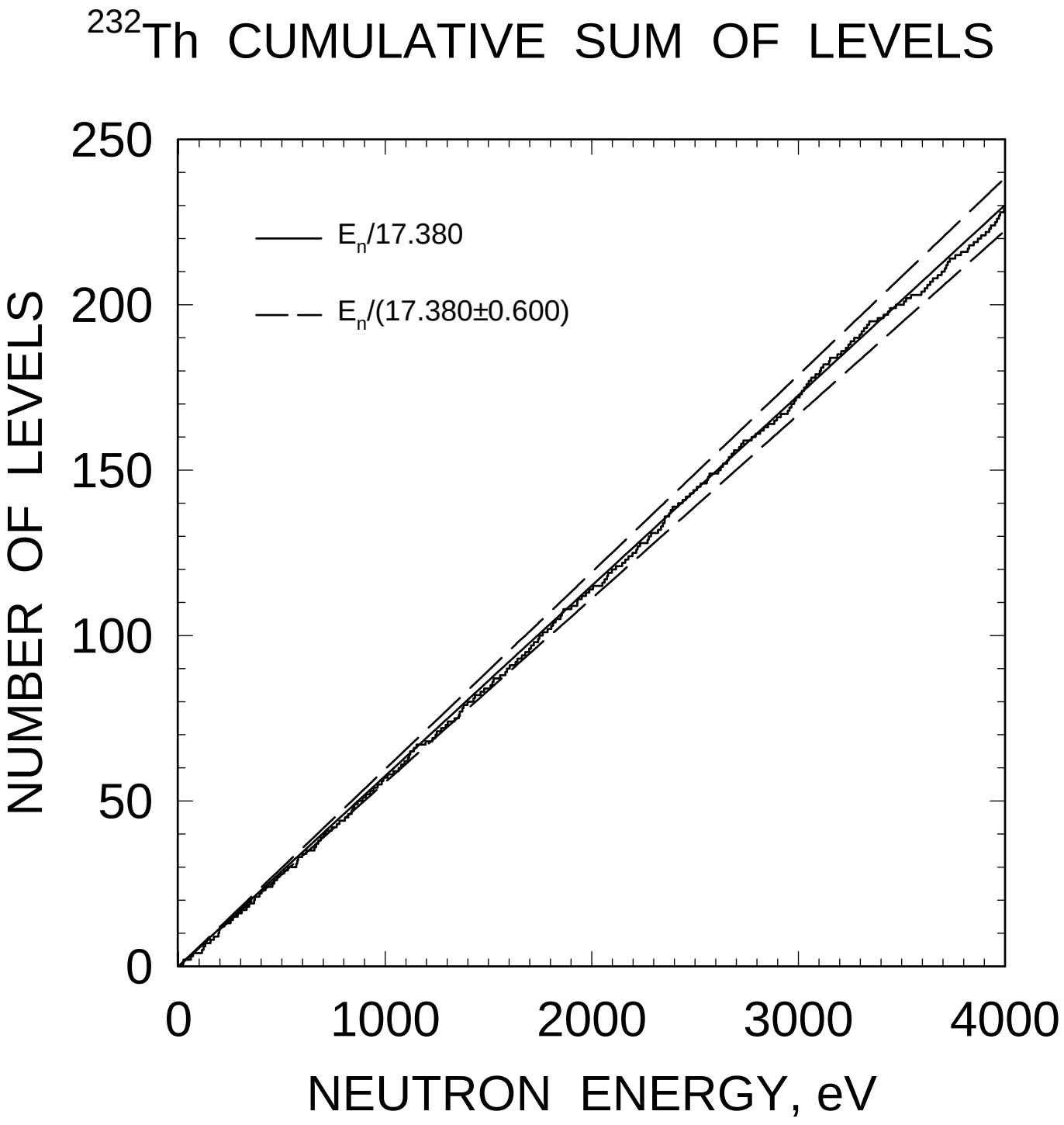
232Th CUMULATIVE SUM OF LEVELS
250
200
150
100
50
0
NUMBER OF LEVELS
En/17.380
En/(17.380±0.600)
0
1000
2000
3000
4000
NEUTRON ENERGY, eV

FIG. 1

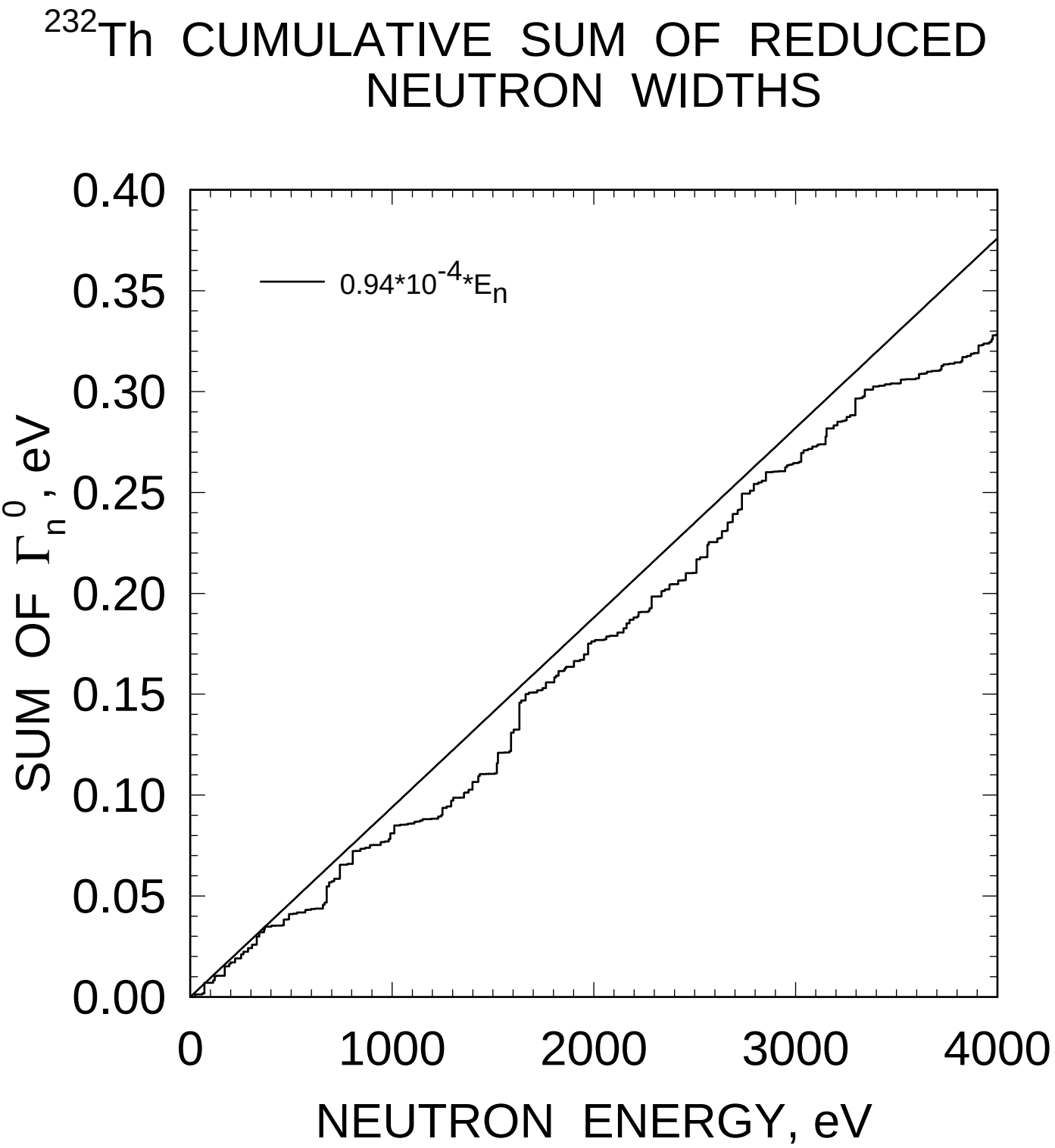
232Th CUMULATIVE SUM OF REDUCED NEUTRON WIDTHS
0.94*10-4*En
SUM OF Γn0, eV
0.40
0.35
0.30
0.25
0.20
0.15
0.10
0.05
0.00
0
1000
2000
3000
4000
NEUTRON ENERGY, eV

FIG. 2

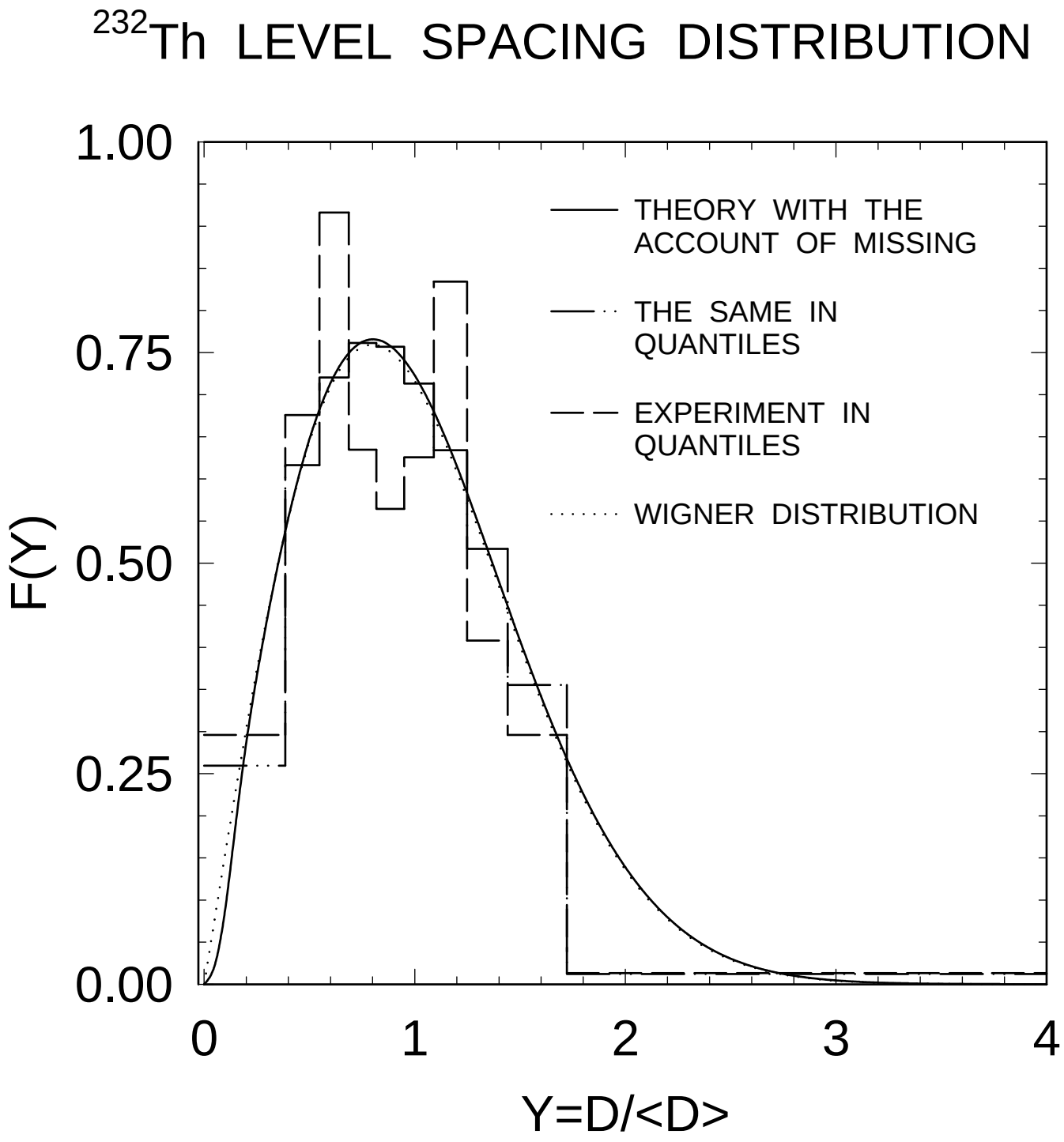
232Th LEVEL SPACING DISTRIBUTION
1.00
0.75
0.50
0.25
0.00
F(Y)
0
1
2
3
4
Y=D/<D>
THEORY WITH THE ACCOUNT OF MISSING
THE SAME IN QUANTILES
EXPERIMENT IN QUANTILES
WIGNER DISTRIBUTION

FIG. 3

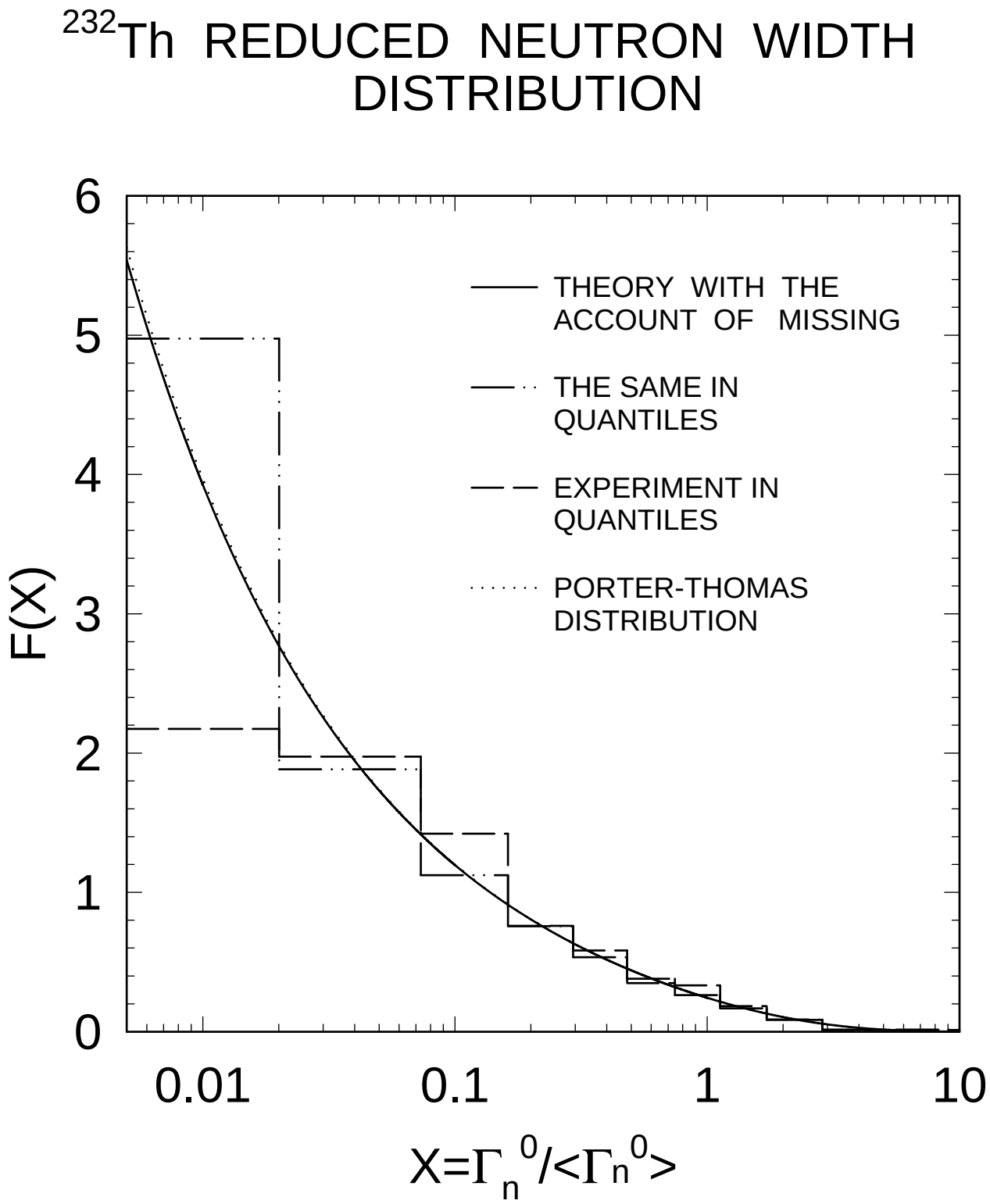
232Th REDUCED NEUTRON WIDTH DISTRIBUTION
THEORY WITH THE ACCOUNT OF MISSING
THE SAME IN QUANTILES
EXPERIMENT IN QUANTILES
PORTER-THOMAS DISTRIBUTION
F(X)
0
1
2
3
4
5
6
0.01
0.1
1
10
X=Γn0/<Γn0>

FIG. 4

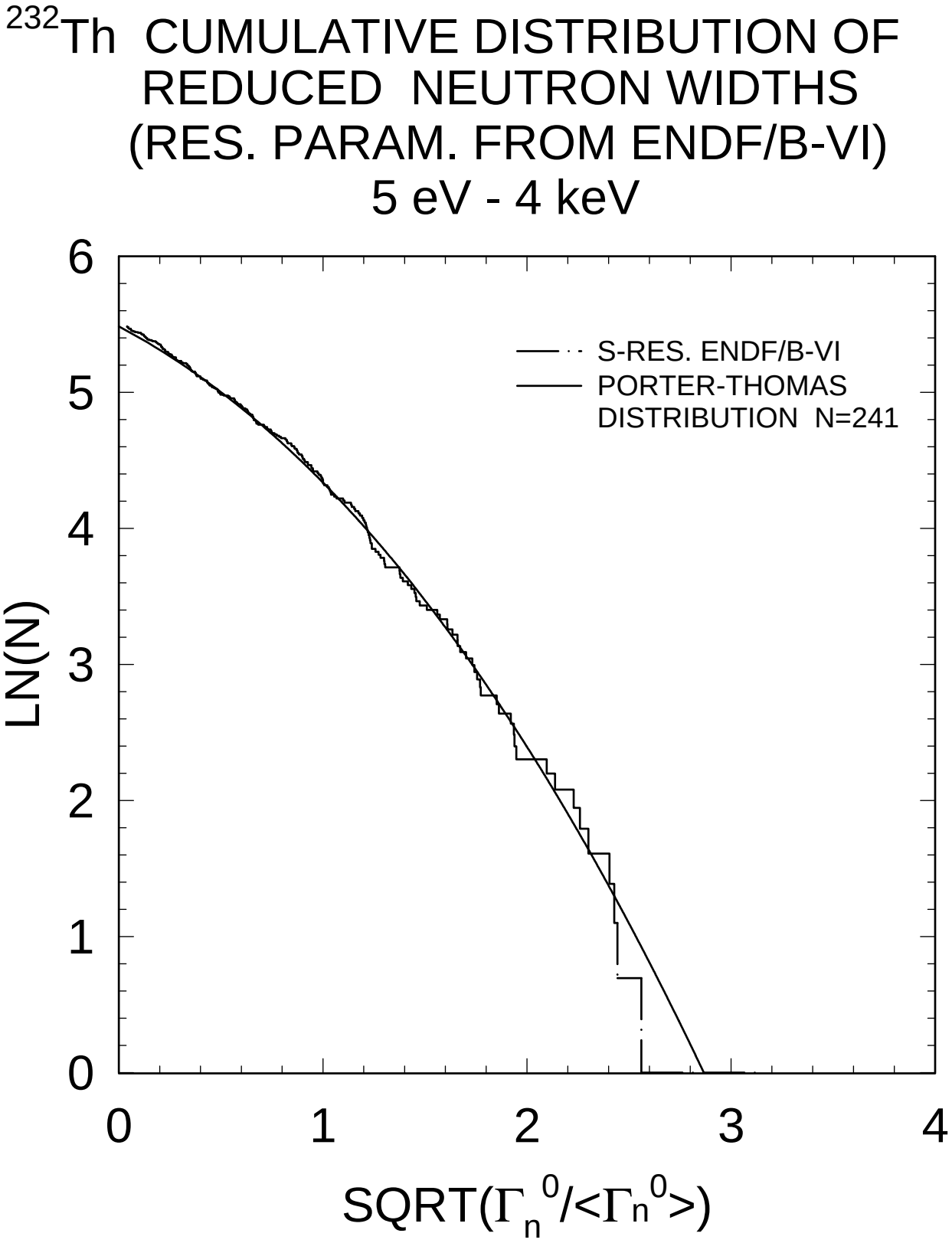
232Th CUMULATIVE DISTRIBUTION OF
REDUCED NEUTRON WIDTHS
(RES. PARAM. FROM ENDF/B-VI)
5 eV - 4 keV
S-RES. ENDF/B-VI
PORTER-THOMAS
DISTRIBUTION N=241
LN(N)
SQRT(Γn0/<Γn0>)
0
1
2
3
4
5
6

FIG. 5

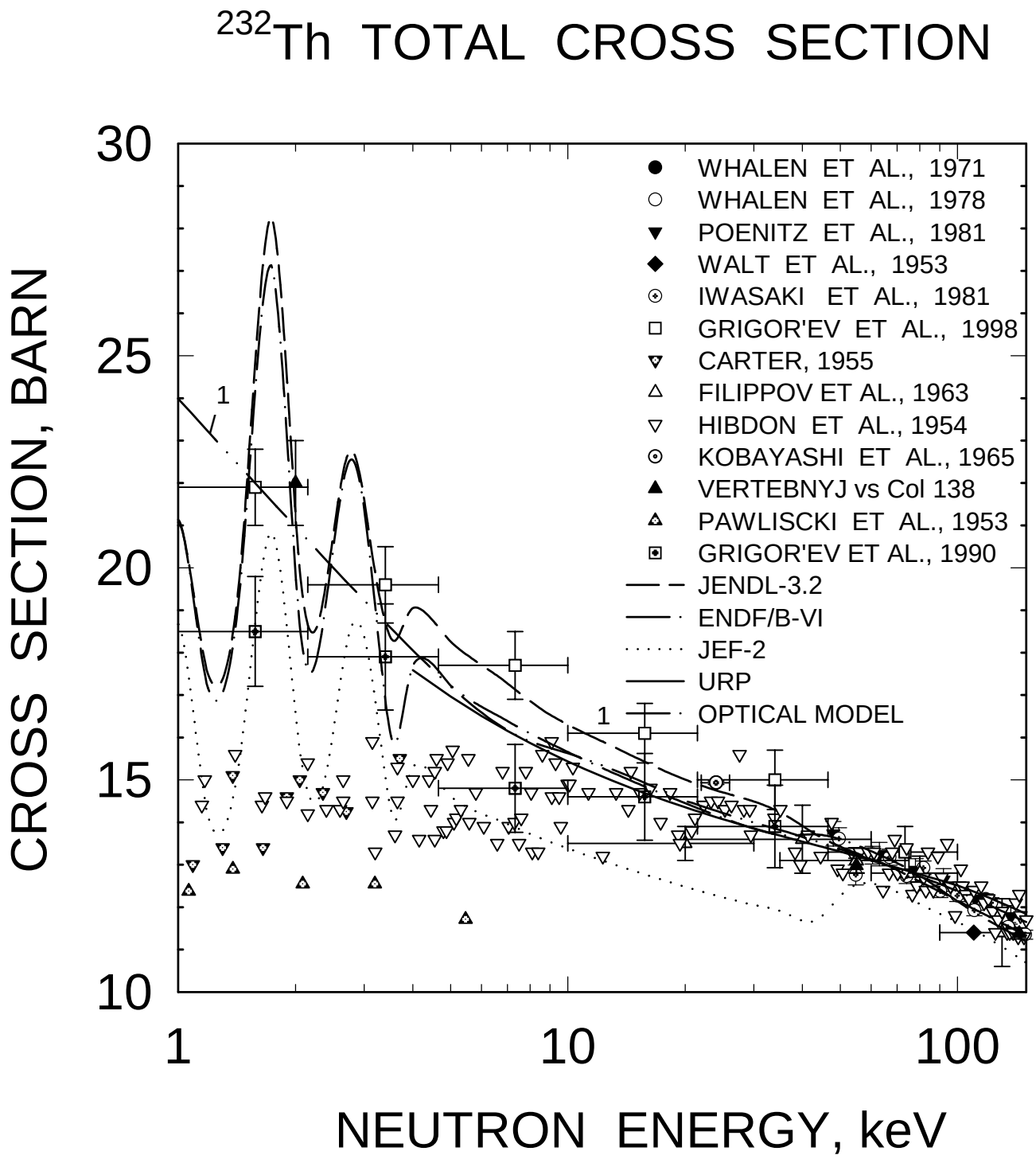
232Th TOTAL CROSS SECTION
CROSS SECTION, BARN
NEUTRON ENERGY, keV
30
25
20
15
10
1
10
100
1
1
WHALEN ET AL., 1971
WHALEN ET AL., 1978
POENITZ ET AL., 1981
WALT ET AL., 1953
IWASAKI ET AL., 1981
GRIGOR'EV ET AL., 1998
CARTER, 1955
FILIPPOV ET AL., 1963
HIBDON ET AL., 1954
KOBAYASHI ET AL., 1965
VERTEBNYJ vs Col 138
PAWLISCKI ET AL., 1953
GRIGOR'EV ET AL., 1990
JENDL-3.2
ENDF/B-VI
JEF-2
URP
OPTICAL MODEL

FIG. 6

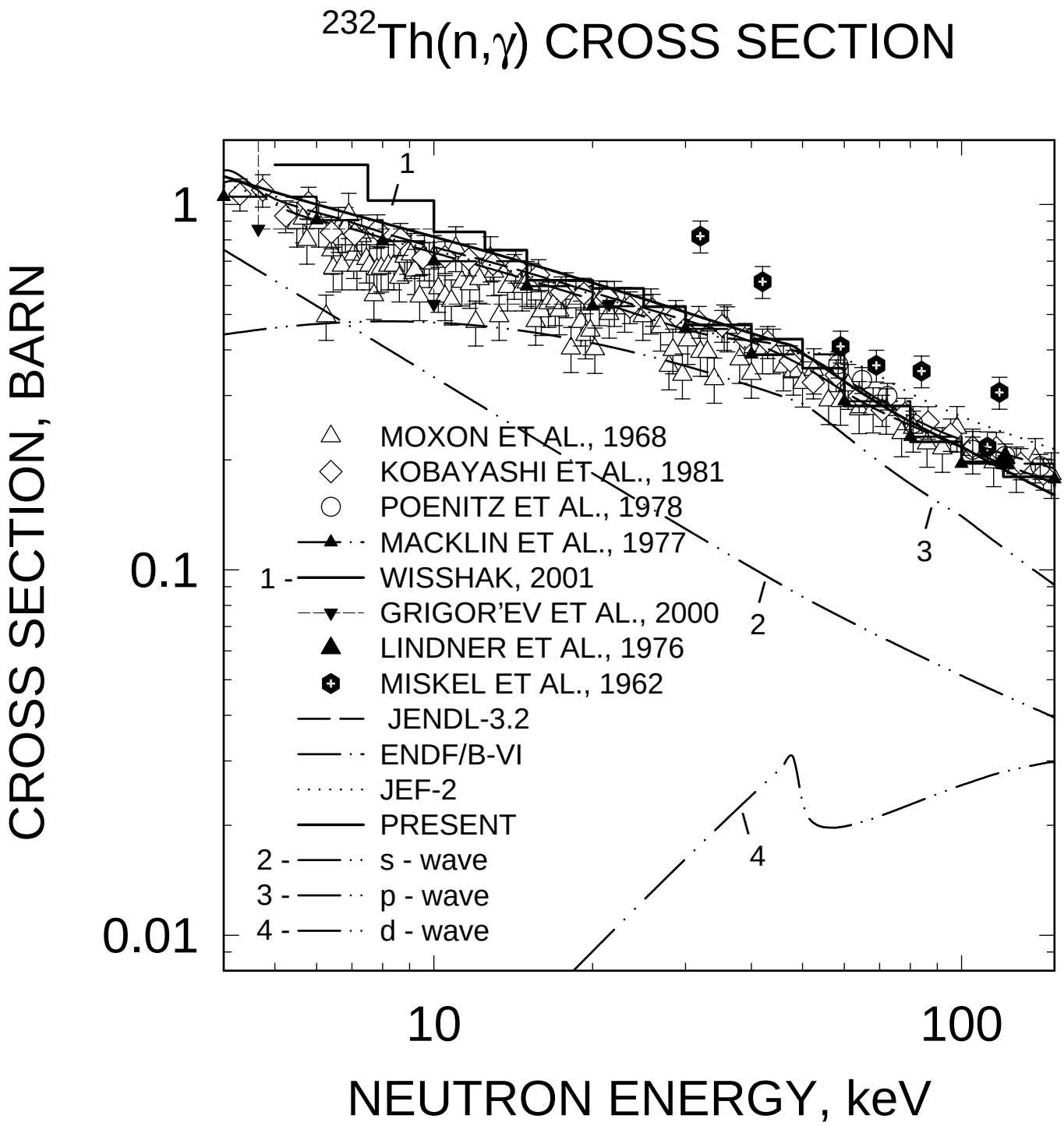
232Th(n,γ) CROSS SECTION
CROSS SECTION, BARN
1
0.1
0.01
10
100
NEUTRON ENERGY, keV
1
2
3
4
MOXON ET AL., 1968
KOBAYASHI ET AL., 1981
POENITZ ET AL., 1978
MACKLIN ET AL., 1977
1 - WISSHAK, 2001
GRIGOR'EV ET AL., 2000
LINDNER ET AL., 1976
MISKEL ET AL., 1962
JENDL-3.2
ENDF/B-VI
JEF-2
PRESENT
2 - s - wave
3 - p - wave
4 - d - wave

FIG. 7

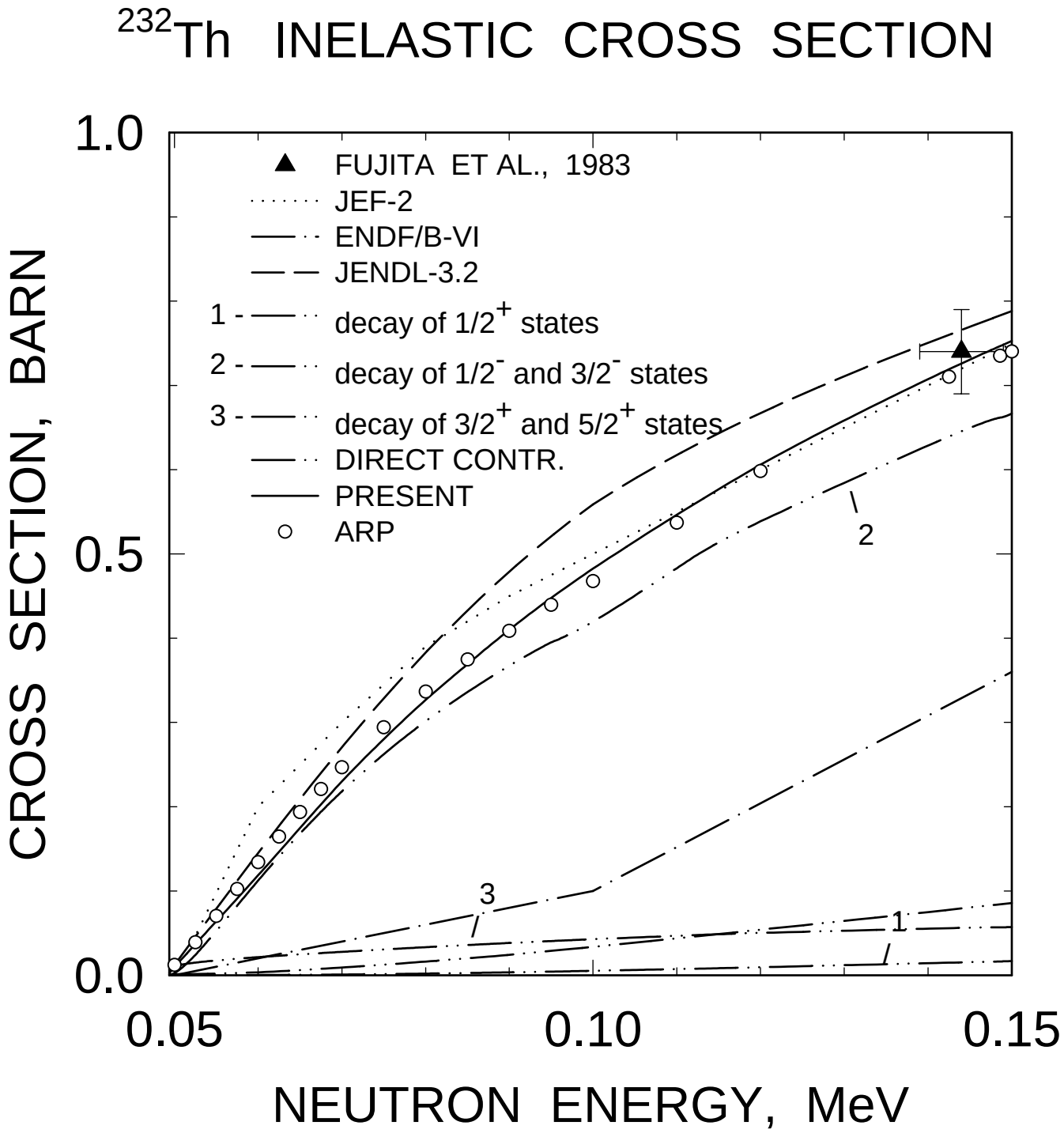
232Th INELASTIC CROSS SECTION
FUJITA ET AL., 1983
JEF-2
ENDF/B-VI
JENDL-3.2
1 - decay of 1/2+ states
2 - decay of 1/2- and 3/2- states
3 - decay of 3/2+ and 5/2+ states
DIRECT CONTR.
PRESENT
ARP
1
2
3
CROSS SECTION, BARN
NEUTRON ENERGY, MeV
1.0
0.5
0.0
0.05
0.10
0.15

FIG. 8

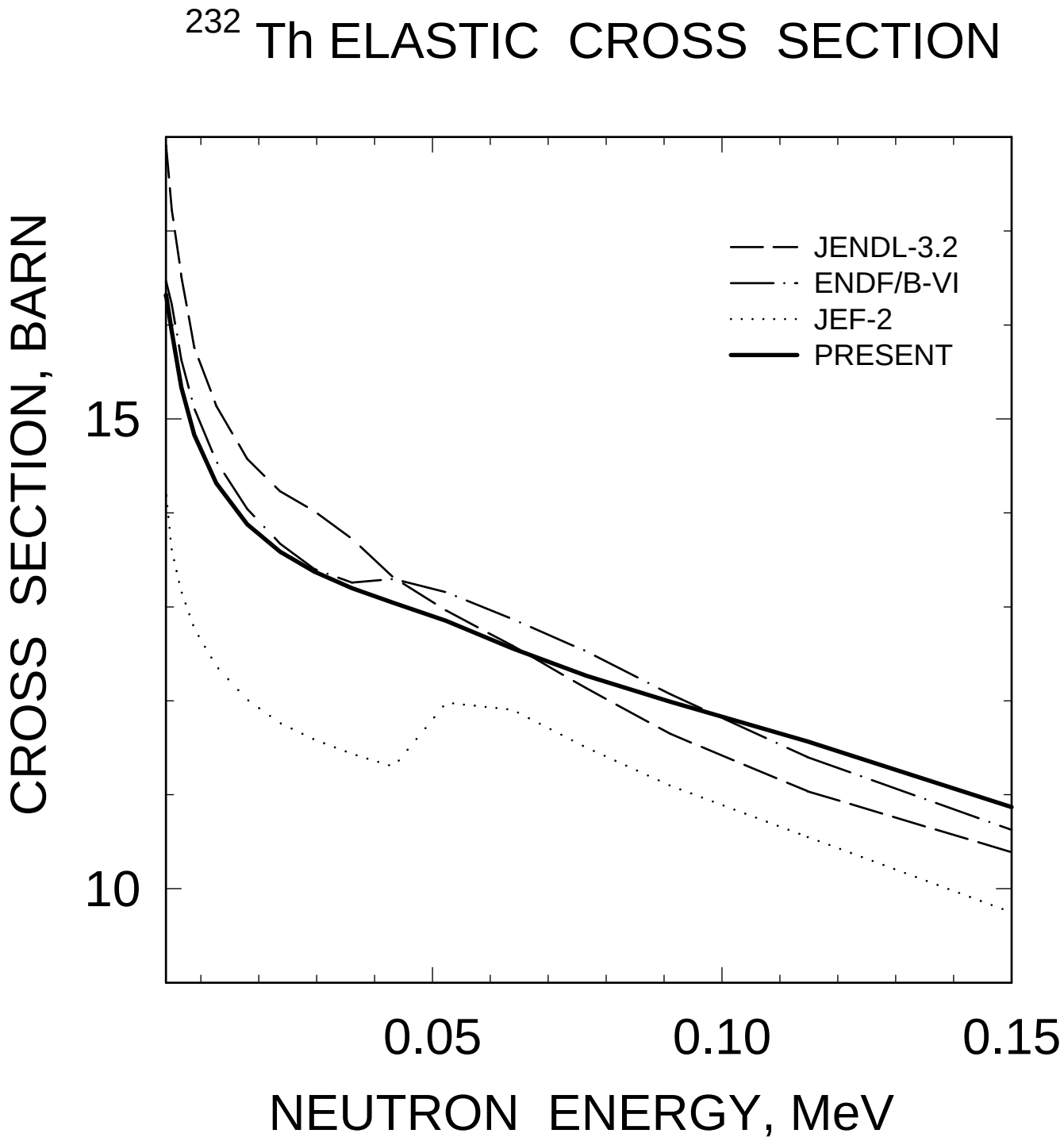
232 Th ELASTIC CROSS SECTION
CROSS SECTION, BARN
15
10
0.05
0.10
0.15
NEUTRON ENERGY, MeV
JENDL-3.2
ENDF/B-VI
JEF-2
PRESENT

FIG. 9

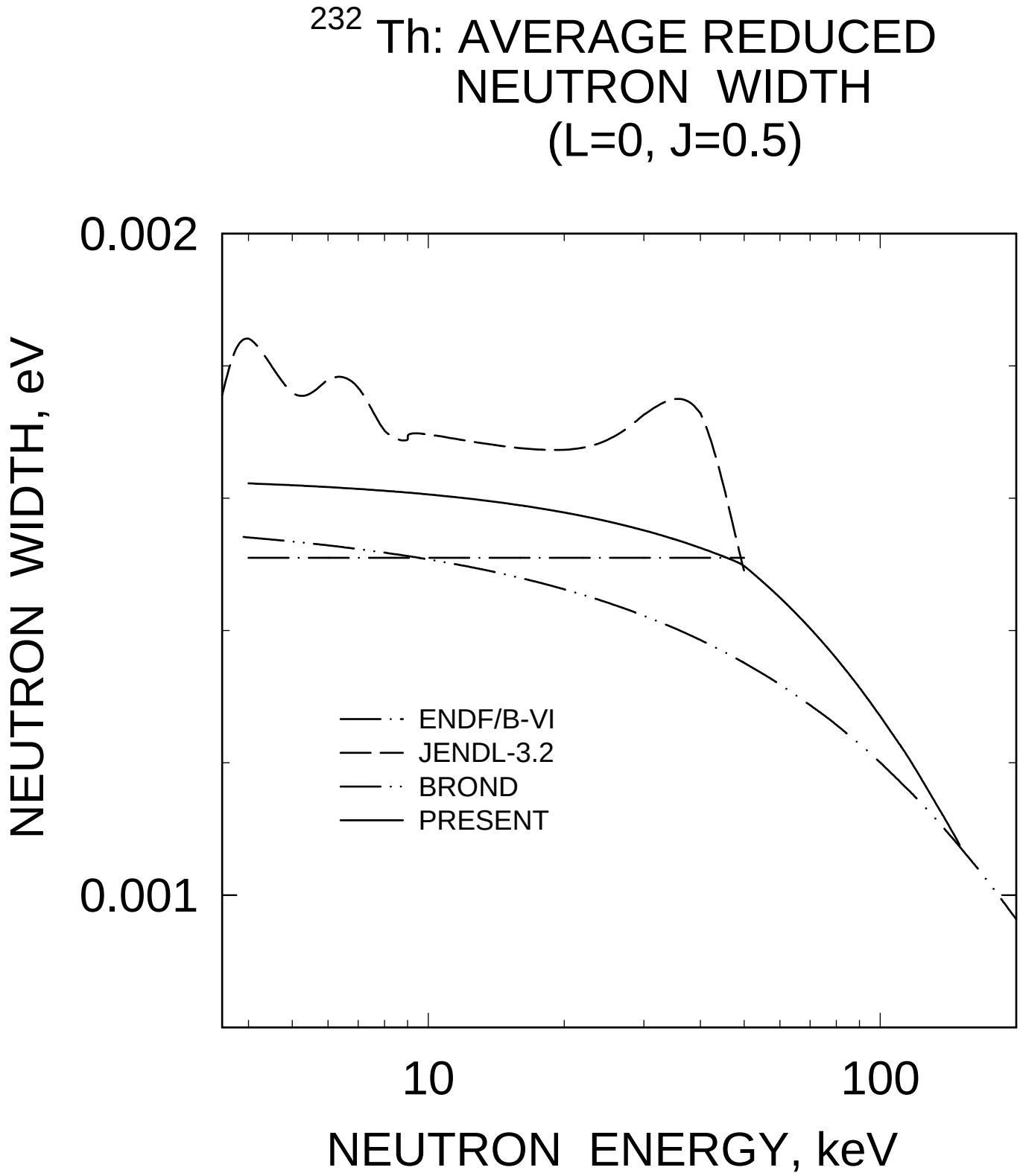
232 Th: AVERAGE REDUCED
NEUTRON WIDTH
(L=0, J=0.5)
0.002
0.001
NEUTRON WIDTH, eV
ENDF/B-VI
JENDL-3.2
BROND
PRESENT
10
100
NEUTRON ENERGY, keV

FIG. 10

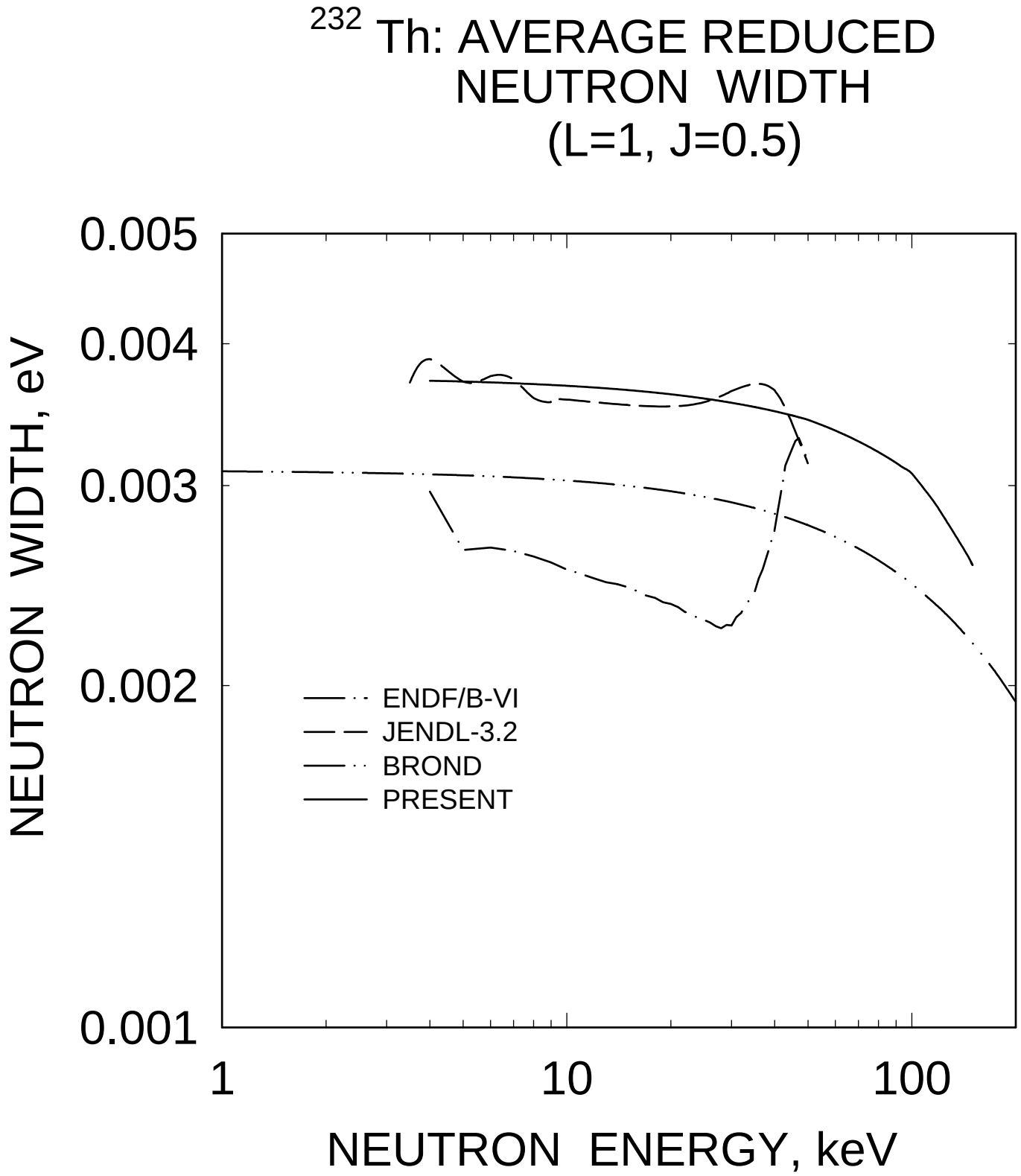
232 Th: AVERAGE REDUCED
NEUTRON WIDTH
(L=1, J=0.5)
0.005
0.004
0.003
0.002
0.001
NEUTRON WIDTH, eV
1
10
100
NEUTRON ENERGY, keV
ENDF/B-VI
JENDL-3.2
BROND
PRESENT

FIG. 11

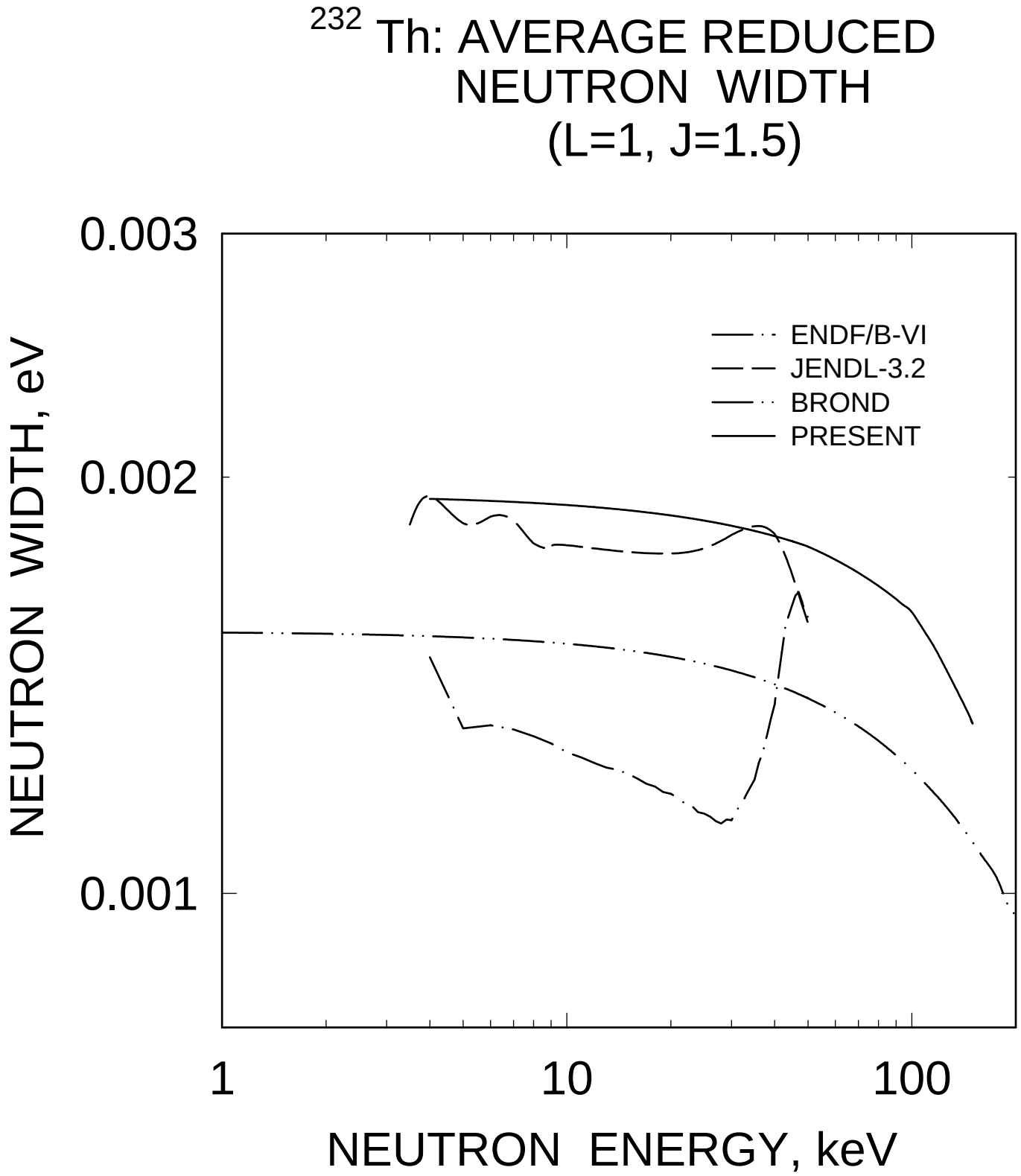
232 Th: AVERAGE REDUCED
NEUTRON WIDTH
(L=1, J=1.5)
0.003
0.002
0.001
NEUTRON WIDTH, eV
ENDF/B-VI
JENDL-3.2
BROND
PRESENT
1
10
100
NEUTRON ENERGY, keV

FIG. 12

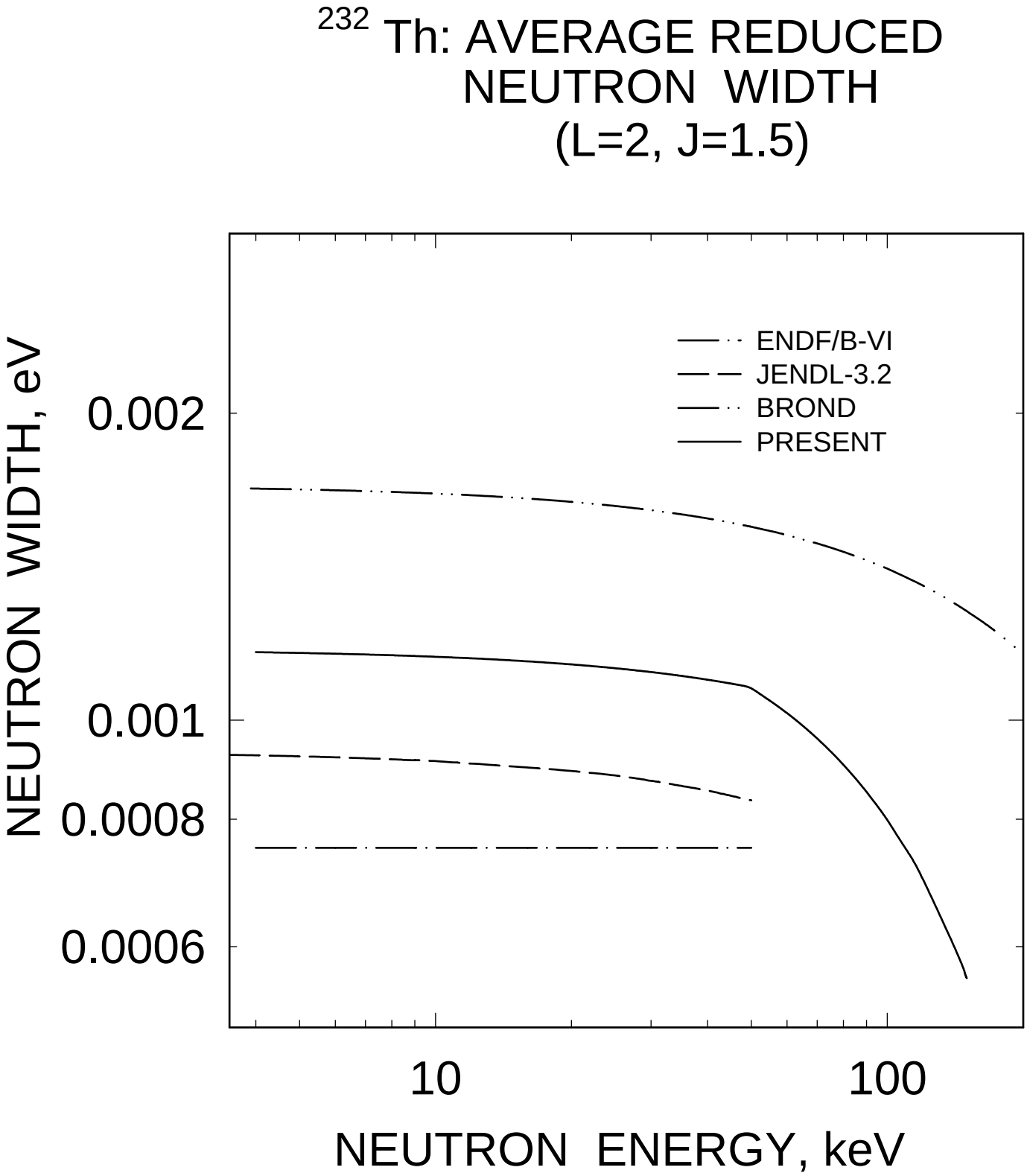
232 Th: AVERAGE REDUCED NEUTRON WIDTH (L=2, J=1.5)
ENDF/B-VI
JENDL-3.2
BROND
PRESENT
NEUTRON WIDTH, eV
0.002
0.001
0.0008
0.0006
10
100
NEUTRON ENERGY, keV

FIG. 13

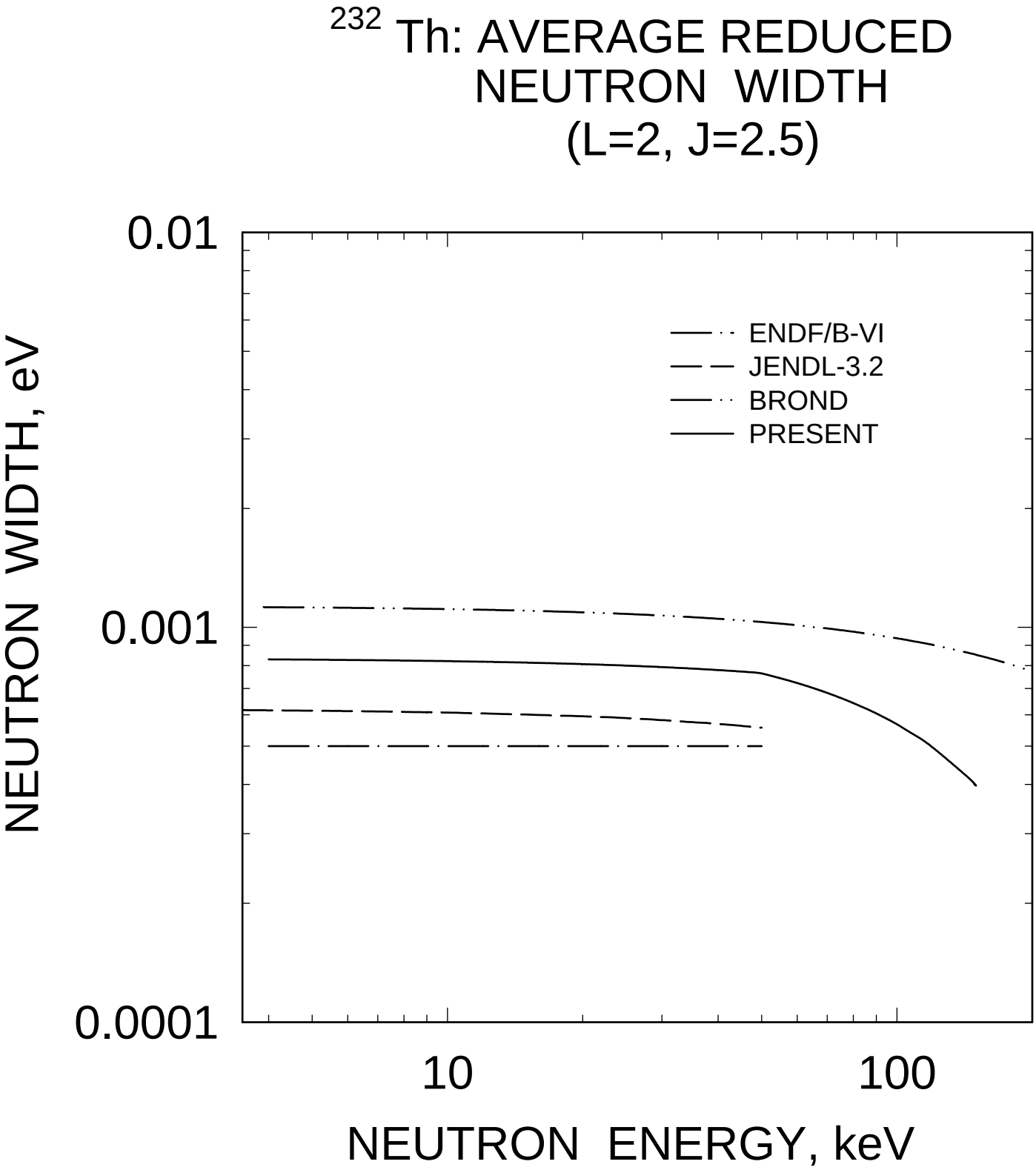
232 Th: AVERAGE REDUCED
NEUTRON WIDTH
(L=2, J=2.5)
0.01
0.001
0.0001
NEUTRON WIDTH, eV
ENDF/B-VI
JENDL-3.2
BROND
PRESENT
10
100
NEUTRON ENERGY, keV

FIG. 14

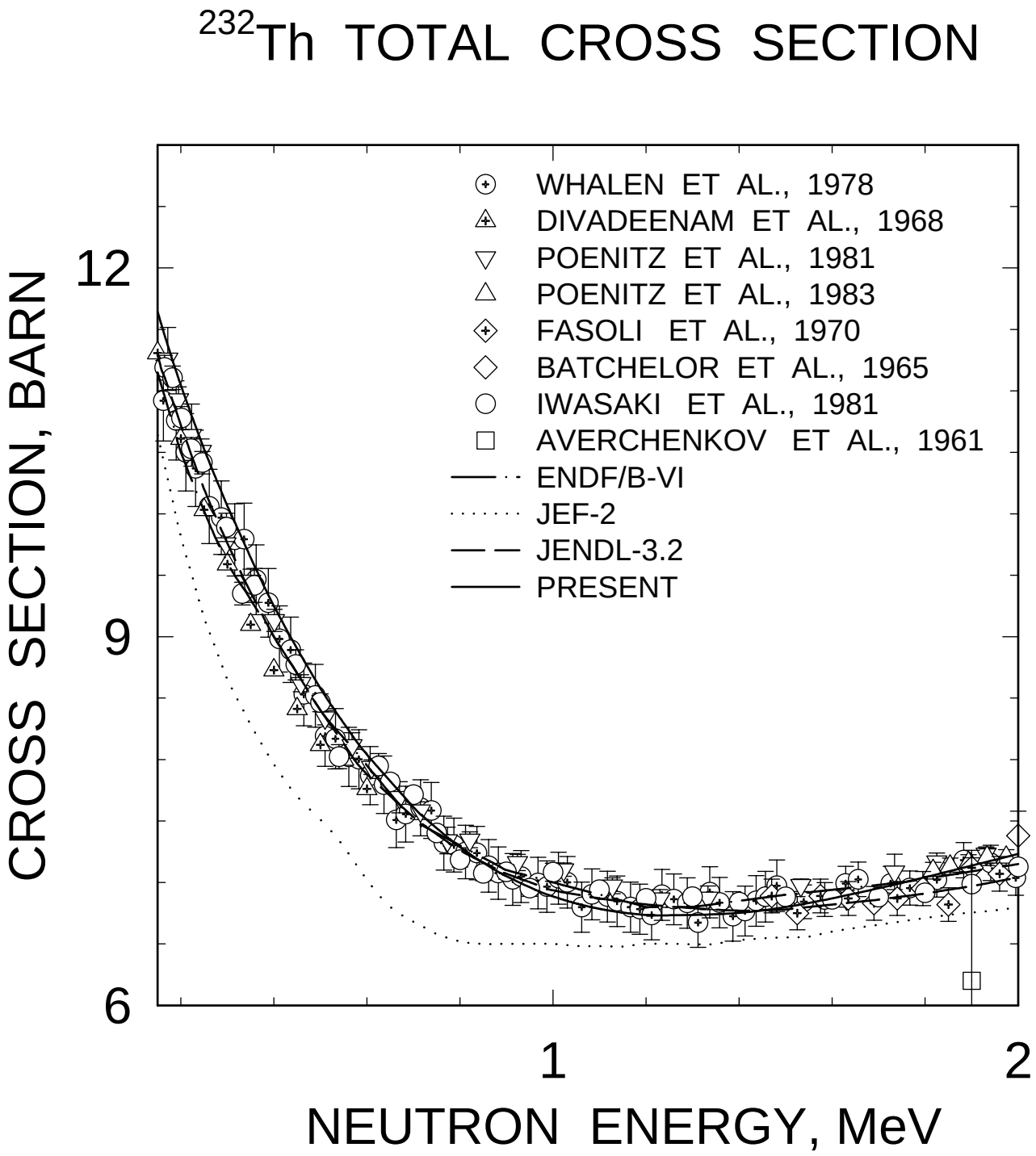
232Th TOTAL CROSS SECTION
WHALEN ET AL., 1978
DIVADEENAM ET AL., 1968
POENITZ ET AL., 1981
POENITZ ET AL., 1983
FASOLI ET AL., 1970
BATCHELOR ET AL., 1965
IWASAKI ET AL., 1981
AVERCHENKOV ET AL., 1961
ENDF/B-VI
JEF-2
JENDL-3.2
PRESENT
CROSS SECTION, BARN
12
9
6
1
2
NEUTRON ENERGY, MeV

FIG. 15

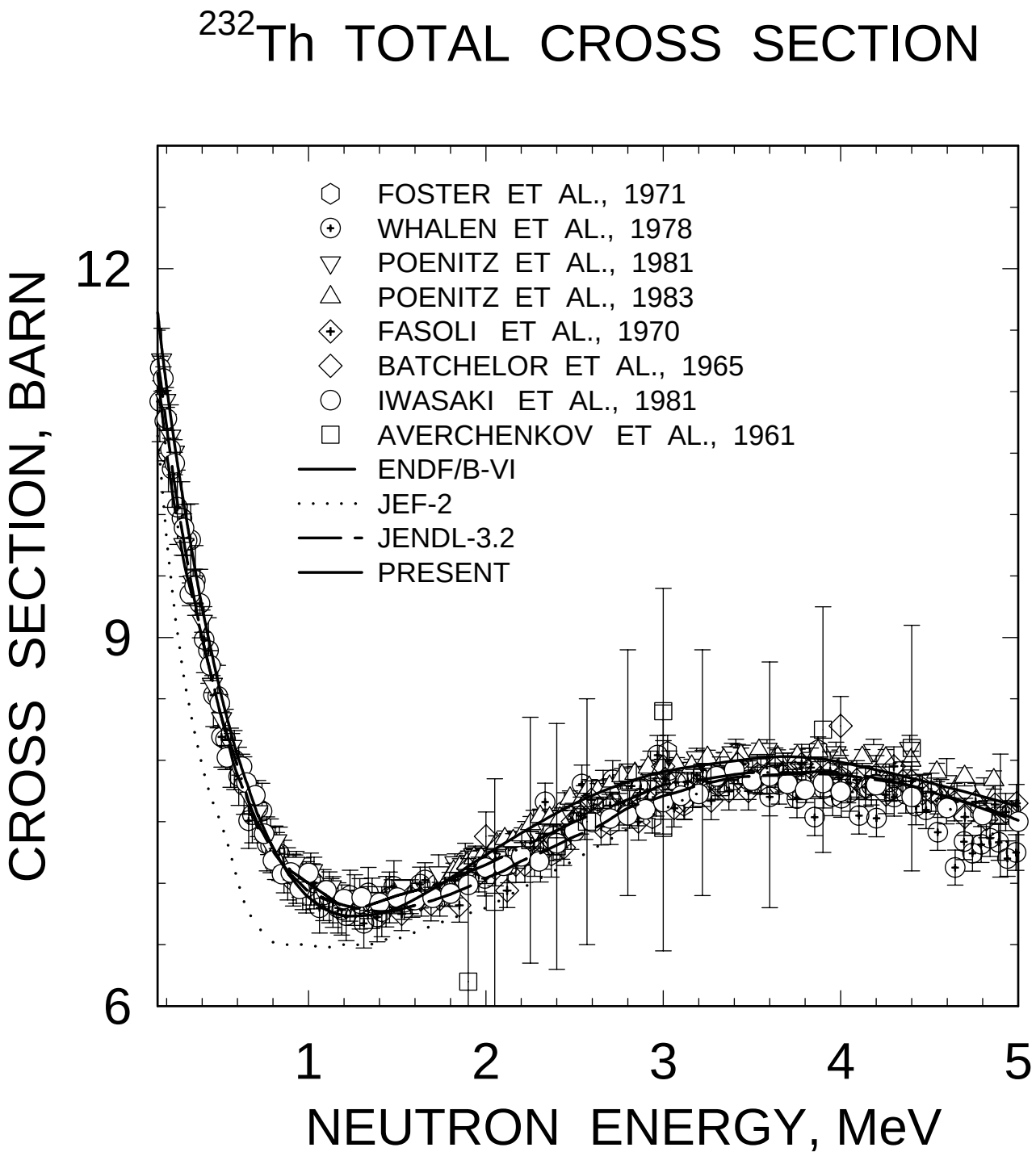
232Th TOTAL CROSS SECTION
FOSTER ET AL., 1971
WHALEN ET AL., 1978
POENITZ ET AL., 1981
POENITZ ET AL., 1983
FASOLI ET AL., 1970
BATCHELOR ET AL., 1965
IWASAKI ET AL., 1981
AVERCHENKOV ET AL., 1961
ENDF/B-VI
JEF-2
JENDL-3.2
PRESENT
CROSS SECTION, BARN
12
9
6
1
2
3
4
5
NEUTRON ENERGY, MeV

FIG. 16

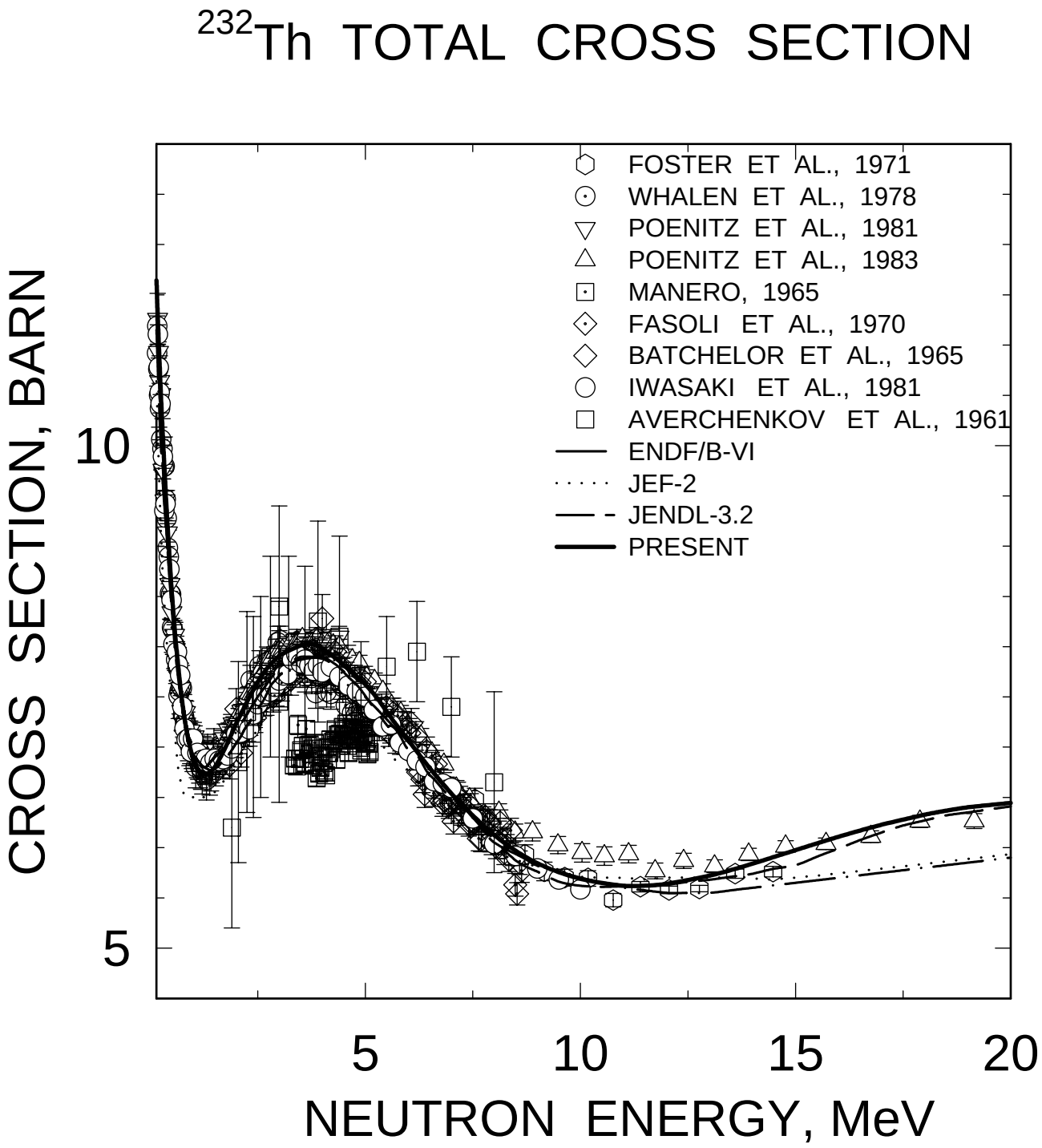
232Th TOTAL CROSS SECTION
FOSTER ET AL., 1971
WHALEN ET AL., 1978
POENITZ ET AL., 1981
POENITZ ET AL., 1983
MANERO, 1965
FASOLI ET AL., 1970
BATCHELOR ET AL., 1965
IWASAKI ET AL., 1981
AVERCHENKOV ET AL., 1961
ENDF/B-VI
JEF-2
JENDL-3.2
PRESENT
CROSS SECTION, BARN
10
5
5
10
15
20
NEUTRON ENERGY, MeV

FIG. 17

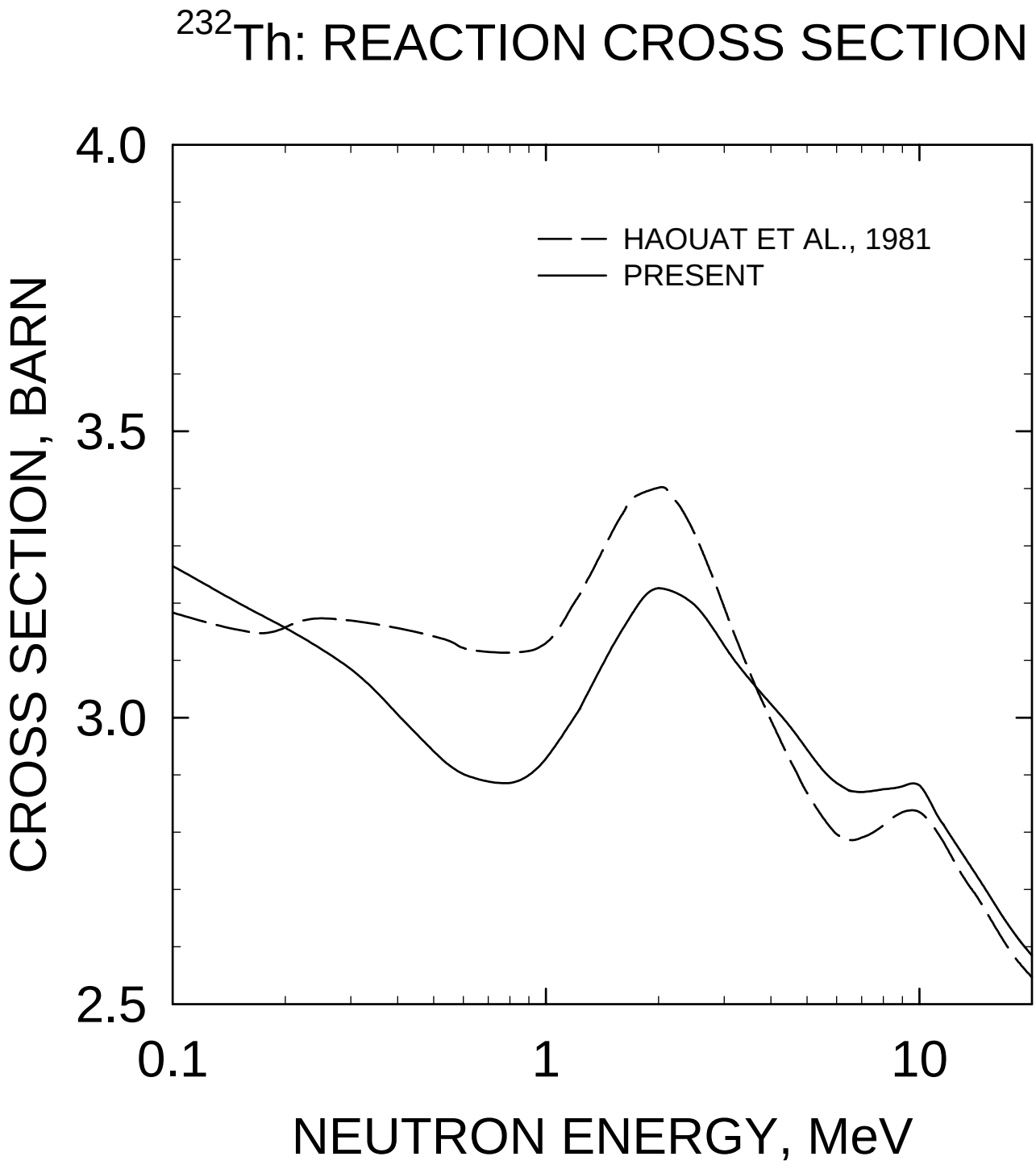
232Th: REACTION CROSS SECTION
HAOUAT ET AL., 1981
PRESENT
CROSS SECTION, BARN
4.0
3.5
3.0
2.5
0.1
1
10
NEUTRON ENERGY, MeV

FIG. 18

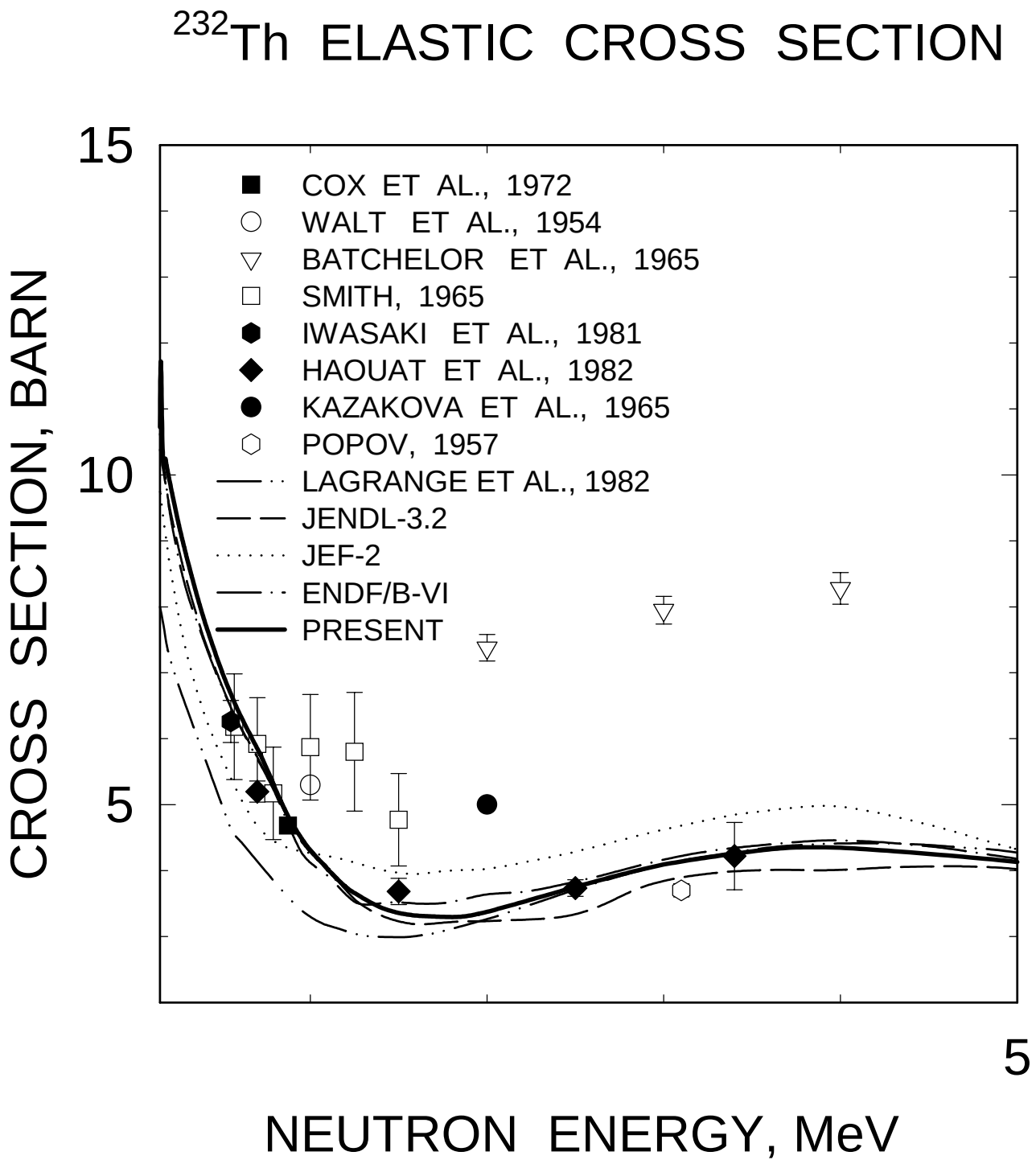
232Th ELASTIC CROSS SECTION
15
10
5
CROSS SECTION, BARN
COX ET AL., 1972
WALT ET AL., 1954
BATCHELOR ET AL., 1965
SMITH, 1965
IWASAKI ET AL., 1981
HAOUAT ET AL., 1982
KAZAKOVA ET AL., 1965
POPOV, 1957
LAGRANGE ET AL., 1982
JENDL-3.2
JEF-2
ENDF/B-VI
PRESENT
5
NEUTRON ENERGY, MeV

FIG. 19

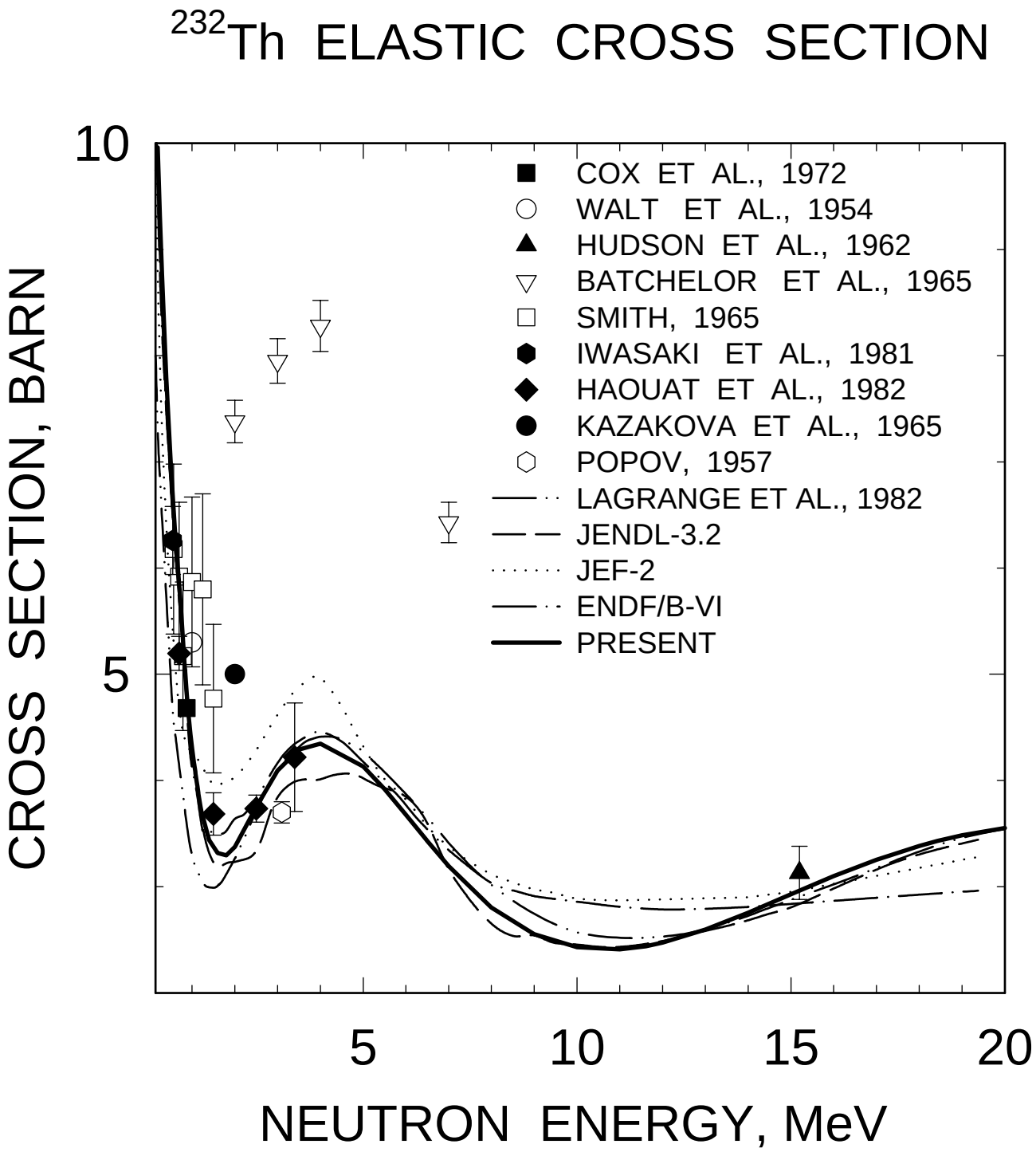
232Th ELASTIC CROSS SECTION
CROSS SECTION, BARN
NEUTRON ENERGY, MeV
10
5
5
10
15
20
COX ET AL., 1972
WALT ET AL., 1954
HUDSON ET AL., 1962
BATCHELOR ET AL., 1965
SMITH, 1965
IWASAKI ET AL., 1981
HAOUAT ET AL., 1982
KAZAKOVA ET AL., 1965
POPOV, 1957
LAGRANGE ET AL., 1982
JENDL-3.2
JEF-2
ENDF/B-VI
PRESENT

FIG. 20

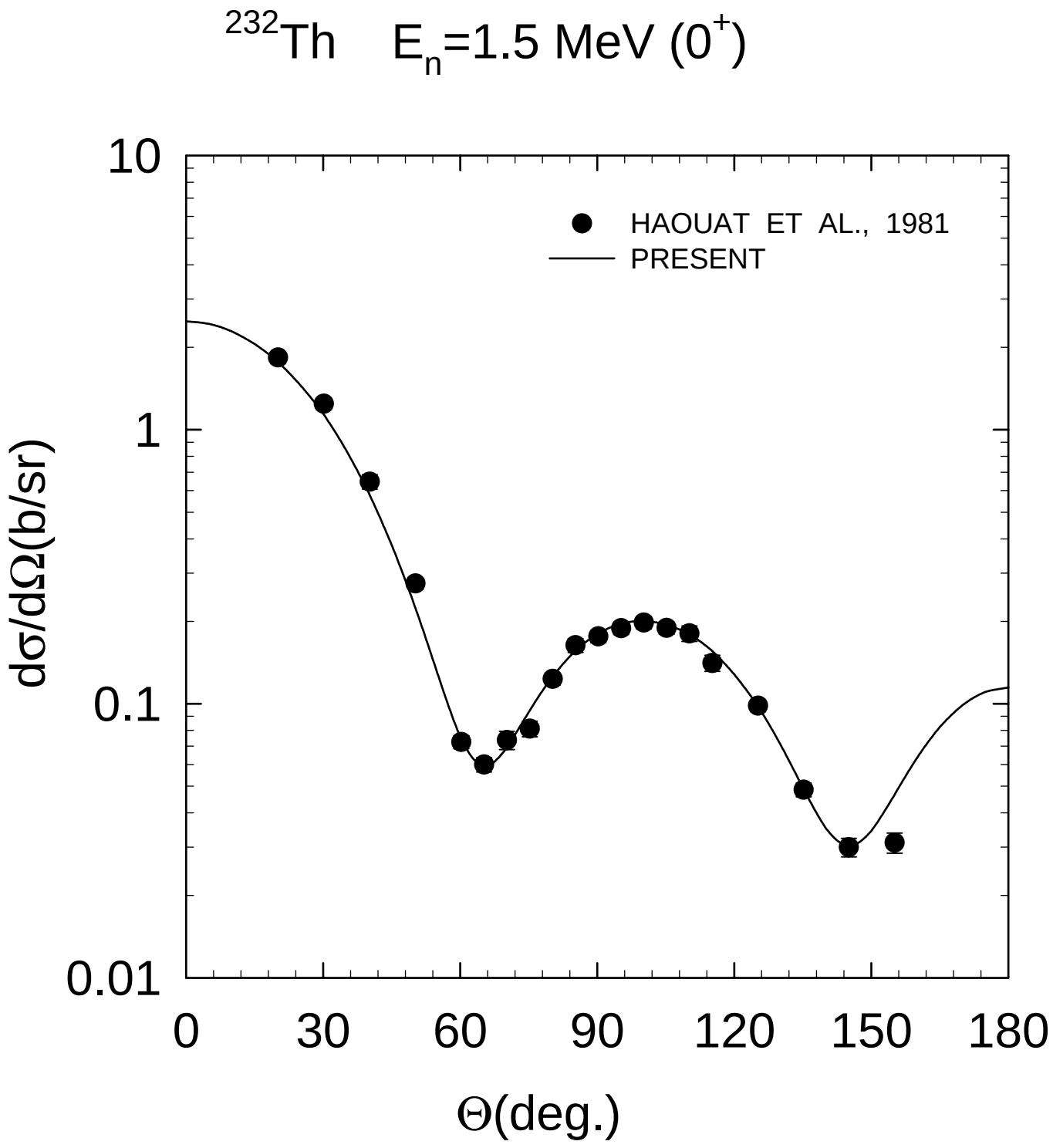
232Th En=1.5 MeV (0+)
HAOUAT ET AL., 1981
PRESENT
dσ/dΩ(b/sr)
10
1
0.1
0.01
0
30
60
90
120
150
180
Θ(deg.)

FIG. 21

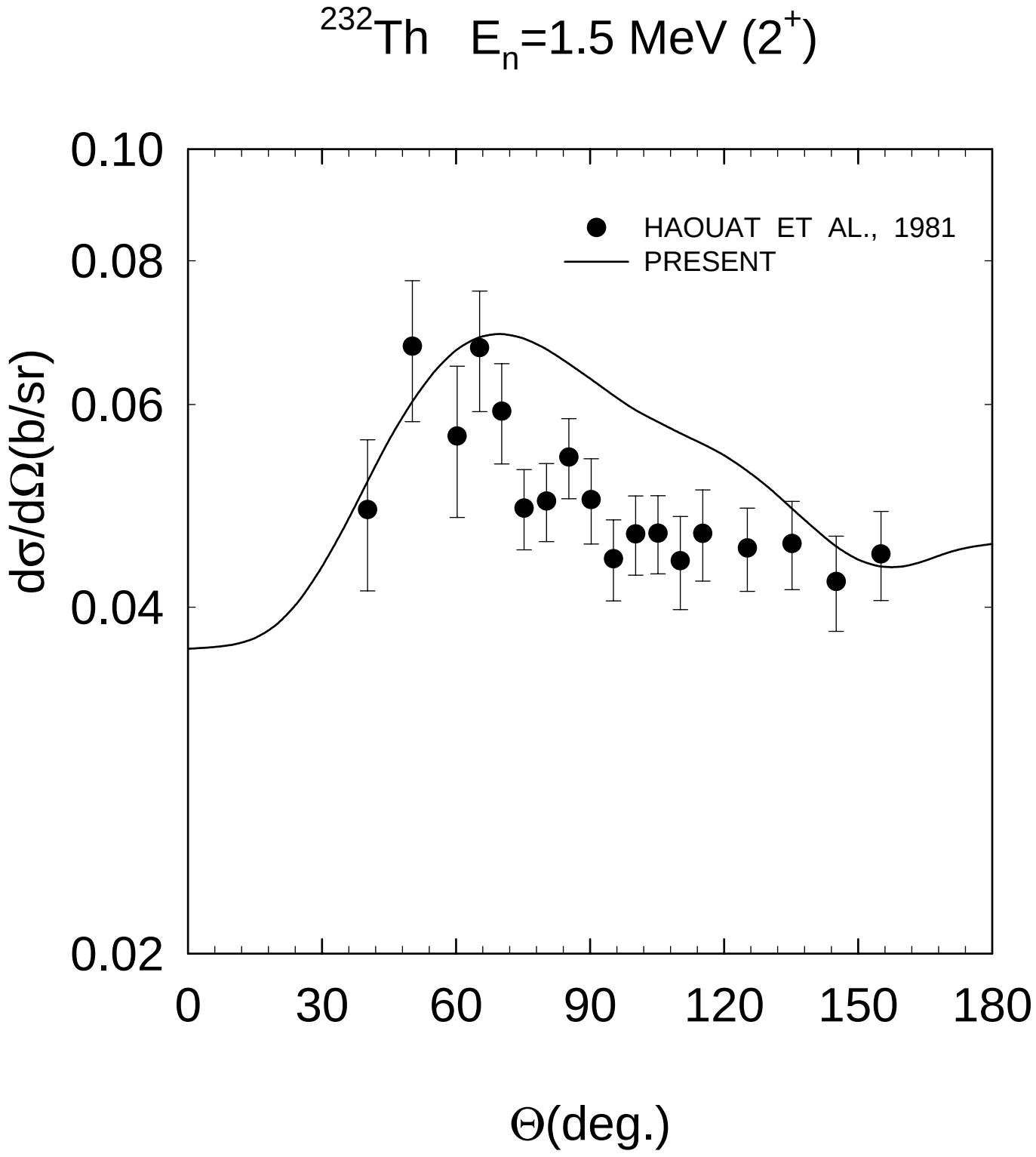
232Th En=1.5 MeV (2+)
HAOUAT ET AL., 1981
PRESENT
dσ/dΩ(b/sr)
0.10
0.08
0.06
0.04
0.02
0
30
60
90
120
150
180
Θ(deg.)

FIG. 22

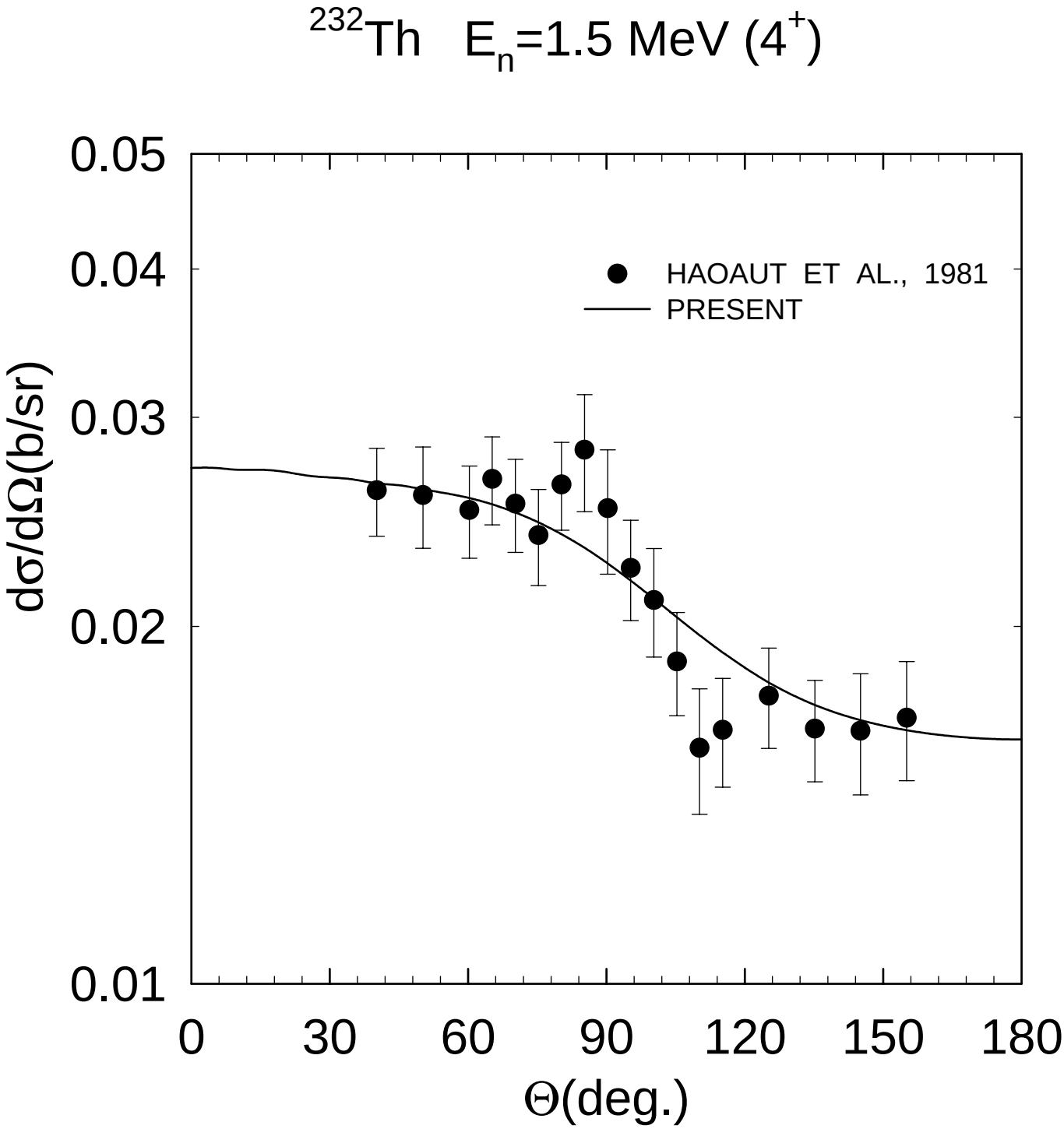
232Th En=1.5 MeV (4+)
HAOAUT ET AL., 1981
PRESENT
dσ/dΩ(b/sr)
0.05
0.04
0.03
0.02
0.01
0
30
60
90
120
150
180
Θ(deg.)

FIG. 23

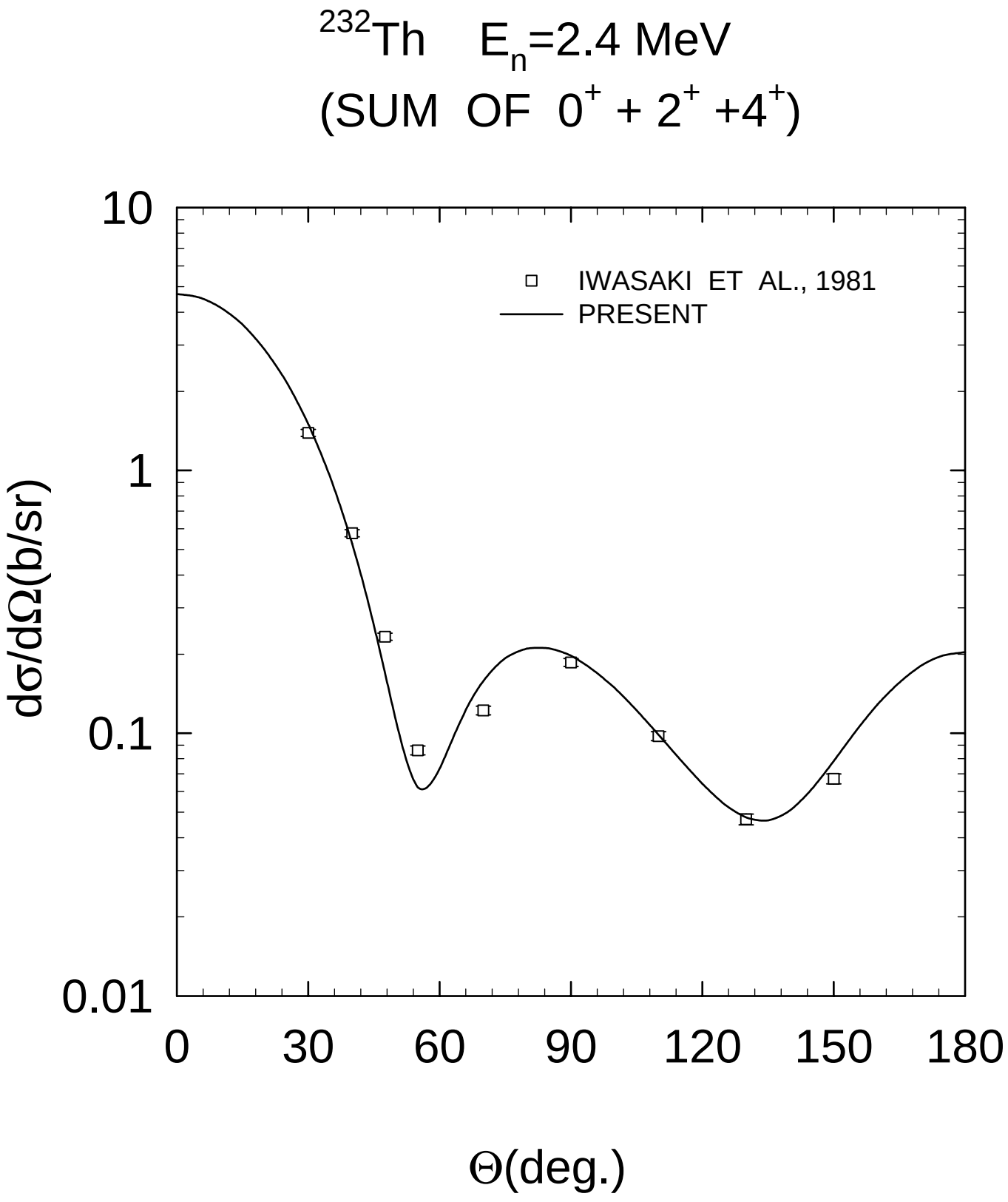
^{232}Th E_n=2.4 MeV
(SUM OF $0^+ + 2^+ + 4^+$)
IWASAKI ET AL., 1981
PRESENT
10
1
0.1
0.01
dσ/dΩ(b/sr)
0
30
60
90
120
150
180
Θ(deg.)

FIG. 24

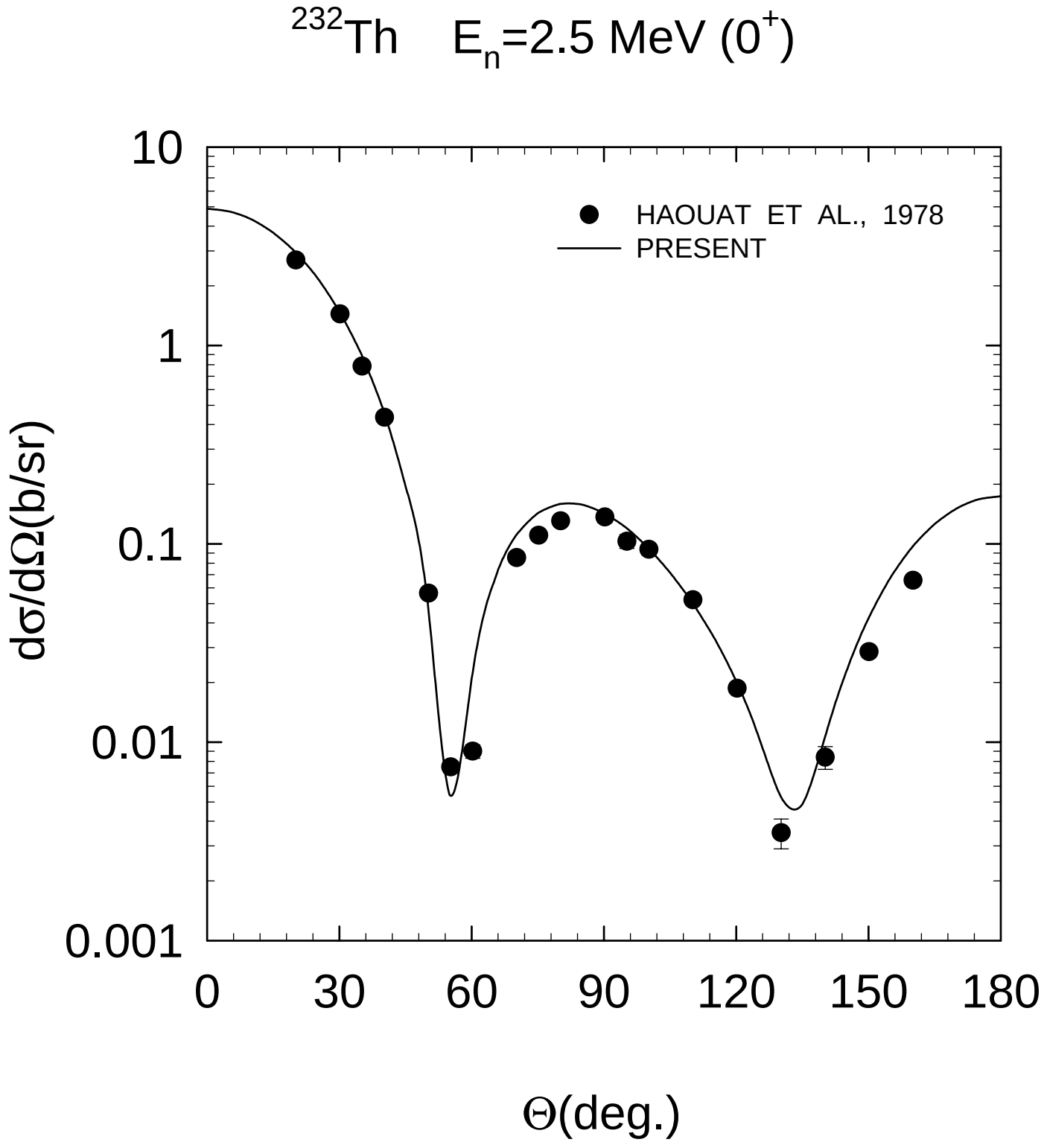
^{232}Th E_n=2.5 MeV (0^+)
HAOUAT ET AL., 1978
PRESENT
10
1
0.1
0.01
0.001
dσ/dΩ(b/sr)
0
30
60
90
120
150
180
Θ(deg.)

FIG. 25

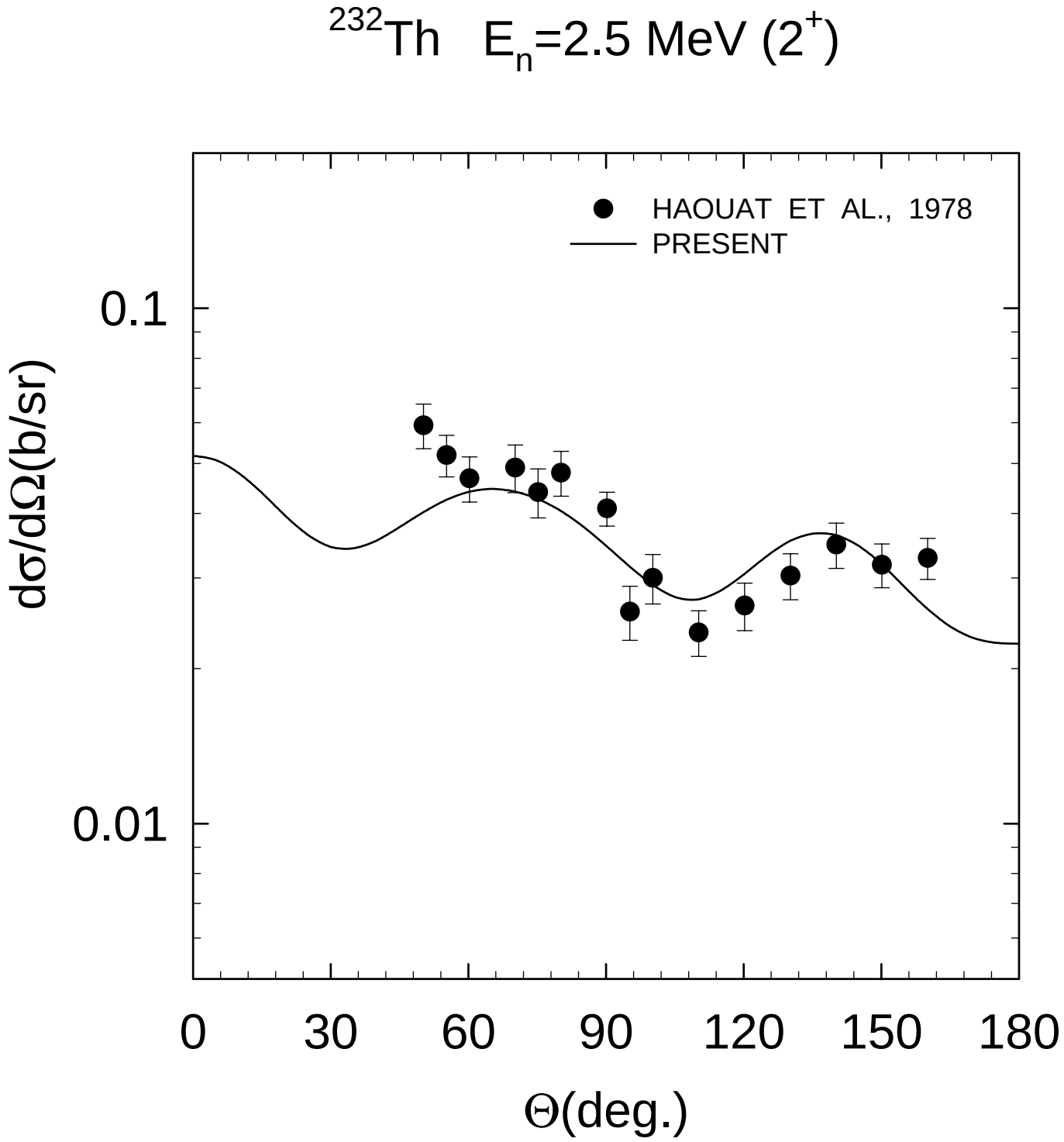
232Th En=2.5 MeV (2+)
HAOUAT ET AL., 1978
PRESENT
0.1
0.01
dσ/dΩ(b/sr)
0
30
60
90
120
150
180
Θ(deg.)

FIG. 26

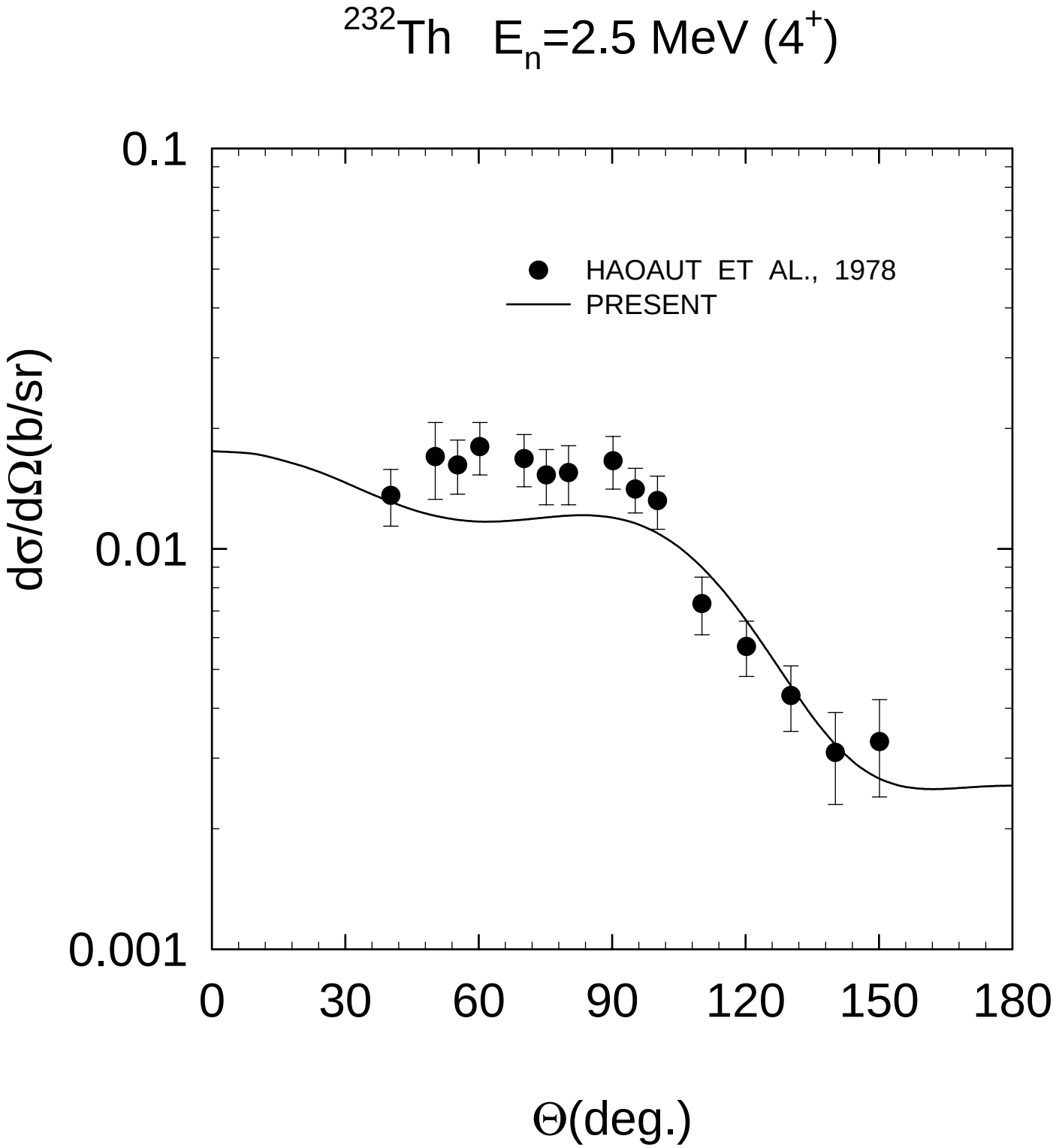
232Th En=2.5 MeV (4+)
HAOAUT ET AL., 1978
PRESENT
dσ/dΩ(b/sr)
0.1
0.01
0.001
0
30
60
90
120
150
180
Θ(deg.)

FIG. 27

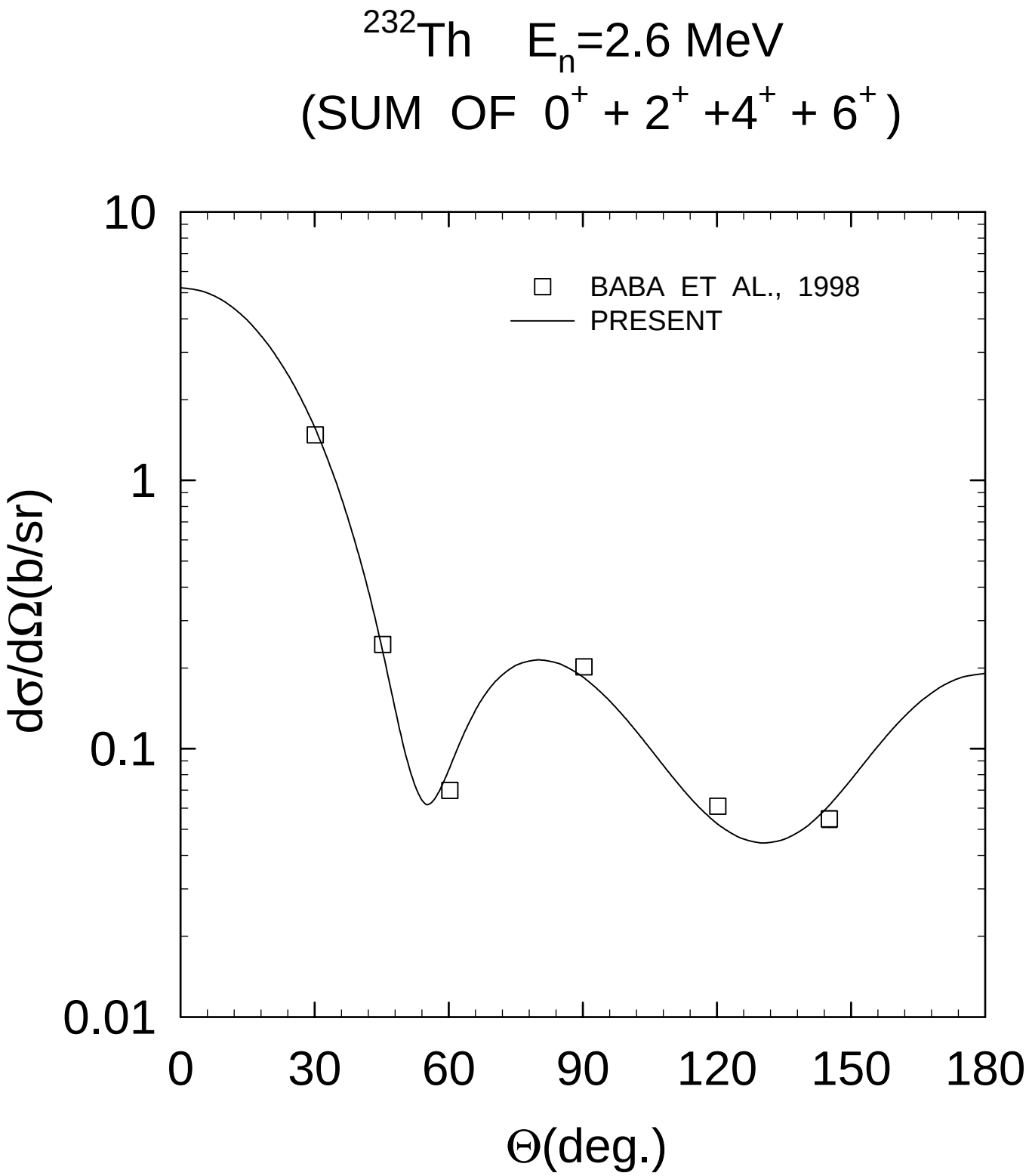
^{232}Th E_n=2.6 MeV
(SUM OF $0^+ + 2^+ + 4^+ + 6^+$)
BABA ET AL., 1998
PRESENT
10
1
0.1
0.01
dσ/dΩ(b/sr)
0
30
60
90
120
150
180
Θ(deg.)

FIG. 28

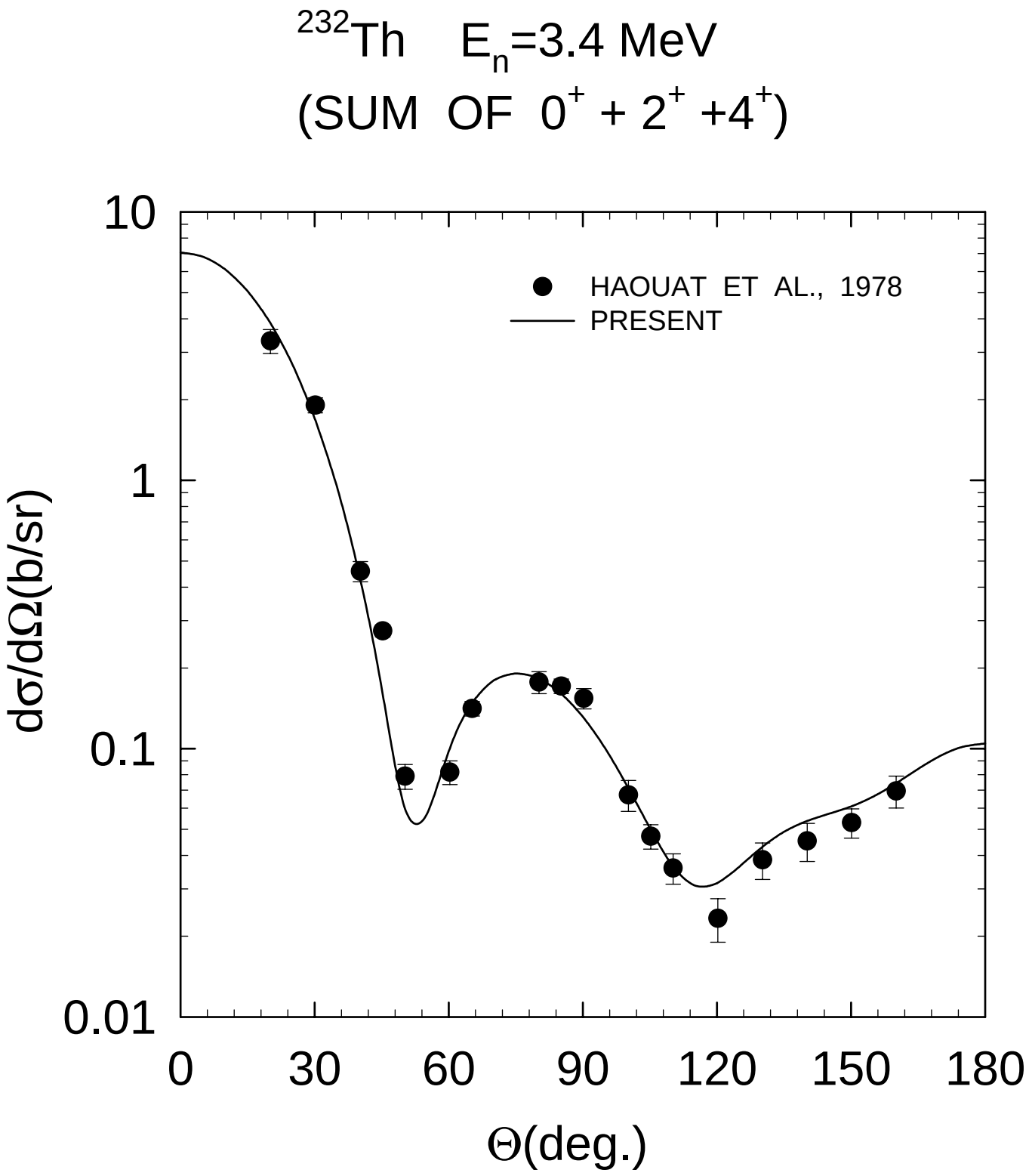
^{232}Th E_n=3.4 MeV
(SUM OF $0^+ + 2^+ + 4^+$)
HAOUAT ET AL., 1978
PRESENT
dσ/dΩ(b/sr)
10
1
0.1
0.01
0
30
60
90
120
150
180
Θ(deg.)

FIG. 29

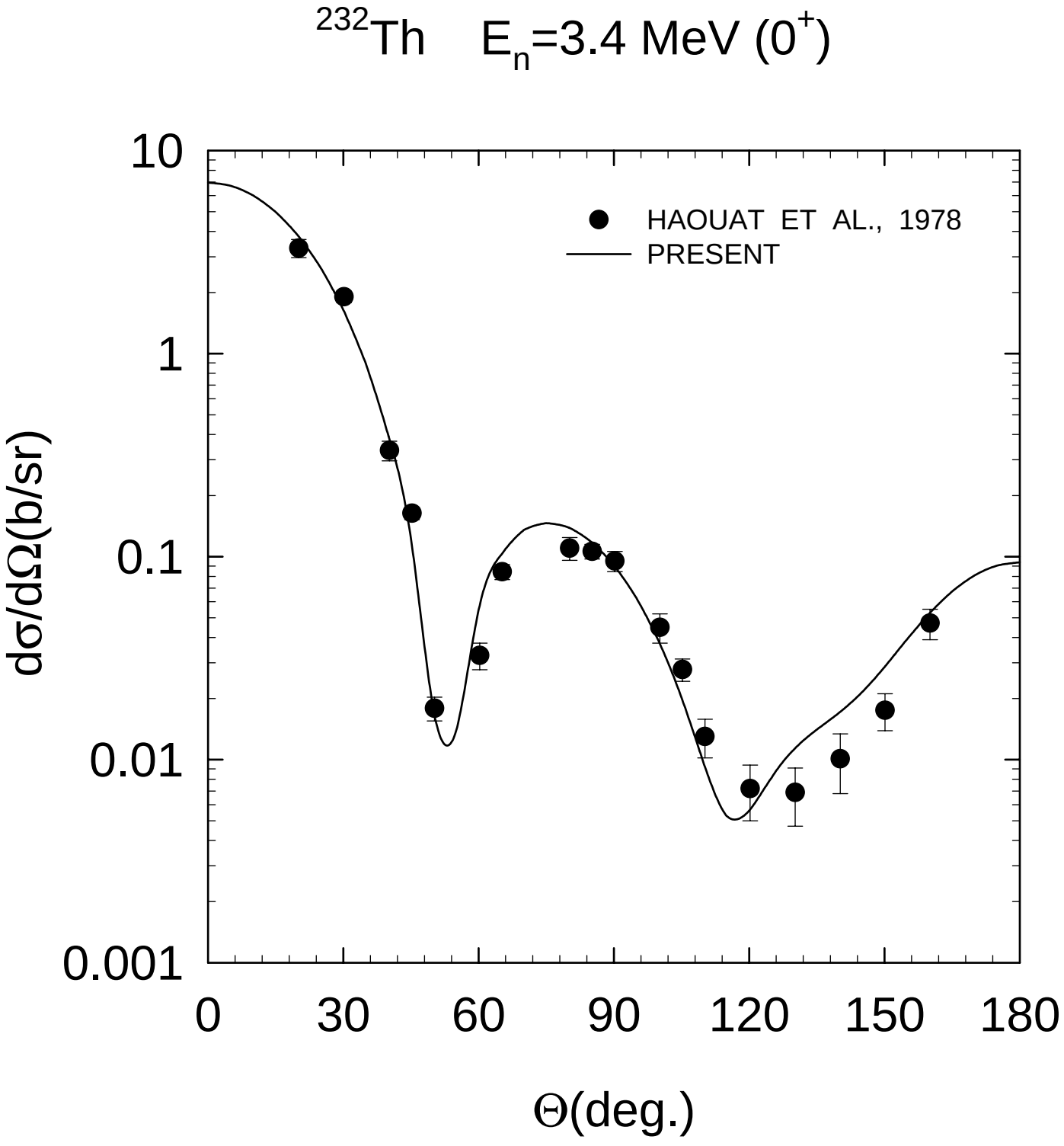
232Th En=3.4 MeV (0+)
HAOUAT ET AL., 1978
PRESENT
dσ/dΩ(b/sr)
10
1
0.1
0.01
0.001
0
30
60
90
120
150
180
Θ(deg.)

FIG. 30

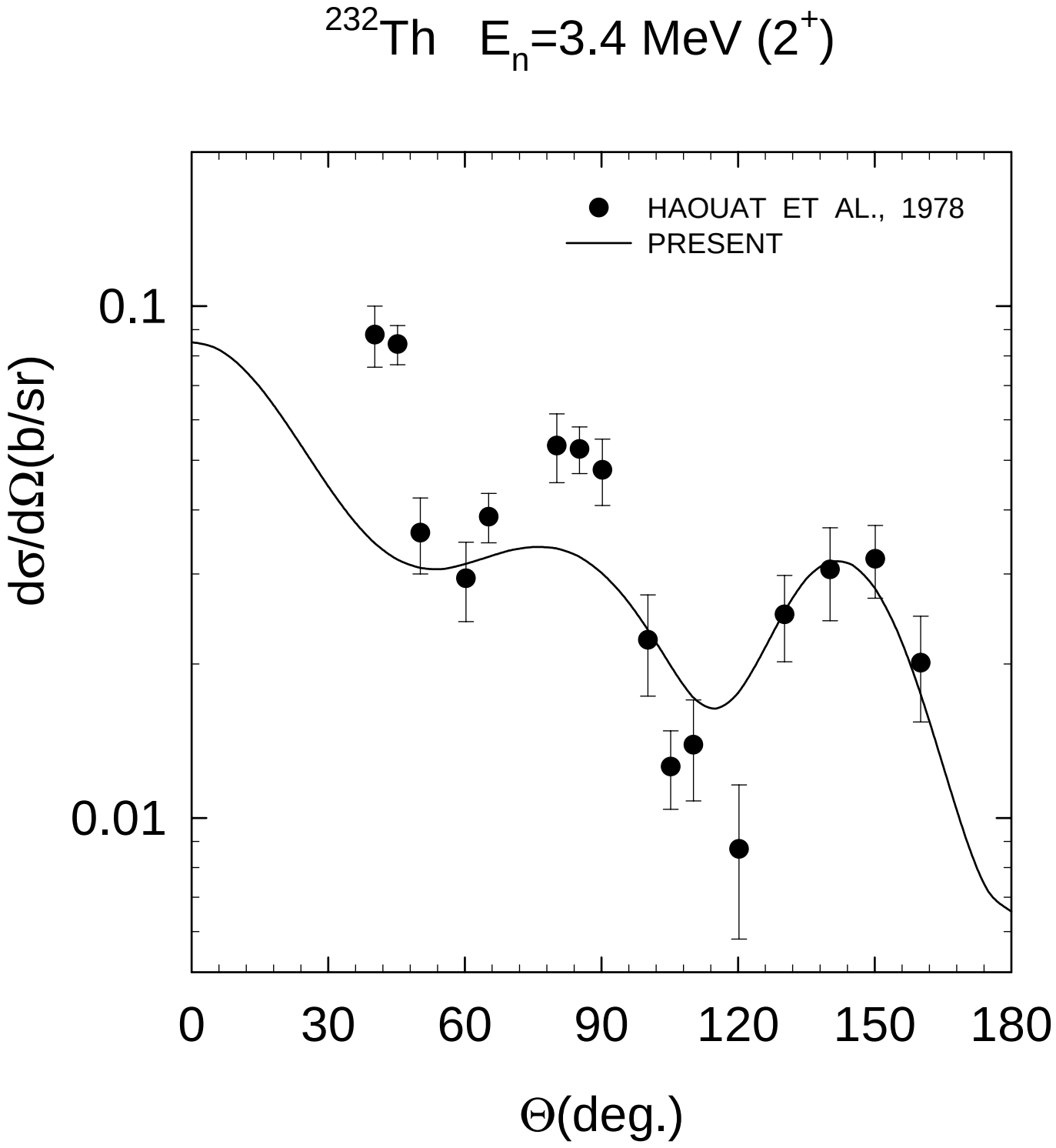
232Th En=3.4 MeV (2+)
HAOUAT ET AL., 1978
PRESENT
0.1
0.01
dσ/dΩ(b/sr)
0
30
60
90
120
150
180
Θ(deg.)

FIG. 31

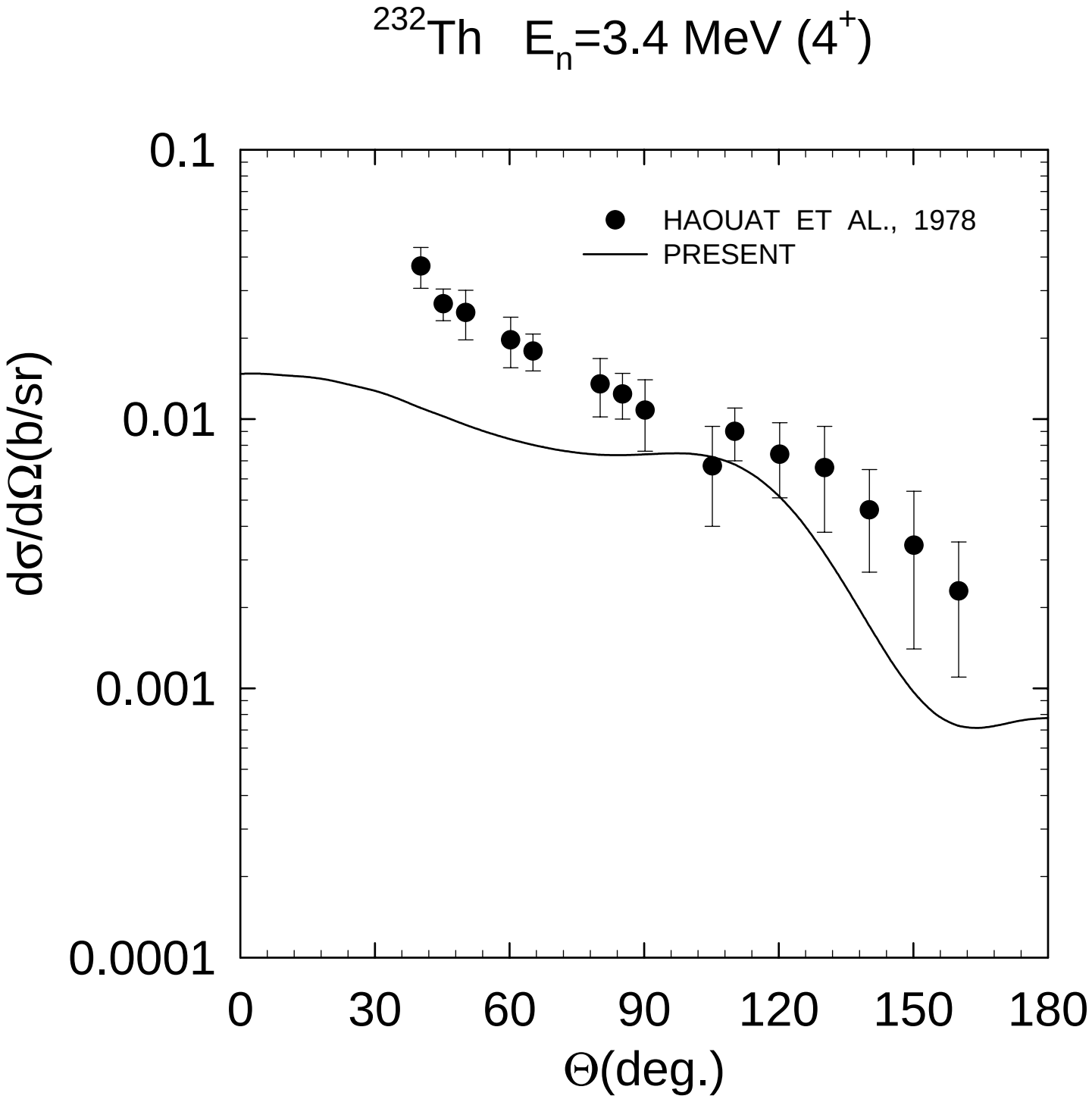
^{232}Th E_n=3.4 MeV (4^+)
HAOUAT ET AL., 1978
PRESENT
0.1
0.01
0.001
0.0001
dσ/dΩ(b/sr)
0
30
60
90
120
150
180
Θ(deg.)

FIG. 32

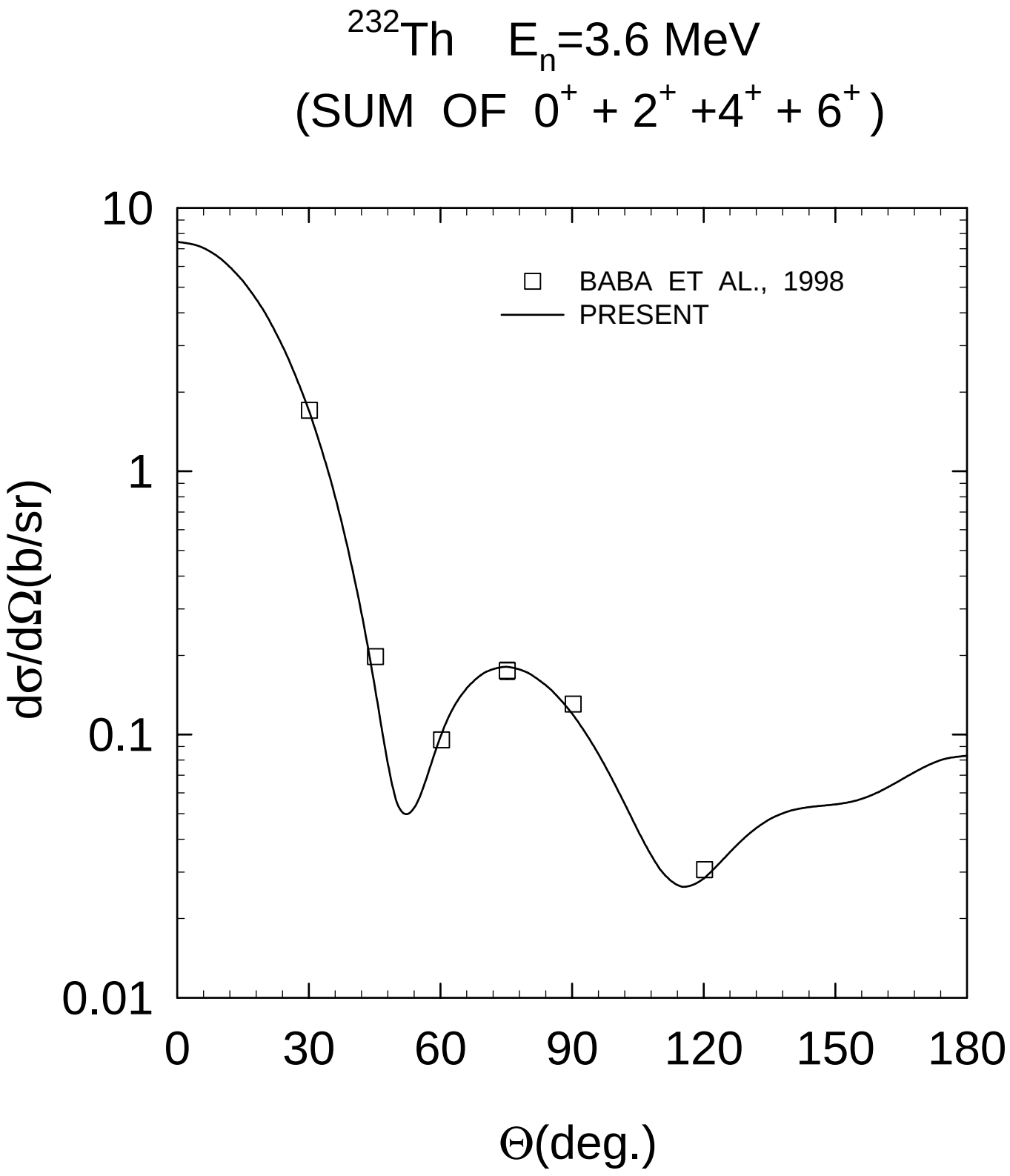
^{232}Th E_n=3.6 MeV
(SUM OF $0^+ + 2^+ + 4^+ + 6^+$)
BABA ET AL., 1998
PRESENT
10
1
0.1
0.01
dσ/dΩ(b/sr)
0
30
60
90
120
150
180
Θ(deg.)

FIG. 33

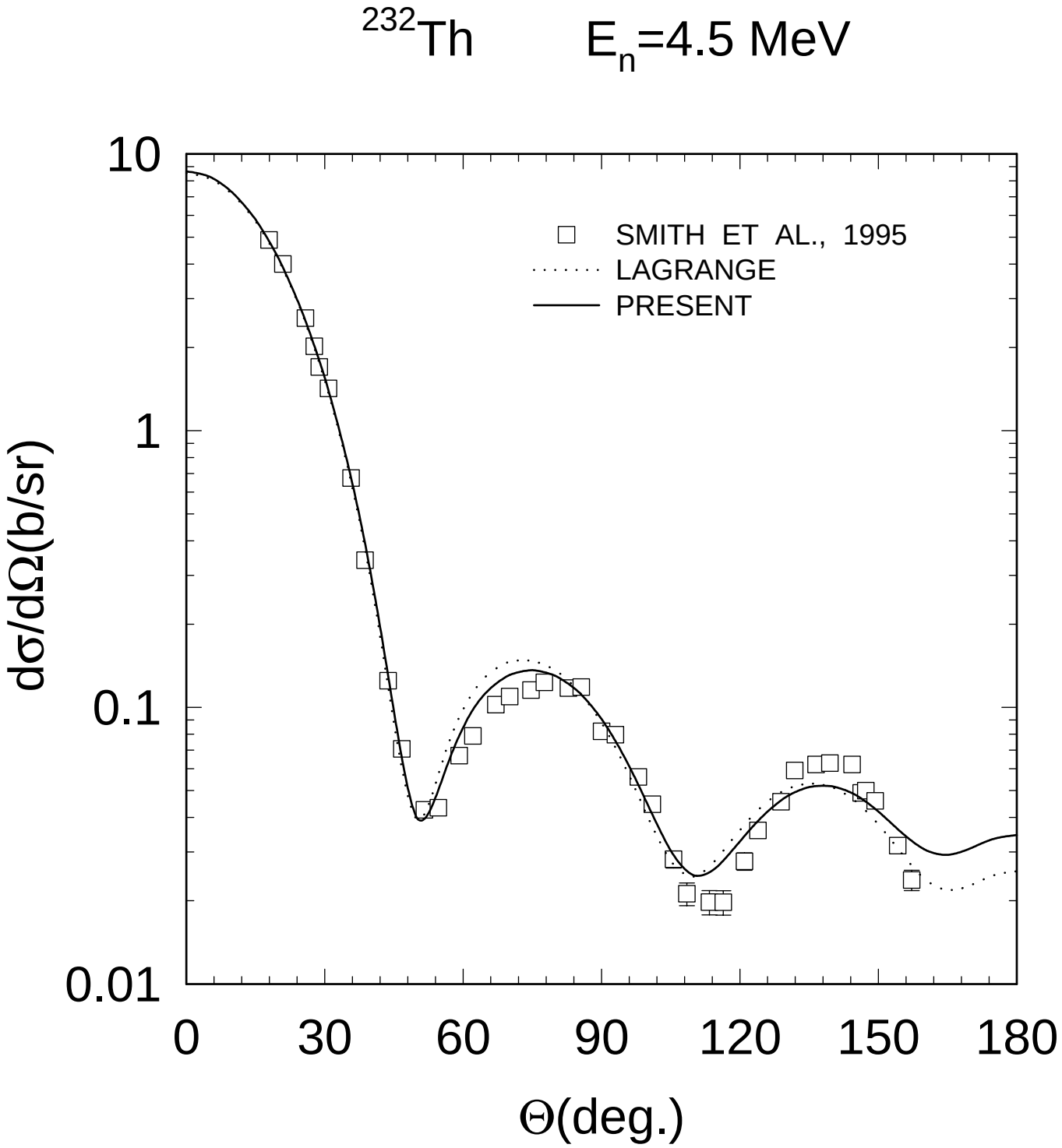
232Th
En=4.5 MeV
SMITH ET AL., 1995
LAGRANGE
PRESENT
dσ/dΩ(b/sr)
10
1
0.1
0.01
0
30
60
90
120
150
180
Θ(deg.)

FIG. 34

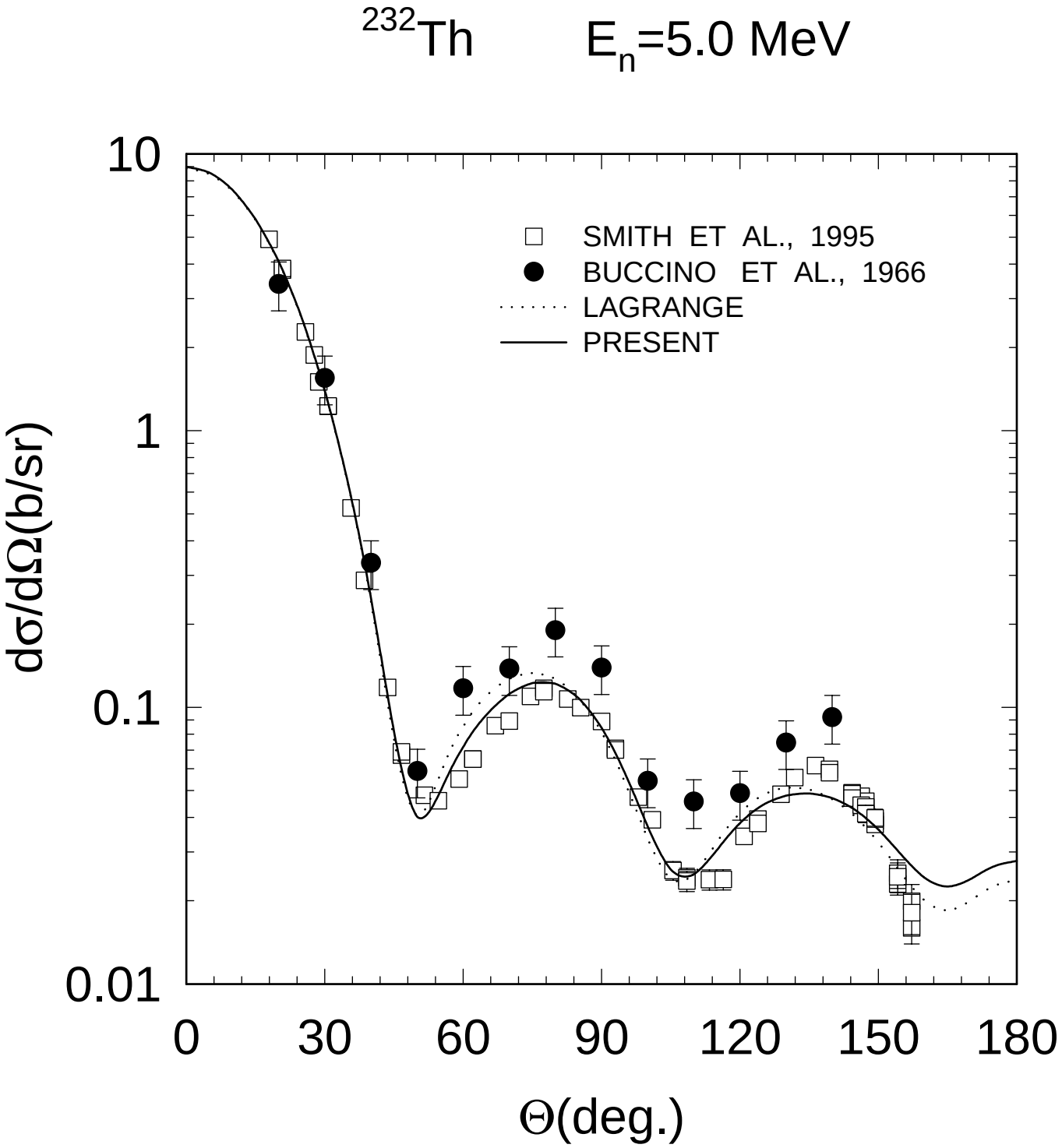
232Th
En=5.0 MeV
SMITH ET AL., 1995
BUCCINO ET AL., 1966
LAGRANGE
PRESENT
dσ/dΩ(b/sr)
10
1
0.1
0.01
0
30
60
90
120
150
180
Θ(deg.)

FIG. 35

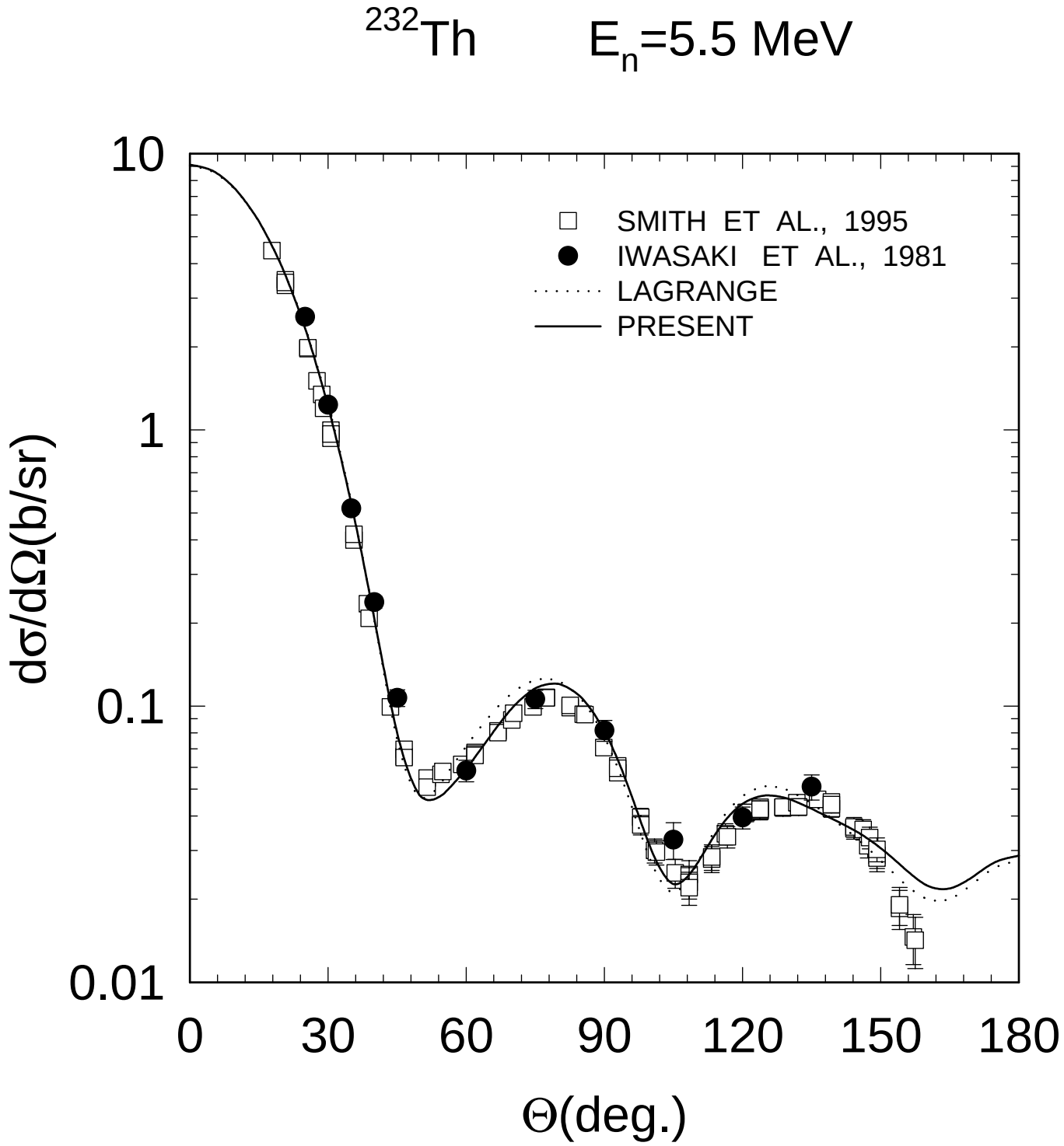
232Th
En=5.5 MeV
SMITH ET AL., 1995
IWASAKI ET AL., 1981
LAGRANGE
PRESENT
dσ/dΩ(b/sr)
10
1
0.1
0.01
0
30
60
90
120
150
180
Θ(deg.)

FIG. 36

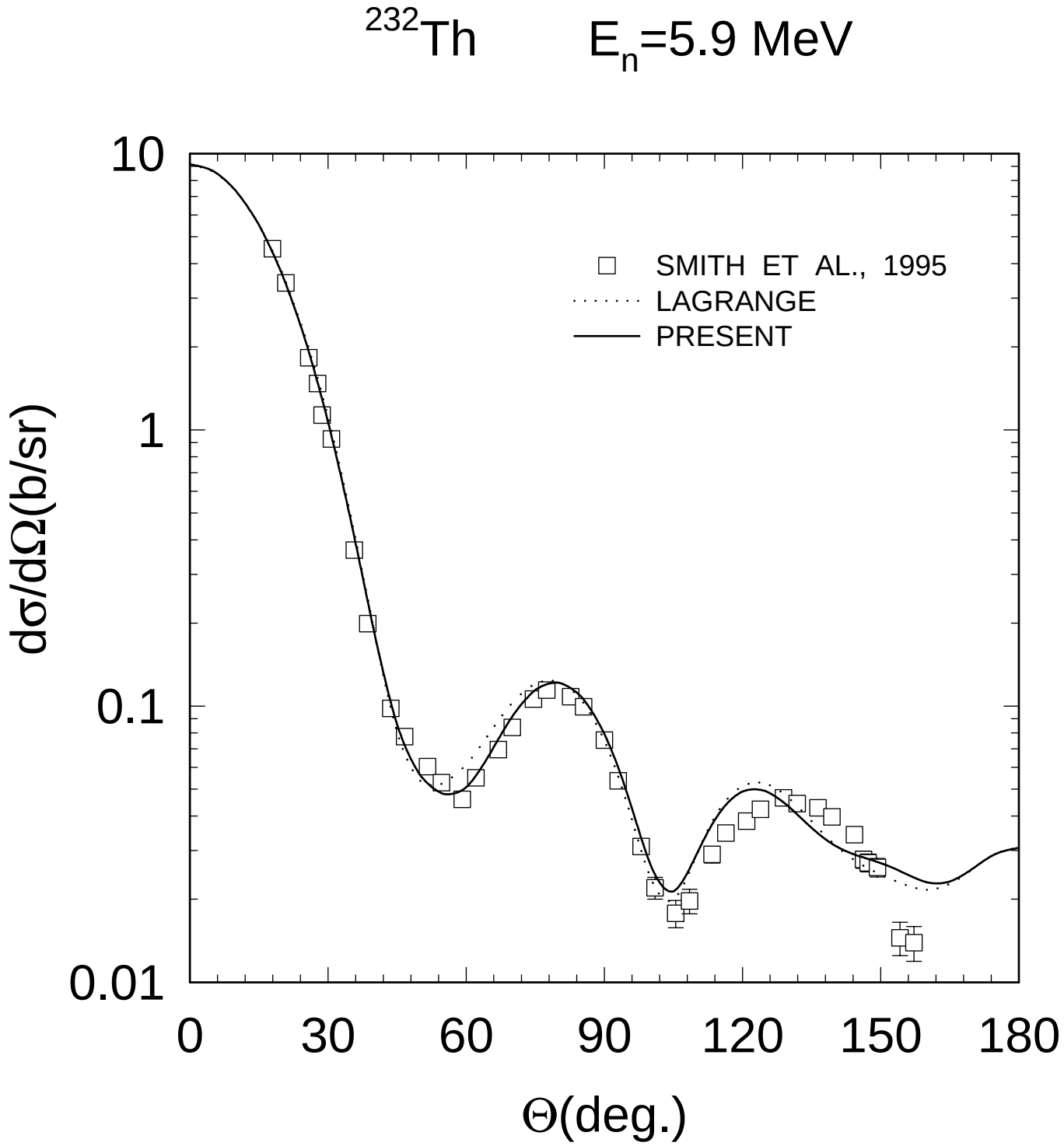
232Th
En=5.9 MeV
SMITH ET AL., 1995
LAGRANGE
PRESENT
dσ/dΩ(b/sr)
10
1
0.1
0.01
0
30
60
90
120
150
180
Θ(deg.)

FIG. 37

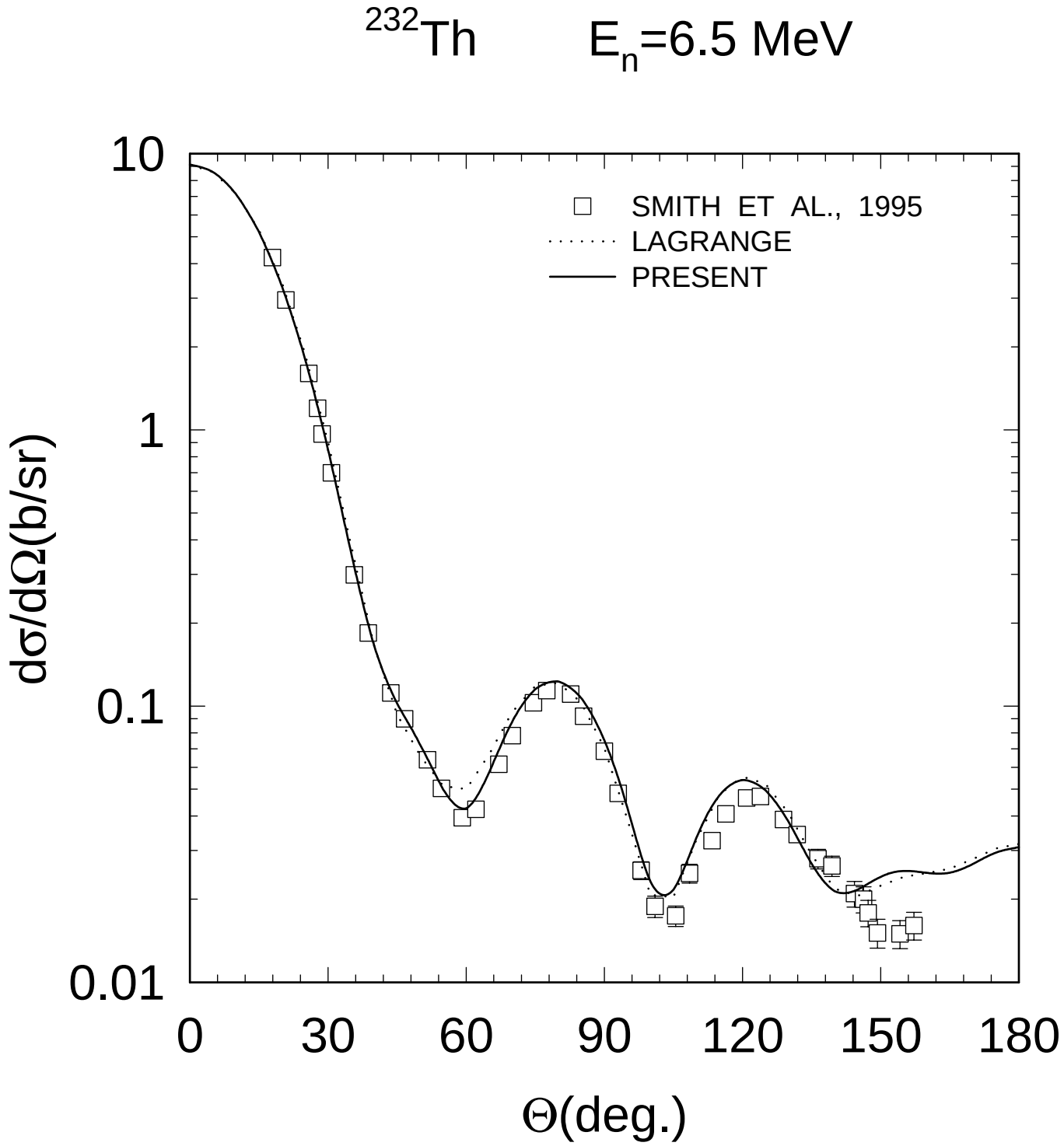
232Th
En=6.5 MeV
SMITH ET AL., 1995
LAGRANGE
PRESENT
dσ/dΩ(b/sr)
10
1
0.1
0.01
0
30
60
90
120
150
180
Θ(deg.)

FIG. 38

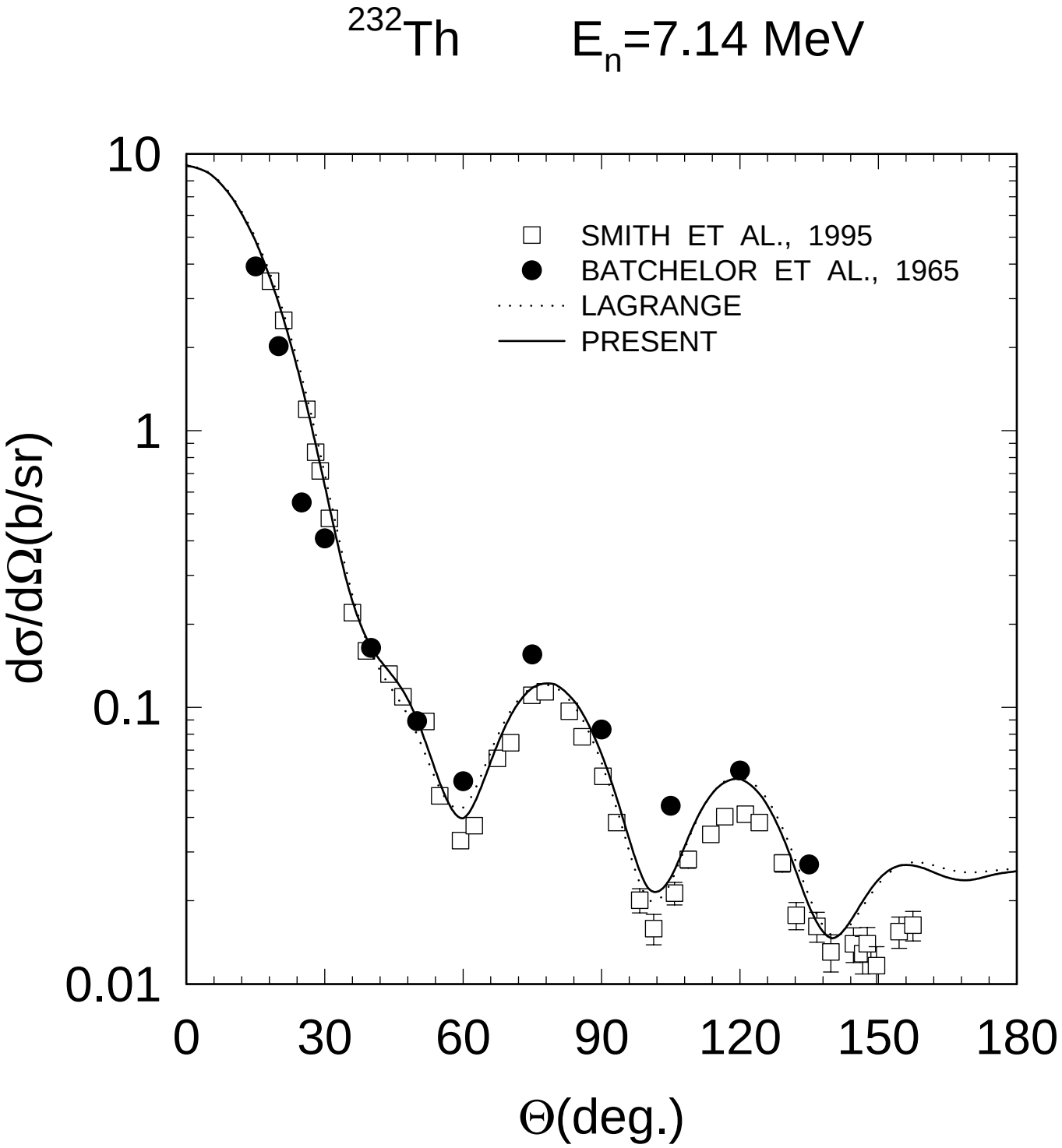
232Th
En=7.14 MeV
SMITH ET AL., 1995
BATCHELOR ET AL., 1965
LAGRANGE
PRESENT
dσ/dΩ(b/sr)
10
1
0.1
0.01
0
30
60
90
120
150
180
Θ(deg.)

FIG. 39

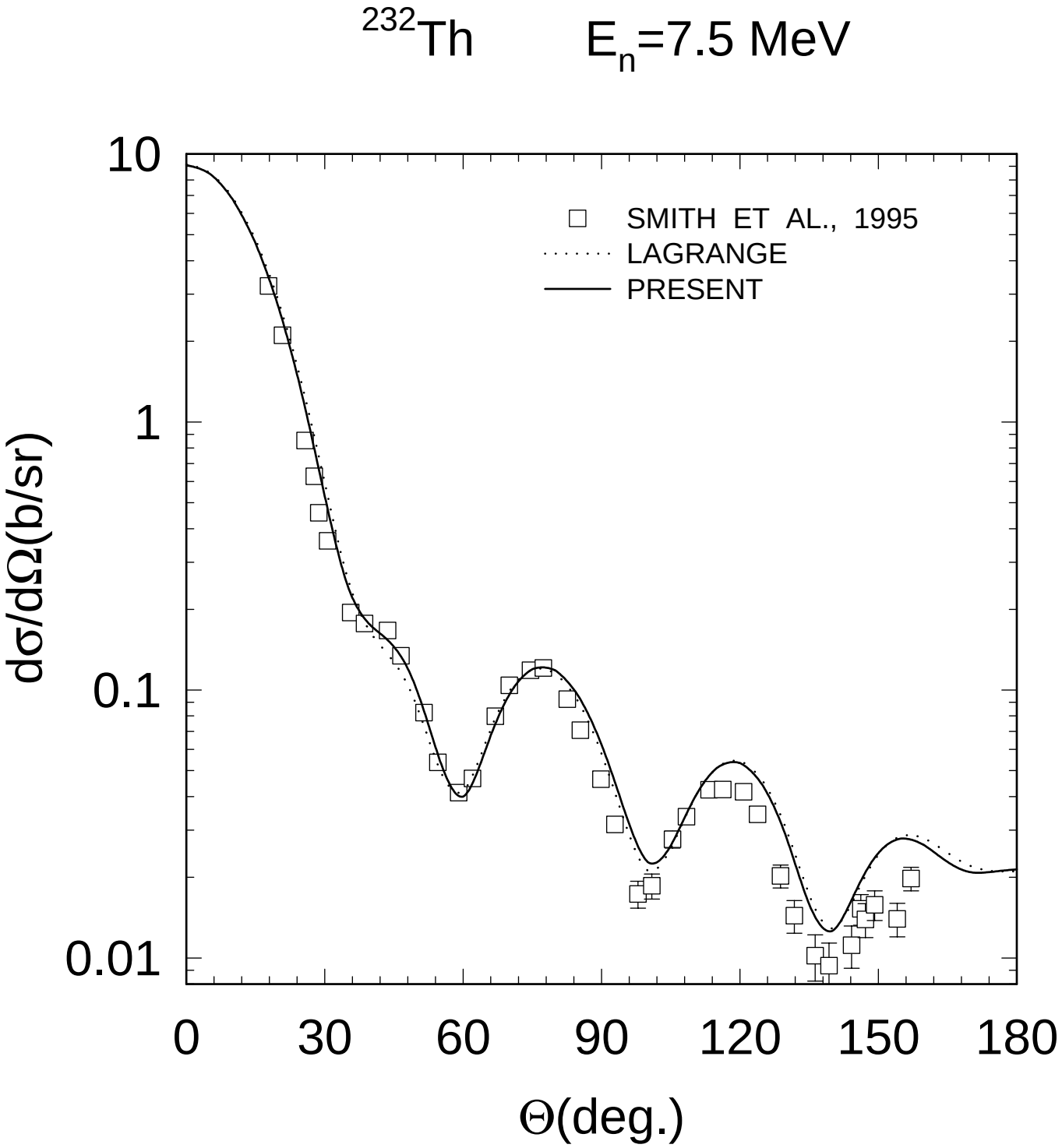
232Th
En=7.5 MeV
SMITH ET AL., 1995
LAGRANGE
PRESENT
dσ/dΩ(b/sr)
10
1
0.1
0.01
0
30
60
90
120
150
180
Θ(deg.)

FIG. 40

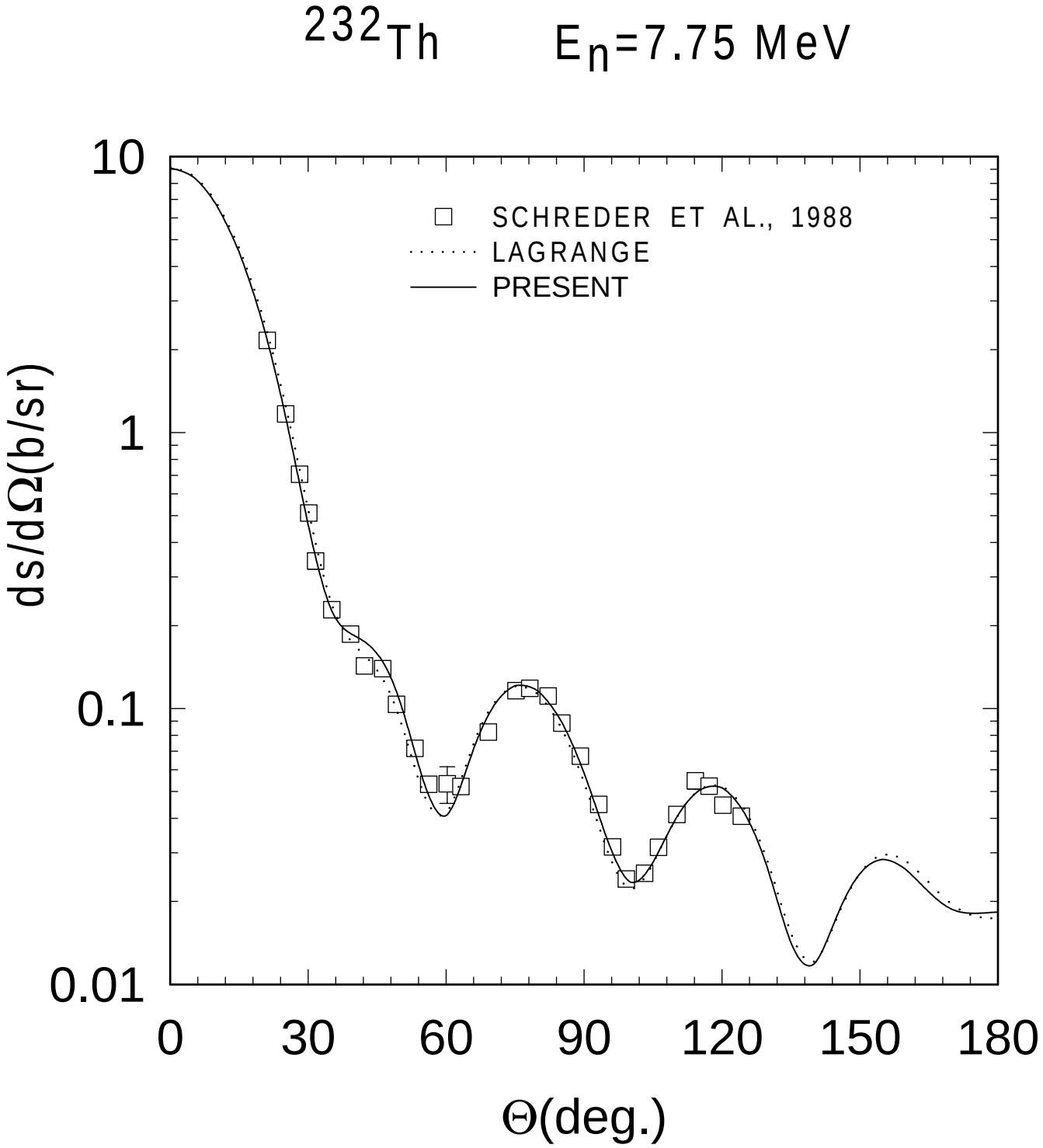
232Th
En=7.75 MeV
SCHREDER ET AL., 1988
LAGRANGE
PRESENT
ds/dΩ(b/sr)
10
1
0.1
0.01
0
30
60
90
120
150
180
Θ(deg.)

FIG. 41

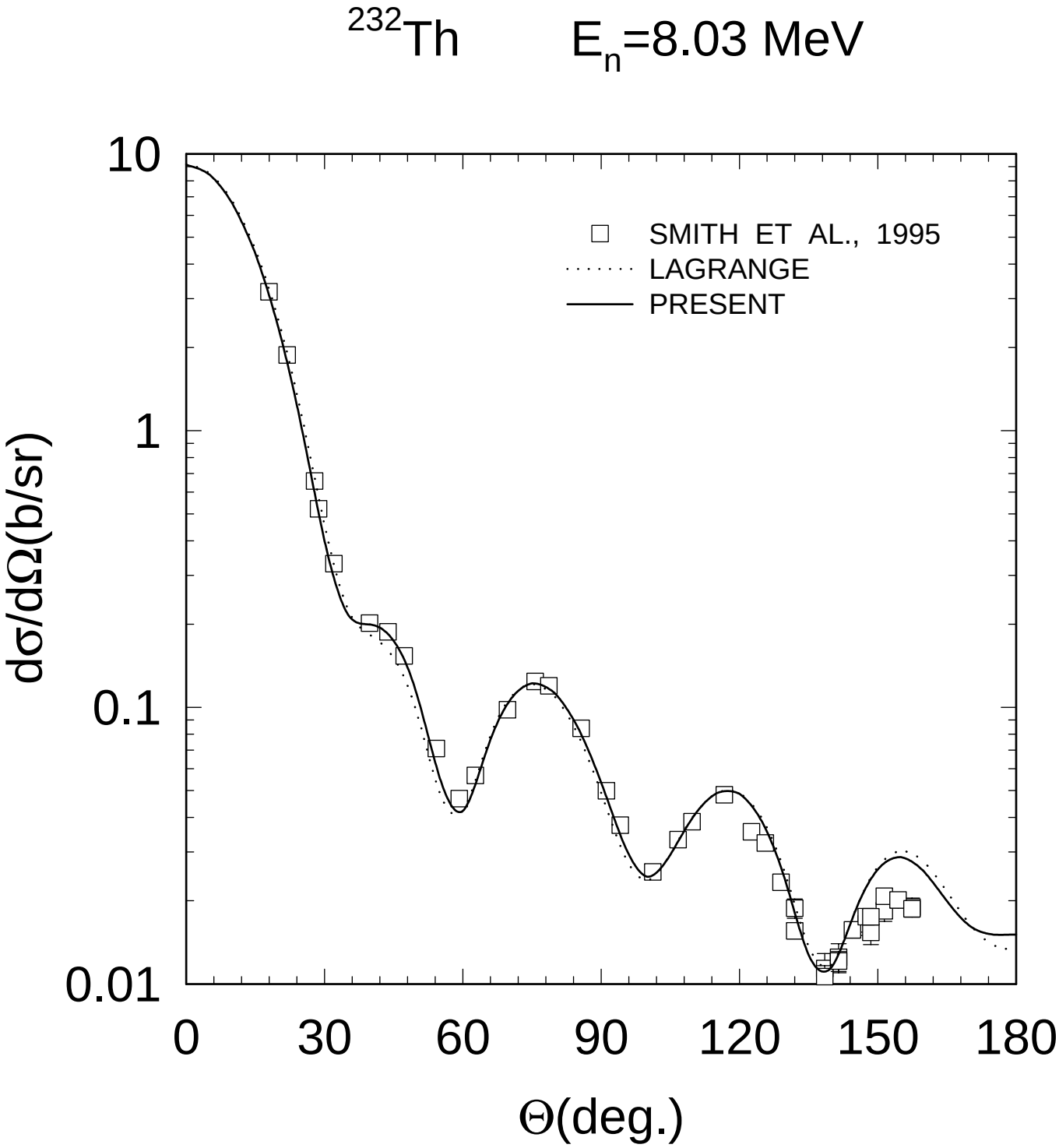
232Th
En=8.03 MeV
SMITH ET AL., 1995
LAGRANGE
PRESENT
10
1
0.1
0.01
dσ/dΩ(b/sr)
0
30
60
90
120
150
180
Θ(deg.)

FIG. 42

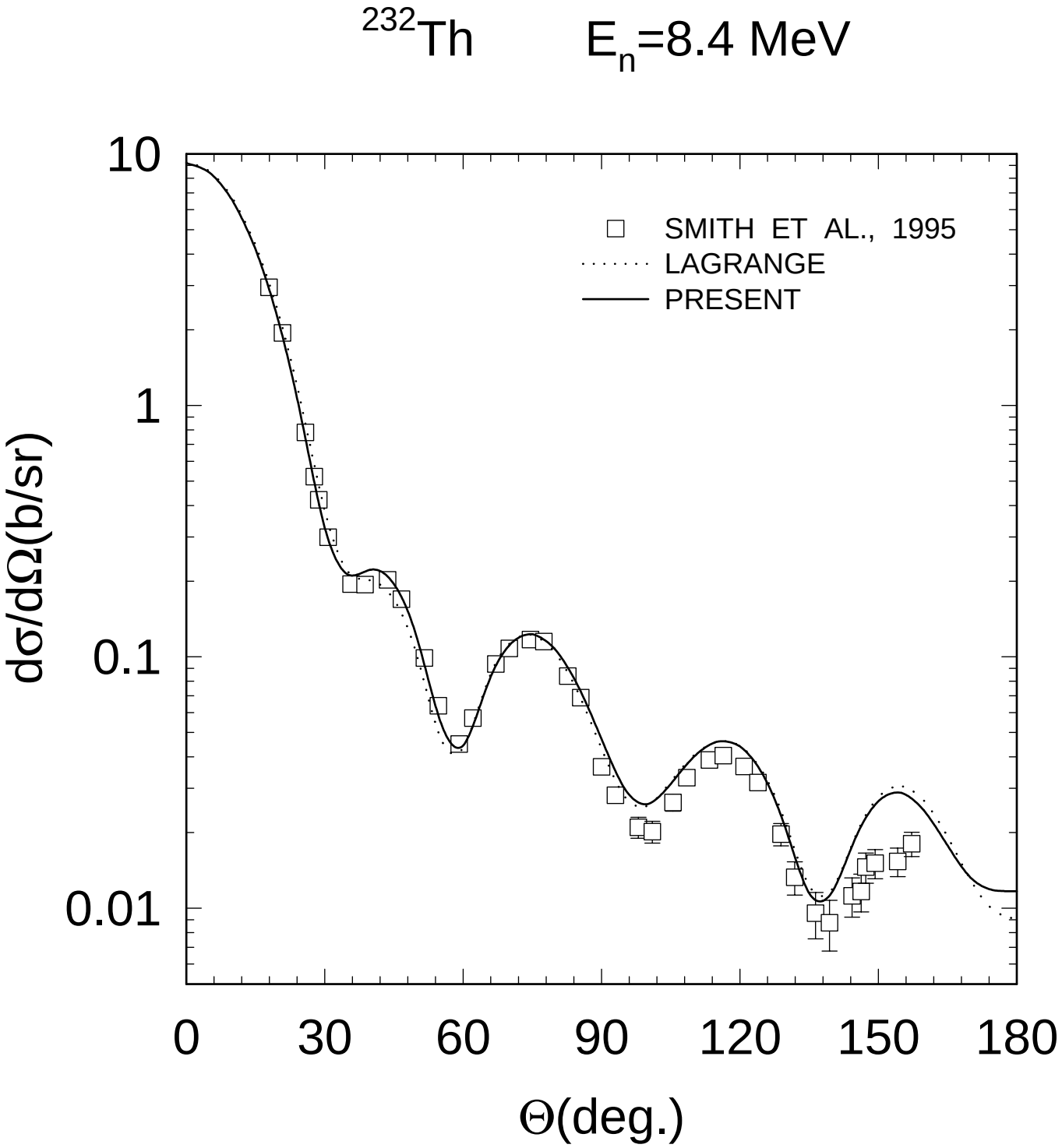
232Th
En=8.4 MeV
SMITH ET AL., 1995
LAGRANGE
PRESENT
dσ/dΩ(b/sr)
10
1
0.1
0.01
0
30
60
90
120
150
180
Θ(deg.)

FIG. 43

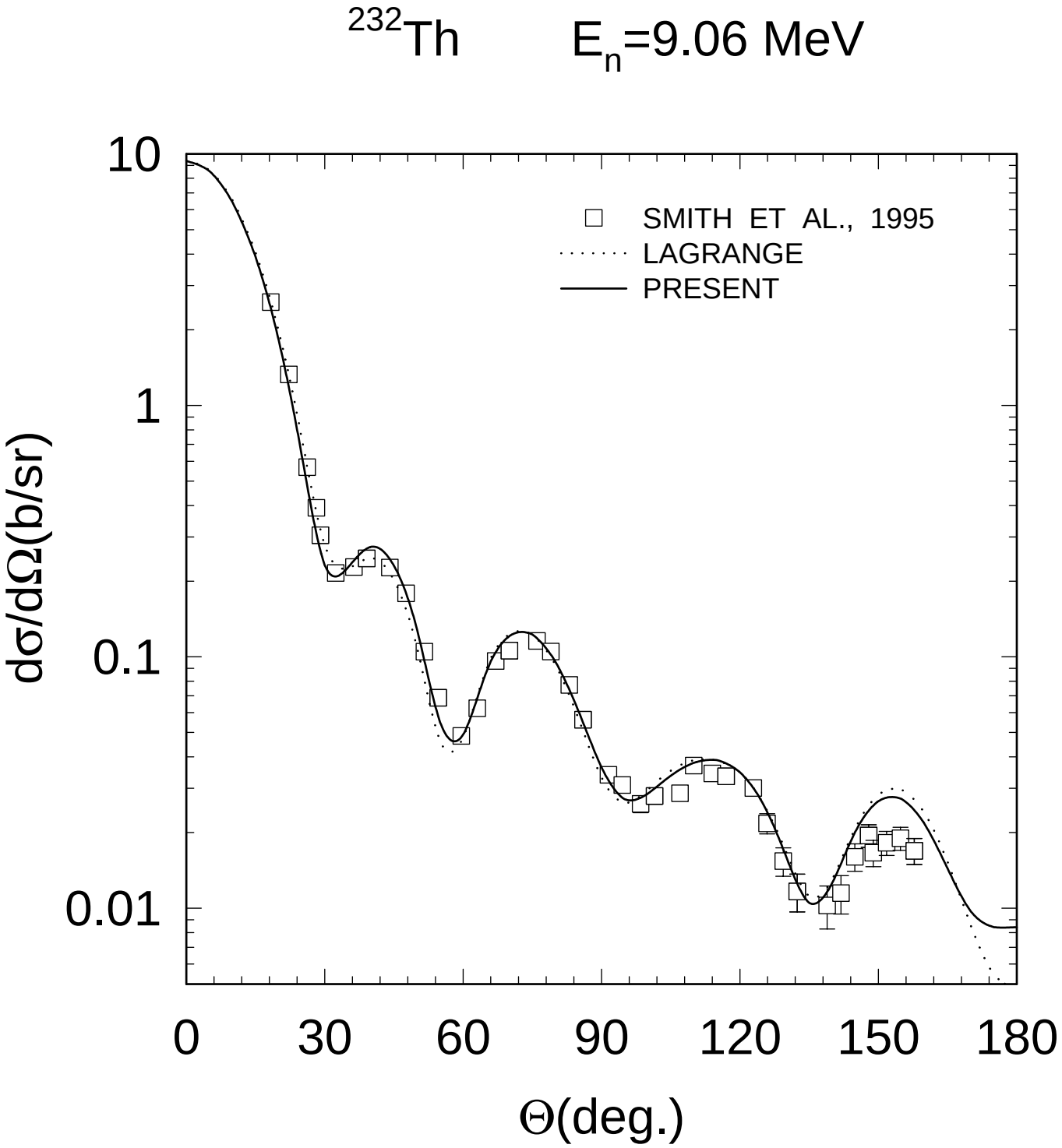
232Th
En=9.06 MeV
SMITH ET AL., 1995
LAGRANGE
PRESENT
dσ/dΩ(b/sr)
10
1
0.1
0.01
0
30
60
90
120
150
180
Θ(deg.)

FIG. 44

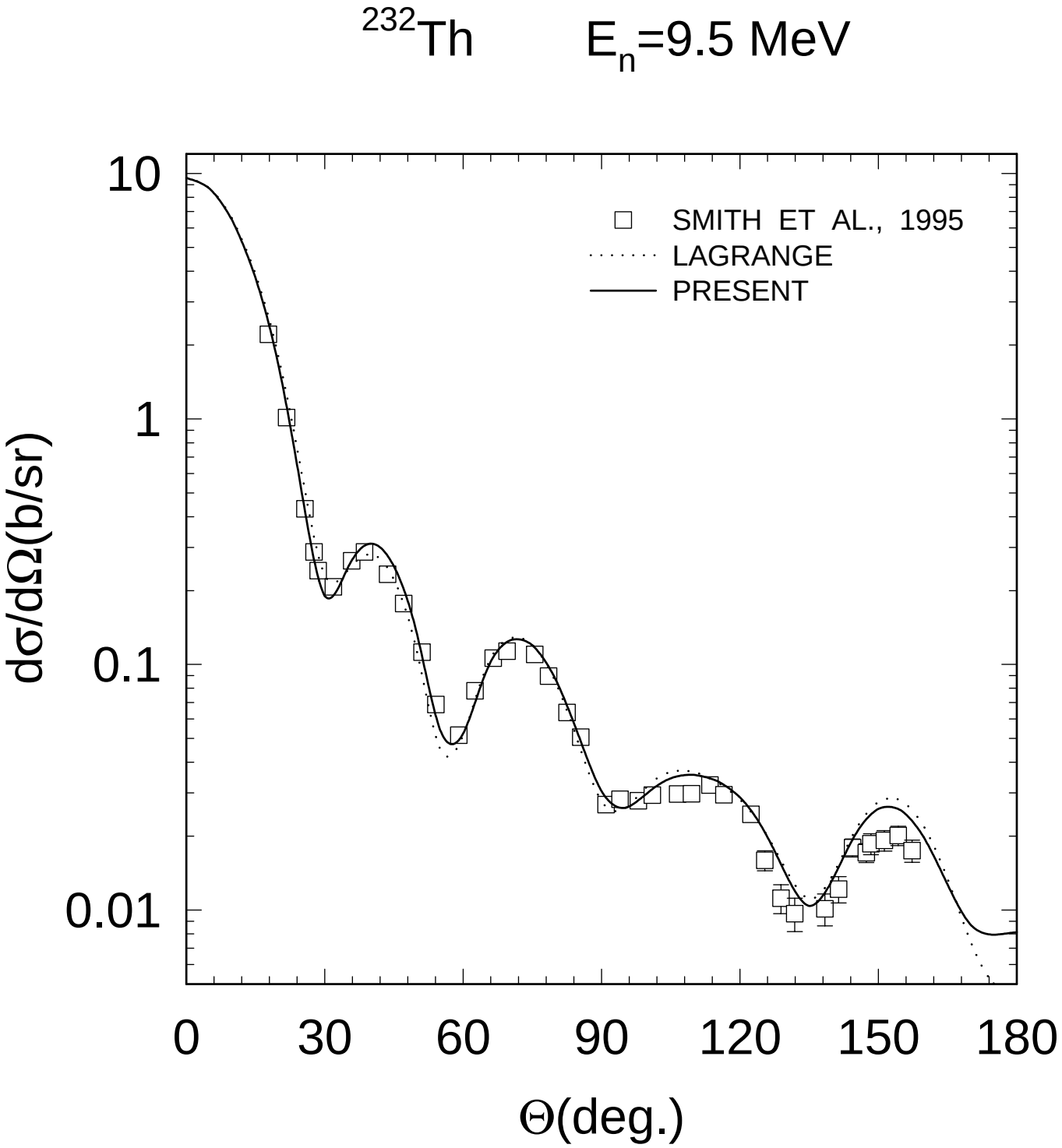
232Th
En=9.5 MeV
SMITH ET AL., 1995
LAGRANGE
PRESENT
dσ/dΩ(b/sr)
10
1
0.1
0.01
0
30
60
90
120
150
180
Θ(deg.)

FIG. 45

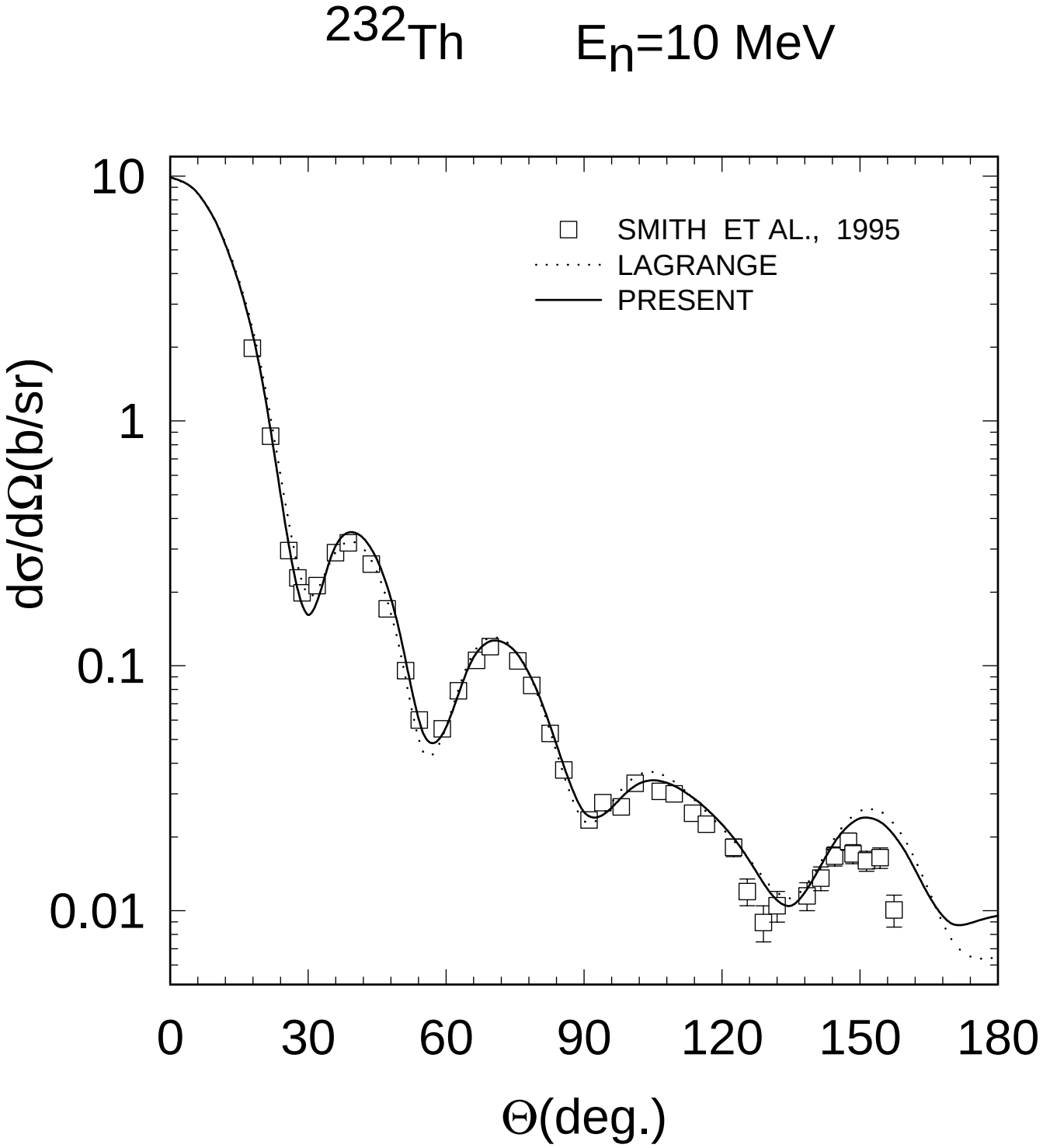
232Th
En=10 MeV
SMITH ET AL., 1995
LAGRANGE
PRESENT
dσ/dΩ(b/sr)
10
1
0.1
0.01
0
30
60
90
120
150
180
Θ(deg.)

FIG. 46

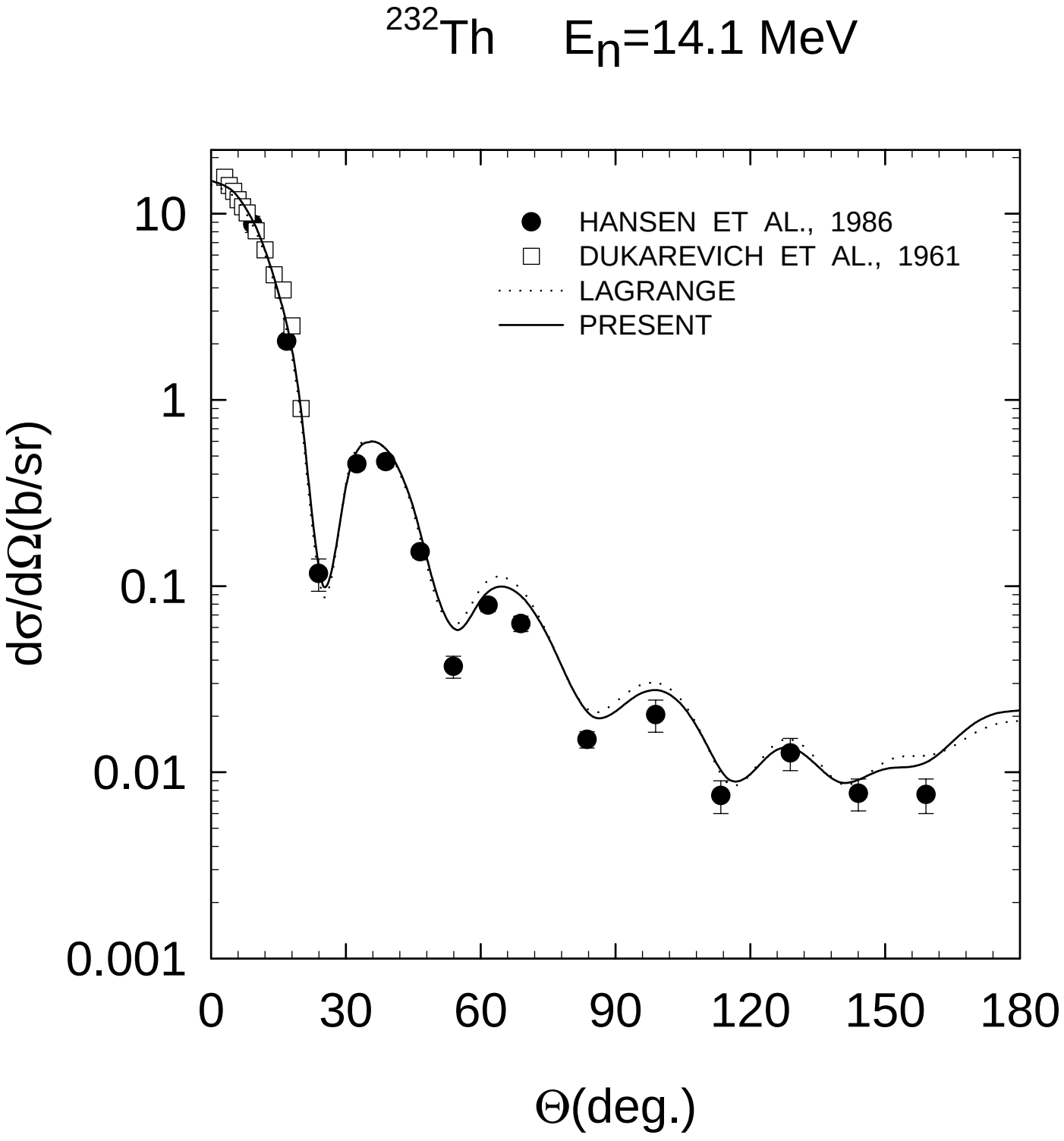
232Th En=14.1 MeV
HANSEN ET AL., 1986
DUKAREVICH ET AL., 1961
LAGRANGE
PRESENT
dσ/dΩ(b/sr)
10
1
0.1
0.01
0.001
0
30
60
90
120
150
180
Θ(deg.)

FIG. 47

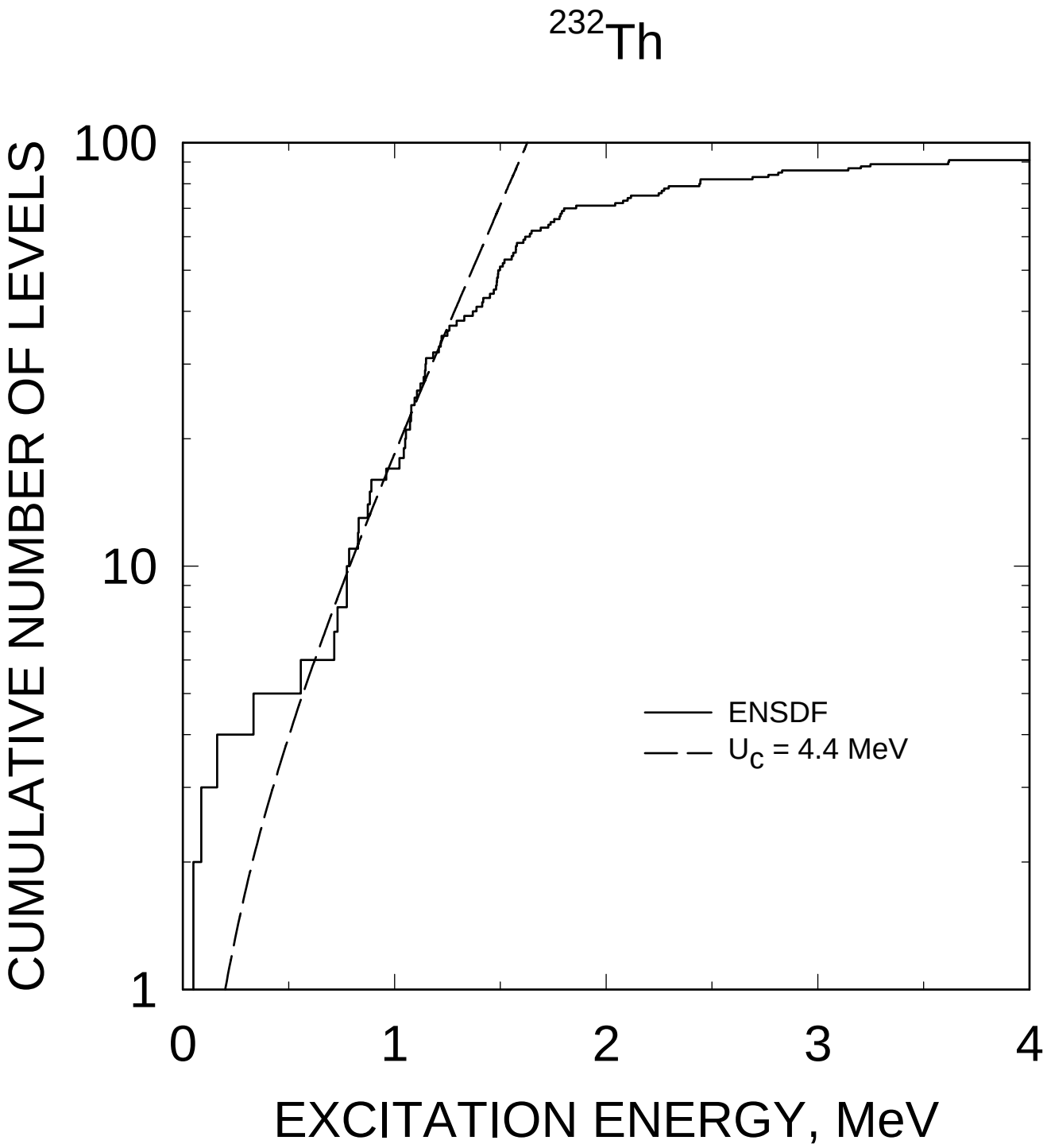
232Th
100
10
1
CUMULATIVE NUMBER OF LEVELS
0
1
2
3
4
EXCITATION ENERGY, MeV
ENSDF
Uc = 4.4 MeV

FIG. 48

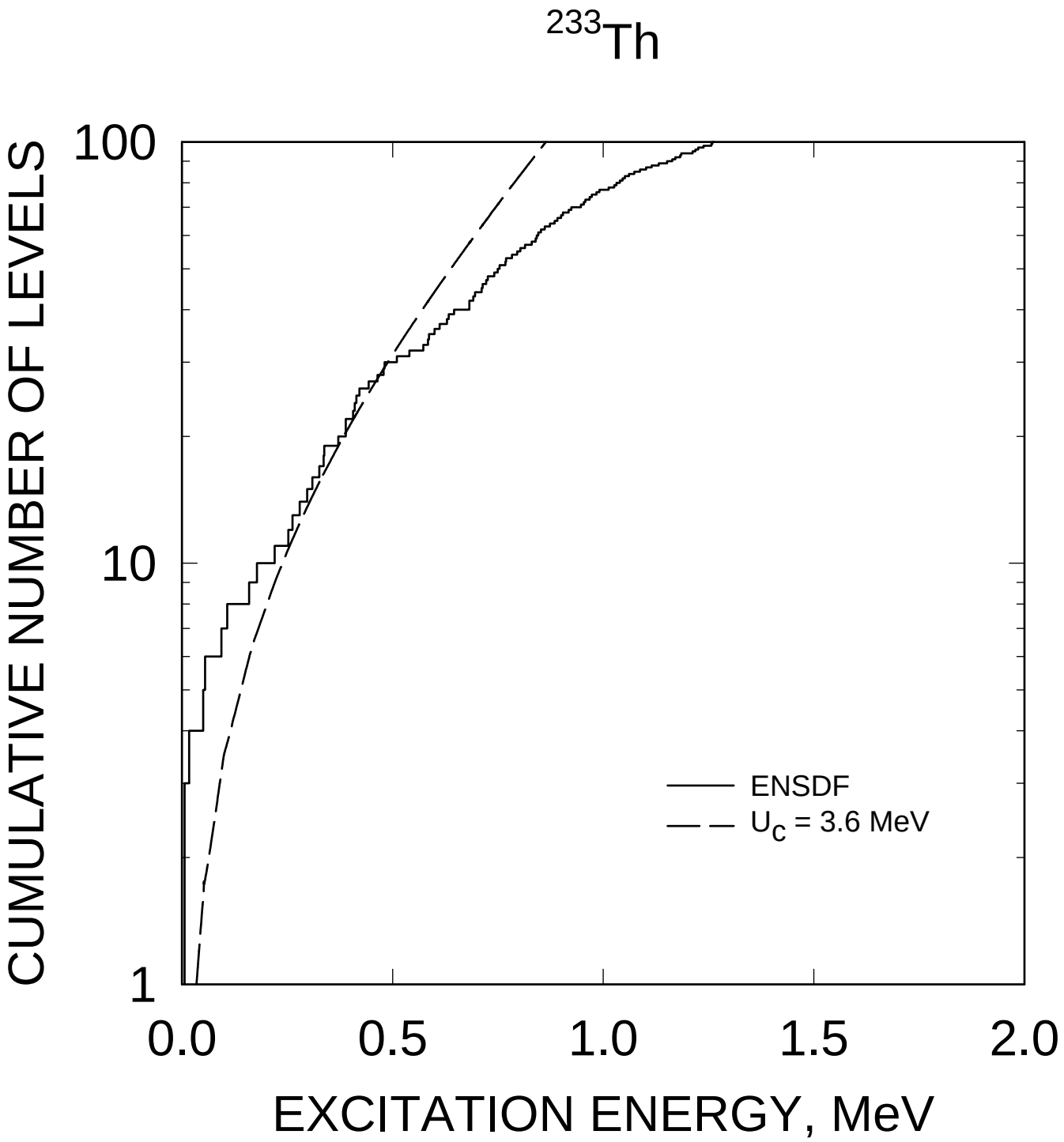
233Th
CUMULATIVE NUMBER OF LEVELS
100
10
1
0.0
0.5
1.0
1.5
2.0
EXCITATION ENERGY, MeV
ENSDF
Uc = 3.6 MeV

FIG. 49

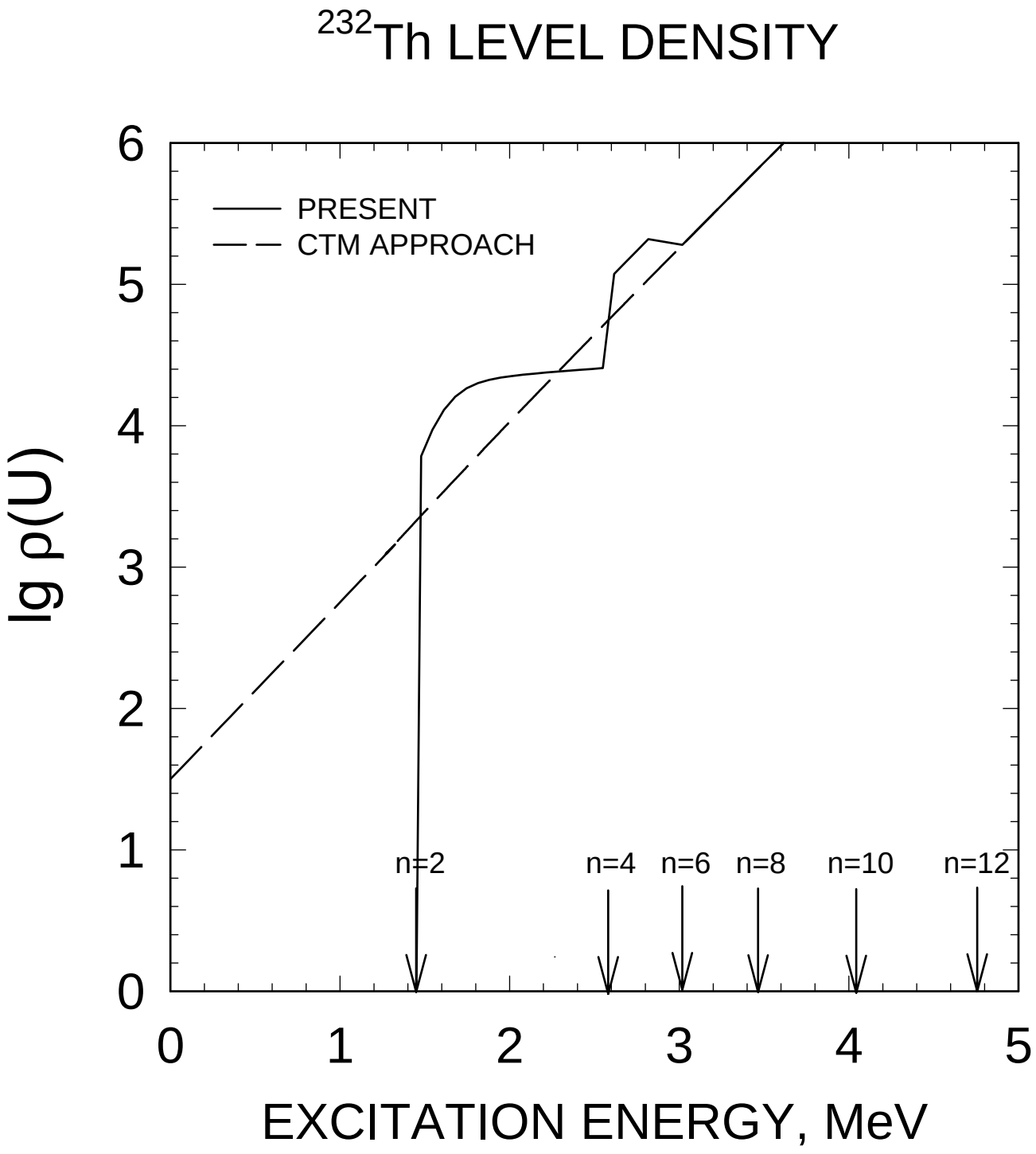
232Th LEVEL DENSITY
PRESENT
CTM APPROACH
lg ρ(U)
EXCITATION ENERGY, MeV
n=2
n=4
n=6
n=8
n=10
n=12
0
1
2
3
4
5
6

FIG. 50

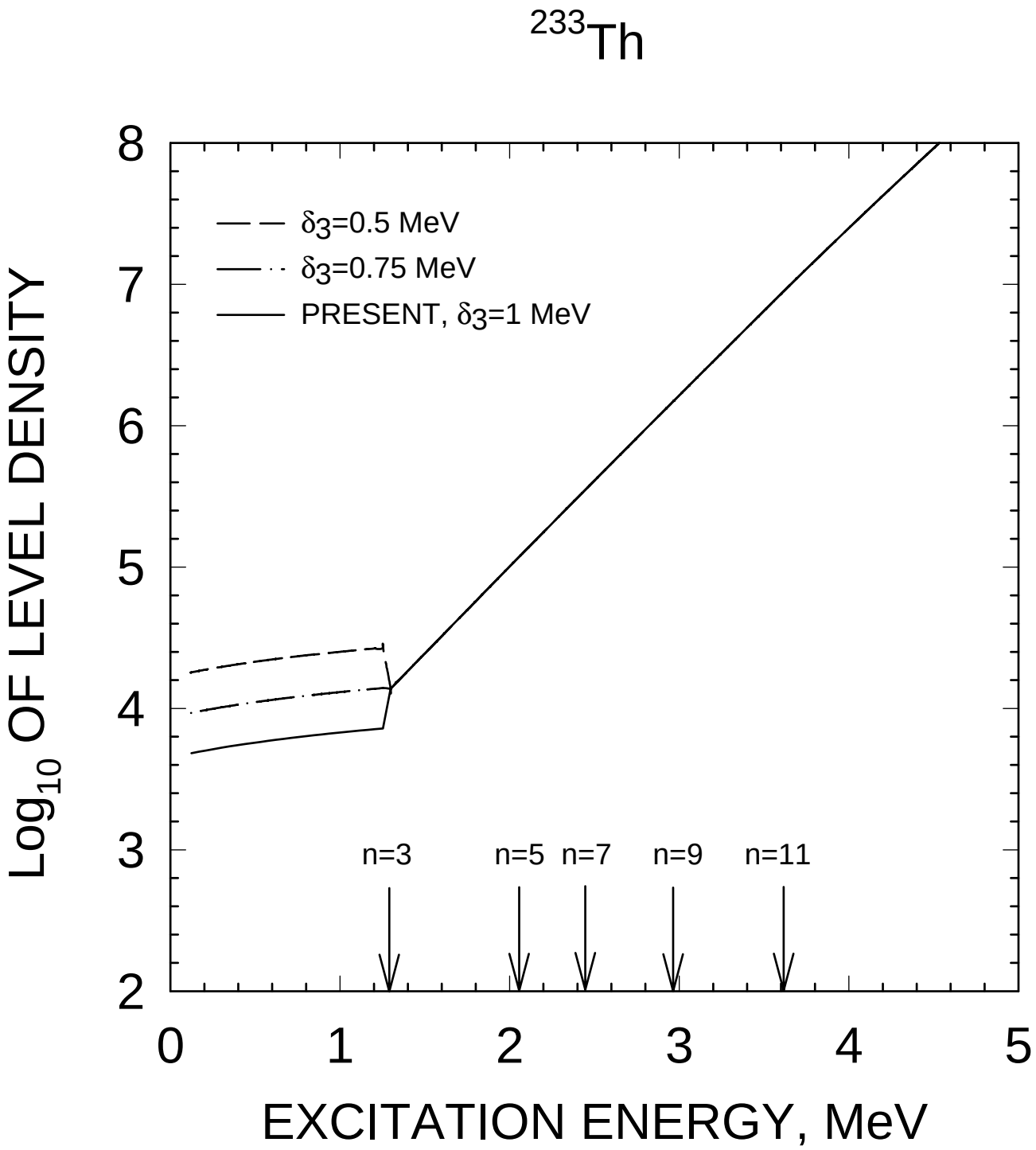
233Th
δ3=0.5 MeV
δ3=0.75 MeV
PRESENT, δ3=1 MeV
n=3
n=5
n=7
n=9
n=11
Log10 OF LEVEL DENSITY
EXCITATION ENERGY, MeV
0
1
2
3
4
5
2
3
4
5
6
7
8

FIG. 51

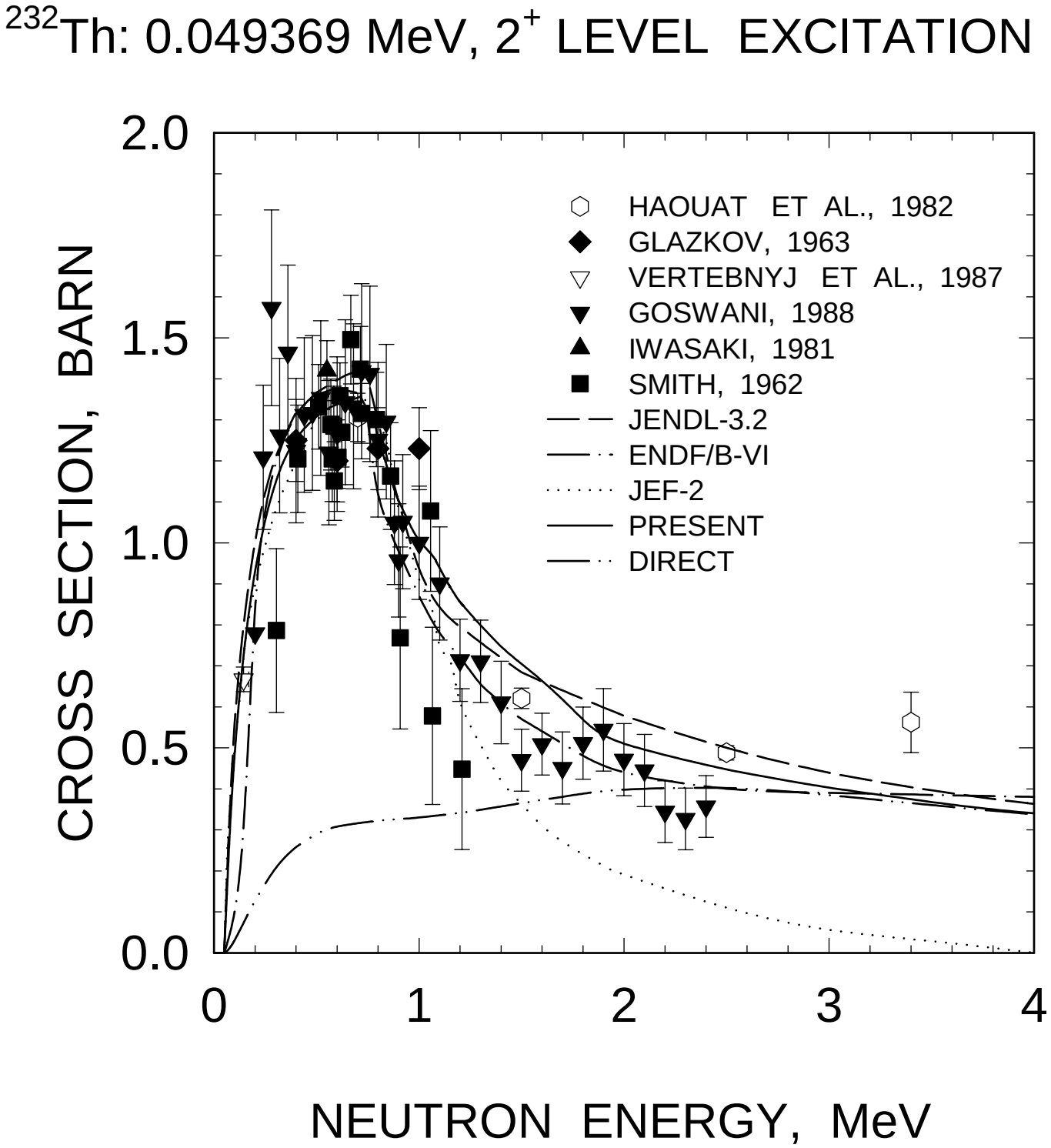
232Th: 0.049369 MeV, 2+ LEVEL EXCITATION
CROSS SECTION, BARN
NEUTRON ENERGY, MeV
2.0
1.5
1.0
0.5
0.0
0
1
2
3
4
HAOUAT ET AL., 1982
GLAZKOV, 1963
VERTEBNYJ ET AL., 1987
GOSWANI, 1988
IWASAKI, 1981
SMITH, 1962
JENDL-3.2
ENDF/B-VI
JEF-2
PRESENT
DIRECT

FIG. 52

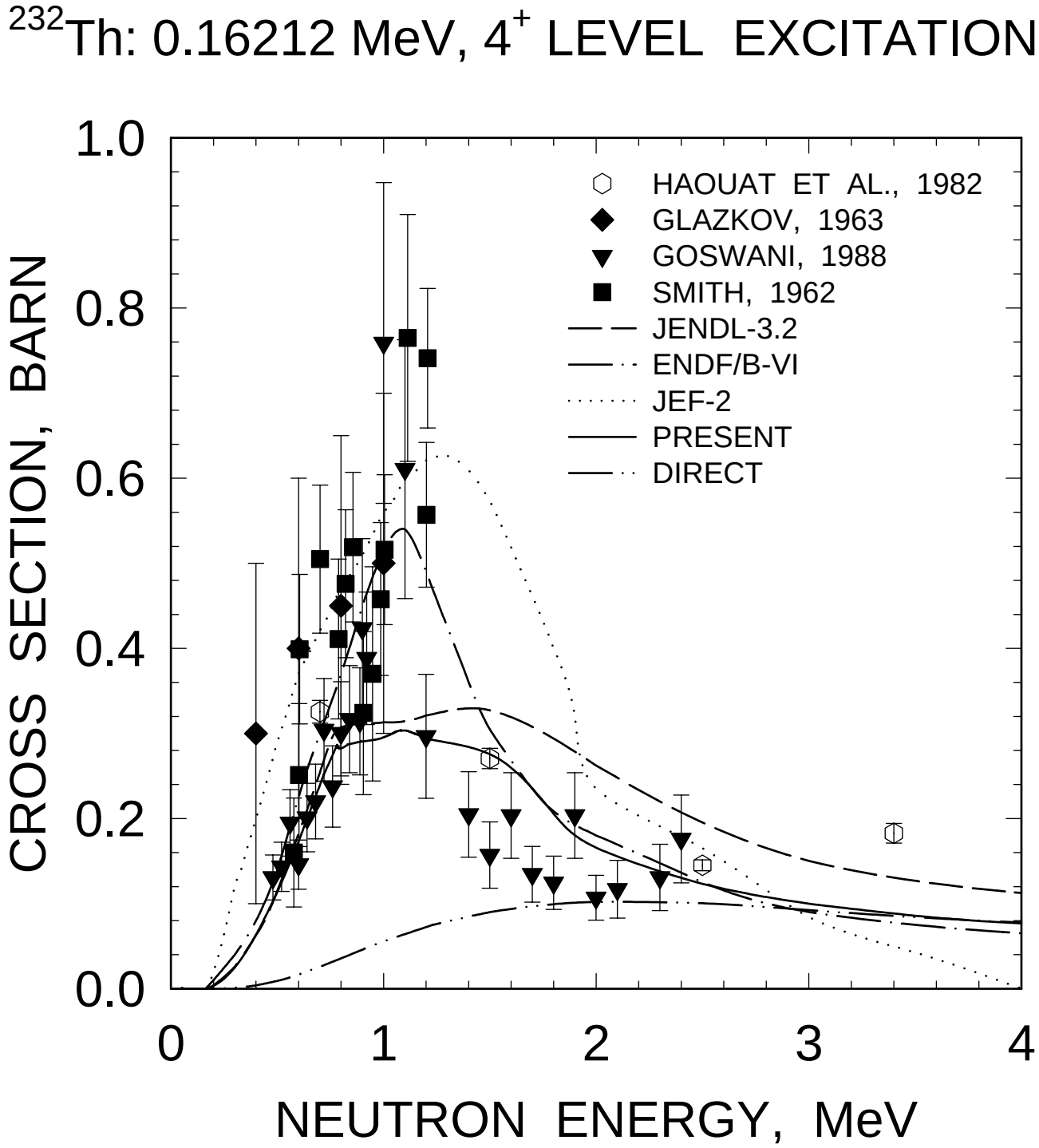
232Th: 0.16212 MeV, 4+ LEVEL EXCITATION
HAOUAT ET AL., 1982
GLAZKOV, 1963
GOSWANI, 1988
SMITH, 1962
JENDL-3.2
ENDF/B-VI
JEF-2
PRESENT
DIRECT
CROSS SECTION, BARN
NEUTRON ENERGY, MeV
0.0
0.2
0.4
0.6
0.8
1.0
0
1
2
3
4

FIG. 53

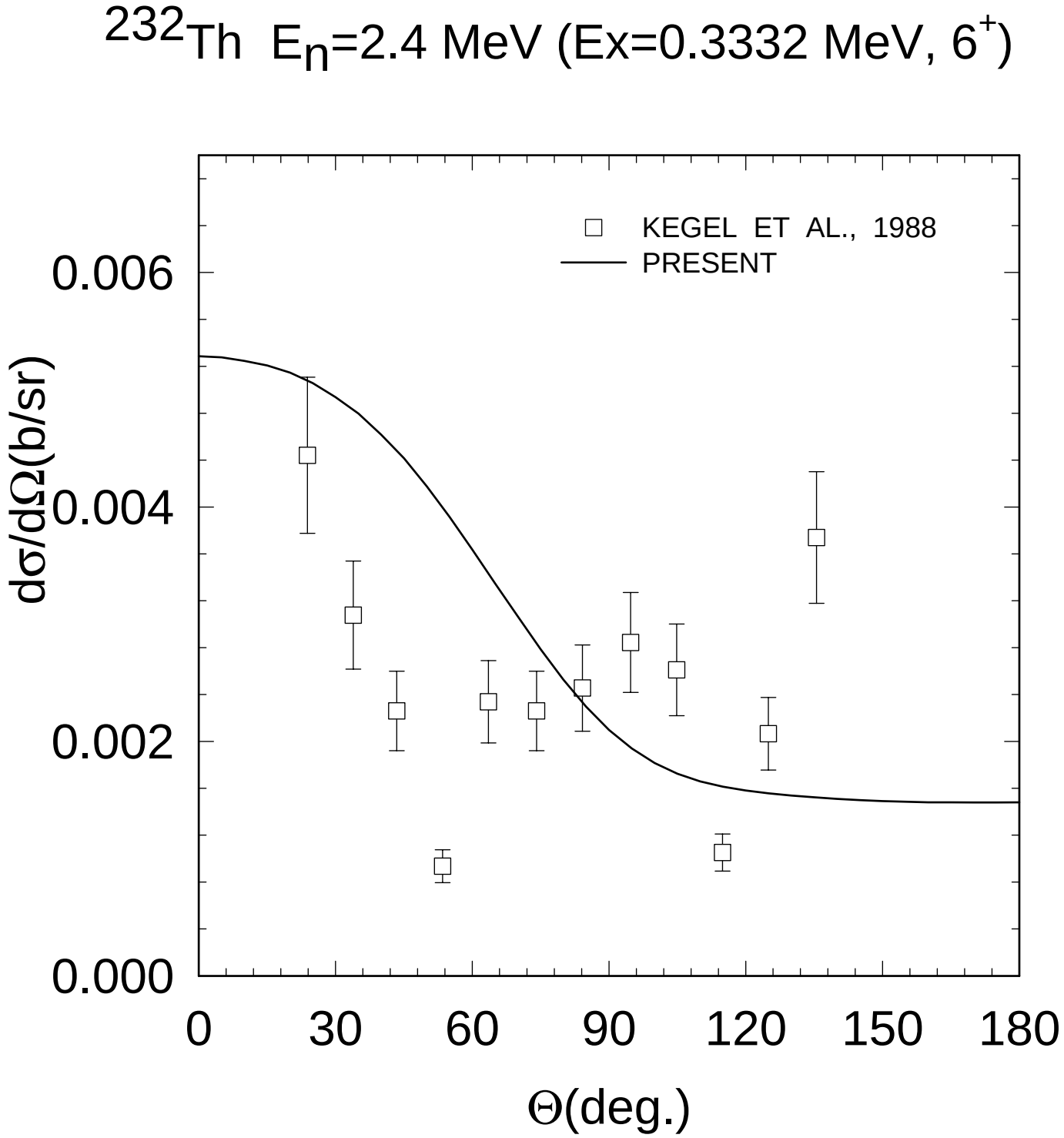
232Th En=2.4 MeV (Ex=0.3332 MeV, 6+)
KEGEL ET AL., 1988
PRESENT
0.006
0.004
0.002
0.000
dσ/dΩ(b/sr)
0
30
60
90
120
150
180
Θ(deg.)

FIG. 54

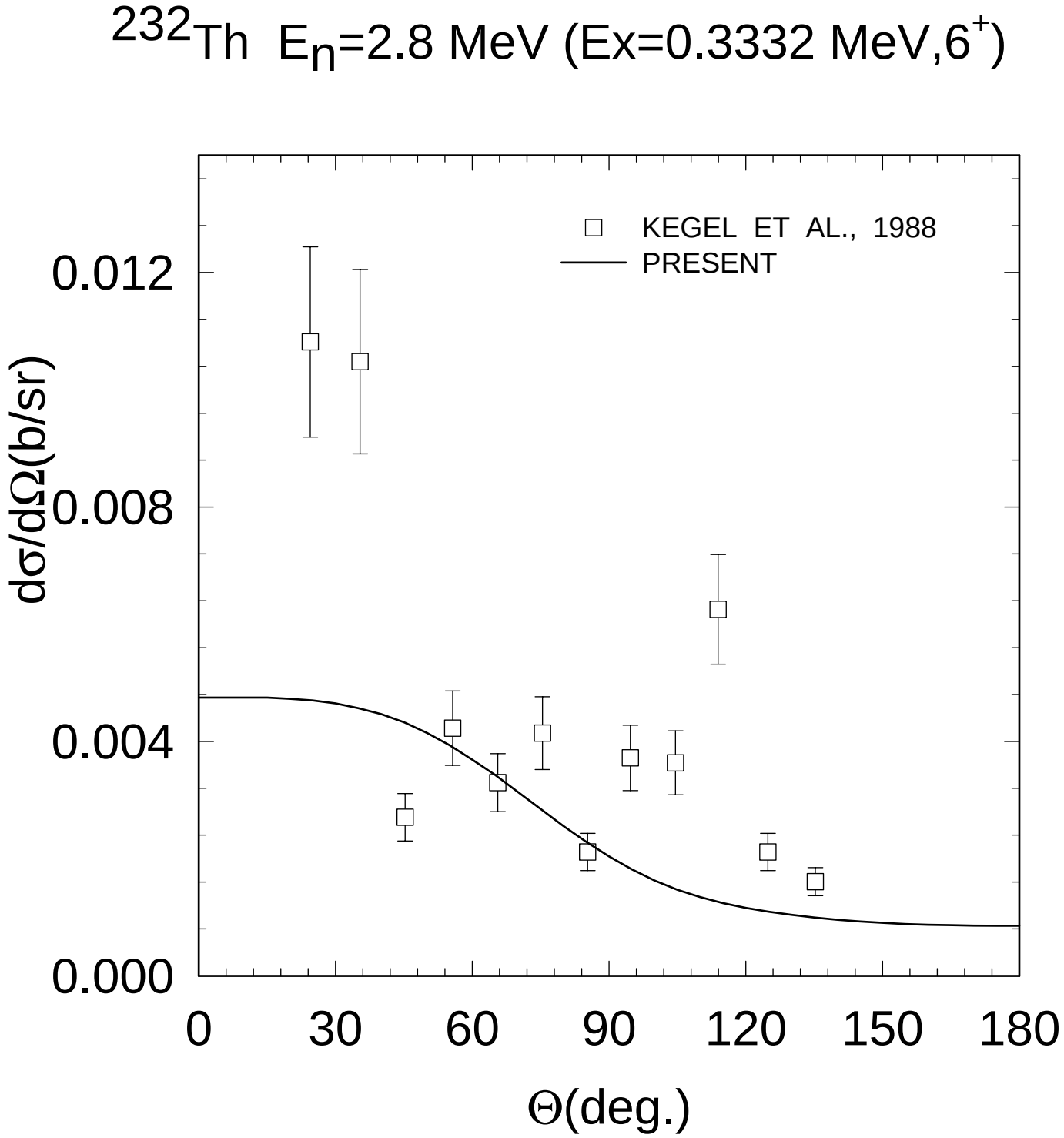
232Th En=2.8 MeV (Ex=0.3332 MeV,6+)
KEGEL ET AL., 1988
PRESENT
dσ/dΩ(b/sr)
0.012
0.008
0.004
0.000
0
30
60
90
120
150
180
Θ(deg.)

FIG. 55

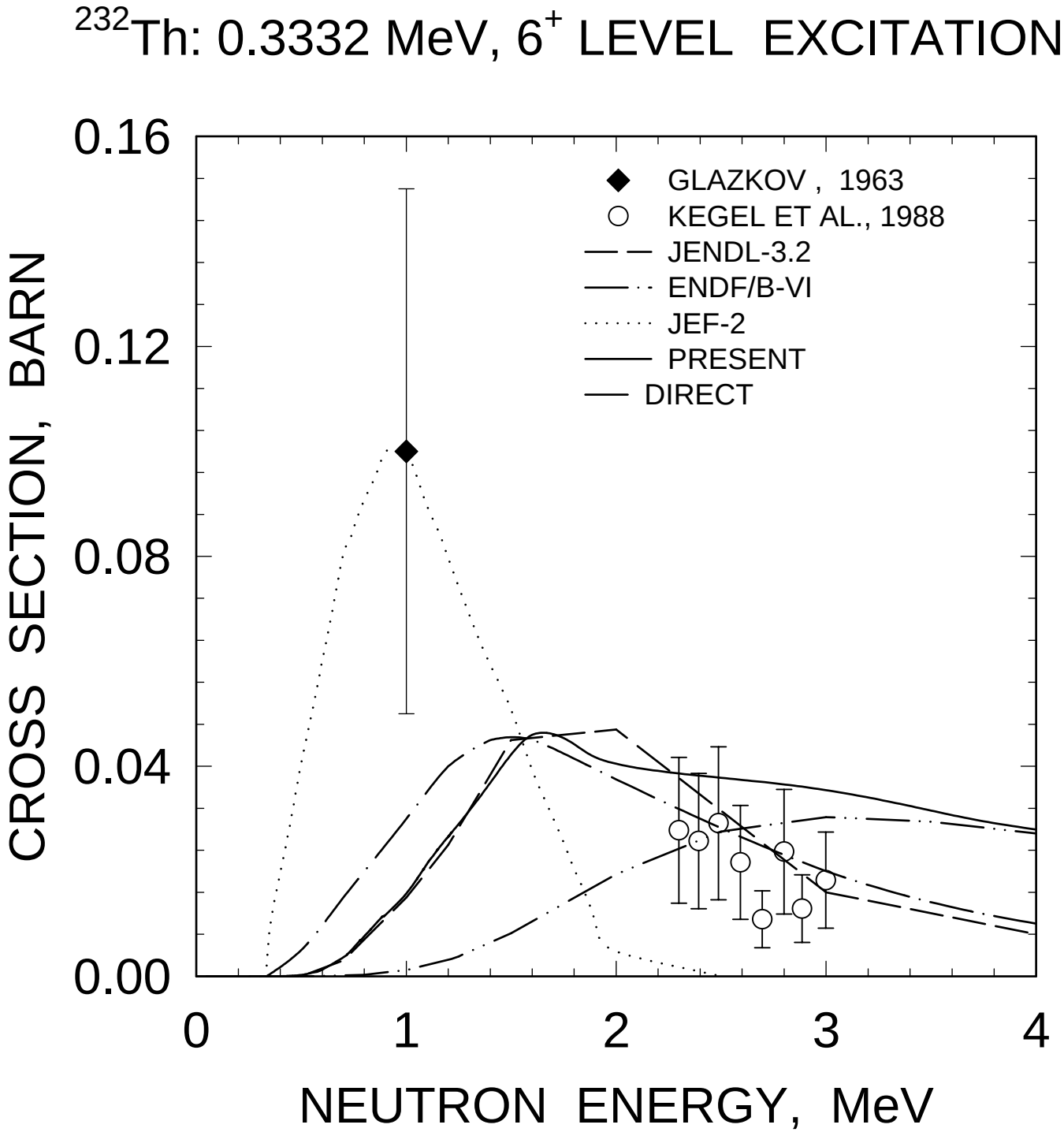
232Th: 0.3332 MeV, 6+ LEVEL EXCITATION
GLAZKOV , 1963
KEGEL ET AL., 1988
JENDL-3.2
ENDF/B-VI
JEF-2
PRESENT
DIRECT
CROSS SECTION, BARN
0.16
0.12
0.08
0.04
0.00
0
1
2
3
4
NEUTRON ENERGY, MeV

FIG. 56

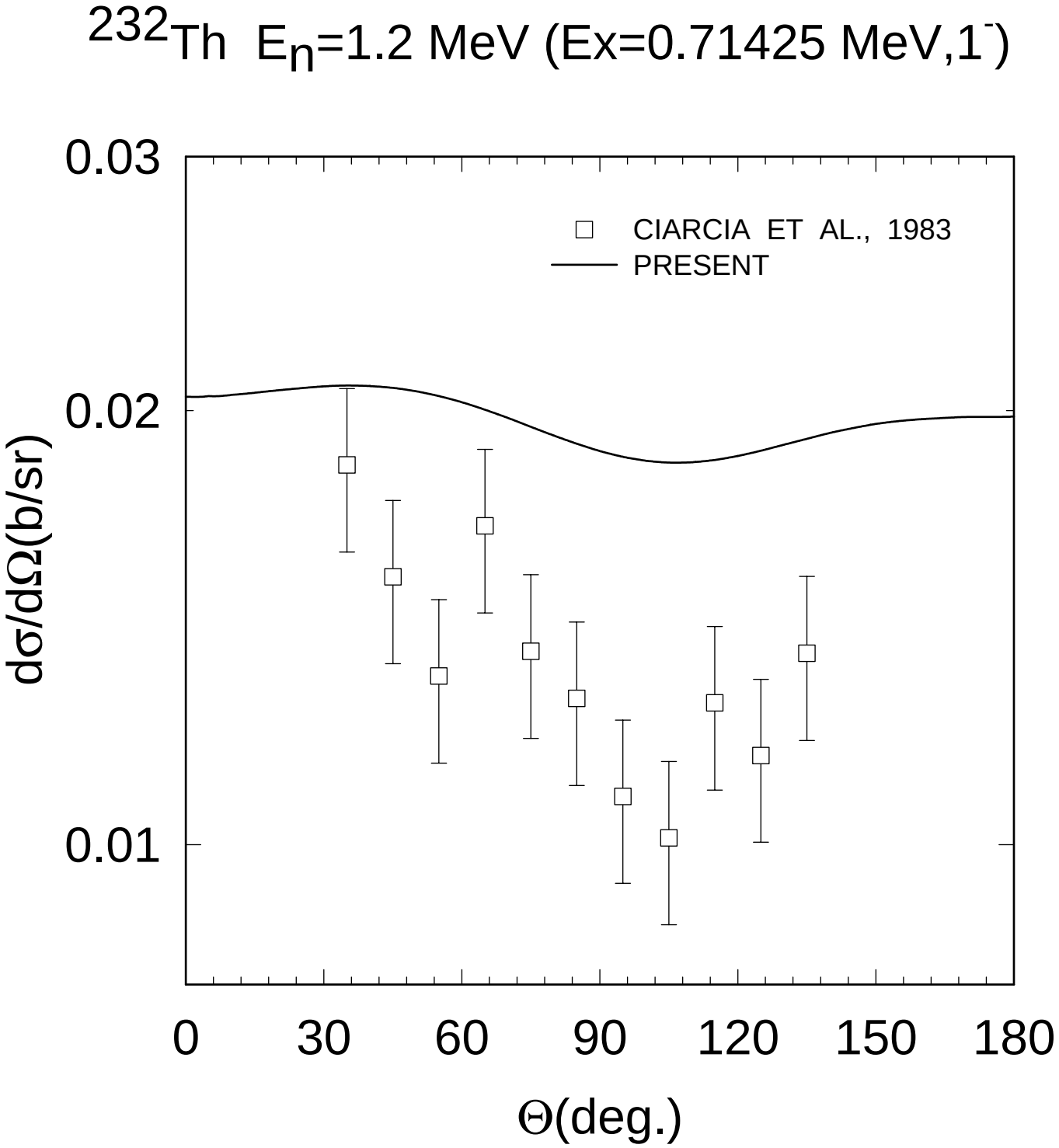
232Th En=1.2 MeV (Ex=0.71425 MeV,1-)
CIARCIA ET AL., 1983
PRESENT
0.03
0.02
0.01
dσ/dΩ(b/sr)
0
30
60
90
120
150
180
Θ(deg.)

FIG. 57

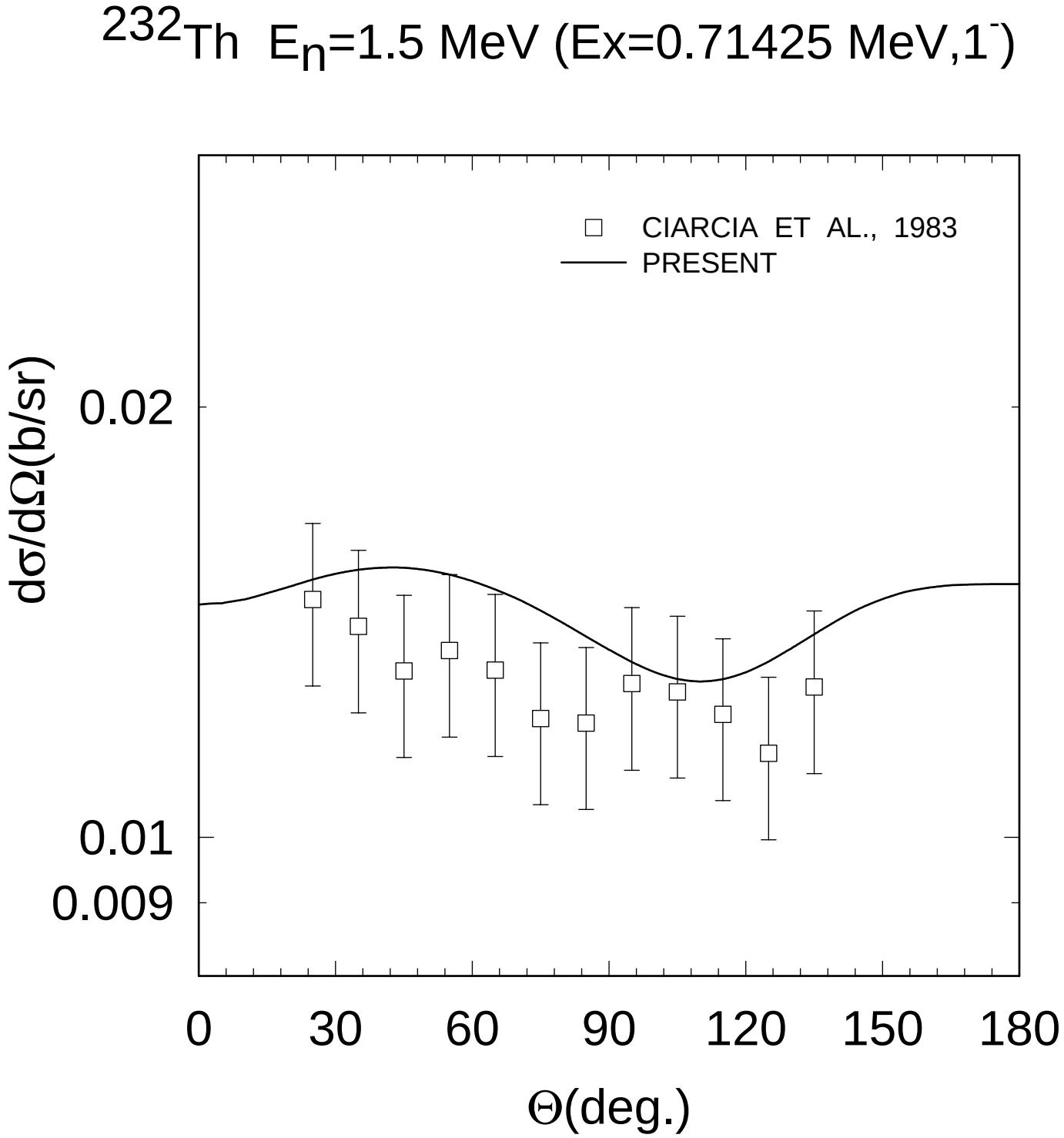
232Th En=1.5 MeV (Ex=0.71425 MeV,1-)
CIARCIA ET AL., 1983
PRESENT
dσ/dΩ(b/sr)
0.02
0.01
0.009
0
30
60
90
120
150
180
Θ(deg.)

FIG. 58

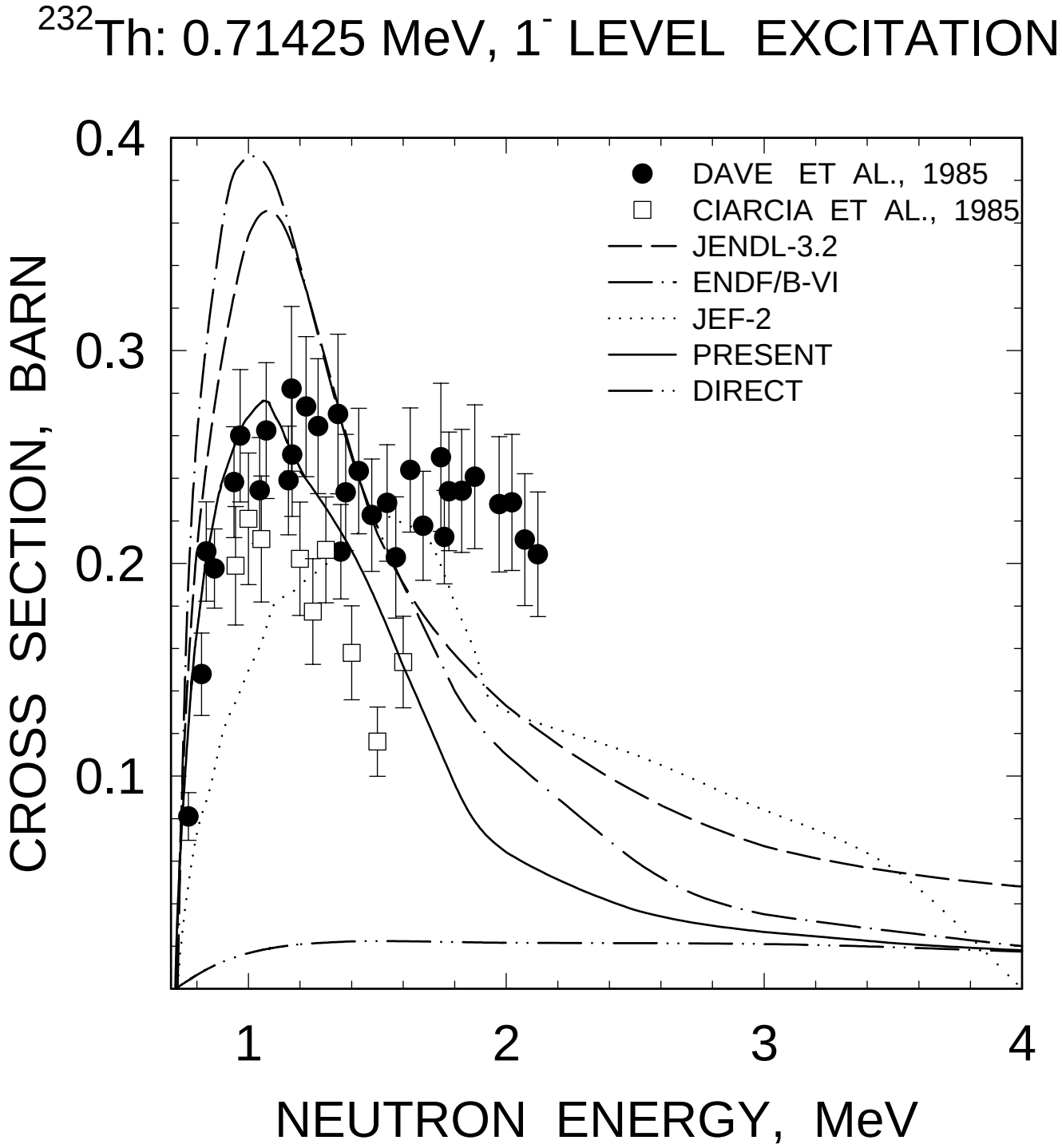
232Th: 0.71425 MeV, 1- LEVEL EXCITATION
DAVE ET AL., 1985
CIARCIA ET AL., 1985
JENDL-3.2
ENDF/B-VI
JEF-2
PRESENT
DIRECT
CROSS SECTION, BARN
0.4
0.3
0.2
0.1
1
2
3
4
NEUTRON ENERGY, MeV

FIG. 59

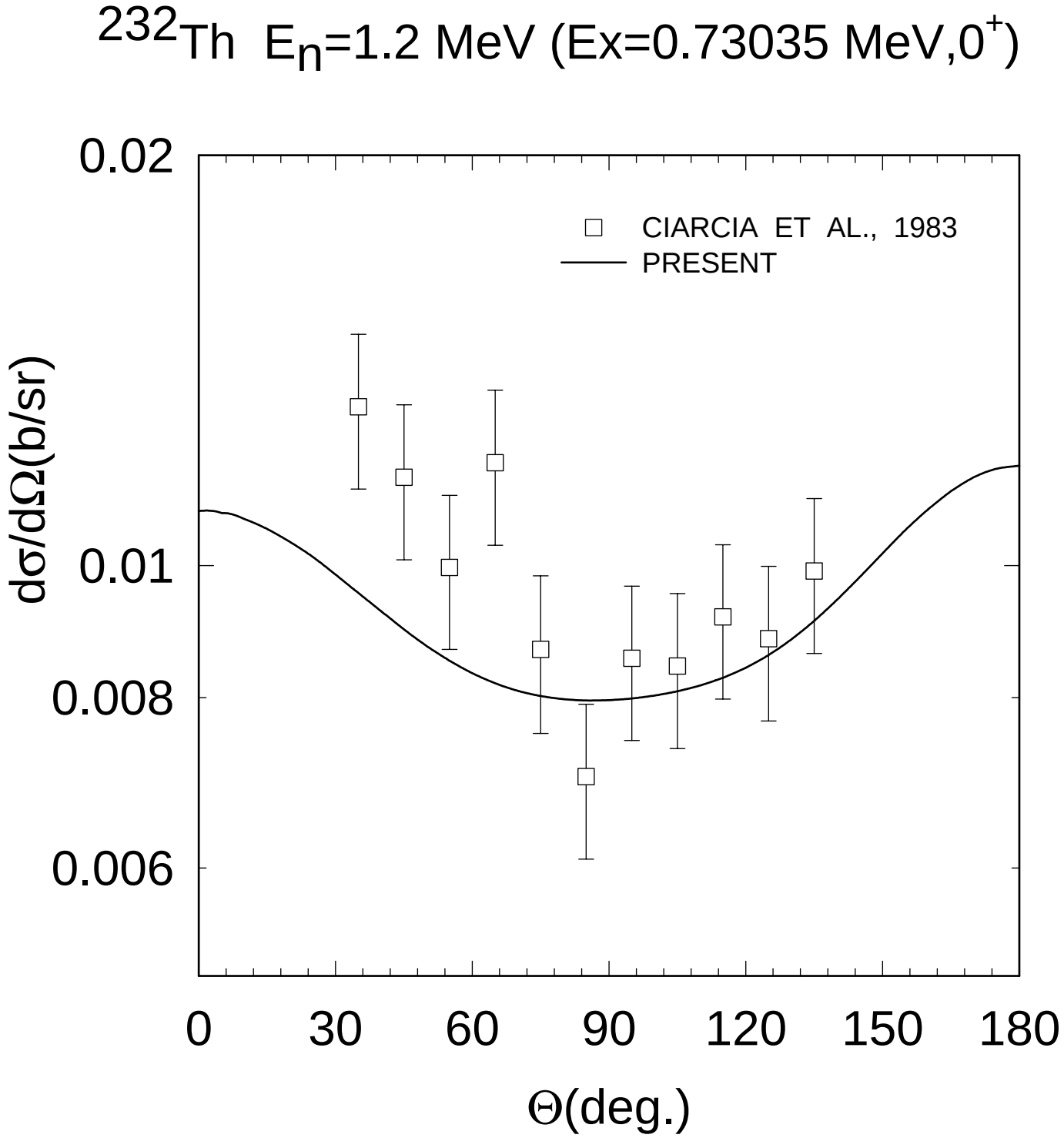
232Th En=1.2 MeV (Ex=0.73035 MeV,0+)
CIARCIA ET AL., 1983
PRESENT
dσ/dΩ(b/sr)
0.02
0.01
0.008
0.006
0
30
60
90
120
150
180
Θ(deg.)

FIG. 60

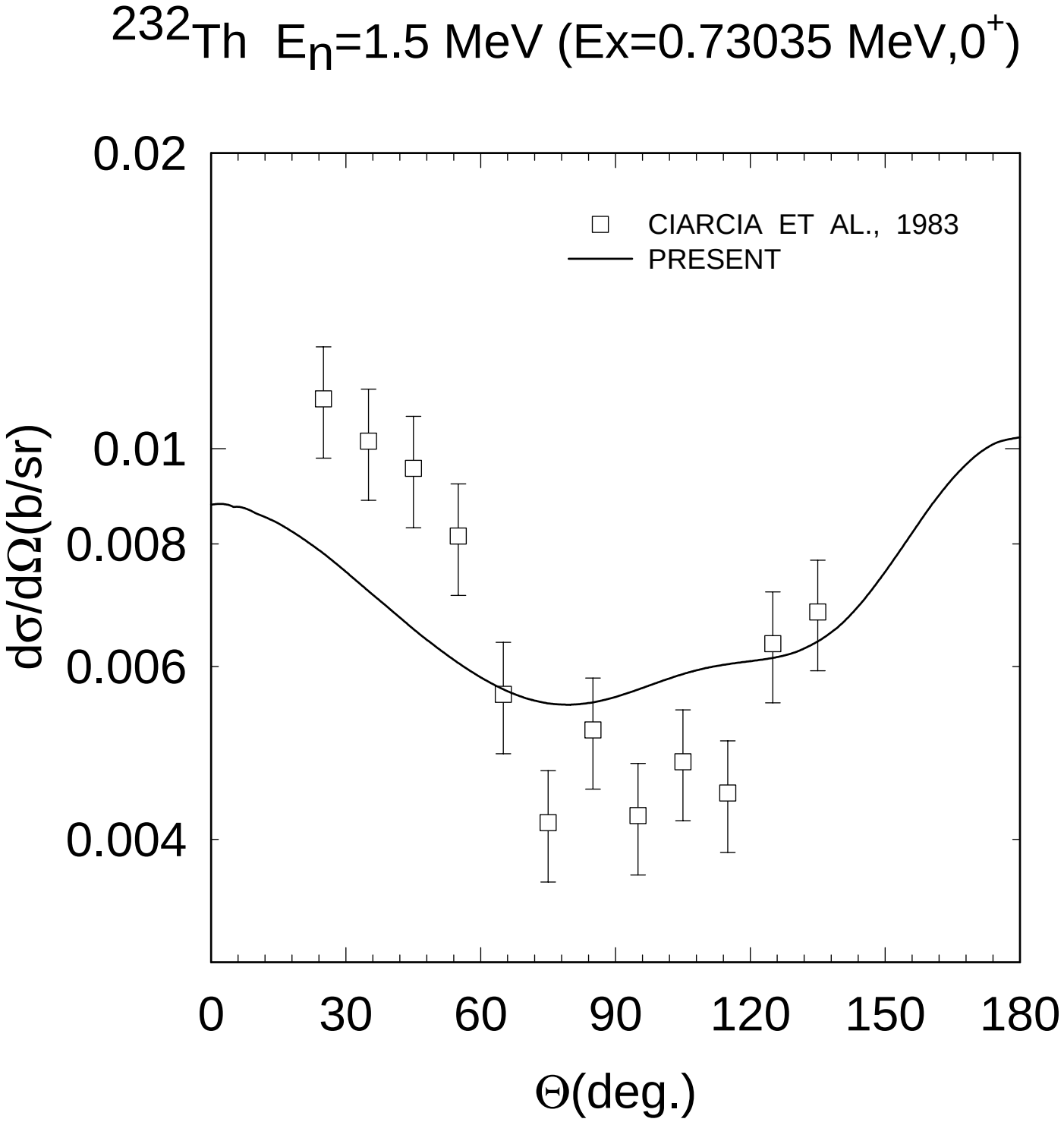
232Th En=1.5 MeV (Ex=0.73035 MeV,0+)
CIARCIA ET AL., 1983
PRESENT
dσ/dΩ(b/sr)
0.02
0.01
0.008
0.006
0.004
0
30
60
90
120
150
180
Θ(deg.)

FIG. 61

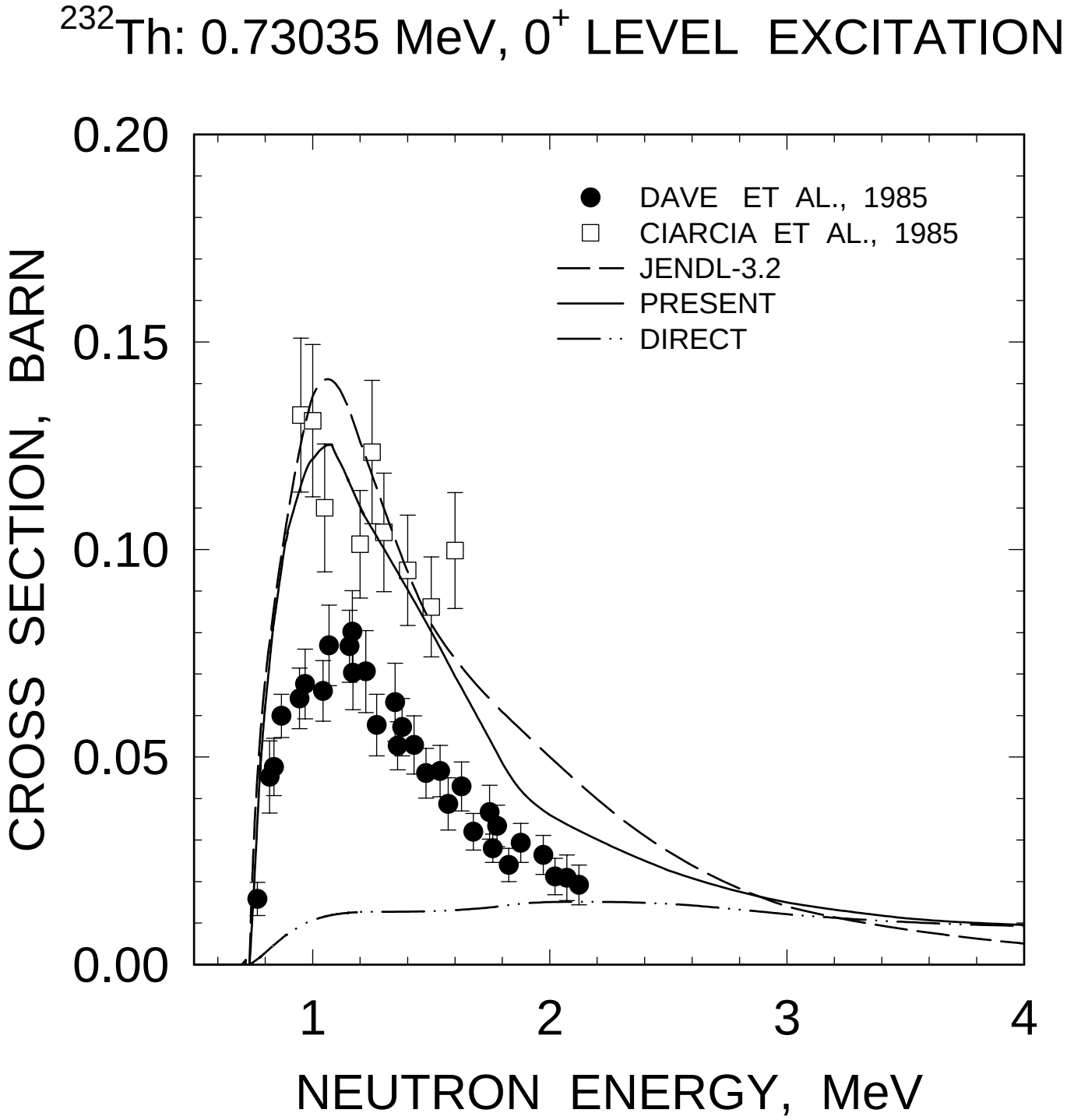
232Th: 0.73035 MeV, 0+ LEVEL EXCITATION
DAVE ET AL., 1985
CIARCIA ET AL., 1985
JENDL-3.2
PRESENT
DIRECT
CROSS SECTION, BARN
0.20
0.15
0.10
0.05
0.00
1
2
3
4
NEUTRON ENERGY, MeV

FIG. 62

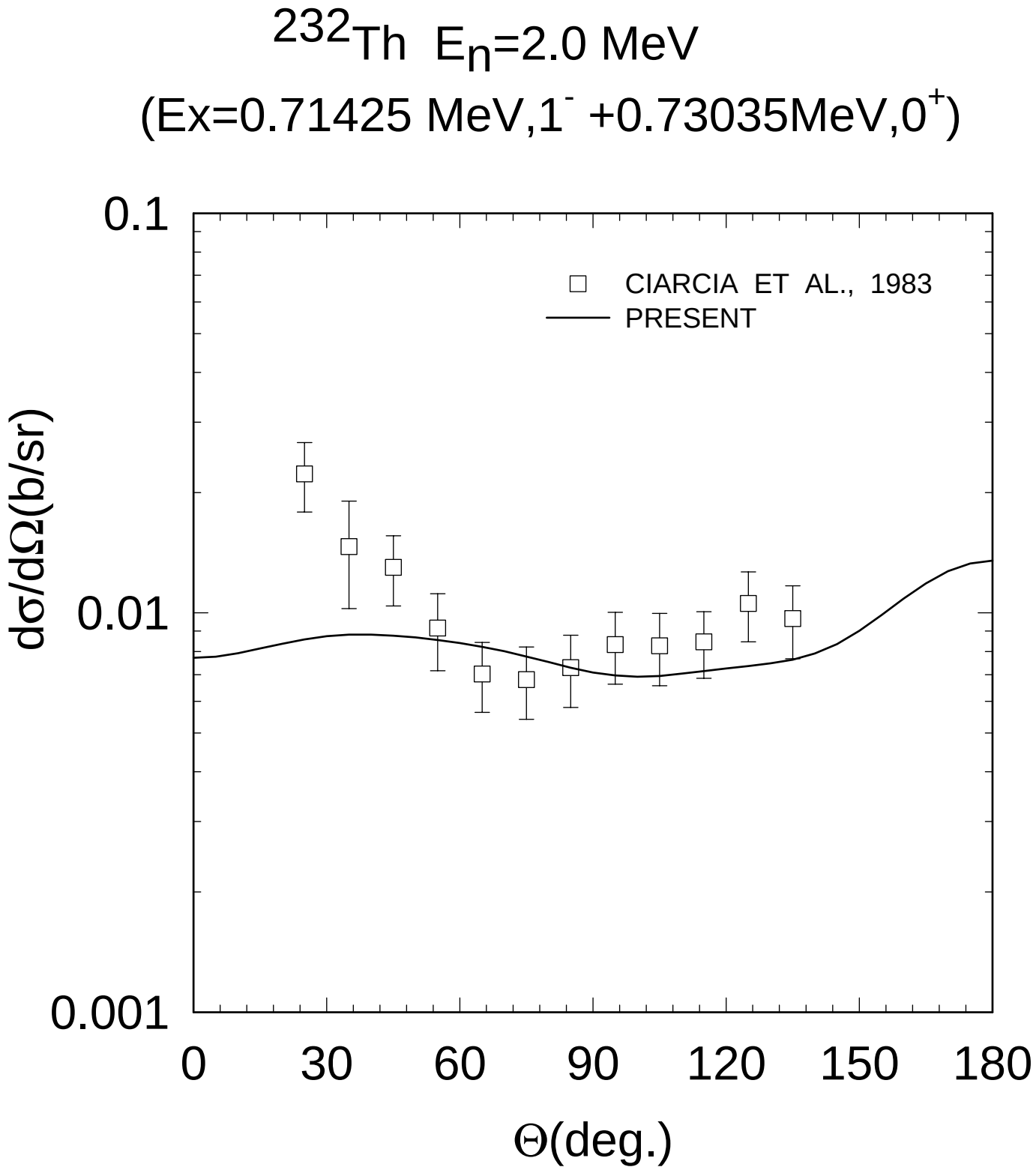
232Th En=2.0 MeV
(Ex=0.71425 MeV,1- +0.73035MeV,0+)
CIARCIA ET AL., 1983
PRESENT
dσ/dΩ(b/sr)
0.1
0.01
0.001
0
30
60
90
120
150
180
Θ(deg.)

FIG. 63

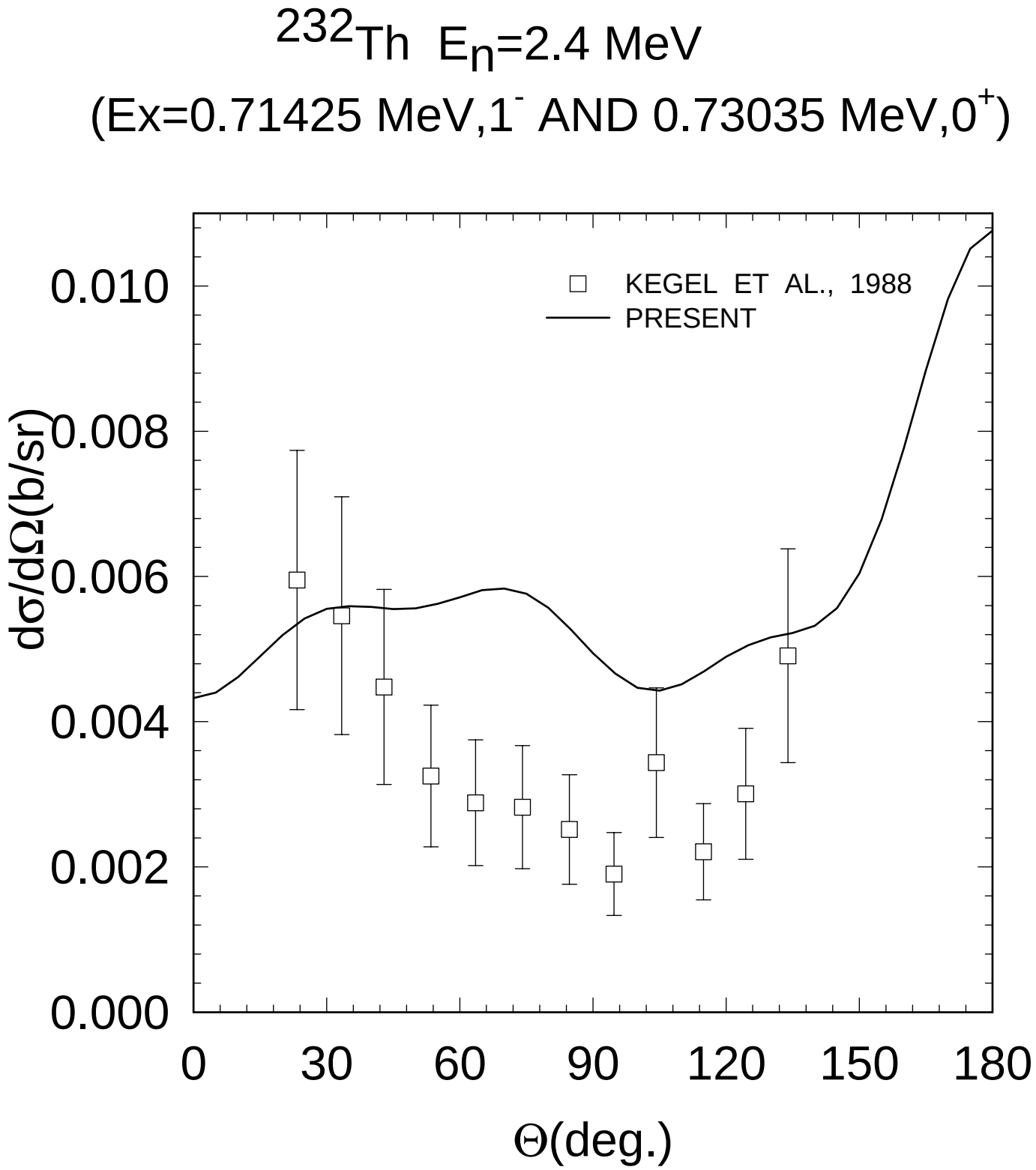
232Th En=2.4 MeV
(Ex=0.71425 MeV,1- AND 0.73035 MeV,0+)
KEGEL ET AL., 1988
PRESENT
dσ/dΩ(b/sr)
0.010
0.008
0.006
0.004
0.002
0.000
0
30
60
90
120
150
180
Θ(deg.)

FIG. 64

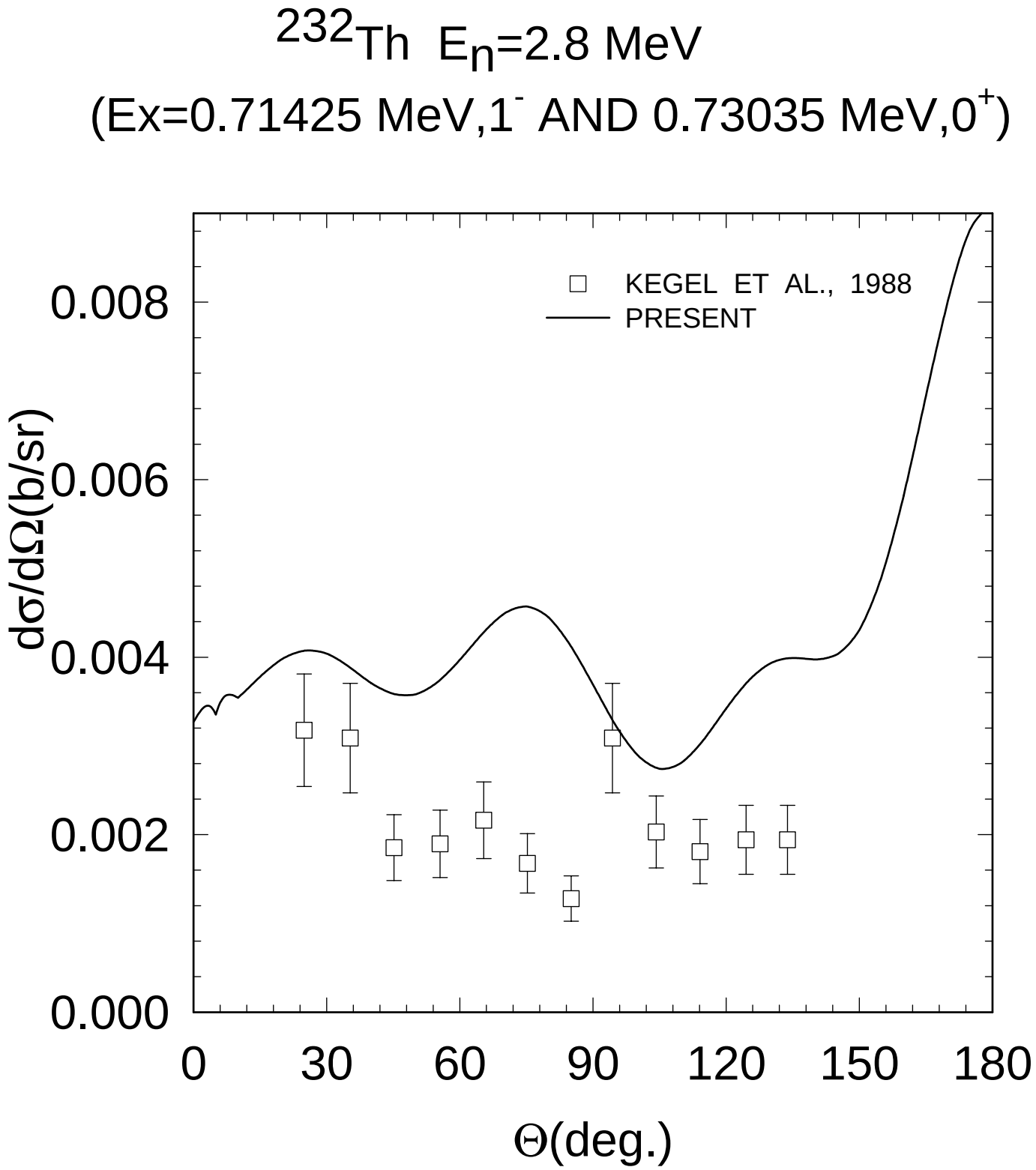
232Th En=2.8 MeV
(Ex=0.71425 MeV,1- AND 0.73035 MeV,0+)
KEGEL ET AL., 1988
PRESENT
dσ/dΩ(b/sr)
0.008
0.006
0.004
0.002
0.000
0
30
60
90
120
150
180
Θ(deg.)

FIG. 65

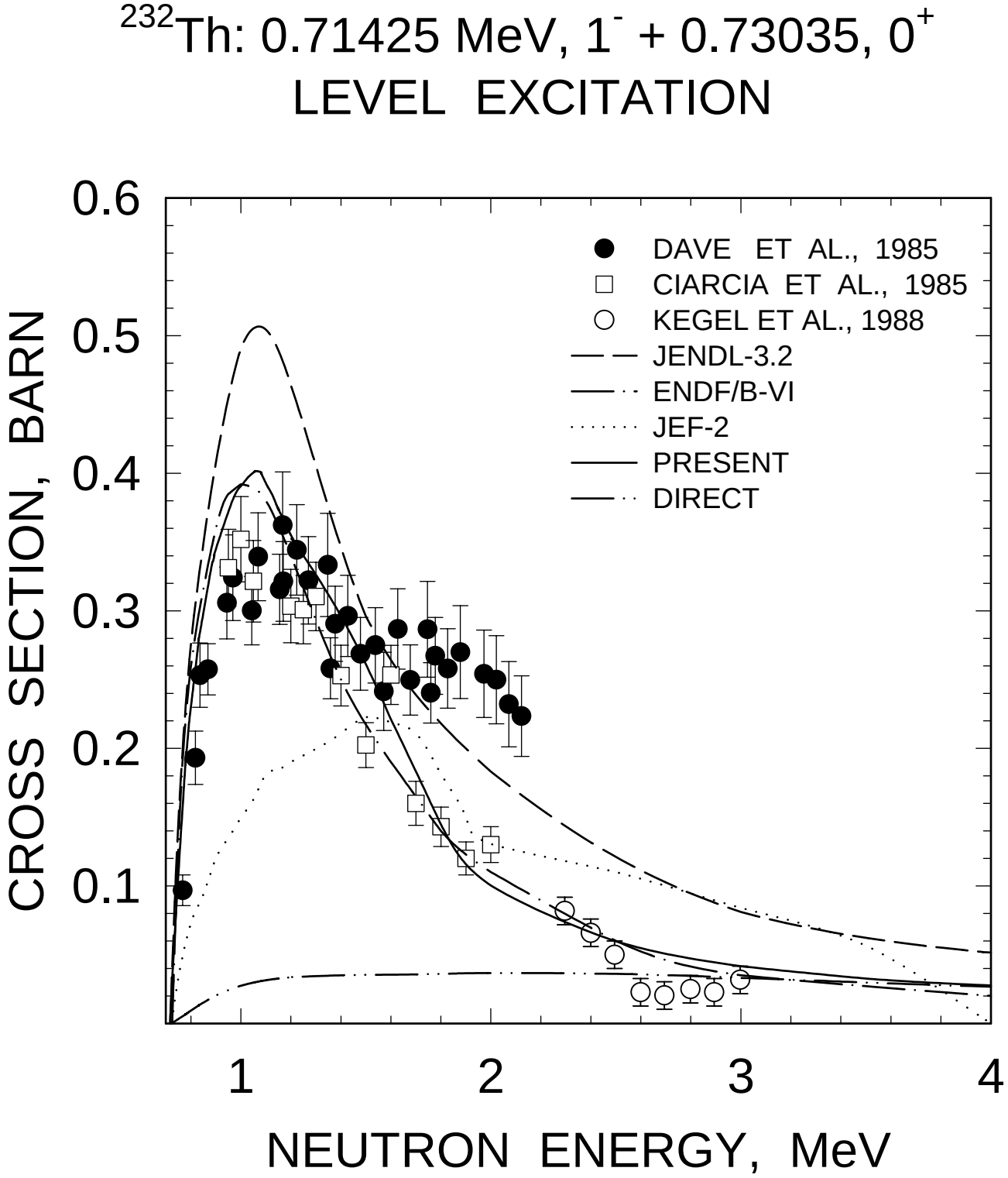
232Th: 0.71425 MeV, 1- + 0.73035, 0+
LEVEL EXCITATION
DAVE ET AL., 1985
CIARCIA ET AL., 1985
KEGEL ET AL., 1988
JENDL-3.2
ENDF/B-VI
JEF-2
PRESENT
DIRECT
CROSS SECTION, BARN
0.6
0.5
0.4
0.3
0.2
0.1
1
2
3
4
NEUTRON ENERGY, MeV

FIG. 66

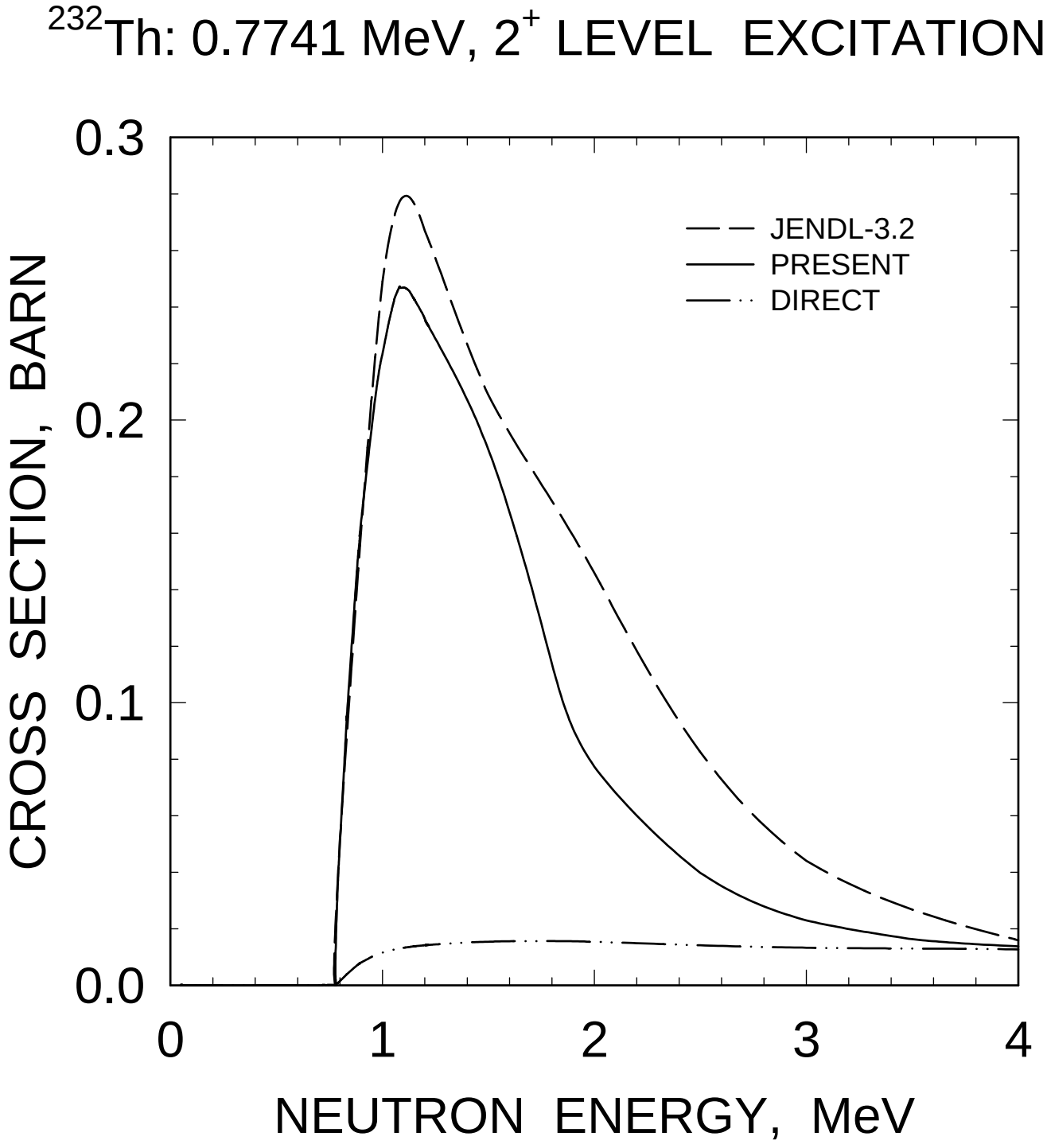
232Th: 0.7741 MeV, 2+ LEVEL EXCITATION
JENDL-3.2
PRESENT
DIRECT
CROSS SECTION, BARN
0.0
0.1
0.2
0.3
0
1
2
3
4
NEUTRON ENERGY, MeV

FIG. 67

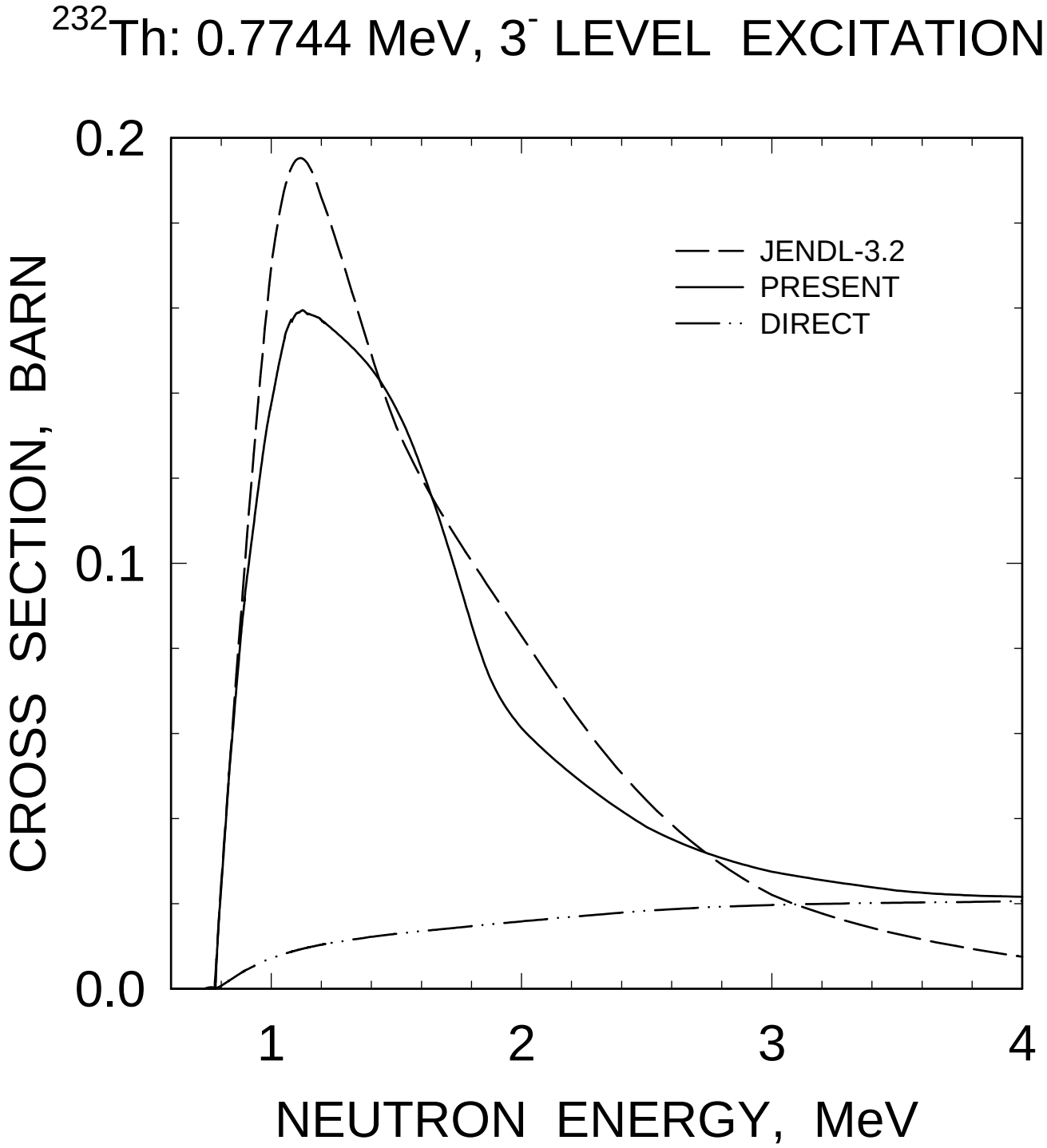
232Th: 0.7744 MeV, 3- LEVEL EXCITATION
0.2
0.1
0.0
CROSS SECTION, BARN
JENDL-3.2
PRESENT
DIRECT
1
2
3
4
NEUTRON ENERGY, MeV

FIG. 68

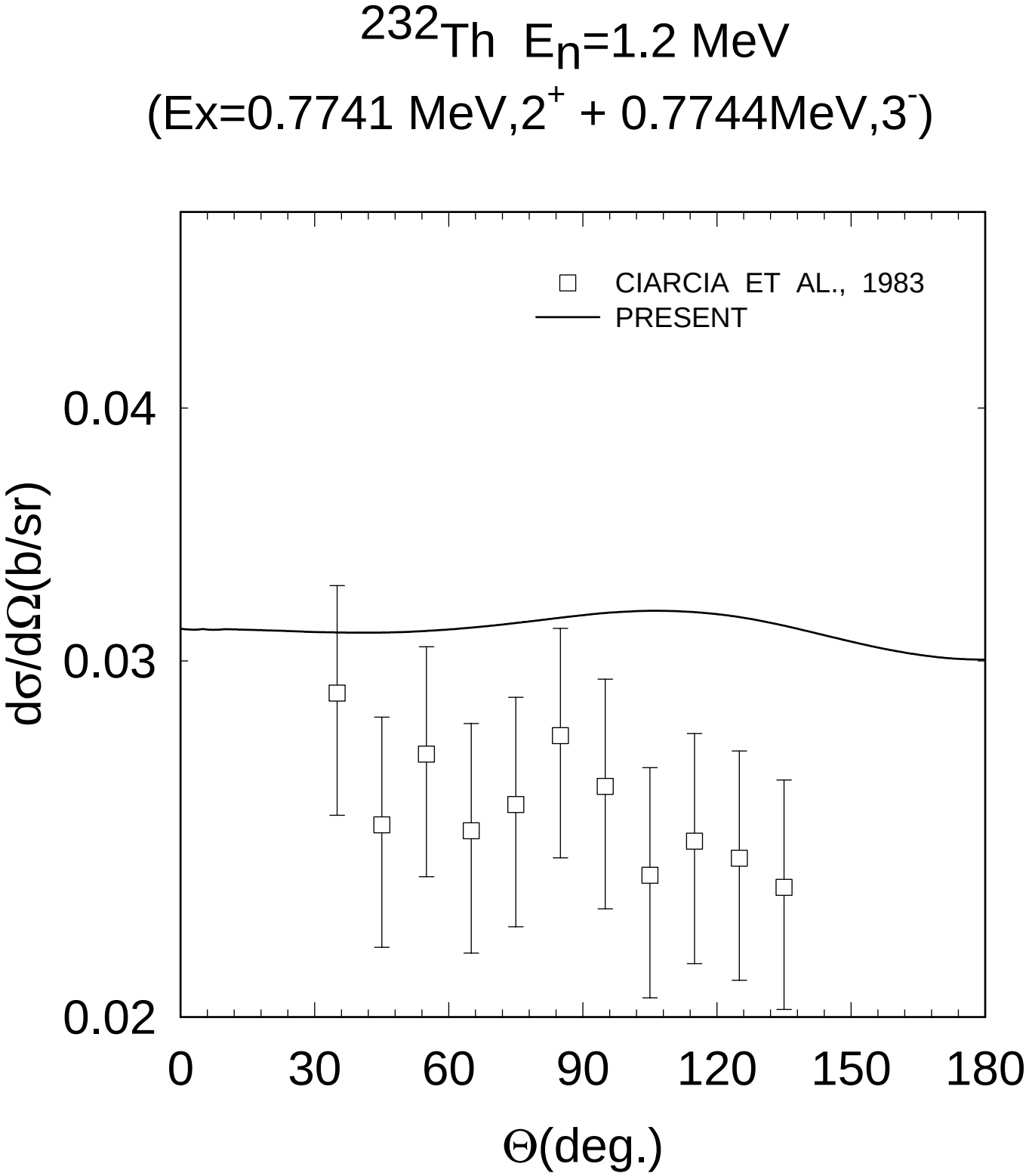
232Th En=1.2 MeV
(Ex=0.7741 MeV,2+ + 0.7744MeV,3-)
CIARCIA ET AL., 1983
PRESENT
0.04
0.03
0.02
dσ/dΩ(b/sr)
0
30
60
90
120
150
180
Θ(deg.)

FIG. 69

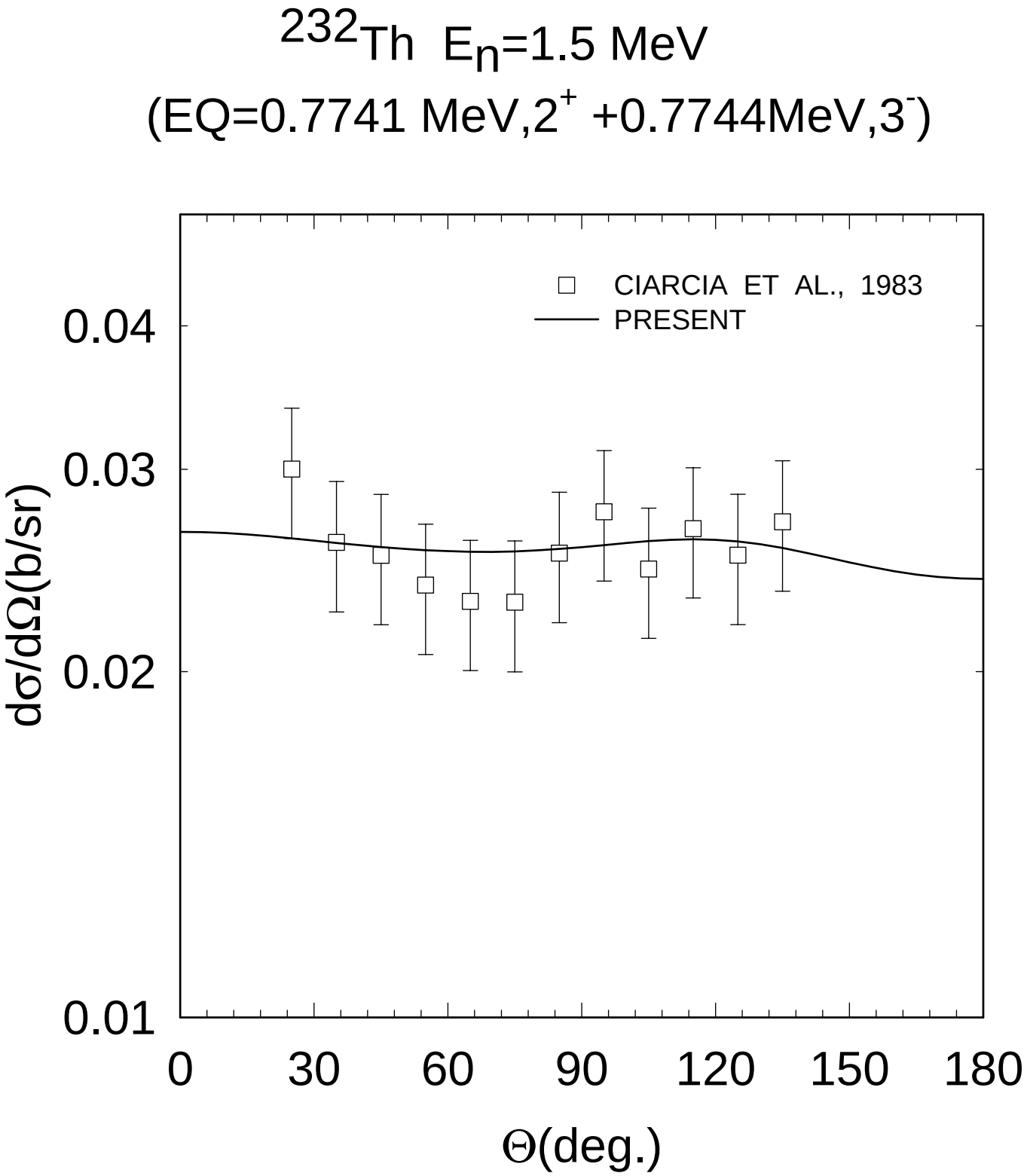
232Th En=1.5 MeV
(EQ=0.7741 MeV,2+ +0.7744MeV,3-)
CIARCIA ET AL., 1983
PRESENT
0.04
0.03
0.02
0.01
dσ/dΩ(b/sr)
0
30
60
90
120
150
180
Θ(deg.)

FIG. 70

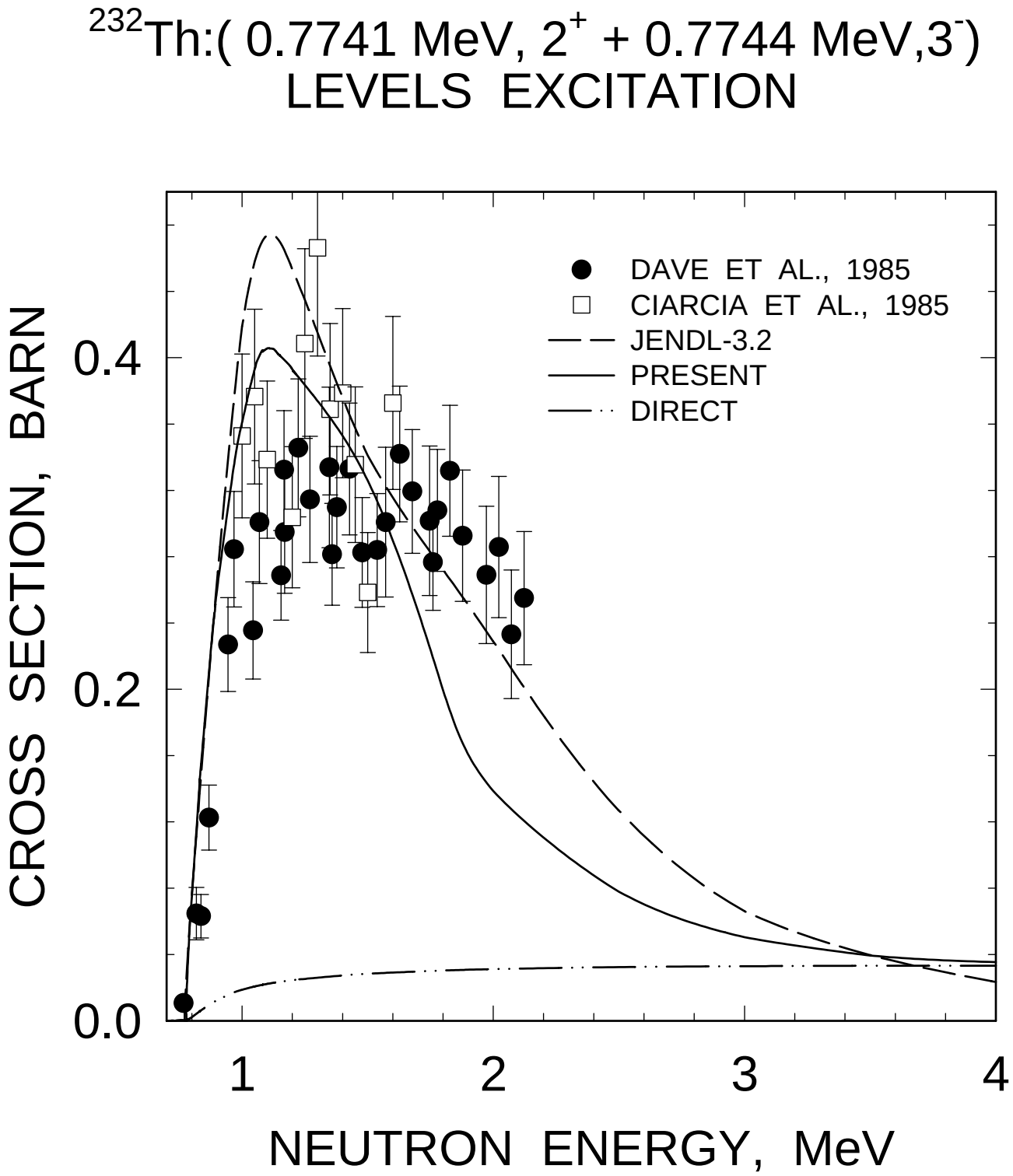
232Th:(0.7741 MeV, 2+ + 0.7744 MeV,3-)
LEVELS EXCITATION
DAVE ET AL., 1985
CIARCIA ET AL., 1985
JENDL-3.2
PRESENT
DIRECT
CROSS SECTION, BARN
0.0
0.2
0.4
1
2
3
4
NEUTRON ENERGY, MeV

FIG. 71

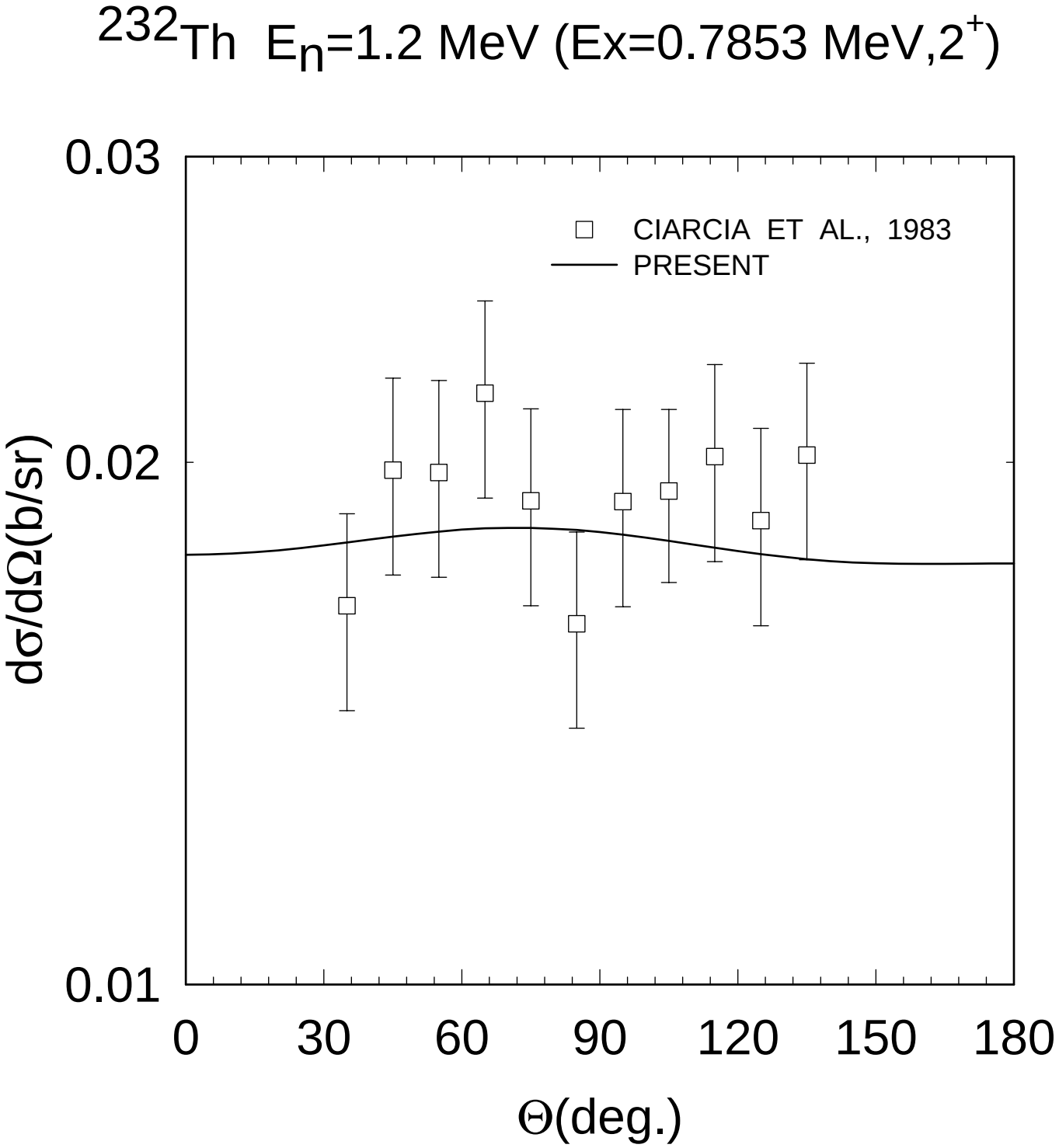
232Th En=1.2 MeV (Ex=0.7853 MeV,2+)
CIARCIA ET AL., 1983
PRESENT
0.03
0.02
0.01
dσ/dΩ(b/sr)
0
30
60
90
120
150
180
Θ(deg.)

FIG. 72

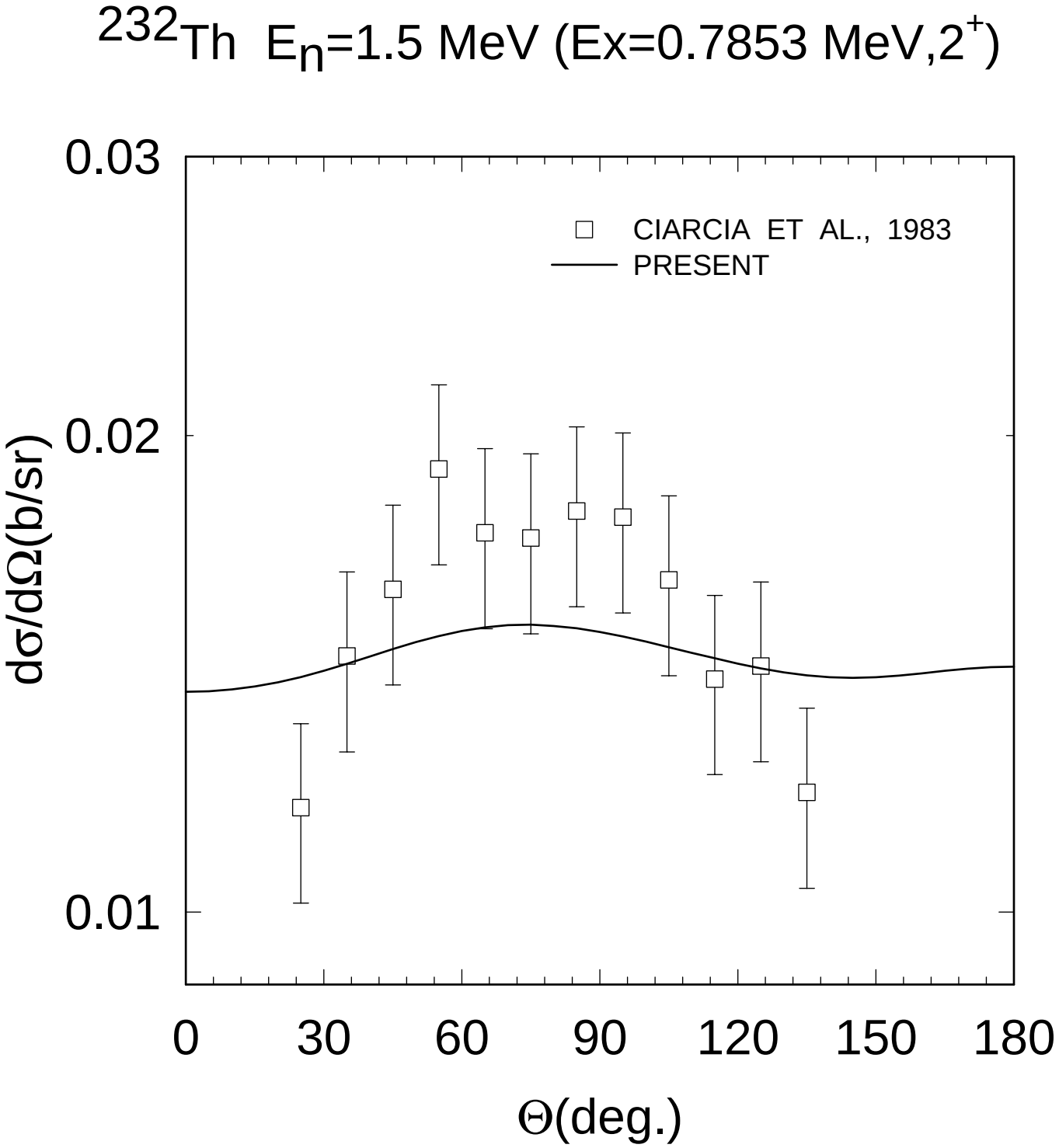
232Th En=1.5 MeV (Ex=0.7853 MeV,2+)
CIARCIA ET AL., 1983
PRESENT
0.03
0.02
0.01
dσ/dΩ(b/sr)
0
30
60
90
120
150
180
Θ(deg.)

FIG. 73

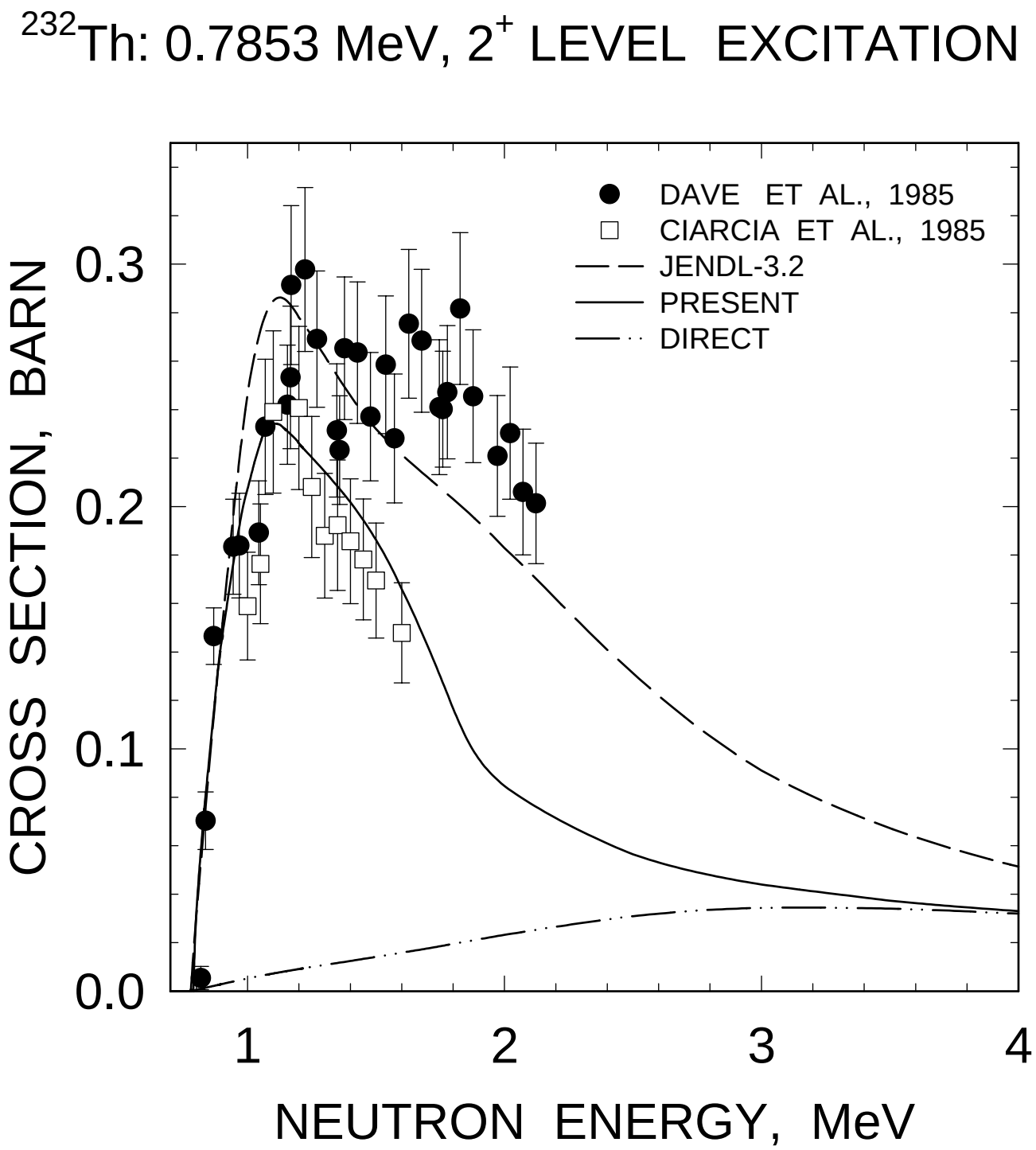
232Th: 0.7853 MeV, 2+ LEVEL EXCITATION
DAVE ET AL., 1985
CIARCIA ET AL., 1985
JENDL-3.2
PRESENT
DIRECT
CROSS SECTION, BARN
0.0
0.1
0.2
0.3
1
2
3
4
NEUTRON ENERGY, MeV

FIG. 74

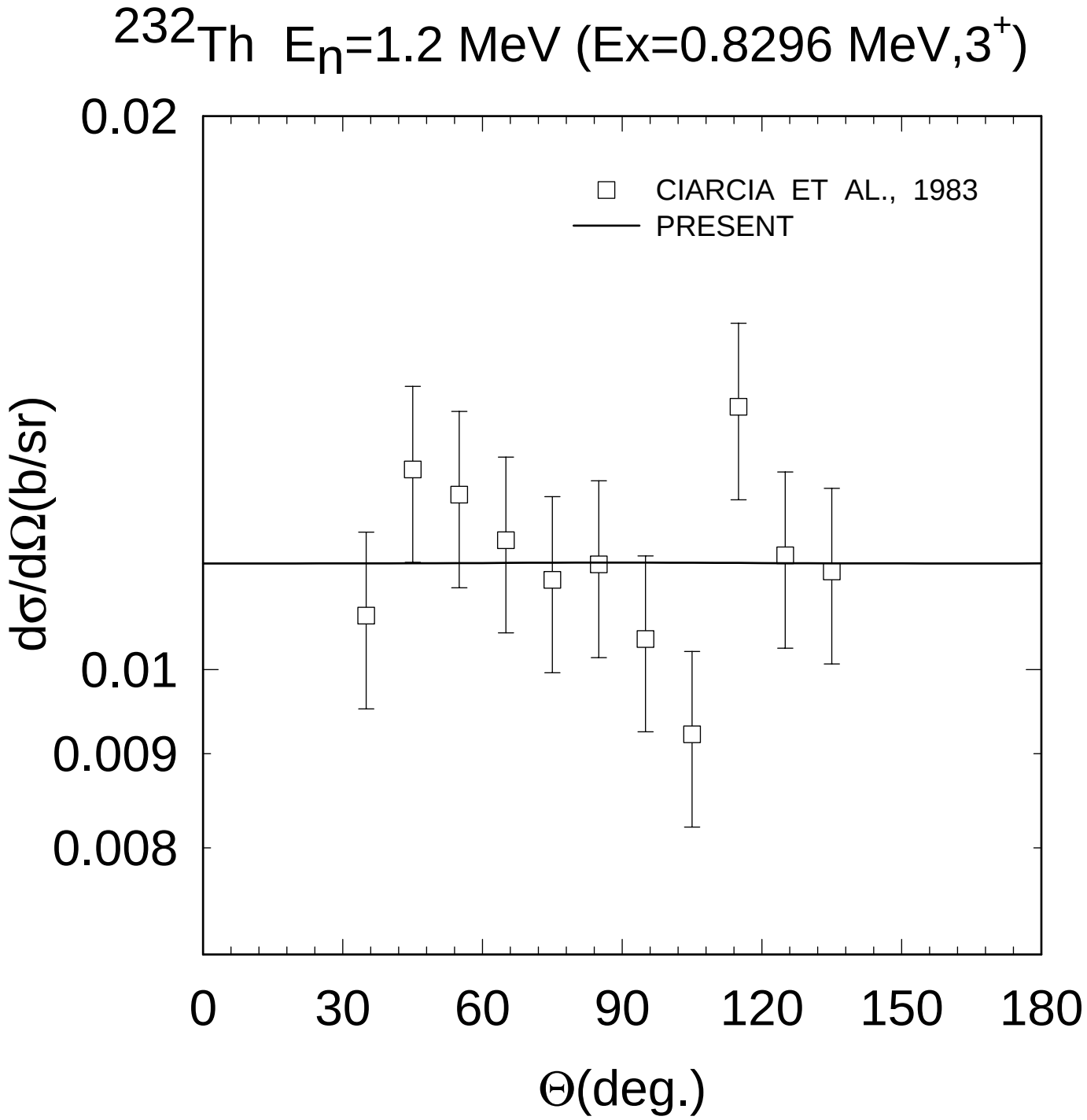
232Th En=1.2 MeV (Ex=0.8296 MeV,3+)
CIARCIA ET AL., 1983
PRESENT
dσ/dΩ(b/sr)
0.02
0.01
0.009
0.008
0
30
60
90
120
150
180
Θ(deg.)

FIG. 75

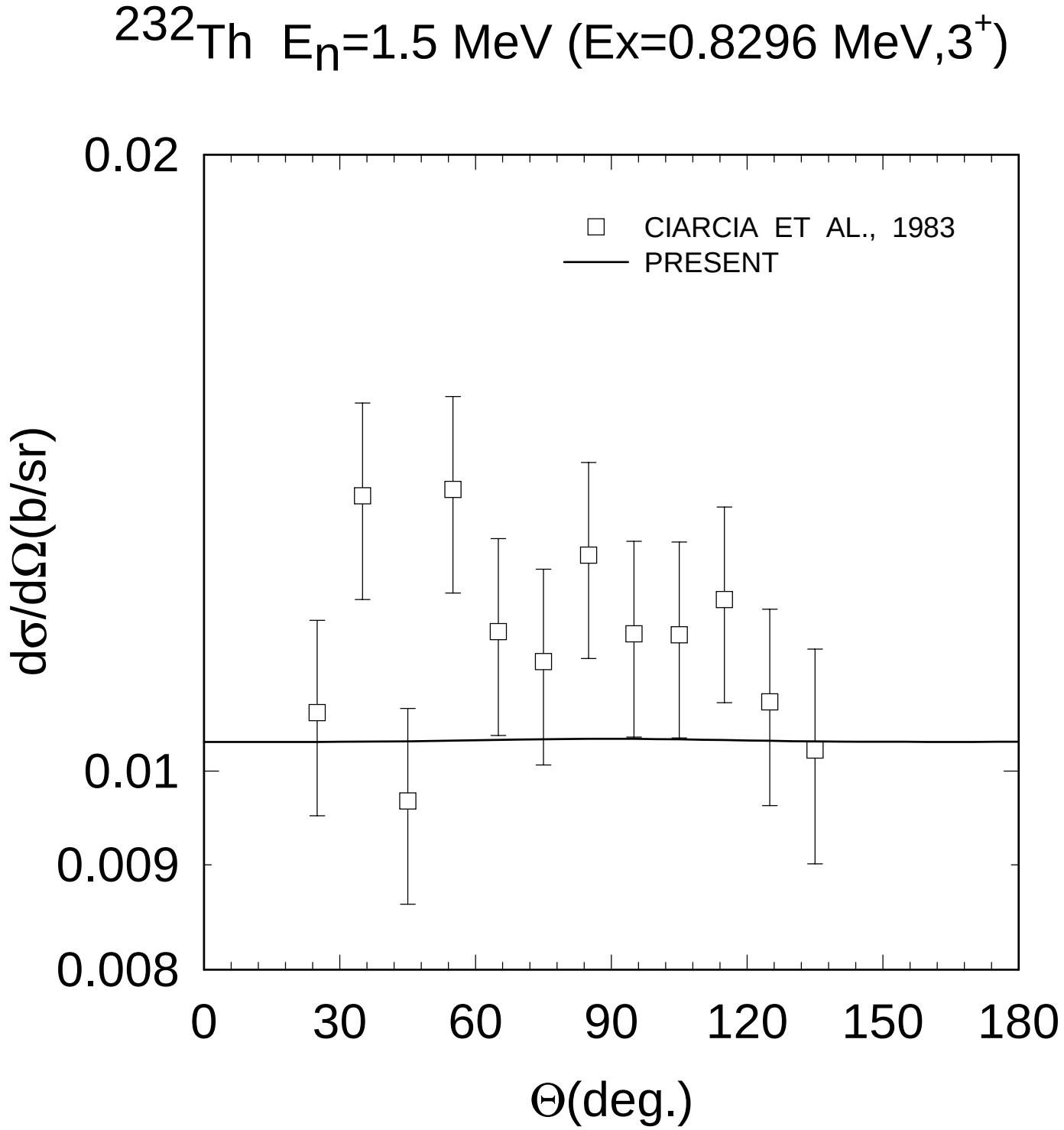
232Th En=1.5 MeV (Ex=0.8296 MeV,3+)
CIARCIA ET AL., 1983
PRESENT
dσ/dΩ(b/sr)
0.02
0.01
0.009
0.008
0
30
60
90
120
150
180
Θ(deg.)

FIG. 76

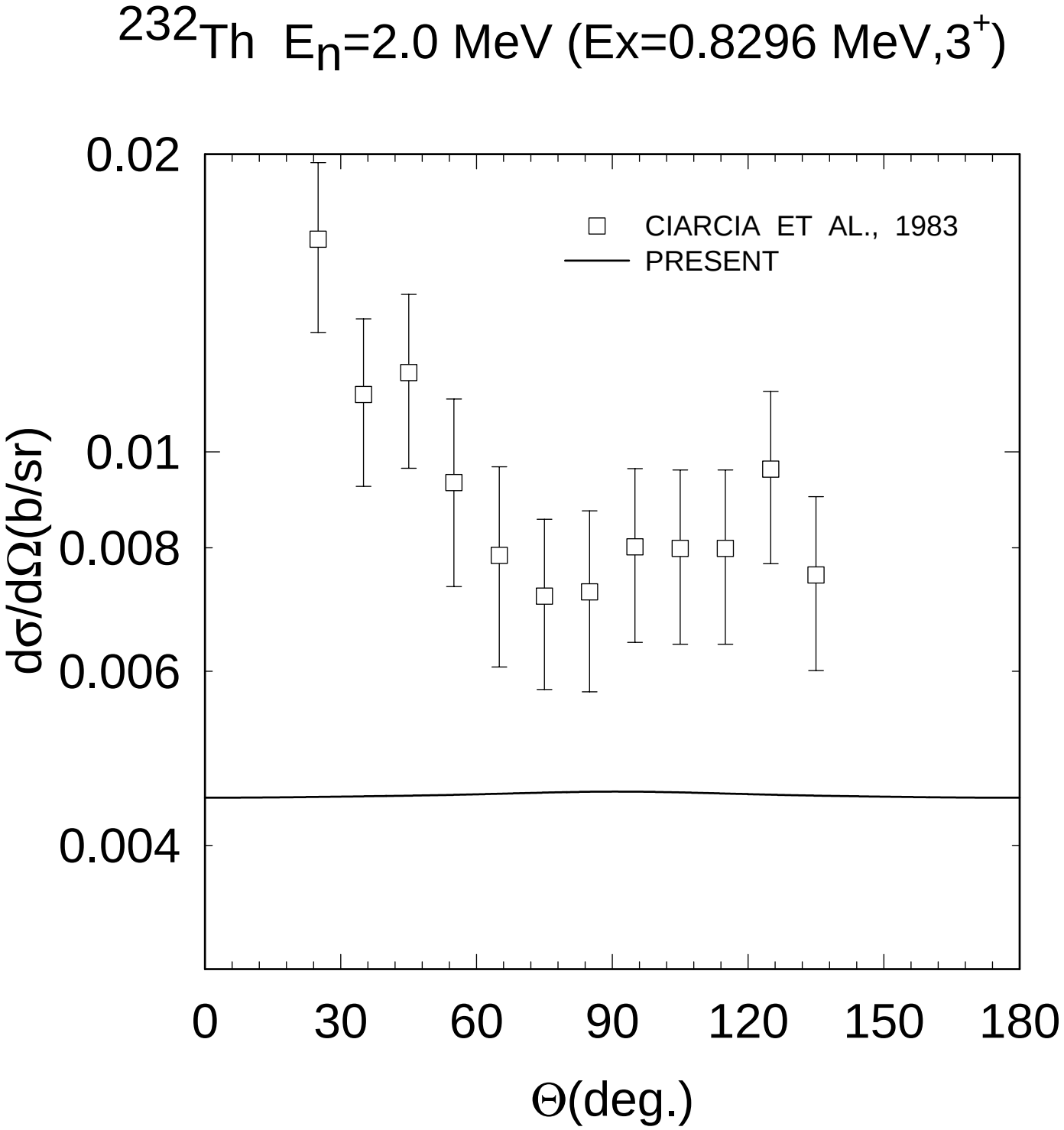
232Th En=2.0 MeV (Ex=0.8296 MeV,3+)
CIARCIA ET AL., 1983
PRESENT
dσ/dΩ(b/sr)
0.02
0.01
0.008
0.006
0.004
0
30
60
90
120
150
180
Θ(deg.)

FIG. 77

^{232}Th: 0.8296 MeV, (3^+) LEVEL EXCITATION

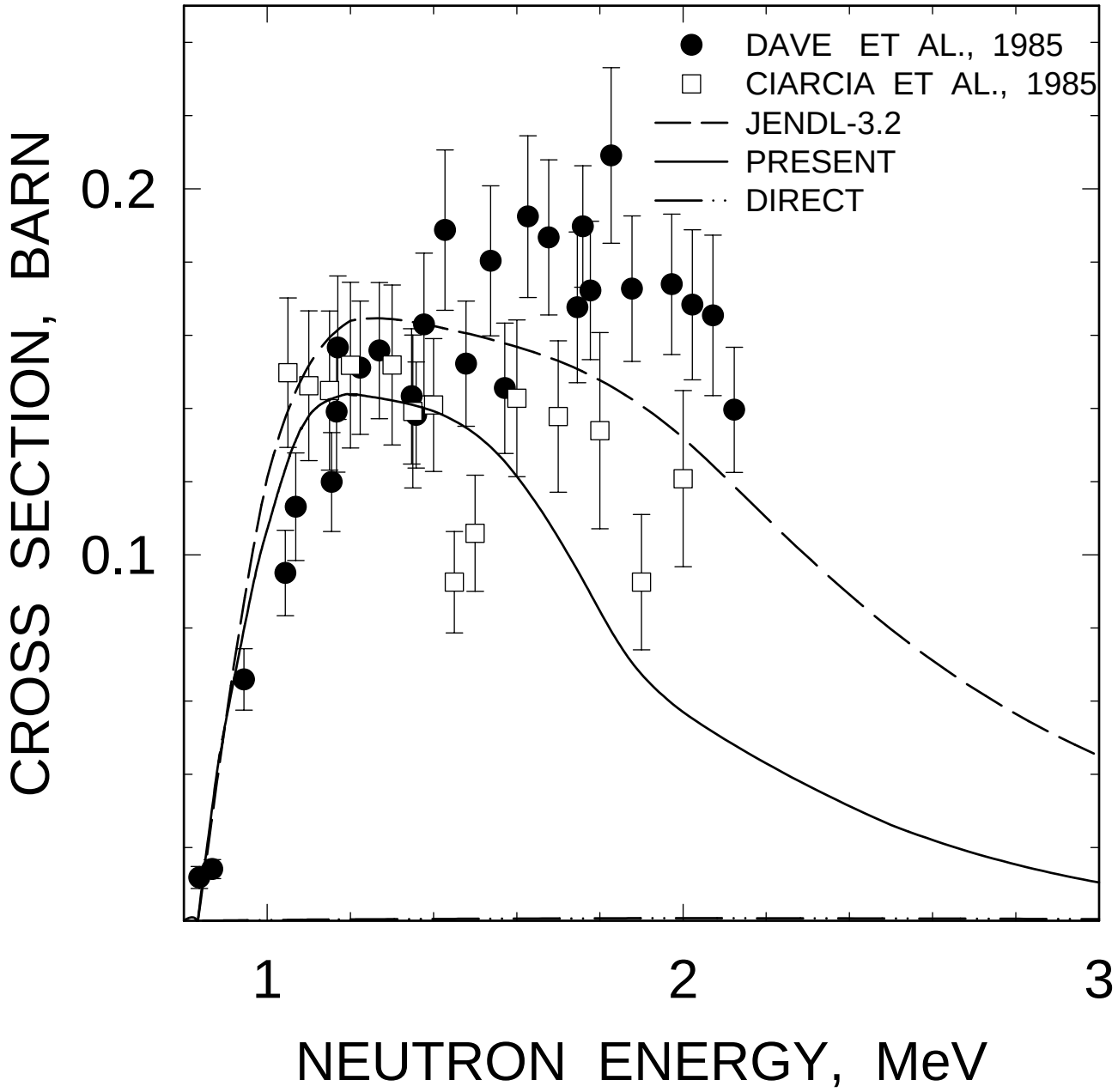

FIG. 78

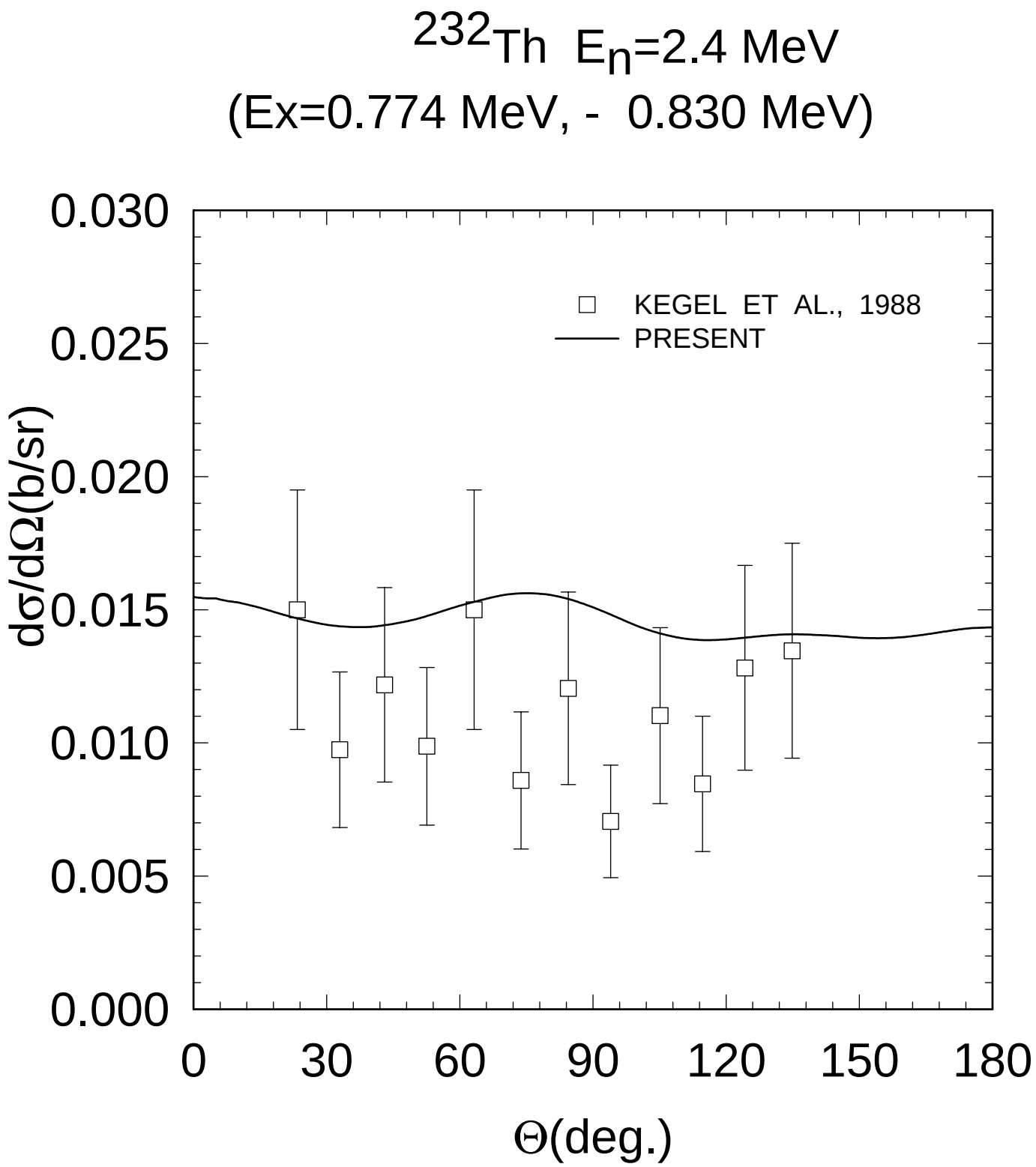
232Th En=2.4 MeV
(Ex=0.774 MeV, - 0.830 MeV)
KEGEL ET AL., 1988
PRESENT
dσ/dΩ(b/sr)
0.030
0.025
0.020
0.015
0.010
0.005
0.000
0
30
60
90
120
150
180
Θ(deg.)

FIG. 79

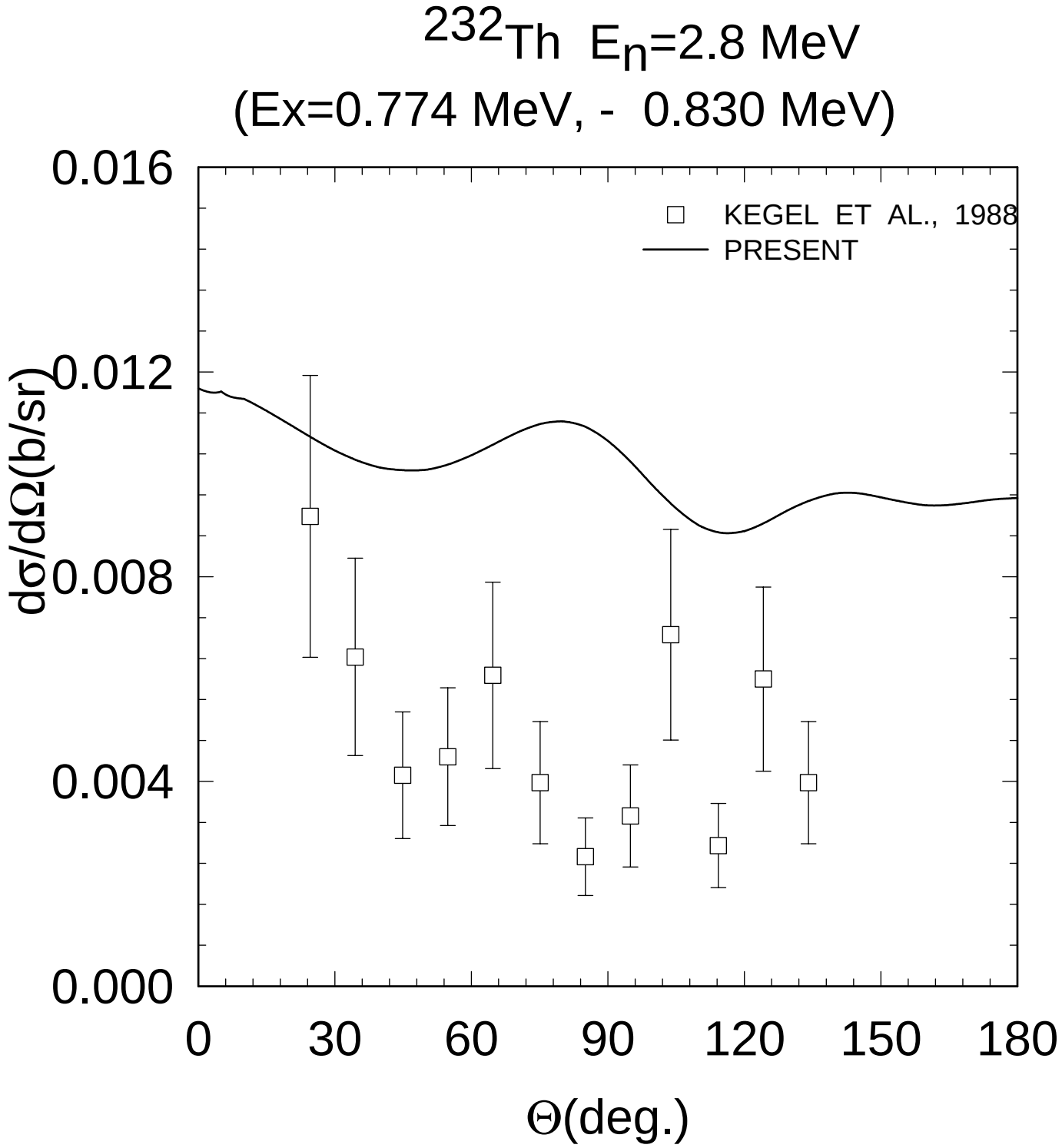
232Th En=2.8 MeV
(Ex=0.774 MeV, - 0.830 MeV)
KEGEL ET AL., 1988
PRESENT
dσ/dΩ(b/sr)
0.016
0.012
0.008
0.004
0.000
0
30
60
90
120
150
180
Θ(deg.)

FIG. 80

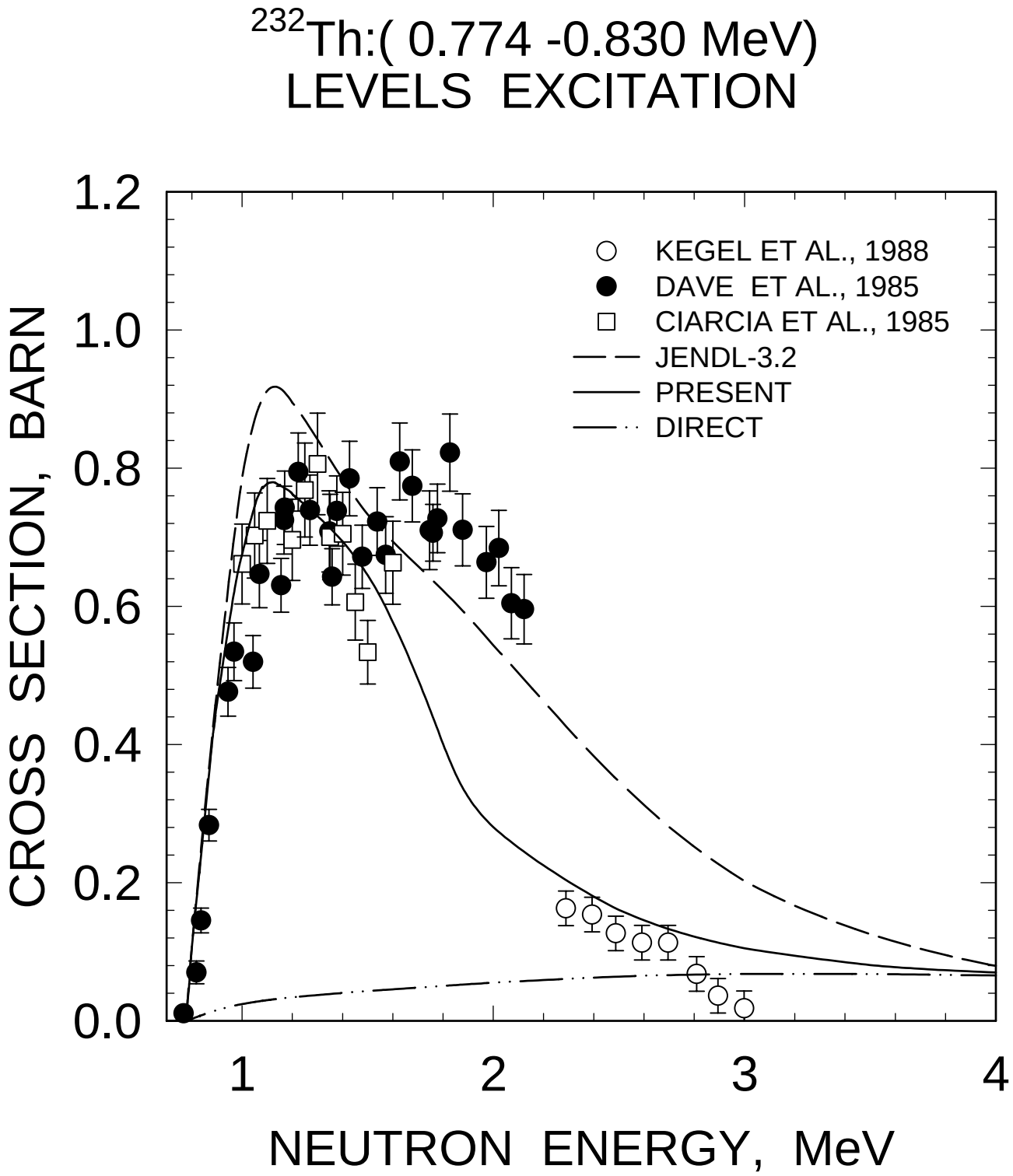
232Th:(0.774 -0.830 MeV)
LEVELS EXCITATION
KEGEL ET AL., 1988
DAVE ET AL., 1985
CIARCIA ET AL., 1985
JENDL-3.2
PRESENT
DIRECT
CROSS SECTION, BARN
NEUTRON ENERGY, MeV
0.0
0.2
0.4
0.6
0.8
1.0
1.2
1
2
3
4

FIG. 81

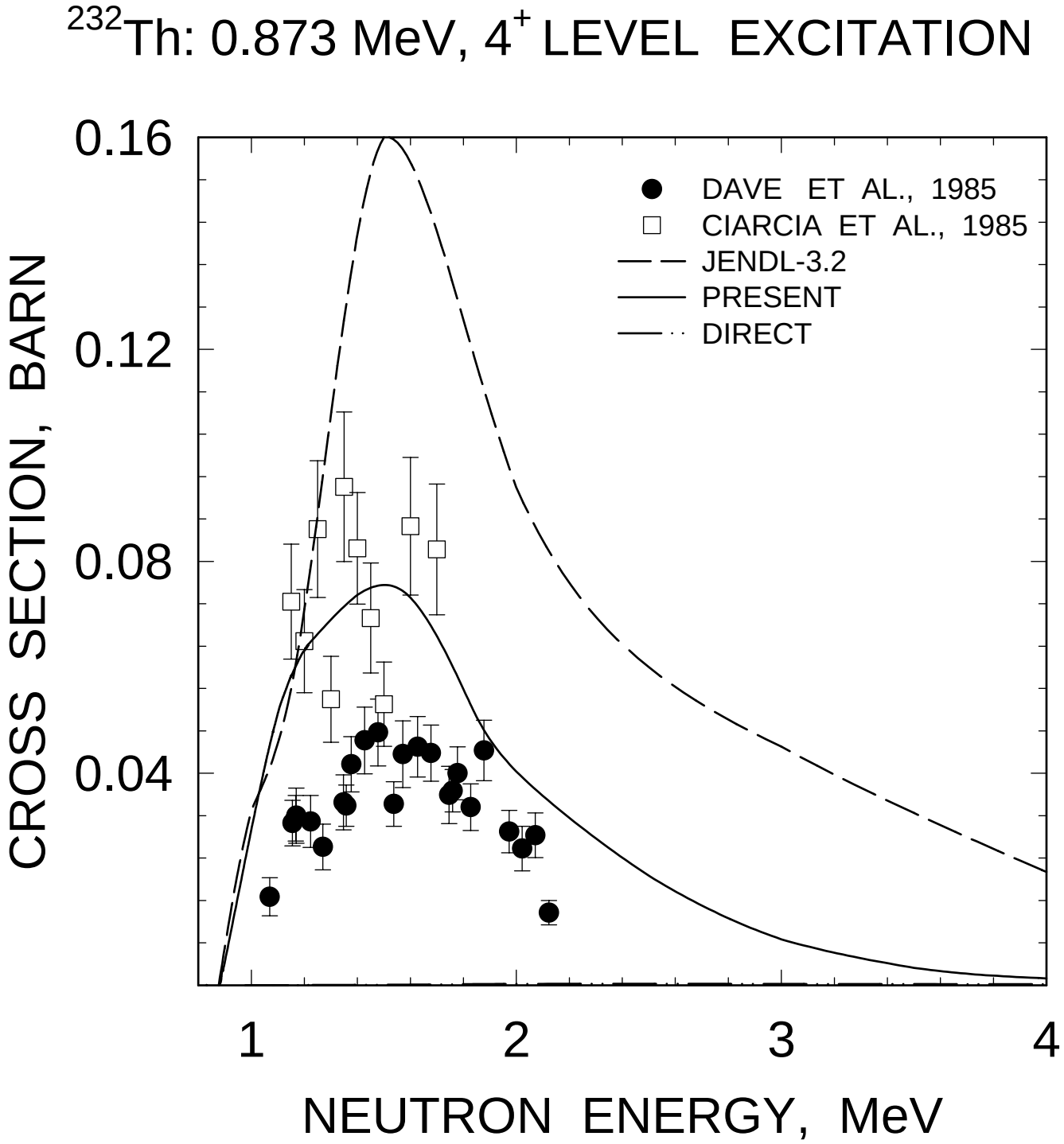
^{232}Th: 0.873 MeV, 4^{+} LEVEL EXCITATION
DAVE ET AL., 1985
CIARCIA ET AL., 1985
JENDL-3.2
PRESENT
DIRECT
CROSS SECTION, BARN
0.16
0.12
0.08
0.04
1
2
3
4
NEUTRON ENERGY, MeV

FIG. 82

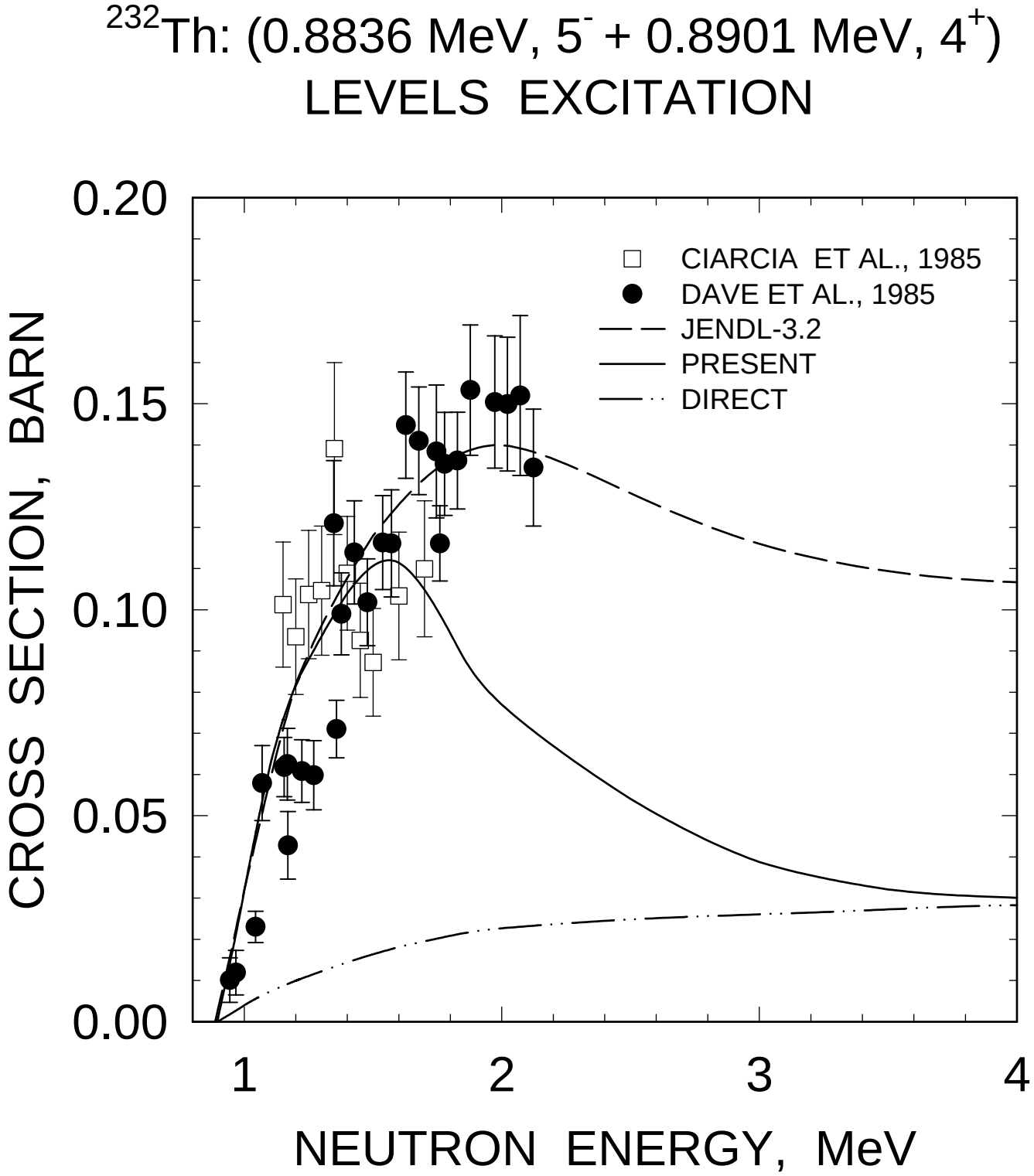
^{232}Th: (0.8836 MeV, 5$^-$ + 0.8901 MeV, 4$^+$)
LEVELS EXCITATION
CIARCIA ET AL., 1985
DAVE ET AL., 1985
JENDL-3.2
PRESENT
DIRECT
CROSS SECTION, BARN
0.20
0.15
0.10
0.05
0.00
1
2
3
4
NEUTRON ENERGY, MeV

FIG. 83

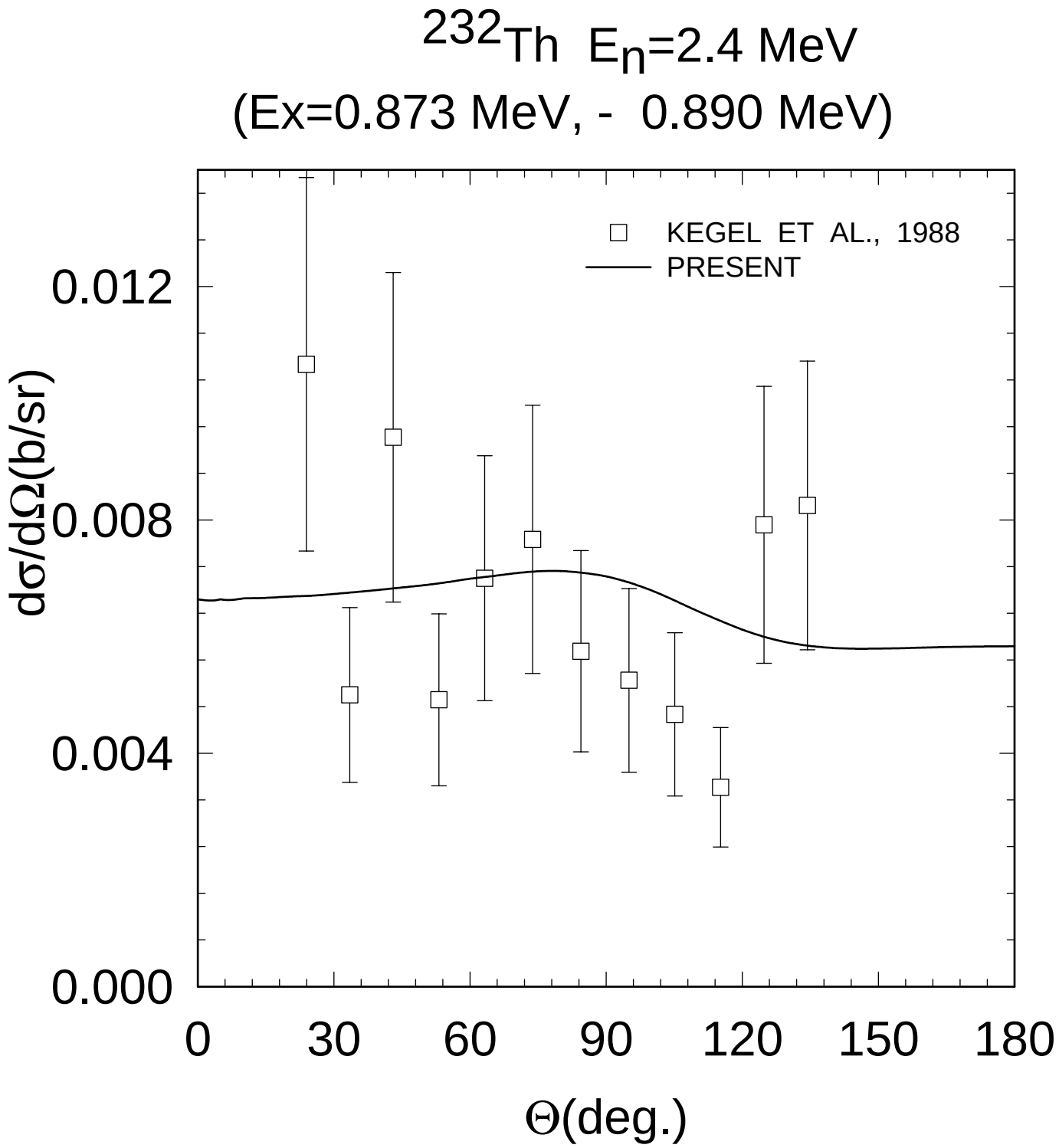
232Th En=2.4 MeV
(Ex=0.873 MeV, - 0.890 MeV)
KEGEL ET AL., 1988
PRESENT
dσ/dΩ(b/sr)
0.012
0.008
0.004
0.000
0
30
60
90
120
150
180
Θ(deg.)

FIG. 84

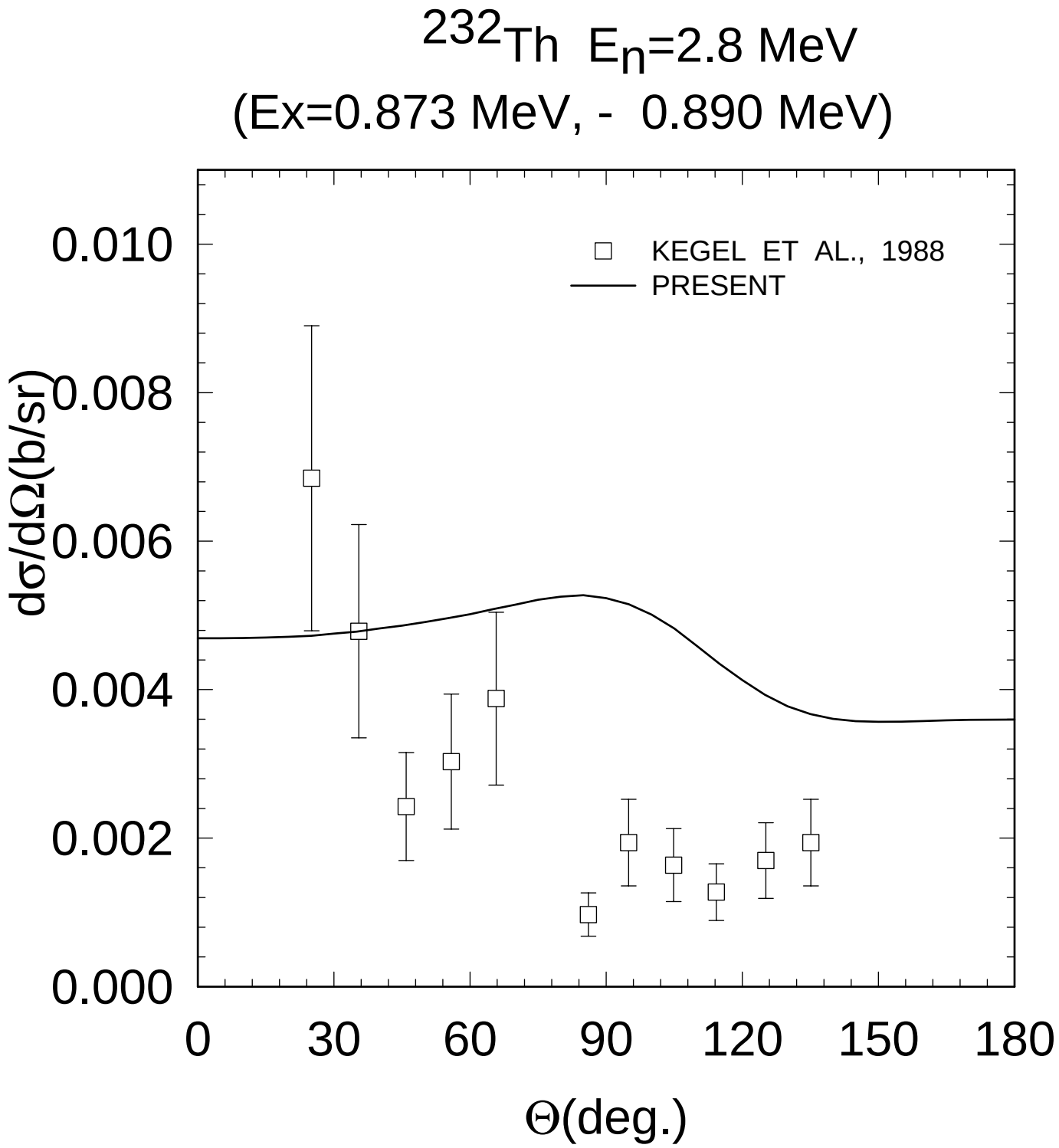
232Th En=2.8 MeV
(Ex=0.873 MeV, - 0.890 MeV)
KEGEL ET AL., 1988
PRESENT
dσ/dΩ(b/sr)
0.010
0.008
0.006
0.004
0.002
0.000
0
30
60
90
120
150
180
Θ(deg.)

FIG. 85

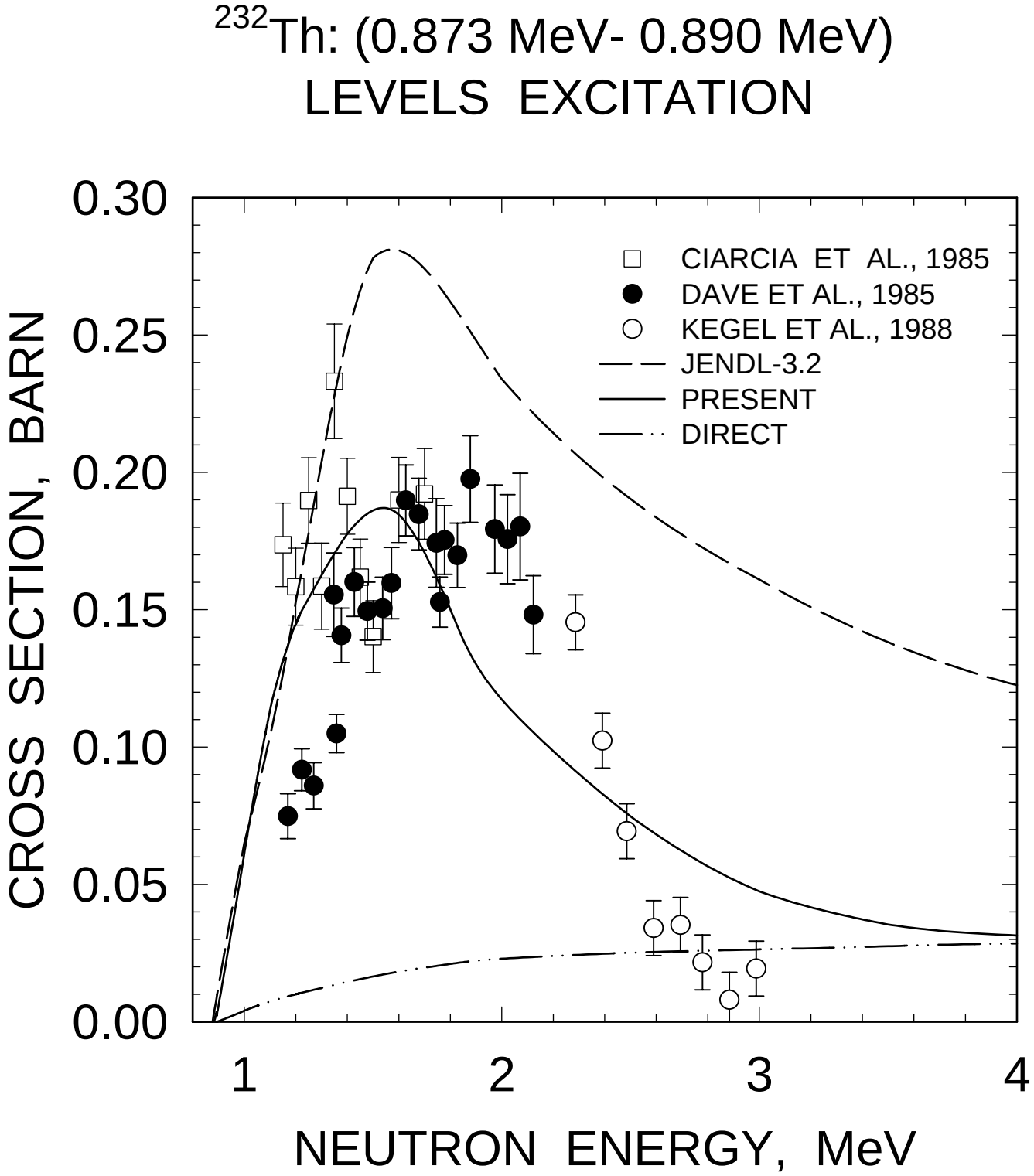
232Th: (0.873 MeV- 0.890 MeV)
LEVELS EXCITATION
CIARCIA ET AL., 1985
DAVE ET AL., 1985
KEGEL ET AL., 1988
JENDL-3.2
PRESENT
DIRECT
CROSS SECTION, BARN
0.30
0.25
0.20
0.15
0.10
0.05
0.00
1
2
3
4
NEUTRON ENERGY, MeV

FIG. 86

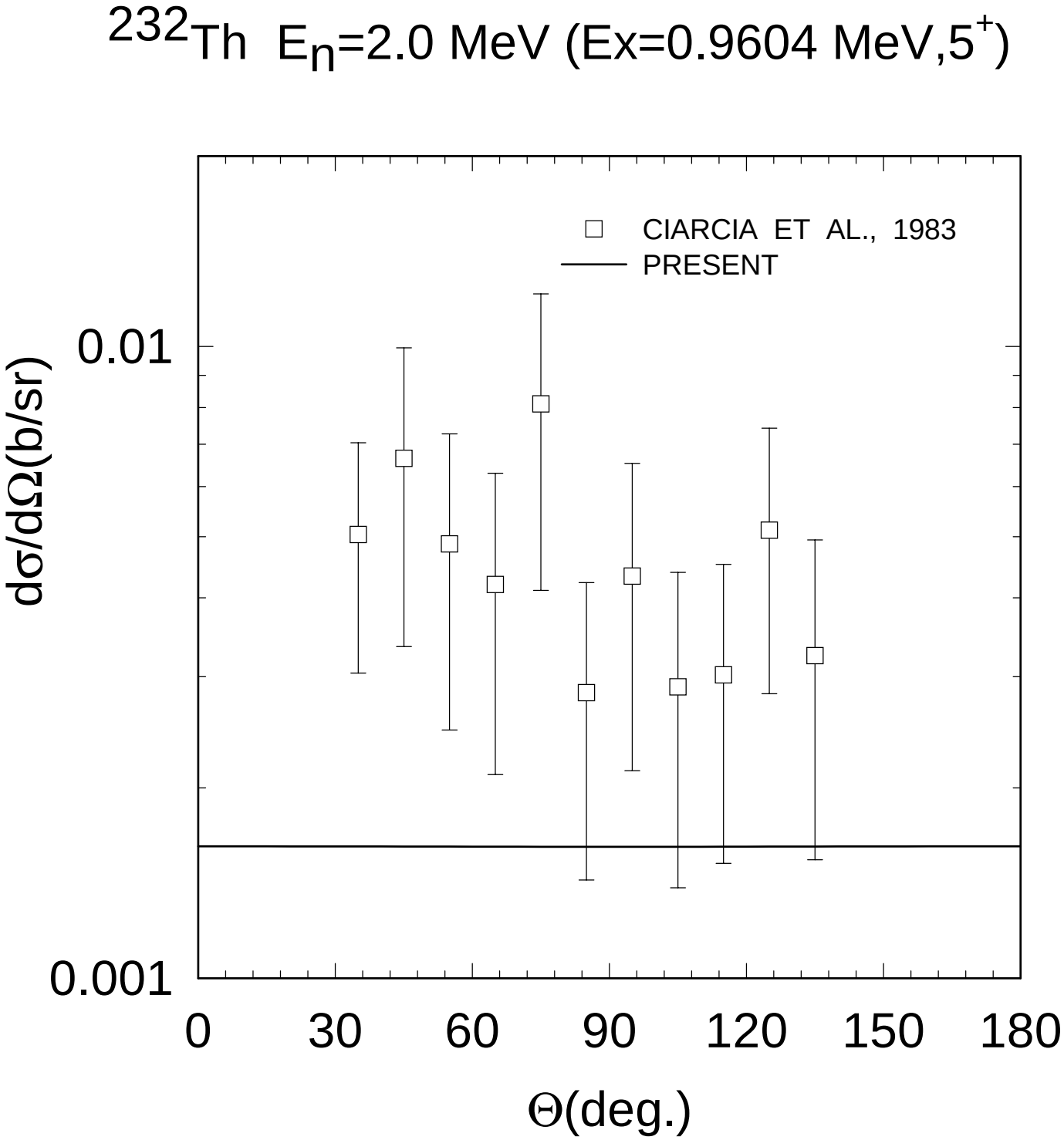
232Th En=2.0 MeV (Ex=0.9604 MeV,5+)
CIARCIA ET AL., 1983
PRESENT
0.01
0.001
dσ/dΩ(b/sr)
0
30
60
90
120
150
180
Θ(deg.)

FIG. 87

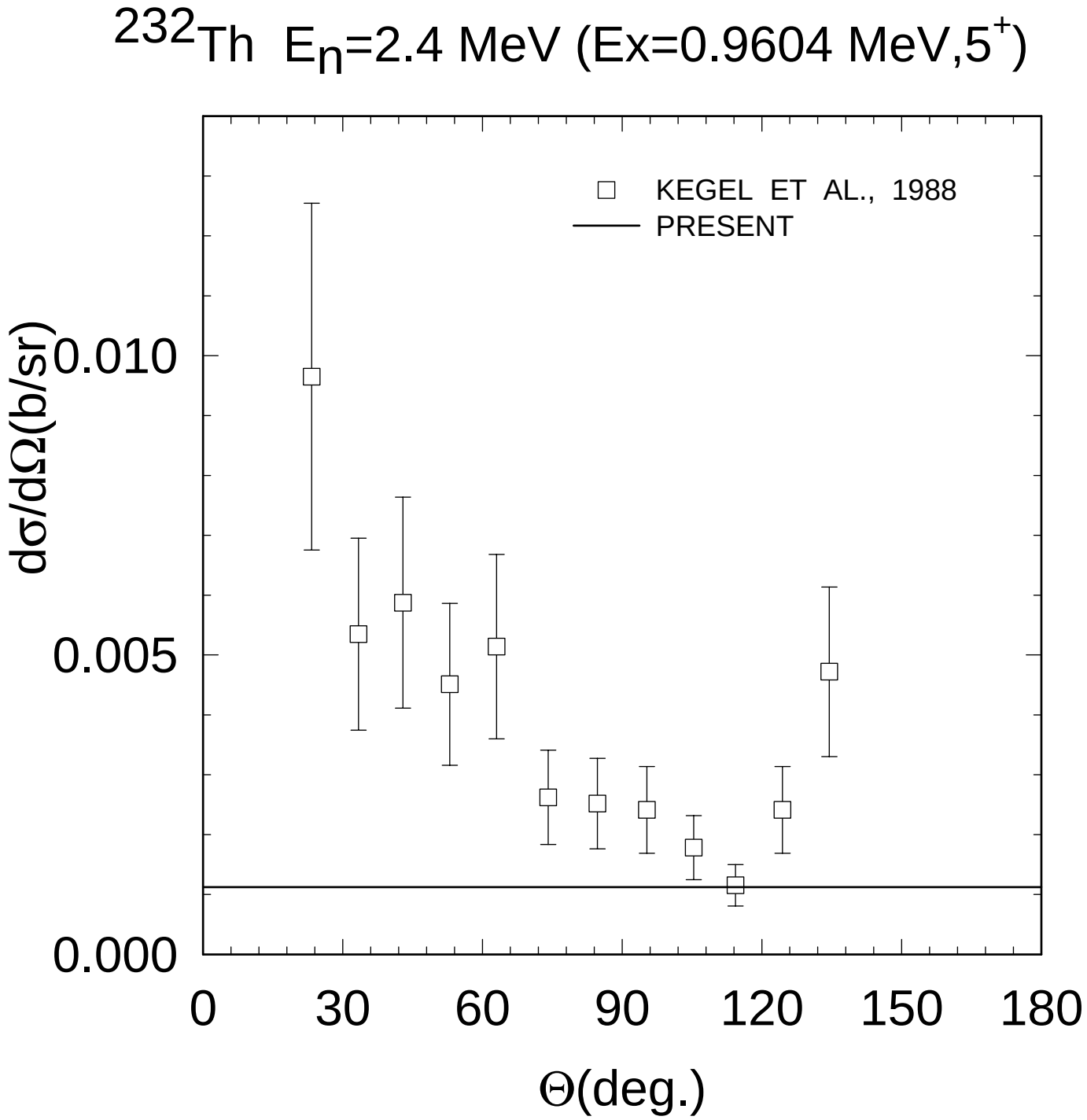
232Th En=2.4 MeV (Ex=0.9604 MeV,5+)
KEGEL ET AL., 1988
PRESENT
dσ/dΩ(b/sr)
0.010
0.005
0.000
0
30
60
90
120
150
180
Θ(deg.)

FIG. 88

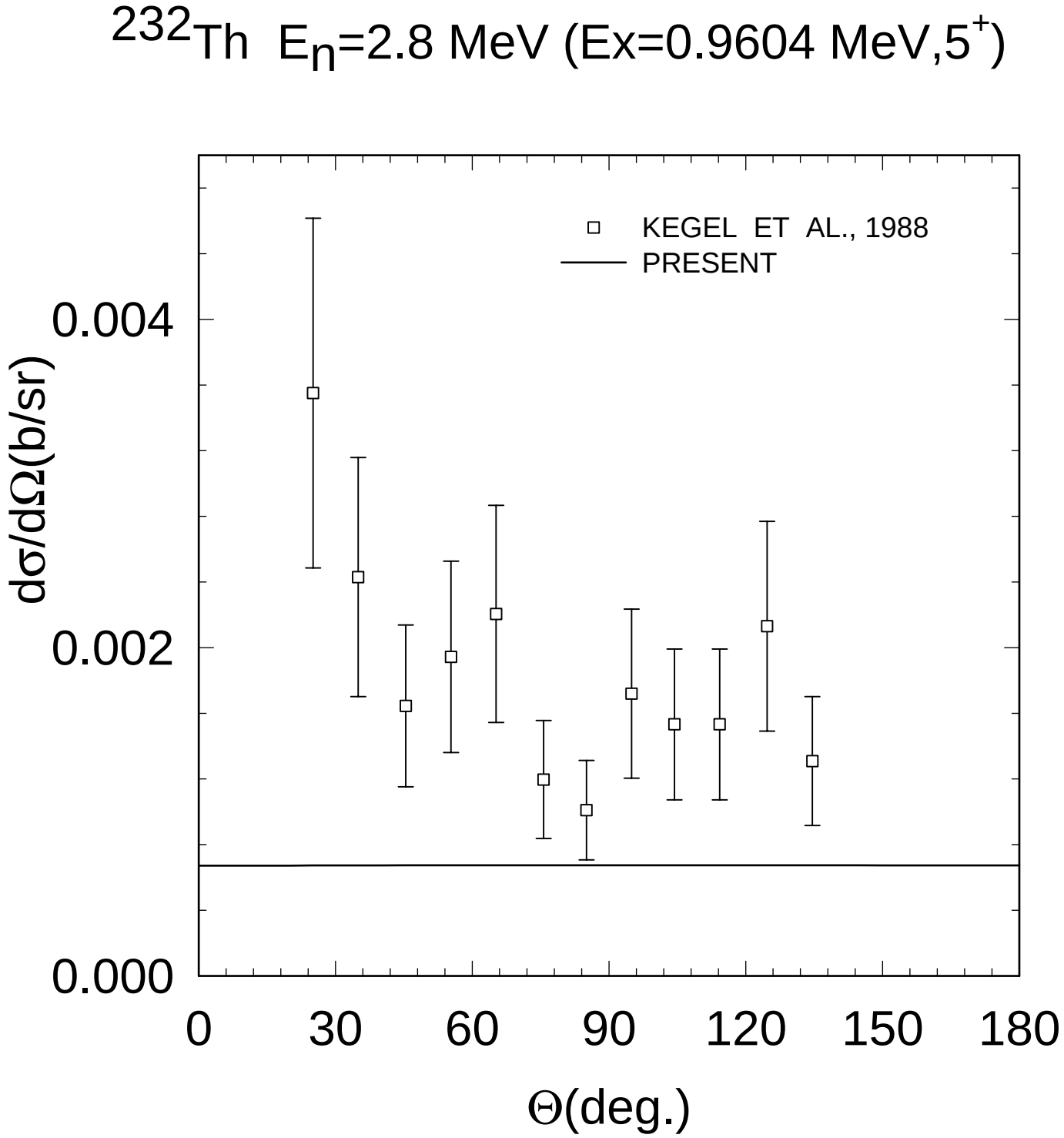
232Th En=2.8 MeV (Ex=0.9604 MeV,5+)
KEGEL ET AL., 1988
PRESENT
dσ/dΩ(b/sr)
0.004
0.002
0.000
0
30
60
90
120
150
180
Θ(deg.)

FIG. 89

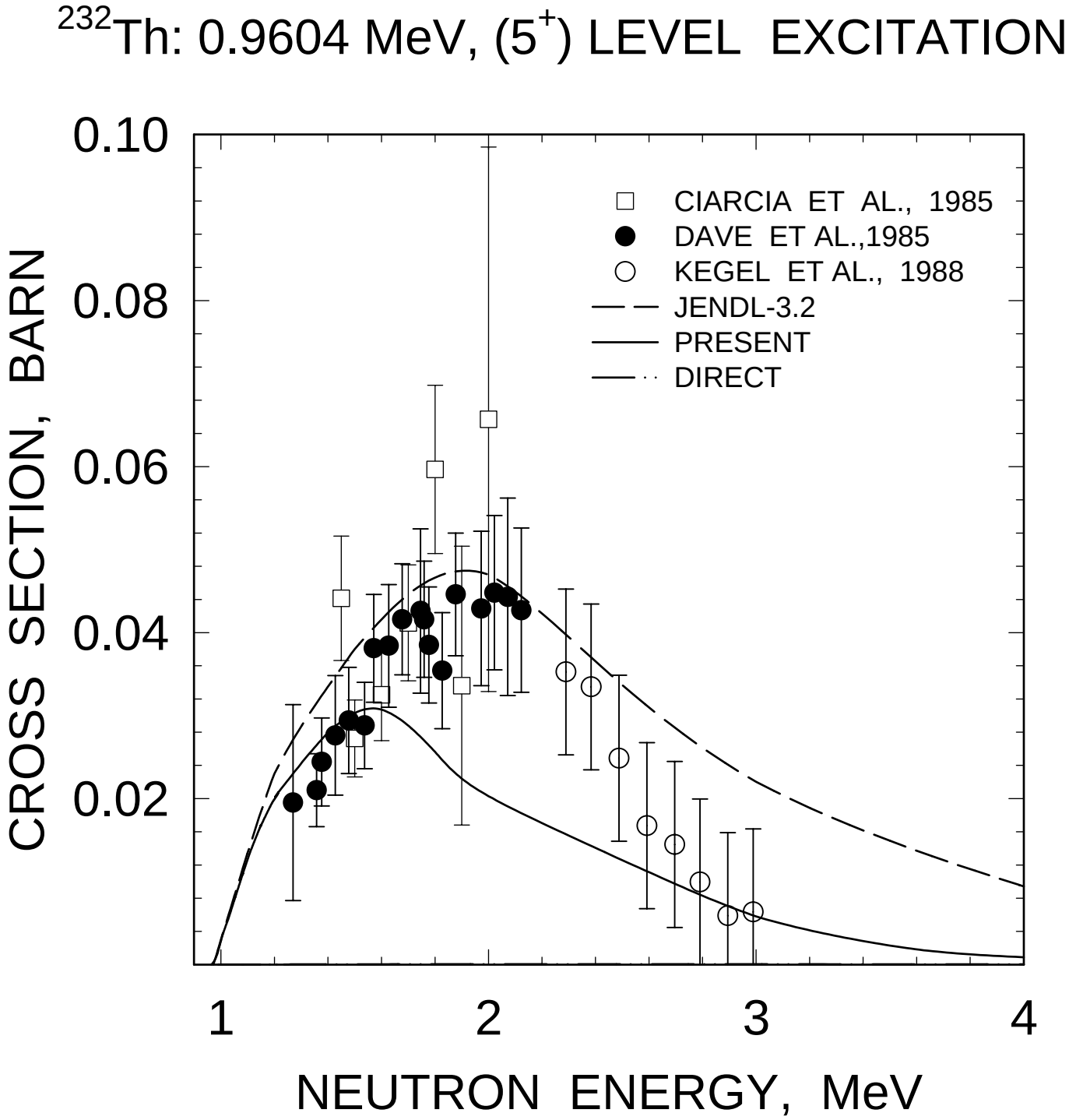
232Th: 0.9604 MeV, (5+) LEVEL EXCITATION
CIARCIA ET AL., 1985
DAVE ET AL.,1985
KEGEL ET AL., 1988
JENDL-3.2
PRESENT
DIRECT
CROSS SECTION, BARN
0.10
0.08
0.06
0.04
0.02
1
2
3
4
NEUTRON ENERGY, MeV

FIG. 90

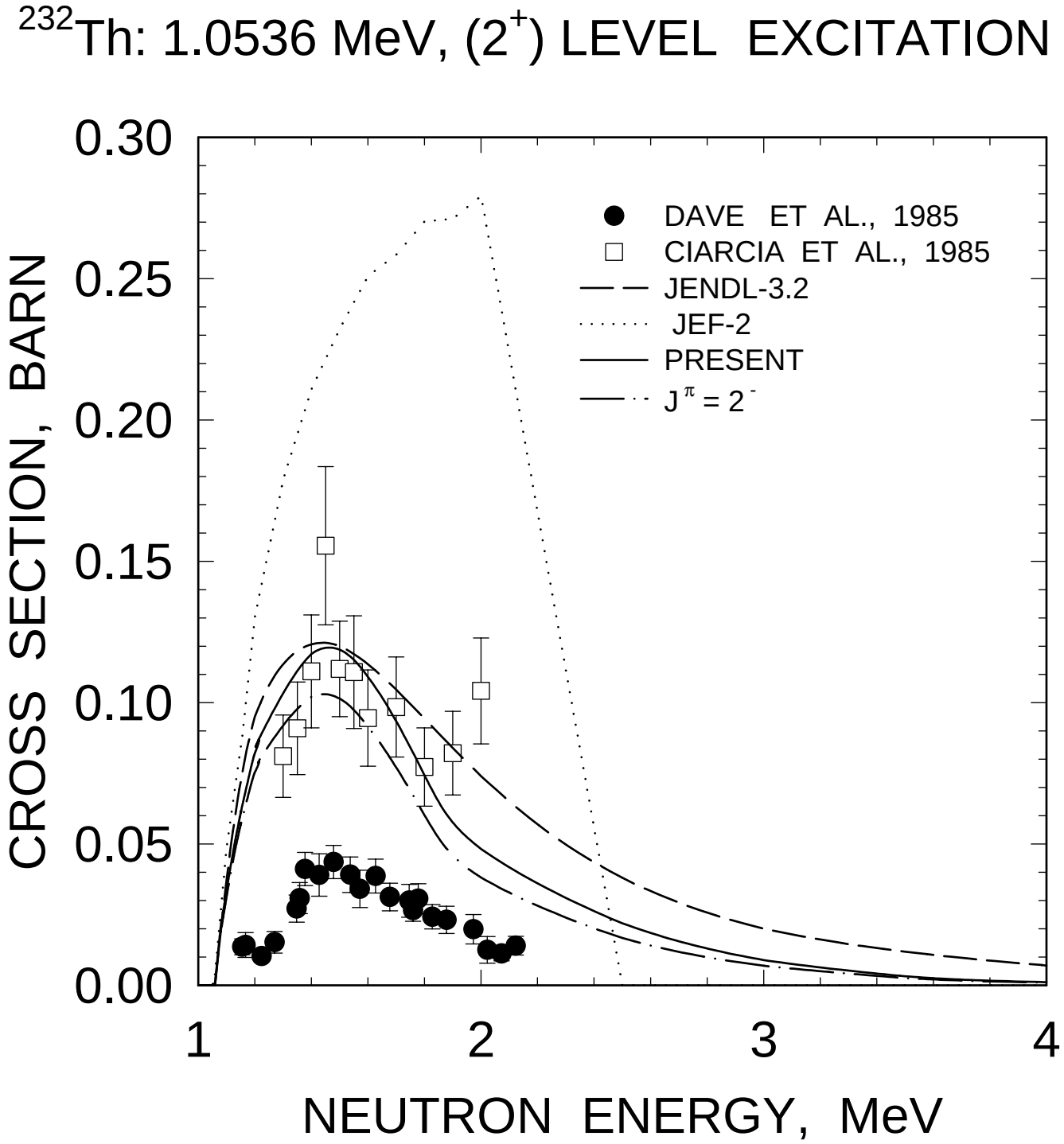
232Th: 1.0536 MeV, (2+) LEVEL EXCITATION
DAVE ET AL., 1985
CIARCIA ET AL., 1985
JENDL-3.2
JEF-2
PRESENT
J π = 2 -
CROSS SECTION, BARN
0.30
0.25
0.20
0.15
0.10
0.05
0.00
1
2
3
4
NEUTRON ENERGY, MeV

FIG. 91

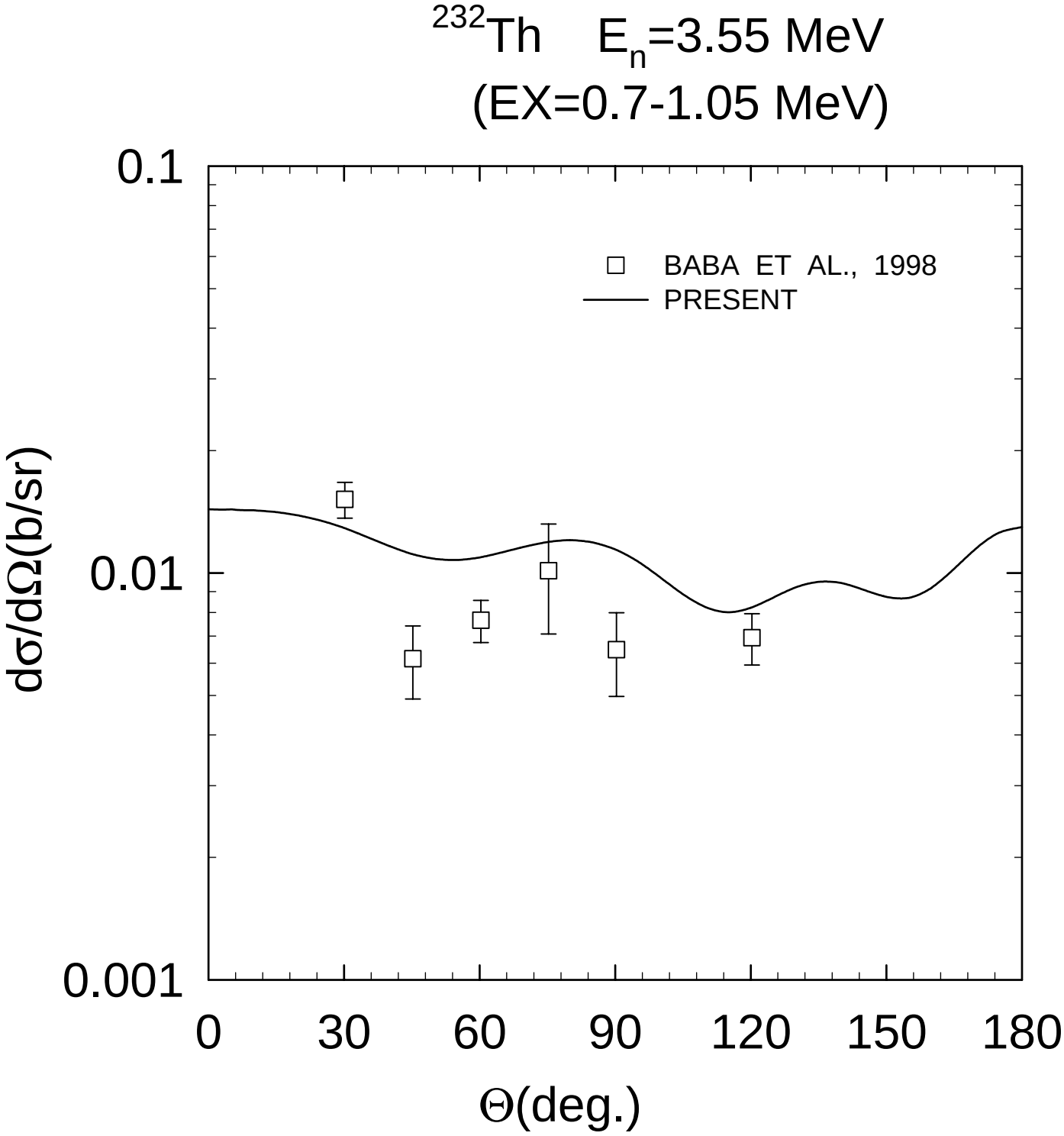
232Th En=3.55 MeV
(EX=0.7-1.05 MeV)
BABA ET AL., 1998
PRESENT
0.1
0.01
0.001
dσ/dΩ(b/sr)
0
30
60
90
120
150
180
Θ(deg.)

FIG. 92

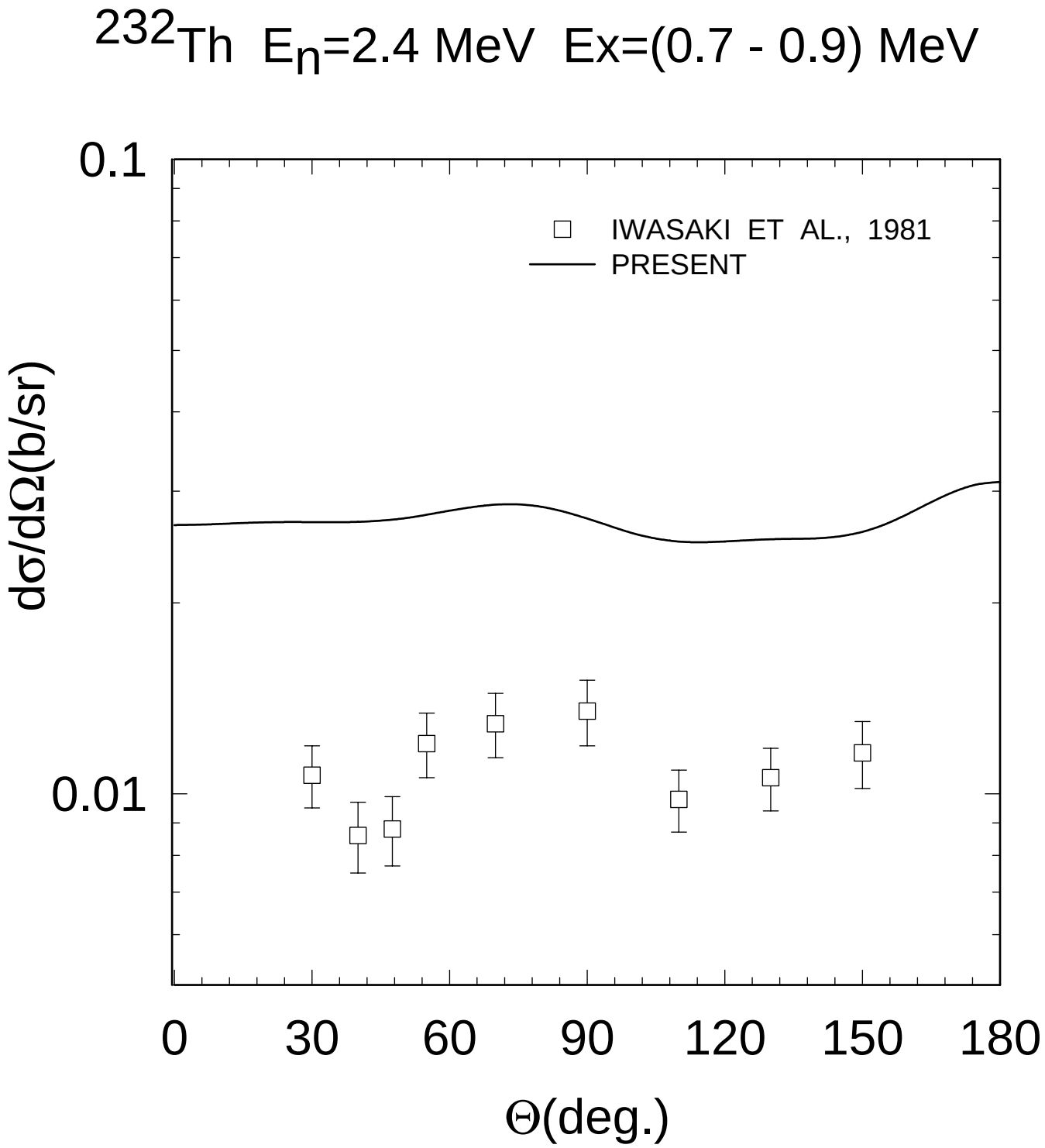
232Th En=2.4 MeV Ex=(0.7 - 0.9) MeV
IWASAKI ET AL., 1981
PRESENT
dσ/dΩ(b/sr)
0.1
0.01
0
30
60
90
120
150
180
Θ(deg.)

FIG. 93

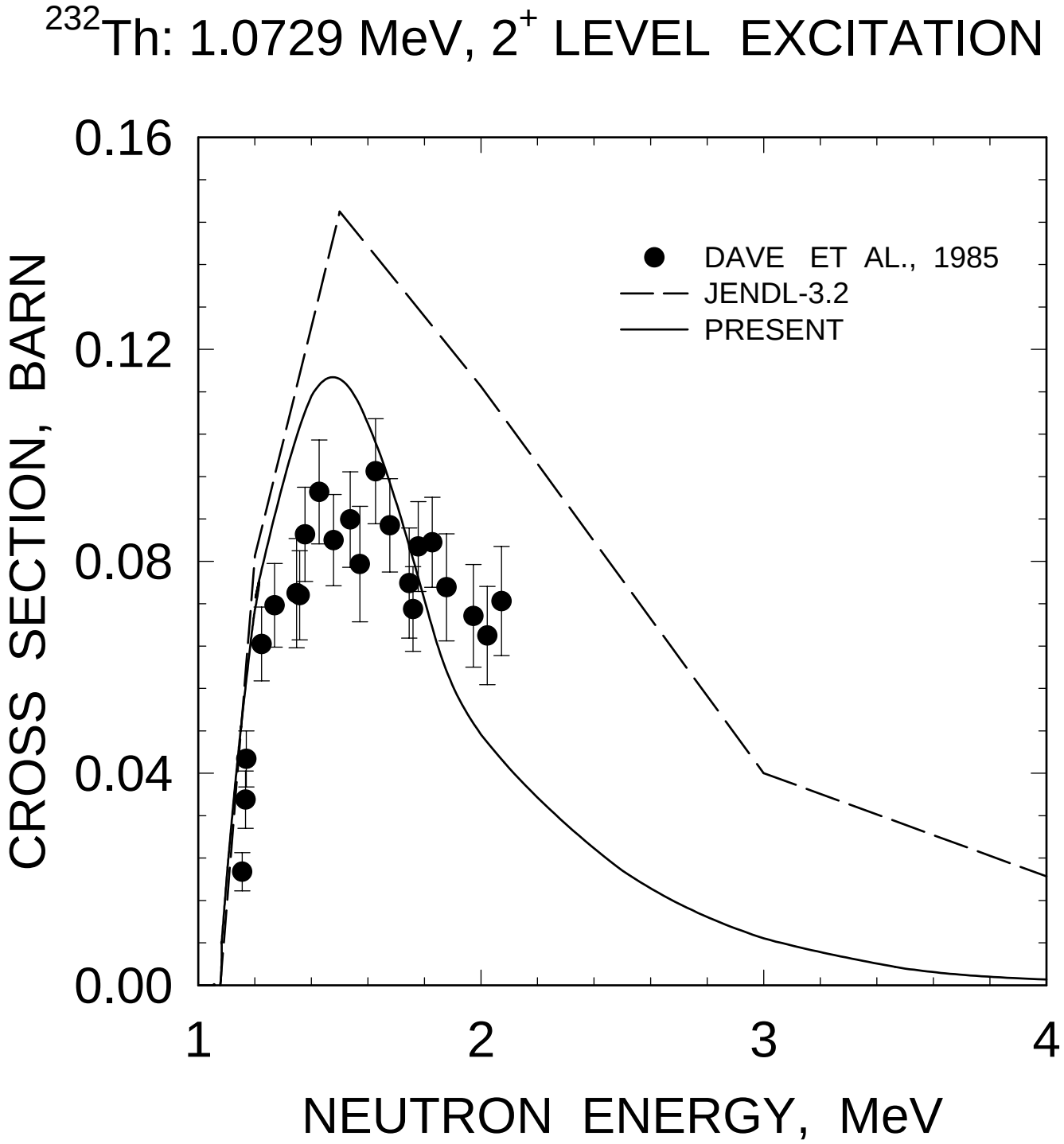
232Th: 1.0729 MeV, 2+ LEVEL EXCITATION
0.16
0.12
0.08
0.04
0.00
CROSS SECTION, BARN
1
2
3
4
NEUTRON ENERGY, MeV
DAVE ET AL., 1985
JENDL-3.2
PRESENT

FIG. 94

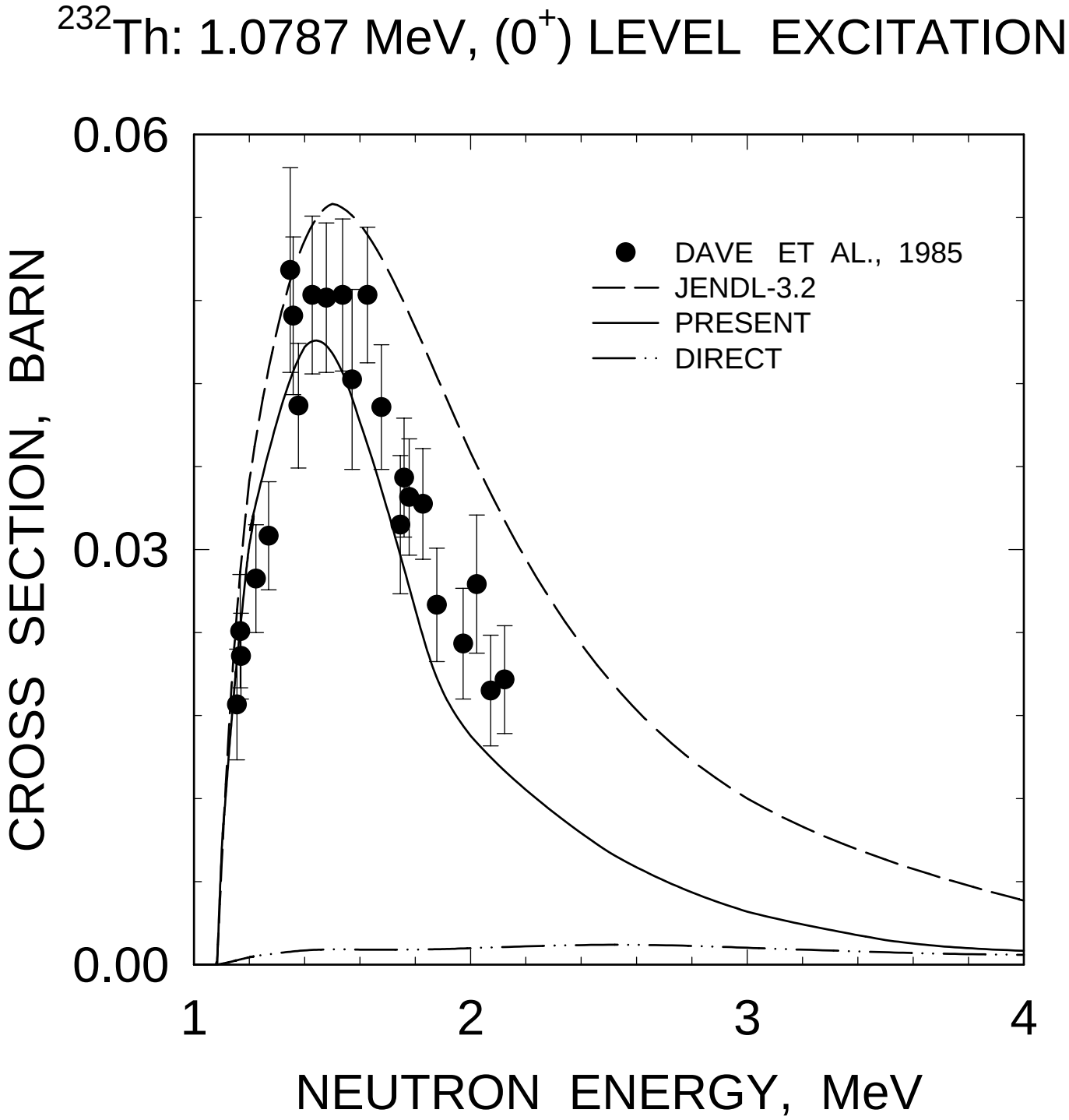
232Th: 1.0787 MeV, (0+) LEVEL EXCITATION
0.06
0.03
0.00
CROSS SECTION, BARN
1
2
3
4
NEUTRON ENERGY, MeV
DAVE ET AL., 1985
JENDL-3.2
PRESENT
DIRECT

FIG. 95

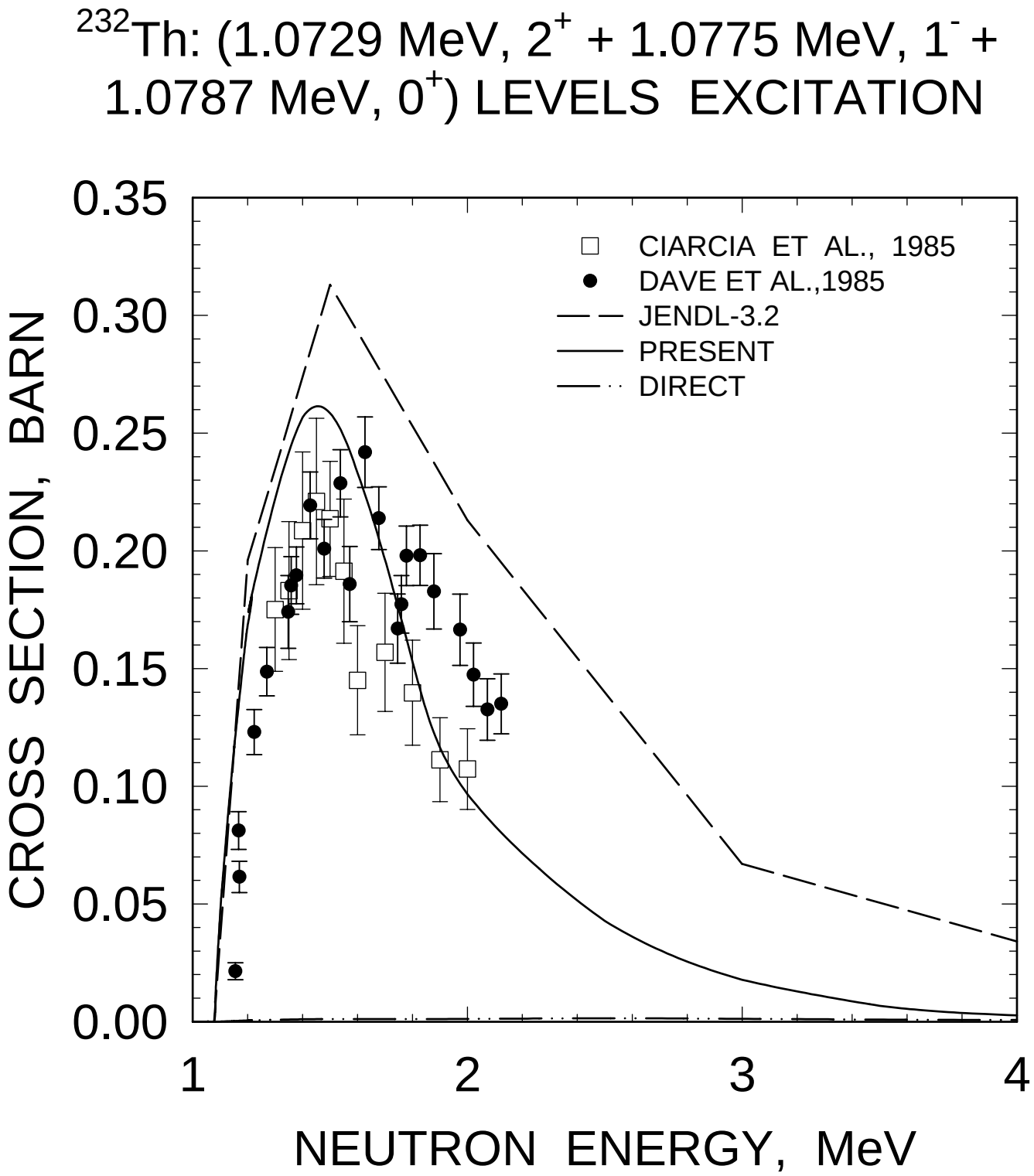
^{232}Th: (1.0729 MeV, 2$^+$ + 1.0775 MeV, 1$^-$ + 1.0787 MeV, 0$^+$) LEVELS EXCITATION
CIARCIA ET AL., 1985
DAVE ET AL.,1985
JENDL-3.2
PRESENT
DIRECT
CROSS SECTION, BARN
0.35
0.30
0.25
0.20
0.15
0.10
0.05
0.00
1
2
3
4
NEUTRON ENERGY, MeV

FIG. 96

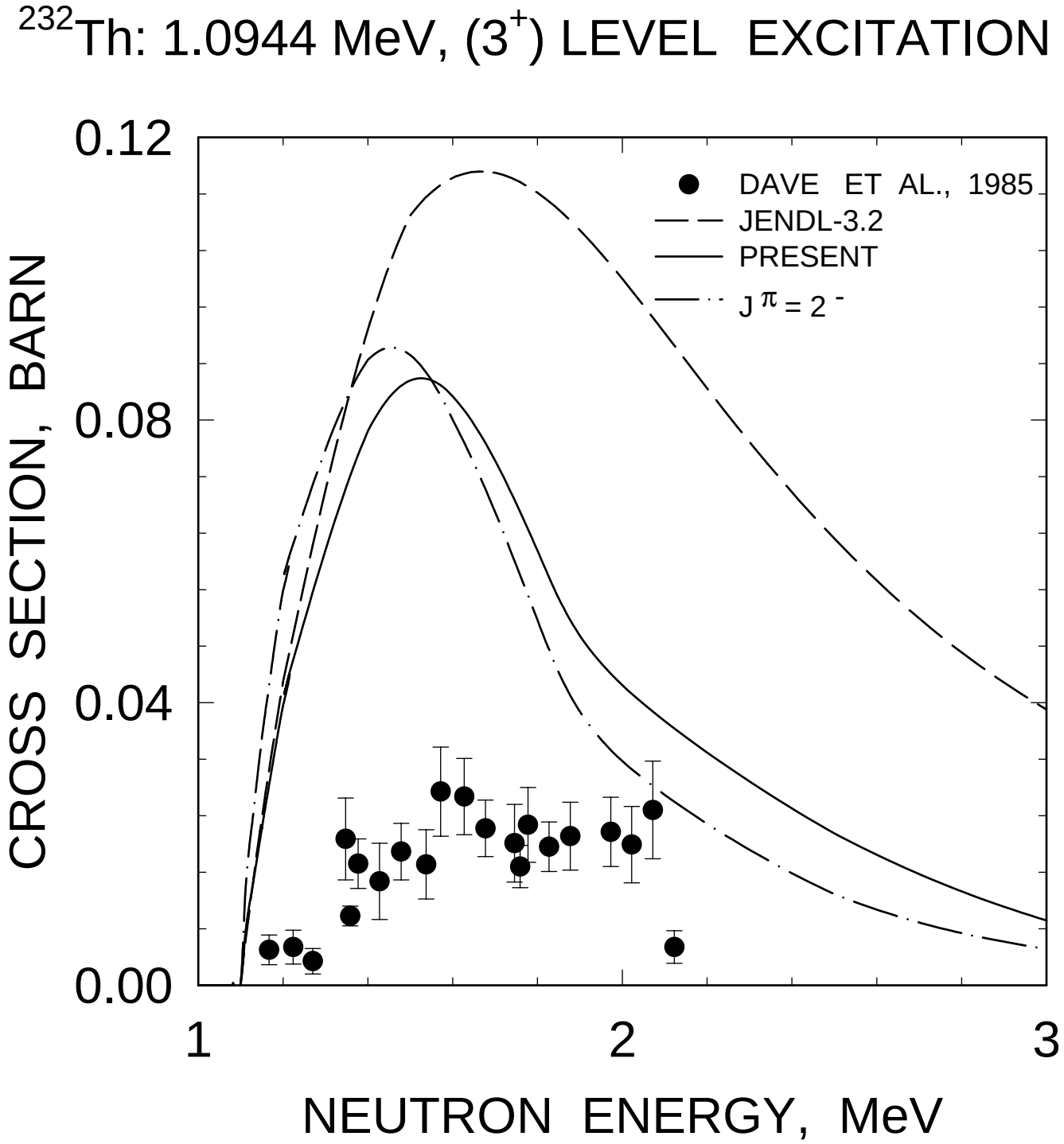
232Th: 1.0944 MeV, (3+) LEVEL EXCITATION
DAVE ET AL., 1985
JENDL-3.2
PRESENT
J π = 2 -
CROSS SECTION, BARN
0.12
0.08
0.04
0.00
1
2
3
NEUTRON ENERGY, MeV

FIG. 97

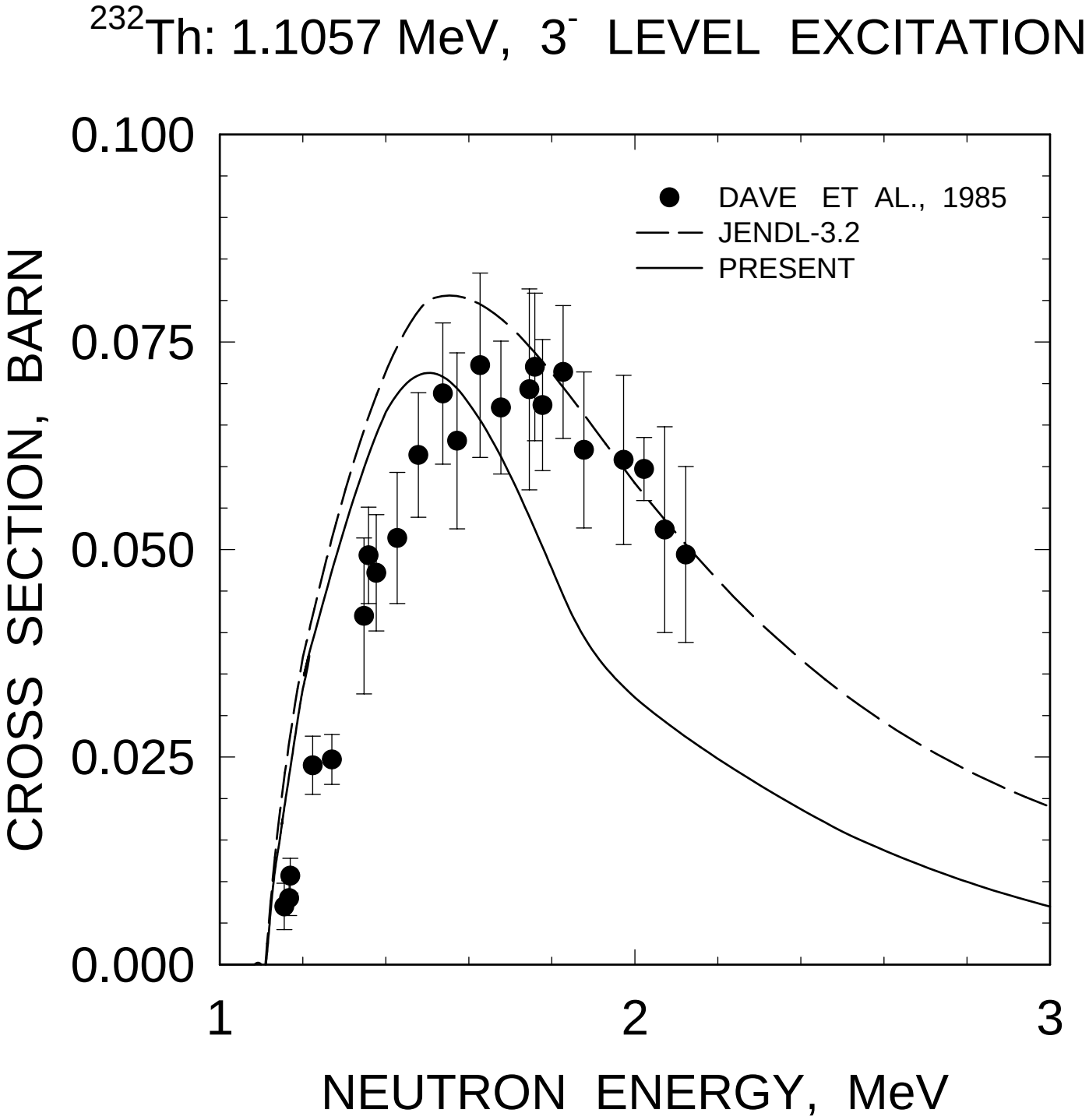
232Th: 1.1057 MeV, 3- LEVEL EXCITATION
DAVE ET AL., 1985
JENDL-3.2
PRESENT
CROSS SECTION, BARN
0.100
0.075
0.050
0.025
0.000
1
2
3
NEUTRON ENERGY, MeV

FIG. 98

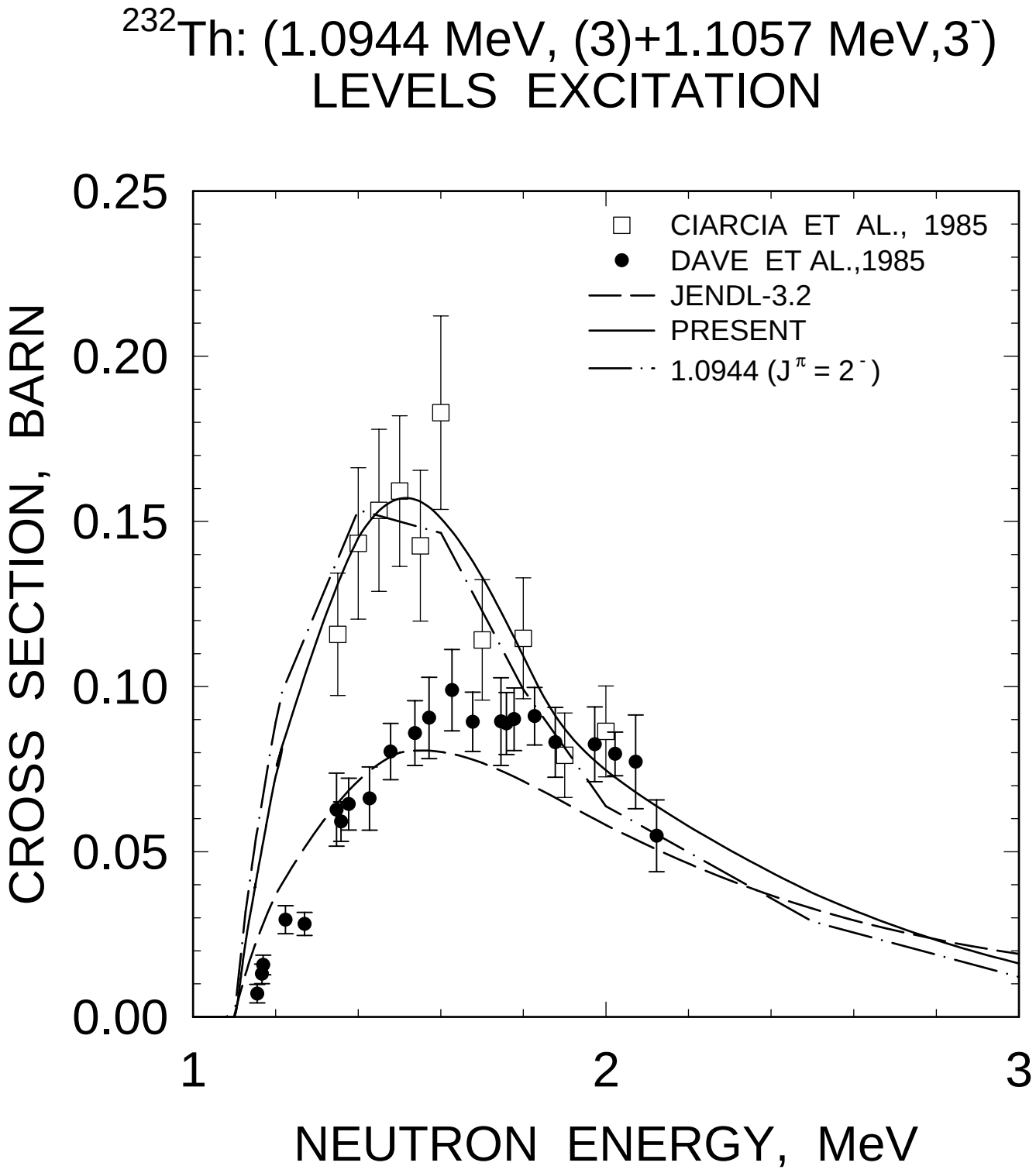
232Th: (1.0944 MeV, (3)+1.1057 MeV,3-)
LEVELS EXCITATION
CIARCIA ET AL., 1985
DAVE ET AL.,1985
JENDL-3.2
PRESENT
1.0944 (Jπ = 2-)
CROSS SECTION, BARN
0.25
0.20
0.15
0.10
0.05
0.00
1
2
3
NEUTRON ENERGY, MeV

FIG. 99

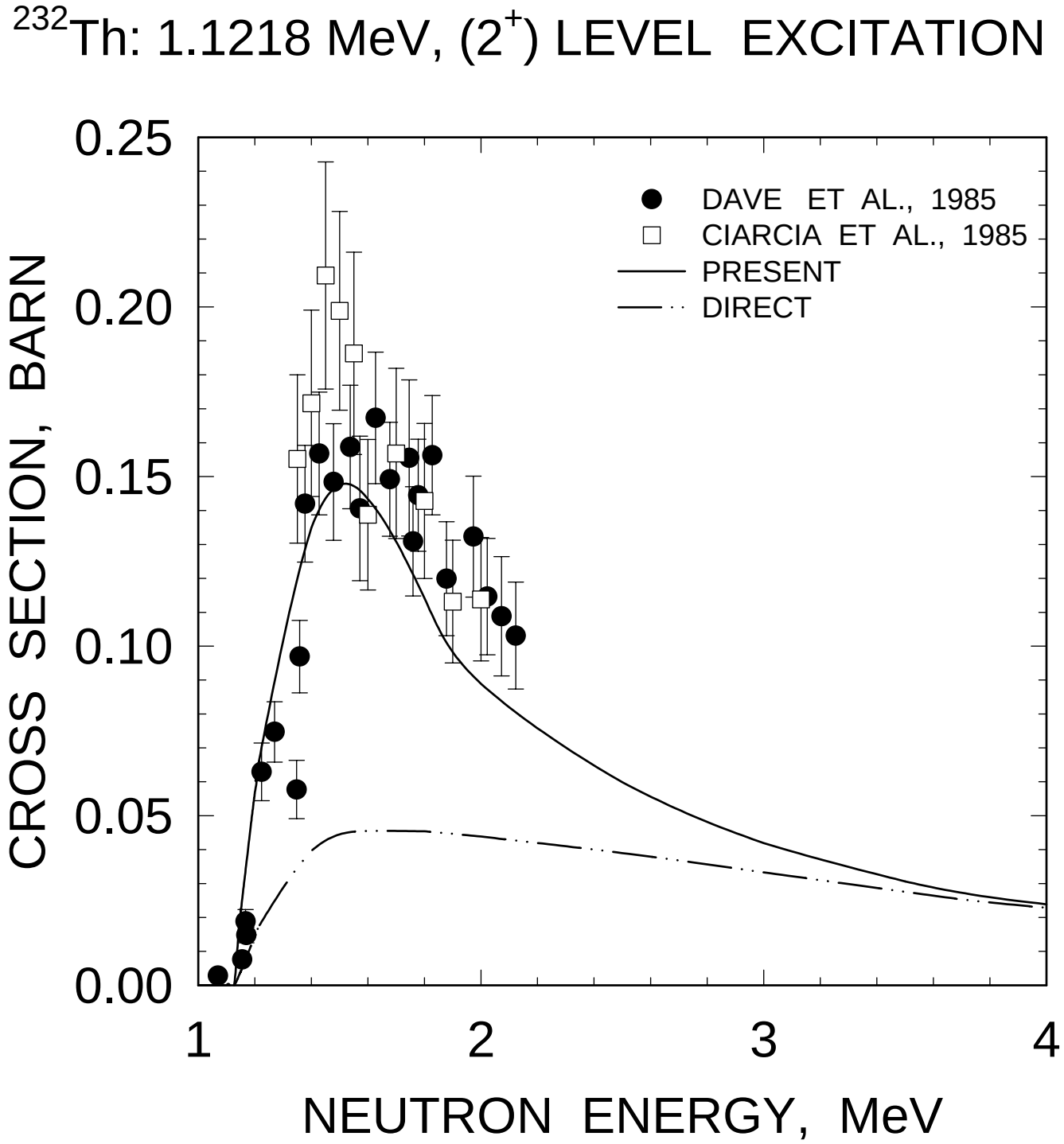
^{232}Th: 1.1218 MeV, (2^{+}) LEVEL EXCITATION
DAVE ET AL., 1985
CIARCIA ET AL., 1985
PRESENT
DIRECT
CROSS SECTION, BARN
0.25
0.20
0.15
0.10
0.05
0.00
1
2
3
4
NEUTRON ENERGY, MeV

FIG. 100

^{232}Th: (1.1433 MeV, (4^-)+ 1.1483 MeV,(4^+))
LEVELS EXCITATION

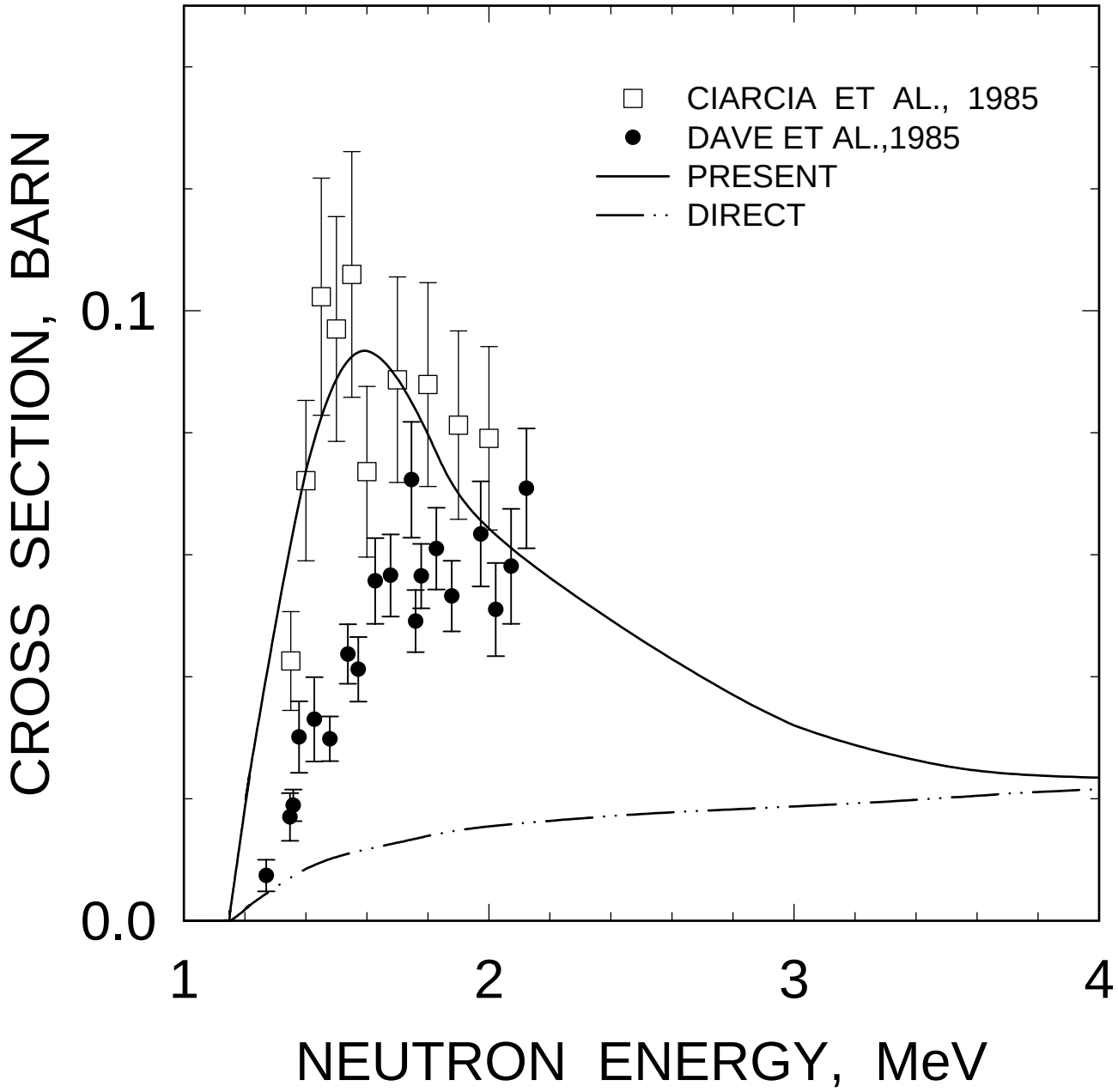

FIG. 101

^{232}Th: 1.1825 MeV, 3^- LEVEL EXCITATION

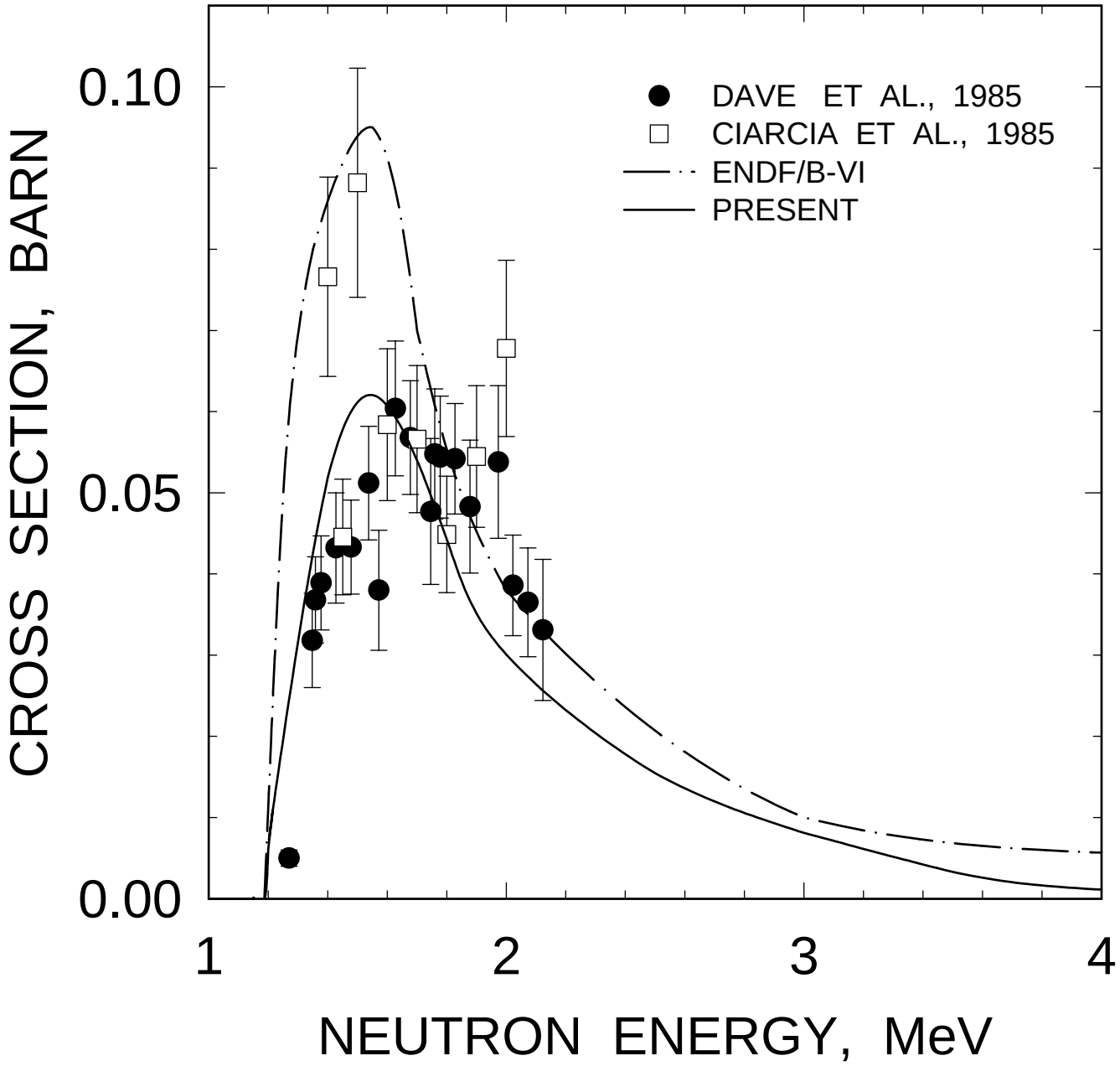

FIG. 102

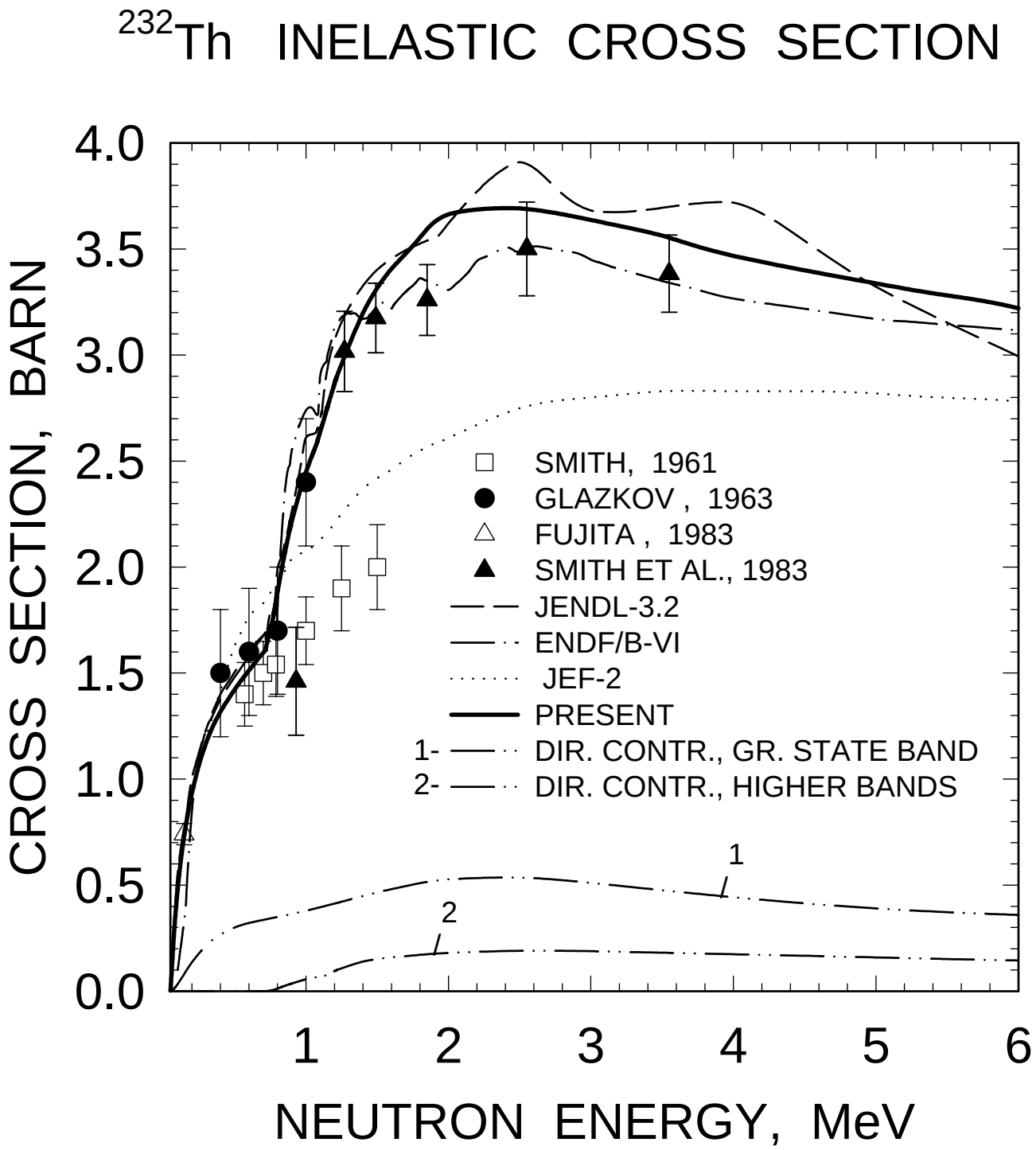
232Th INELASTIC CROSS SECTION
CROSS SECTION, BARN
NEUTRON ENERGY, MeV
4.0
3.5
3.0
2.5
2.0
1.5
1.0
0.5
0.0
1
2
3
4
5
6
SMITH, 1961
GLAZKOV , 1963
FUJITA , 1983
SMITH ET AL., 1983
JENDL-3.2
ENDF/B-VI
JEF-2
PRESENT
1- DIR. CONTR., GR. STATE BAND
2- DIR. CONTR., HIGHER BANDS
1
2

FIG. 103

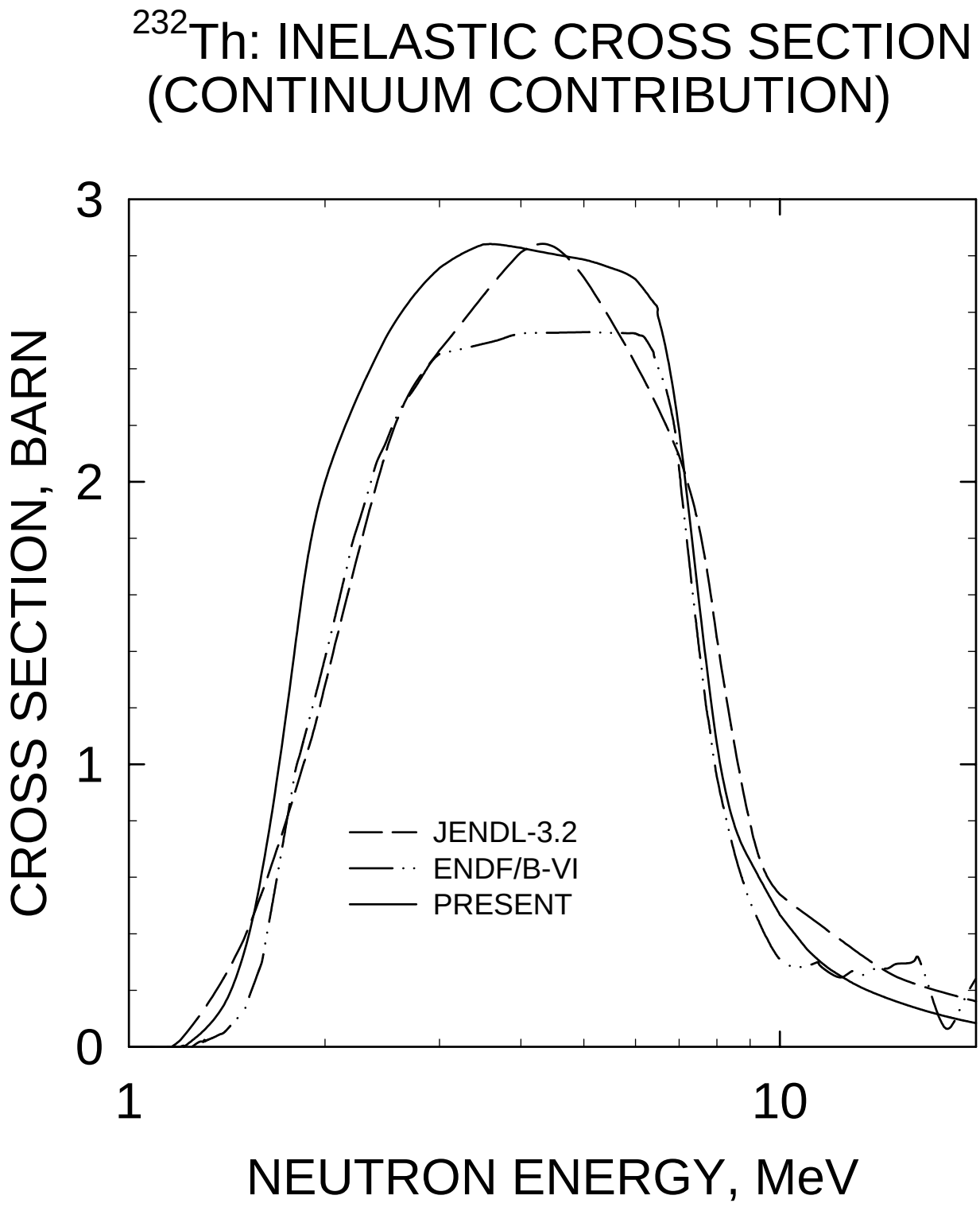
232Th: INELASTIC CROSS SECTION
(CONTINUUM CONTRIBUTION)
CROSS SECTION, BARN
NEUTRON ENERGY, MeV
0
1
2
3
1
10
JENDL-3.2
ENDF/B-VI
PRESENT

FIG. 104

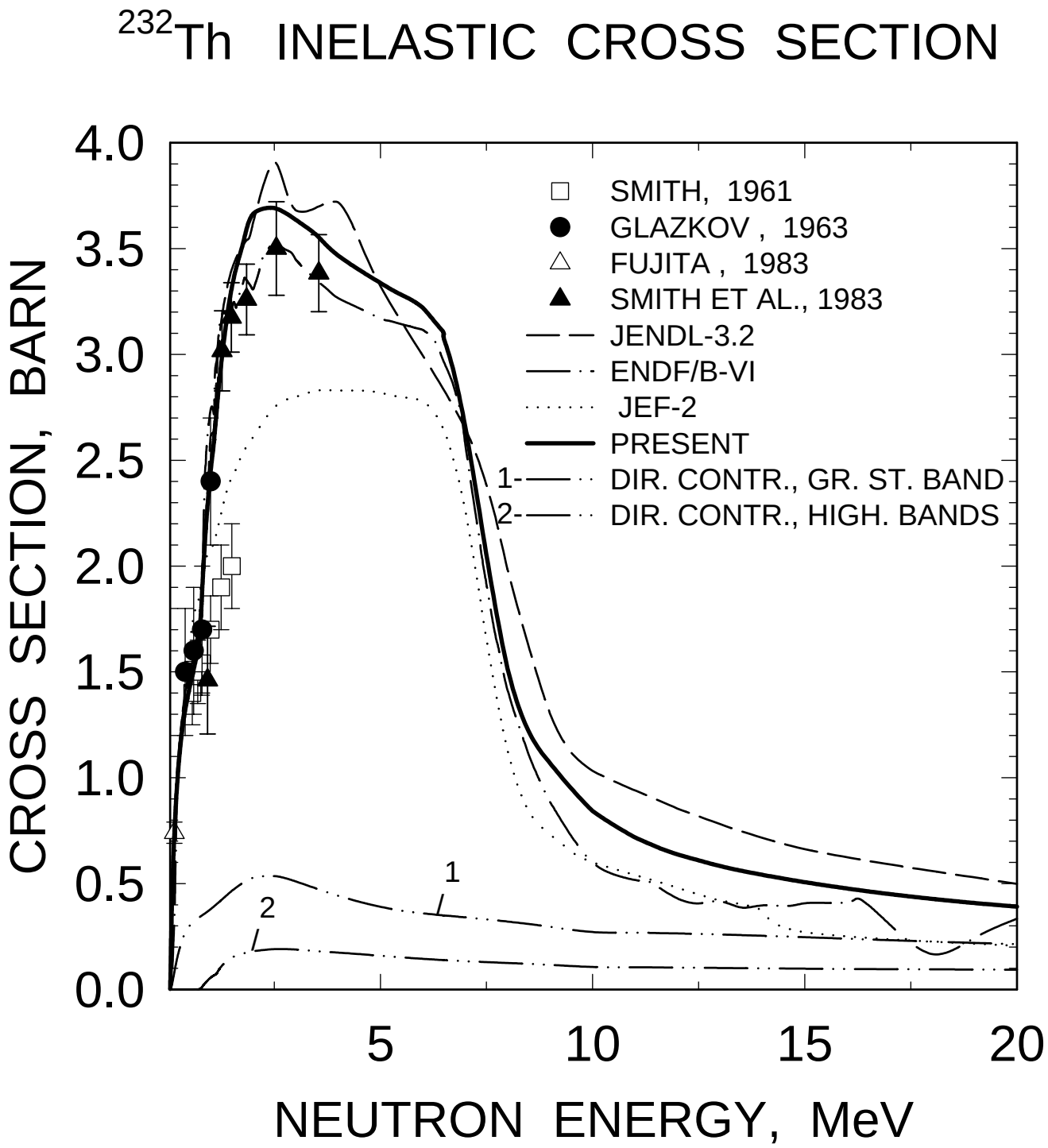
232Th INELASTIC CROSS SECTION
CROSS SECTION, BARN
NEUTRON ENERGY, MeV
4.0
3.5
3.0
2.5
2.0
1.5
1.0
0.5
0.0
5
10
15
20
SMITH, 1961
GLAZKOV , 1963
FUJITA , 1983
SMITH ET AL., 1983
JENDL-3.2
ENDF/B-VI
JEF-2
PRESENT
1- DIR. CONTR., GR. ST. BAND
2- DIR. CONTR., HIGH. BANDS
1
2

FIG. 105

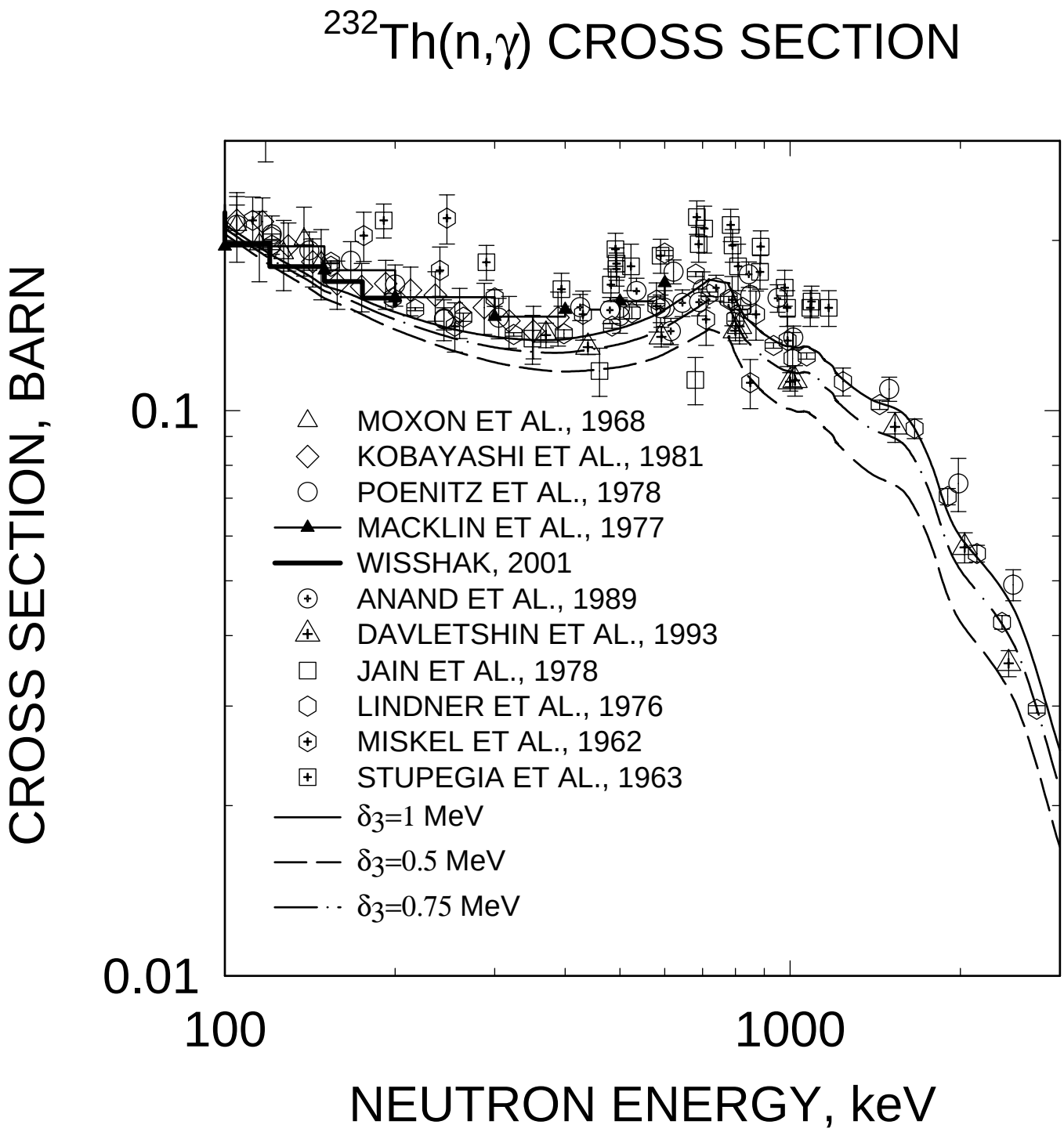
232Th(n,γ) CROSS SECTION
CROSS SECTION, BARN
0.1
0.01
100
1000
NEUTRON ENERGY, keV
MOXON ET AL., 1968
KOBAYASHI ET AL., 1981
POENITZ ET AL., 1978
MACKLIN ET AL., 1977
WISSHAK, 2001
ANAND ET AL., 1989
DAVLETSHIN ET AL., 1993
JAIN ET AL., 1978
LINDNER ET AL., 1976
MISKEL ET AL., 1962
STUPEGIA ET AL., 1963
δ3=1 MeV
δ3=0.5 MeV
δ3=0.75 MeV

FIG. 106

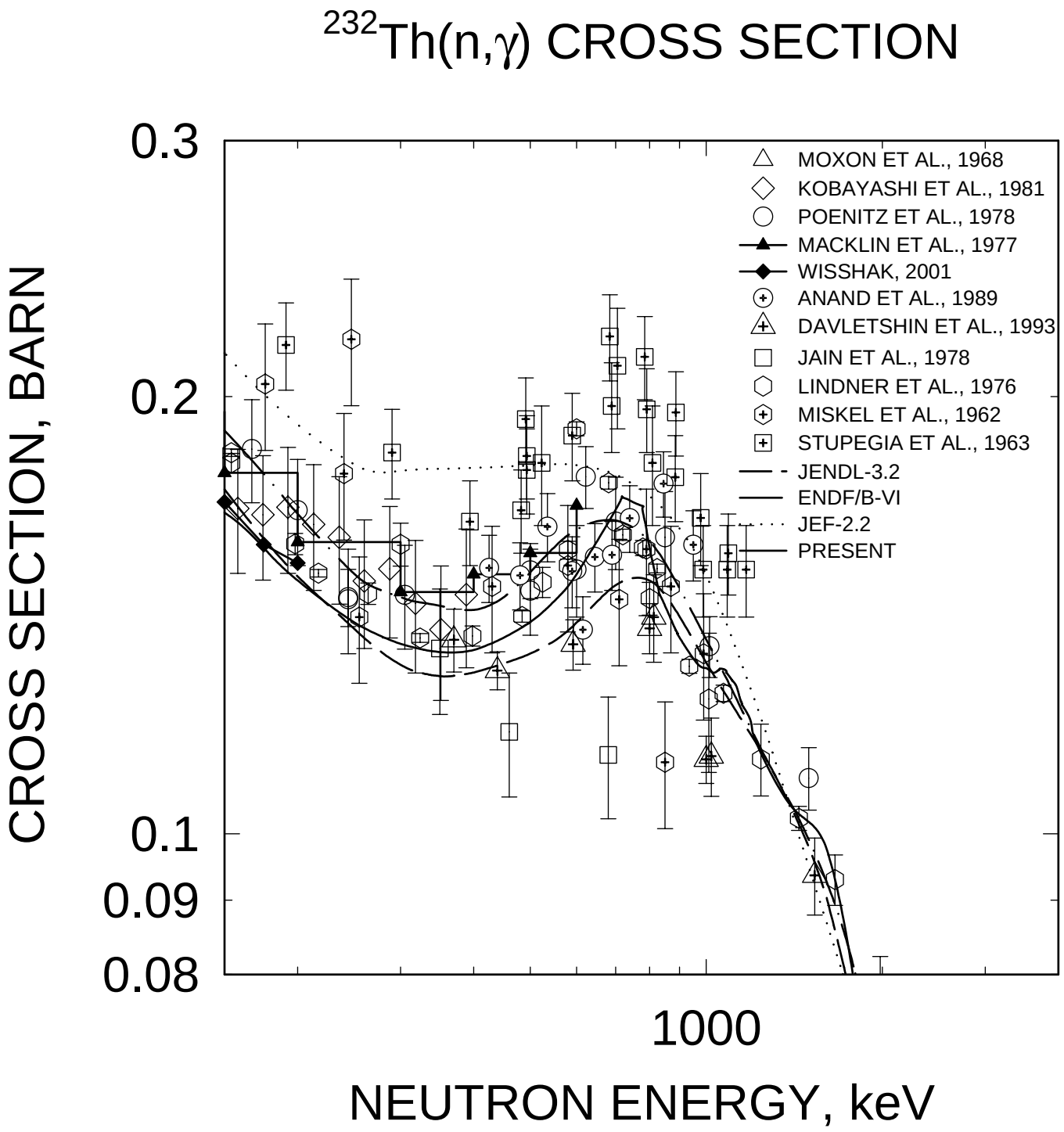
232Th(n,γ) CROSS SECTION
0.3
0.2
0.1
0.09
0.08
CROSS SECTION, BARN
1000
NEUTRON ENERGY, keV
MOXON ET AL., 1968
KOBAYASHI ET AL., 1981
POENITZ ET AL., 1978
MACKLIN ET AL., 1977
WISSHAK, 2001
ANAND ET AL., 1989
DAVLETSHIN ET AL., 1993
JAIN ET AL., 1978
LINDNER ET AL., 1976
MISKEL ET AL., 1962
STUPEGIA ET AL., 1963
JENDL-3.2
ENDF/B-VI
JEF-2.2
PRESENT

FIG. 107

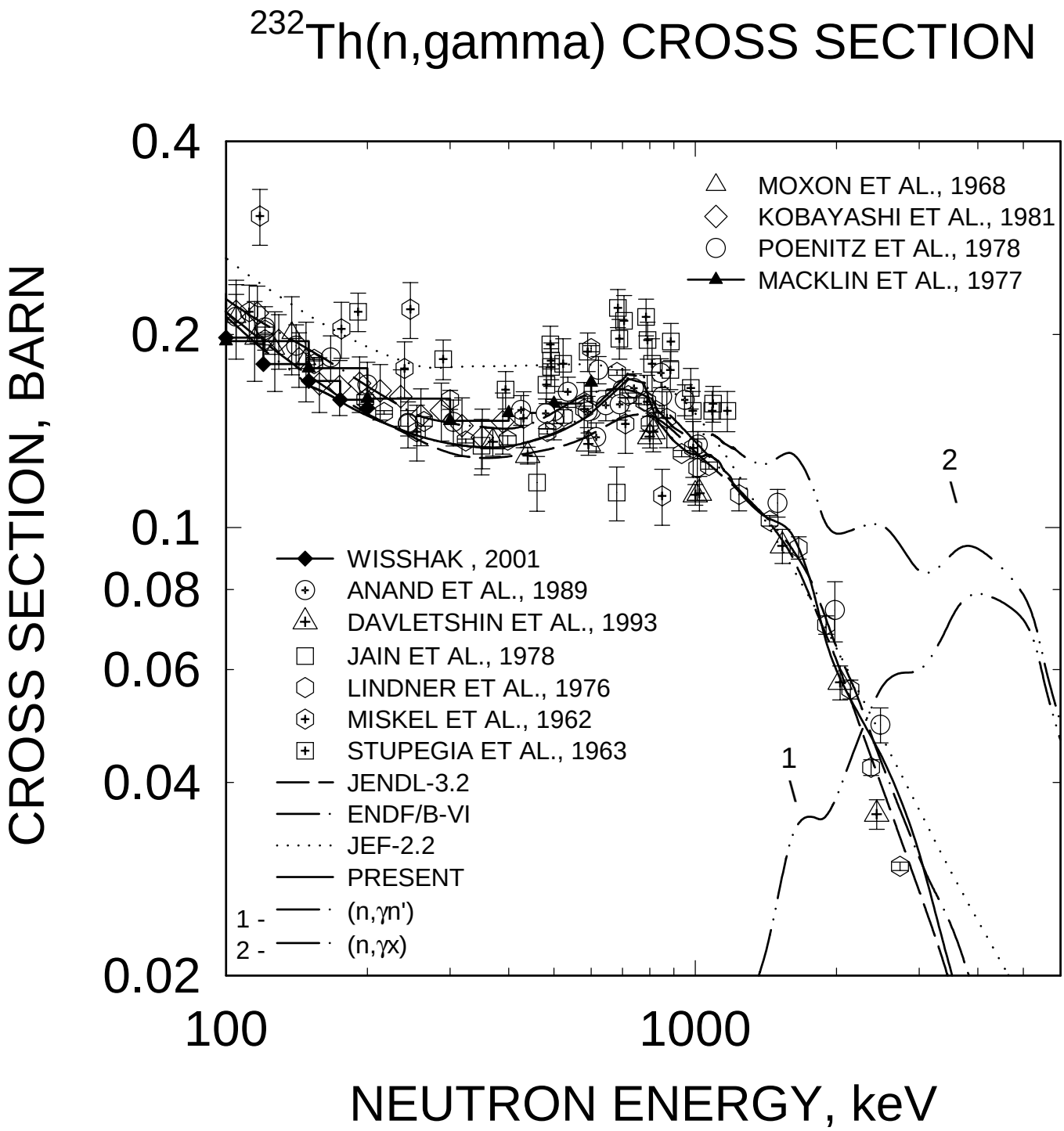
232Th(n,gamma) CROSS SECTION
CROSS SECTION, BARN
NEUTRON ENERGY, keV
0.4
0.2
0.1
0.08
0.06
0.04
0.02
100
1000
MOXON ET AL., 1968
KOBAYASHI ET AL., 1981
POENITZ ET AL., 1978
MACKLIN ET AL., 1977
WISSHAK , 2001
ANAND ET AL., 1989
DAVLETSHIN ET AL., 1993
JAIN ET AL., 1978
LINDNER ET AL., 1976
MISKEL ET AL., 1962
STUPEGIA ET AL., 1963
JENDL-3.2
ENDF/B-VI
JEF-2.2
PRESENT
1 - (n,γn')
2 - (n,γx)
1
2

FIG. 108

^{232}Th FISSION CROSS SECTION

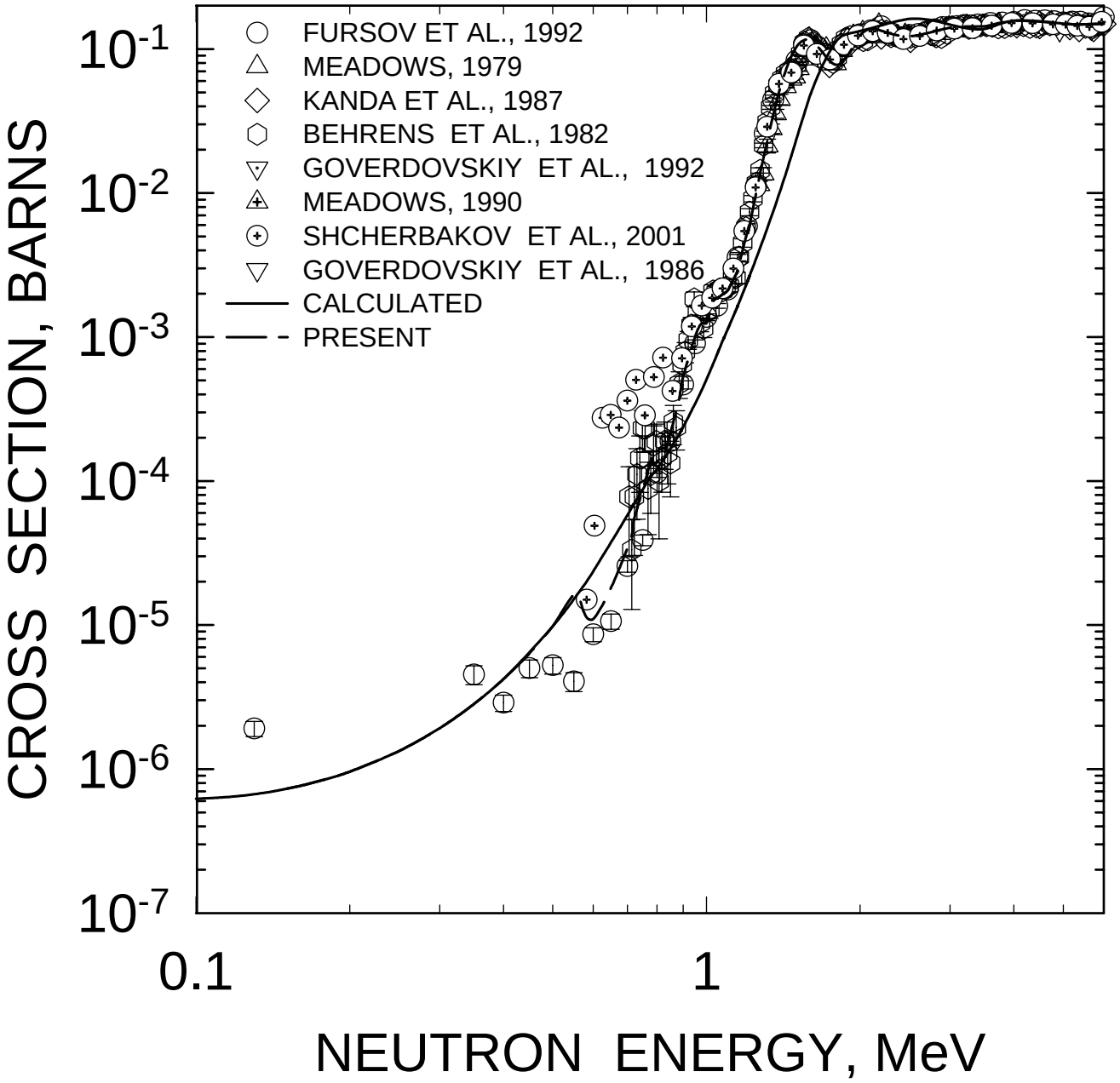

FIG. 109

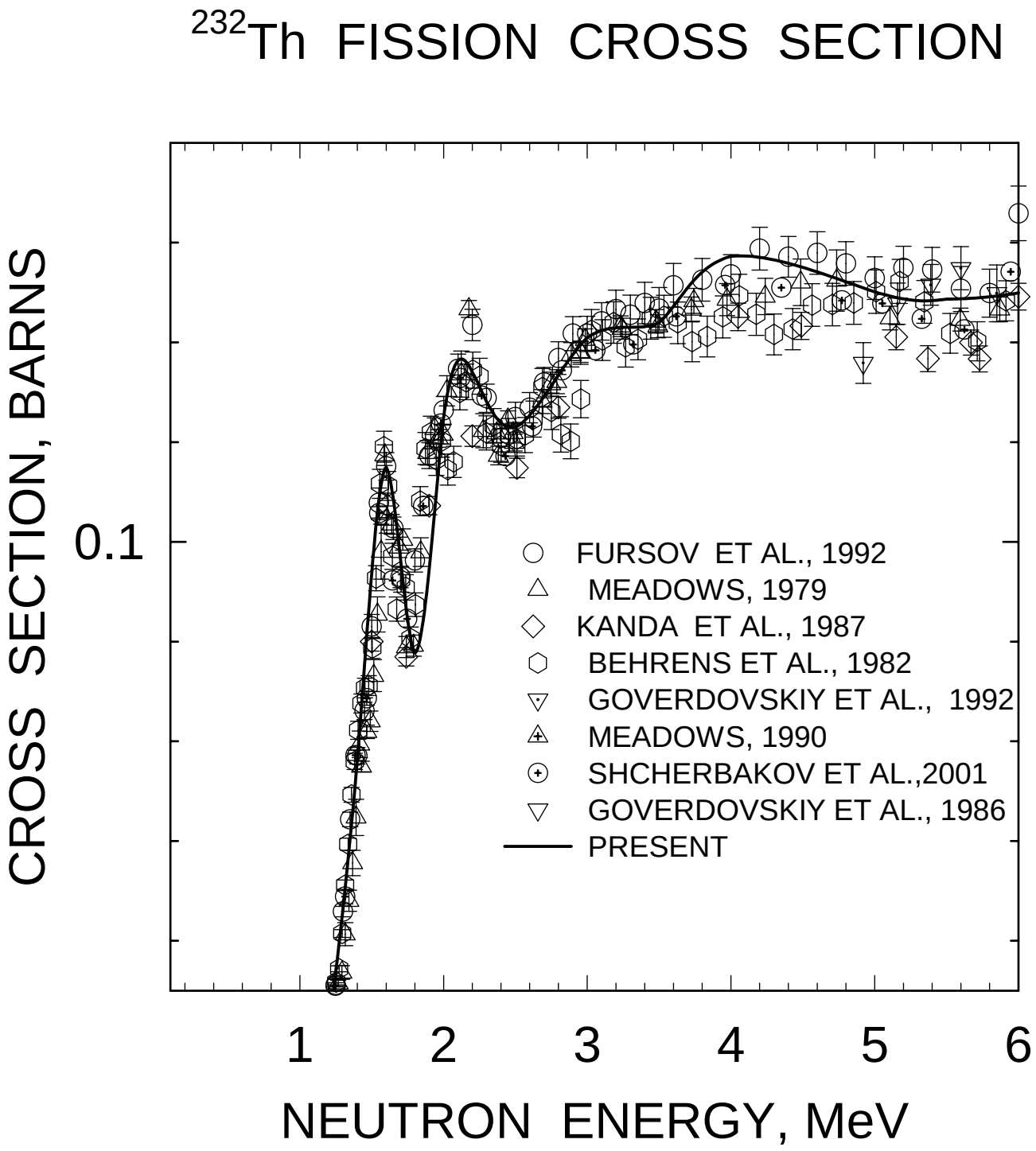
232Th FISSION CROSS SECTION
CROSS SECTION, BARNS
0.1
1
2
3
4
5
6
NEUTRON ENERGY, MeV
FURSOV ET AL., 1992
MEADOWS, 1979
KANDA ET AL., 1987
BEHRENS ET AL., 1982
GOVERDOVSKIY ET AL., 1992
MEADOWS, 1990
SHCHERBAKOV ET AL.,2001
GOVERDOVSKIY ET AL., 1986
PRESENT

FIG. 110

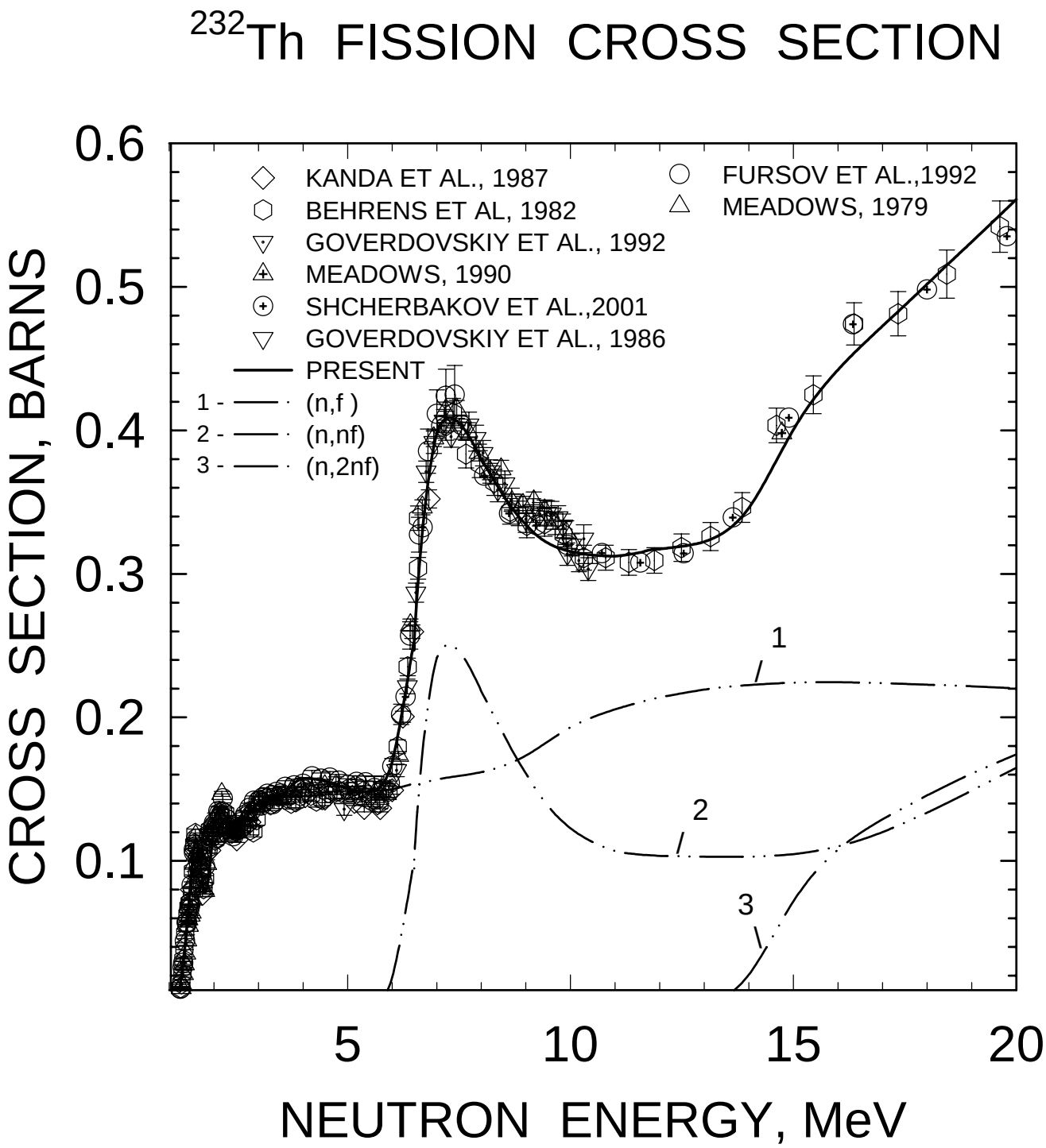
232Th FISSION CROSS SECTION
KANDA ET AL., 1987
BEHRENS ET AL, 1982
GOVERDOVSKIY ET AL., 1992
MEADOWS, 1990
SHCHERBAKOV ET AL.,2001
GOVERDOVSKIY ET AL., 1986
FURSOV ET AL.,1992
MEADOWS, 1979
PRESENT
1 - (n,f)
2 - (n,nf)
3 - (n,2nf)
CROSS SECTION, BARNS
0.6
0.5
0.4
0.3
0.2
0.1
5
10
15
20
NEUTRON ENERGY, MeV

FIG. 111

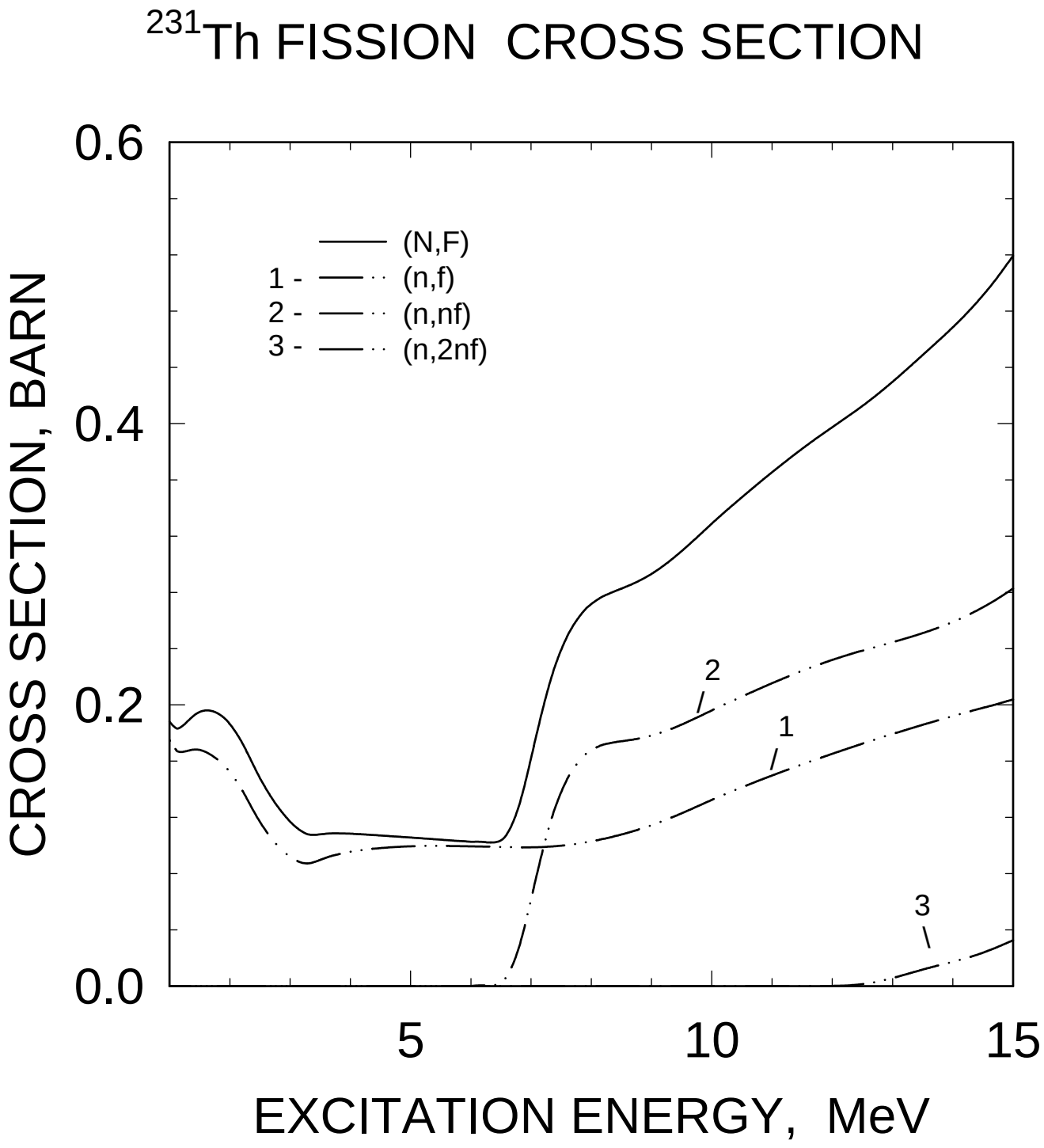
231Th FISSION CROSS SECTION
0.6
0.4
0.2
0.0
CROSS SECTION, BARN
(N,F)
1 - (n,f)
2 - (n,nf)
3 - (n,2nf)
2
1
3
5
10
15
EXCITATION ENERGY, MeV

FIG. 112

^{232}Th(n,f) CHANCE FISSION CONTRIBUTIONS

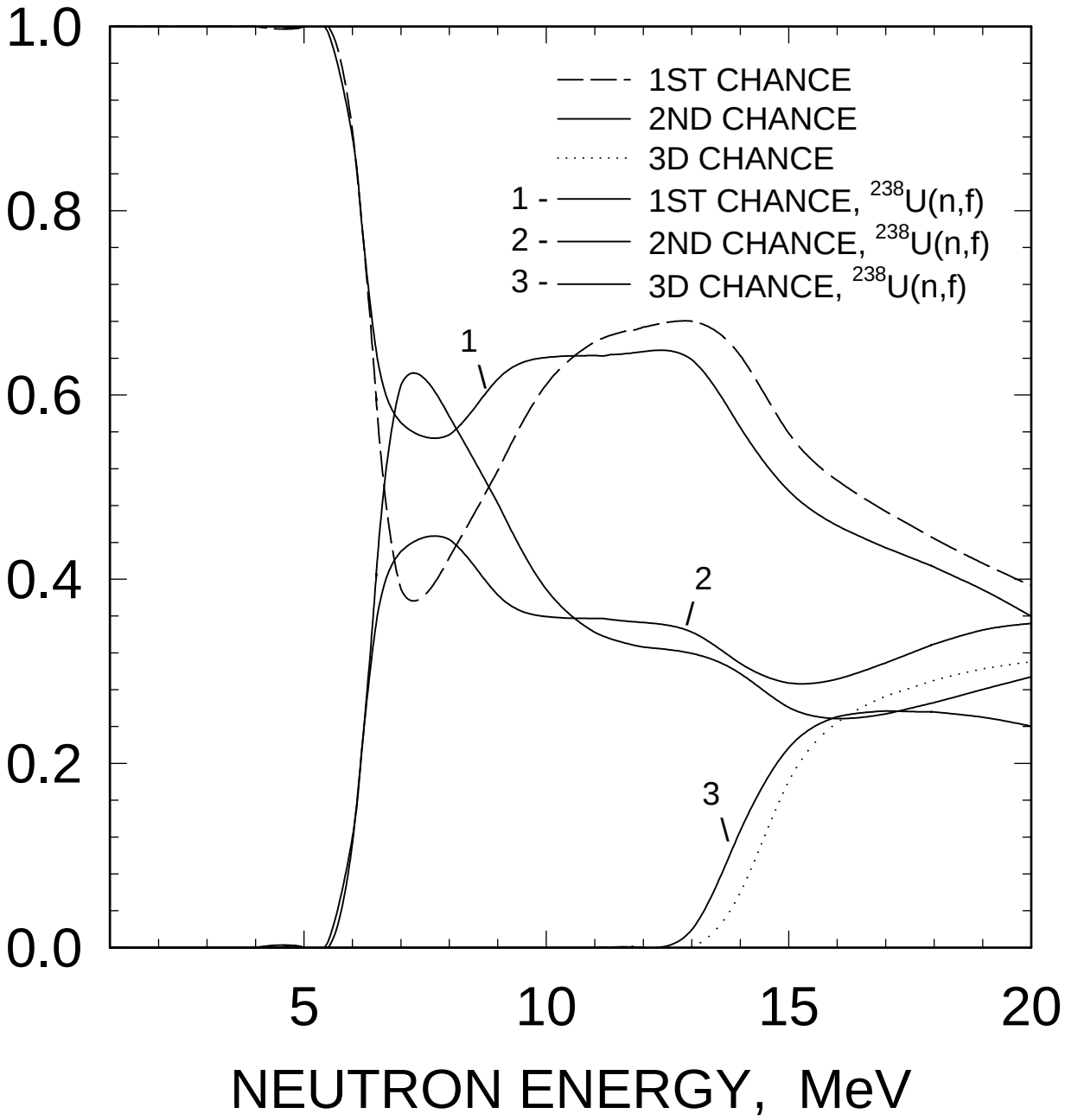

FIG. 113

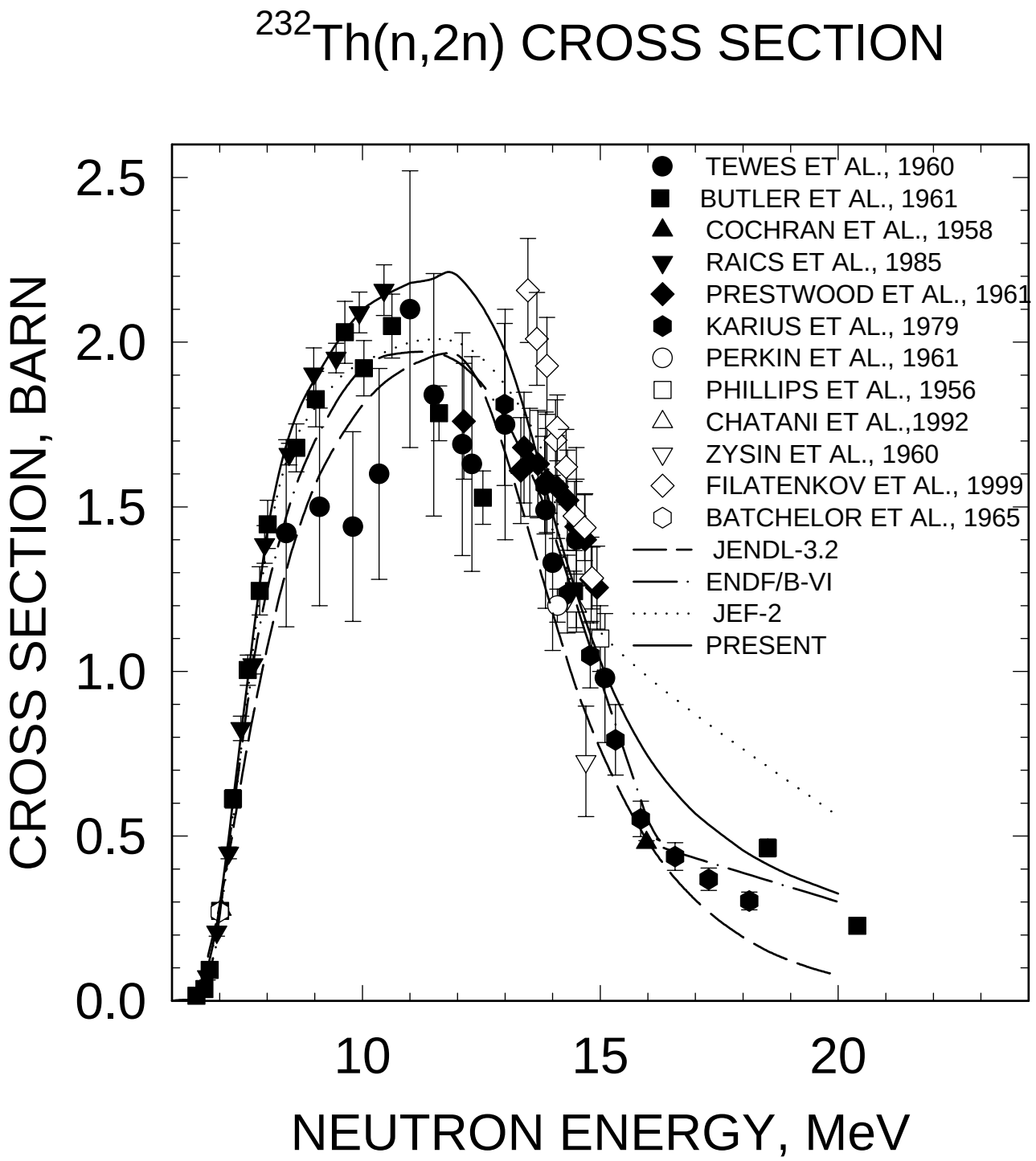
232Th(n,2n) CROSS SECTION
CROSS SECTION, BARN
NEUTRON ENERGY, MeV
0.0
0.5
1.0
1.5
2.0
2.5
10
15
20
TEWES ET AL., 1960
BUTLER ET AL., 1961
COCHRAN ET AL., 1958
RAICS ET AL., 1985
PRESTWOOD ET AL., 1961
KARIUS ET AL., 1979
PERKIN ET AL., 1961
PHILLIPS ET AL., 1956
CHATANI ET AL.,1992
ZYSIN ET AL., 1960
FILATENKOV ET AL., 1999
BATCHELOR ET AL., 1965
JENDL-3.2
ENDF/B-VI
JEF-2
PRESENT

FIG. 114

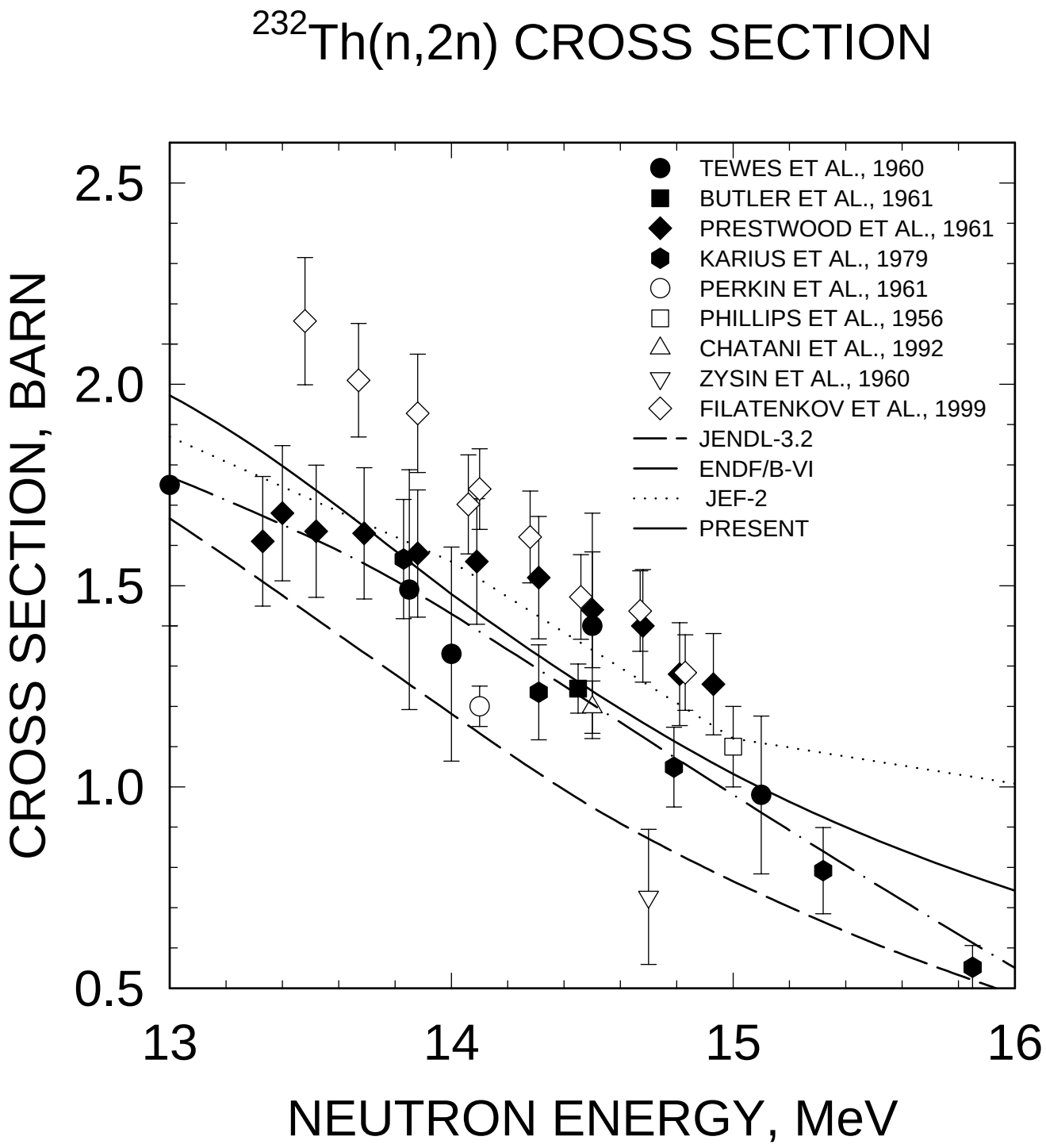
232Th(n,2n) CROSS SECTION
TEWES ET AL., 1960
BUTLER ET AL., 1961
PRESTWOOD ET AL., 1961
KARIUS ET AL., 1979
PERKIN ET AL., 1961
PHILLIPS ET AL., 1956
CHATANI ET AL., 1992
ZYSIN ET AL., 1960
FILATENKOV ET AL., 1999
JENDL-3.2
ENDF/B-VI
JEF-2
PRESENT
CROSS SECTION, BARN
2.5
2.0
1.5
1.0
0.5
13
14
15
16
NEUTRON ENERGY, MeV

FIG. 115

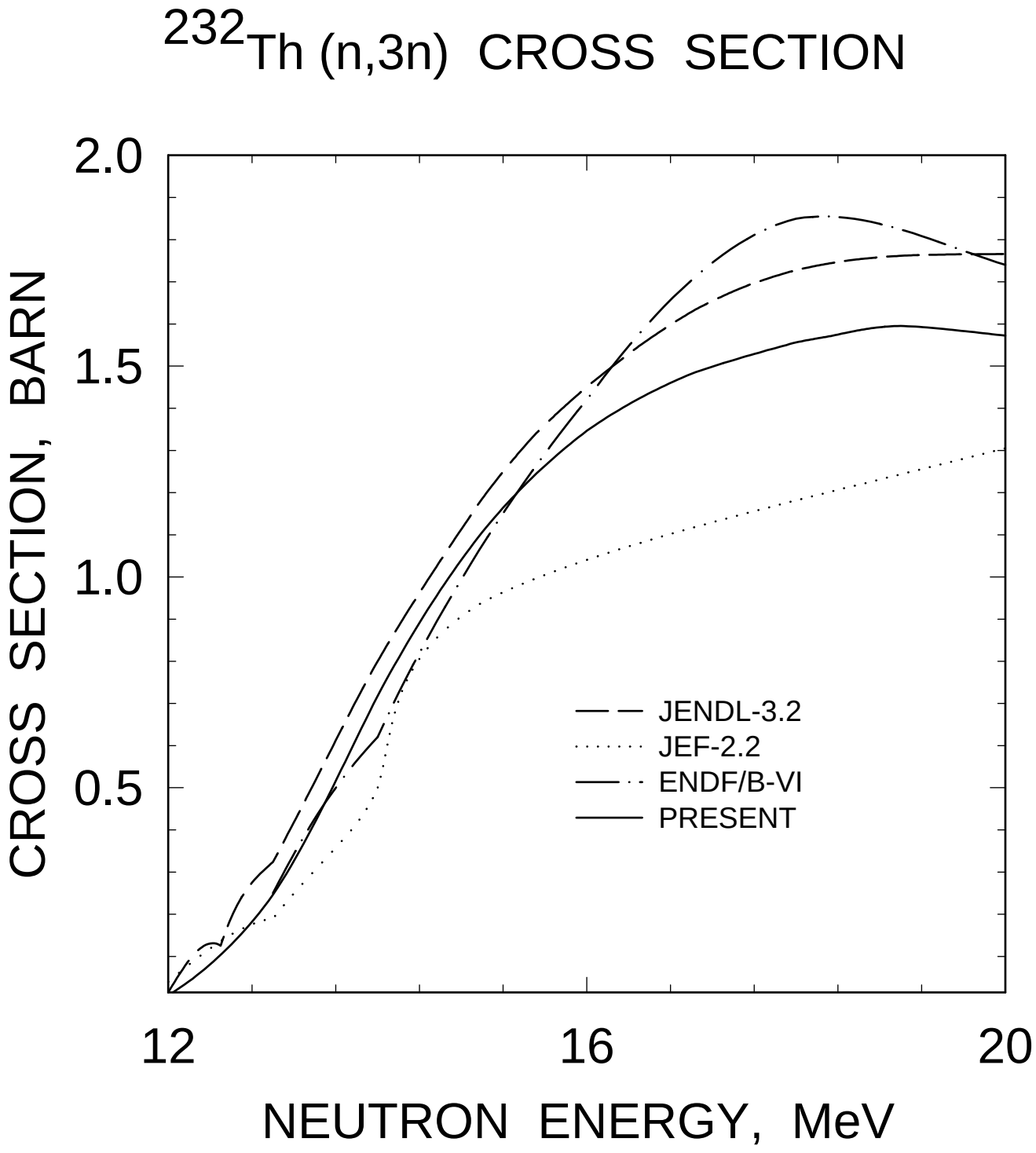
232Th (n,3n) CROSS SECTION
2.0
1.5
1.0
0.5
CROSS SECTION, BARN
12
16
20
NEUTRON ENERGY, MeV
JENDL-3.2
JEF-2.2
ENDF/B-VI
PRESENT

FIG. 116

^{232}Th PFNS, E_n=1.4 MeV.

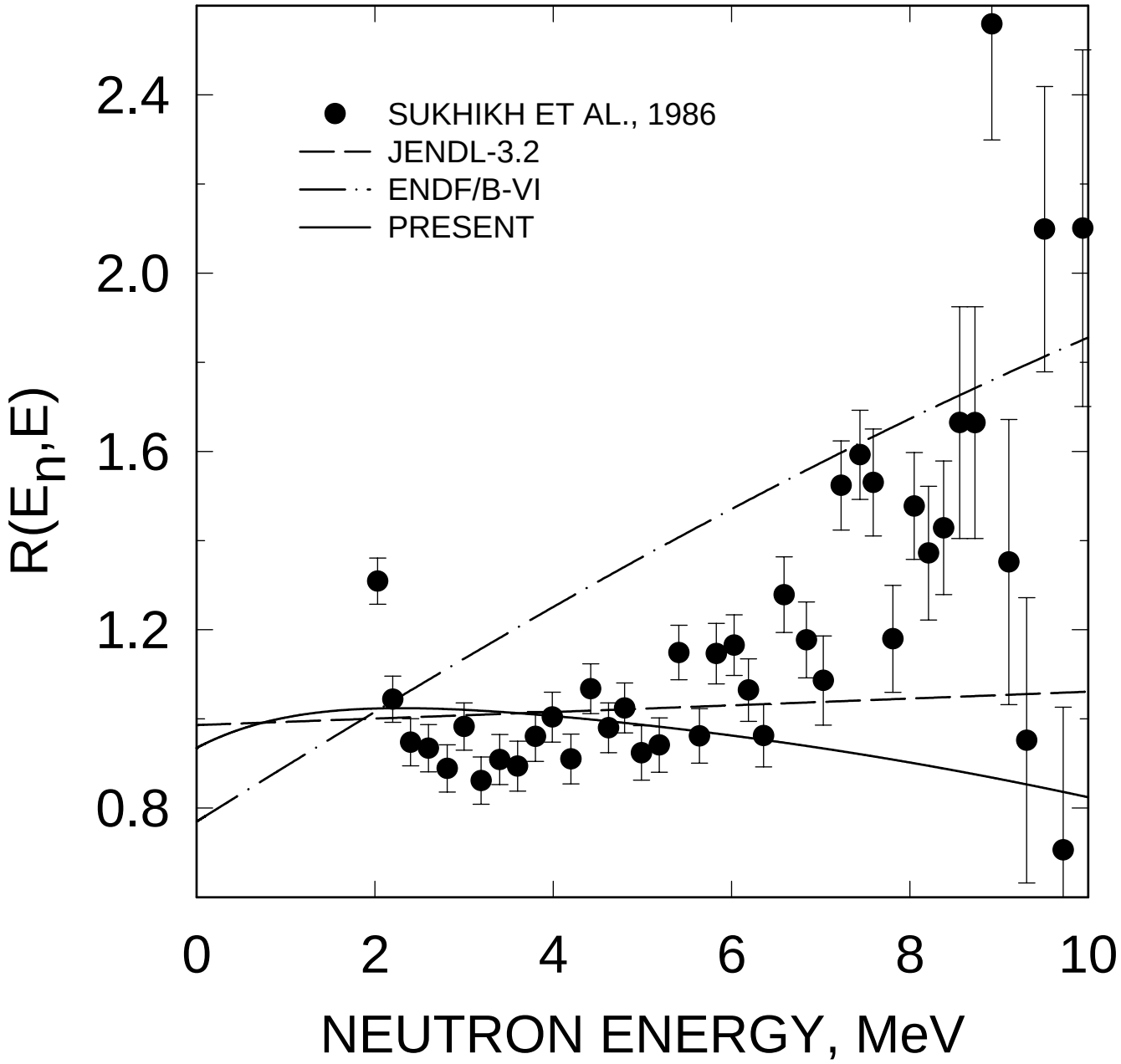

FIG. 117

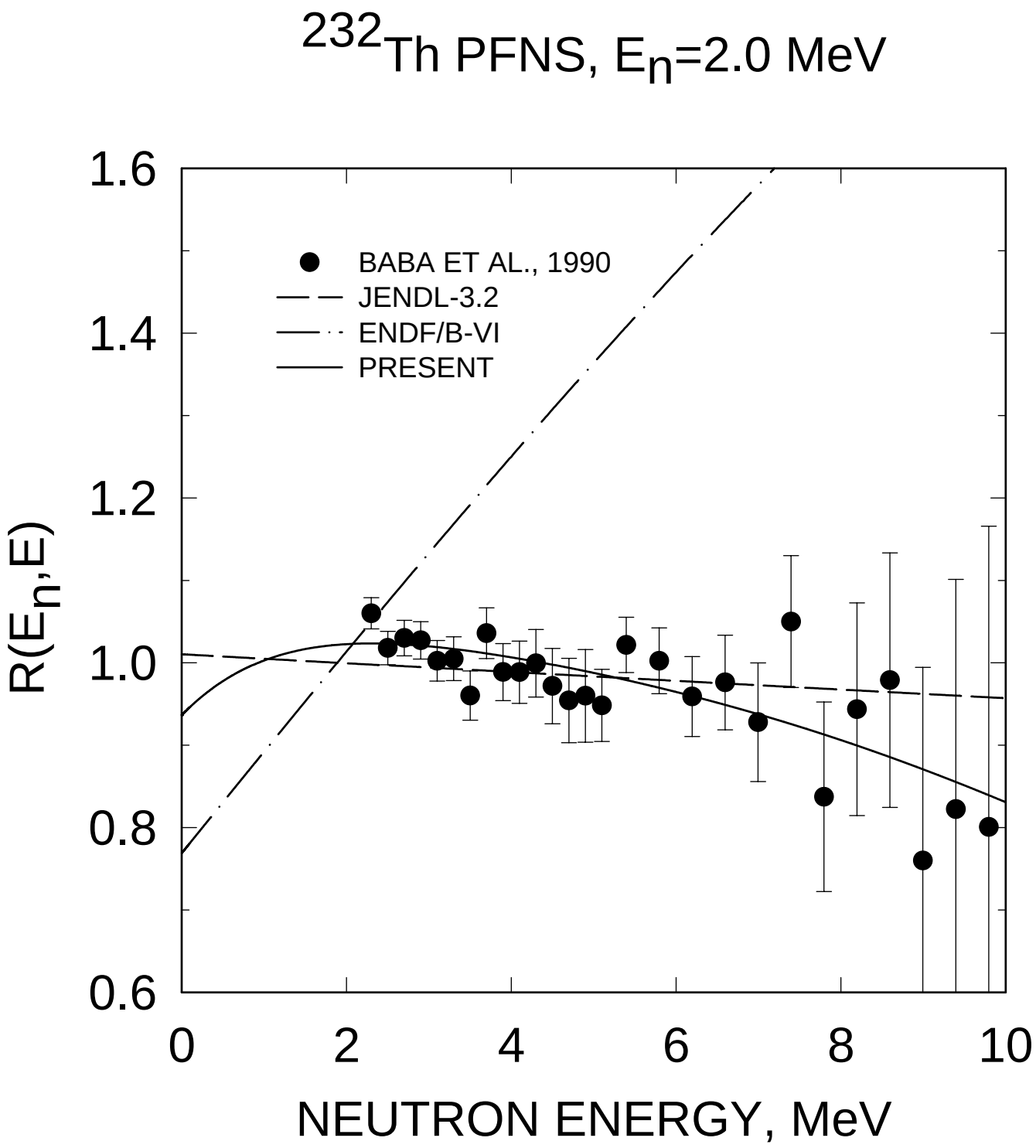
232Th PFNS, En=2.0 MeV
BABA ET AL., 1990
JENDL-3.2
ENDF/B-VI
PRESENT
R(En,E)
1.6
1.4
1.2
1.0
0.8
0.6
0
2
4
6
8
10
NEUTRON ENERGY, MeV

FIG. 118

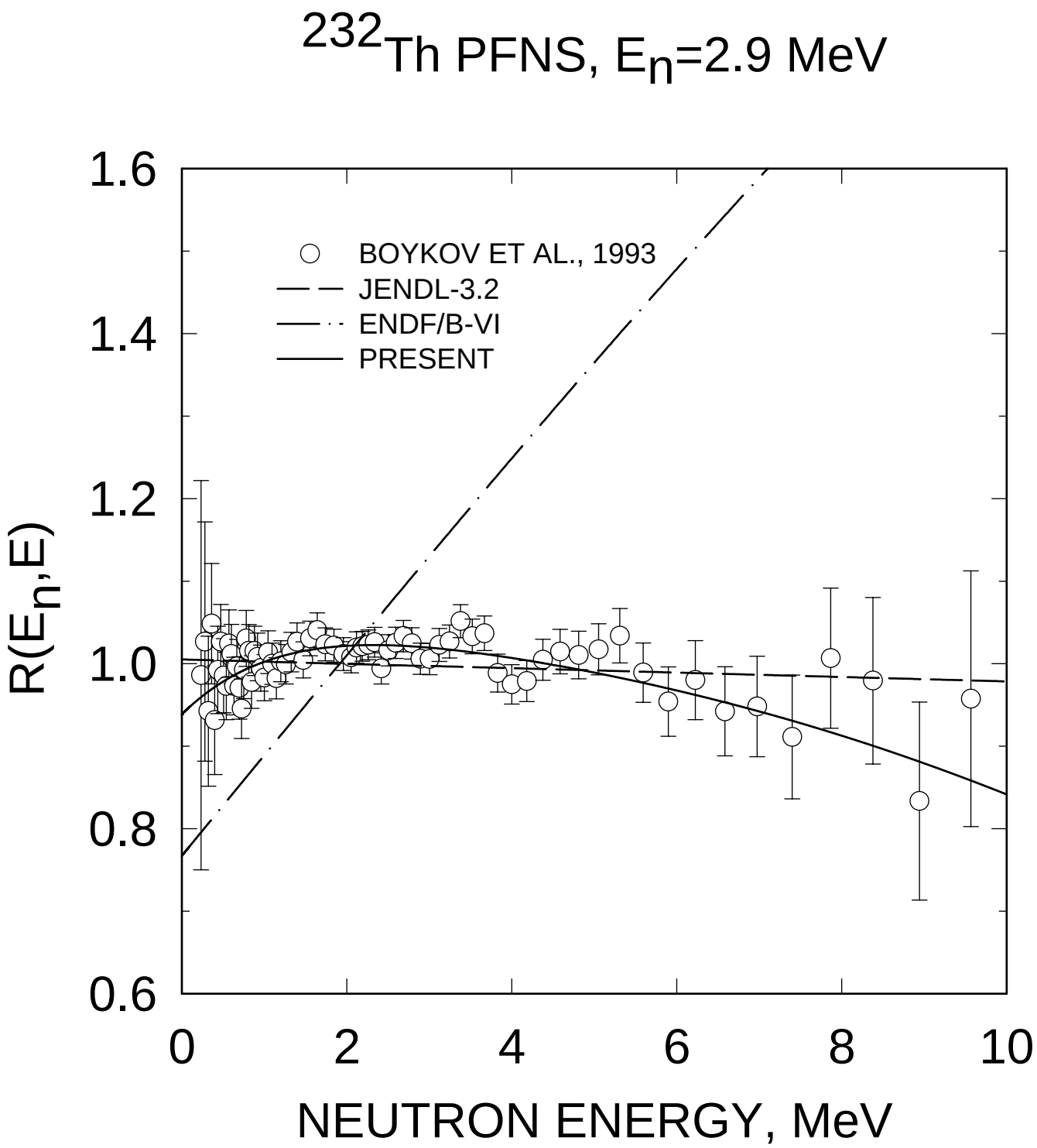
232Th PFNS, En=2.9 MeV
BOYKOV ET AL., 1993
JENDL-3.2
ENDF/B-VI
PRESENT
R(En,E)
1.6
1.4
1.2
1.0
0.8
0.6
0
2
4
6
8
10
NEUTRON ENERGY, MeV

FIG. 119

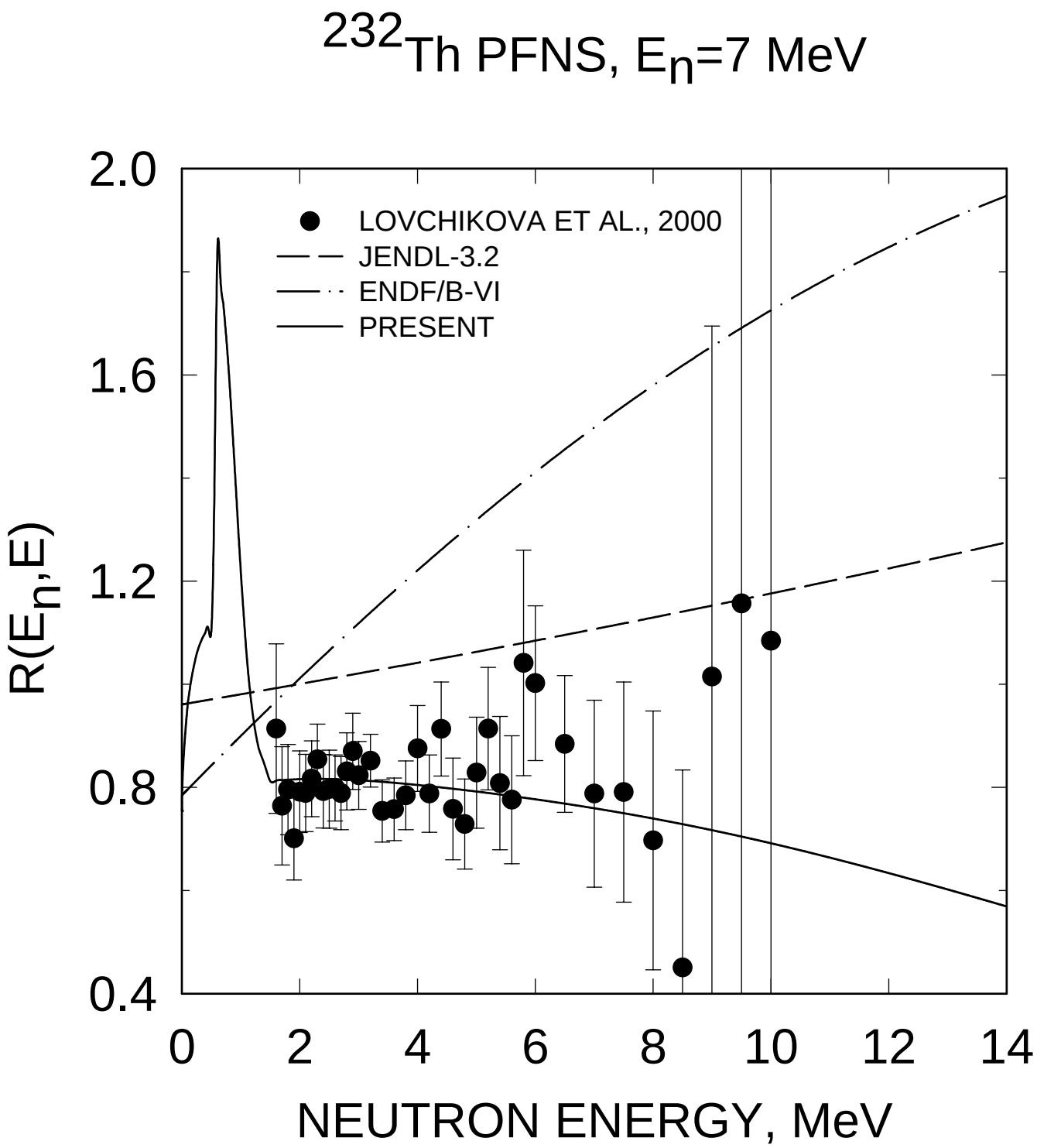
232Th PFNS, En=7 MeV
LOVCHIKOVA ET AL., 2000
JENDL-3.2
ENDF/B-VI
PRESENT
R(En,E)
2.0
1.6
1.2
0.8
0.4
0
2
4
6
8
10
12
14
NEUTRON ENERGY, MeV

FIG. 120

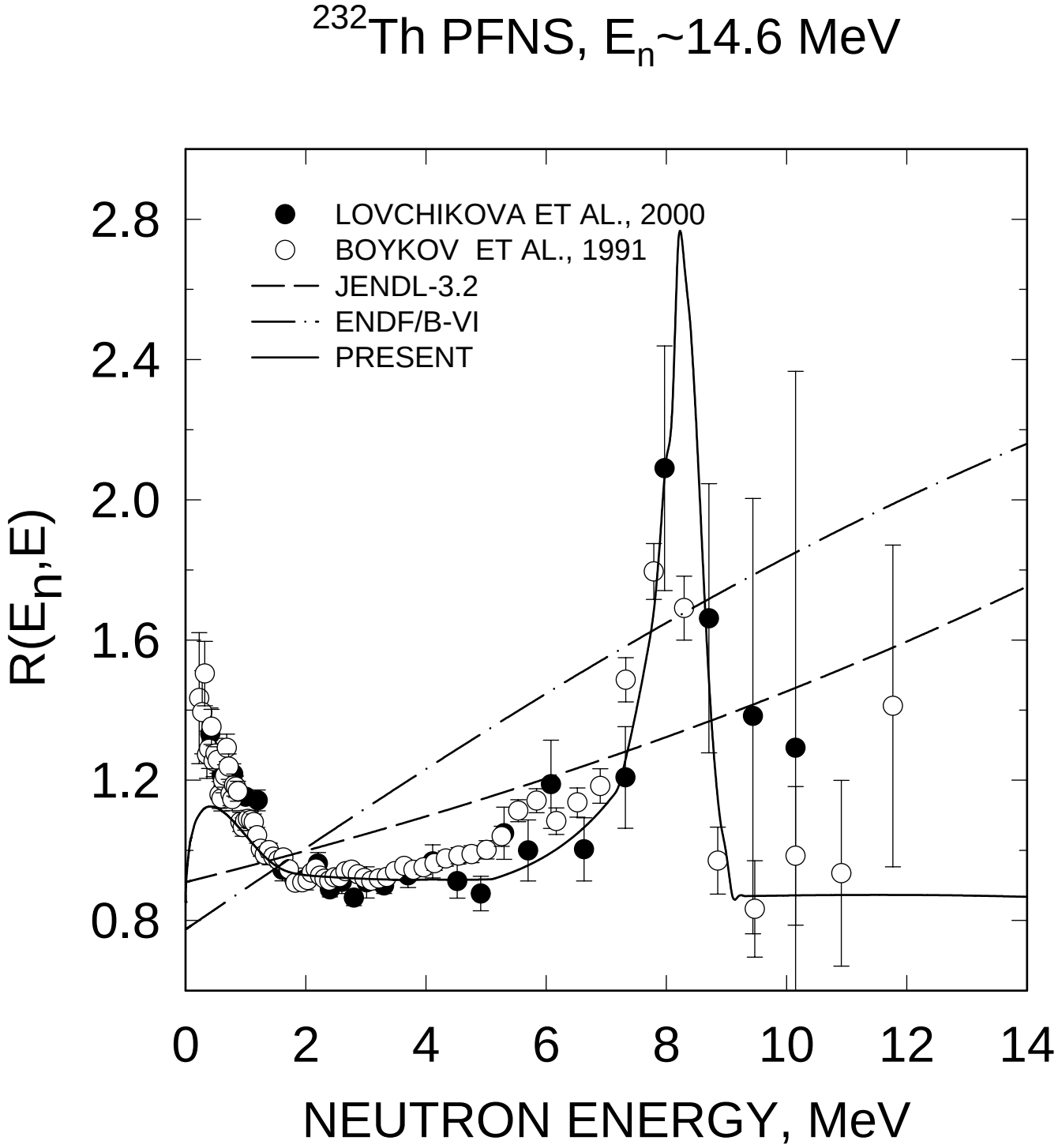
232Th PFNS, En~14.6 MeV
LOVCHIKOVA ET AL., 2000
BOYKOV ET AL., 1991
JENDL-3.2
ENDF/B-VI
PRESENT
R(En,E)
2.8
2.4
2.0
1.6
1.2
0.8
0
2
4
6
8
10
12
14
NEUTRON ENERGY, MeV

FIG. 121

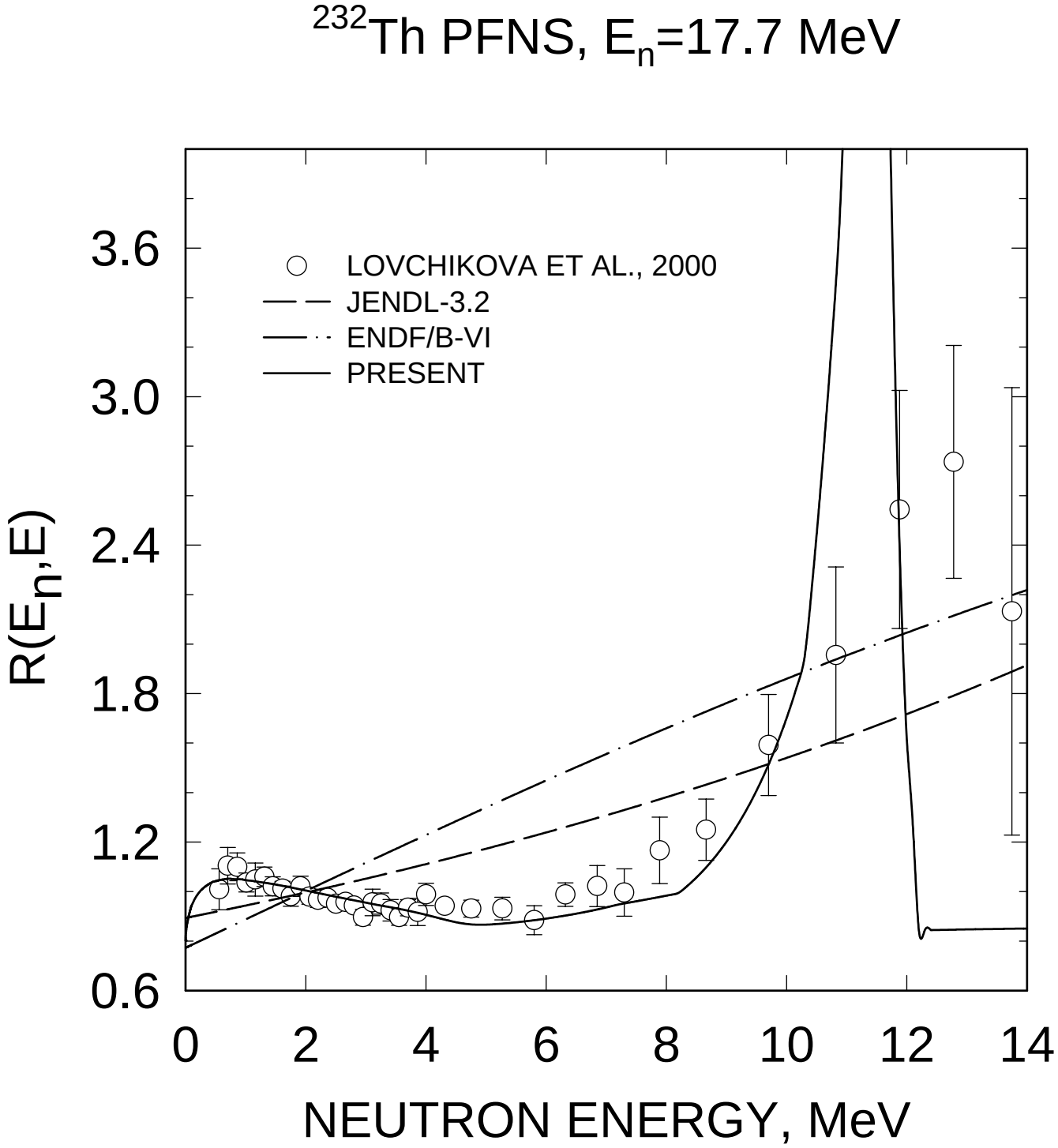
232Th PFNS, En=17.7 MeV
LOVCHIKOVA ET AL., 2000
JENDL-3.2
ENDF/B-VI
PRESENT
R(En,E)
3.6
3.0
2.4
1.8
1.2
0.6
0
2
4
6
8
10
12
14
NEUTRON ENERGY, MeV

FIG. 122

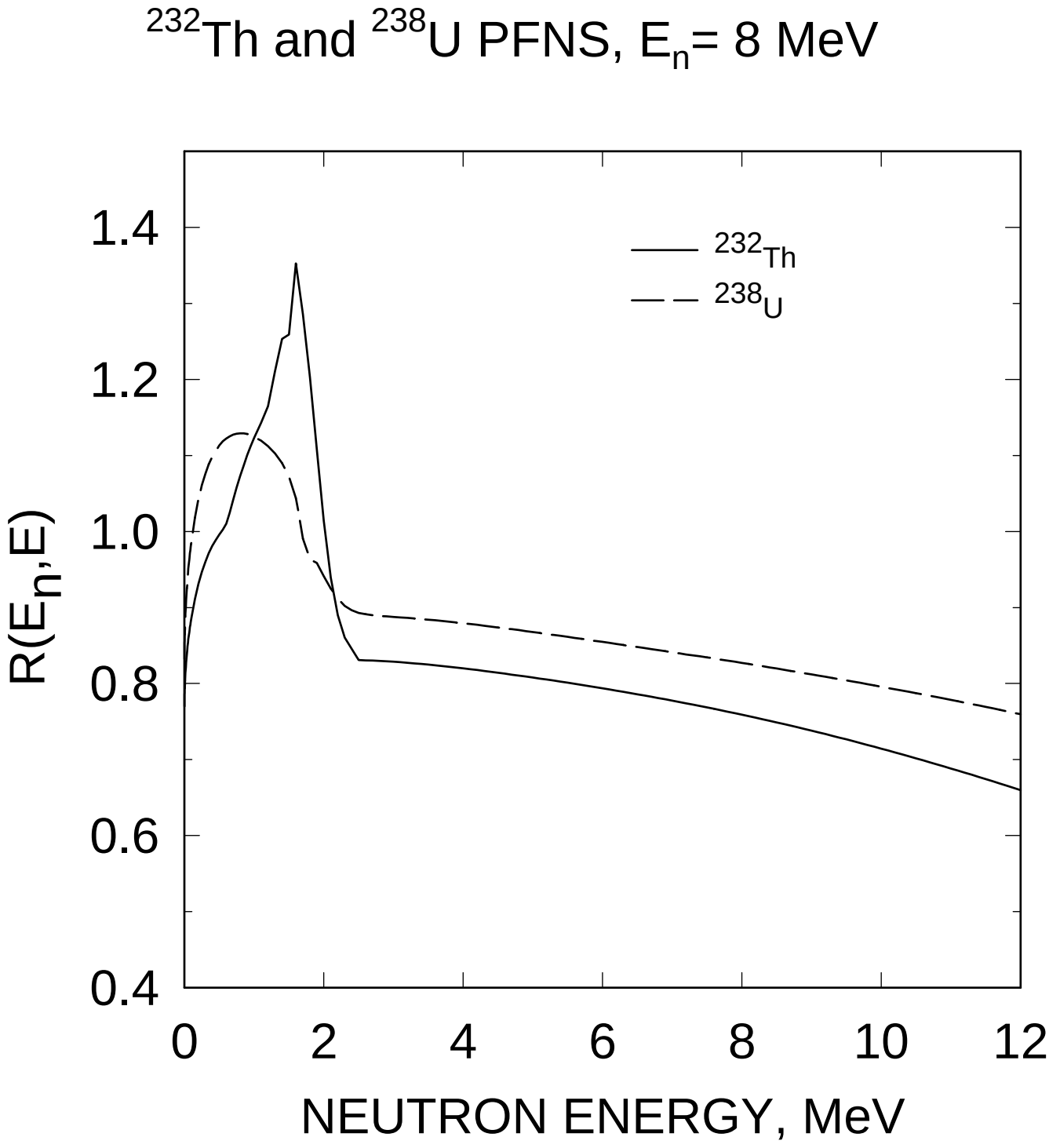
232Th and 238U PFNS, En= 8 MeV
232Th
238U
R(En,E)
1.4
1.2
1.0
0.8
0.6
0.4
0
2
4
6
8
10
12
NEUTRON ENERGY, MeV

FIG. 123

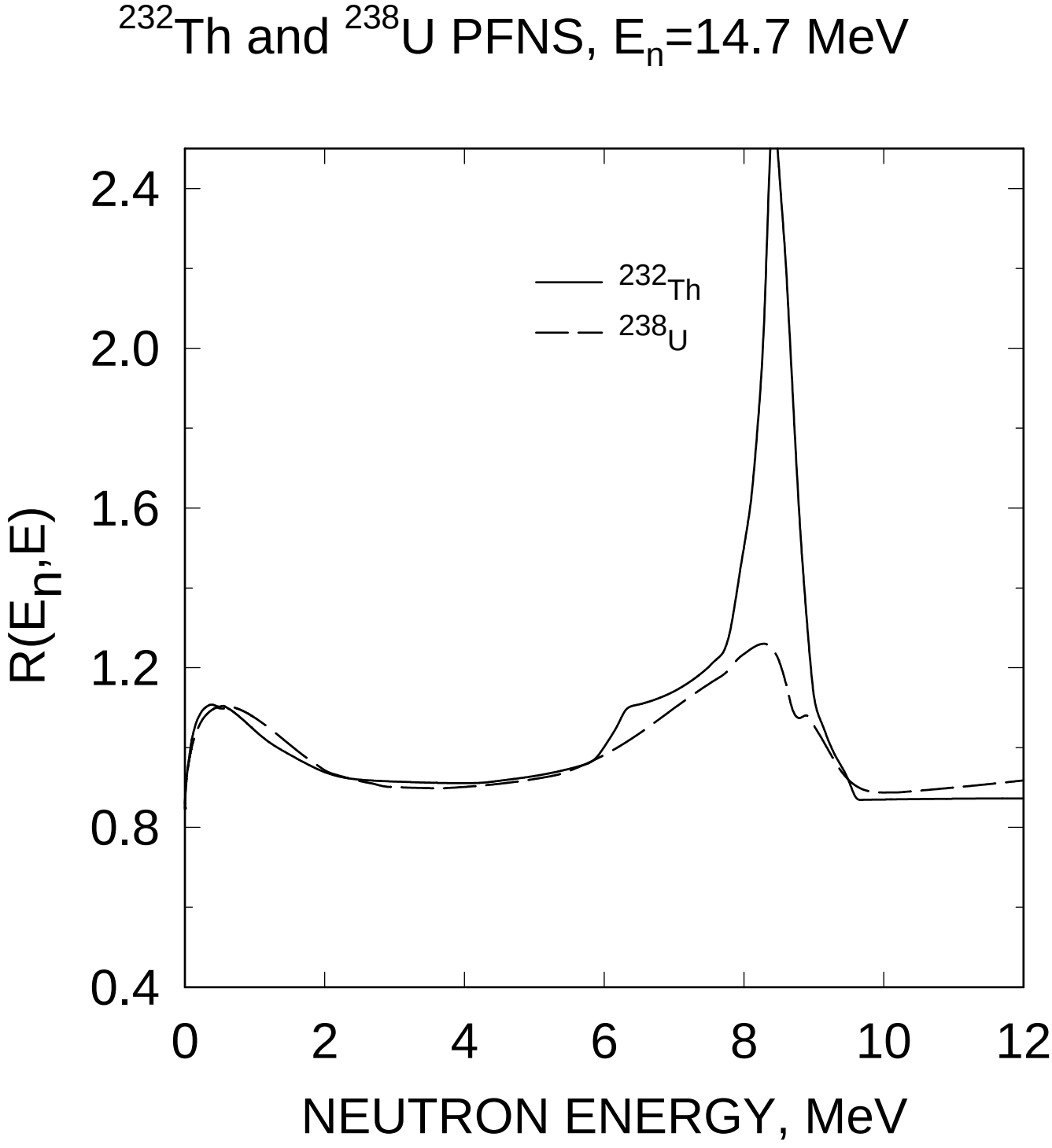
232Th and 238U PFNS, En=14.7 MeV
2.4
2.0
1.6
1.2
0.8
0.4
R(En,E)
232Th
238U
0
2
4
6
8
10
12
NEUTRON ENERGY, MeV

FIG. 124

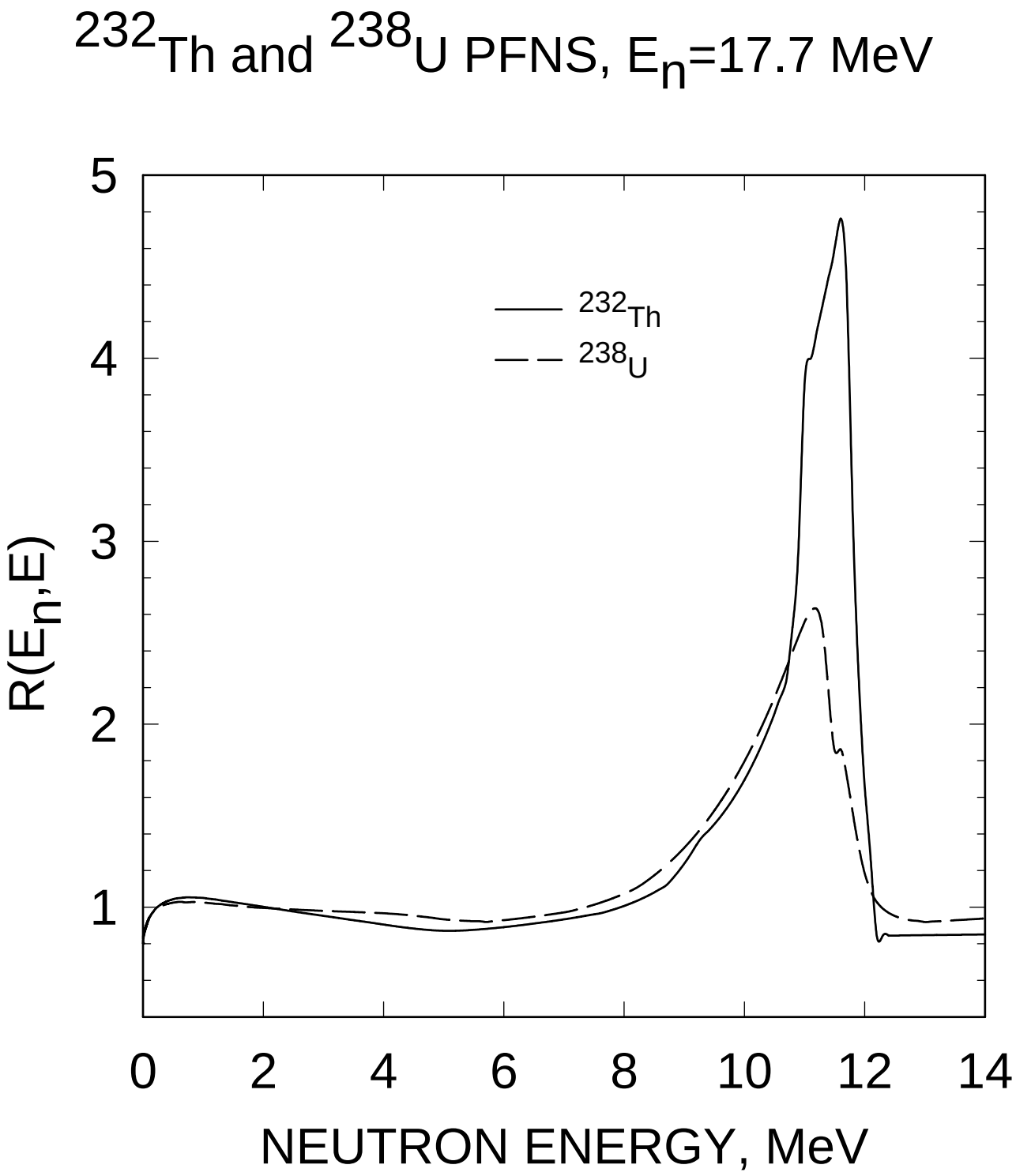
232Th and 238U PFNS, En=17.7 MeV
232Th
238U
R(En,E)
NEUTRON ENERGY, MeV
0
2
4
6
8
10
12
14
1
2
3
4
5

FIG. 125

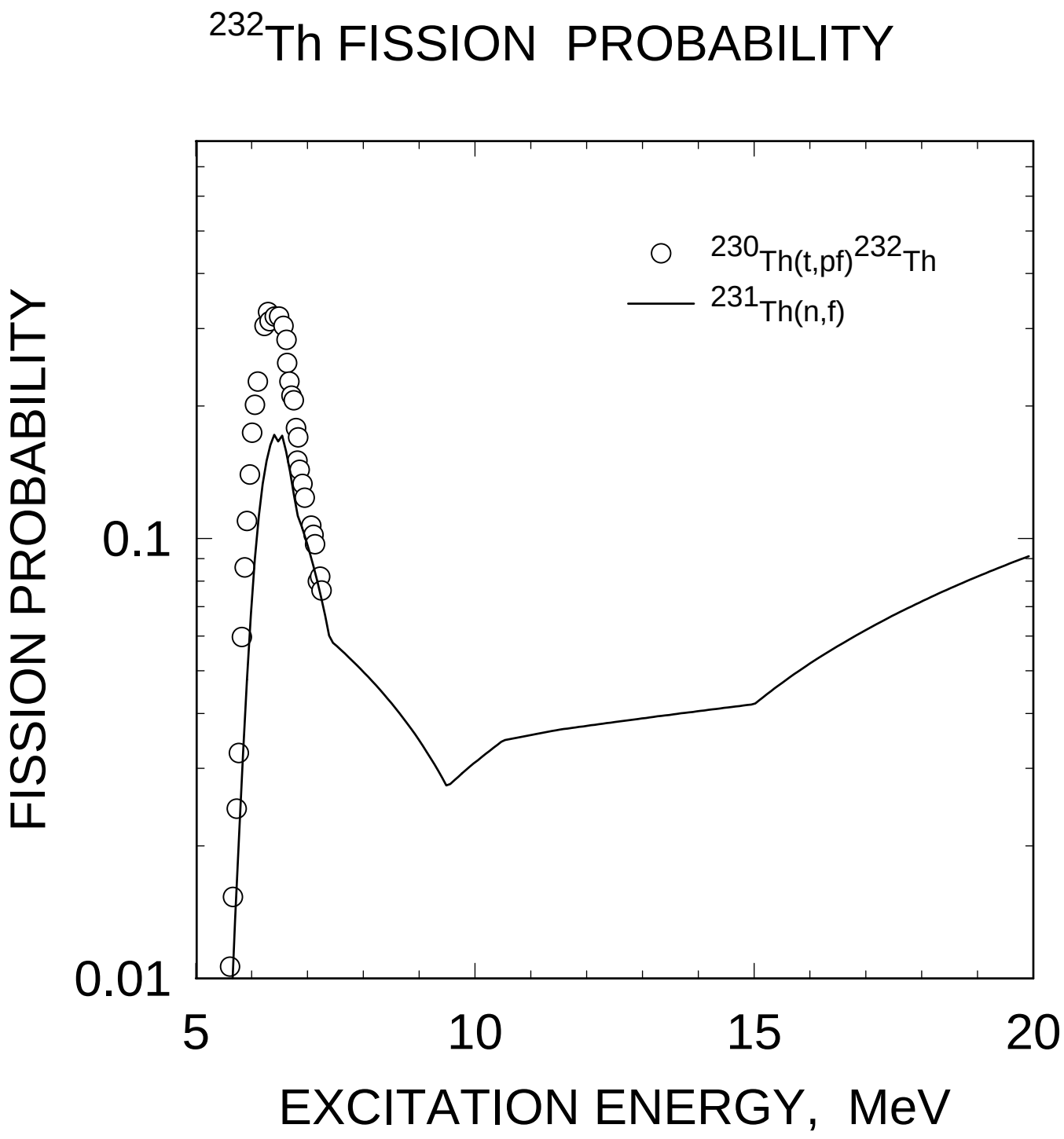
232Th FISSION PROBABILITY
230Th(t,pf)232Th
231Th(n,f)
FISSION PROBABILITY
0.1
0.01
5
10
15
20
EXCITATION ENERGY, MeV

FIG. 126

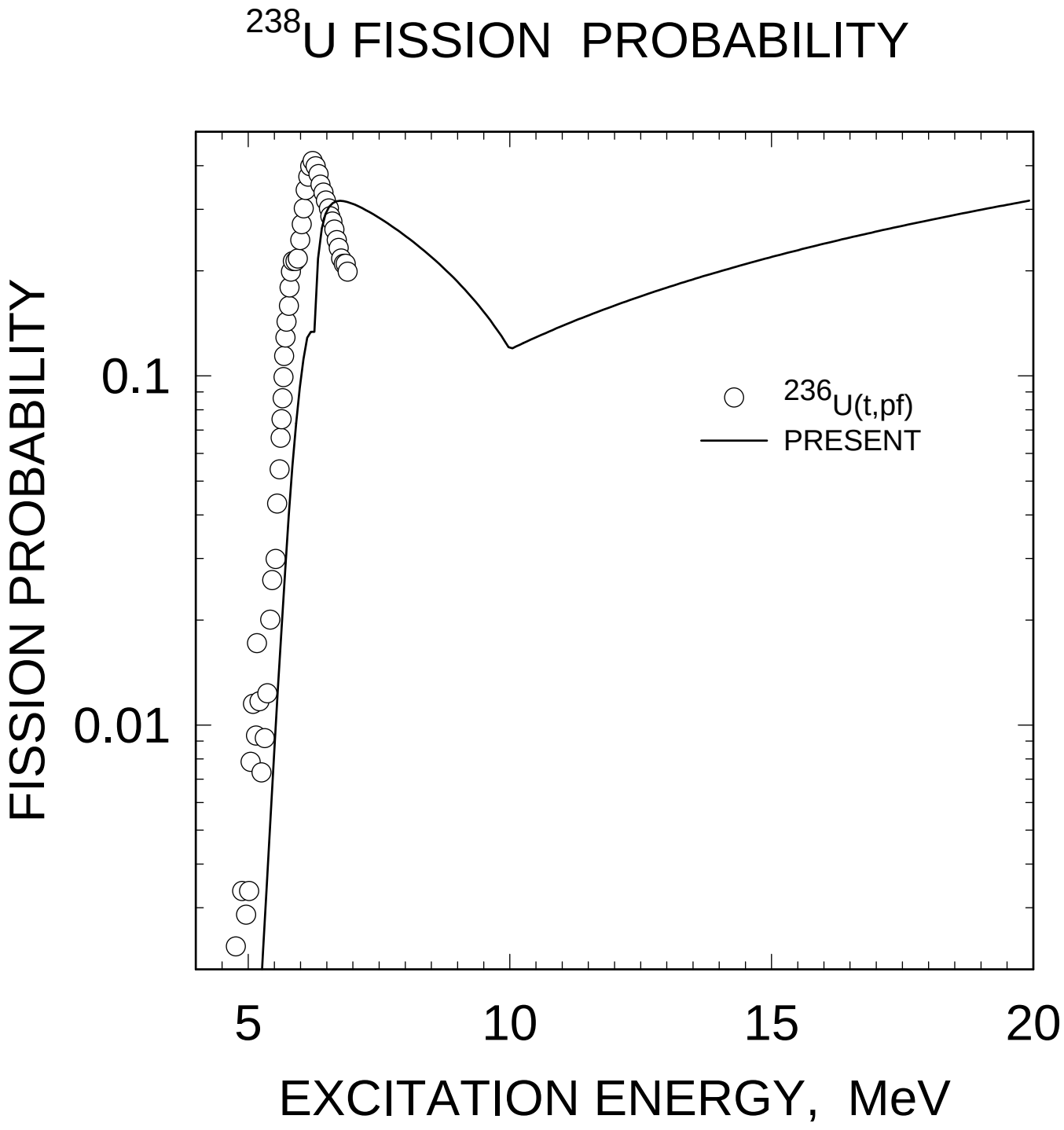
238U FISSION PROBABILITY
FISSION PROBABILITY
0.1
0.01
236U(t,pf)
PRESENT
5
10
15
20
EXCITATION ENERGY, MeV

FIG. 127

^{232}Th, NEUTRON MULTIPLICIY

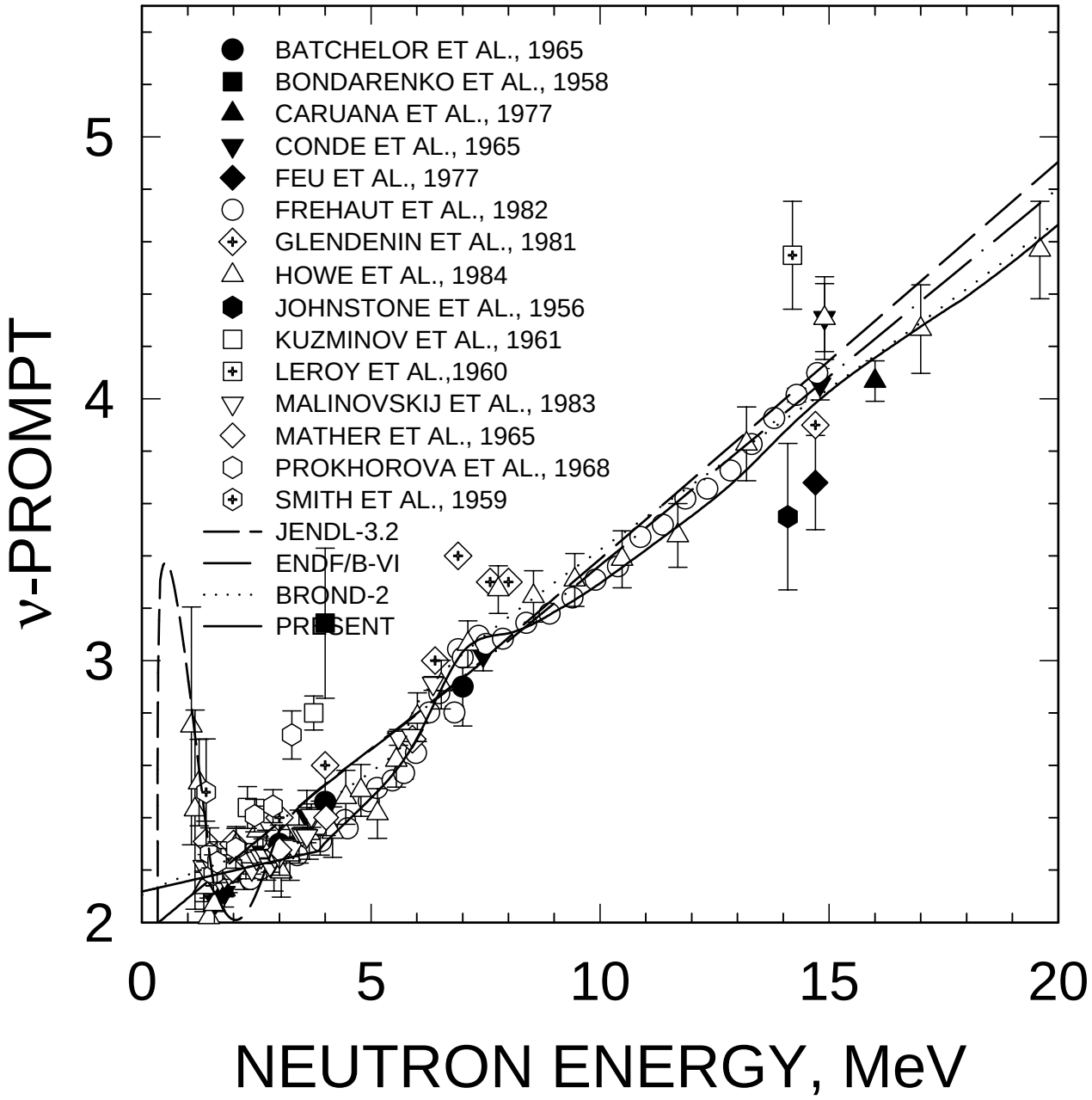

FIG. 128

^{232}Th(n,f) NEUTRON MULTIPLICITY

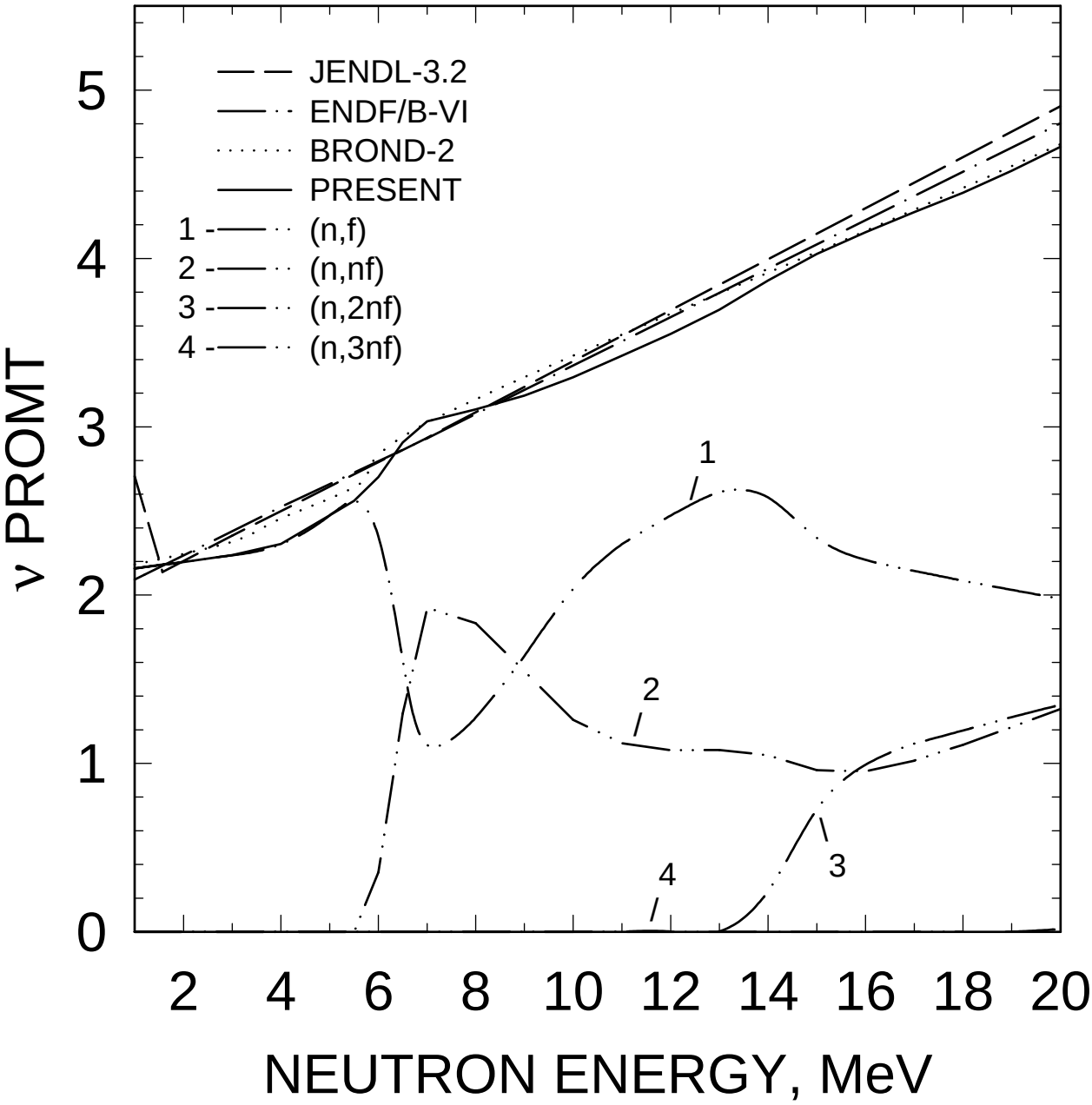

FIG. 129

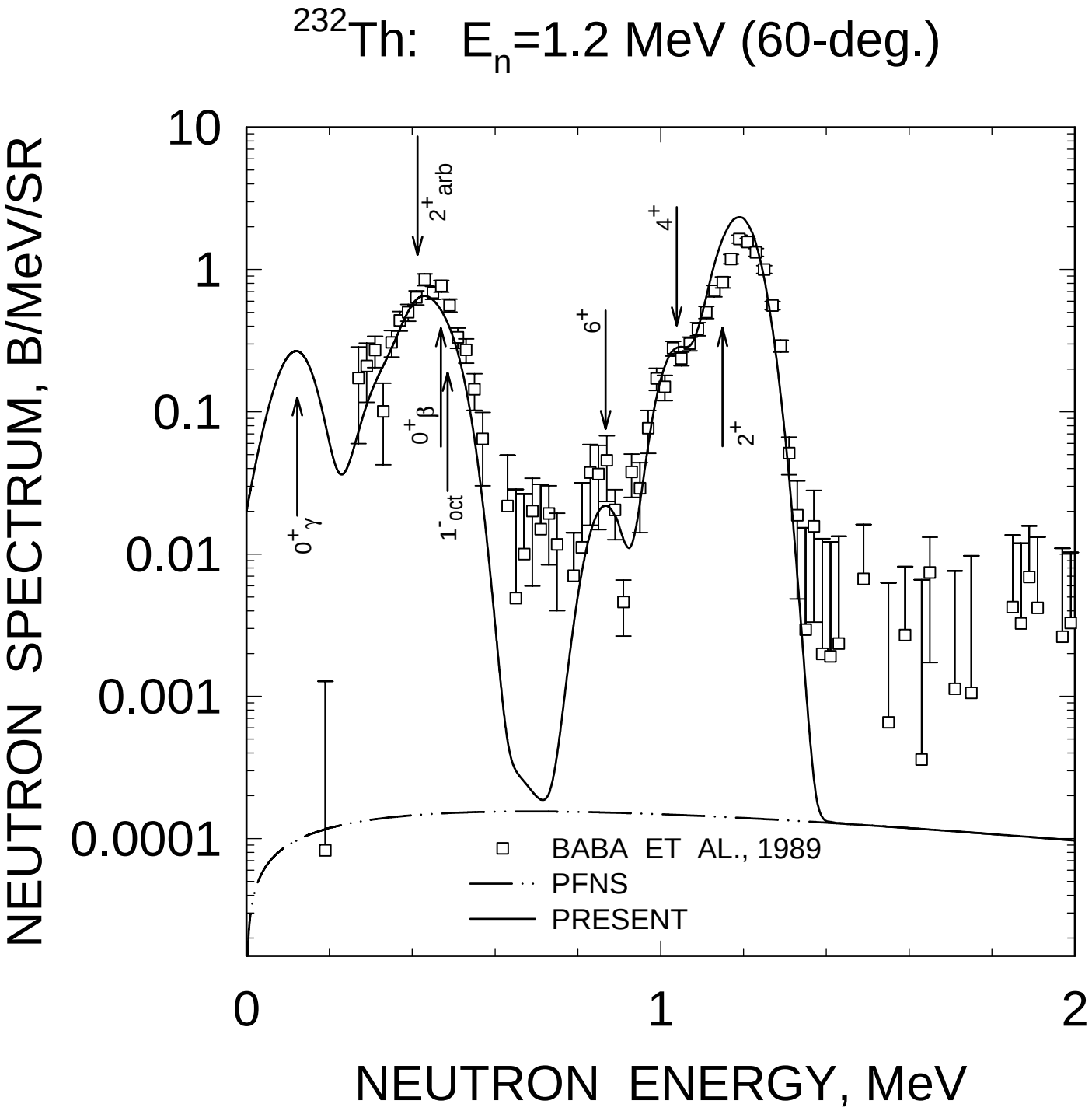
232Th: En=1.2 MeV (60-deg.)
NEUTRON SPECTRUM, B/MeV/SR
10
1
0.1
0.01
0.001
0.0001
0
1
2
NEUTRON ENERGY, MeV
0+γ
0+β
1-oct
2+arb
6+
4+
2+
BABA ET AL., 1989
PFNS
PRESENT

FIG. 130

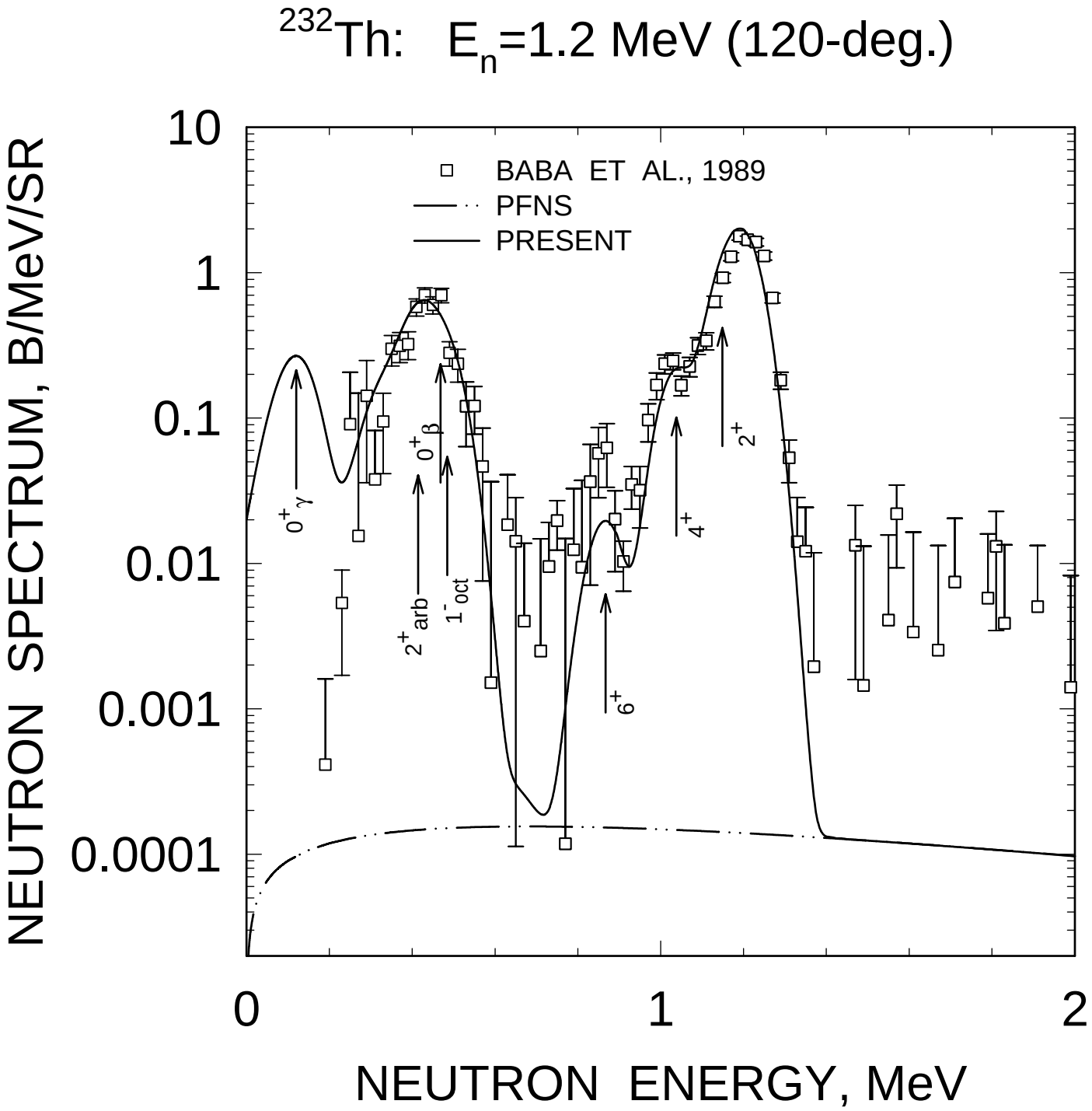
232Th: En=1.2 MeV (120-deg.)
BABA ET AL., 1989
PFNS
PRESENT
NEUTRON SPECTRUM, B/MeV/SR
NEUTRON ENERGY, MeV
10
1
0.1
0.01
0.001
0.0001
0
1
2
0+γ
0+β
2+arb
1-oct
6+
4+
2+

FIG. 131

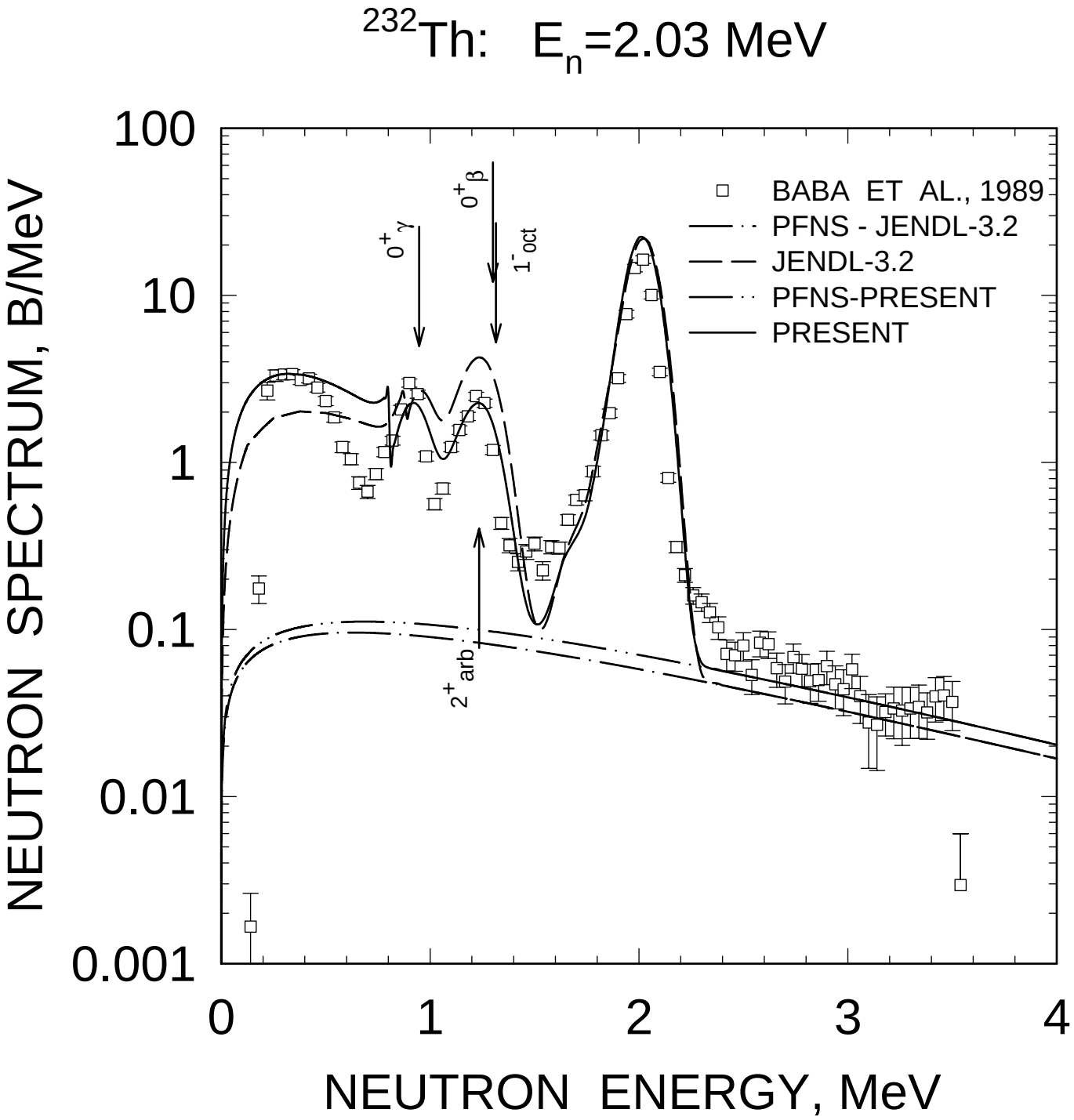
232Th: En=2.03 MeV
NEUTRON SPECTRUM, B/MeV
NEUTRON ENERGY, MeV
100
10
1
0.1
0.01
0.001
0
1
2
3
4
BABA ET AL., 1989
PFNS - JENDL-3.2
JENDL-3.2
PFNS-PRESENT
PRESENT
0+γ
0+β
1-oct
2+arb

FIG. 132

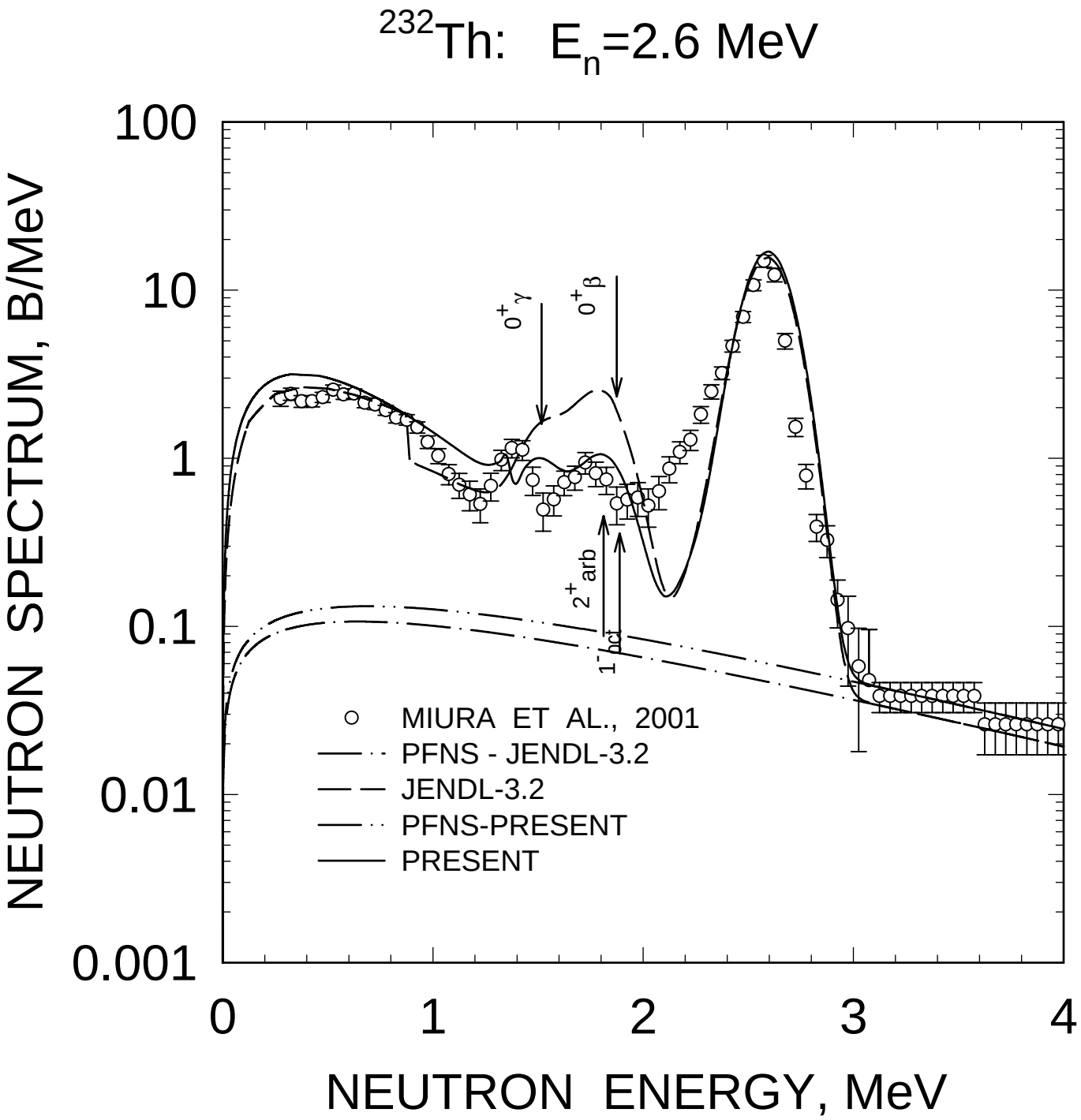
232Th: En=2.6 MeV
NEUTRON SPECTRUM, B/MeV
NEUTRON ENERGY, MeV
100
10
1
0.1
0.01
0.001
0
1
2
3
4
0+γ
0+β
2+arb
1-bd
MIURA ET AL., 2001
PFNS - JENDL-3.2
JENDL-3.2
PFNS-PRESENT
PRESENT

FIG. 133

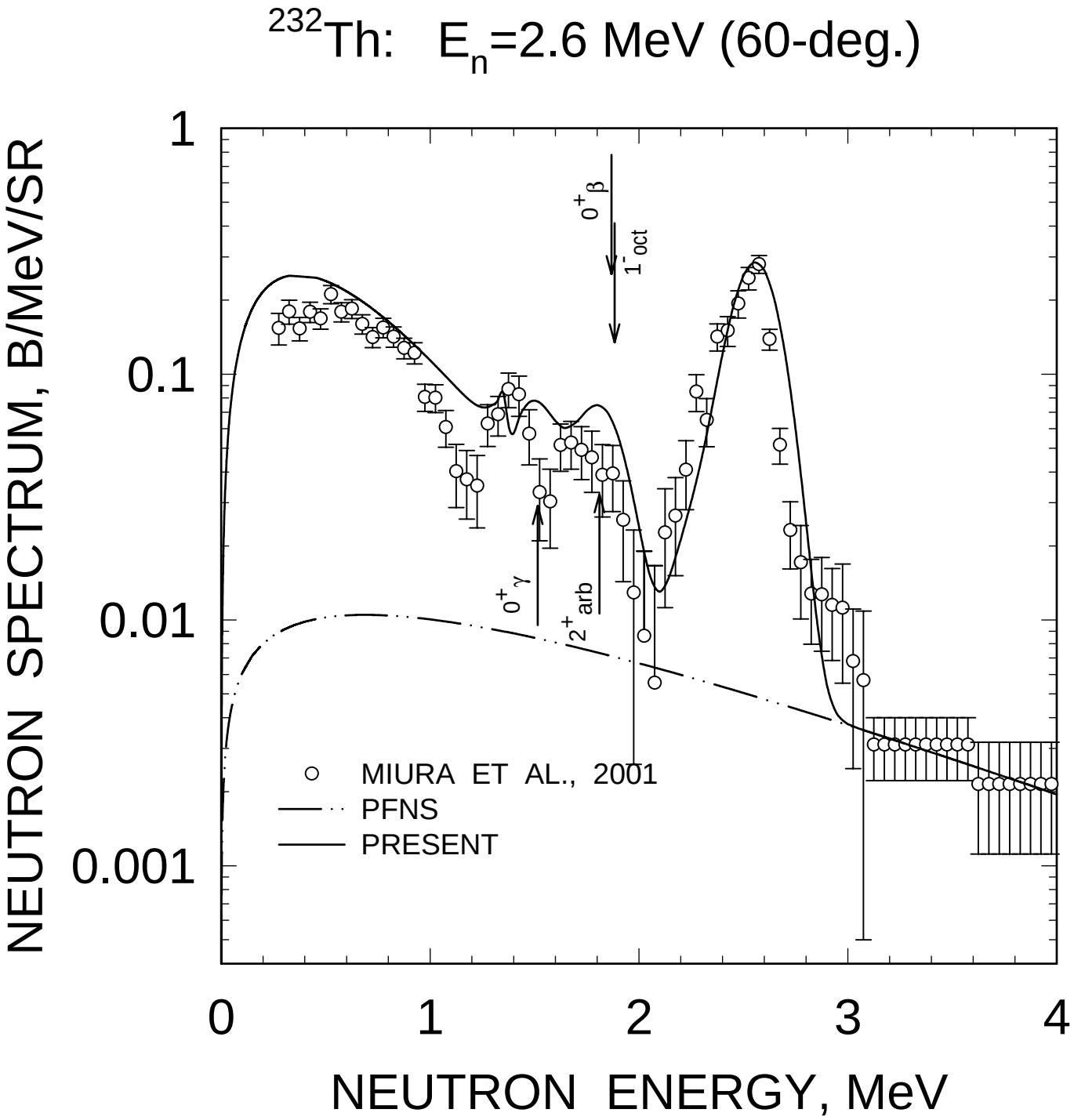
232Th: En=2.6 MeV (60-deg.)
NEUTRON SPECTRUM, B/MeV/SR
1
0.1
0.01
0.001
0
1
2
3
4
NEUTRON ENERGY, MeV
0+β
1- oct
0+γ
2+arb
MIURA ET AL., 2001
PFNS
PRESENT

FIG. 134

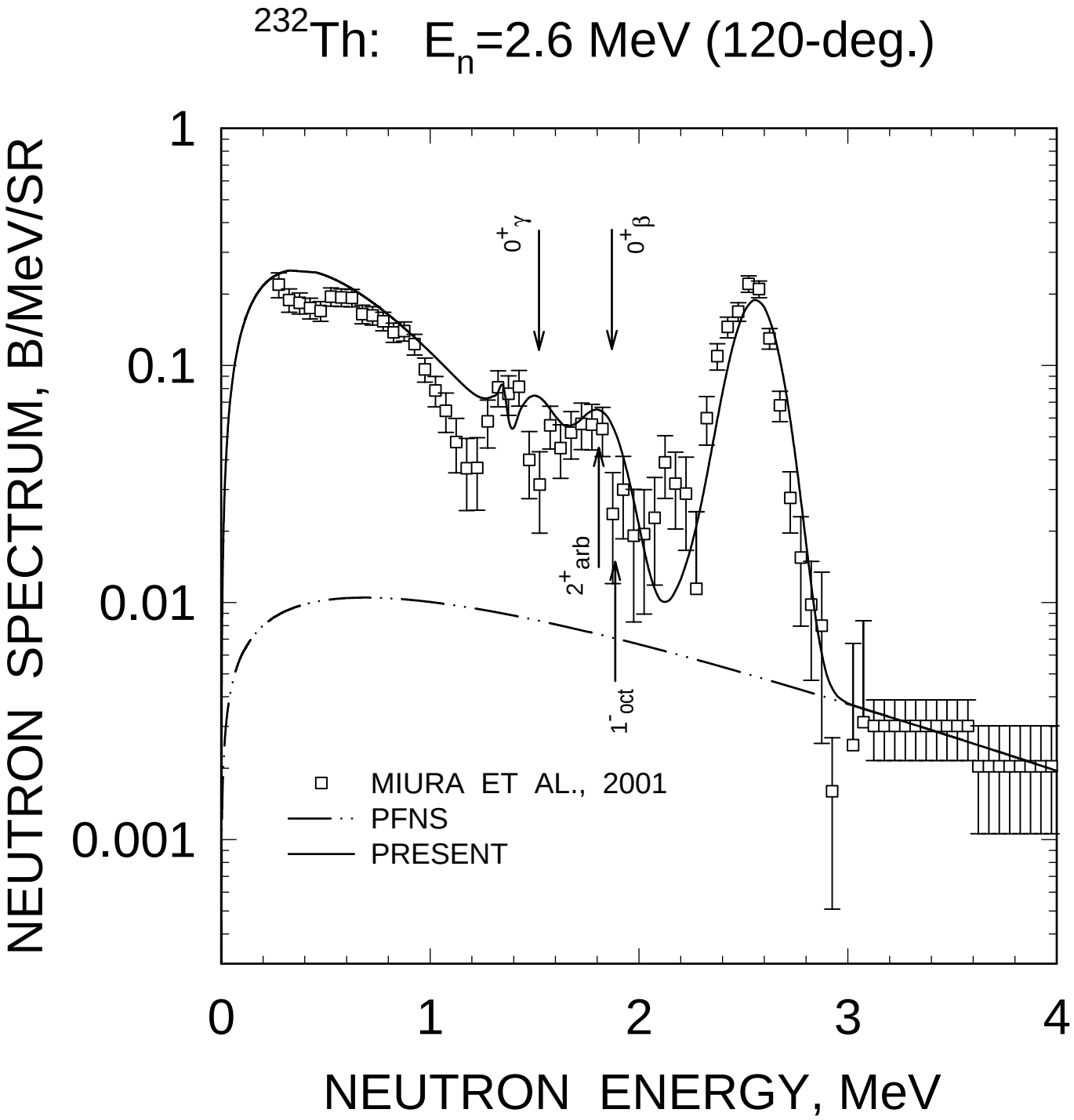
232Th: En=2.6 MeV (120-deg.)
NEUTRON SPECTRUM, B/MeV/SR
1
0.1
0.01
0.001
0
1
2
3
4
NEUTRON ENERGY, MeV
0+γ
0+β
2+arb
1-oct
MIURA ET AL., 2001
PFNS
PRESENT

FIG. 135

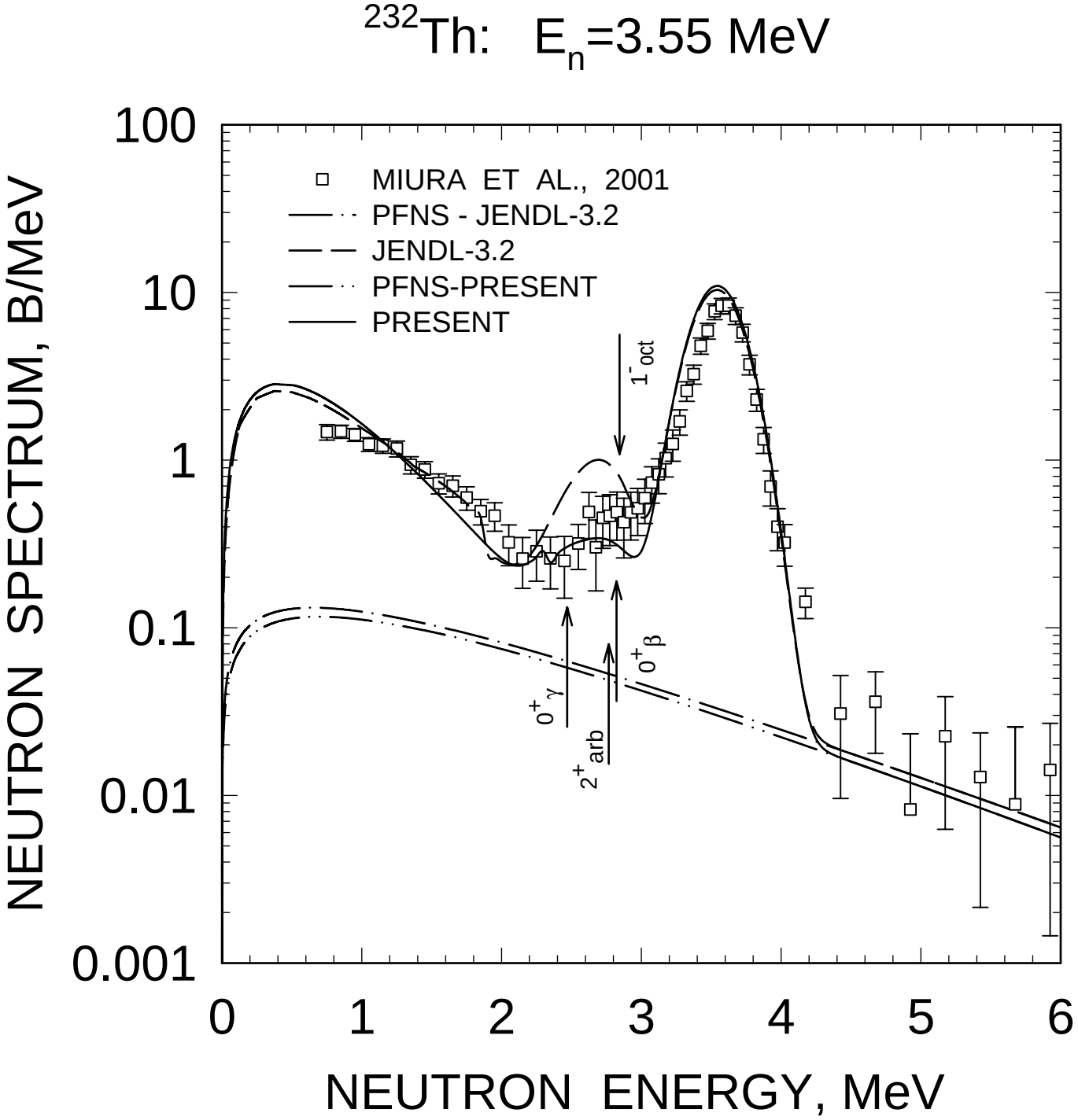
232Th: En=3.55 MeV
MIURA ET AL., 2001
PFNS - JENDL-3.2
JENDL-3.2
PFNS-PRESENT
PRESENT
1- oct
0+ γ
2+ arb
0+ β
NEUTRON SPECTRUM, B/MeV
NEUTRON ENERGY, MeV
100
10
1
0.1
0.01
0.001
0
1
2
3
4
5
6

FIG. 136

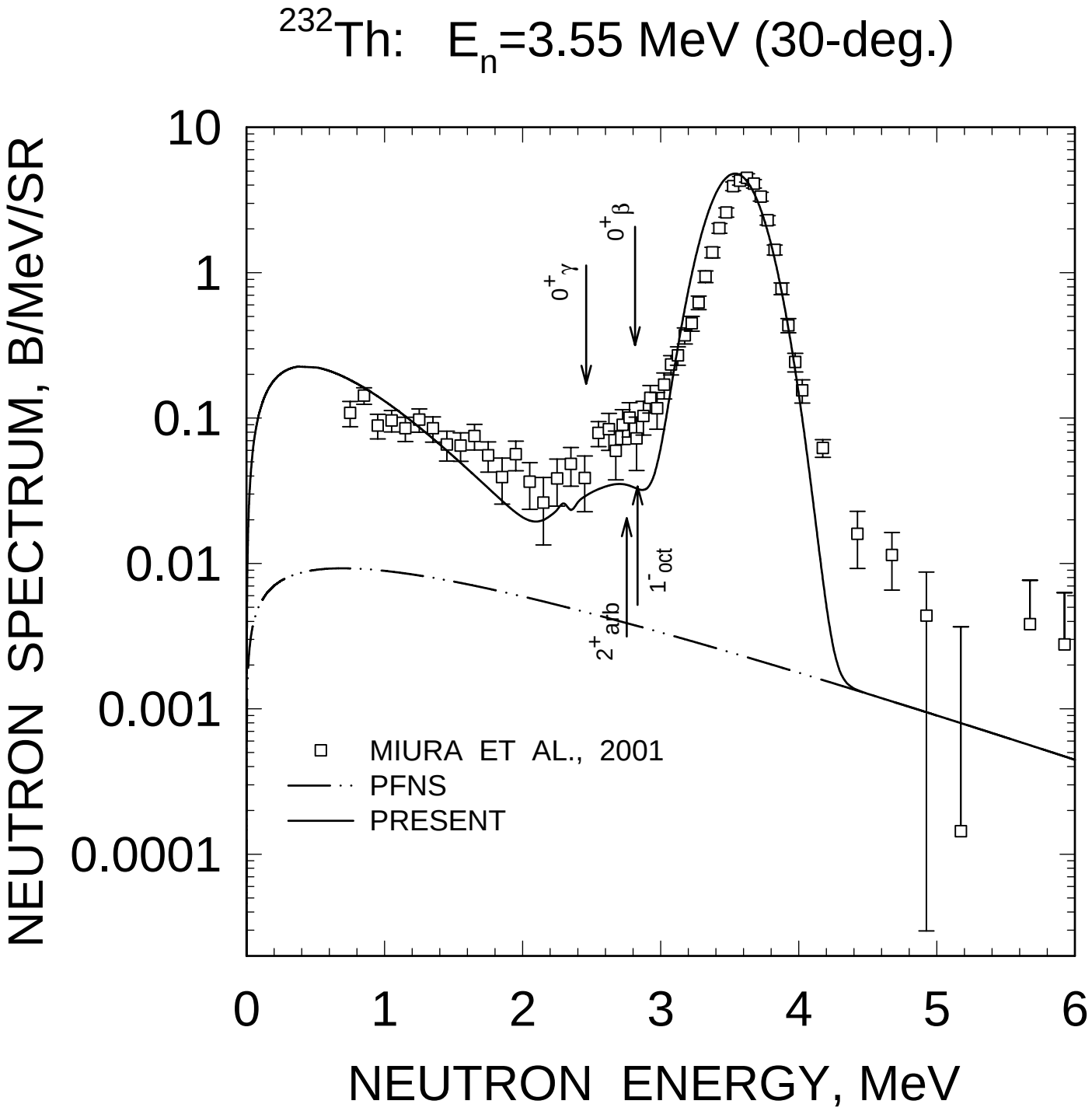
232Th: En=3.55 MeV (30-deg.)
NEUTRON SPECTRUM, B/MeV/SR
10
1
0.1
0.01
0.001
0.0001
0
1
2
3
4
5
6
NEUTRON ENERGY, MeV
0+γ
0+β
1-oct
2+a/b
MIURA ET AL., 2001
PFNS
PRESENT

FIG. 137

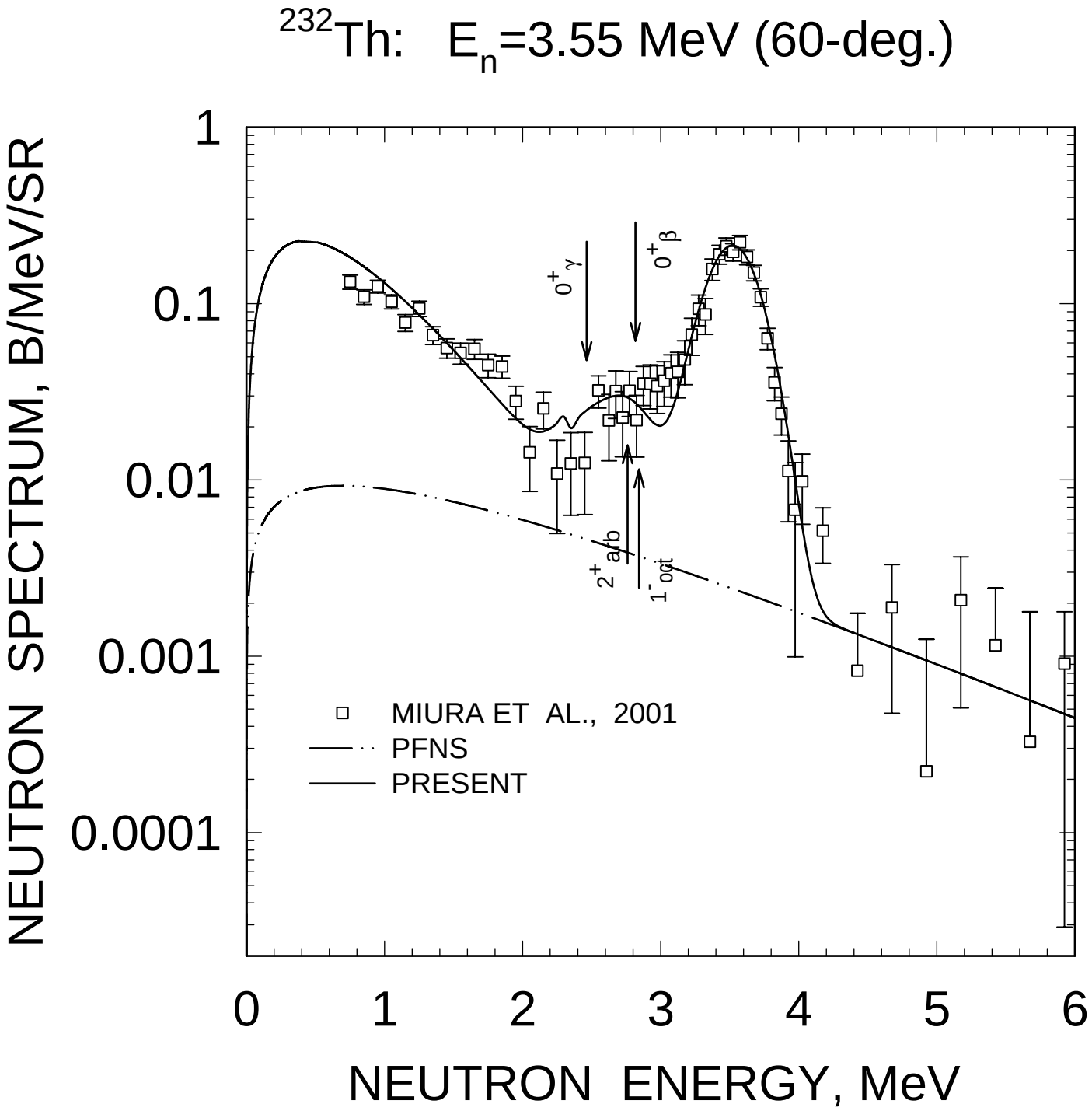
232Th: En=3.55 MeV (60-deg.)
NEUTRON SPECTRUM, B/MeV/SR
1
0.1
0.01
0.001
0.0001
0
1
2
3
4
5
6
NEUTRON ENERGY, MeV
0+γ
0+β
2+a/b
1-oct
MIURA ET AL., 2001
PFNS
PRESENT

FIG. 138

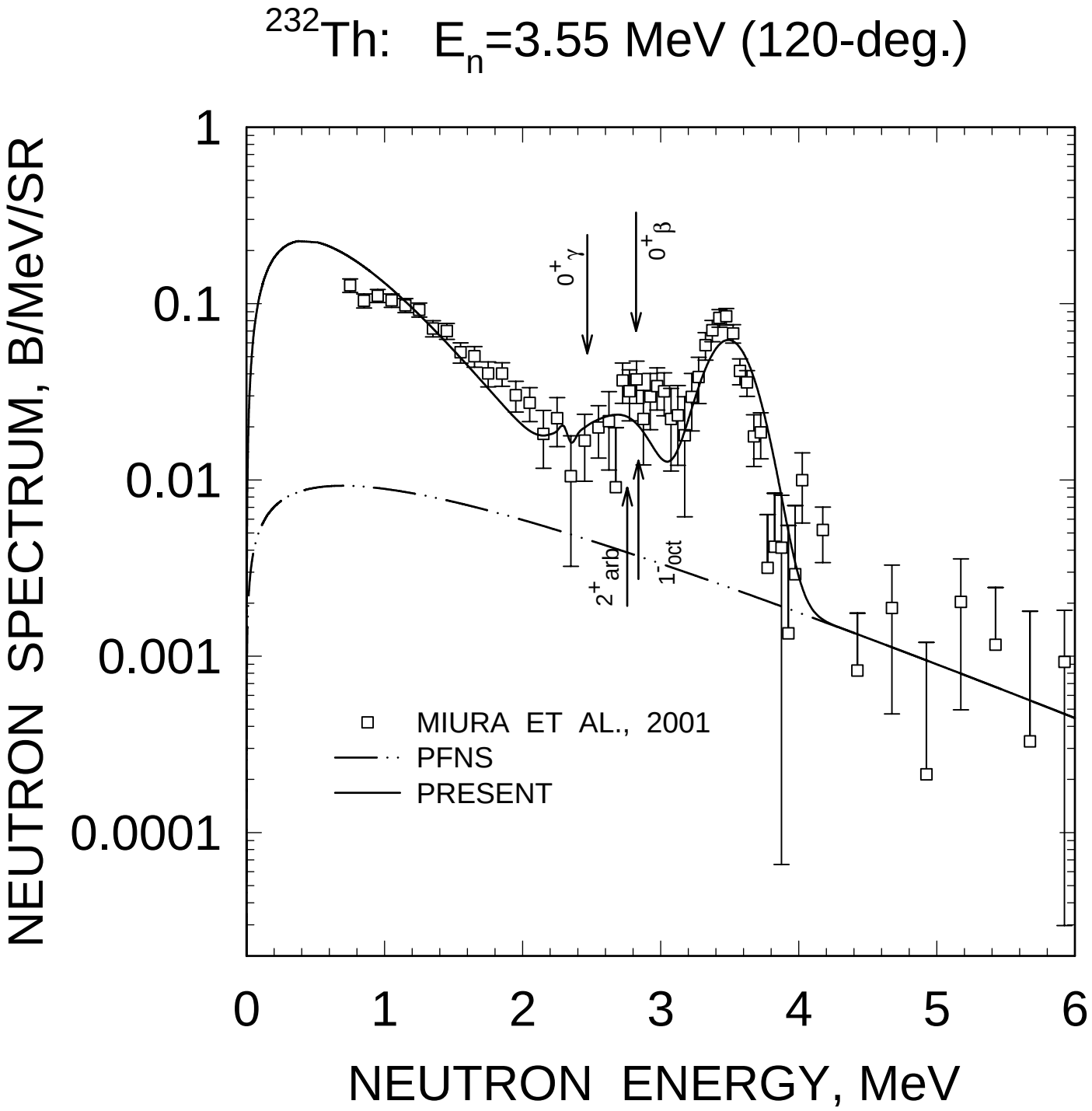
232Th: En=3.55 MeV (120-deg.)
NEUTRON SPECTRUM, B/MeV/SR
1
0.1
0.01
0.001
0.0001
0
1
2
3
4
5
6
NEUTRON ENERGY, MeV
0+γ
0+β
2+arb
1-oct
MIURA ET AL., 2001
PFNS
PRESENT

FIG. 139

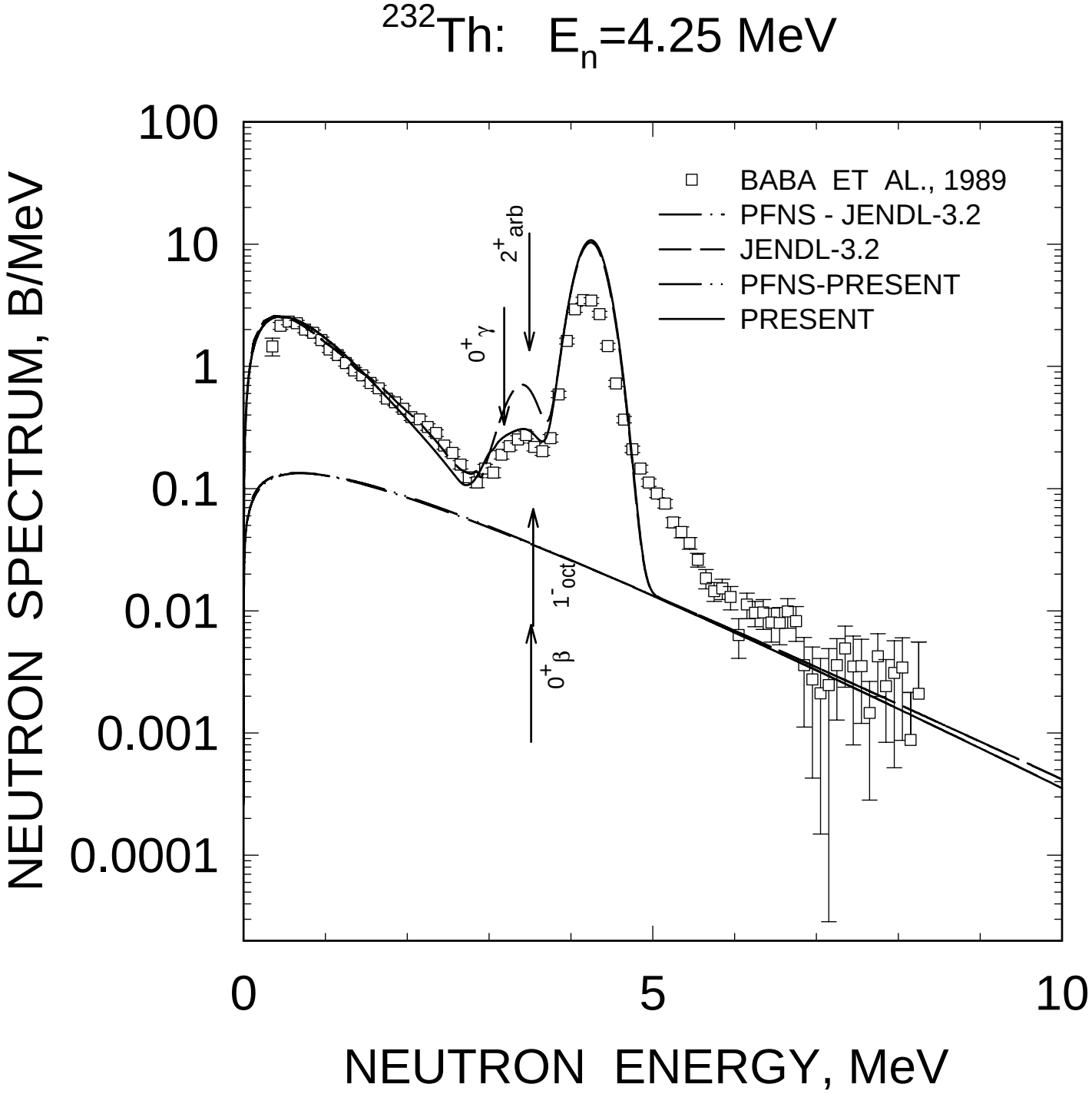
232Th: En=4.25 MeV
BABA ET AL., 1989
PFNS - JENDL-3.2
JENDL-3.2
PFNS-PRESENT
PRESENT
2+arb
0+γ
1-oct
0+β
100
10
1
0.1
0.01
0.001
0.0001
0
5
10
NEUTRON SPECTRUM, B/MeV
NEUTRON ENERGY, MeV

FIG. 140

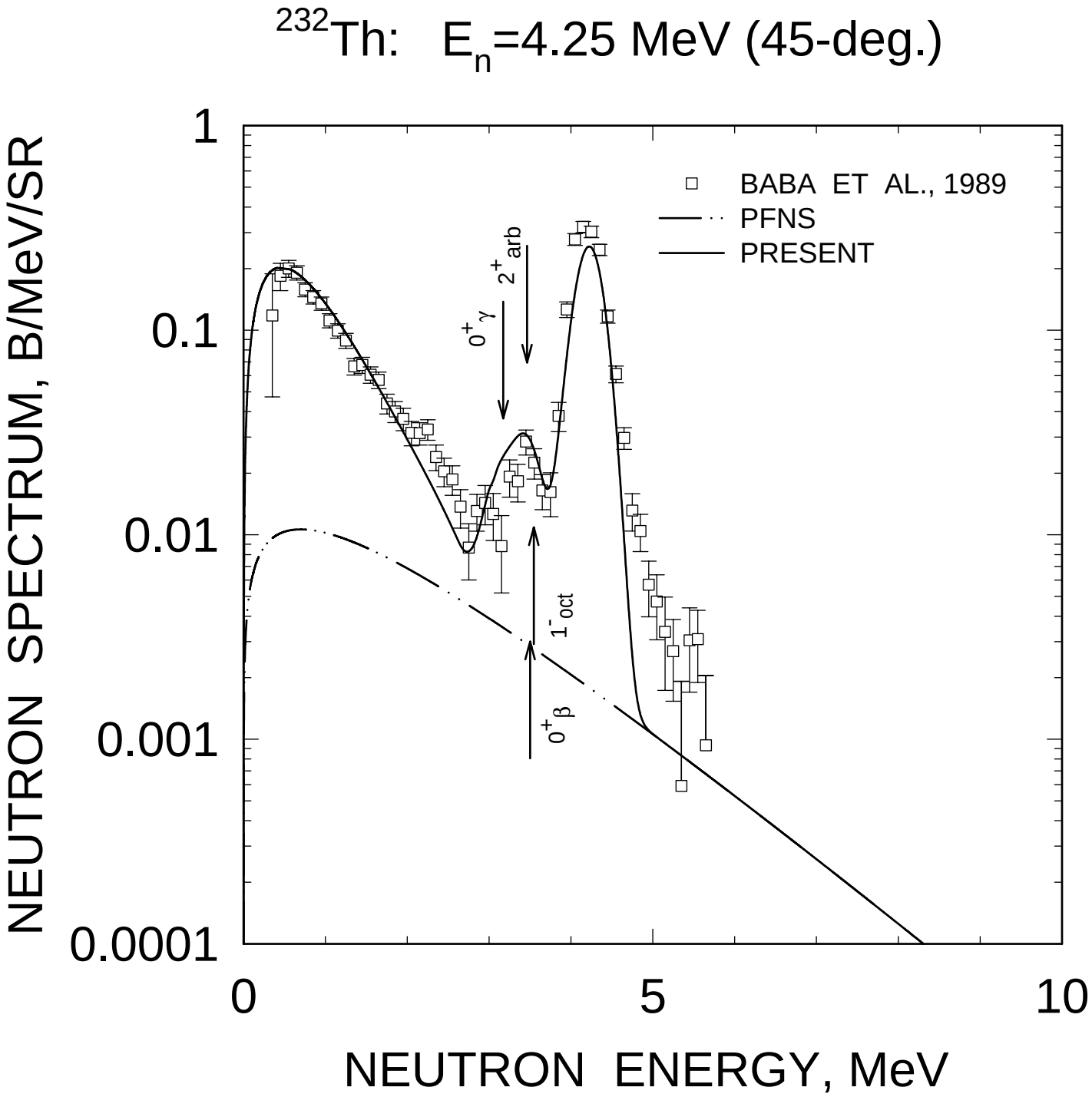
232Th: En=4.25 MeV (45-deg.)
BABA ET AL., 1989
PFNS
PRESENT
0+γ
2+arb
1-oct
0+β
NEUTRON SPECTRUM, B/MeV/SR
NEUTRON ENERGY, MeV
1
0.1
0.01
0.001
0.0001
0
5
10

FIG. 141

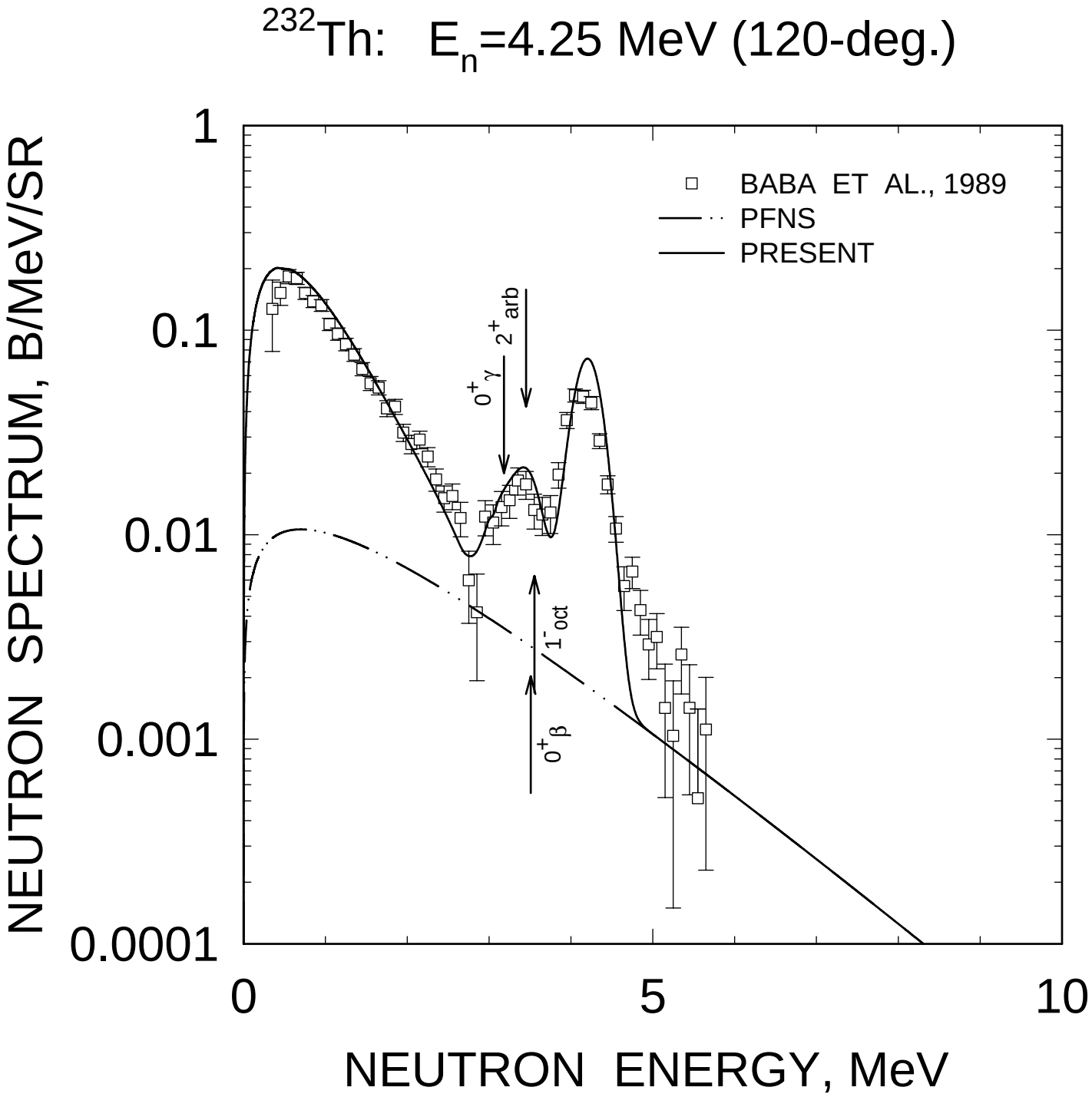
232Th: En=4.25 MeV (120-deg.)
BABA ET AL., 1989
PFNS
PRESENT
0+γ
2+arb
1-oct
0+β
NEUTRON SPECTRUM, B/MeV/SR
NEUTRON ENERGY, MeV
1
0.1
0.01
0.001
0.0001
0
5
10

FIG. 142

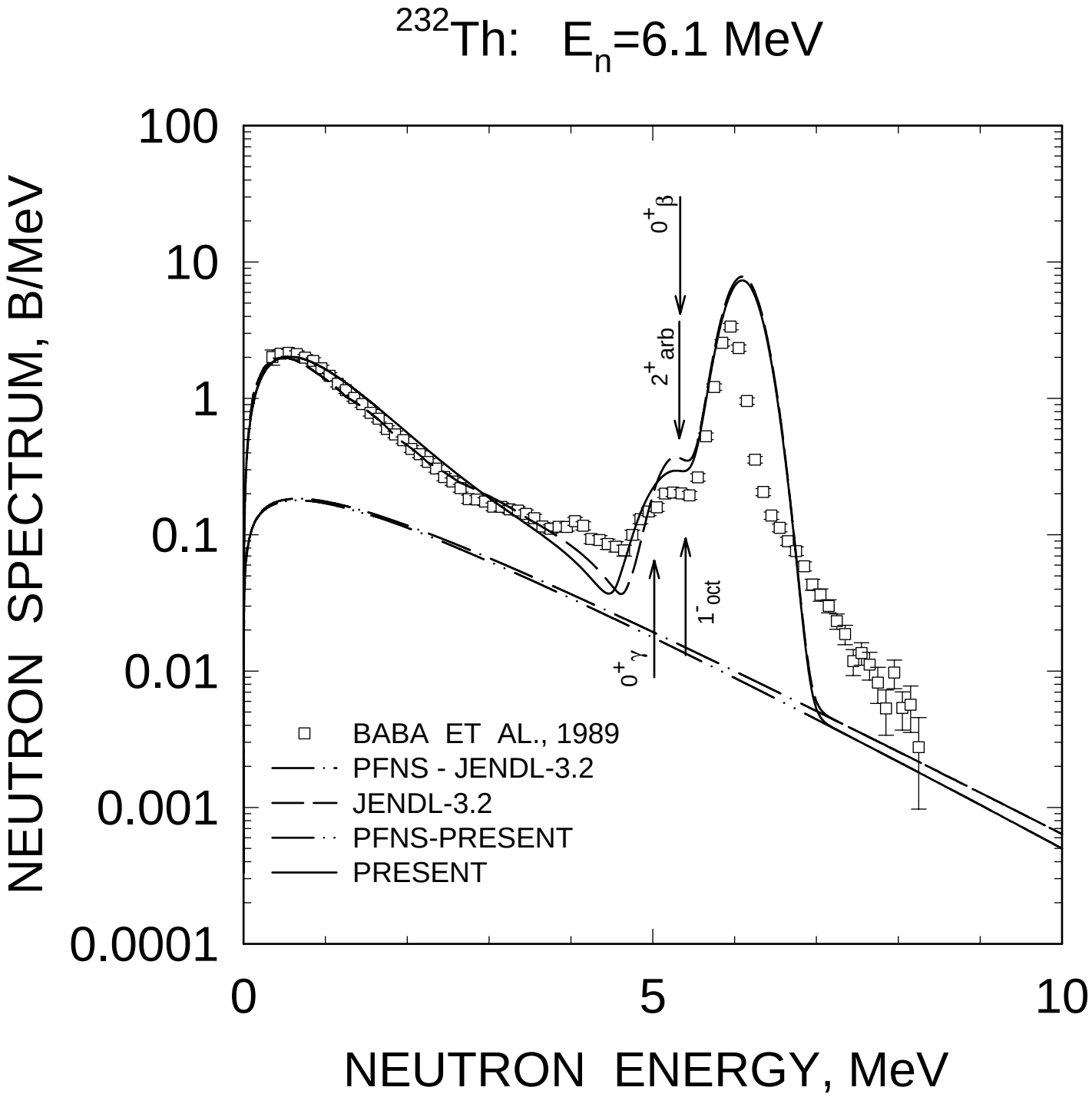
232Th: En=6.1 MeV
NEUTRON SPECTRUM, B/MeV
NEUTRON ENERGY, MeV
100
10
1
0.1
0.01
0.001
0.0001
0
5
10
0+β
2+arb
1-oct
0+γ
BABA ET AL., 1989
PFNS - JENDL-3.2
JENDL-3.2
PFNS-PRESENT
PRESENT

FIG. 143

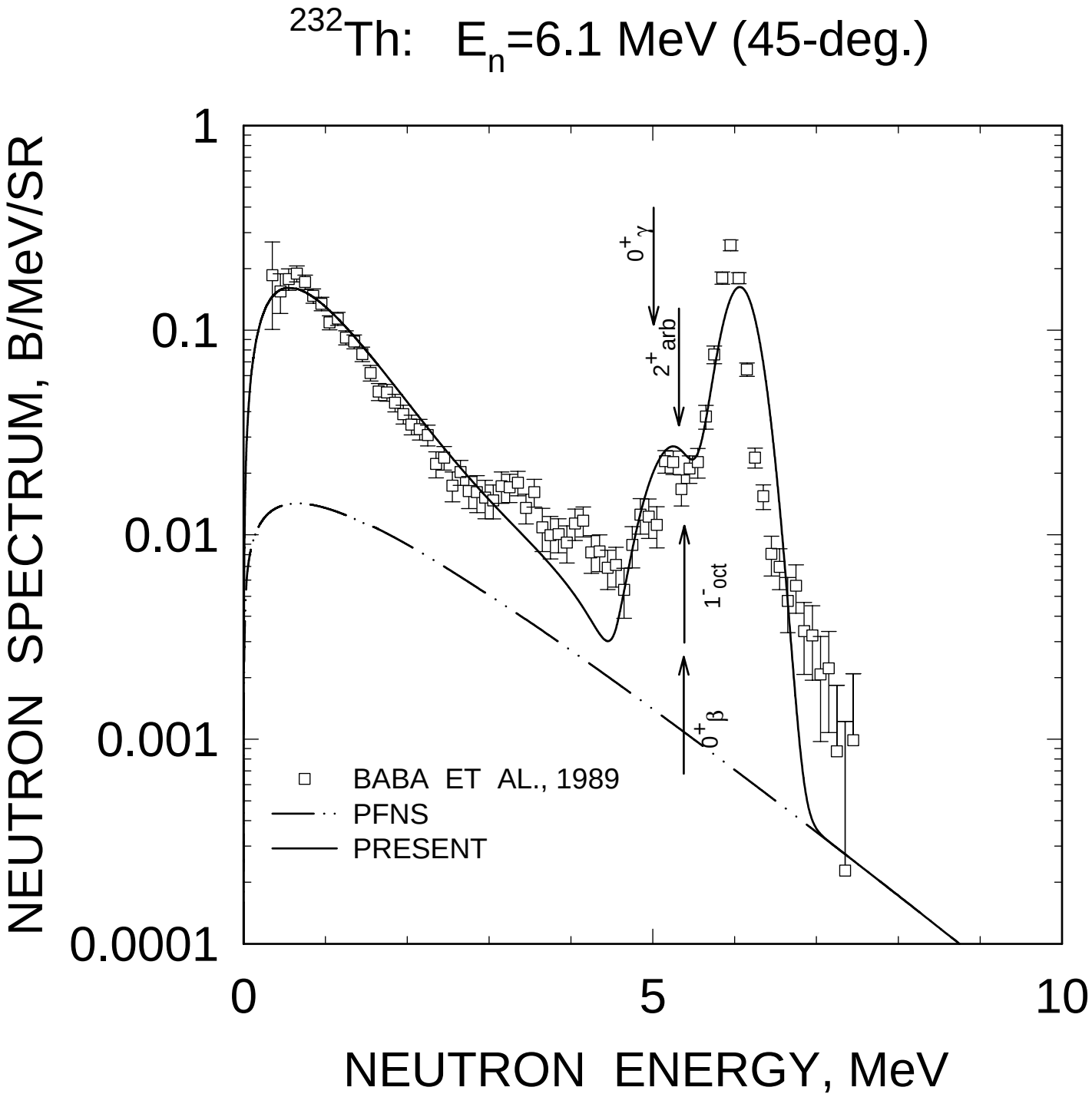
232Th: En=6.1 MeV (45-deg.)
NEUTRON SPECTRUM, B/MeV/SR
1
0.1
0.01
0.001
0.0001
0
5
10
NEUTRON ENERGY, MeV
0+γ
2+arb
1-oct
0+β
BABA ET AL., 1989
PFNS
PRESENT

FIG. 144

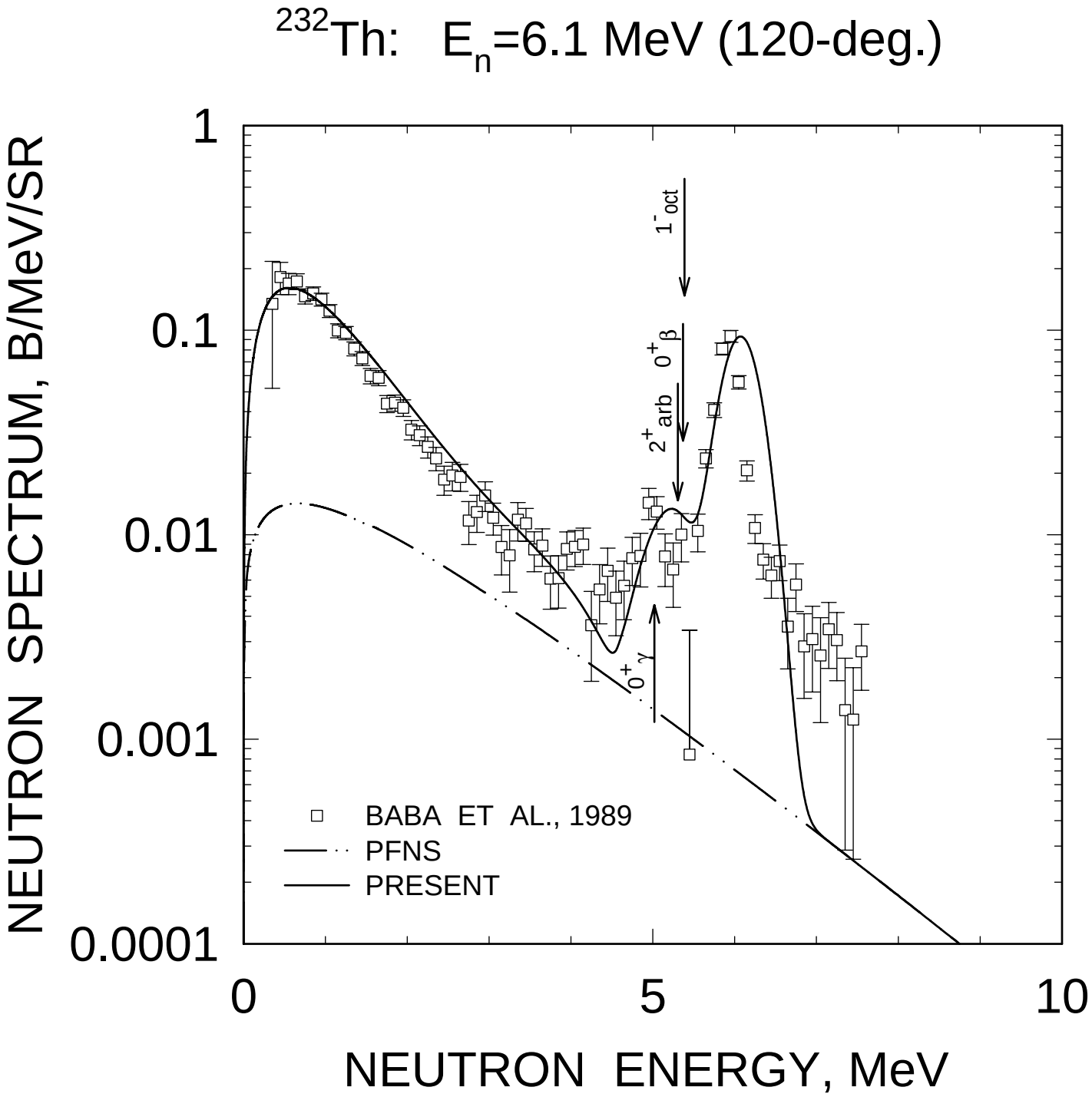
232Th: En=6.1 MeV (120-deg.)
NEUTRON SPECTRUM, B/MeV/SR
1
0.1
0.01
0.001
0.0001
0
5
10
NEUTRON ENERGY, MeV
1- oct
0+ β
2+ arb
0+ γ
BABA ET AL., 1989
PFNS
PRESENT

FIG. 145

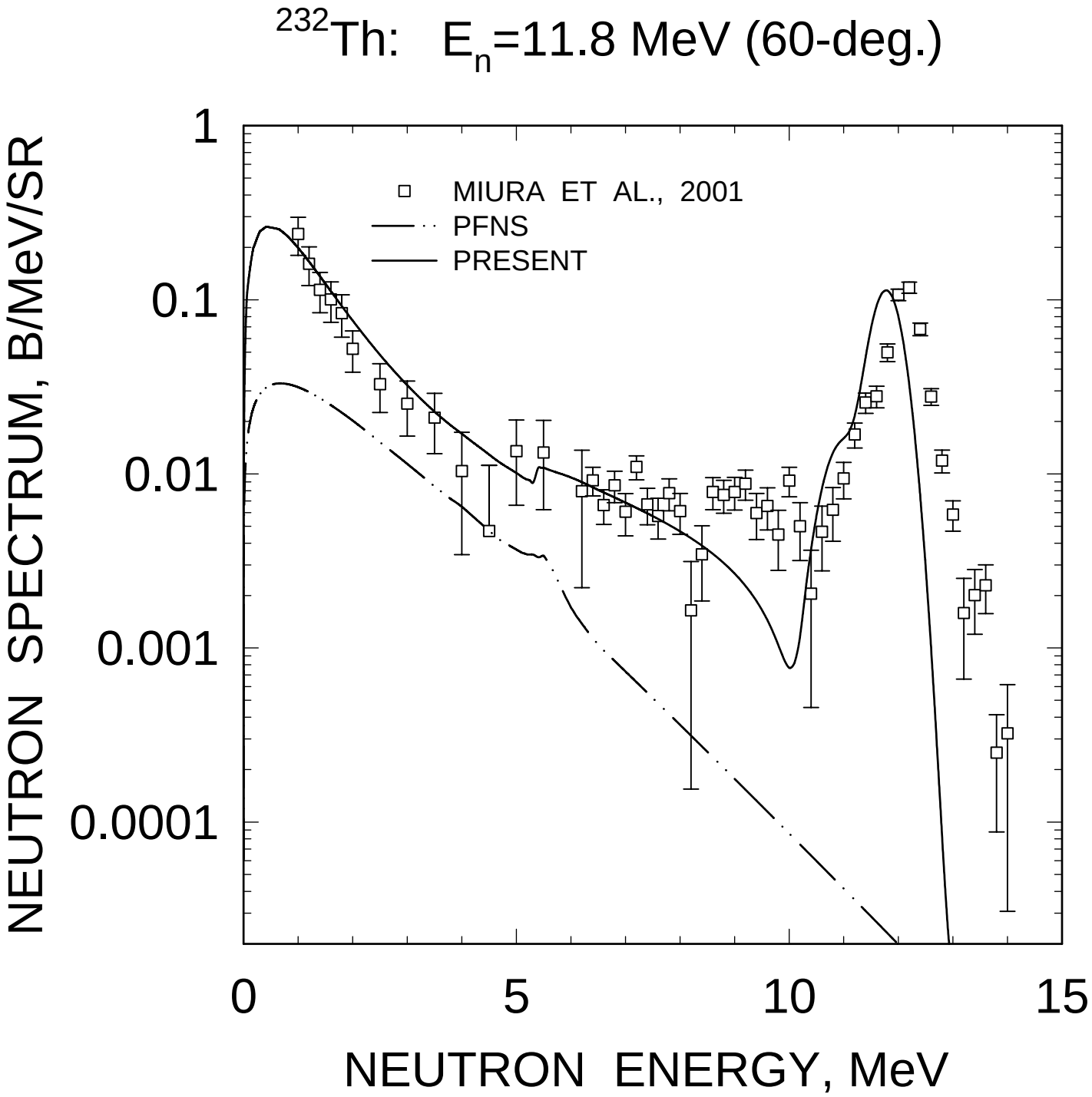
232Th: En=11.8 MeV (60-deg.)
MIURA ET AL., 2001
PFNS
PRESENT
NEUTRON SPECTRUM, B/MeV/SR
1
0.1
0.01
0.001
0.0001
0
5
10
15
NEUTRON ENERGY, MeV

FIG. 146

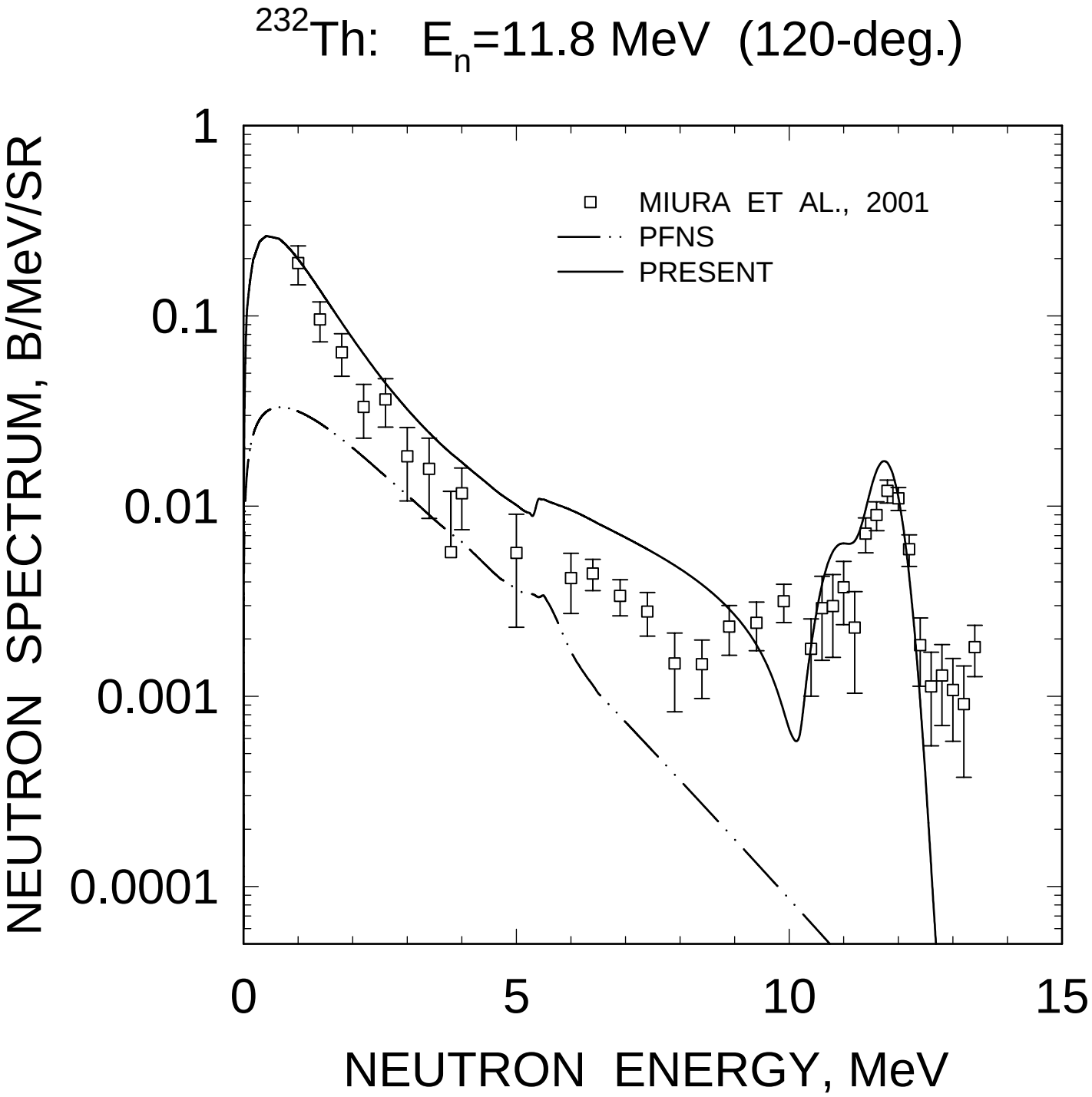
232Th: En=11.8 MeV (120-deg.)
MIURA ET AL., 2001
PFNS
PRESENT
NEUTRON SPECTRUM, B/MeV/SR
1
0.1
0.01
0.001
0.0001
0
5
10
15
NEUTRON ENERGY, MeV

FIG. 147

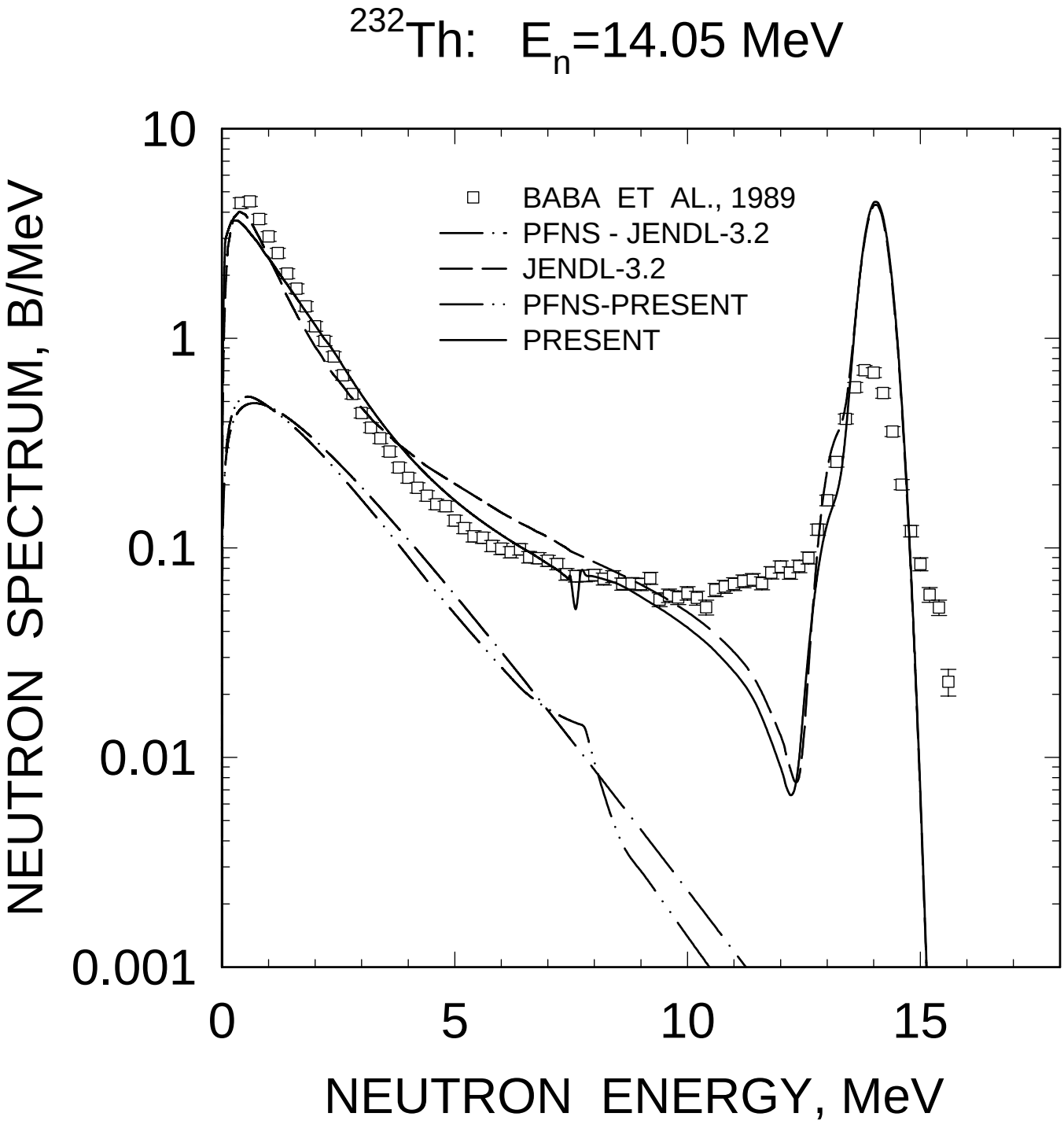
232Th: En=14.05 MeV
BABA ET AL., 1989
PFNS - JENDL-3.2
JENDL-3.2
PFNS-PRESENT
PRESENT
NEUTRON SPECTRUM, B/MeV
NEUTRON ENERGY, MeV
10
1
0.1
0.01
0.001
0
5
10
15

FIG. 148

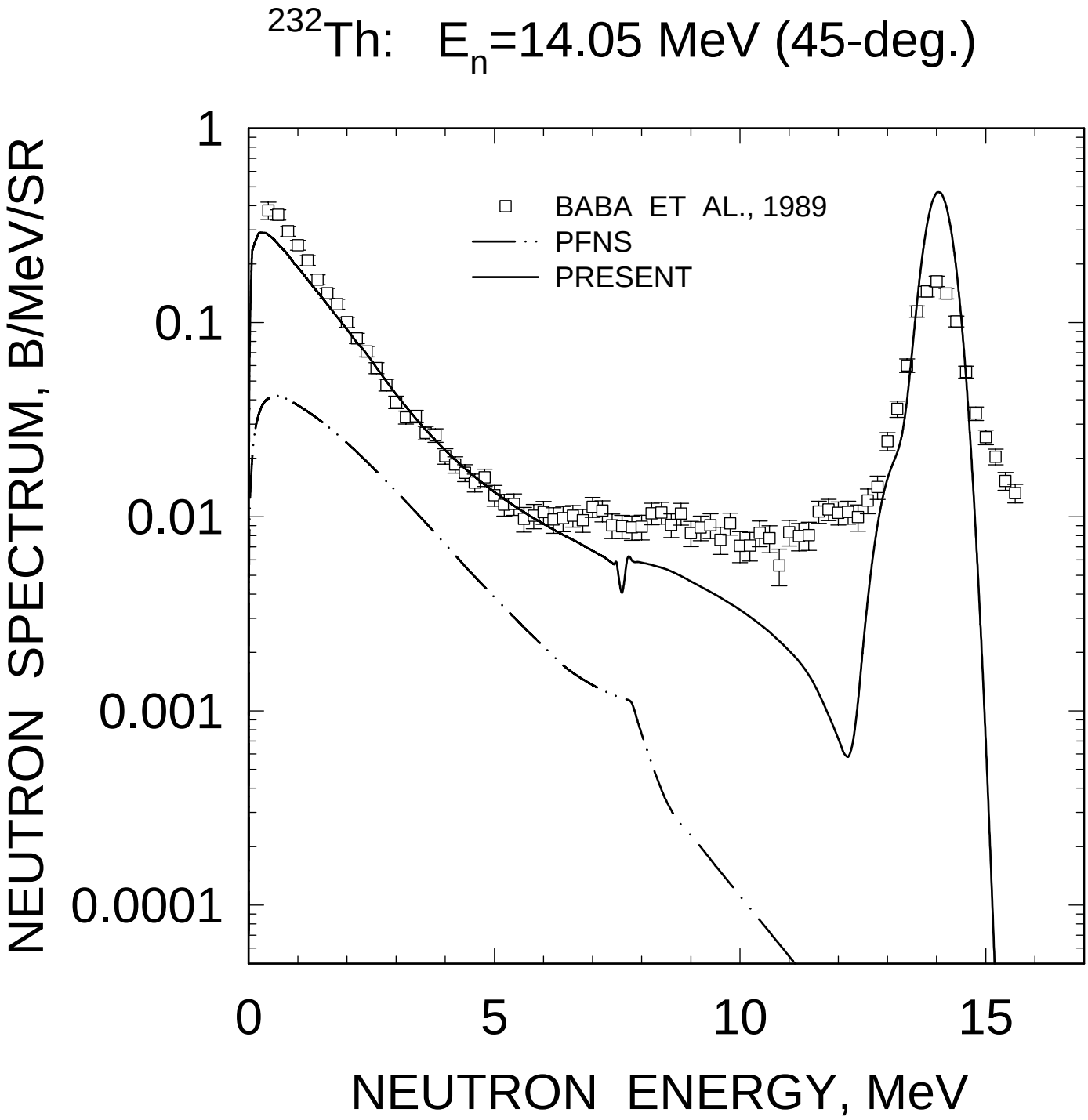
232Th: En=14.05 MeV (45-deg.)
BABA ET AL., 1989
PFNS
PRESENT
NEUTRON SPECTRUM, B/MeV/SR
1
0.1
0.01
0.001
0.0001
0
5
10
15
NEUTRON ENERGY, MeV

FIG. 149

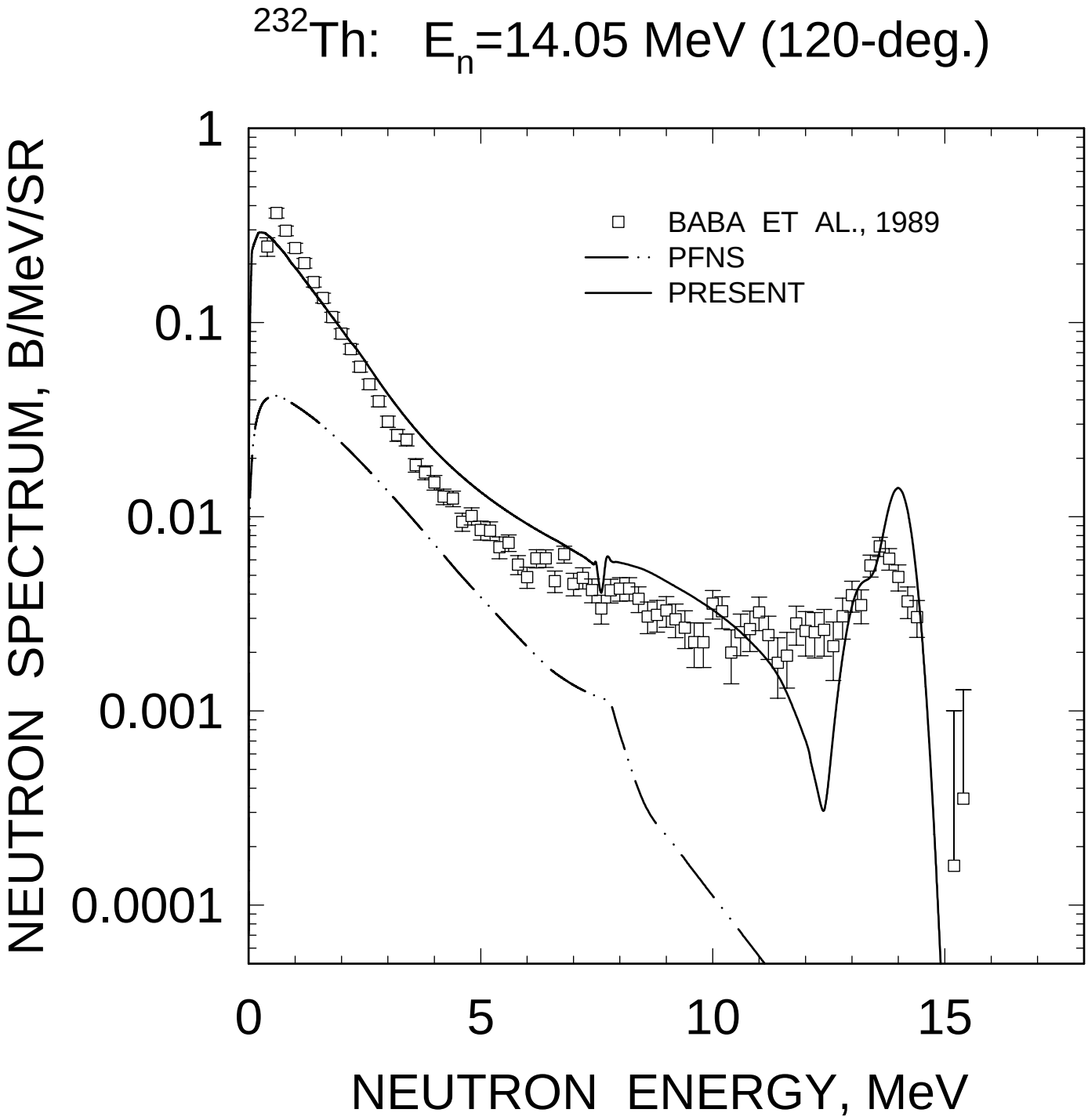
232Th: En=14.05 MeV (120-deg.)
BABA ET AL., 1989
PFNS
PRESENT
NEUTRON SPECTRUM, B/MeV/SR
1
0.1
0.01
0.001
0.0001
0
5
10
15
NEUTRON ENERGY, MeV

FIG. 150

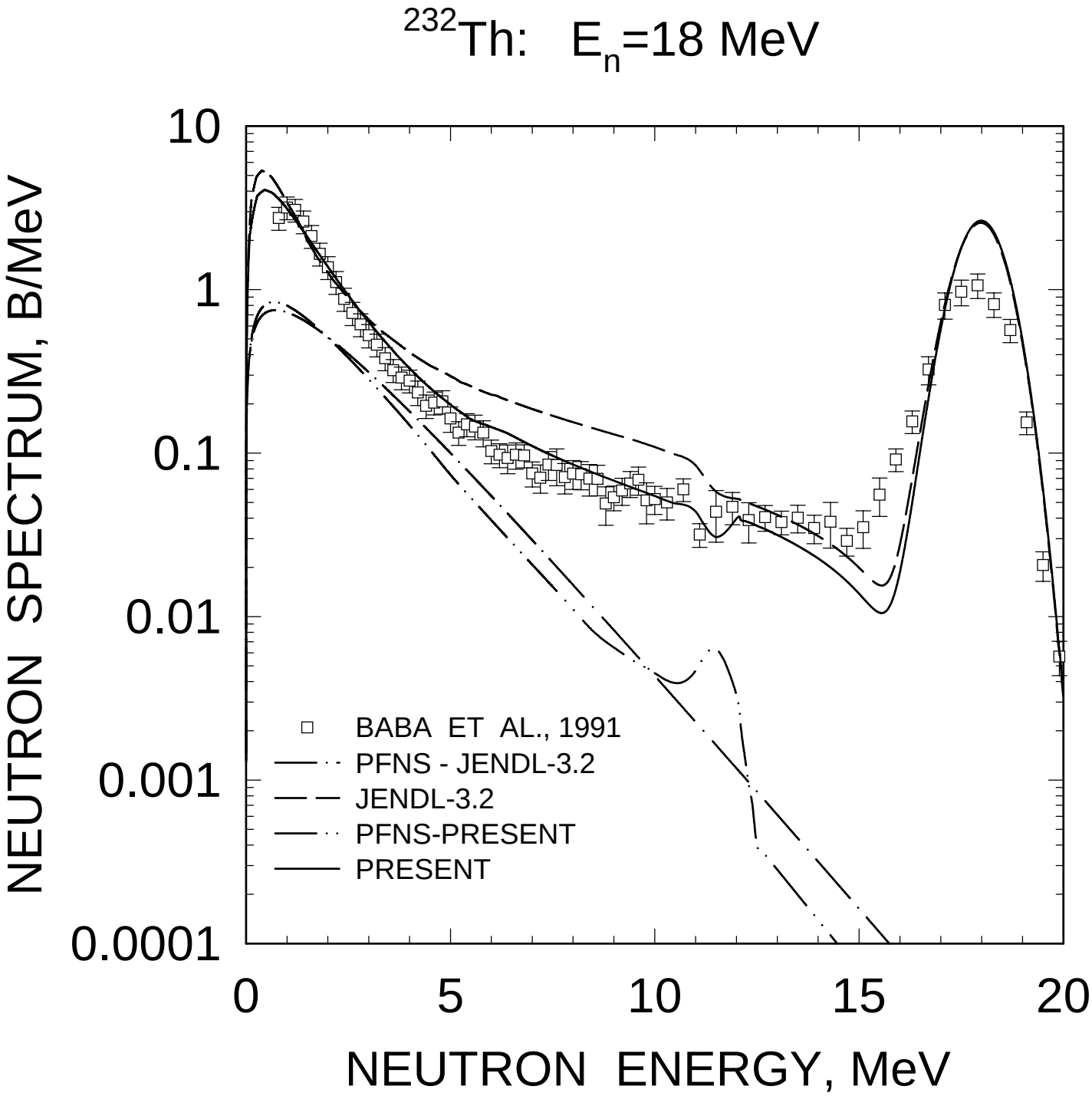
232Th: En=18 MeV
NEUTRON SPECTRUM, B/MeV
10
1
0.1
0.01
0.001
0.0001
0
5
10
15
20
NEUTRON ENERGY, MeV
BABA ET AL., 1991
PFNS - JENDL-3.2
JENDL-3.2
PFNS-PRESENT
PRESENT

FIG. 151

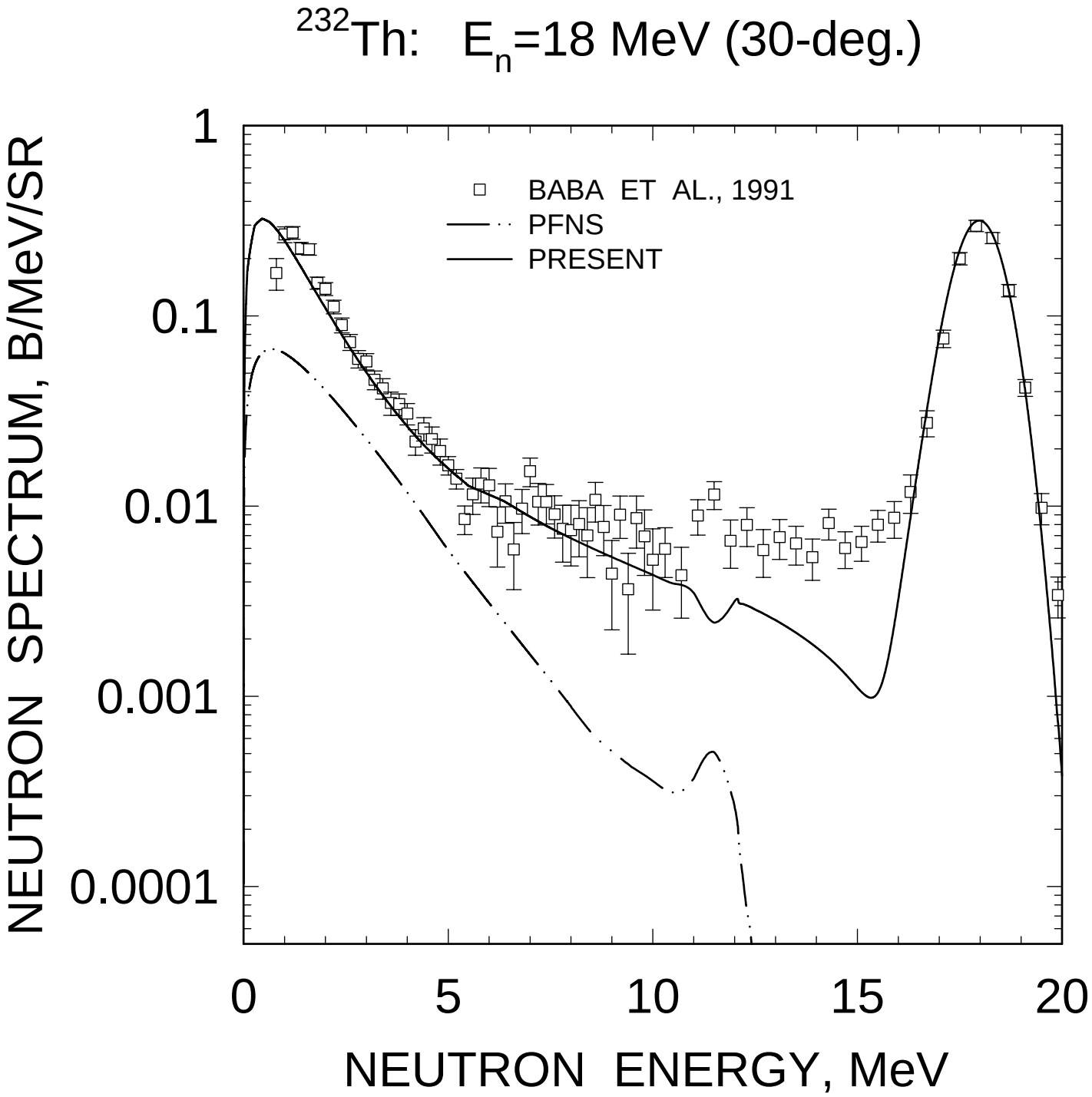
232Th: En=18 MeV (30-deg.)
BABA ET AL., 1991
PFNS
PRESENT
NEUTRON SPECTRUM, B/MeV/SR
1
0.1
0.01
0.001
0.0001
0
5
10
15
20
NEUTRON ENERGY, MeV

FIG. 152

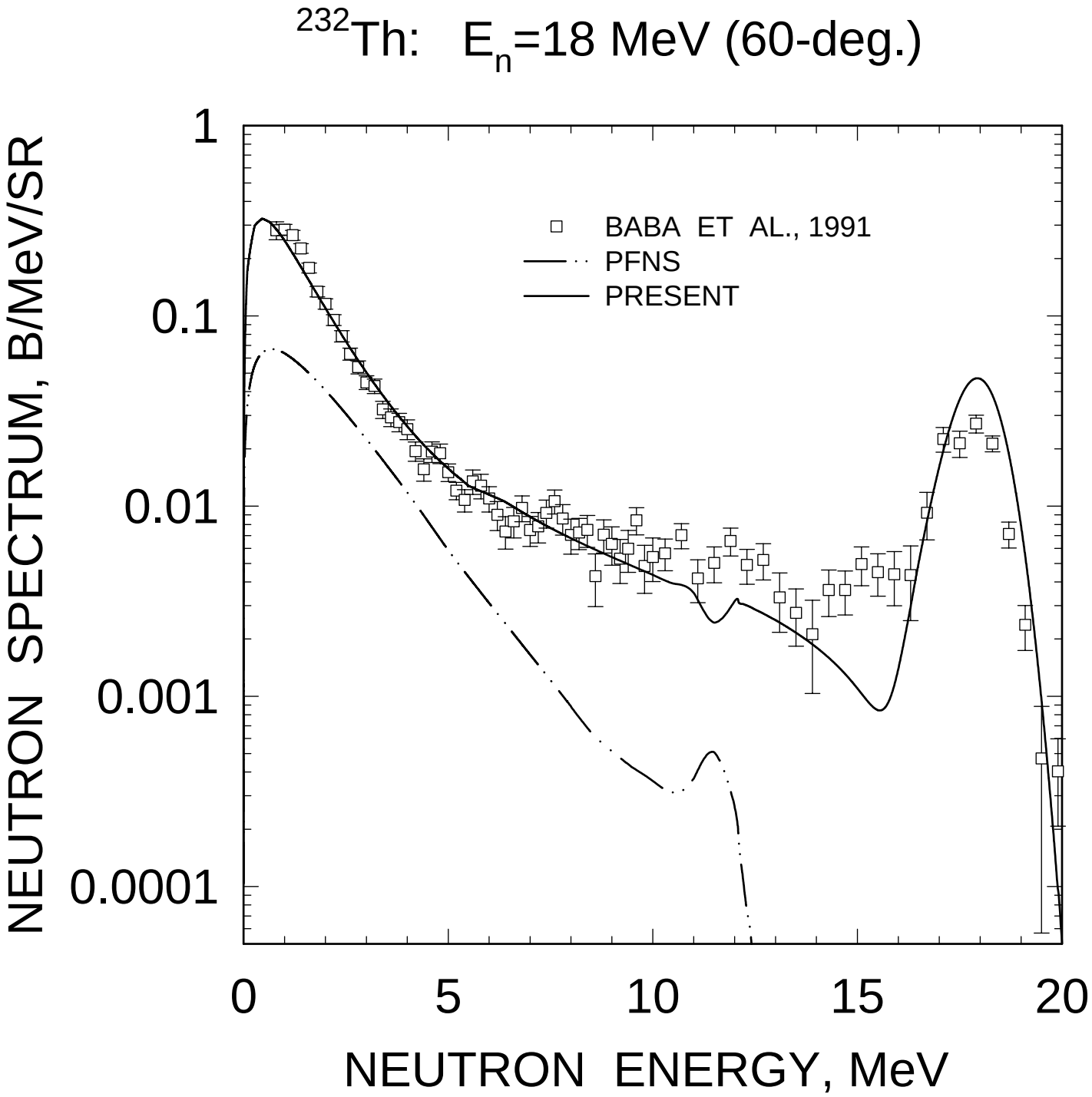
232Th: En=18 MeV (60-deg.)
BABA ET AL., 1991
PFNS
PRESENT
NEUTRON SPECTRUM, B/MeV/SR
1
0.1
0.01
0.001
0.0001
0
5
10
15
20
NEUTRON ENERGY, MeV

FIG. 153

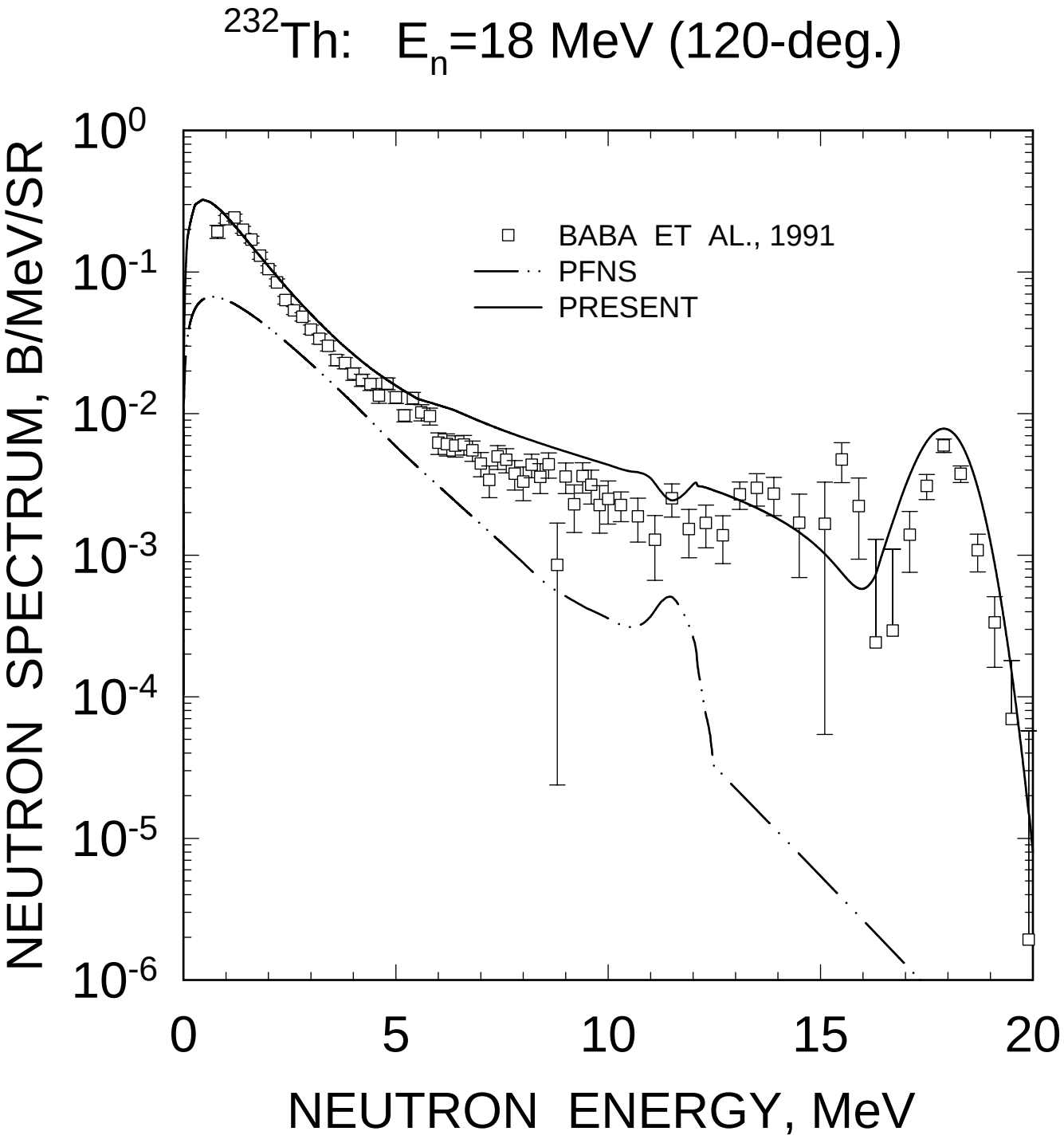
232Th: En=18 MeV (120-deg.)
BABA ET AL., 1991
PFNS
PRESENT
NEUTRON SPECTRUM, B/MeV/SR
NEUTRON ENERGY, MeV
10^0
10^-1
10^-2
10^-3
10^-4
10^-5
10^-6
0
5
10
15
20

FIG. 154

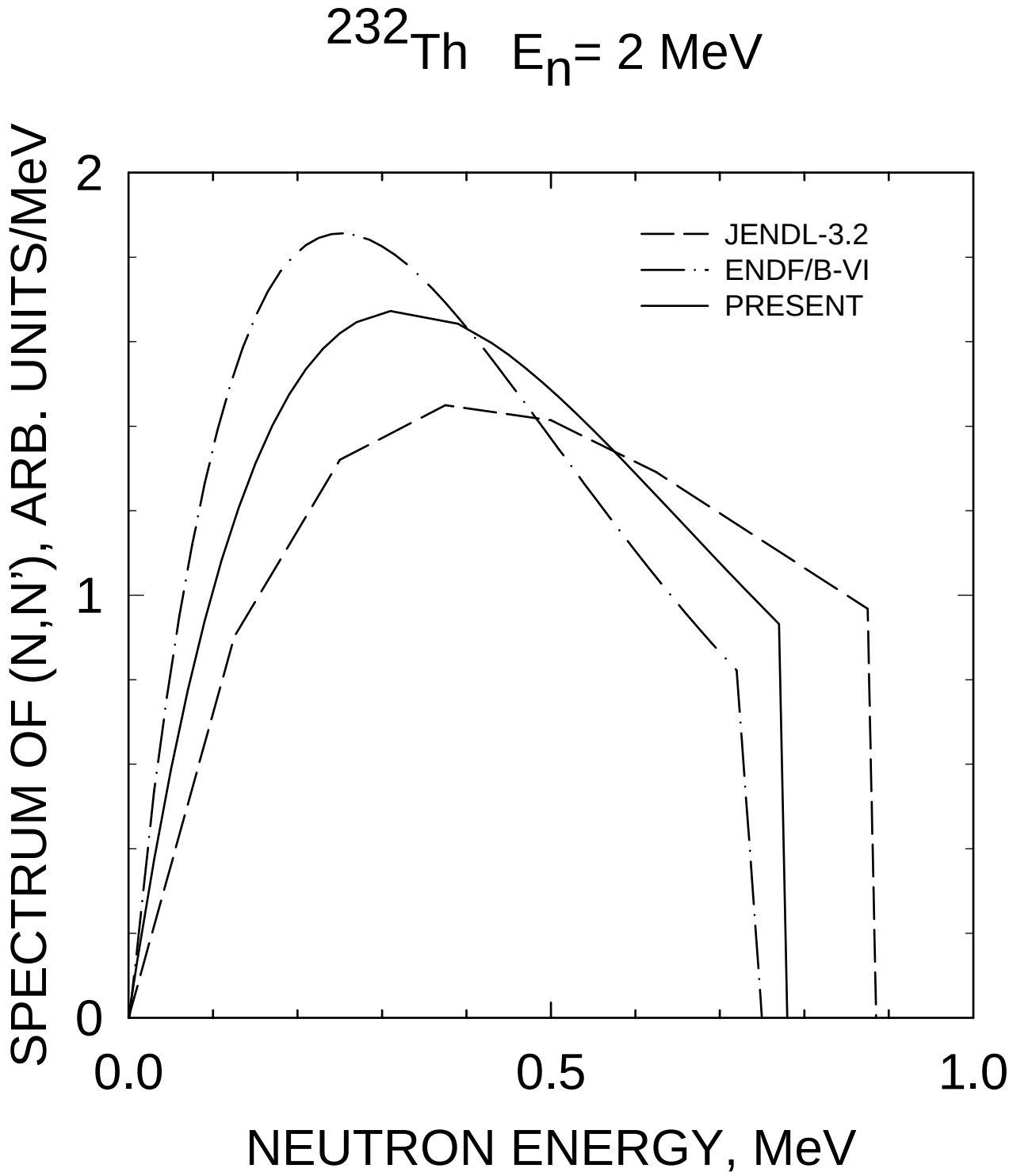
232Th En= 2 MeV
SPECTRUM OF (N,N'), ARB. UNITS/MeV
2
1
0
0.0
0.5
1.0
NEUTRON ENERGY, MeV
JENDL-3.2
ENDF/B-VI
PRESENT

FIG. 155

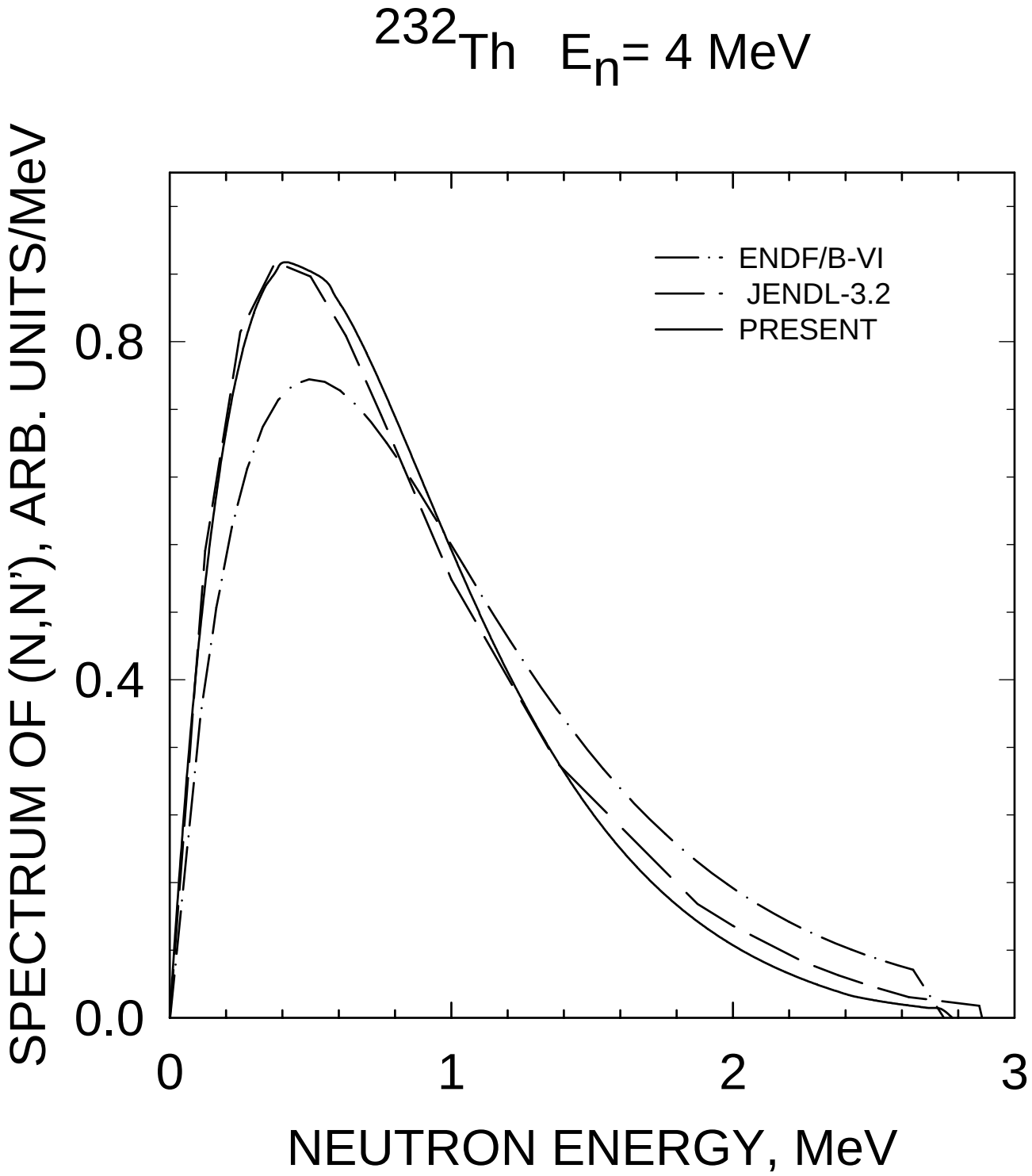
232Th En= 4 MeV
ENDF/B-VI
JENDL-3.2
PRESENT
SPECTRUM OF (N,N'), ARB. UNITS/MeV
0.0
0.4
0.8
0
1
2
3
NEUTRON ENERGY, MeV

FIG. 156

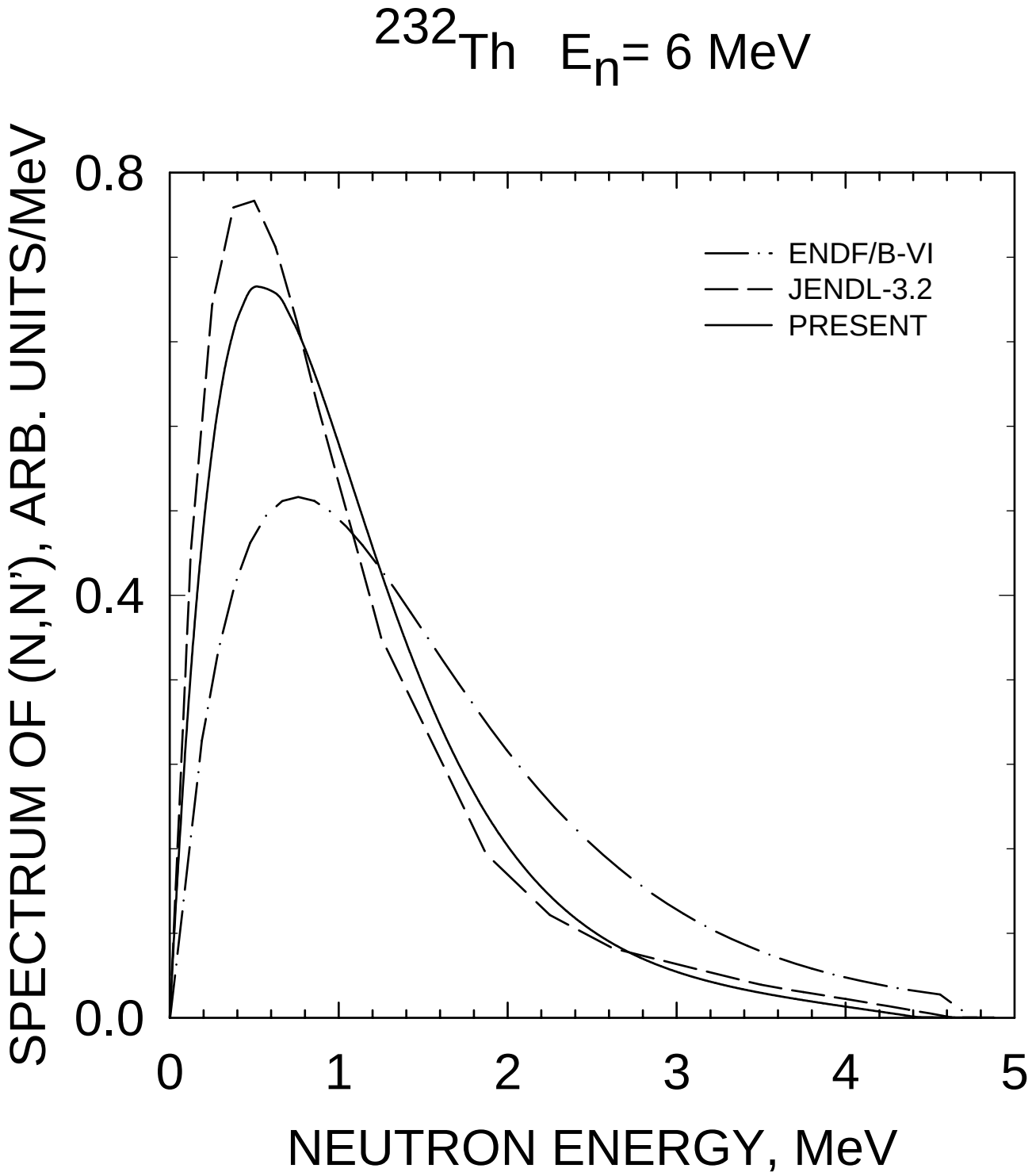
232Th En= 6 MeV
SPECTRUM OF (N,N'), ARB. UNITS/MeV
0.8
0.4
0.0
0
1
2
3
4
5
NEUTRON ENERGY, MeV
ENDF/B-VI
JENDL-3.2
PRESENT

FIG. 157

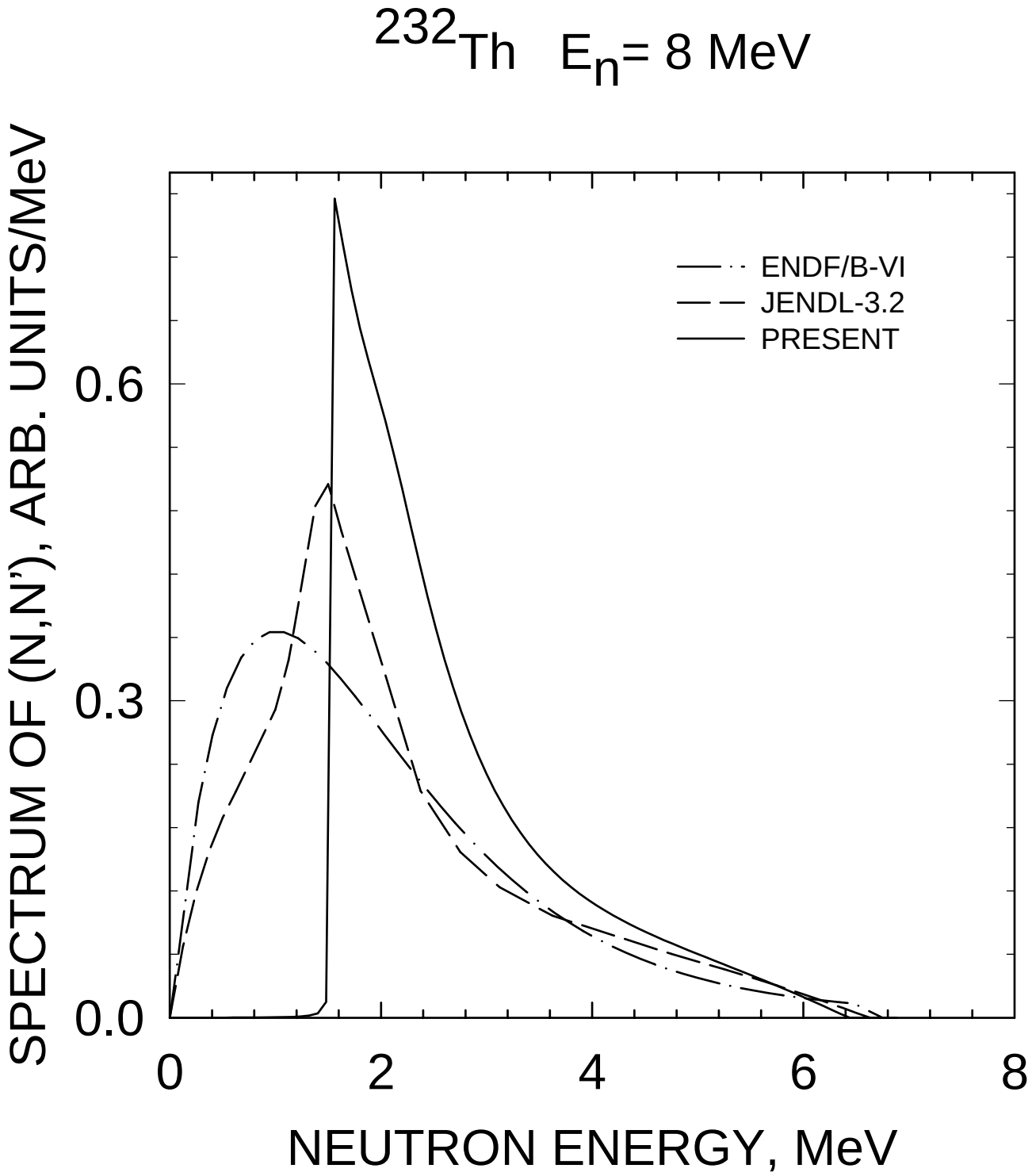
232Th En= 8 MeV
ENDF/B-VI
JENDL-3.2
PRESENT
SPECTRUM OF (N,N'), ARB. UNITS/MeV
0.0
0.3
0.6
0
2
4
6
8
NEUTRON ENERGY, MeV

FIG. 158

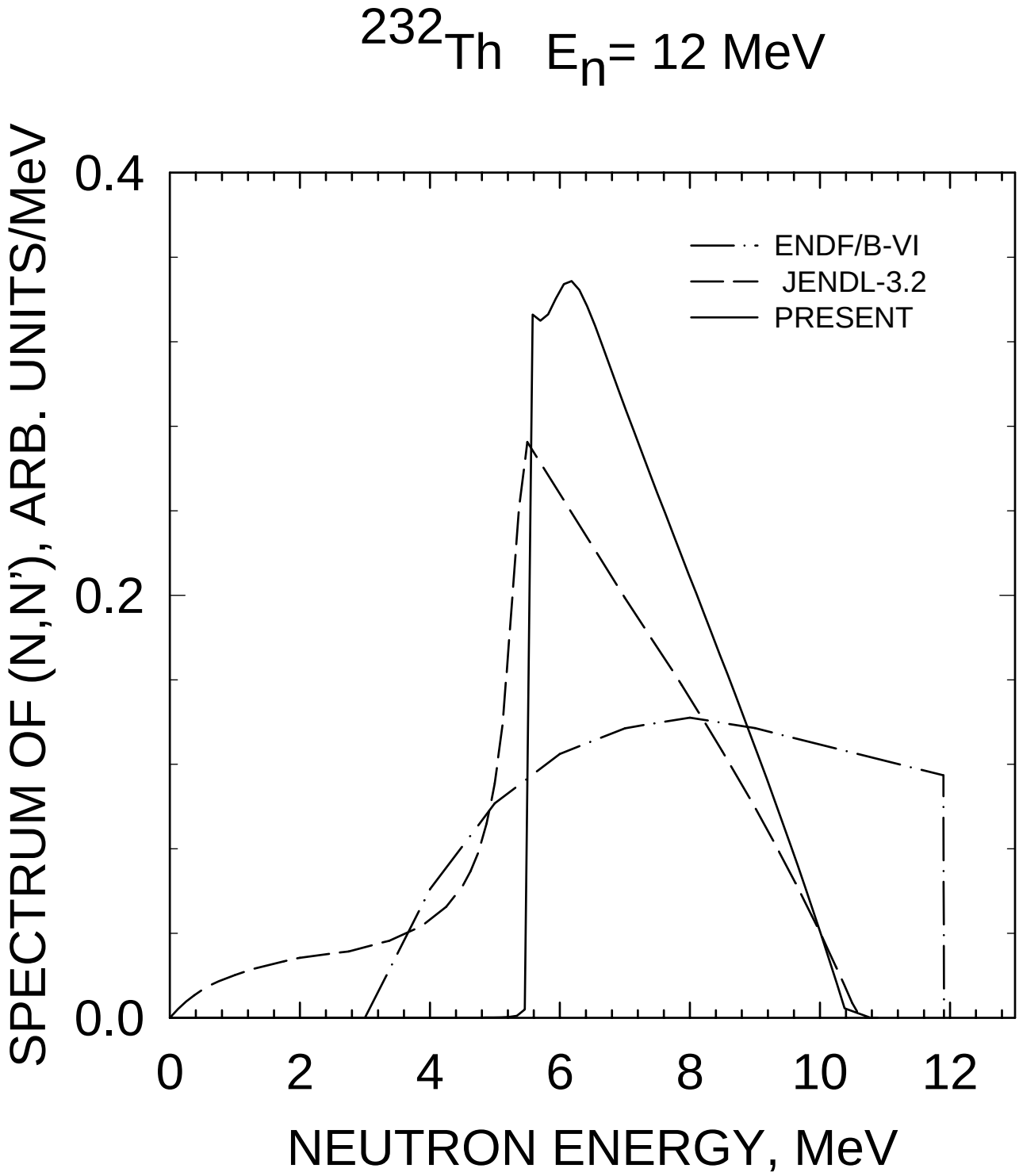
232Th En= 12 MeV
ENDF/B-VI
JENDL-3.2
PRESENT
SPECTRUM OF (N,N'), ARB. UNITS/MeV
0.4
0.2
0.0
0
2
4
6
8
10
12
NEUTRON ENERGY, MeV

FIG. 159

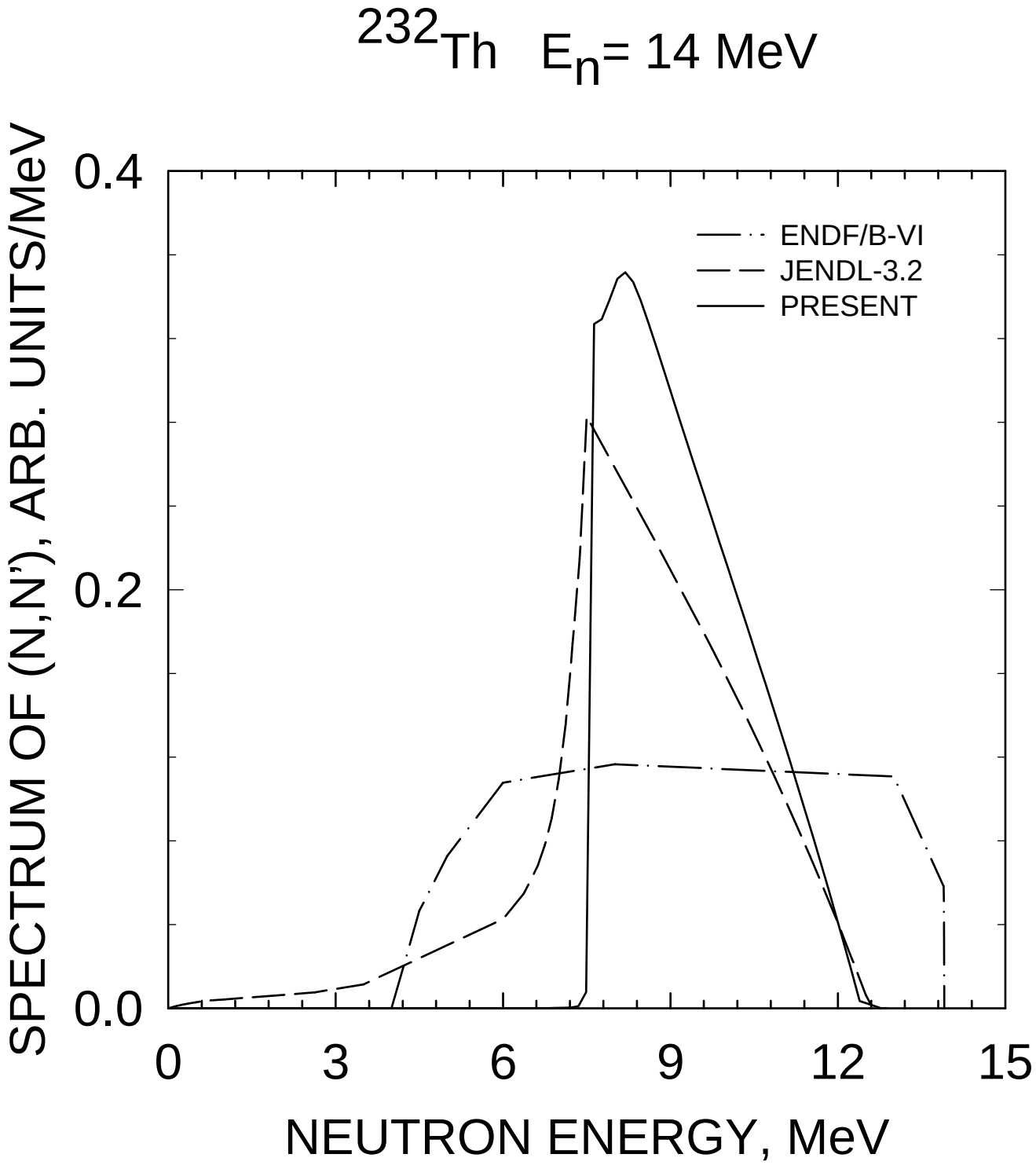
232Th En= 14 MeV
ENDF/B-VI
JENDL-3.2
PRESENT
SPECTRUM OF (N,N'), ARB. UNITS/MeV
0.4
0.2
0.0
0
3
6
9
12
15
NEUTRON ENERGY, MeV

FIG. 160

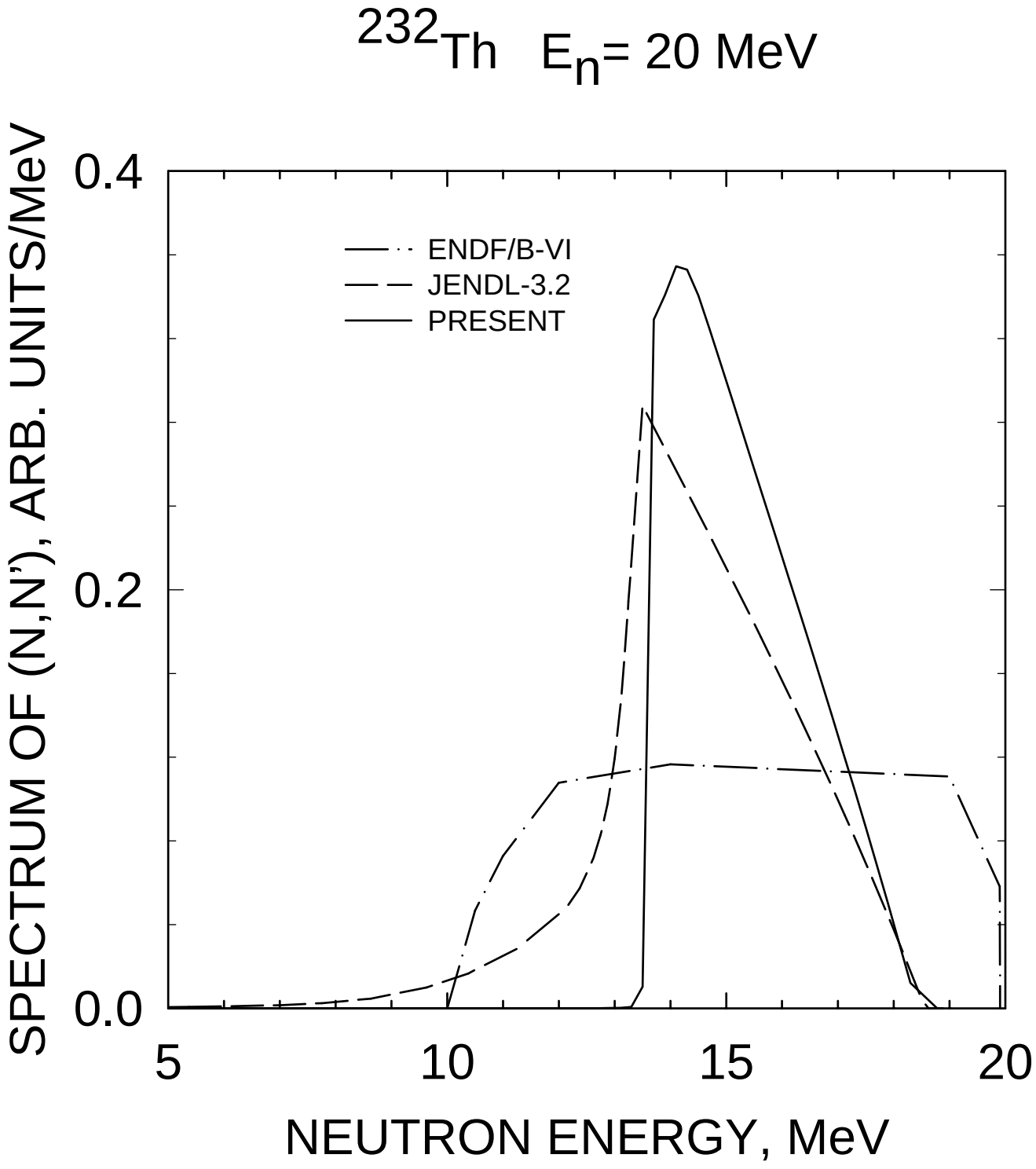
232Th En= 20 MeV
ENDF/B-VI
JENDL-3.2
PRESENT
SPECTRUM OF (N,N'), ARB. UNITS/MeV
0.4
0.2
0.0
5
10
15
20
NEUTRON ENERGY, MeV

FIG. 161

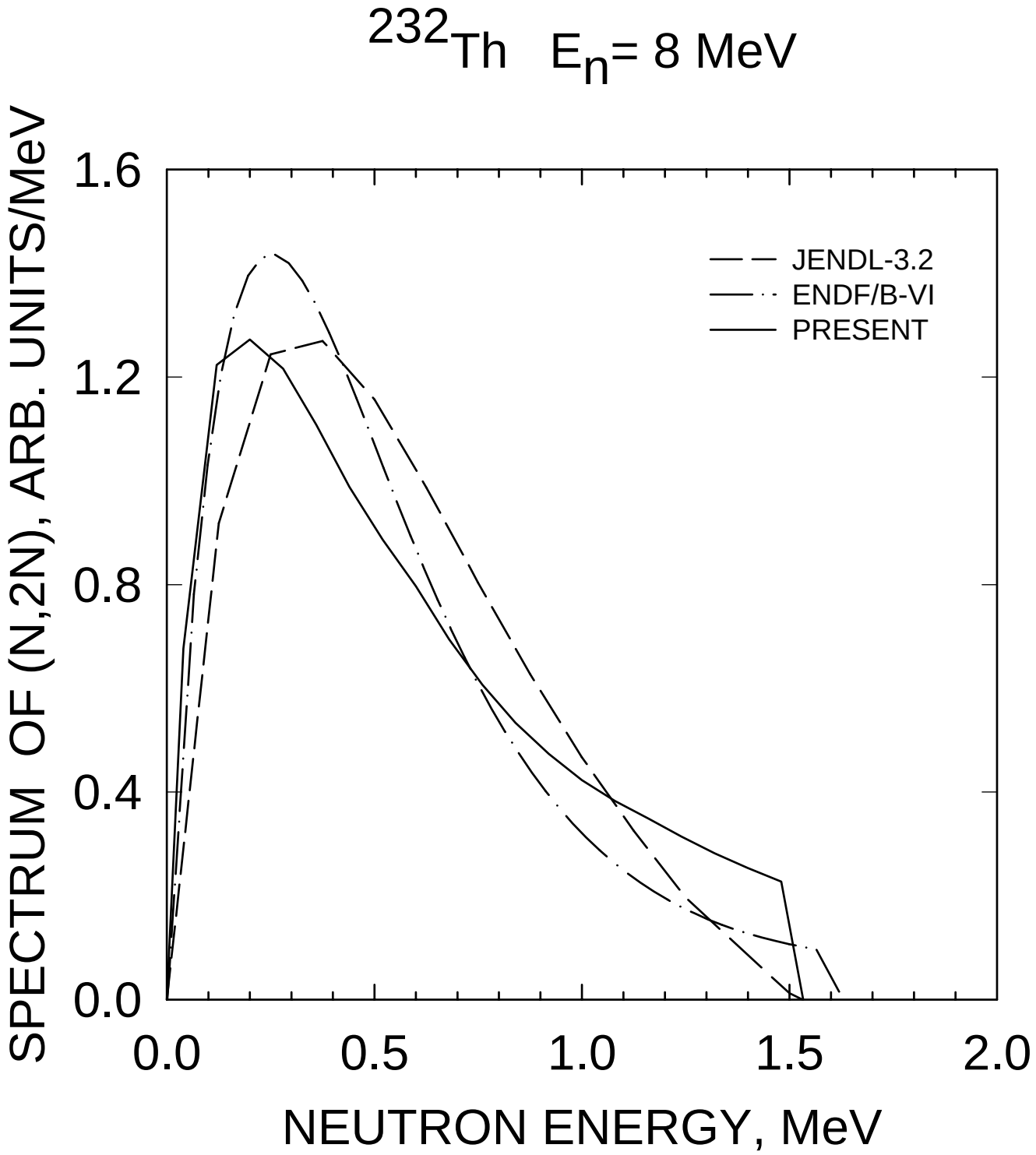
232Th En= 8 MeV
SPECTRUM OF (N,2N), ARB. UNITS/MeV
1.6
1.2
0.8
0.4
0.0
0.0
0.5
1.0
1.5
2.0
NEUTRON ENERGY, MeV
JENDL-3.2
ENDF/B-VI
PRESENT

FIG. 162

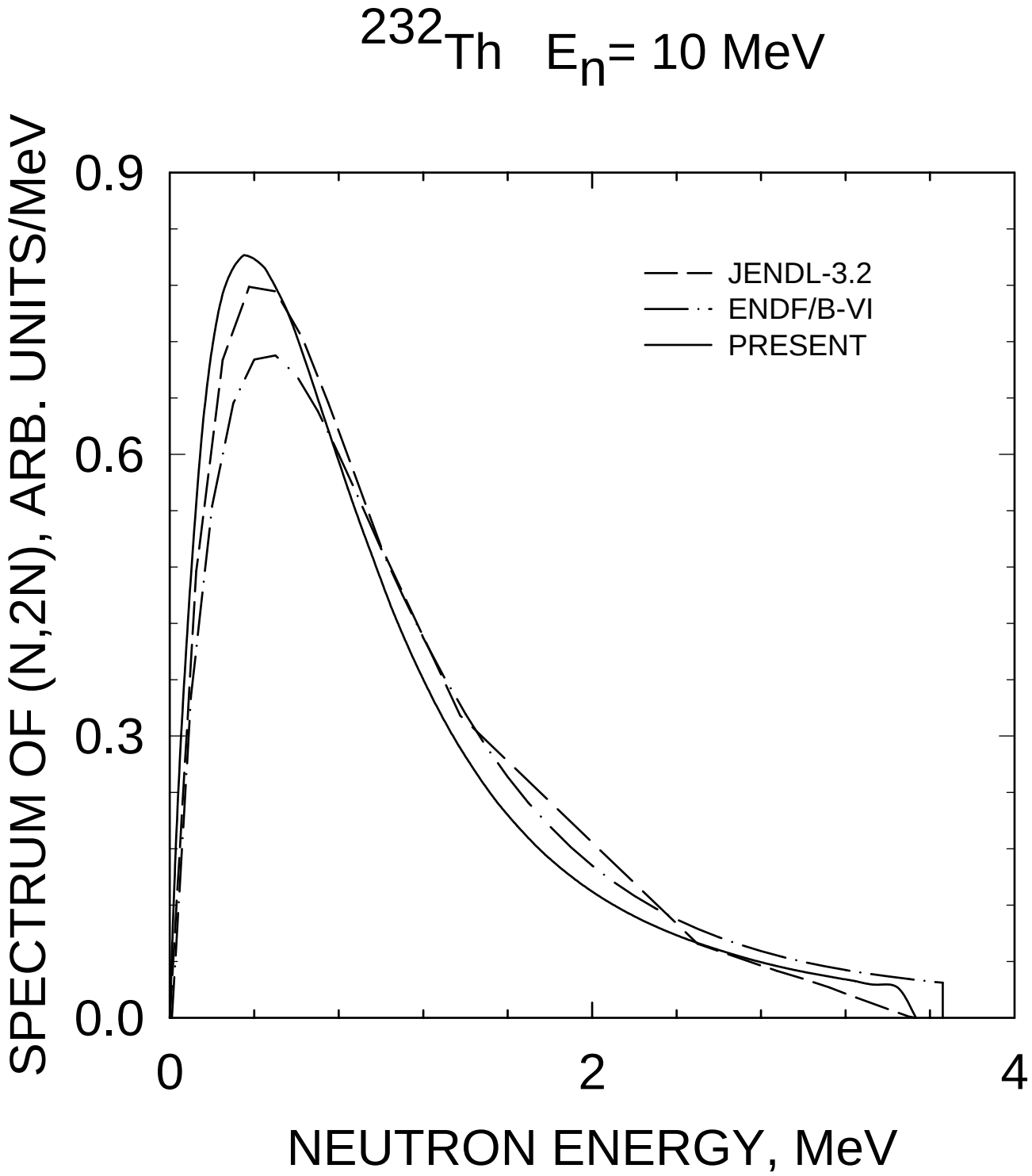
232Th En= 10 MeV
SPECTRUM OF (N,2N), ARB. UNITS/MeV
0.9
0.6
0.3
0.0
0
2
4
NEUTRON ENERGY, MeV
JENDL-3.2
ENDF/B-VI
PRESENT

FIG. 163

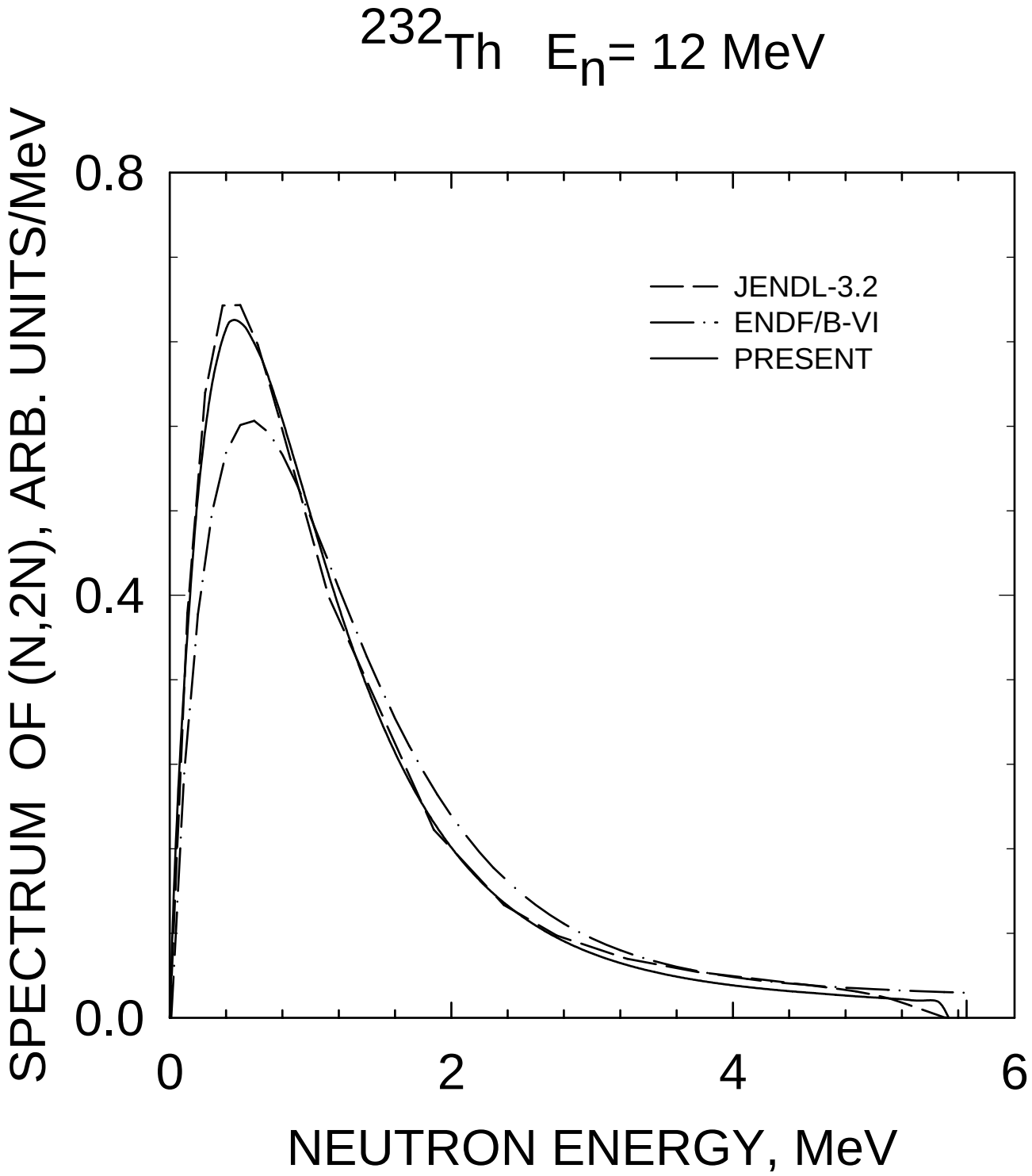
232Th En= 12 MeV
SPECTRUM OF (N,2N), ARB. UNITS/MeV
0.8
0.4
0.0
0
2
4
6
NEUTRON ENERGY, MeV
JENDL-3.2
ENDF/B-VI
PRESENT

FIG. 164

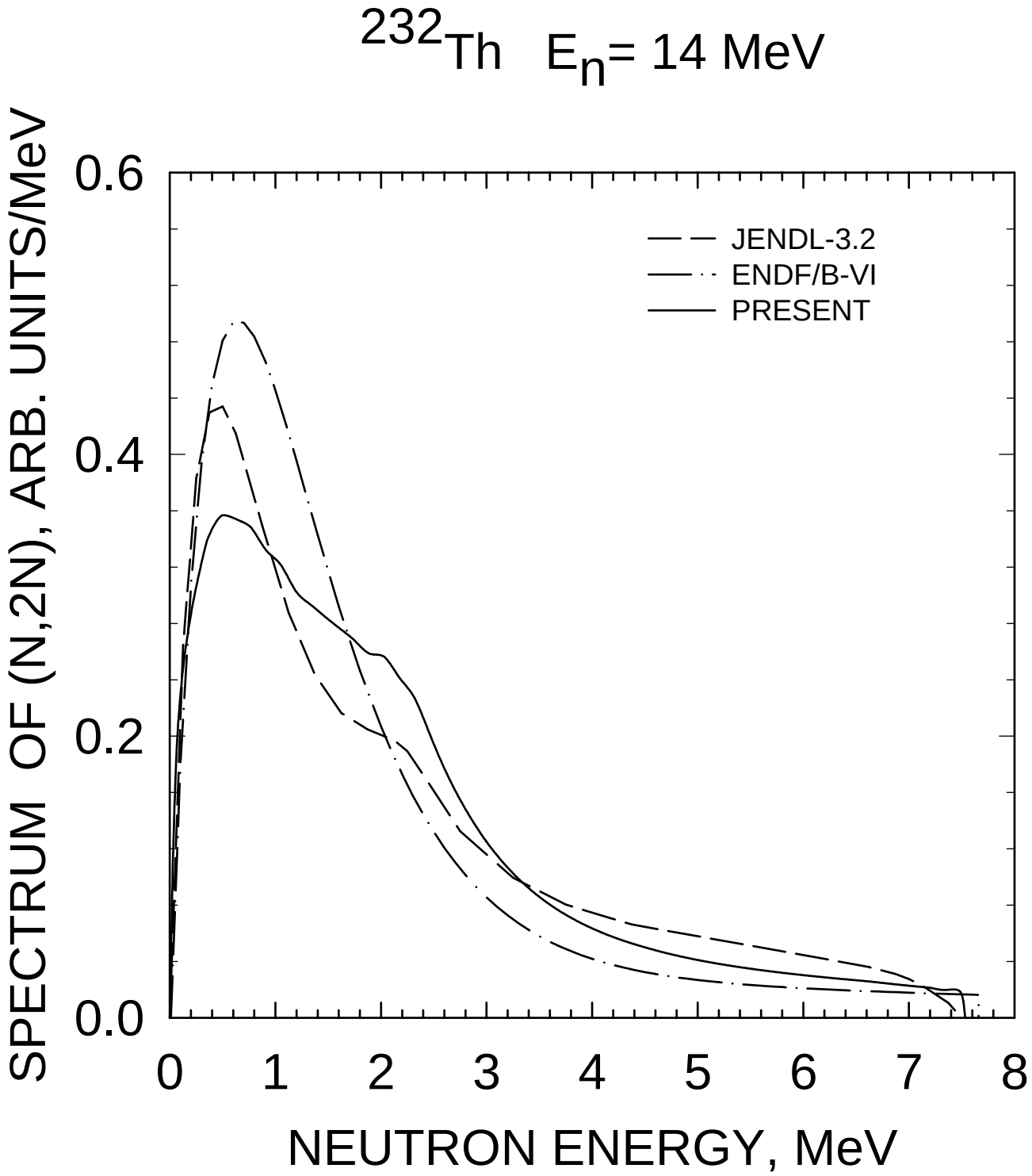
232Th En= 14 MeV
SPECTRUM OF (N,2N), ARB. UNITS/MeV
0.6
0.4
0.2
0.0
0
1
2
3
4
5
6
7
8
NEUTRON ENERGY, MeV
JENDL-3.2
ENDF/B-VI
PRESENT

FIG.165

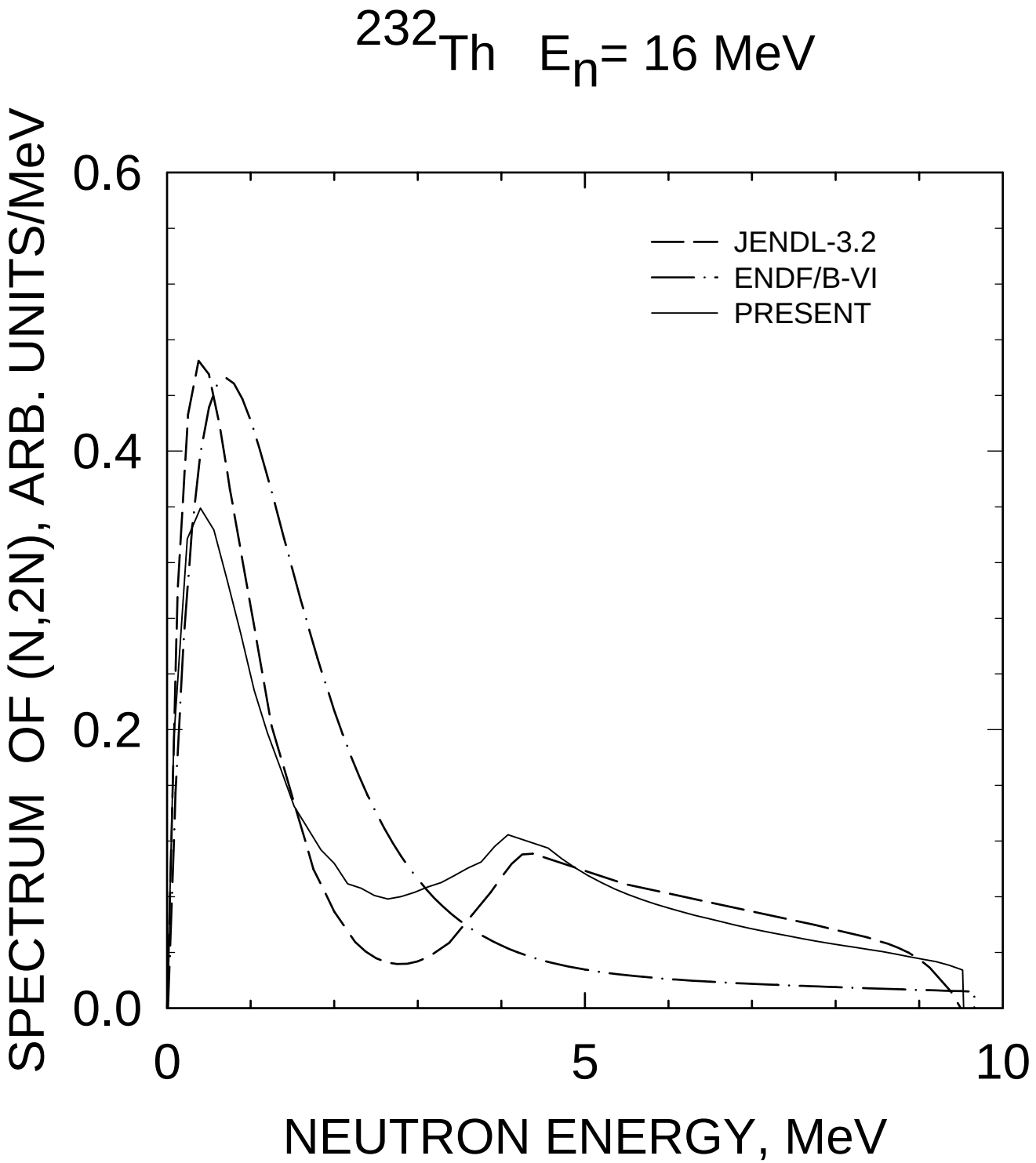
232Th En= 16 MeV
SPECTRUM OF (N,2N), ARB. UNITS/MeV
0.6
0.4
0.2
0.0
0
5
10
NEUTRON ENERGY, MeV
JENDL-3.2
ENDF/B-VI
PRESENT

FIG. 166

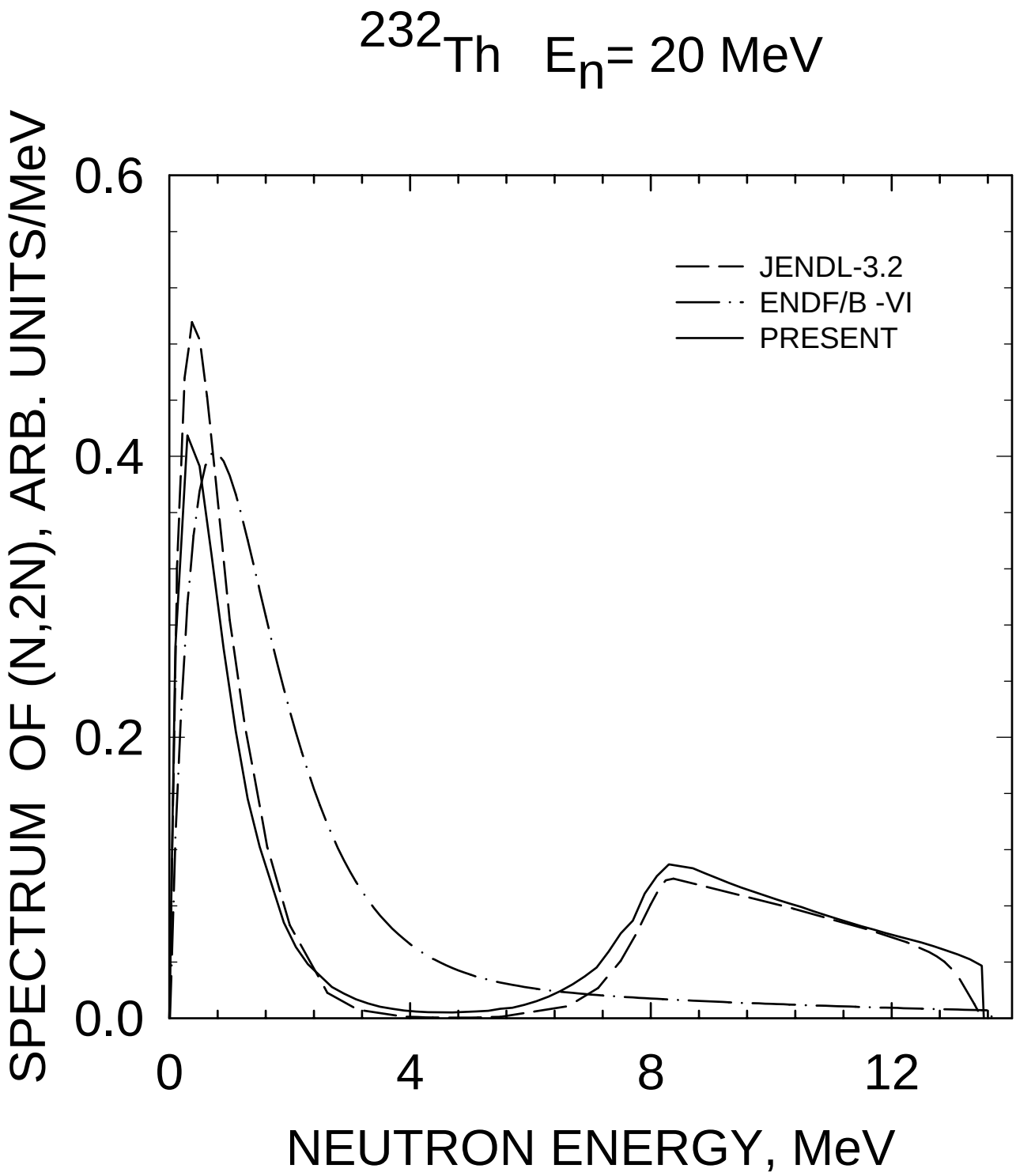
232Th En= 20 MeV
SPECTRUM OF (N,2N), ARB. UNITS/MeV
0.6
0.4
0.2
0.0
0
4
8
12
NEUTRON ENERGY, MeV
JENDL-3.2
ENDF/B -VI
PRESENT

FIG. 167

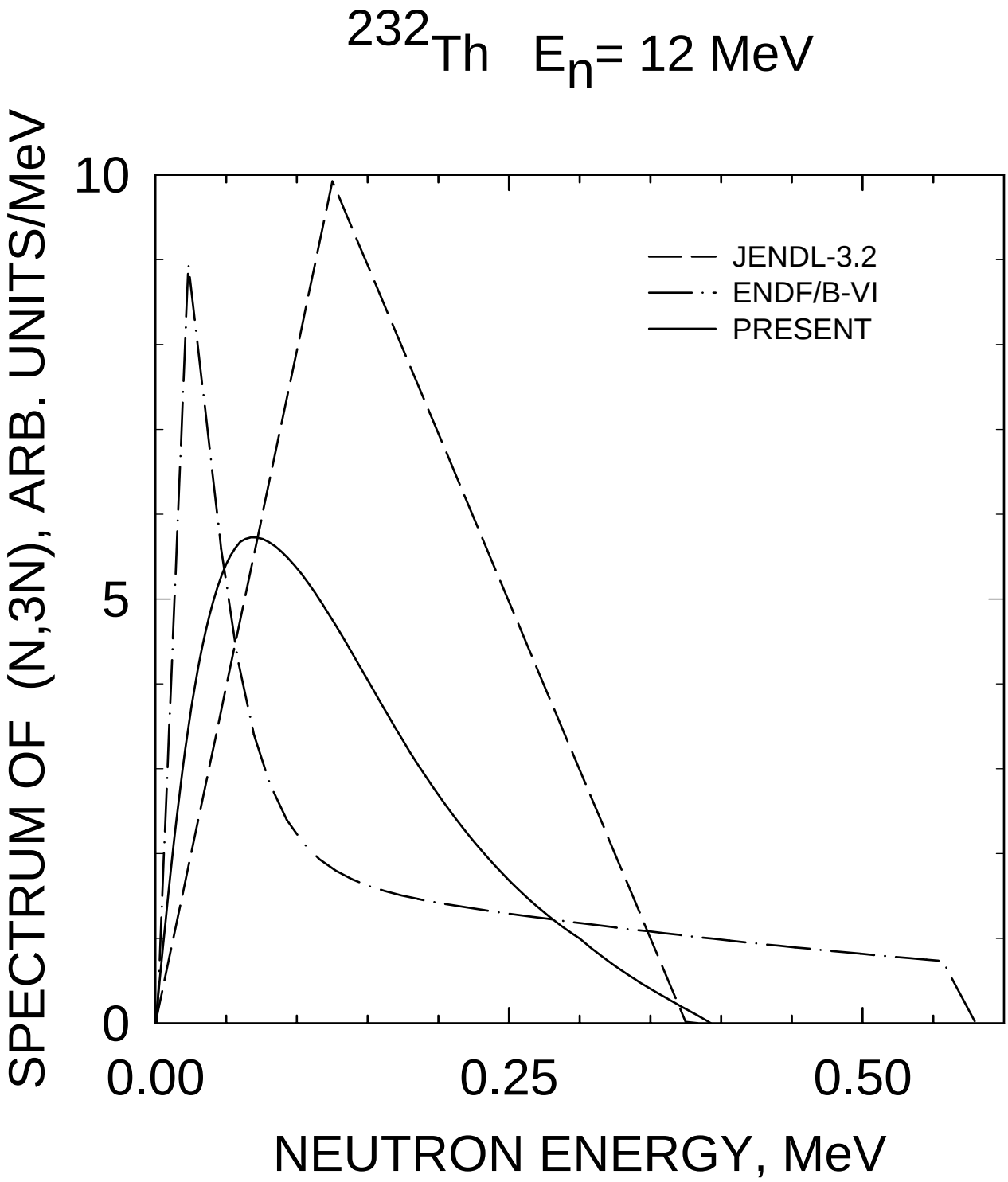
232Th En= 12 MeV
SPECTRUM OF (N,3N), ARB. UNITS/MeV
10
5
0
0.00
0.25
0.50
NEUTRON ENERGY, MeV
JENDL-3.2
ENDF/B-VI
PRESENT

FIG. 168

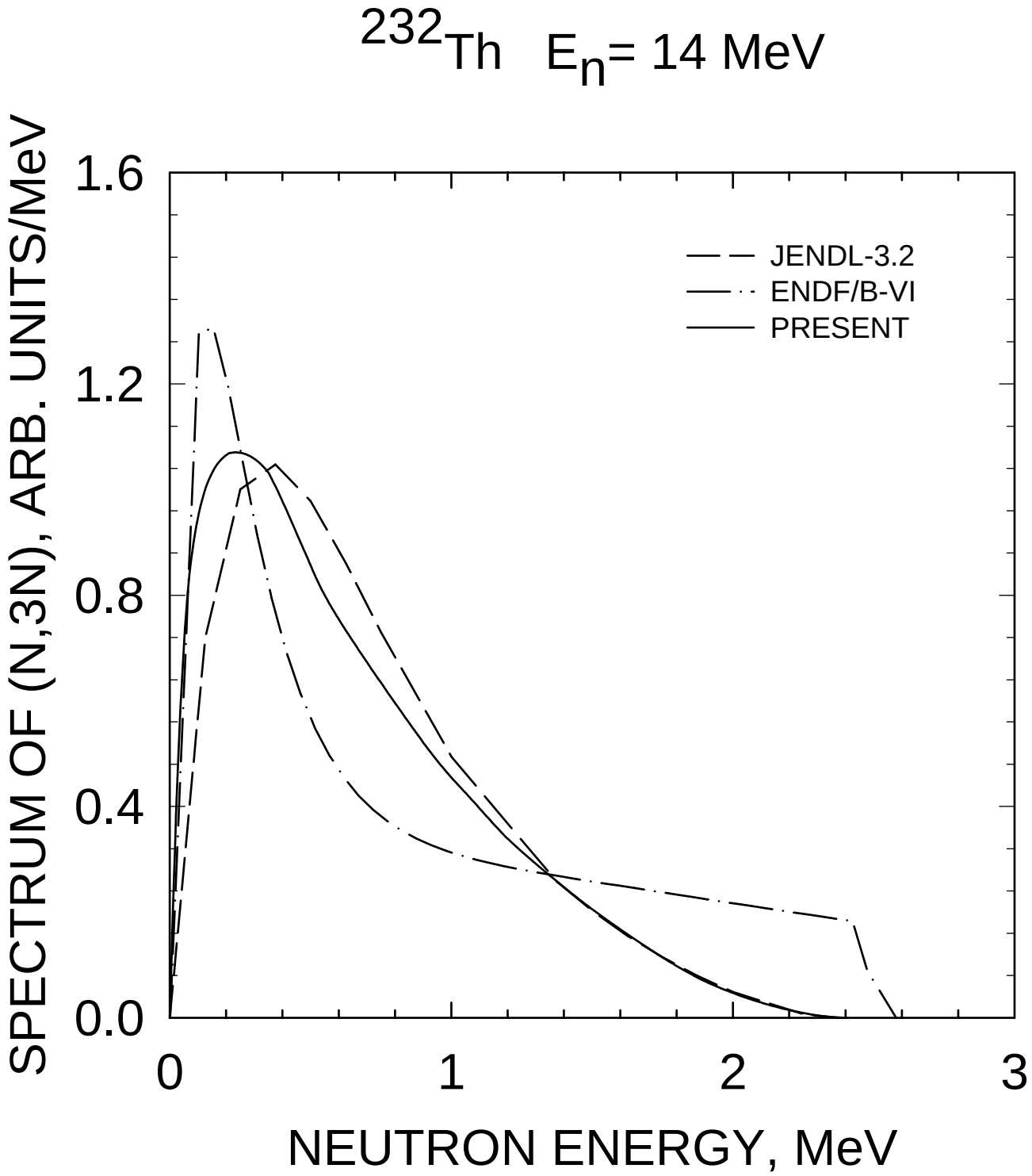
232Th En= 14 MeV
SPECTRUM OF (N,3N), ARB. UNITS/MeV
1.6
1.2
0.8
0.4
0.0
0
1
2
3
NEUTRON ENERGY, MeV
JENDL-3.2
ENDF/B-VI
PRESENT

FIG. 169

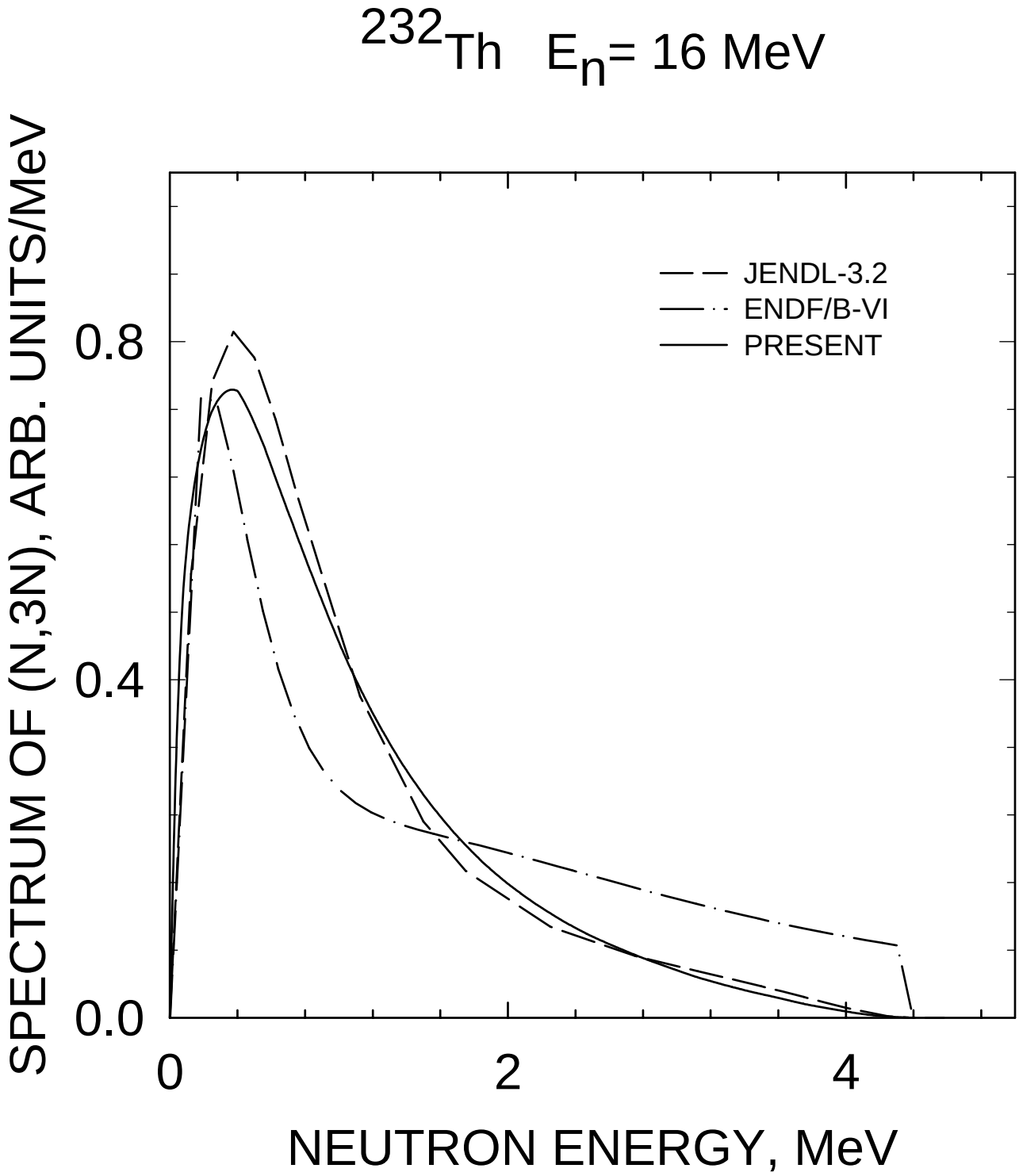
232Th En= 16 MeV
JENDL-3.2
ENDF/B-VI
PRESENT
SPECTRUM OF (N,3N), ARB. UNITS/MeV
0.0
0.4
0.8
0
2
4
NEUTRON ENERGY, MeV

FIG. 170

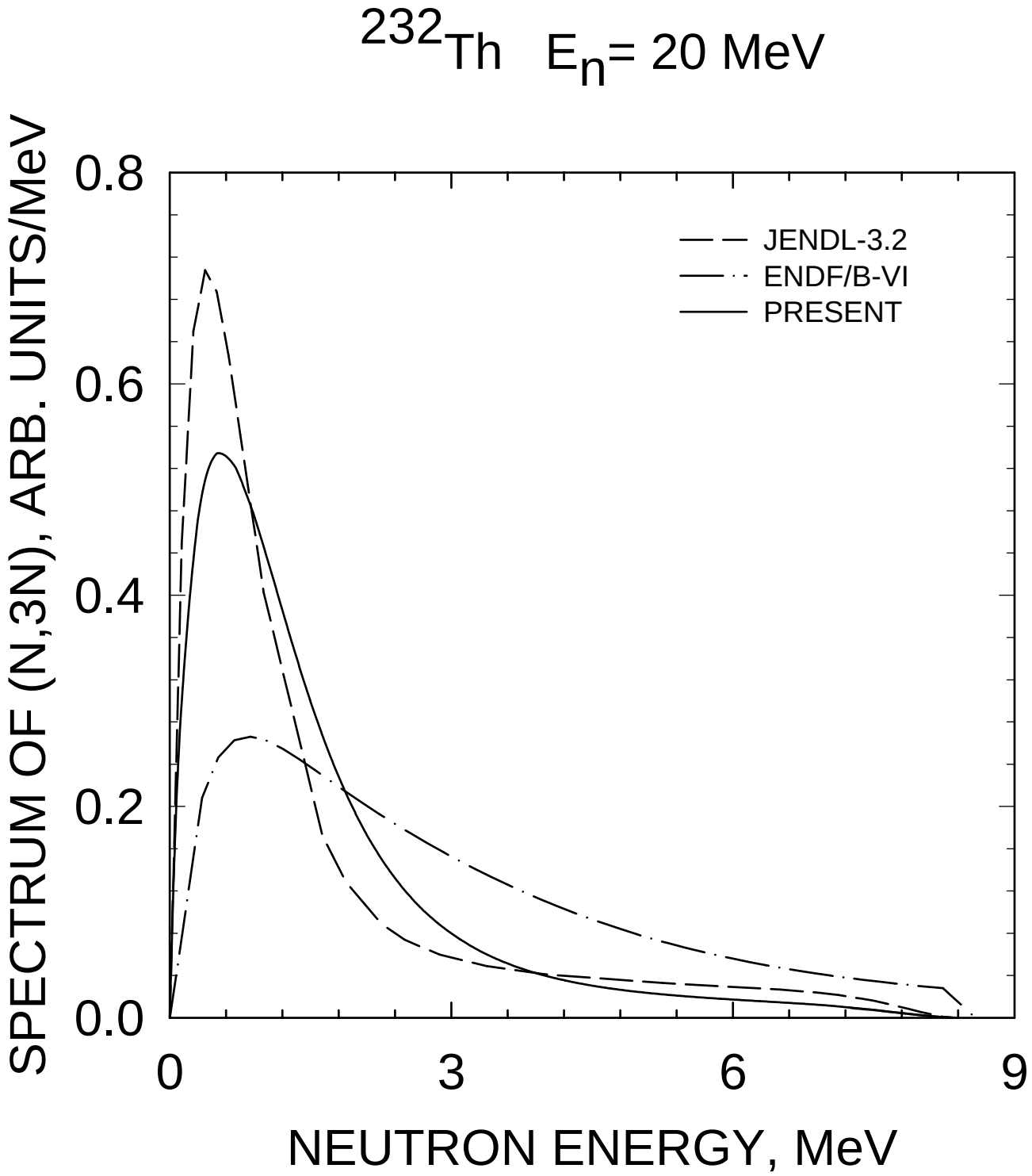
232Th En= 20 MeV
SPECTRUM OF (N,3N), ARB. UNITS/MeV
0.8
0.6
0.4
0.2
0.0
0
3
6
9
NEUTRON ENERGY, MeV
JENDL-3.2
ENDF/B-VI
PRESENT

FIG. 171

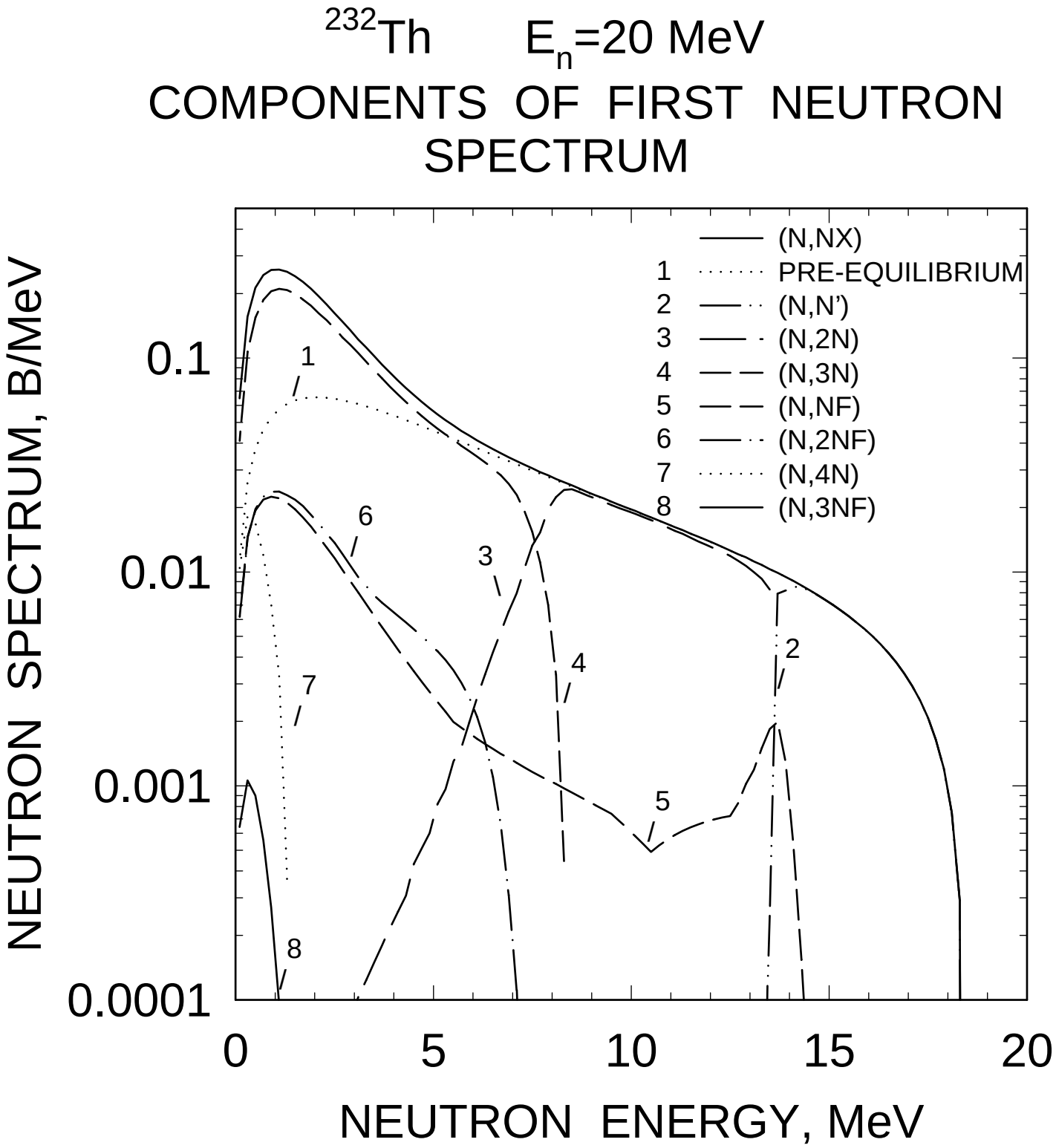
232Th En=20 MeV
COMPONENTS OF FIRST NEUTRON SPECTRUM
(N,NX)
1 PRE-EQUILIBRIUM
2 (N,N')
3 (N,2N)
4 (N,3N)
5 (N,NF)
6 (N,2NF)
7 (N,4N)
8 (N,3NF)
NEUTRON SPECTRUM, B/MeV
0.1
0.01
0.001
0.0001
0
5
10
15
20
NEUTRON ENERGY, MeV

FIG. 172

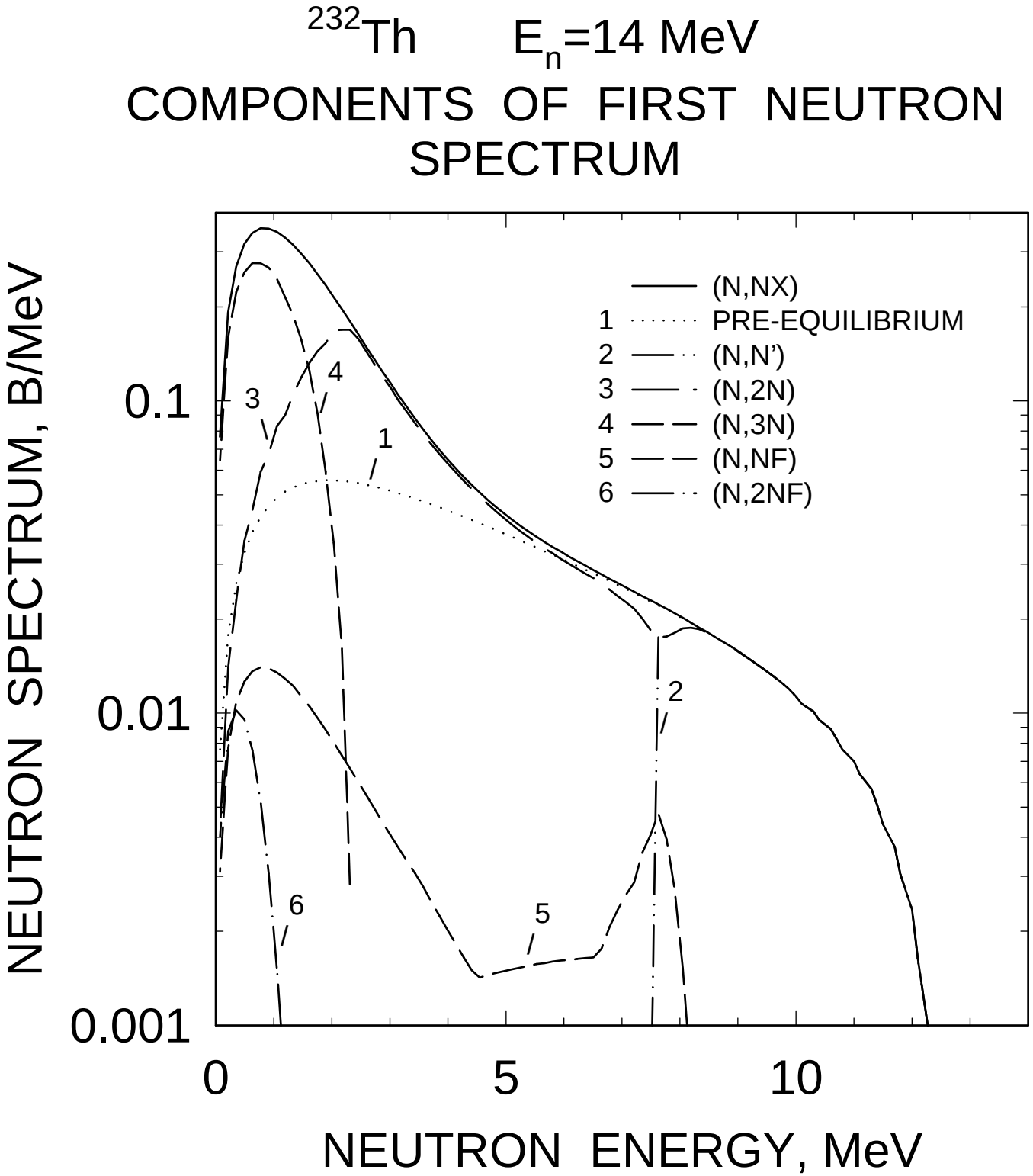
232Th En=14 MeV
COMPONENTS OF FIRST NEUTRON SPECTRUM
(N,NX)
1 PRE-EQUILIBRIUM
2 (N,N')
3 (N,2N)
4 (N,3N)
5 (N,NF)
6 (N,2NF)
NEUTRON SPECTRUM, B/MeV
0.1
0.01
0.001
0
5
10
NEUTRON ENERGY, MeV

FIG. 173

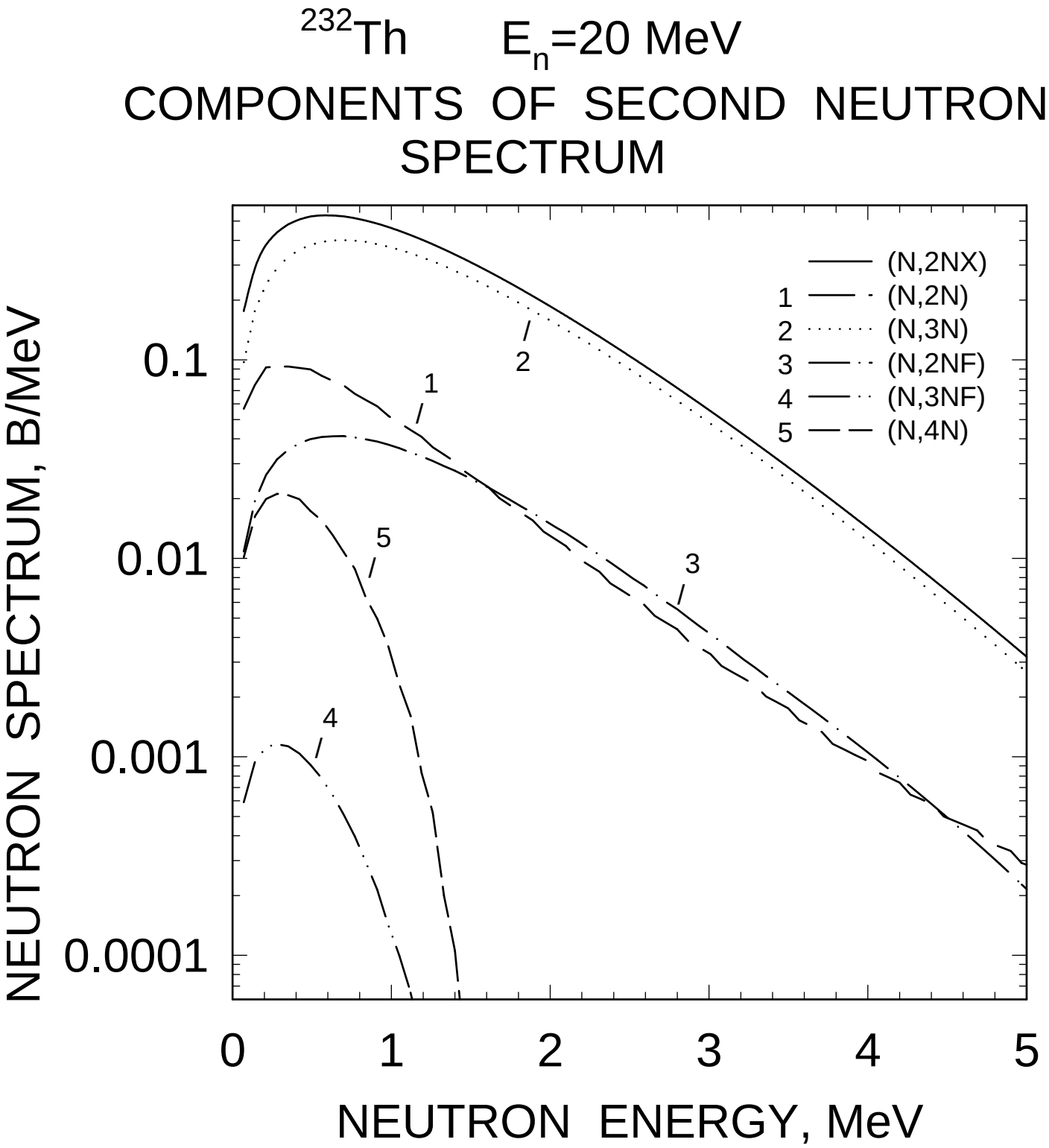
232Th En=20 MeV
COMPONENTS OF SECOND NEUTRON SPECTRUM
(N,2NX)
1 (N,2N)
2 (N,3N)
3 (N,2NF)
4 (N,3NF)
5 (N,4N)
0.1
0.01
0.001
0.0001
NEUTRON SPECTRUM, B/MeV
0
1
2
3
4
5
NEUTRON ENERGY, MeV

FIG. 174

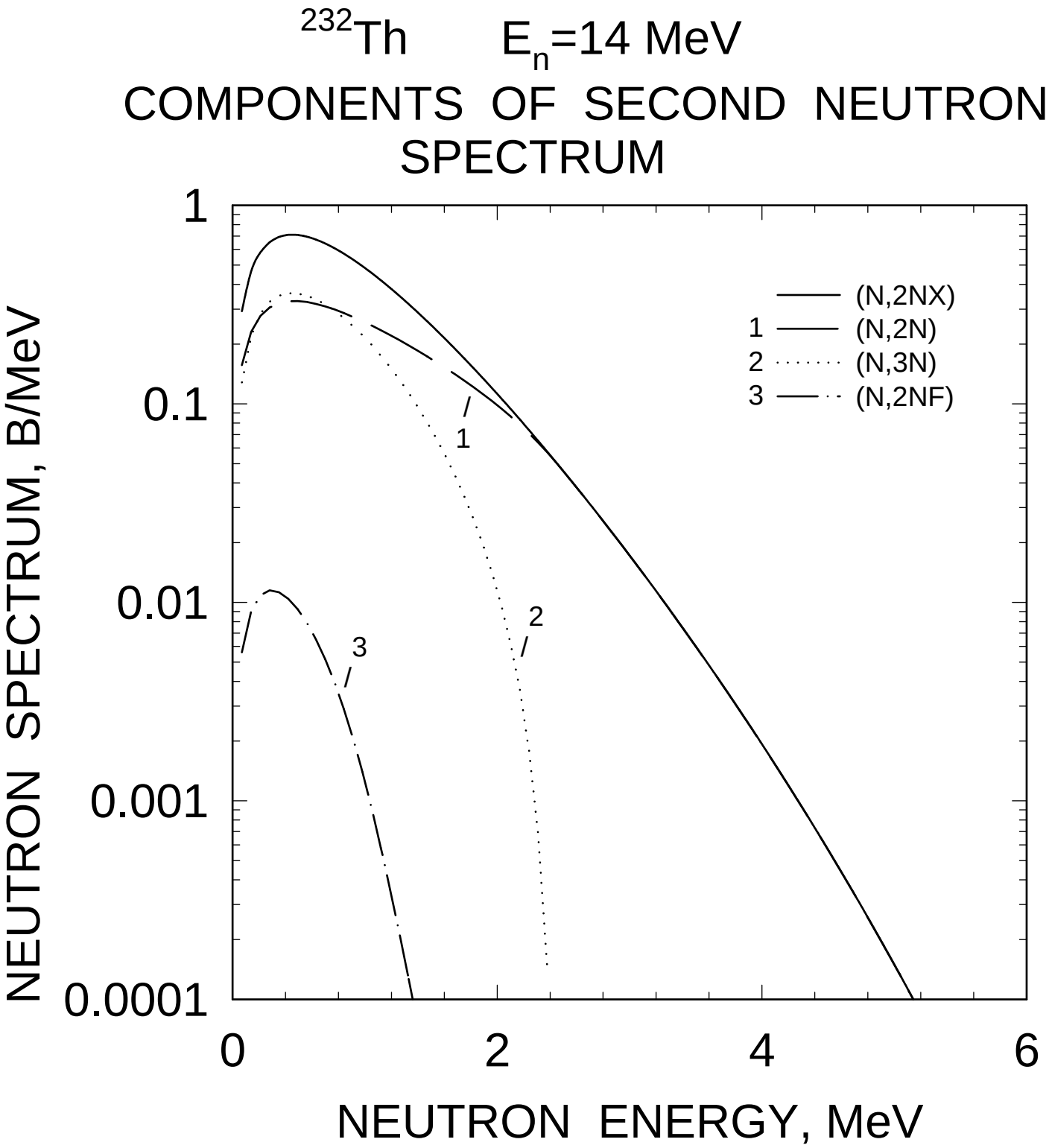
232Th En=14 MeV
COMPONENTS OF SECOND NEUTRON SPECTRUM
NEUTRON SPECTRUM, B/MeV
NEUTRON ENERGY, MeV
1
0.1
0.01
0.001
0.0001
0
2
4
6
(N,2NX)
1 (N,2N)
2 (N,3N)
3 (N,2NF)
1
2
3

FIG. 175

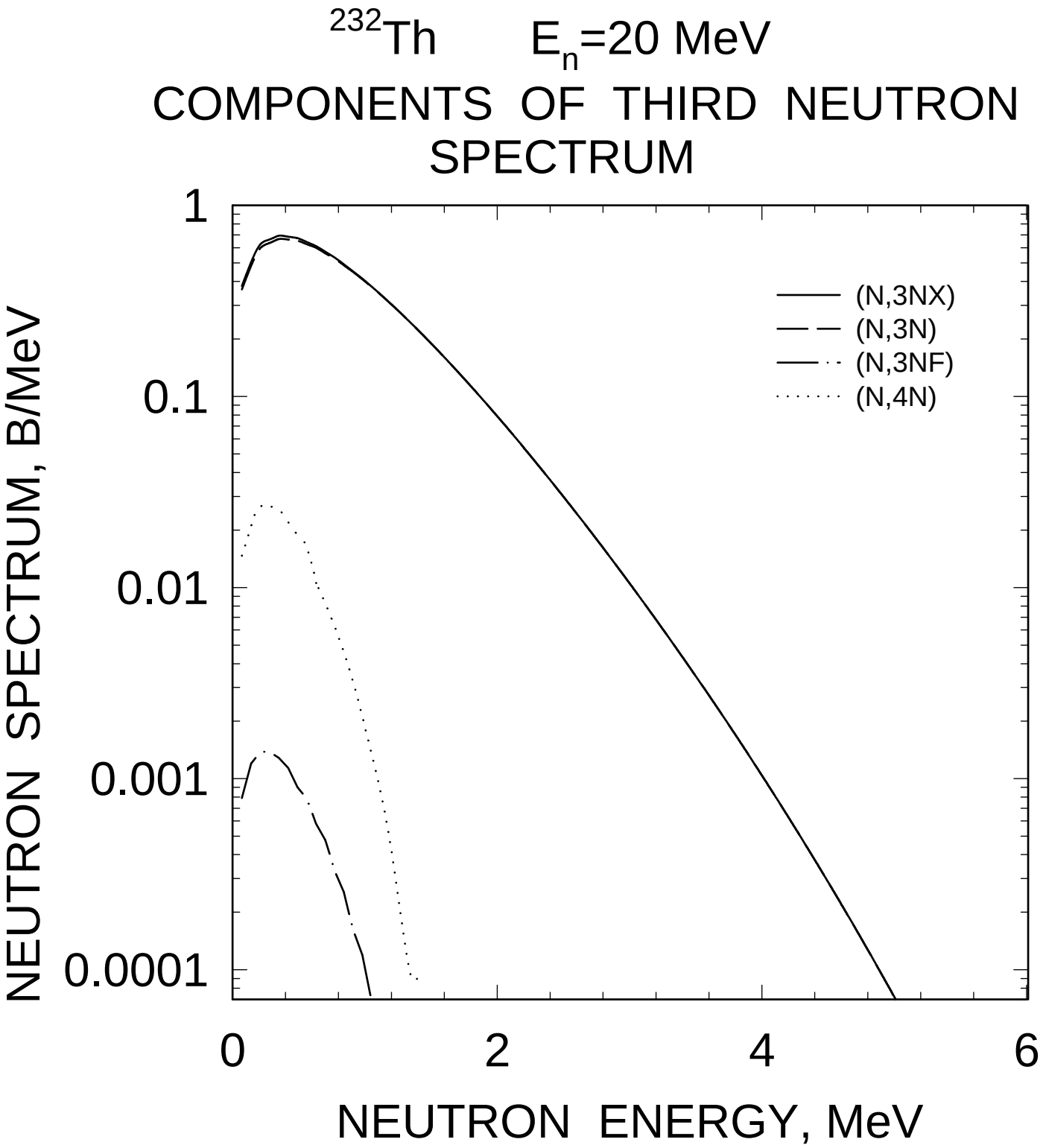
232Th En=20 MeV
COMPONENTS OF THIRD NEUTRON SPECTRUM
NEUTRON SPECTRUM, B/MeV
1
0.1
0.01
0.001
0.0001
0
2
4
6
NEUTRON ENERGY, MeV
(N,3NX)
(N,3N)
(N,3NF)
(N,4N)

FIG. 176

Nuclear Data Section
International Atomic Energy Agency
P.O. Box 100
A-1400 Vienna
Austria

e-mail: services@iaeand.iaea.org
fax: (43-1) 26007
cable: INATOM VIENNA
telex: 1-12645
telephone: (43-1) 2600-21710

Online: TELNET or FTP: iaeand.iaea.org
username: IAEANDS for interactive Nuclear Data Information System
usernames: ANONYMOUS for FTP file transfer;
FENDL2 for FTP file transfer of FENDL-2.0;
RIPL for FTP file transfer of RIPL;
NDSONL for FTP access to files saved in “NDIS” Telnet session.
Web: http://www-nds.iaea.org